

**THE IMPACT OF TROPICAL CYCLONES ON THE GEOMORPHIC
EVOLUTION OF BOLIVAR PENINSULA, TEXAS**

A Thesis

by

BILLY UTAH HALES, JR.

Submitted to the Office of Graduate Studies of
Texas A&M University
in partial fulfillment of the requirements for the degree of

MASTER OF SCIENCE

May 2012

Major Subject: Geography

The Impact of Tropical Cyclones on the Geomorphic Evolution of

Bolivar Peninsula, Texas

Copyright 2012 Billy Utah Hales, Jr.

**THE IMPACT OF TROPICAL CYCLONES ON THE GEOMORPHIC
EVOLUTION OF BOLIVAR PENINSULA, TEXAS**

A Thesis

by

BILLY UTAH HALES, JR.

Submitted to the Office of Graduate Studies of
Texas A&M University
in partial fulfillment of the requirements for the degree of

MASTER OF SCIENCE

Approved by:

Co-Chairs of Committee,	Douglas J. Sherman
	Hongxing Liu
Committee Member,	John Rick Giardino
Head of Department,	Vatche Tchakerian

May 2012

Major Subject: Geography

ABSTRACT

The Impact of Tropical Cyclones on the Geomorphic Evolution of Bolivar Peninsula,
Texas. (May 2012)

Billy Utah Hales, Jr., B.S., Texas A&M University - Kingsville

Co-Chairs of Advisory Committee: Dr. Douglas J. Sherman
Dr. Hongxing Liu

Annually, tropical cyclones do tremendous damage and are agents of long-term coastal change. To test this idea of different tropical cyclones delivering consistent coastal change, a landform with such evolution is needed. One such landform is a spit. What contributions do tropical cyclones give toward the evolution of a spit, and do tropical cyclones give the same kinds of impacts? To determine if tropical cyclones have similar impacts, shoreline and volumetric change from four storms impacting Bolivar Peninsula are considered. Being a southwest-trended spit at a length of 33.5 kilometers, storm impacts are measured in the form of one dimensional shoreline and two dimensional volumetric change. These impacts are abstracted into shoreline change and volumetric change patterns. These patterns are identified and compared for differences between each storm and similarity among all storms.

Results indicate that shoreline accretionary zones vary alongshore. Results from Hurricane Ike indicate an accretionary zone ten kilometers from the distal end. Shoreline change patterns for Hurricane Rita show an unstable accretionary zone at four kilometers from the distal end. Results for Tropical Storm Fay indicate an unstable accretionary

zone that begins at the distal end and continues to the middle of the spit. In terms of similarity for shoreline change, all patterns from storms demonstrated erosion near Rollover Fish Pass.

One dimensional volumetric change patterns were entirely erosive for Hurricanes Rita and Ike, and Tropical Storm Fay had by small zones of accretion near the distal portion of the spit. Tropical Storm Josephine demonstrated an accretion zone between the middle and distal portion of the spit. Results from two dimensional volumetric change patterns suggest a threshold for inland penetration. Tropical Storm Fay showed a ten to twenty meter wide pattern of erosion around five kilometers from the distal end and near the proximal end of the spit, and Hurricane Rita demonstrated a twenty meter wide pattern of erosion near the distal end. Hurricane Ike had erosive penetration of up to 200 meters around fifteen kilometers from the distal end. Results suggest that certain storms reinforce the standard spit growth model, and others work against it.

DEDICATION

It is my desire to dedicate this work to my parents—who have shown great patience and understanding during my scholastic career. It is my hope that the fruits of my work will eventually profit them and make their efforts worthwhile.

ACKNOWLEDGEMENTS

In terms of general academic life, I would first like to acknowledge Dr. Douglas J. Sherman and Dr. Hongxing Liu for their wisdom, patience, and overall support for me during this time in my life. Furthermore, I would like to acknowledge Dr. John “Rick” Giardino for his advice on handling the various pitfalls that one can fall into during graduate school—I fell into at least half of them! Thanks and best wishes for a good future are in order for another individual I’d like to acknowledge, Dr. Jaehyung Yu—who gave me much of my foundation in geomatics.

Furthermore, I’d like to acknowledge the help and technical expertise of Qiusheng Wu, Dr. Haibin Su, and Dr. Lei Wang. They were instrumental in helping me understand the many software tools that I used and contributed to. I’d also like to acknowledge Tiffany Hepner and John Anderson at the Bureau of Economic Geology for helping me solve several problems.

I thank and acknowledge the State of Texas Department of Higher Education for funding me for two years and giving me a fascinating research opportunity. I’d also like to acknowledge Dr. Mark Lorang, who gave me a chance to perform when no one had any real idea of my potential. Lastly, I’d like to acknowledge Dr. Thomas Lee McGehee, for giving me the intellectual and professional foundation upon which I’m building this work on.

TABLE OF CONTENTS

	Page
ABSTRACT	iii
DEDICATION	v
ACKNOWLEDGEMENTS	vi
TABLE OF CONTENTS	vii
LIST OF FIGURES.....	xi
LIST OF TABLES	xxii
 CHAPTER	
I INTRODUCTION.....	1
Research Purpose	1
Study Area.....	2
Objectives.....	2
II SPIT GEOMORPHOLOGY AND TROPICAL CYCLONE IMPACTS.....	4
Spits.....	4
Spit Geomorphology	4
Spit Evolution.....	6
Natural Processes	11
Anthropogenic Features and Resultant Processes	14
Tropical Cyclones	15
Tropical Storm Impacts	19
Tropical Storm Josephine.....	24
Tropical Storm Fay.....	27
Hurricane Rita	30
Hurricane Ike.....	33

CHAPTER	Page
III DATA AND METHODS.....	38
Data Availability	38
LiDAR Remote Sensing.....	38
Datasets	40
Shoreline Extraction Methods.....	43
Data Processing.....	43
LAS Data Preparation	43
LiDAR Co-Registration	44
Land/Water Object Segmentation	47
Noise Reduction	49
Morphology Operator.....	50
Spurious Object Removal.....	52
Boundary Tracing and Vectorization	52
Vector Shoreline Corrections	52
Level One Corrections	55
Level Two Corrections.....	56
Level Three Corrections.....	58
Level Four Corrections.....	61
Shoreline Change Analysis	62
Setting Up Polygon Constraints	64
Shoreline Segment Constraint.....	69
Linear Shoreline Change Analysis	72
Area Shoreline Change Analysis.....	73
Linear Shoreline Change Classification	74
Volumetric Change Analysis	76
Coastal Change Map	77
Spurious Object Removal.....	77
Morphological Operations.....	79
Object Identification.....	79
Vectorize Boundaries of Objects.....	80
Compute Volumetric Attributes	80
Manual Corrections of Morphological Patches.....	81
Identification of Proper Spacing	81
Semivariogram Analysis	82
Fractal Scaling Range Analysis.....	91
Shifting Window Analysis	96
Pattern Extraction.....	102
Linear Referencing for Pattern Extraction	102
Pattern Extraction from Previous Publications	103
Pattern Extraction from Shoreline Change.....	103

CHAPTER	Page
Pattern Extraction from Volumetric Change.....	105
Two-Dimensional Pattern Extraction.....	106
One-Dimensional Pattern Extraction	108
Pattern Change Analysis	109
IV ANALYSIS OF STORM IMPACT PATTERNS.....	110
Shoreline Change Patterns	110
Shoreline Change Pattern - Tropical Storm Fay	110
Shoreline Change Pattern - Hurricane Rita.....	112
Shoreline Change Pattern - Hurricane Ike.....	117
Volumetric Change Patterns.....	120
1D Volumetric Change Patterns.....	120
2D Volumetric Change Patterns.....	121
1D Volume Change Patterns – Tropical Storm Josephine	123
1D Volume Change Patterns – Tropical Storm Fay.....	126
2D Volume Change Patterns – Tropical Storm Fay.....	126
1D Volume Change Patterns – Hurricanes Ike and Rita.....	135
2D Volume Change Patterns – Hurricane Rita	135
2D Volume Change Patterns – Hurricane Ike	146
Shoreline Change Pattern Comparisons.....	155
Pattern Comparison – Tropical Storm Fay to Hurricane Rita	155
Pattern Comparison – Tropical Storm Fay to Hurricane Ike	155
Pattern Comparison – Hurricane Rita to Hurricane Ike	158
Pattern Comparison – All Storms.....	158
Volume Change Pattern Comparisons	161
1D Comparison - T.S. Josephine to T.S. Fay	161
1D Comparison – T.S. Josephine to H. Ike and H. Rita.....	164
1D Comparison – T.S. Fay to H. Ike and H. Rita	168
2D Comparison – T.S. Fay to H. Rita	168
2D Comparison – T.S. Fay to H. Ike.....	180
1D Comparison – Hurricane Rita to Hurricane Ike.....	188
2D Comparison – Hurricane Rita to Hurricane Ike.....	188
2D Pattern Similarity – All Storms	196
Impacts Derived From 2D Volumetric Change Patterns.....	203
V DISCUSSION	204
Shoreline Change Patterns	204
Volumetric Change Patterns.....	208
Synthesis.....	217

CHAPTER	Page
VI SUMMARY AND CONCLUSIONS.....	221
Summary	221
Conclusions	223
Future Work	227
LITERATURE CITED	228
APPENDIX A	236
APPENDIX B	264
APPENDIX C	269
APPENDIX D	285
APPENDIX E.....	370
VITA	379

LIST OF FIGURES

		Page
Figure 1.1	Location map of study area – Bolivar Peninsula.....	3
Figure 2.1	Catastrophic erosion at Rollover Fish Pass shortly after opening.	7
Figure 2.2	Beach aggradation since jetty construction 1856-2010.....	8
Figure 2.3	Outline of rotational instability.	10
Figure 2.4	Time-steps through one-dimensional model showing the evolution of a flying spit through a response to wave-angle climate.	12
Figure 2.5	Graph demonstrating typical proximity of highest wind speed with respect to distance from the eye of the storm and this relationship to the tropical storm intensity.	17
Figure 2.6	Two different representations of wind speed distribution from models that contrast different wind speeds at different sides of the hurricane relative to the direction of motion.....	18
Figure 2.7	Illustration of variables D_{high}/D_{low} and R_{high}/R_{low} for the storm impact model.	21
Figure 2.8	Four different regimes of coastal impact from tropical cyclones, illustrated.	22
Figure 2.9	BEST storm track of Tropical Storm Josephine.....	25
Figure 2.10	Wind speeds and directions within a 12 hour window around the closest location to Tropical Storm Josephine.	26
Figure 2.11	BEST storm track of Tropical Storm Fay.	28

	Page
Figure 2.12	Wind/wave speeds and directions within a 12 hour window around the closest location to Tropical Storm Fay..... 29
Figure 2.13	BEST storm track of Hurricane Rita 31
Figure 2.14	Wind speeds and directions within a 12 hour window at the study area..... 32
Figure 2.15	BEST storm track of Hurricane Ike..... 34
Figure 2.16	Wind speeds and directions within a 12 hour window around the landfall of Hurricane Ike 35
Figure 2.17	Interpolated inundation map that occurred as a result of the incipient Hurricane Ike storm surge. 37
Figure 3.1	Depiction of the multiple returns depicted in LiDAR data. 41
Figure 3.2	Point spacing and layout of original LiDAR point data on top of the IDW interpolated imagery derived from the July 2006 dataset..... 41
Figure 3.3	Scene from FP_SE quadrangle from post-Rita dataset. 46
Figure 3.4	Alpha portion (tail) of a normal distribution. 46
Figure 3.5	Initial results of the object oriented land-water image segmentation..... 49
Figure 3.6	Before (top) and after (bottom) captions of the smoothing effect that the morphology operator has on a shoreline. 51
Figure 3.7	Before (top) and after (bottom) captions depicting the removal of spurious objects. 53
Figure 3.8	Raster polylines before vectorization. 54

	Page
Figure 3.9	Figure from Price (2006) that shows how a line is defined by two nodes and vertices that bound it. 56
Figure 3.10	An example of the ‘loop’ structure found in vector shorelines that result from level two corrections. 57
Figure 3.11	Examples of dangle topological errors that are commonly encountered during level two corrections. 59
Figure 3.12	An example of using the ‘Modify Feature’ tool and the ‘Sketch Properties’ window in ArcGIS Desktop to find topological errors. 60
Figure 3.13	Before and after the PAEK smoothing algorithm on a shoreline after Level 4 corrections image in the background is 1999 NASA LiDAR imagery. 63
Figure 3.14	Illustration of dynamic segmentation as compared to the traditional arc-node model of other linear features. 65
Figure 3.15	An illustration of the dynamic segmentation process for Hurricane Ike shoreline change. 67
Figure 3.16	Correct orientation for both base and target shorelines (left), and incorrect orientation for both base and target shoreline (right). 68
Figure 3.17	Generated linear shoreline change polylines between pre-Ike and post-Ike shorelines. 70
Figure 3.18	Classified linear shoreline change. 75
Figure 3.19	Hurricane Ike coastal change map with blue being accretion, red being erosion, and transparent being no change beyond error. 78
Figure 3.20	Semivariogram generated from raw shoreline change data from Hurricanes Ike, Rita, and Tropical Storm Fay. 83

	Page
Figure 3.21 Semivariogram representing the 30 point running median residual from shoreline change data of Hurricanes Ike, Rita, and Tropical Storm Fay.....	84
Figure 3.22 Semivariogram representing the 100 point running median residual from shoreline change data of Hurricanes Ike, Rita, and Tropical Storm Fay.....	85
Figure 3.23 Semivariogram representing the 200 point running median residual from shoreline change data of Hurricanes Ike, Rita, and Tropical Storm Fay.....	86
Figure 3.24 Trended semivariograms that have been transformed in a manner similar to that of Dolan, Fenster, and Holme (1992).	90
Figure 3.25 Fractal analysis for Hurricane Ike	92
Figure 3.26 Fractal analysis for Hurricane Rita.....	93
Figure 3.27 Fractal analysis for Tropical Storm Fay.....	94
Figure 3.28 Results of shoreline change derived from shifting window analysis of shoreline impacts from Tropical Storm Fay.	97
Figure 3.29 Results of shoreline change derived from shifting window analysis of shoreline impacts from Tropical Storm Fay.	98
Figure 3.30 Spatially sensitive alongshore locations, as identified by shifting window analysis.	99
Figure 3.31 Results of shoreline change derived from the shifting window analysis of shoreline impacts from Hurricane Ike.	100
Figure 3.32 Pattern representation extracted from Figure 11 in Gibeaut et al. (2002).	104

	Page
Figure 3.33	With points, it is possible to do summary statistics and counts in order to establish a pattern for tropical storm response and long term change. 107
Figure 4.1	Pattern of shoreline erosion and accretion as a result of Tropical Storm Fay. 111
Figure 4.2	Detrended shoreline impacts from Tropical Storm Fay. 113
Figure 4.3	Pattern of shoreline erosion and accretion as a result of Hurricane Rita. 115
Figure 4.4	Detrended shoreline impacts from Hurricane Rita. 116
Figure 4.5	Pattern of shoreline erosion and accretion as a result of Hurricane Ike. 118
Figure 4.6	Detrended shoreline impacts from Hurricane Ike. 119
Figure 4.7	Instruction map that illustrates how to interpret 2D volumetric patterns. 122
Figure 4.8	1D alongshore volumetric pattern generated by Tropical Storm Josephine. 124
Figure 4.9	Detrended volumetric change for Tropical Storm Josephine, as derived from estimates from Gibeaut et al. (2002). 125
Figure 4.10	1D alongshore volumetric pattern generated by Tropical Storm Fay. 127
Figure 4.11	Detrended volumetric change for Tropical Storm Fay, as derived from values obtained by Coastal Morphology Analyst and then derived as discussed in Chapter 3. 128
Figure 4.12	Sections A-D of 2D volumetric change patterns – Tropical Storm Fay. 129

	Page
Figure 4.13	Sections D-G of 2D volumetric change patterns – Tropical Storm Fay. 130
Figure 4.14	Sections G-J of 2D volumetric change patterns – Tropical Storm Fay. 131
Figure 4.15	Sections J-M of 2D volumetric change patterns – Tropical Storm Fay. 132
Figure 4.16	Sections M-P of 2D volumetric change patterns – Tropical Storm Fay. 133
Figure 4.17	Sections P-S of 2D volumetric change patterns – Tropical Storm Fay. 134
Figure 4.18	Human developments that have occurred between the pre and post-Rita LiDAR imagery. 136
Figure 4.19	Localized areas of overwash from Hurricane Rita. 137
Figure 4.20	Sections A-D of 2D volumetric change patterns – Hurricane Rita. 138
Figure 4.21	Sections D-G of 2D volumetric change patterns – Hurricane Rita. 139
Figure 4.22	Sections G-J of 2D volumetric change patterns – Hurricane Rita. 140
Figure 4.23	Sections J-M of 2D volumetric change patterns – Hurricane Rita. 141
Figure 4.24	Sections M-P of 2D volumetric change patterns – Hurricane Rita. 142
Figure 4.25	Sections P-S of 2D volumetric change patterns – Hurricane Rita. 143

	Page
Figure 4.26	Human developments that have occurred between the pre and post-Rita LiDAR imagery. 144
Figure 4.27	Localized areas of overwash from Hurricane Rita 145
Figure 4.28	Detrended volumetric change from Hurricane Ike, as derived from values obtained by Coastal Morphology Analyst and then derived as discussed in Chapter 3. 147
Figure 4.29	1D alongshore volumetric pattern – Hurricane Ike 148
Figure 4.30	Sections A-D of 2D volumetric change patterns – Hurricane Ike 149
Figure 4.31	Sections D-F of 2D volumetric change patterns – Hurricane Ike 150
Figure 4.32	Sections G-J of 2D volumetric change patterns – Hurricane Ike 151
Figure 4.33	Sections J-M of 2D volumetric change patterns – Hurricane Ike 152
Figure 4.34	Sections M-P of 2D volumetric change patterns – Hurricane Ike 153
Figure 4.35	Sections P-S of 2D volumetric change patterns – Hurricane Ike 154
Figure 4.36	Alongshore shoreline change pattern comparison – Tropical Storm Fay to Hurricane Rita. 156
Figure 4.37	Alongshore shoreline change pattern comparison – Tropical Storm Fay to Hurricane Ike 157
Figure 4.38	Alongshore shoreline change pattern comparison – Tropical Storm Fay to Hurricane Ike 159

	Page
Figure 4.39 Alongshore shoreline change pattern comparison – all storms.	160
Figure 4.40 Alongshore volume change pattern comparison – Tropical Storm Josephine to Tropical Storm Fay.	162
Figure 4.41 Comparison of detrended alongshore impacts from Tropical Storms Josephine and Fay.	163
Figure 4.42 Alongshore volume change pattern comparison – Tropical Storm Josephine to Hurricanes Rita and Ike.	165
Figure 4.43 Comparison of detrended alongshore impacts from Tropical Storm Josephine and Hurricane Rita.	166
Figure 4.44 Comparison of detrended alongshore impacts from Tropical Storm Josephine and Hurricane Ike.	167
Figure 4.45 Alongshore volume change pattern comparison – Tropical Storm Fay to Hurricanes Rita and Ike.	169
Figure 4.46 Comparison of detrended alongshore impacts from Tropical Storm Fay and Hurricane Rita.	170
Figure 4.47 Comparison of detrended alongshore impacts from Tropical Storm Fay and Hurricane Ike.	171
Figure 4.48 Sections A-D of 2D volumetric change pattern comparison – Tropical Storm Fay to Hurricane Rita.	174
Figure 4.49 Sections D-G of 2D volumetric change pattern comparison – Tropical Storm Fay to Hurricane Rita.	175
Figure 4.50 Sections G-J of 2D volumetric change pattern comparison – Tropical Storm Fay to Hurricane Rita.	176
Figure 4.51 Sections J-M of 2D volumetric change pattern comparison – Tropical Storm Fay to Hurricane Rita.	177

	Page
Figure 4.52	Sections M-P of 2D volumetric change pattern comparison – Tropical Storm Fay to Hurricane Rita. 178
Figure 4.53	Sections P-S of 2D volumetric change pattern comparison – Tropical Storm Fay to Hurricane Rita. 179
Figure 4.54	Sections A-D of 2D volumetric change pattern comparison – Tropical Storm Fay to Hurricane Ike. 181
Figure 4.55	Sections D-G of 2D volumetric change pattern comparison – Tropical Storm Fay to Hurricane Ike. 182
Figure 4.56	Sections G-J of 2D volumetric change pattern comparison – Tropical Storm Fay to Hurricane Ike. 183
Figure 4.57	Sections J-M of 2D volumetric change pattern comparison – Tropical Storm Fay to Hurricane Ike. 184
Figure 4.58	Sections M-P of 2D volumetric change pattern comparison – Tropical Storm Fay to Hurricane Ike. 186
Figure 4.59	Sections P-S of 2D volumetric change pattern comparison – Tropical Storm Fay to Hurricane Ike. 187
Figure 4.60	Comparison of detrended alongshore impacts from Hurricanes Ike and Rita. 189
Figure 4.61	Sections A-D of 2D volumetric change pattern comparison – Hurricane Rita to Hurricane Ike. 190
Figure 4.62	Sections D-G of 2D volumetric change pattern comparison – Hurricane Rita to Hurricane Ike. 191
Figure 4.63	Sections G-J of 2D volumetric change pattern comparison – Hurricane Rita to Hurricane Ike. 192
Figure 4.64	Sections J-M of 2D volumetric change pattern comparison – Hurricane Rita to Hurricane Ike. 193
Figure 4.65	Sections M-P of 2D volumetric change pattern comparison – Hurricane Rita to Hurricane Ike. 194

	Page
Figure 4.66	Sections P-S of 2D volumetric change pattern comparison – Hurricane Rita to Hurricane Ike. 195
Figure 4.67	Sections A-D of 2D volumetric change pattern comparison – all storms. 197
Figure 4.68	Sections D-G of 2D volumetric change pattern comparison – all storms. 198
Figure 4.69	Sections G-J of 2D volumetric change pattern comparison – all storms. 199
Figure 4.70	Sections J-M of 2D volumetric change pattern comparison – all storms. 200
Figure 4.71	Sections M-P of 2D volumetric change pattern comparison – all storms. 201
Figure 4.72	Sections P-S of 2D volumetric change pattern comparison – all storms. 202
Figure 5.1	Alongshore shoreline erosion from Tropical Storm Fay and Hurricanes Ike and Rita. 205
Figure 5.2	Caption of alongshore trends in volumetric change from Tropical Storm Josephine compared to long-term shoreline change. 206
Figure 5.3	Details of how a stream outlet changes in shape and how the shoreline accretes as a result of Tropical Storm Fay and erodes from Hurricane Rita. 210
Figure 5.4	Three images of before Tropical Storm Fay, after Tropical Storm Fay, and after Hurricane Ike to demonstrate that stream outlets are highly dynamic environments. 211
Figure 5.5.	Details of how damages on the geotube from Tropical Storm Fay and Hurricane Rita caused a back-scarping and even scour patterns from Hurricane Rita. 212

	Page
Figure 5.6. Detail of extreme beach change as a result of Hurricane Ike.....	214
Figure 5.7 All alongshore trends from 1D volumetric change analysis.	215

LIST OF TABLES

	Page
Table 2.1. Configuration of storms included in this study.	36
Table 3.1. Table of storm events, data availability, and what analyses are performed to establish patterns for these events.	39
Table 3.2. LiDAR data format and sources.....	42
Table 3.3. Ranges obtained from semivariogram analyses.	91
Table 3.4. Total 500 meter pattern bins that change character during the shifting window analysis.	102
Table 4.1. Values of erosion and accretion extracted from 2D volumetric patterns of Hurricanes Ike and Rita and Tropical Storm Fay.	203

CHAPTER I

INTRODUCTION

Research Purpose

Tropical cyclones are agents of coastal change in the Northern Gulf of Mexico (Doran *et al.*, 2009; Gibeaut, Gutierrez, and Hepner, 2002; McBride, Byrnes and Hiland, 1995). Shorelines are often used to measure the geomorphic change that has been brought by these storms (Gutierrez *et al.*, 2001; Gibeaut, Gutierrez, and Hepner, 2002; McBride, Byrnes and Hiland, 1995). Within the last ten years, Light Detection and Ranging (LiDAR) technology has been utilized to measure coastal change caused by the impacts of tropical and extra-tropical cyclones on coastal barriers (Sallenger *et al.*, 2001; Sallenger *et al.*, 2003; Doran *et al.*, 2009). Spits, peninsular coastal features that protrude from the mainland as a tail of sediment, have a predictable evolution based on wave climate (Ashton, Murray, and Littlewood, 2007; Gibeaut, Gutierrez, and Hepner, 2002; King and McCullagh, 1971), which is a summary of wave conditions that typically consists of wave period, height averaged and sorted by direction (Davidson-Arnott, 2010). The purpose of this study is to establish the role of environmental factors and tropical cyclones in the geomorphology of a coastal barrier through pattern analysis of the impacts of these storms with utilization of pre and post-storm LiDAR data and past analyses like that of Gibeaut, Gutierrez, and Hepner (2002).

Study Area

This study of patterns, coastal change, and coastal storms focuses on the beach face of Bolivar Peninsula (Figure 1.1). Roughly 33.5 kilometers long, Bolivar Peninsula is a low-lying spit with very low offshore gradient (Shepard, 1960). Pointing southwest off of High Island, this fine sand spit is in an environment that is microtidal and wave-dominated (LeBlanc and Hodgson, 1959; Gibeaut, Gutierrez, and Hepner, 2002). Because of its antecedent geomorphology, Bolivar Peninsula is relatively vulnerable to the impact of coastal storms (Doran *et al.*, 2009; Sallenger, 2000; Gibeaut, Gutierrez, and Hepner, 2002; Stockdon *et al.*, 2007).

Objectives

Given that barrier spits have a defined long-term evolution (Gibeaut, Gutierrez, and Hepner, 2002; McBride *et al.*, 1995; Morton, 1975; Morton, 1997) and that tropical cyclones play a role in long-term barrier evolution (Fenster *et al.*, 2002), do different tropical cyclones have the same defined effect on a barrier spit? To answer this question, this work has two objectives:

1. Identify patterns of erosion and accretion in 2D (shoreline change) and 3D (volumetric change) that were caused by Hurricanes Ike and Rita and Tropical Storms Josephine and Fay.
2. Compare these patterns to each other individually and cumulatively to evaluate for similarity and difference.

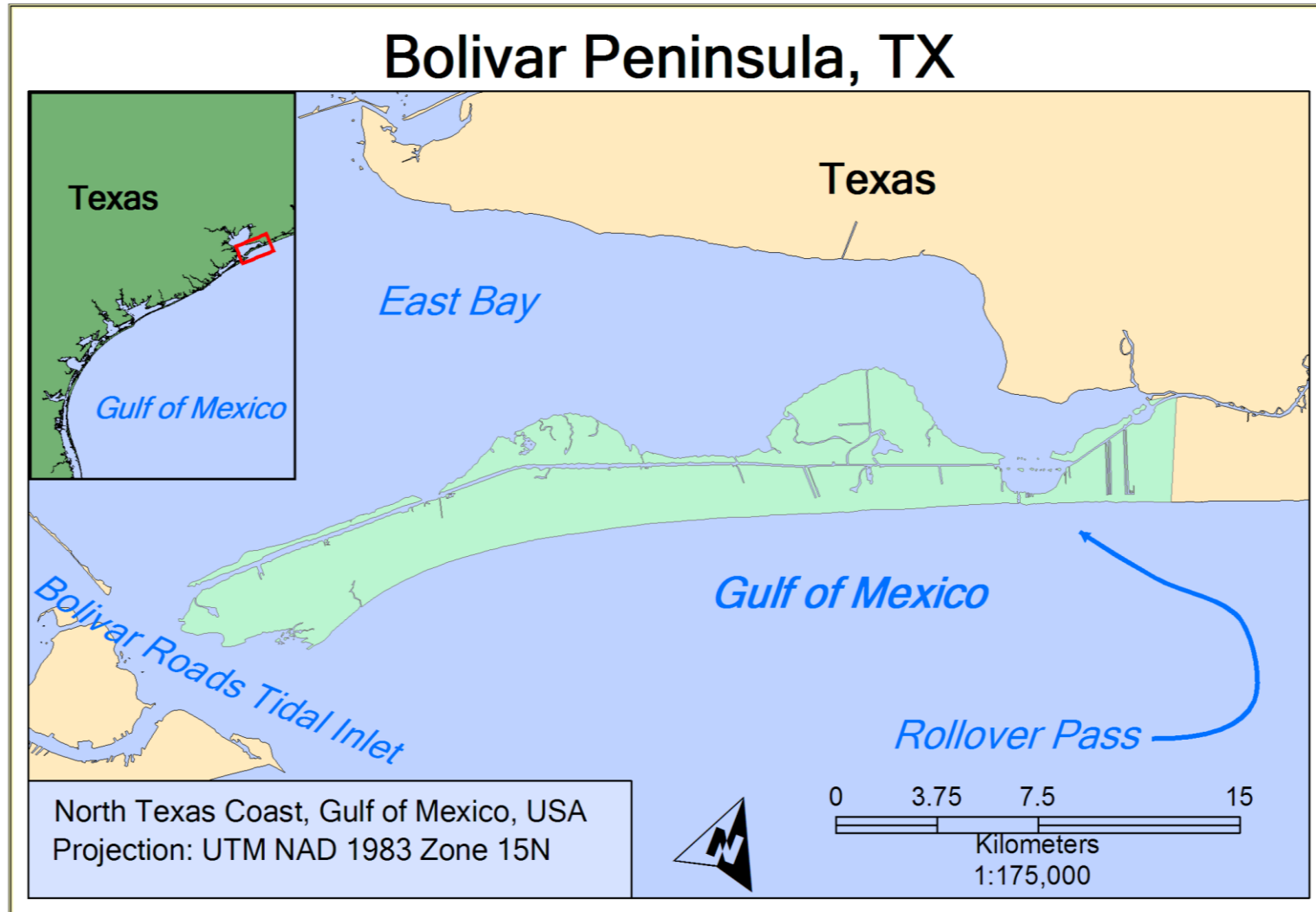


Figure 1.1. Location map of study area – Bolivar Peninsula.

CHAPTER II

SPIT GEOMORPHOLOGY AND TROPICAL CYCLONE IMPACTS

Spits

Spits often occur in areas where a coastline changes direction abruptly (Gilbert, 1890). They are the result of sediment gradually building outward from this rapid change in the trend of a shoreline. This sediment builds outward because of wave-angle climate and longshore drift. The longshore drift, a shore-parallel current, is the result of incipient waves striking the coastline obliquely (Evans, 1942). This longshore drift carries sediment to the area of dramatic shoreline change, and gradually builds outward until a tail of sediment has appeared (Evans, 1942).

In terms of composition, spits are most often found to be composed of sand. However, spits can also be composed of shingle—such as Hurst Castle Spit (King and McCullagh, 1971). The mesoscale shape of a spit is also influenced greatly by wave angle climate, and can produce shapes such as flying spits (Ashton, Murray, and Littlewood, 2007), complex spits such as Cape Cod (Johnson, 1919), or compound recurved spits such as Sandy Hook (Johnson, 1919) and Hurst Castle Spit (King and McCullagh, 1971). From these observations, Bolivar Peninsula could be considered a gently recurving sandy spit.

Spit Geomorphology

The geomorphology of a barrier spit is quite similar to that of a barrier island. In fact, it is thought that the breaching of barrier spits explain the formation of some barrier islands (Fisher, 1968). Given that, barrier spits consist of several sub-environments that

act together as a system. Since spits are similar to barrier islands, it is appropriate to consider the geomorphology of barrier islands.

Oertel (1985) stated that barrier islands have six major sub-environments, these are the backbarrier lagoon, the inlets and their deltas, the barrier island, the barrier platform, and the shoreface. Of interest in this study is the shoreface, the barrier spit—as adapted from Oertel (1985), and the inlets sub-environment. Other sub-environments are present on Bolivar Peninsula, but these other sub-environments have no data coverage.

In Oertel (1985), the barrier island sub-environment covers the subaerial portion of the barrier feature. This sub-environment can have several sedimentary regimes (Oertel 1985). For Bolivar Peninsula, data coverage allows us to observe changes in the beach and the foredunes/dune ridges. The beach is noted by an accumulation of fine sand, and this fine sand beach can vary in width of nearly 90 meters at parts of the distal portion of the spit to 40 meters or less near the proximal end of the spit. Dune height varies from a maximum of 4 meters to an average of roughly 2 meters in height above mean high water. These dune elevations were low enough to be overcome by the storm surge of Hurricane Ike—which was nearly 15 feet (Berg, 2009). The low elevation of the dunes coupled with the relatively low beach slope (Shepard, 1960), can allow for major devastation in the event of a storm—which is what happened in the case of Hurricane Ike (Berg, 2009). These environments do interact with each other to form a system, the barrier system (Oertel, 1985).

Spit Evolution

Extracted from earlier works, three likely scenarios for barrier spit evolution were postulated by Hoyt (1967). In his paper, he advocated that large coastal barrier islands are likely formed by submergence of antecedent dune formations. He also pointed out that spits may just be a step toward barrier island evolution by barrier spit breaching. However, he found this not as plausible because there were not—by his observation—good examples of a barrier island resultant from this process. Fisher (1968), in reply to Hoyt (1967), also set out the idea that barrier islands formation can easily be explained by the formation of beach ridges through littoral drift. Littoral drift is a process of alongshore sediment transport caused by currents that form as a result of residual momentum of obliquely-striking waves on a coastline (Davidson-Arnott, 2010).

It is been known that there are two large contributors to the shape and evolution of a barrier spit in the natural environment. Those factors are wave climate (Ashton, Murray, and Littlewood, 2007; King and McCullagh, 1971) and coastal storms (Fenster, Dolan, and Morton, 2002; Morton, 2002; Morton and Sallenger, 2003). However, it is undeniable that there are man-made factors and features that play a role in the evolution of a barrier spit (Bales and Holley, 1989; Kraus, 1999; Prather and Sorenson, 1972; Morang, 2006). These man-made features include artificially-dredged inlets like Rollover Fish Pass, (Figure 2.1; Prather and Sorenson, 1972) and the constructed features that bound natural inlets like North Jetty that bounds Bolivar Roads Tidal Inlet, as shown in (Figure 2.2).

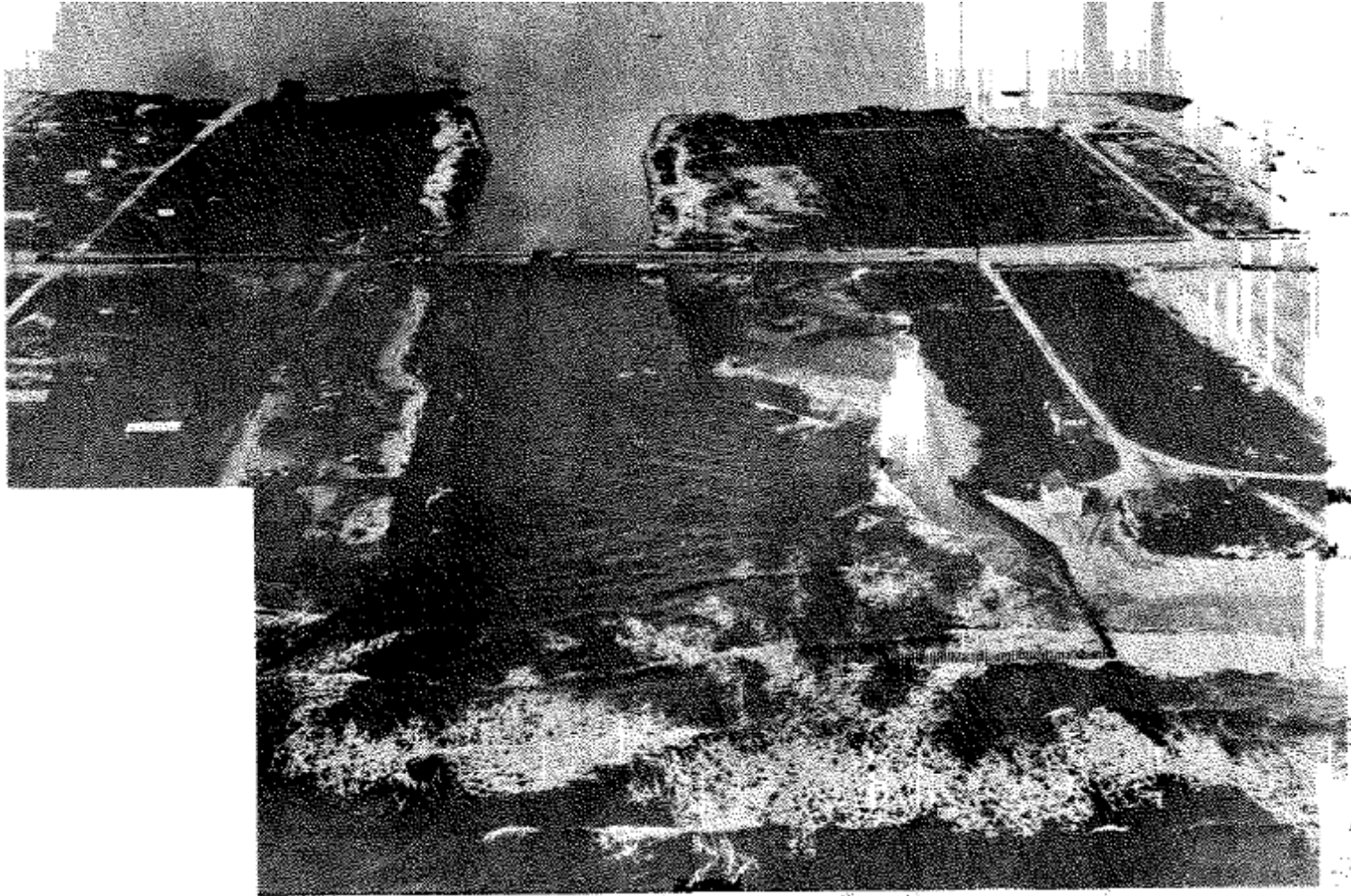


Figure 2.1. Catastrophic erosion at Rollover Fish Pass shortly after opening. (Prather and Sorenson 1972)

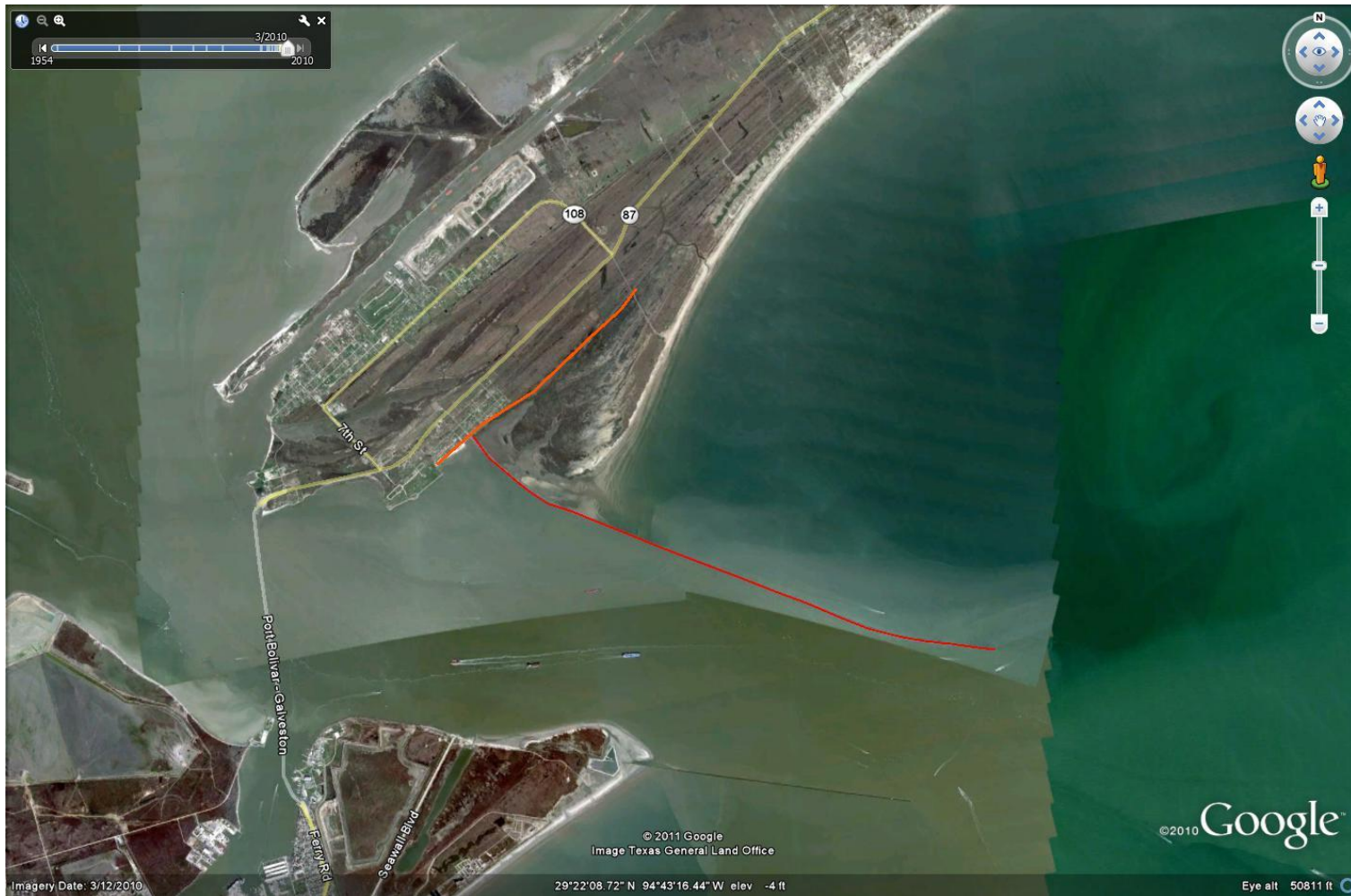


Figure 2.2. Beach aggradation since Jetty construction 1856-2010. Red line is outline of North Jetty. Orange line is outline of 1856 shoreline. Image from Google Earth. (adapted from Anderson, 2007)

Originally noted by Leatherman, Rice, and Goldsmith (1982) in their analysis of Virginia shorelines, coastal barriers can undergo a mesoscale process known as rotational instability. With the process of rotational stability, one side of a coastal barrier accretes and the other side erodes. The result is a mesoscale change that tends to bode a change in barrier island shape. This type of mesoscale behavior was noted in the Chandeleur islands from the work of McBride, Byrnes, and Hiland (1995), (Figure 2.3). The significance of these two studies demonstrates a consistent pattern of alongshore erosion and accretion. Both studies involved observations from long-term shoreline change data, but the environments are quite different.

The largest difference between these environments is the tidal influence. In Leatherman, Rice, and Goldsmith (1982), a mesotidal (2-4m) environment is observed and in McBride and Byrnes, a microtidal (<2m) environment is observed. In a microtidal environment that is analogous to that of McBride, Byrnes, and Hiland (1995), Bolivar Peninsula shows long-term shoreline change patterns consistent with rotational instability and spit accretion (Gibeaut, Gutierrez, and Hepner, 2002; Morton, 1975; Morton, 1983; Morton, 1997; McBride, Byrnes, and Hiland, 1995). This phenomenon is illustrated in Morton (1983)—where the shoreline is shown to gradually accrete at the distal end of the spit and erode at the proximal end. As demonstrated in the next two sections, natural and anthropogenic factors play a role in rotational instability in the case of Bolivar Peninsula.

c. Rotational Instability ⑧

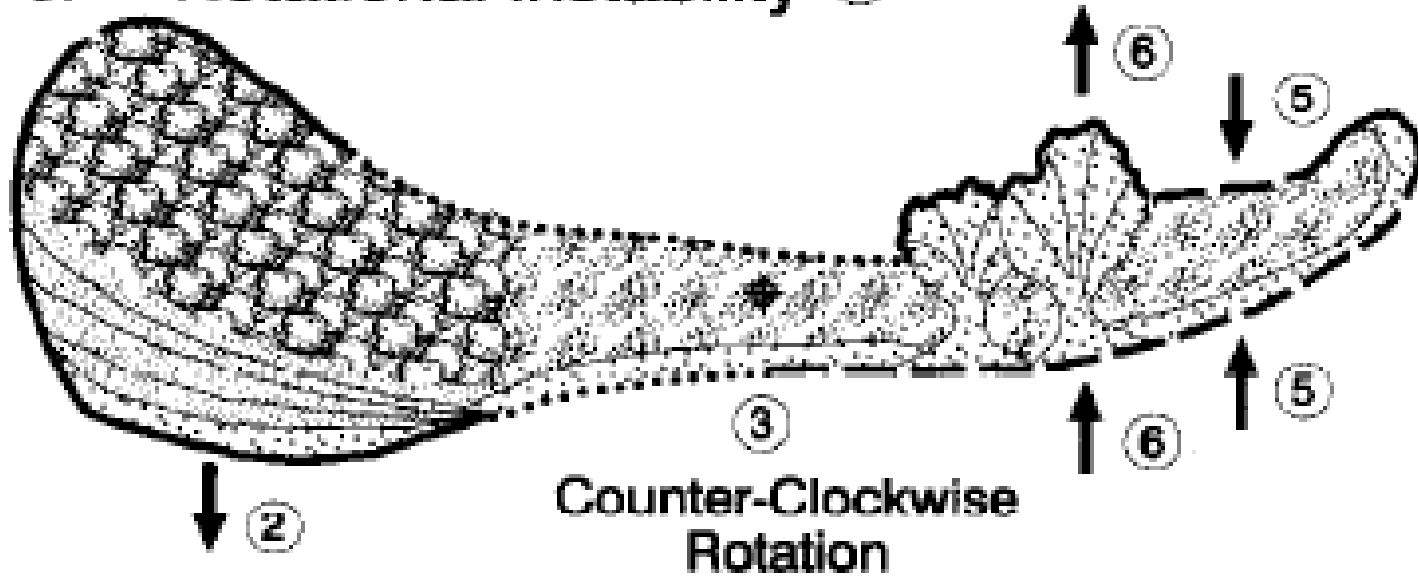


Figure 2.3. Outline of rotational instability. The left side of this island would be equivalent to the distal portion of Bolivar Peninsula, and the right side would be the proximal end. (McBride, Byrnes, and Hiland, 1995)

Natural Processes

Some of the earliest published work done on spits is that of Johnson (1919). He used mesoscale shape and habit of different spits to deduce their possible origin and evolution. However like his advisor, William Morrison Davis, he was entrenched in the belief that the evolution of geomorphic phenomena is cyclic and can be given biological paradigms such as age. Hence he believed in ‘young’ and ‘old’ geomorphic features.

It was his estimation that ‘younger’ shorelines were very complex and that features such as barrier spits and islands represent a maturing of that coastline. However, this ideology of young and old does not address what factors or processes are really at work. It only addresses an observation, but gives no concrete manner by which this smoothing of the shoreline could occur.

To understand the factors that play a role in the evolution of a spit, more recent work uses different types of modeling to describe the important factors at work in the genesis and evolution of spits. King and McCullagh (1971) used a weighted process-response model to generate spits of different shapes. With some experimentation, they were able to simulate a spit that was very similar to Hurst Castle Spit, a shingle spit off the coast of Britain. In Ashton, Murray, and Littlewood (2007), a one dimensional model was used to simulate the affect of variable angle climates on spits (Figure 2.4). This approach uses a contour method, Equation (2.1) that describes the plan-view evolution of a shoreline.

$$\frac{\partial y}{\partial t} = -\mu \frac{\partial^2 y}{\partial x^2} \quad (2.1)$$

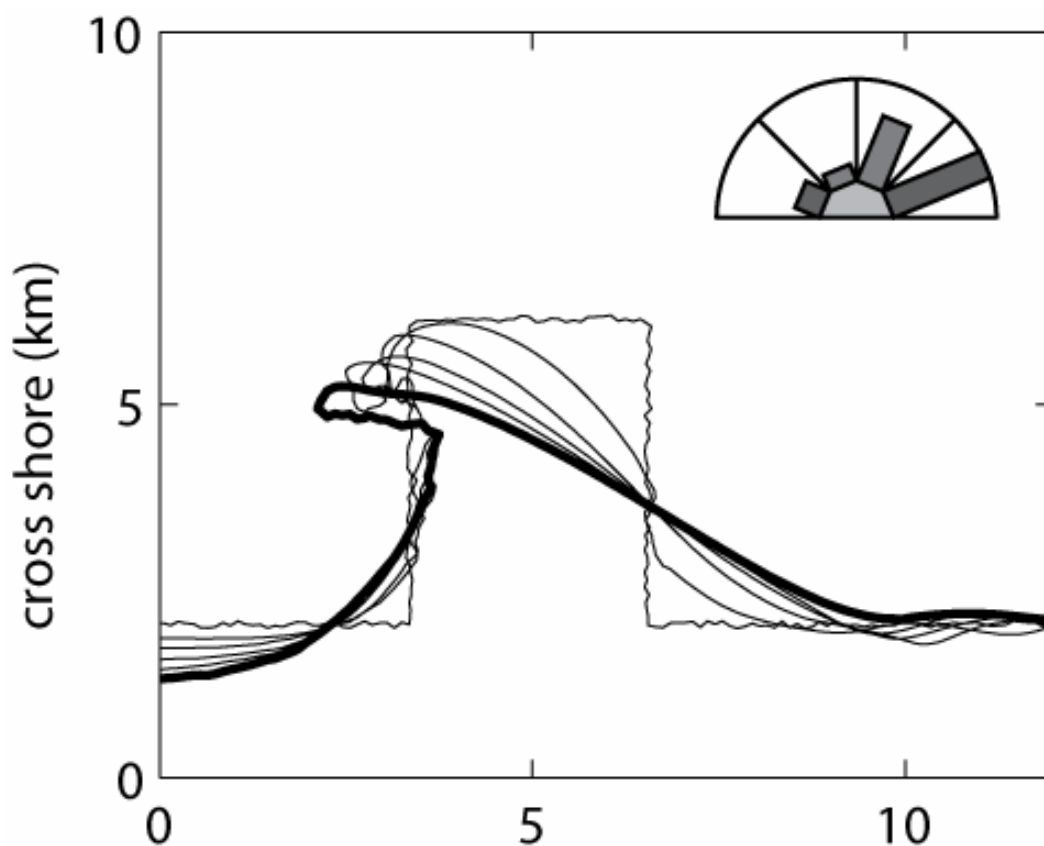


Figure 2.4. Time-steps through one-dimensional model showing the evolution of a flying spit through a response to wave-angle climate. The wave angle climate is shown through a ‘wind rose’ at the upper right. This wind rose details the dominant direction that the wind is coming from. In this case, east by southeast is the dominant incipient wind? direction. (Ashton, Murray, and Littlewood 2007)

In this approach, the partial derivative of ‘y’ with respect to ‘t’ represents coastal change with respect to time and the double partial derivative of ‘y’ with respect to ‘x’ describes coastal curvature/shape (Ashton, Murray, and Littlewood, 2007). Particularly, diffusivity, ‘ μ ’, explains the effect of the change in wave-angle climate on a coastline. This was elaborated within the framework of the deep-water CERC formula,

(Equation 2.2) as shown in Ashton, Murray, and Littlewood (2007).

$$\mu = \frac{K}{D} T^{1/5} H_0^{12/5} \left\{ \cos^{1/5}(\varphi_0 - \theta) \left[\left(\frac{6}{5} \right) \sin^2(\varphi_0 - \theta) - \cos^2(\varphi_0 - \theta) \right] \right\} \quad (2.2)$$

‘K’ is an empirical constant that Ashton Murray and Littlewood (2007) set at $0.34 \text{ m}^{3/5} \text{ s}^{-6/5}$ —although it is interesting to note that different literature have found values between 0.2 to 0.39 (Wang, Ebersole, and Smith, 2002). ‘D’ represents depth in meters, ‘T’ represents wave period in terms of seconds and H_0 is the deep water wave height in terms of meters. Terms that deserve particular attention are those in curly braces, which describe the geometry of incipient waves. The notable variable is the relative angle between wave groups to the shore ($\varphi_0 - \theta$). With this variable in consideration, this formula states that waves that approach the shoreline more obliquely will render the most change. It also suggests that waves that approach the shore at a more normal direction render less affect or morphological change.

From the work of Ashton, Murray, and Littlewood (2007), the findings were that regardless of the trends in changing wave-angle climate, a spit will work to achieve equilibrium or 90 degrees relative angle to the wave angle climate. With these models, the workers were able to simulate a flying spit and a cape, an example shown in Figure 2.3. Although the studies by Ashton, Murray, and Littlewood (2007) and King and McCullagh (1971) are far removed in time, technique, and have differing modeling paradigms, both of these studies came to the conclusion that wave climate and shoreline orientation were the most important environmental factors in the evolution of a barrier spit.

Anthropogenic Features and Resultant Processes

Anthropogenic features on the beach face of Bolivar Peninsula include geotubes, the North Jetty, and Rollover Fish Pass. Geotubes were the most recently constructed in 2001 because of the widespread dune erosion brought by Tropical Storms Josephine and Frances (Gibeaut, Gutierrez, and Hepner, 2002; Gibeaut *et al.*, 2002, Gibeaut *et al.*, 2008). According to the findings of Gibeaut *et al.* (2002), the geotubes played a role in the narrowing of beaches, and these geotubes presented the apparent management and maintenance difficulties in keeping them covered with sand. To add to these findings, the geotubes ultimately did fail in the oncoming storm surge and waves brought forth by Hurricane Ike (McLellan and Lee, 2009). This failure is detailed by the deflation of these geotubes and the localized scour that occurred at areas where the geotubes met and possibly at areas where they were compromised by debris (McLellan and Lee, 2009; Potts, 2010).

The original North Jetty was built in 1876 and went through several modifications and fortifications thereafter (Sargent and Bottin, 1989). However, this Jetty failed because it was unsustainable when made from wood and sediment (Sargent and Bottin, 1989). From aerial photography, one can see sediment that has accumulated at the northern side of the North Jetty from the baffled littoral drift and spit accretion of Bolivar Peninsula—in a manner analogous to those observations of (Kraus, 1999), (Figure 2.2).

Another anthropogenic feature, Rollover Fish Pass opened in 1955 with the hopes of providing a better habitat for fish in East Bay (Bales and Holley, 1989; Prather

and Sorenson, 1972). Because of incongruencies in the tidal cycle between East Bay and the Gulf of Mexico, the tidal prism—the volume of water that passes through a given feature because of tidal changes—from the newly-dredged Rollover Fish Pass resulted in coastal erosion and the inlet widened as a result (Prather and Sorenson, 1972) (Figure 2.1). From the work of Prather and Sorenson (1972), it was estimated that Rollover Fish Pass was attributable to the loss of around 24,000 m³/yr of sediment. However, conclusions from Bales and Holley (1989) show generally agreeing measurements of 6700 m³/yr to 20,000 m³/yr of sediment from beach erosion rates, but also had sediment loss an order of magnitude above at around 240,000 m³/yr to 290,000 m³/yr from dredging rates for the Gulf Intracoastal Water Way just northwest of Rollover Bay. Regardless of the estimate, it is generally agreed by both studies that the shorelines near Rollover Pass are in a state of erosion relative to other shorelines. Fenster and Dolan (1996) found that inlets can cause coastal change within several kilometers around them.

Tropical Cyclones

Tropical cyclones are defined as storms that fall within subtropical and tropical regions (Longshore, 2008). These storms, when powerful enough, are considered a Hurricane in the North Atlantic (Longshore, 2008; Simpson and Riehl, 1981). It should be noted that the line between Hurricane and Tropical Storm is steeped in historical significance and is somewhat arbitrary (Dorst, 2004). However arbitrary, it is acknowledged that a Hurricane represents the mature stage of a tropical cyclone with winds increasing in intensity and more closely packed around the eye wall, as shown in Figures 2.5 and 2.6 (Longshore, 2008; Simpson and Riehl, 1981).

Hurricanes are further described in terms of peak sustained wind speed by the Saffir-Simpson Hurricane Wind Scale (Saffir-Simpson Team, 2012). Winds are measured at sustained one minute intervals at a standard of 10 meters above a relatively flat surface (Saffir-Simpson Team, 2012). A Category 1 Hurricane is thought to be able to threaten buildings that are not very structurally sound, whereas a Category 5 Hurricane can deliver complete devastation to an area (Saffir-Simpson Team, 2012). It should be noted that this scale does not consider other factors such as barometric pressure—as it did in its earliest days (Saffir-Simpson Team, 2012). The strength of the Saffir-Simpson Hurricane Wind Scale is in its simplicity, but its weakness is also in its simplicity. Factors such as storm surge can vary greatly between different storms of the same category (East, Turco, and Mason, 2008; Islam *et al.*, 2009).

Another notable feature of the tropical cyclone is the location of strongest winds. In general, with some notable exceptions, the tropical cyclone is strongest in the right side of the storm—relative to direction of movement in the storm, as shown in Figure 2.6 (Simpson and Reihl, 1981).

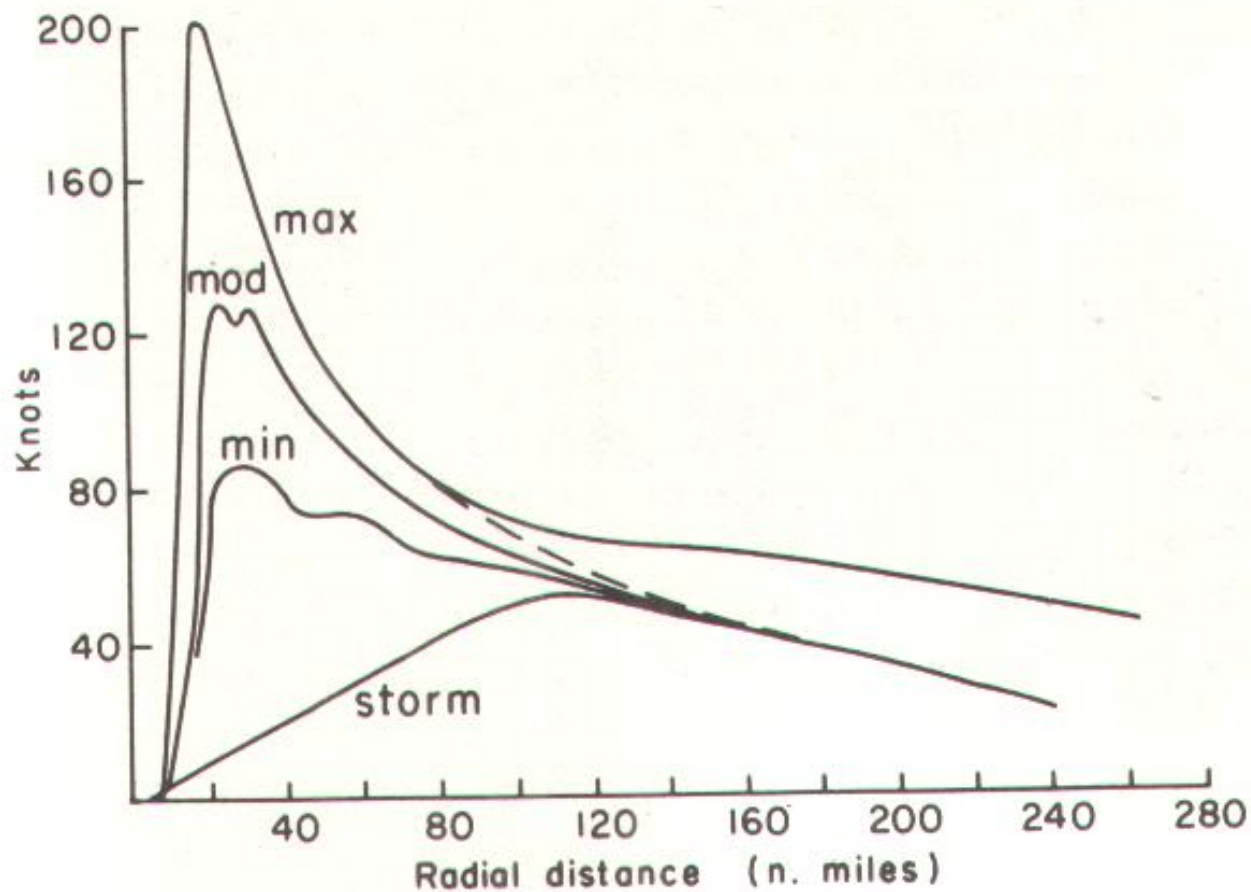


Figure 2.5. Graph demonstrating typical proximity of highest wind speed with respect to distance from the eye of the storm and this relationship to the tropical storm intensity. 'Min', 'Mod', and 'Max' correspond to Minimum, Moderate, and Maximum Hurricane intensity and 'Storm' corresponds to a tropical storm. (Simpson and Riehl, 1981)

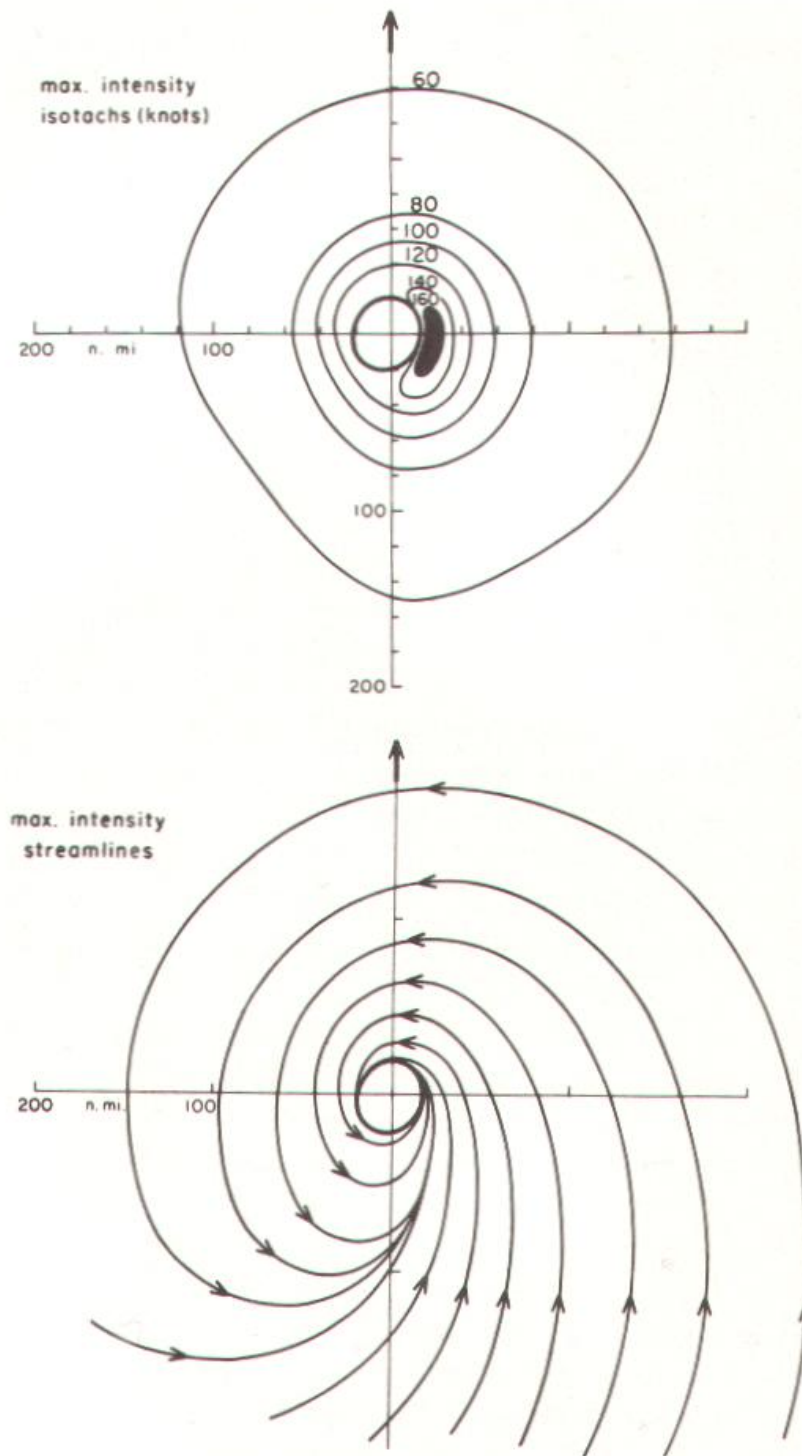


Figure 2.6. Two different representations of wind speed distribution from models that contrast different wind speeds at different sides of the hurricane relative to the direction of motion (at the top of each drawing) (Simpson and Riehl, 1981)

Tropical Cyclone Impacts

In the following sections, four tropical cyclones will be discussed in terms of the coastal change that they have wrought. These storms will be characterized by their relative distance from the study area, the side of the storm that the study area was in at landfall, and the intensity of the storm via the Saffir-Simpson Hurricane Wind scale at the point where the storm is closest to the study area.

In Gibeaut, Gutierrez, and Hepner, (2002), the impact of Tropical Storms Josephine and Frances are used to establish an empirically derived threshold that is found by multiplying water level with water level standard deviation. Gibeaut, Gutierrez, and Hepner (2002) showed that there is a threshold upon which significant shoreline change is expected to occur. Josephine just exceeded this threshold, and Frances went further above this threshold (Gibeaut, Gutierrez, and Hepner, 2002). This methodology and underlying logic implies that there is a role that the landform itself plays when it comes to eventual impact of a tropical cyclone once it approaches land. This should come as no surprise, but often other notables scales omit the landform altogether.

Morton (2002) looks into the different factors, storm-specific and barrier-specific, that can account for the variable responses of a barrier system to a particular storm. Morton and Sallenger (2003) build on the work of Morton (2002) by looking at the washover penetration of barrier complexes along the eastern United States as the result of different extreme or catastrophic coastal storms. One particular event, washout (Morton, 2002; Morton and Sallenger, 2003) is caused by flow of water out of the

lagoon over the barrier complex and into the ocean. The effects of washout were documented in many of the scour patterns by Potts (2010) with respect to Hurricane Ike.

The most important message from the works of Morton (2002) and Morton and Sallenger (2003) is that storms have varying effects based on distance from the eye, which side of the storm that landfall is made relative to the area in question, and features relating to the intensity of the storm and the barrier's ability to resist storm forcing. This important linkage between driving forces, the storm, and resisting forces, the barrier landform, was actually formulated in Sallenger (2000), and given application in Stockdon *et al.* (2007).

In Sallenger (2000), a storm impact scale was derived that takes into account the properties of wave runup with storm surge 'R' and dunes 'D'. Each variable is then further categorized as 'high' or 'low'. Thus R_{high} and R_{low} correspond to the highest and lowest swash elevations during a storm (Figure 2.7). These 'R' values correspond to storm forcing, however they are related to the landform by virtue of beach slope. The next parameter of interest is 'D'. D_{high} and D_{low} correspond to the height of the dune crest and toe (Sallenger, 2000). This parameter is a measure of the barrier's ability to resist the erosive forcing wrought by the storm. These four parameters can be formulated to create four distinct regimes of storm impact: swash, collision, overwash, and inundation (Figure 2.8; Sallenger, 2000). These impact levels are determined by a series

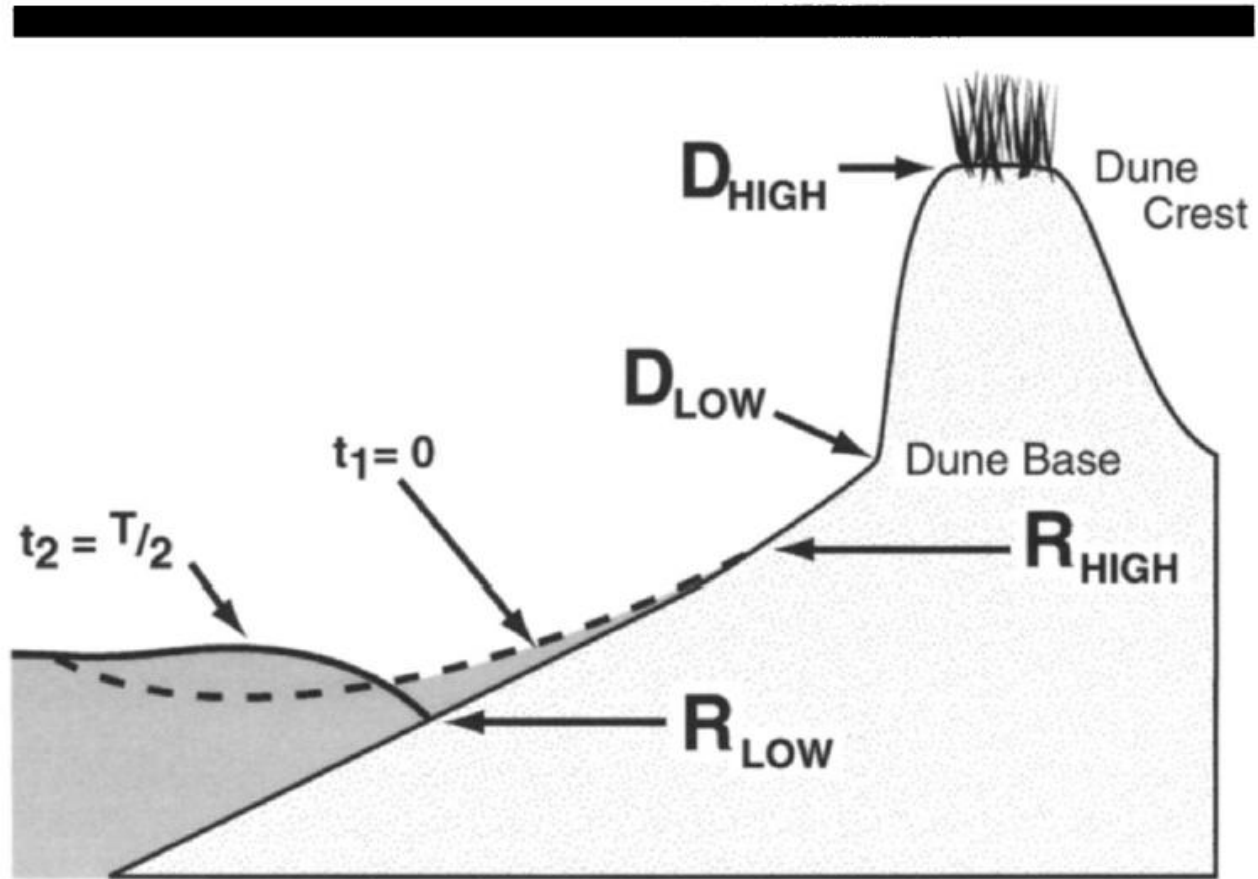


Figure 2.7. Illustration of variables D_{high}/D_{low} and R_{high}/R_{low} for the storm impact model. (Sallenger, 2000)

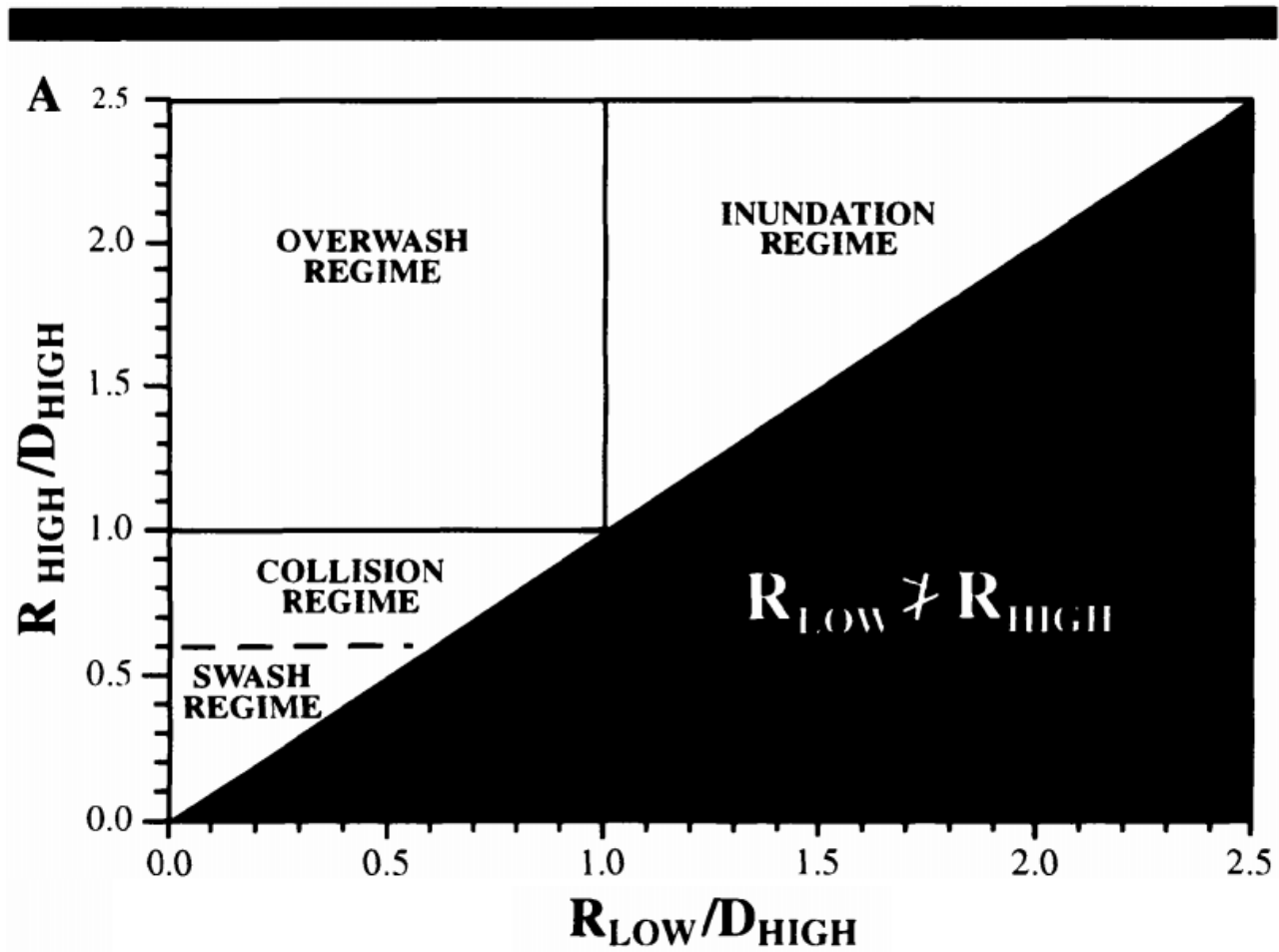


Figure 2.8. Four different regimes of coastal impact from Tropical Cyclones. (Sallenger, 2000)

of inequalities. The left hand side of these inequalities is constant, which is $R_{\text{high}}/D_{\text{high}}$ (Sallenger 2000). The advantage of this approach is that storm damage is quantified and taken into account. With more work, there could be a possibility to forecast potential damages with some better degree of accuracy (Morton, 2002). However, the issue is that this model requires apriori knowledge of the storm's path and barrier island parameters, and the models based on this approach have had limited success (Stockdon, 2007).

Houser, Hapke, and Hamilton (2008) did a novel statistical analysis of shoreline change and volume change along the coast of Florida. Specifically, this study suggested that transverse bars and island width could also play a role in these variations. Patterns were used to suggest these controlling factors. They found that island width was highly correlative and out of phase with historic shoreline change. Additionally, this work showed how dune prominence was statistically correlative to the presence of offshore transverse ridges. Through this work, it was shown how analyses can be used to decompose data into patterns, and that these patterns can suggest meaningful relationships with controlling factors—such as offshore transverse ridges or dune prominence.

Tropical Storm Josephine

Tropical Storm Josephine made landfall in Apalachee Bay, Florida around the evening of 7 October 1996 (Pasch, 1997). Estimation of the BEST track for Josephine and wind speed results for the study area based on data from buoy 42035 (NDBC, 2011) shows that the system was closest and most felt in Texas on 6 October at 0400 UTC about 300 miles south of Bolivar Peninsula (Figure 2.9). With the study area being situated on the left side of the storm (Figure 2.6) when it was at its closest, storm intensity was just at a threshold for meaningful dune and shoreline erosion (Gibeaut, Gutierrez, and Hepner, 2002).

According to data from the National Data Bouy Center at station 42035, 22 nautical miles east of Galveston, the wind speed was 12.5 meters per second or 28 miles per hour. Wind direction is estimated by the NDBC (2002) to be average of decomposed unit vectors. After the average is obtained, the actual direction is calculated for $\arctan(u/v)$ (NDBC, 2002). For Tropical Storm Josephine, the estimated wind direction was going southwest leaving from 33 degrees east of north. To estimate wind speed, scalar values for wind speeds were averaged over eight minutes (NDBC, 2002). Further illustration of wind speeds and directions are given in Figure 2.10. Significant wave height, the average of the highest one third of all the waves sampled over a 20 minute sampling period (NDBC, 2002) was calculated as 2.84 meters with a dominant wave period of 9.09 seconds. Directional wave data were not derived for Tropical Storm Josephine.

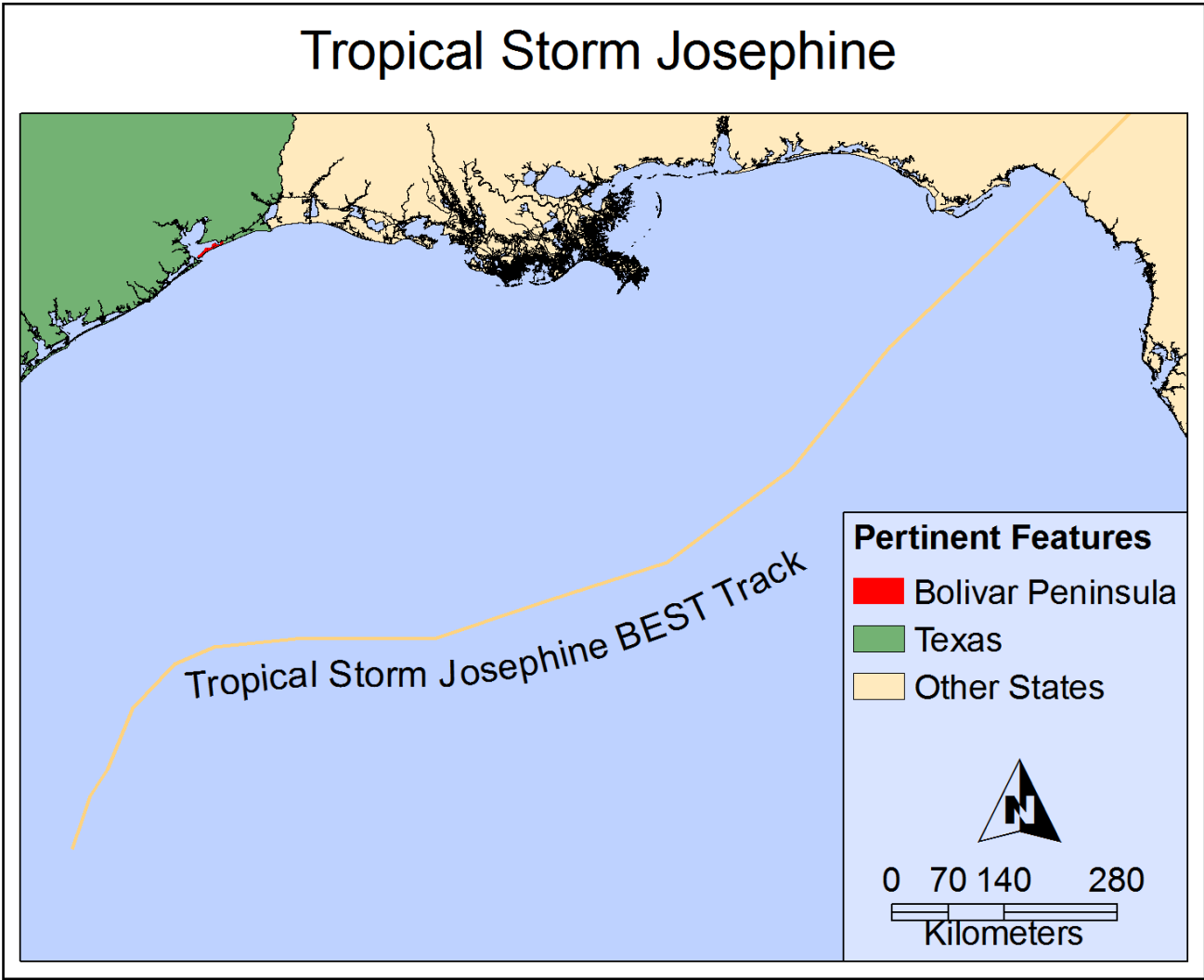


Figure 2.9. BEST storm track of Tropical Storm Josephine (Geospatial Data: NOAA)

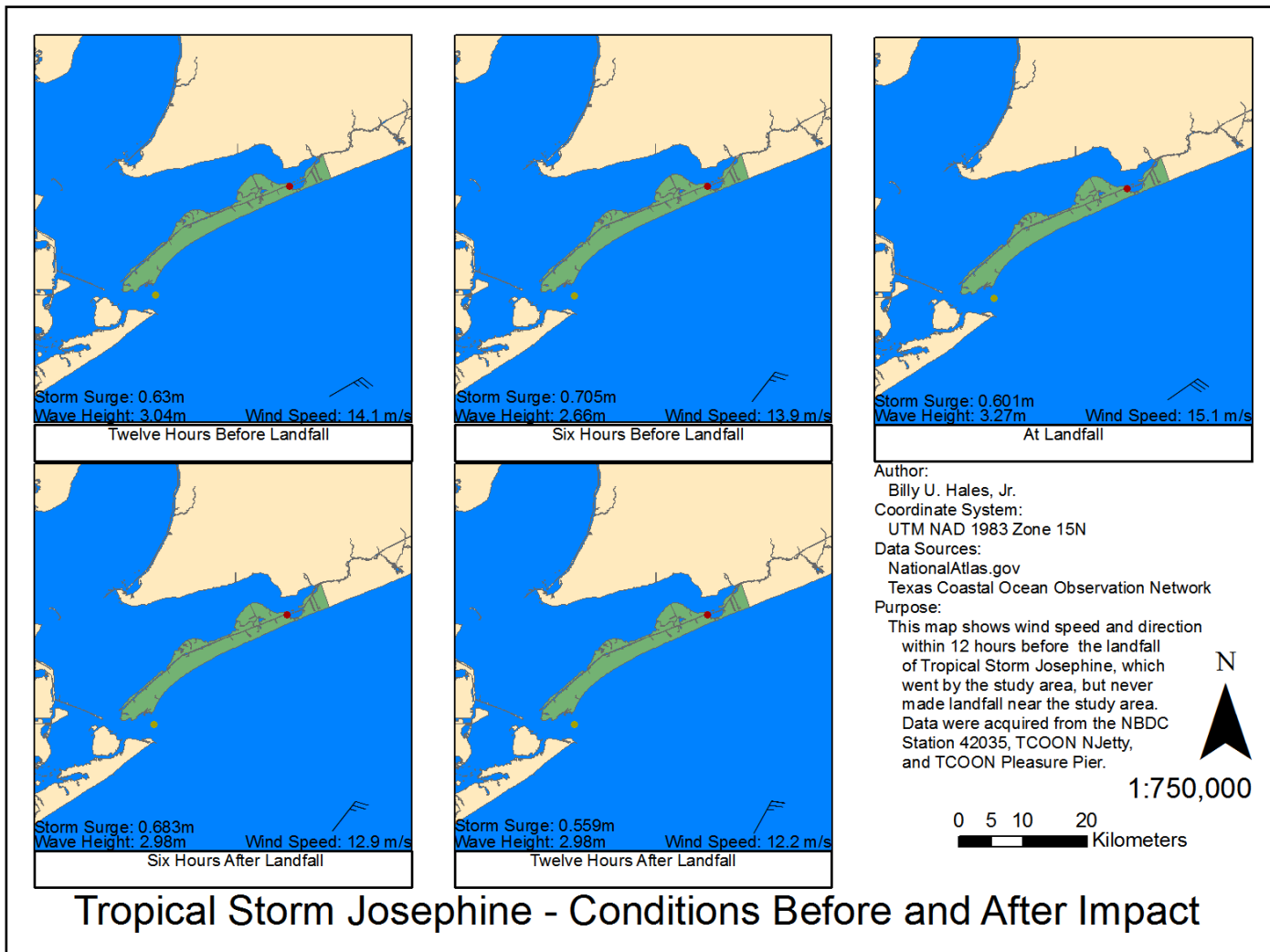


Figure 2.10. Wind speeds and directions within a 12 hour window around the closest location to Tropical Storm Josephine. Over time, wind direction only changed a couple of degrees, and starting to trend more southerly.

Tropical Storm Fay

Tropical Storm Fay made landfall at 7 September 2002 at 0900 UTC near Matagorda Peninsula, TX. The eye of Tropical Storm Fay landed nearly 150 miles south of the study area (Figure 2.11). The estimated maximum wind speeds upon landfall were estimated at 50 kts or approximately 58 miles per hour. Bolivar Peninsula was subjected to sustained winds of approximately 33 kts or roughly 38 miles per hour (Stewart, 2003). One hour after landfall, wind speeds were reported by National Data Buoy Center Station 42035 to be coming from the east southeast at 12.8 meters per second or approximately 29 miles per hour (NDBC, 2011). It was reported that Tropical Storm Fay generated a storm surge of roughly 0.66 to 1 meter throughout most of the northern Texas Coast (Stewart, 2003). National Data Bouy Center Buoy 42035 also reported wave heights of 3.48 meters with a period of 8.33 seconds coming from the southeast. Storm surge ranged from 0.9 meters at landfall to 0.5 meters twelve hours after landfall (NDBC, 2011). It should be noted that the prominent wave direction was going in a northwesterly direction during the 24-hour window around the time of landfall (Figure 2.12).

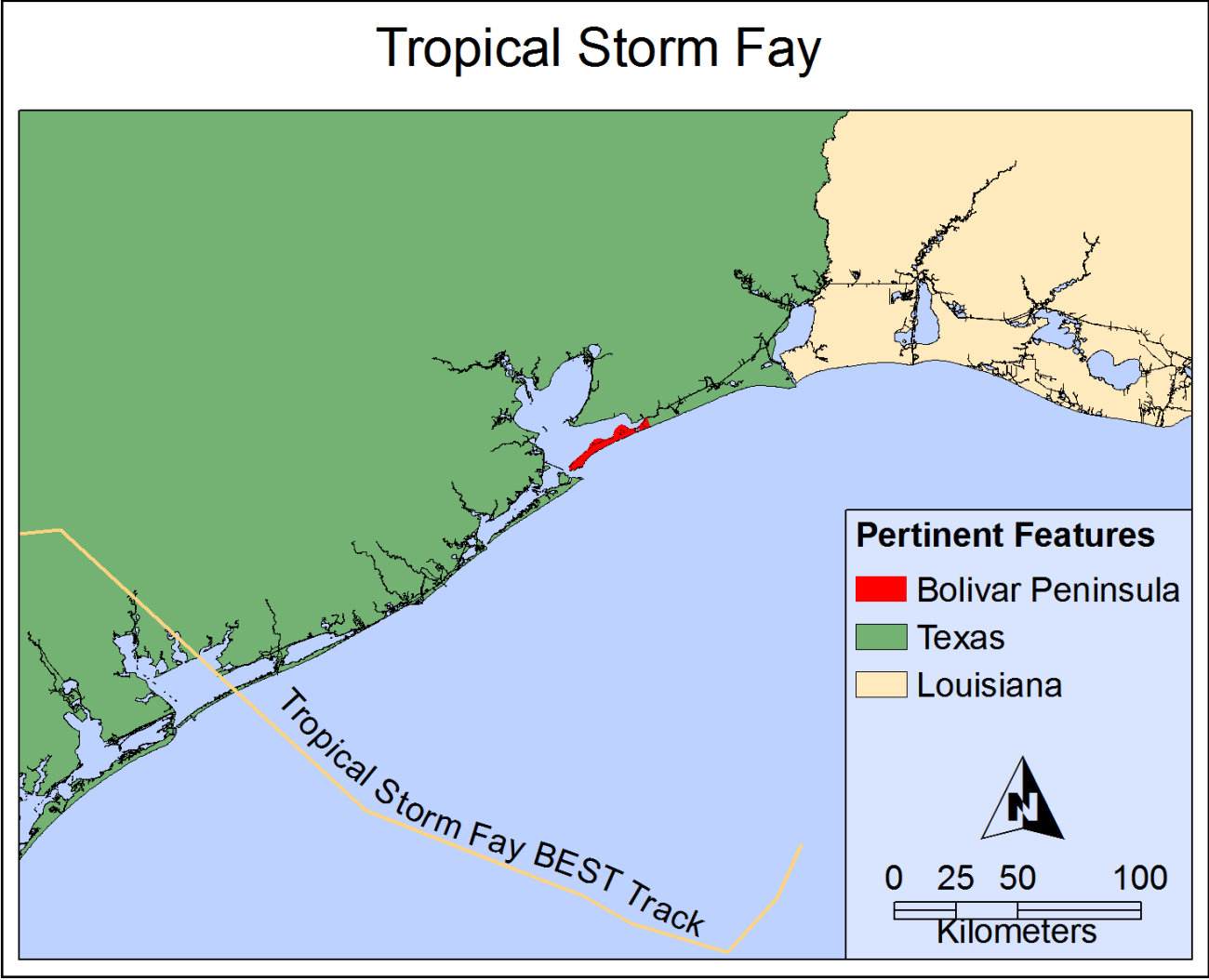


Figure 2.11. BEST storm track of Tropical Storm Fay (Geospatial Data: NOAA).

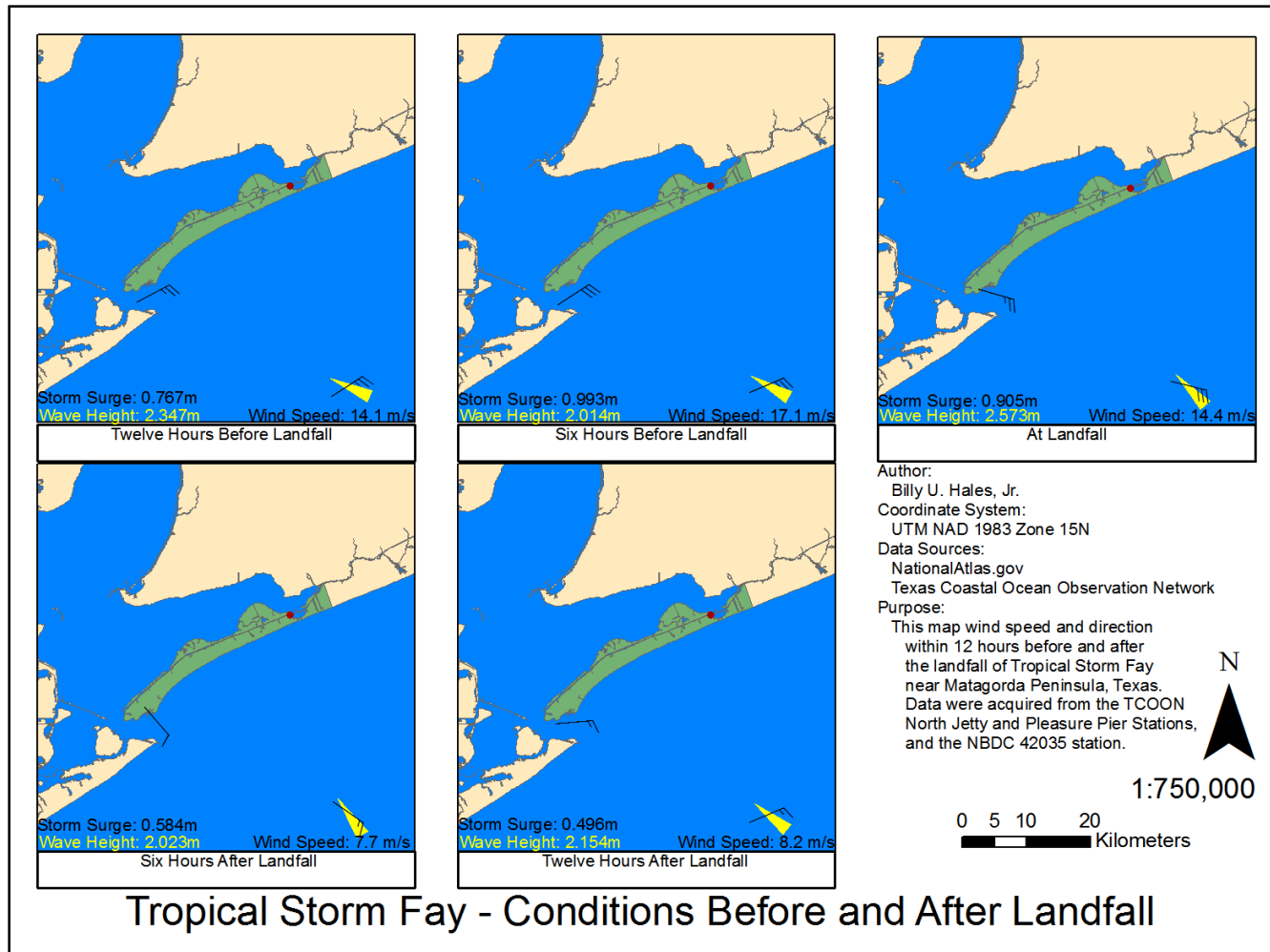


Figure 2.12. Wind/wave speeds and directions within a 12 hour window around the closest location to Tropical Storm Fay. Notice how the wind barbs tend to trend more northerly at landfall and thereafter, and that the waves seem to always point nearly normal to the barrier spit. Wave directions are in yellow.

Hurricane Rita

On 24 September 2005 at 0740 UTC, Hurricane Rita made landfall as a category 3 storm on the Saffir-Simpson Hurricane Wind scale. The center of Hurricane Rita landed slightly east of Sabine Pass (Figure 2.13). This put Bolivar Peninsula on the weaker side of the storm (Gibeaut *et al.*, 2008). The estimated maximum wind speeds upon landfall were 100 knots, approximately 115 miles per hour (Knabb *et al.*, 2006). According to data from the NDBC (2011), wind speeds close to the study area were sustained at 12.5 meters per second or roughly 28 miles per hour and coming from the southwest. Estimated wave height was 2.3 meters and had a period of 6.25 seconds at an angle slightly more westward than the wind direction.

Gibeaut *et al.* (2008) found that the combined storm surge and wave action at the study area was less than those impacts recorded from Tropical Storm Frances in 1998. This finding has importance because Tropical Storm Frances was found to be a benchmark or threshold storm for causing significant morphological change by storm overwash (Gibeaut, Gutierrez, and Hepner, 2002). It should also be noted that the seaward fetch of these winds also contributed to localized flooding along the upper Texas Coast (Knabb *et al.*, 2006).

Hurricane Rita

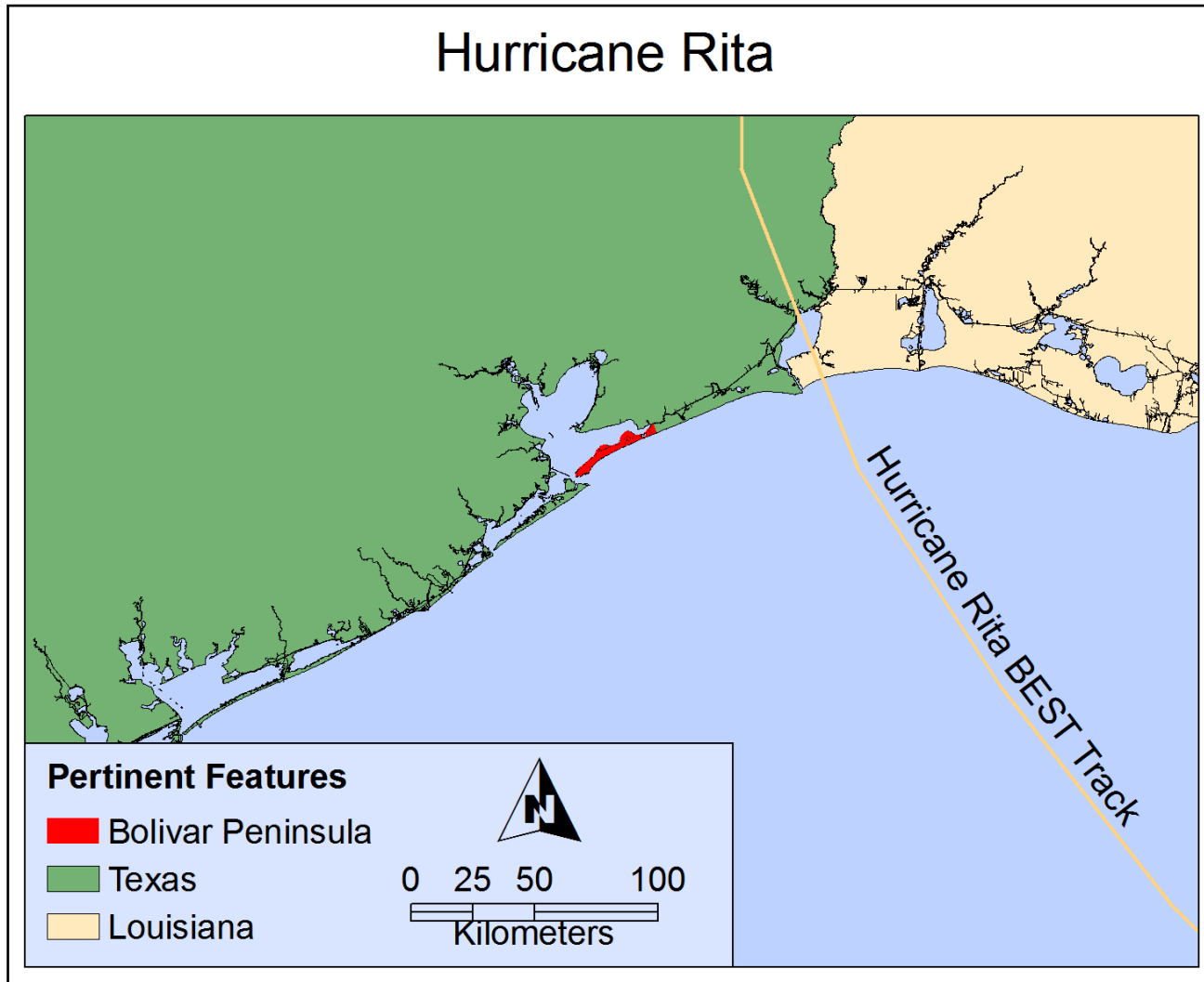


Figure 2.13. BEST storm track of Hurricane Rita (Geospatial Data: NOAA)

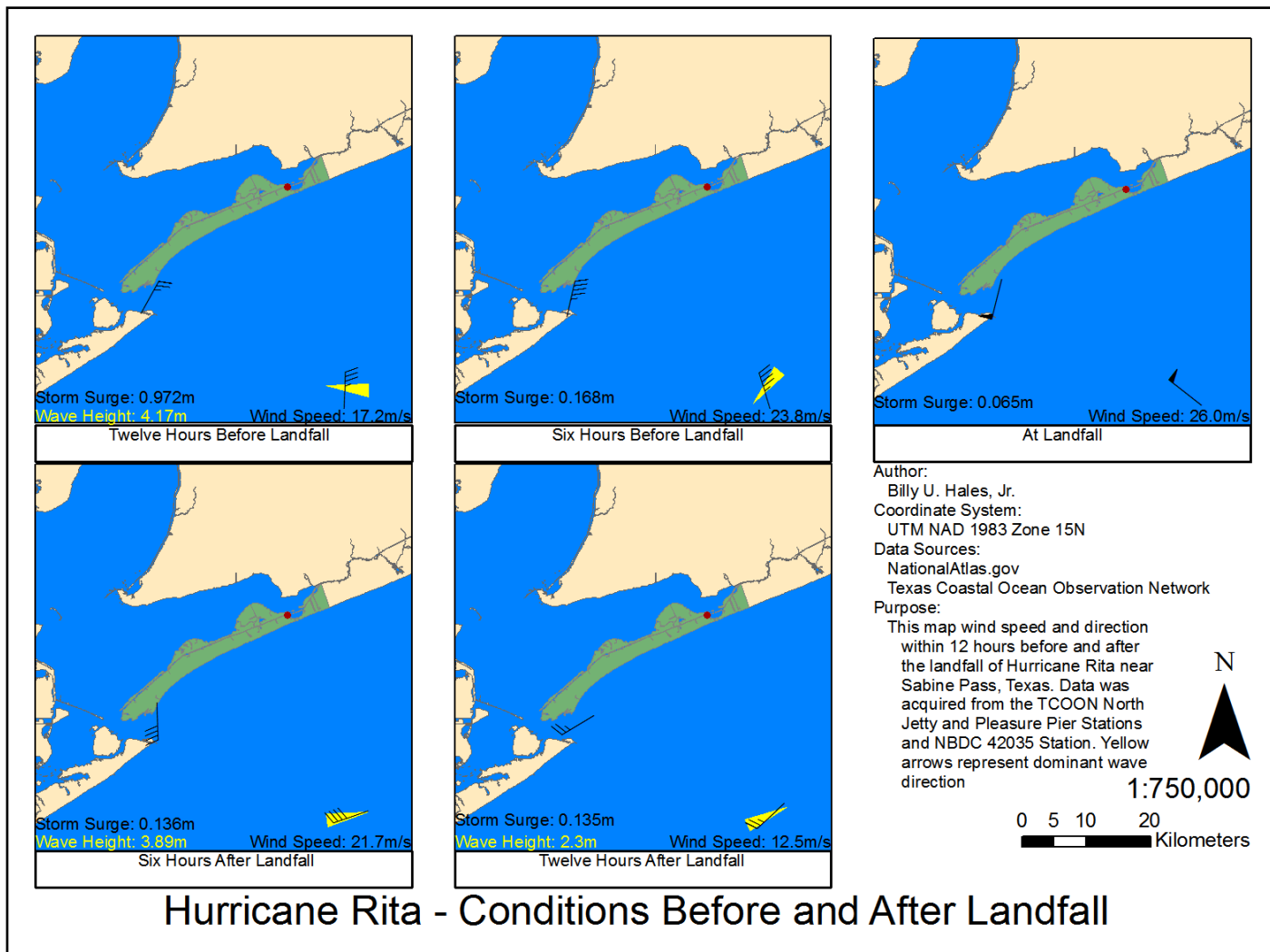


Figure 2.14. Wind speeds and directions within a 12 hour window at the study area. Notice how the wind and then the wave direction changes before and after landfall. Wave directions are in yellow.

Storm surge and wave direction dynamics of Hurricane Rita showed that the wind and waves made a reversal from wind/waves pointing west southwestward before landfall to an easterly direction after landfall (Figure 2.14). Storm surge was around 0.9 meters at 12 hours before landfall, but was quickly depressed by offshore winds by landfall to a value of less than 0.1 meter (NOAA, 2011).

Hurricane Ike

Making landfall on 13 September 2008 at 0700 UTC, Hurricane Ike was a category 2 storm on the Saffir-Simpson Hurricane Wind scale (Berg, 2009). The eye, or center, of the storm made landfall around the northern end of Galveston Island (Figure 2.15), this put Bolivar Peninsula on the immediate ‘right side’ of the hurricane—which means that the study area was subjected to the highest winds, waves (Simpson and Riehl, 1981), and the highest storm surge of approximately 15ft to 20ft (Berg, 2009).

The estimated maximum wind speeds upon landfall were at 95 knots, or approximately 109 miles per hour (Berg, 2009). Data from the National Buoy Center was not actually valid because the buoy had drifted during the storm (NDBC, 2011). However, another buoy operated by the Texas Coastal Ocean Observing Network had data shortly before the landfall of Hurricane Ike (DNR, 2008). This data show sustained wind speeds of 26.2 meters per second or 59 miles per hour coming from the northeast (NDBC, 2011). Wave parameters from buoys were not available (Figure 2.16).

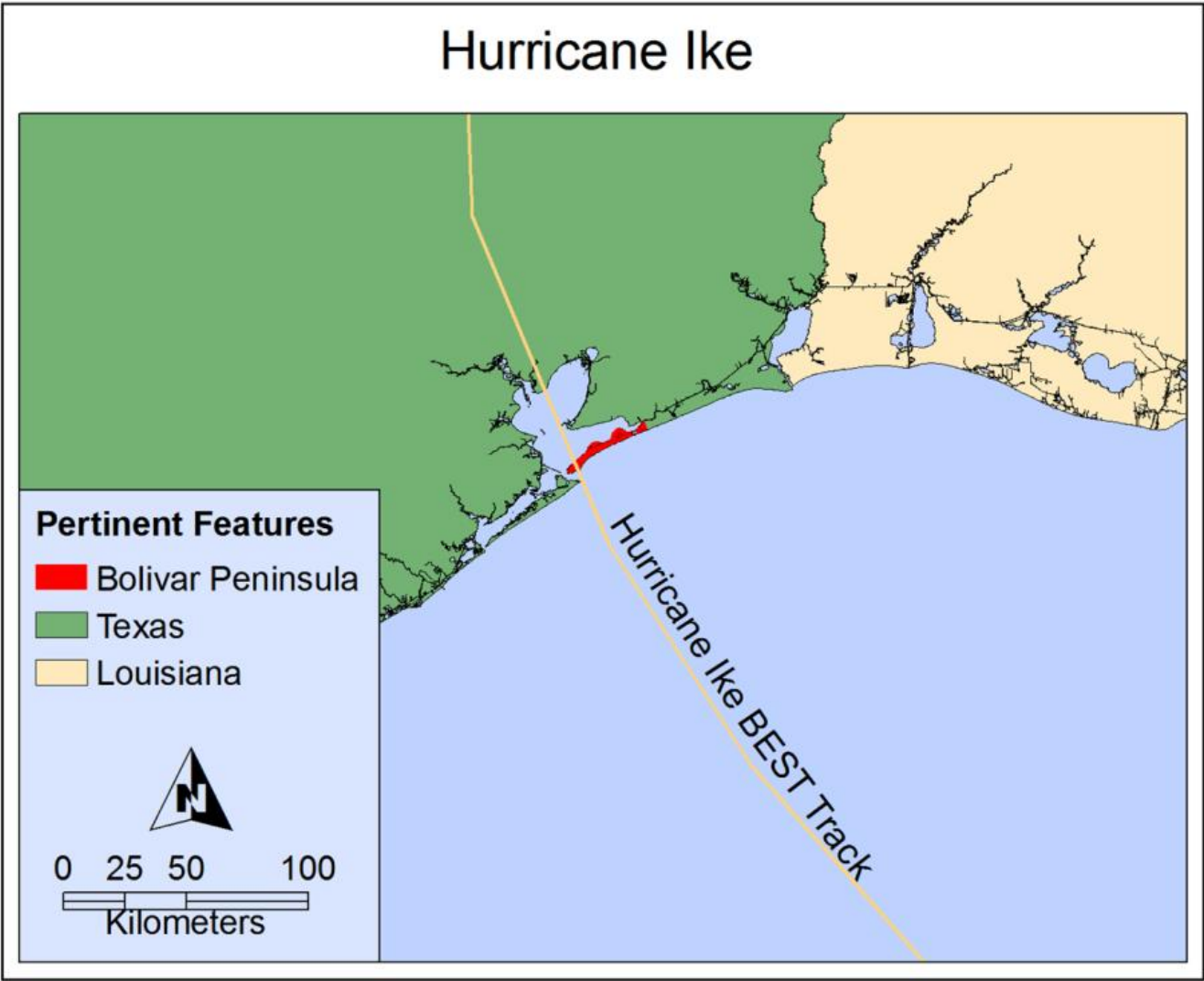


Figure 2.15. BEST storm track of Hurricane Ike. (Geospatial Data: NOAA)

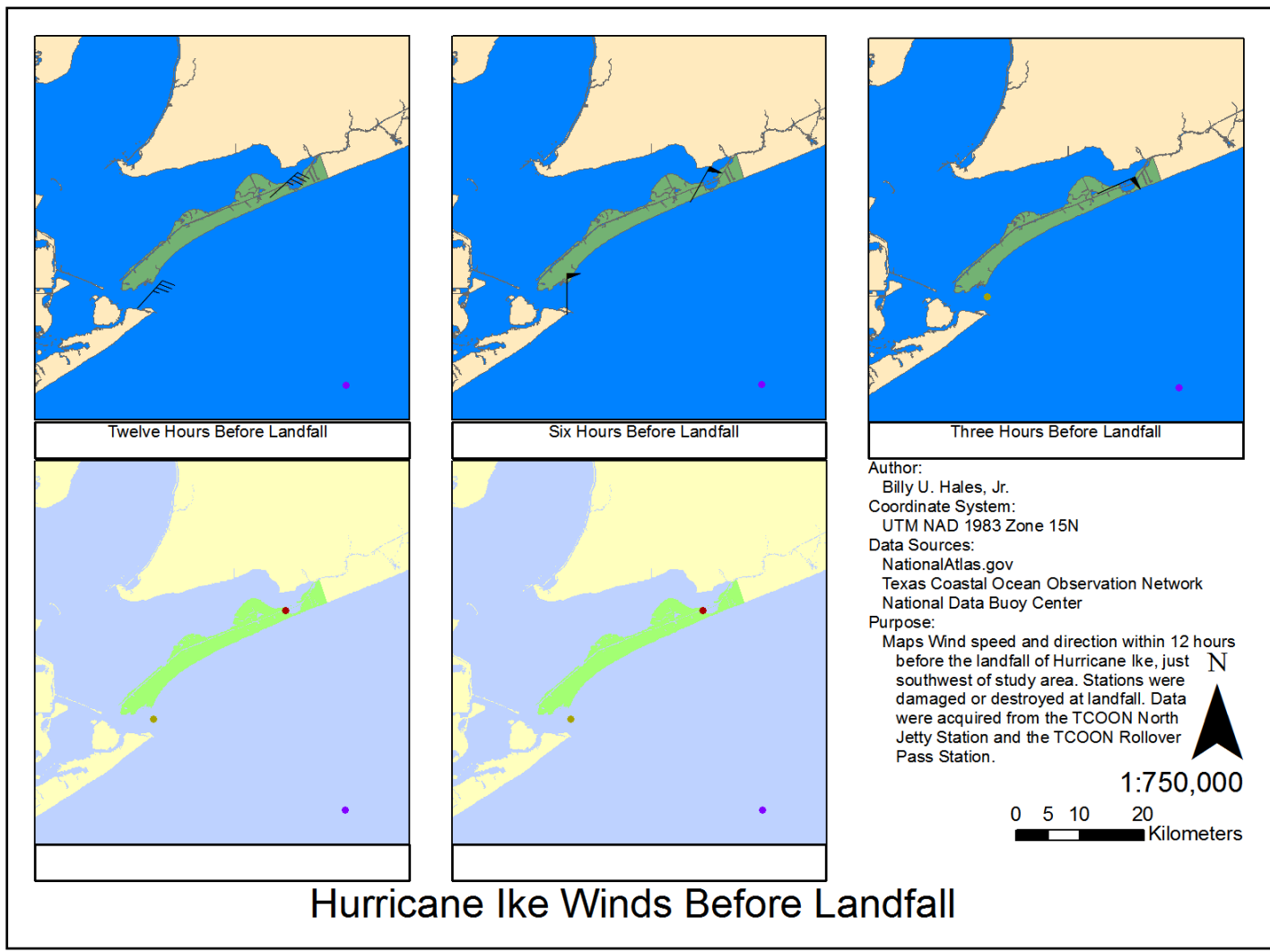


Figure 2.16. Wind speeds and directions within a 12 hour window around the landfall of Hurricane Ike. Landfall and post-landfall observations were not possible because of the stations being destroyed or damaged by the high waves and wind.

Bolivar peninsula had very little to offer in terms of protection from Ike's incoming storm surge (Doran, 2009). This is largely because the natural dune protection was severely compromised because of erosion resulting from Tropical Storms Josephine and Frances (Gibeaut, Gutierrez, and Hepner, 2002). It has also been shown that a great contributor to the damage on Bolivar peninsula was the storm-related ebb flow that occurred after Hurricane Ike had passed over Galveston Bay (Potts, 2010). Bolivar Peninsula, upon the aftermath of Hurricane Ike, was devastated by inundation, (Figure 2.17).

Table 2.1. Configuration of storms included in this study. Symbols Indicate Data Origin

Storm Name	Side of Storm	Distance from Eye (km)	Wind Speed (m/s)*	Wave Height (m)**	Storm Surge (m)***
Josephine	Left	483	12.5	3.27	0.6
Fay	Right	241	12.8	3.48	0.9
Rita	Left	100	12.5	2.3	0.1
Ike***	Right	Direct Impact	27.9	4.9	3.5

* - National Data Buoy Center, at landfall

** - Texas Coastal Ocean Observation Network, at landfall

*** - NOAA Tidal Data

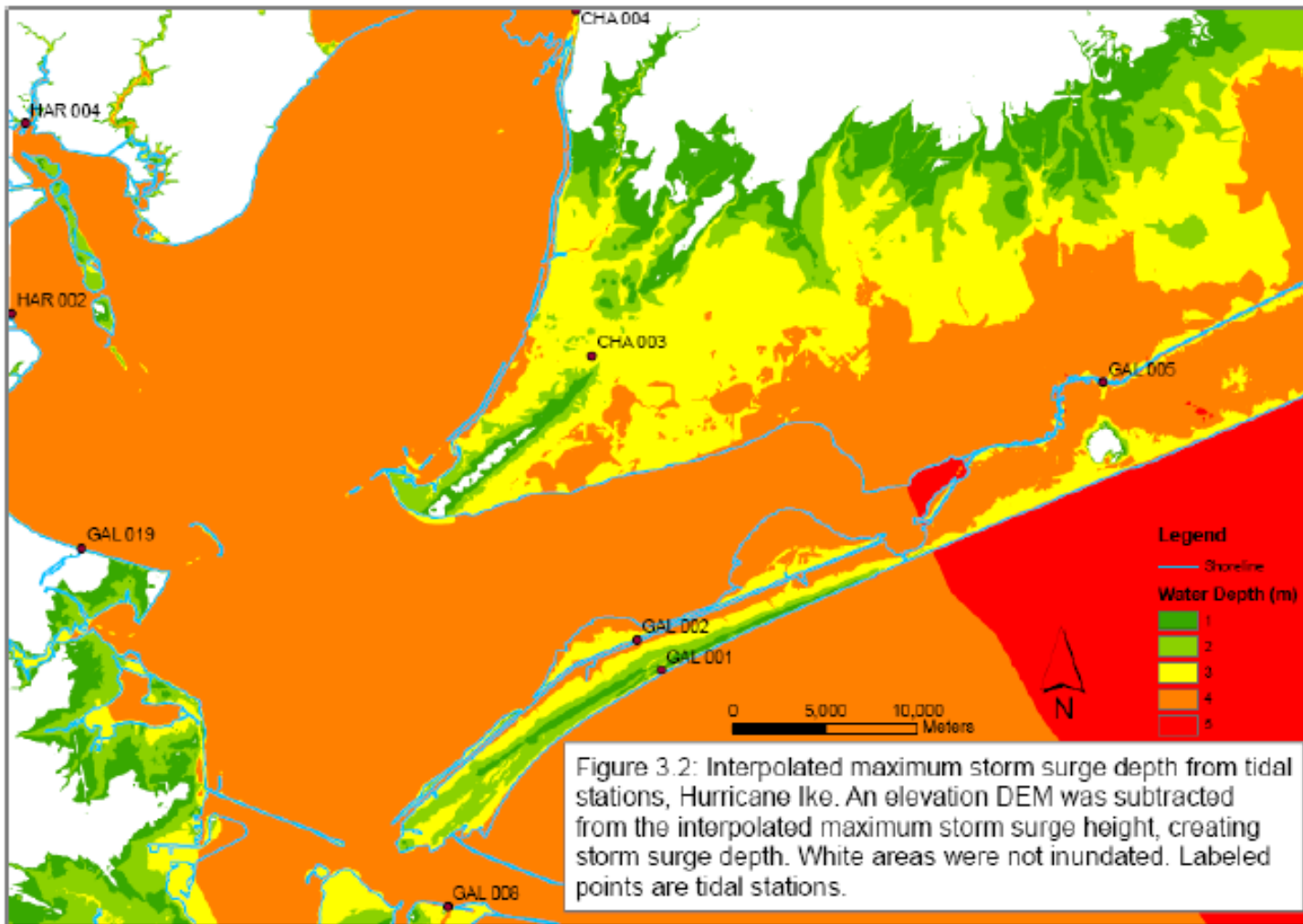


Figure 2.17. Interpolated inundation map that occurred as a result of the Hurricane Ike storm surge. Only white areas were not inundated. (Potts 2010)

CHAPTER III

DATA AND METHODS

Data Availability

This research will examine the geomorphic impacts of four storms on Bolivar Peninsula, TX. Three storms will be analyzed using LiDAR-derived digital elevation models. For these events, shorelines change patterns and volumetric change patterns will be examined. For Tropical Storm Josephine, other data sources are utilized, as no LiDAR data are available. Data availability is shown in Table 3.1.

LiDAR Remote Sensing

LiDAR is a form of active remote sensing that utilizes the timings of signal returns from infrared or blue/green laser pulses to infer surface elevation (Wehr and Lohr, 1999). From a typical LiDAR mission, two products are derived, multiple-return elevation data and laser intensity image (Wehr and Lohr, 1999). Most LiDAR data in this project are collected with an ALTM 1225 LiDAR sensor mounted on a small aircraft, such as a Cessna Stationaire 206 that was featured in Gibeaut *et al.* (2008).

Most LiDAR acquisition systems consist of a sensor, inertial measurement unit (IMU), and a differential GPS (Jensen, 2007). The sensor emits a laser pulse at a given frequency, and the timing between emittance and return can be used to infer distance from the equation (3.1)

$$R = \frac{1}{2}tc \tag{3.1}$$

where R is the range (distance) and t is the time differential between emittance and return, and c is the speed of light (Jensen, 2007). This range, or distance, can then be combined with aircraft attitude and geographic position to infer elevation.

Table 3.1. *Table of storm events, data availability, and what analyses are performed to establish patterns for these events.*

Storm Event	Pre and Post Event Acquisition	Pre;Post Event Data Form	Source	Analyses Performed
T.S. Josephine	09-1997;11-1997	Graph	Gibeaut, Gutierrez, & Hepner (2002)	Volume
T.S. Fay	08-2002;09-2002	LiDAR;	BEG;	Shoreline;
		LiDAR	BEG	Volume
H. Rita	08-2005;10-2005	LiDAR;	BEG;	Shoreline;
		LiDAR	BEG	Volume
H. Ike	July 2006;09-2008	LiDAR;	BEG;	Shoreline;
		LiDAR	USGS	Volume

The IMU allows the analyst to visualize the precise attitude of the aircraft during data acquisition. Terms used to describe attitude include roll, pitch, and yaw. Considering that coordinate axis ‘x’ represents the flight path, ‘y’ is perpendicular to the flight path, and ‘z’ represents elevation above ground, roll, pitch, and yaw can be used describe the relative rotation of an object on the three major axes, x,y, and z, respectively (Wehr and Lohr, 1999). The differential GPS (DGPS) component of a typical LiDAR data acquisition allows the analyst to resolve where in geographic space this mass of elevation values has relevance (Sallenger *et al.* 2001). Using a differentially corrected geographic positioning system that has stations within a certain range of the flight path, accurate ground location can be achieved in LiDAR missions (Sallenger *et al.*, 2001).

All three components, the sensor, IMU, and DGPS, interact to allow coastal investigators to derive a mass of elevation points that are geometrically and geographically accurate.

LiDAR elevation data for the purpose of measuring the impacts of coastal storms can have multiple returns. These returns are used to discern different layers or elevations at which surface features are detected (Jensen, 2007). A return is numbered based on the order upon which it returns to the sensor (Figure 3.1). Typically, the first return implies the top elevation and the last return implies the bottom elevation (Jensen, 2007).

An example of this usage of multiple returns can be described in terms of vegetation stand detection—multiple returns can help vegetation scientists visualize different stands of vegetation at the multiple elevations in the same horizontal location, (Figure 3.1) (Wehr and Lohr, 1999). LiDAR points are typically irregularly spaced (Figure 3.2). The irregularly spaced points are often interpolated into an elevation grid so as to fit the tessellated model of a raster (Jensen, 2005).

Datasets

This project deals with change detection between LiDAR elevations before and after coastal storms. LiDAR elevation can be provided in LAS Binary Point Data, ASCII XYZ data, and ArcINFO GRID format. LiDAR datasets used in this study are in the form of ArcINFO GRID format, obtained from the Bureau of Economic Geology (BEG), the NOAA Coastal Services Center (CSC), and the United States Geological Survey (USGS). These datasets were acquired before and after Hurricanes Ike, Rita, and Tropical Storm Fay (Table 3.1). Sallenger *et al.* (2003) noted that that it is critical that

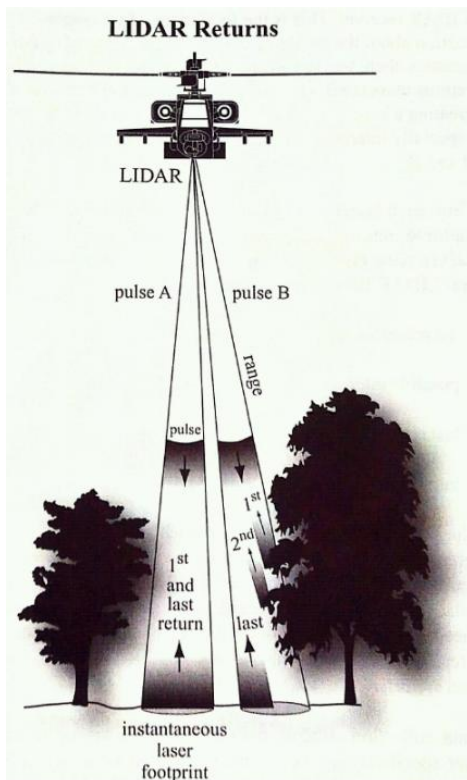


Figure 3.1. Depiction of the multiple returns depicted in LiDAR data. (Jensen, 2007)

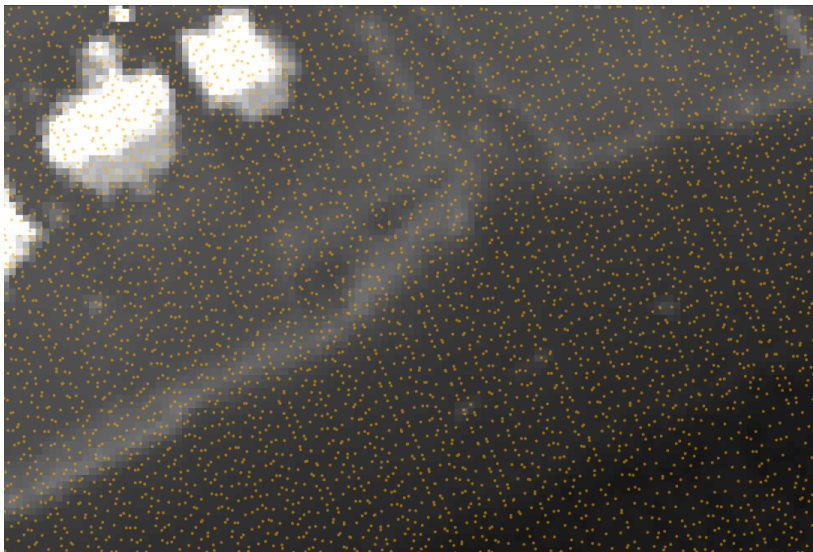


Figure 3.2. Point spacing and layout of original LiDAR point data on top of the IDW interpolated grid derived from the July 2006 dataset.

post-storm event LiDAR imagery be taken as soon as possible after the landfall and dissipation of a coastal storm.

Table 3.2. *LiDAR data format and sources.*

Time Acquired	Format	Resolution	Acquired From	Status
August 2002	GRID	1 meter	BEG	Baseline
September 2002	LAS	Variable	CSC	Post-Fay
August 2005	GRID	1 meter	BEG	Baseline
October 2005	GRID	1 meter	BEG	Post-Rita
July 2006	LAS	Variable	BEG	Baseline
September 2008	GRID	5 meters	USGS	Post-Ike

Elevations in all datasets are vertically referenced to the North American Vertical Datum of 1988 (NAVD 88). All datasets except the September 2008 dataset use the Universal Transverse Mercator (UTM) coordinate system with the North American Datum of 1983 (NAD 83) as the coordinate system datum. The September 2008 dataset originally had the ITRF 2000 coordinate system, and had to translated to WGS 1984 and then to UTM NAD 1983. Post-Ike LiDAR elevation was visually checked for correct alignment with the July 2006 dataset, and it matched all targets—which consisted of buildings and roads.

Shoreline Extraction Methods

To extract shorelines from LiDAR imagery, a set of shoreline feature extraction tools were developed and based on the ArcObjects and Microsoft Visual Studio.NET development environment. In particular, a set of Visual C++.NET-developed dynamically linked libraries (DLLs) with a common graphical user interface (GUI) were developed by Liu *et al.* (2011). These tools involve four major phases of shoreline extraction which are data processing, land/water object segmentation, noise reduction; and boundary tracing and vectorization.

Data Processing

Data processing consists of LAS Data Preparation and LiDAR co-registration with a common datum/dataset.

LAS Data Preparation

Binary LAS data are first converted into three-dimensional ArcView multipoint shapefiles via the LASToMultiPoint tool in ArcGIS® Desktop. The nominal spacing for these multipoint data was set to 0.25 meters such that the most detail was retained in the output multipoint shapefile. Once vector point data is available, as shown in Figure 3.2, this data is interpolated into a grid with an Inverse Distance Weighted approach. The proper parameters for interpolation used a minimum of 3 points, a power value of 1, and a radius of 1.5 meters. This was done to simulate an algorithm performed by the BEG to generate other LiDAR-derived digital elevation models (John Andrews, pers. comm.).

The 2006 baseline dataset had been resampled to five meters using Bilinear Interpolation. This is necessary because the post-storm data for Hurricane Ike are five meters in resolution. Datasets with multiple resolutions should be resampled to the coarsest resolution in order to avoid issues with accuracy and oversampling of data (Jensen, 2007).

There were also significant issues with the post-Rita LiDAR dataset. This issue was with wave-generated noise near the shoreline. This problem was largely ameliorated by usage the ArcGIS Desktop 9.3.1 FocalMin procedure. This procedure involved rotating a 1:5:000 region such that the perspective was shore-parallel. After rotating, a 5 x 1 focal window was used, and only the minimum value was recorded. This procedure was conducted on the observation that there were bands from two different levels of water present in the imagery.

LiDAR Co-Registration

It was demonstrated in Sallenger *et al.* (2001) that there is a need to co-register multi-temporal LiDAR data acquired before and after a storm event. This step is necessary to eliminate systematic error between the two datasets. For this research, all LiDAR datasets were registered to a dataset acquired in December 2008 by the Bureau of Economic Geology. This dataset provided the greatest detail of damage after Hurricane Ike. Based on the greatest detail and extent of damage, the December 2008 dataset would be the most restrictive in terms of finding suitable areas for this coregistration. Rigorous correction for systematic error is based on the same persistent features, which could be used to register all datasets. The features selected for co-

registration are termed as pseudo-invariant features (PIFs) (Liu, Sherman, and Gu, 2007; Liu *et al.*, 2011).

PIFs are features that do not have much vertical or horizontal change between the acquisitions of two different datasets (Liu, Sherman, and Gu, 2007). These features often consist of roads and parking lots, (Figure 3.3). Thus, PIFs were manually identified from hill-shaded image of LIDAR DEMs and stored in ArcView shapefile format.

One problem encountered in the usage of roads as PIFs were extreme elevation changes caused by cars, trucks, and unforeseen storm impacts. This was addressed through the usage of alpha-trimmed means (Liu *et al.*, accepted). This approach looks at a histogram of data, and removes a certain percent threshold of values from the tails of that distribution (Figure 3.4). The alpha-trimmed means approach was originally undertaken using two Python scripts, LidarStatCalc and LidarMaskPy, in Appendix A.

These routines/scripts use the ArcToolbox® raster ‘clip’ function to clip out the PIFs from both LiDAR datasets. From these clips, a difference is found between the December 2008 dataset and the other datasets to be co-registered using the ArcToolbox® ‘minus’ function. From these differences, a histogram is generated, and then 2.5% of each ‘tail’ is removed—leaving 95% of data (Liu *et al.*, accepted).

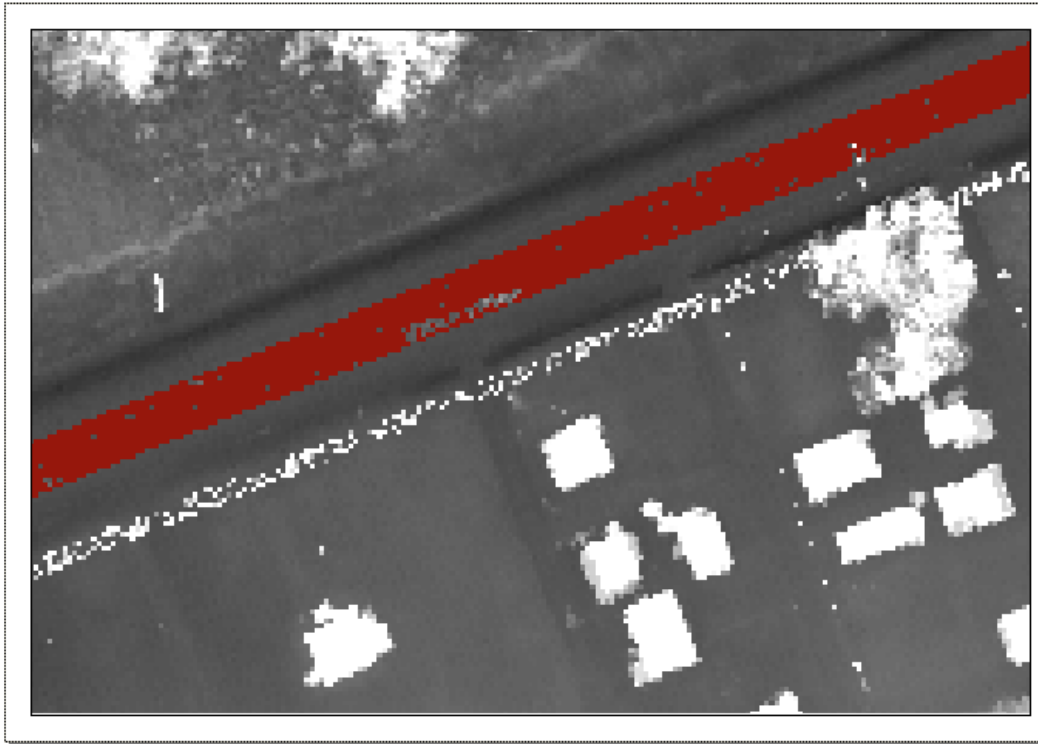


Figure 3.3. Scene from FP_SE quadrangle from post-Rita dataset. The maroon color depicts a PIF that has had the alpha portion trimmed. Notice the blank space in the maroon near the middle of the image. That blank space is most likely a car.

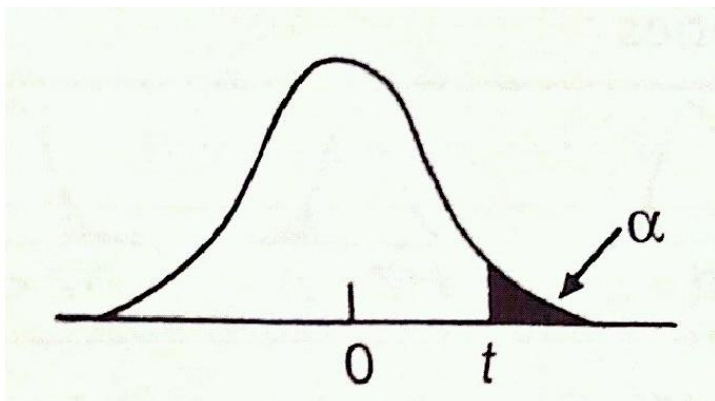


Figure 3.4. Alpha portion (tail) of a normal distribution (Burt, Barber, and Rigby, 2009).

As a result, extreme values are purged from the PIF differences, and a mean is calculated for each quadrangle present in the imagery. Means are calculated from these differences and recorded, as shown in Appendix B. These recorded means are then put in a weighted average scheme such that,

$$E_s = \frac{1}{2}\mu_p L + \frac{1}{2}\mu_p P . \quad (3.2)$$

In equation (3.2), ‘ E_s ’ describes systematic error between LiDAR datasets, ‘ μ_p ’ describes means of difference between LiDAR datasets for each quadrangle, ‘ L ’ describes the fractional length that quadrangle contributes to the shoreline, and P describes the fractional number of pixels that differences in PIFs for that quadrangle contribute to the entire dataset. This equation makes the statement that equally important quadrangles can cover a large geographic and constrained by few PIFs or with many PIFs and constrained by small geographic area.

One systematic difference value between each dataset, the result of this weighting scheme, was considered, Appendix B. This constraint stems from the observation that these datasets are continuous and a different mean correction for each quadrangle would enforce a discontinuity between them. Such discontinuities in dataset corrections or registrations would result in a shoreline with obvious geometric discontinuities.

Land/Water Object Segmentation

Using an object-oriented methodology, it is possible to abstract a coastal environment into two fundamental types of objects, land and water. Methods that

support this delineation of land and water objects largely depend on the type of data being analyzed. Algorithms from Liu *et al.* (2011) demonstrate how this segmentation can be accomplished for LiDAR Elevation data through tidal datum segmentation.

The tidal datum segmentation method has a straight-forward theoretical foundation and consists of simple steps. First, a tidal datum is acquired from a tidal station, Galveston Pleasure Pier in my analysis. Then, a LiDAR elevation raster representing the coastal geomorphology of my study area is segmented into land and water objects based on whether it falls above or below that tidal datum. Land objects are above the tidal datum value, and water objects are below the tidal datum value (Liu *et al.*, 2011). The result of this object extraction is a binary image that has the value '0' representing water and '255' representing land, an example in Figure 3.5.

Using an actual tidal datum to segment the land and water objects is the most reliable in determining the actual shoreline of a coastal feature. This is because aerial photography or satellite imagery is limited to analysis of the presence of the water line (Liu, Sherman, and Gu, 2007). Since the water line varies with tide and climatic conditions throughout the day, this line is prone to movement and can't adequately approximate a more temporally valid shoreline (Liu *et al.*, 2011). Therefore, segmentation of land and water objects via tidal datum is less temporally sensitive. This is because tidal datums are actually averaged water levels over a 19-year period, the tidal

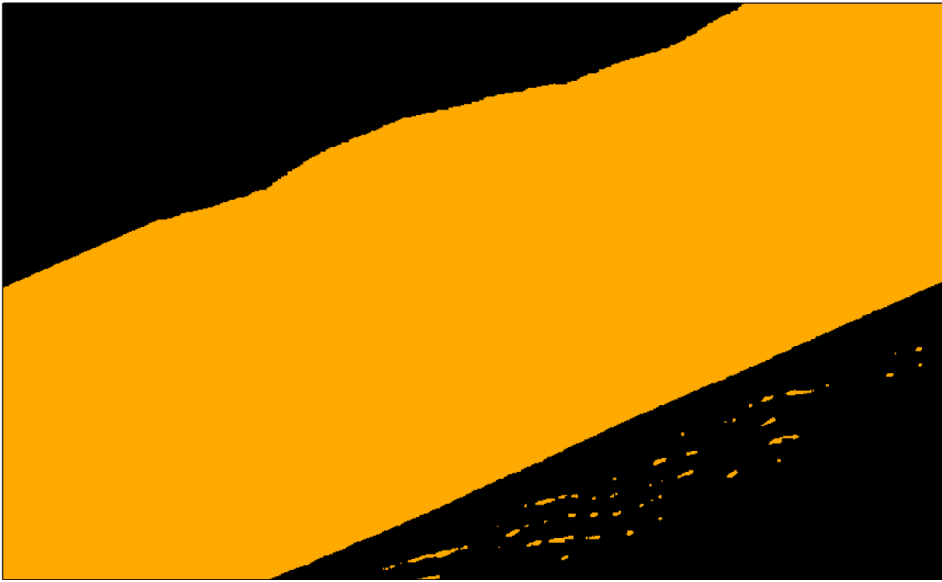


Figure 3.5. Initial results of the object oriented land-water image segmentation. Black would be water and orange would be land.

epoch (Liu, Sherman, and Gu, 2007). The tidal datum used in this study was acquired from the NOAA Pleasure Pier Station (NOAA, 2011) at 0.377 meters above North American Vertical Datum of 1988.

Noise Reduction

After land/water object segmentation, the data often are characterized by very uneven boundaries and holes of variable sizes within each of the objects. Generally, these are considered artifacts in the data and are undesirable (Liu *et al.*, 2011). Noise reduction allows for the filling in of many of these holes and to make the boundaries more smooth. Two tools were developed in Liu *et al.* (2010) and Liu *et al.* (2011), the morphology operator and the spurious object removal tool.

Morphology Operator

After a binary image that represents land and water is generated from the tidal datum intersection method, there is a need to smooth the jagged/noisy edges of the raw shoreline. This can be accomplished with the Morphology Operator (Liu *et al.*, 2011). This operation has two major commands, dilate and erode. The dilate command, ‘d’, recursively adds outer pixels to the edges of a user-specified object by one pixel, and the erode command, ‘e’, recursively reduces the bounds of the outer edge of the given object by one pixel (Liu *et al.*, 2011). Both commands recursively manipulate edge pixels with vertical and horizontal—and not diagonal—connectivity considered. These two commands can be used to eliminate small scale abnormalities/noise and smooth out abnormal jagged edges. Two ancillary commands are the trim and fill commands. With fill, the user can eliminate small one-pixel objects and with trim the user can eliminate small one-pixel dangling objects from the boundary between two different objects (Liu *et al.*, 2011). Commands on these datasets generally consisted of ‘ddeetf’, which means that the features on this image are dilated twice, eroded twice, and then have the trim and fill operations done to them. This results in a smooth shoreline—as detailed in Figure 3.6.



Figure 3.6. Before (top) and after (bottom) captions of the smoothing effect that Morphology Operator has on a shoreline.

Spurious Object Removal

After the Morphology operation, relatively small and spurious features are removed (Liu *et al.*, 2011). This involves the user specifying threshold number of pixels that determine the maximum size of spurious objects. For this study, both land and water objects had spurious objects removed, and the threshold was generally 1000 pixels with pixel resolution of one meter and 40 pixels for datasets with pixel resolution of five meters. This process is demonstrated in Figure 3.7.

Boundary Tracing and Vectorization

Recognizing that the shoreline is the boundary between water and land, a moving window algorithm is employed to derive a binary image in which only borders are considered, as in Liu *et al.* (2011). The two objects in this image are borders and non-borders, as shown in Figure 3.8. The determination of borders and non-borders is made by comparing the focus or center of this roving window to its vertical and horizontal outside members. If one or more pixels are different than the focus, then the pixel is considered a boundary pixel (Liu *et al.*, 2011).

Vector Shoreline Corrections

Despite the intended effects of the morphology operator and the spurious object removal algorithm, there are still noise and topological imperfections in the shoreline data. Raw shoreline data typically have spurious objects that contain more pixels than the threshold of the spurious object removal algorithm, dangles—that are small protrusions which stick out of a vector shoreline, and small box-like artifacts that are generated from thin linear features. To address these problems, four different procedures

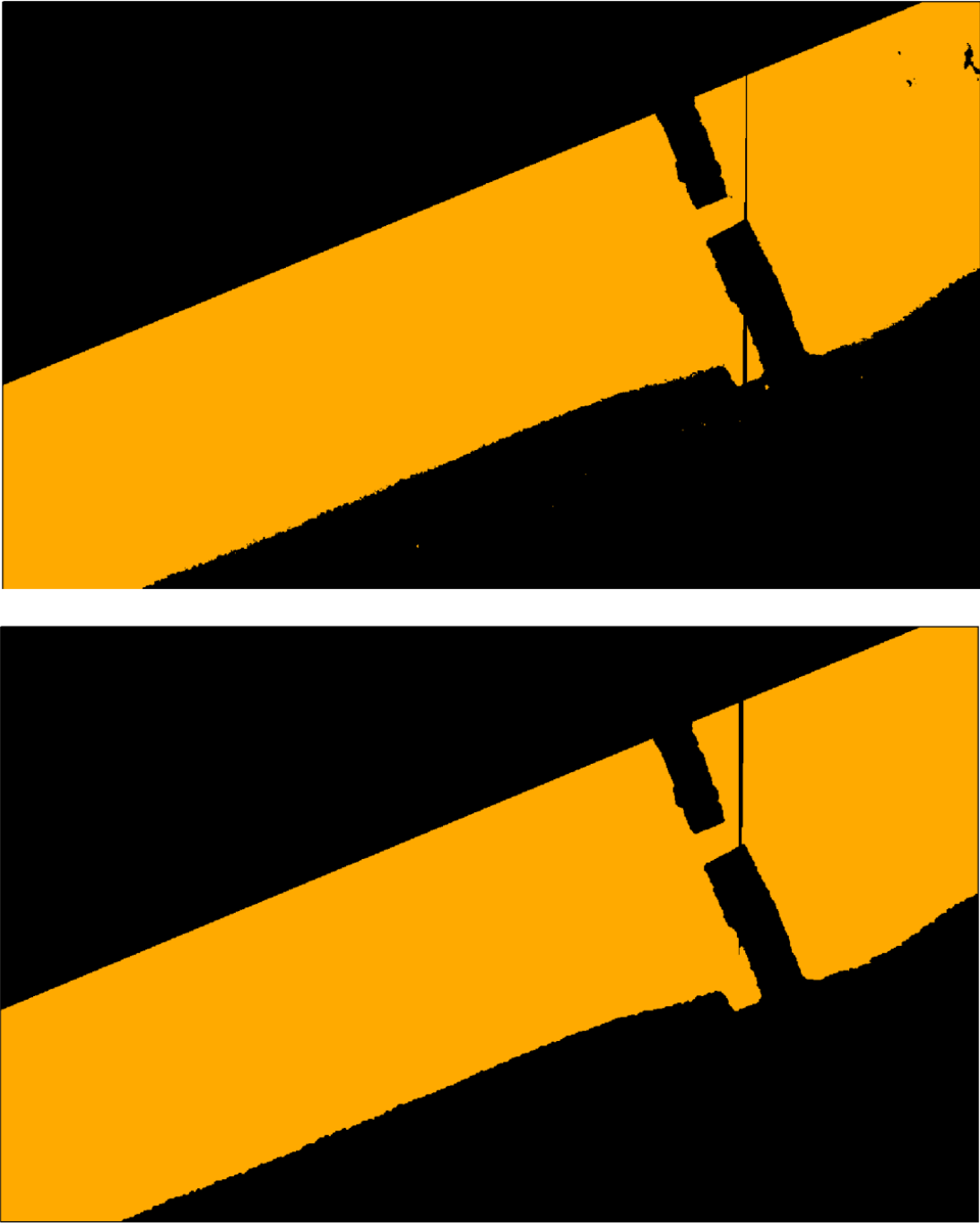


Figure 3.7. Before (top) and after (bottom) captions depicting the removal of spurious objects.

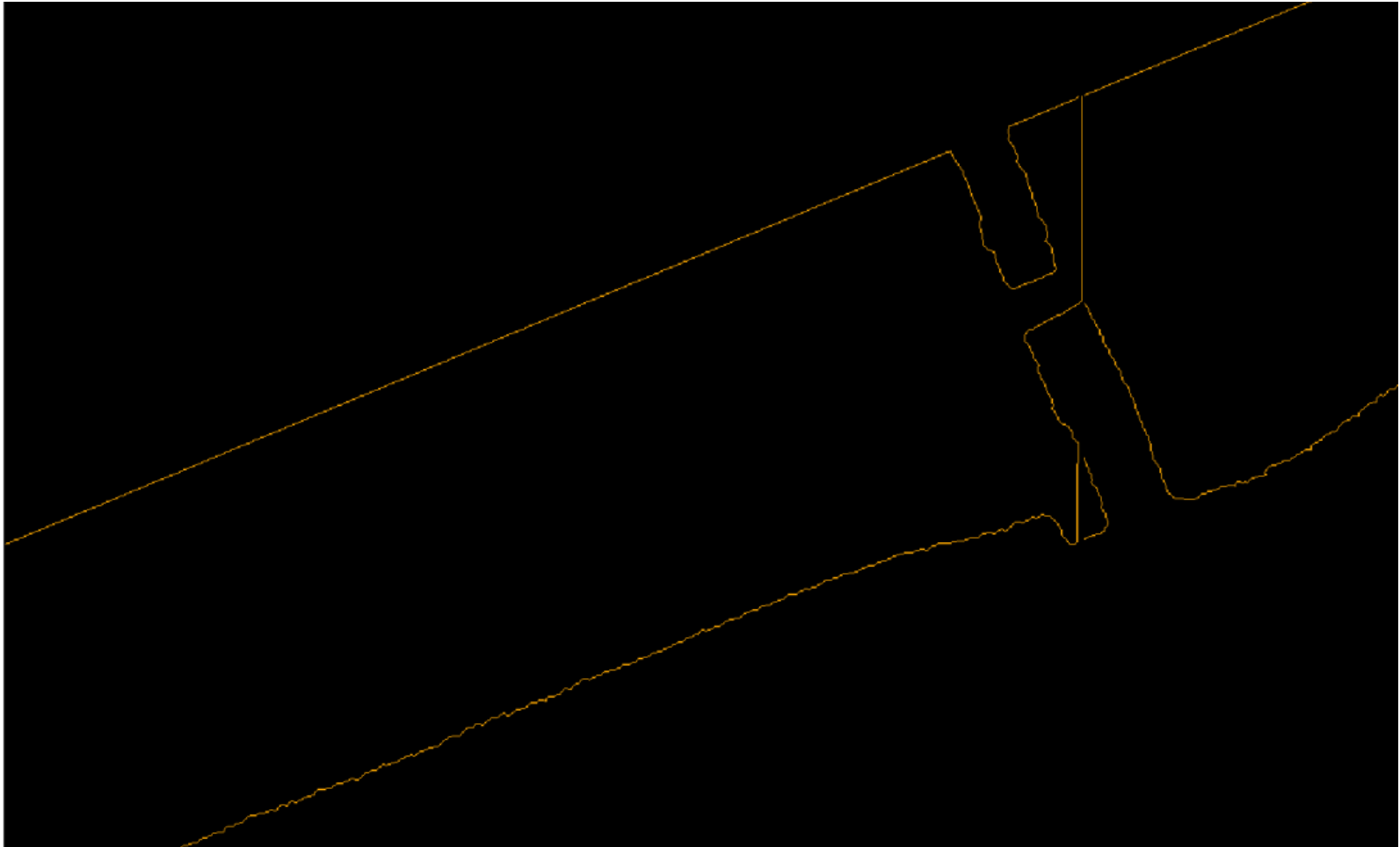


Figure 3.8. Raster polylines before vectorization. Orange denotes border pixels and black denotes non-border pixels.

of vector shoreline correction and smoothing are implemented. These are considered ‘levels’ of correction, and all shorelines begin with a ‘L1’ to ‘L4’ designation to indicate the level of correction that has taken place.

Level One Corrections

Shorelines emerge from coastal imagery in the form of a loop. This loop consists of the bounds of the image on three sides and the actual shoreline on one side. There is inherent advantage in this structure because of the way that ArcGIS® organizes vector polylines.

ArcGIS® organizes vector polylines such that lines are bounded by special vertices termed ‘nodes’ (Price, 2006) on the ends of these lines (Figure 3.9) and at intersections of lines. A loop structure has one set of nodes that denotes the end and beginning of that line. This makes all other nodes automatically indicative of a topological error—since shorelines are continuous lines that denote the bounds of water and land (Liu, Sherman, and Gu, 2007).

The goal of level one corrections is to ensure that all ‘loops’ for each image are closed. Open loops have two nodes—as all other lines do. This makes obviating all other nodes as topological errors a harder task in the next levels of correction. When an open loop is discovered, that loop is closed using the ‘merge’ function in the ArcMap® ‘Editor’ extension.

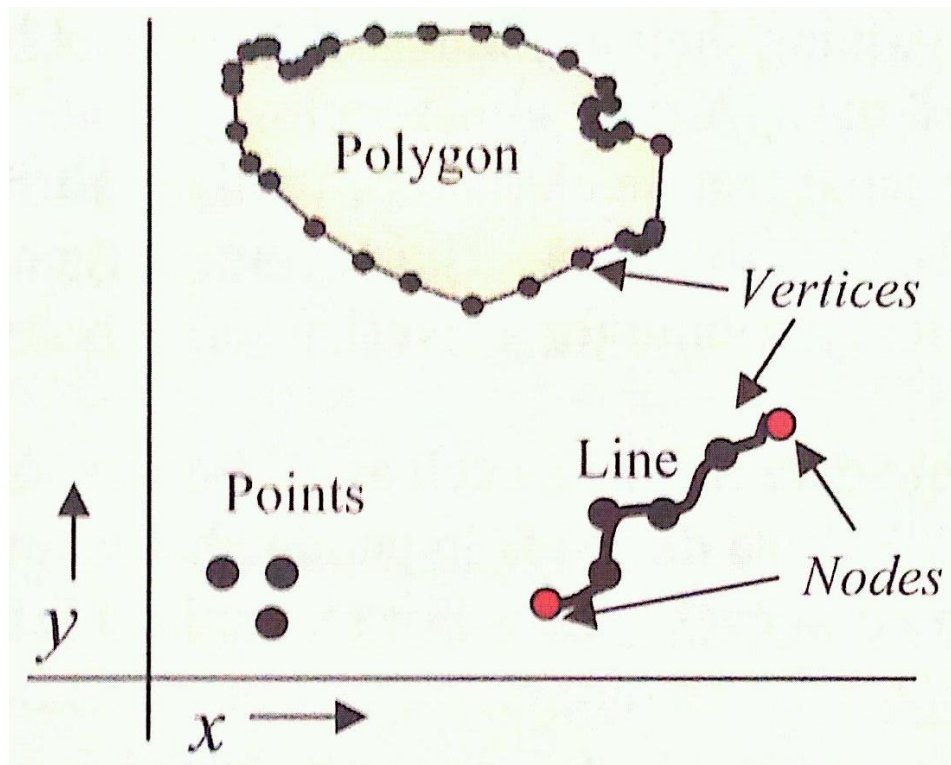


Figure 3.9. Figure from Price (2006) that shows how a line is defined by two nodes and vertices that bound the line.

Level Two Corrections

Level two corrections build upon previous corrections by using these loops as a means of checking topology (Figure 3.10). This is facilitated with the “Check Topology” tool in ArcGIS® Desktop. The first step is to establish a personal geodatabase from all vector loops generated from the segmented LiDAR imagery. This is necessary because shapefiles—the output of the boundary tracing and Vectorization algorithm, represent the spaghetti data model and do not have the ability to scrutinize topology (Demers, 2005).

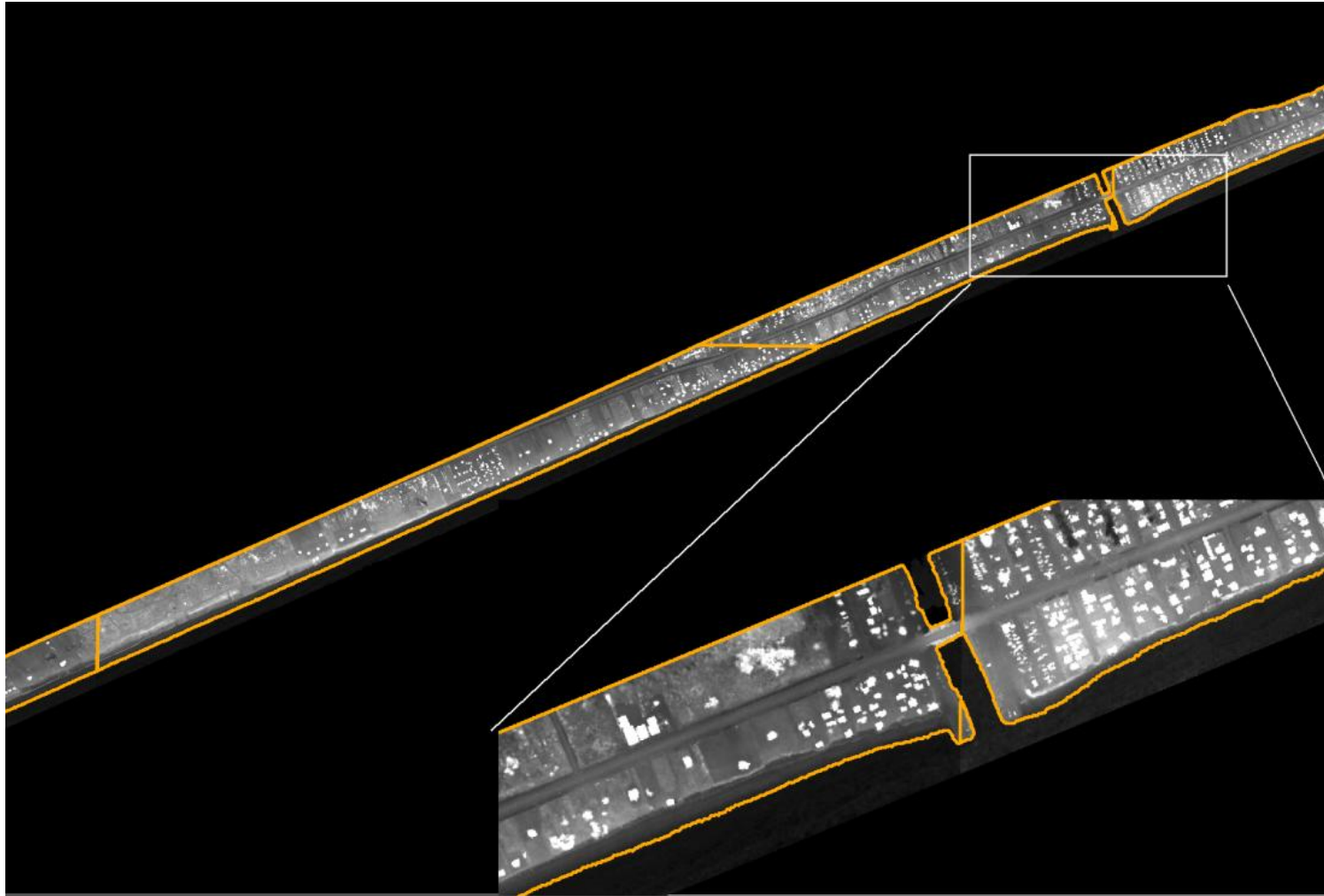


Figure 3.10. An example of the 'loop' structure found in vector shorelines that result from level two corrections. Lower left enhanced zoom is to show the non-shoreline side of the loop representing the southeast portion of the Frozen Point quadrangle and the shoreline sides of that and another loop-quadrangle.

Topological errors fall into several categories. Specifically, the topological errors of interest are known as ‘dangles’. Dangles are single line protrusions that are the result of an overshoot, undershoot, or failure to properly connect a line to its intended target (Demers, 2005). For the purpose of shoreline extraction, all dangles are considered errors, and they are removed. The goal of level two corrections is to eliminate all dangle topological errors. Examples of dangles are shown in Figure 3.11.

Level Three Corrections

Most of the corrections are made at level three. Level three corrections are broken into three main phases. The first phase is to merge all the shoreline extraction results for each quadrangle from step two using the ‘merge’ command from the ‘Data Management’ ArcToolbox. After merging these results from Level Two Corrections, the loops will have three of their non shore-facing sides removed to leave a vector shoreline.

The second phase is to ensure that the shoreline is topologically sound. The second phase takes advantage of the ‘modify feature’ command under the ‘Editor’ extension in ESRI ArcGIS Desktop® (Figure 3.12). This command allows the user to analyze individual features and determine how many vertices are present. Separate features that have few vertices are automatically suspect as being a topological error. Common topological errors involve spurious features of two vertices and box features that have four to five vertices in number.

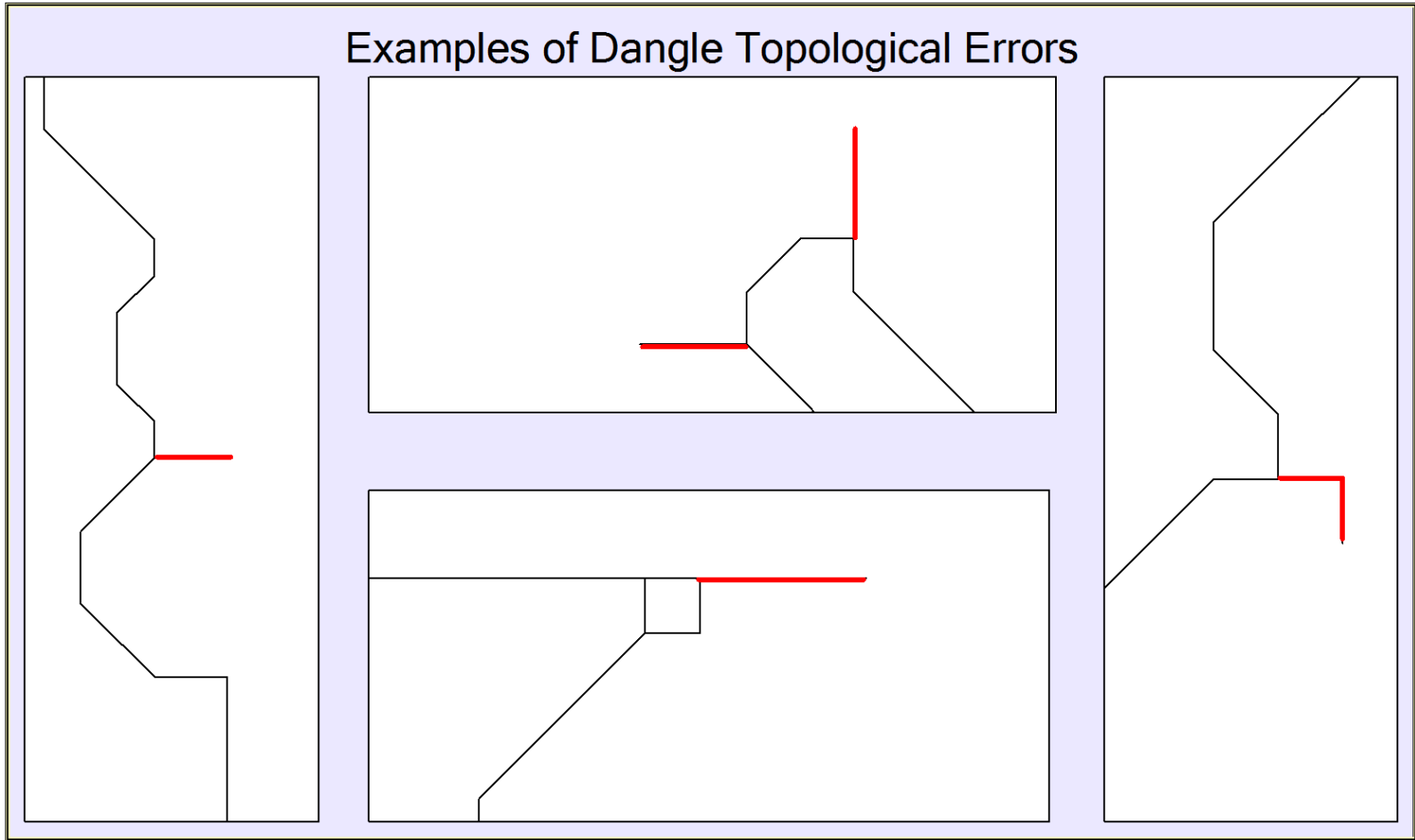


Figure 3.11. Examples of dangle topological errors that are commonly encountered during level two corrections.

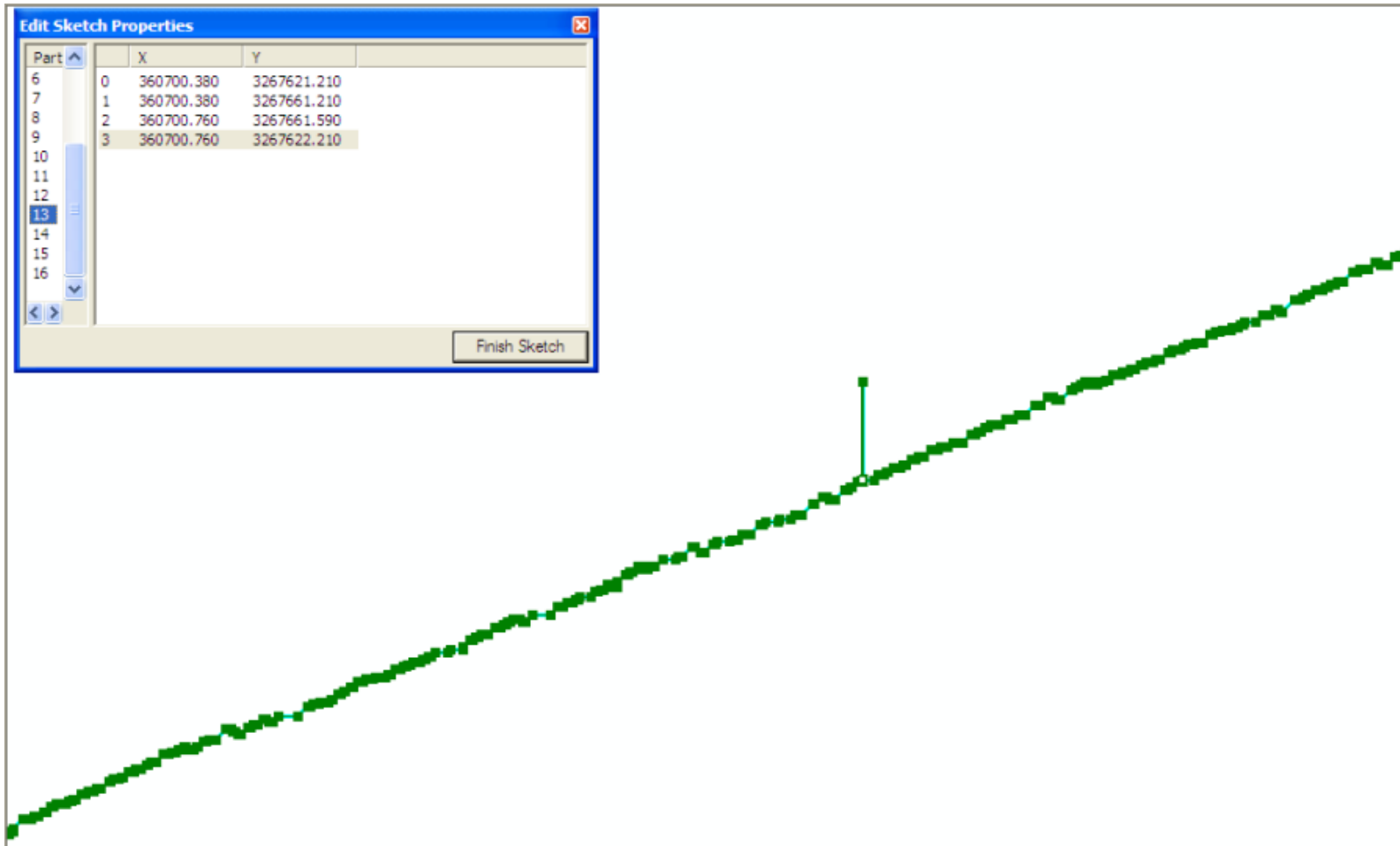


Figure 3.12. An example of using the 'Modify Feature' tool and the 'Sketch Properties' window in ArcGIS Desktop® to find topological errors. Shown is a topological error that resulted from the elimination of non-shoreline sides. This is indicative because there are only 4 vertices on this particular part. Continuous shorelines have thousands of vertices.

If such a feature is found, a correction is made. Corrections often involve the deletion of the erroneous feature or the manual repair of that feature. Once repaired, the features are topologically continuous, and will join automatically. When fully corrected through this phase, shorelines typically contain four to six features that have several thousand vertices each.

The third phase of level three corrections involves the usage of original LiDAR data and aerial photographs to check and validate questionable features. In most cases, original LiDAR data were required for shoreline validation. Aerial photographs were used at times, but this usage of aerial photography are limited because the water line can be distinctly different than the tidal referenced mean high water shoreline derived from LiDAR data (Liu, Sherman, and Gu, 2007).

Level Four Corrections

Level four corrections offer shoreline generalization and even more smoothing to the final shoreline product. Even after morphological smoothing, spurious object removal, manual shoreline corrections and validation, the shoreline itself still has some extra noise and is blocky in appearance. The level four correction process uses the ArcGIS® ‘Smooth Line’ command with the Polynomial Approximation with Exponential Kernel (PAEK) function. This functionality is built into ArcGIS® Desktop, but implemented in the Shoreline Extractor ArcGIS® extension developed by Liu *et al.* (2011).

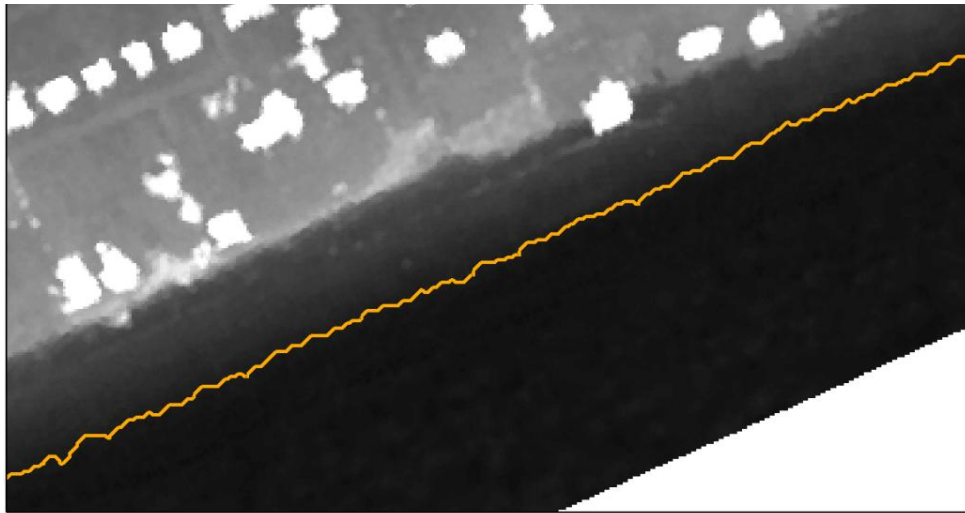
The PAEK function requires a given tolerance in order to smooth the shoreline (ESRI, 2010), and the tolerance used for this work is eight times the resolution of the source imagery. Therefore, shorelines derived from five meter imagery will have a smoothing tolerance of forty meters, and those derived from one meter imagery will have a smoothing tolerance of eight meters. A comparison of the shoreline before and after level four corrections is shown in Figure 3.13.

Shoreline Change Analysis

After two or more shorelines have been obtained, the next step is to calculate linear shoreline change with an algorithm developed by Arias (2003). The linear shoreline change approach used in this work consists of a set of steps to constrain the linear shoreline algorithm in order to generate shore normal linear shoreline differences. When unconstrained, the algorithm outputs unnecessarily erratic and erroneous linear shoreline differences that are not shore-normal.

In order to combat this inadequacy and to ensure that linear shoreline change values are consistent, a decision was made to use shore-normal linear shoreline differences. Despite the opinion of Arias (2003), the topologically constrained method only seems to work on segments of shorelines that have roughly the same length. The greater the difference in length and in the complexity of the base and target shorelines; the greater the angle error in the linear shoreline differences.

To ensure that shoreline differences are shore-normal, the base and target shoreline must be constrained to a length that is approximately equal for both. This task is easy to accomplish for shorelines that are gently changing and not complex. However,



Before the PAEK Function at a Smoothing Tolerance of 8 meters.



After the PAEK Function at a Smoothing Tolerance of 8 meters.

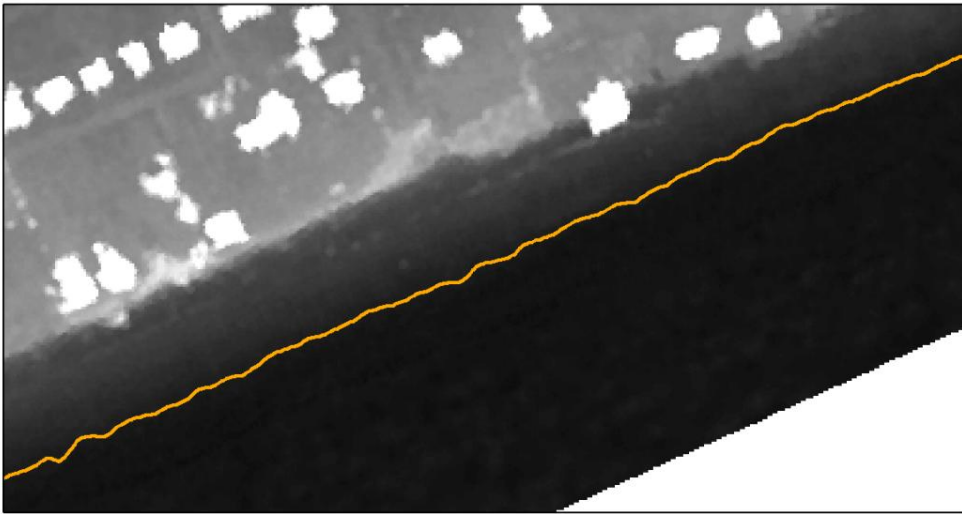


Figure 3.13. Before and after the PAEK smoothing algorithm on a shoreline after level four corrections Image in the background is 1999 NASA LiDAR imagery.

this task is far more difficult with dramatically changing and complex shorelines. To handle these highly complex shoreline change scenarios, a set of procedures reduce the alongshore distance that these shorelines cover. The goal is to reduce the difference in length between these two shorelines.

Setting Up Polygon Constraints

The first step in constraining the shorelines is to generate polygons that act to cut both shorelines to a prescribed shape in order to enforce a set alongshore distance. For this work, the primary goal of this operation is to generate a set of shapefiles that will cut out 100 meter base and target shorelines—as measured from a manually created centerline between both shorelines.

The centerline is constructed by manual inspection and insertion of vertices between both shorelines at a scale of 1:10,000. This center line establishes the position of all constraint polygons for both shorelines and will allow the creation of event features to delimit a 100 meter interval along the shore of the study area.

After a centerline is established, a buffer is generated at a defined distance from the centerline. This buffer will eventually be segmented and used to generate the constraint polygons necessary to enforce an equal-distance constraint. After generating a buffer from the centerline, it is then subjected to dynamic segmentation. Dynamic segmentation allows events, informed by distances along a route feature, to be displayed on any part of that route, rather than at vertices or nodes in the arc-node model used by other linear features (Li, Liu, and Felus, 2001). An example of this is shown in Figure 3.14.

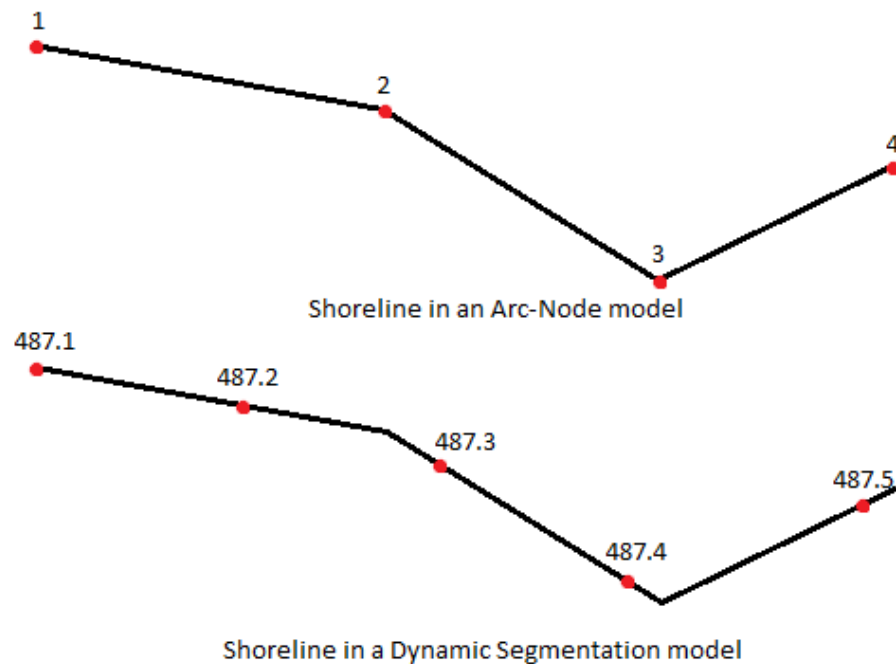


Figure 3.14. Illustration of Dynamic Segmentation as compared to the traditional arc-node model of other linear features. Notice how the ‘events’ in the dynamically segmented model can be at any point on the line, rather than at just nodes or vertices. *adapted from Li, Liu, and Felus (2001)*

The first step in using dynamic segmentation is to establish a route feature—a vector linear dataset that is a component used to obtain measurements and establish locations in dynamic segmentation (Brennan and Harlow, 2004), as shown in Figure 3.15. For this work, the centerline is converted to a route via the ‘Create Route’ feature in ArcGIS® Desktop.

The next step in the dynamic segmentation process is to establish a route event table. The event table specifies discrete points or stretches of a route that have a

particular significance (Brennan and Harlow, 2004). This table specifies the points or routes by provided along-route distances upon which to instantiate the desired features. For this project, the event table specifies the location of points at a single alongshore route at a defined interval of 100 meters, as shown in Figure 3.16. The result of dynamic segmentation in this work is an event layer (Brennan and Harlow, 2004). The event layer specifies the points that represent 100 meter intervals along the centerline.

With event points, it is possible to obtain easting and northing coordinates and an angle normal to the centerline, and to make two sets of points that are at a specified distance normal on both sides of the event points spaced at every 100 meters along the centerline, an example is shown in Figure 3.16. With the user-specified interval of 100 meters, the 'BufferPts' python script will create points at a length of 400 meters normal to the centerline at every event point. These lines will serve to segment the buffer (Figure 3.15). In order for a linear feature to segment a polygon, the 'Construct Features' ArcGIS® Desktop tool must be used. The result is a buffer polygon with cuts at every 100 meters along the centerline.

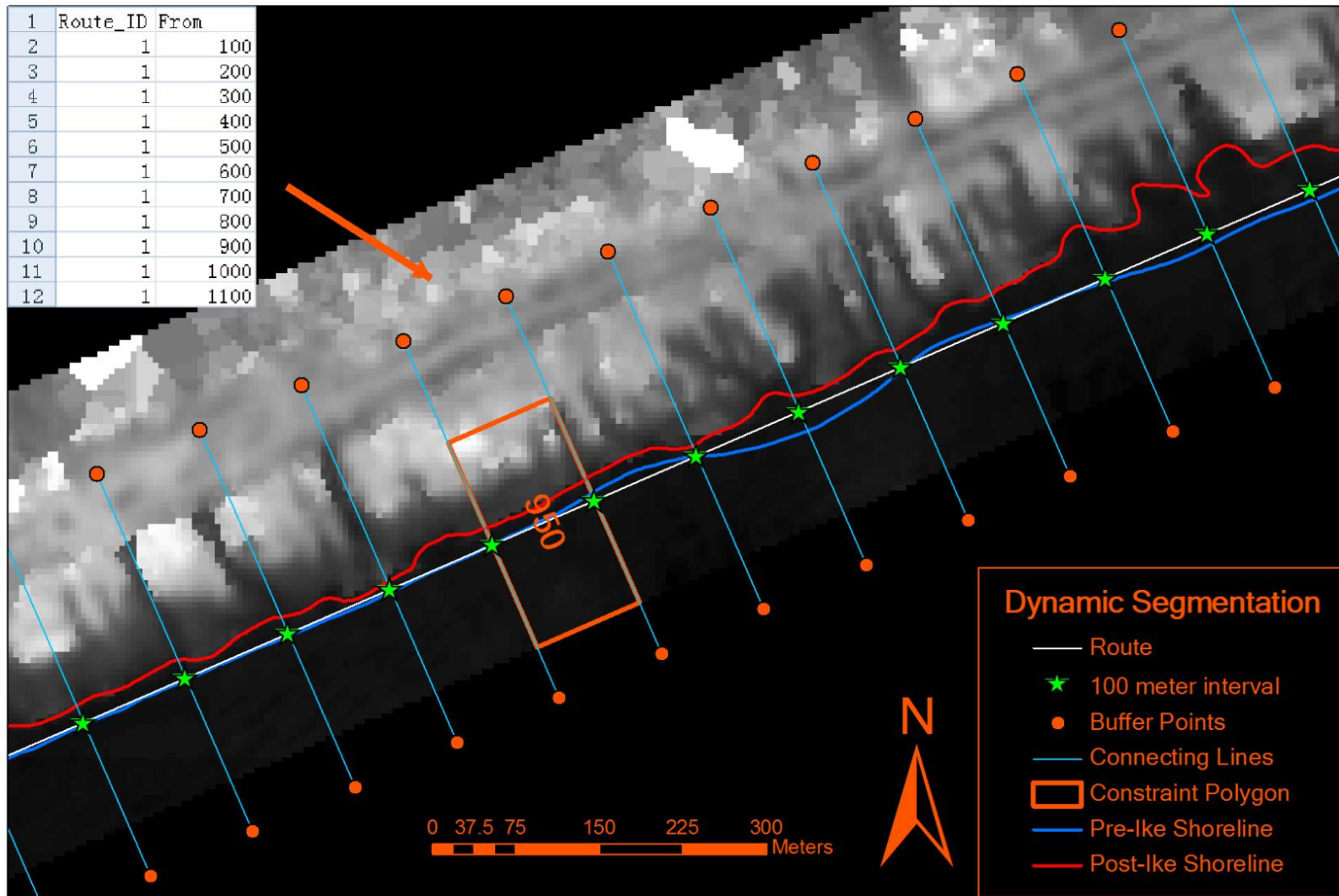


Figure 3.15. An illustration of the dynamic segmentation process for Hurricane Ike shoreline change.

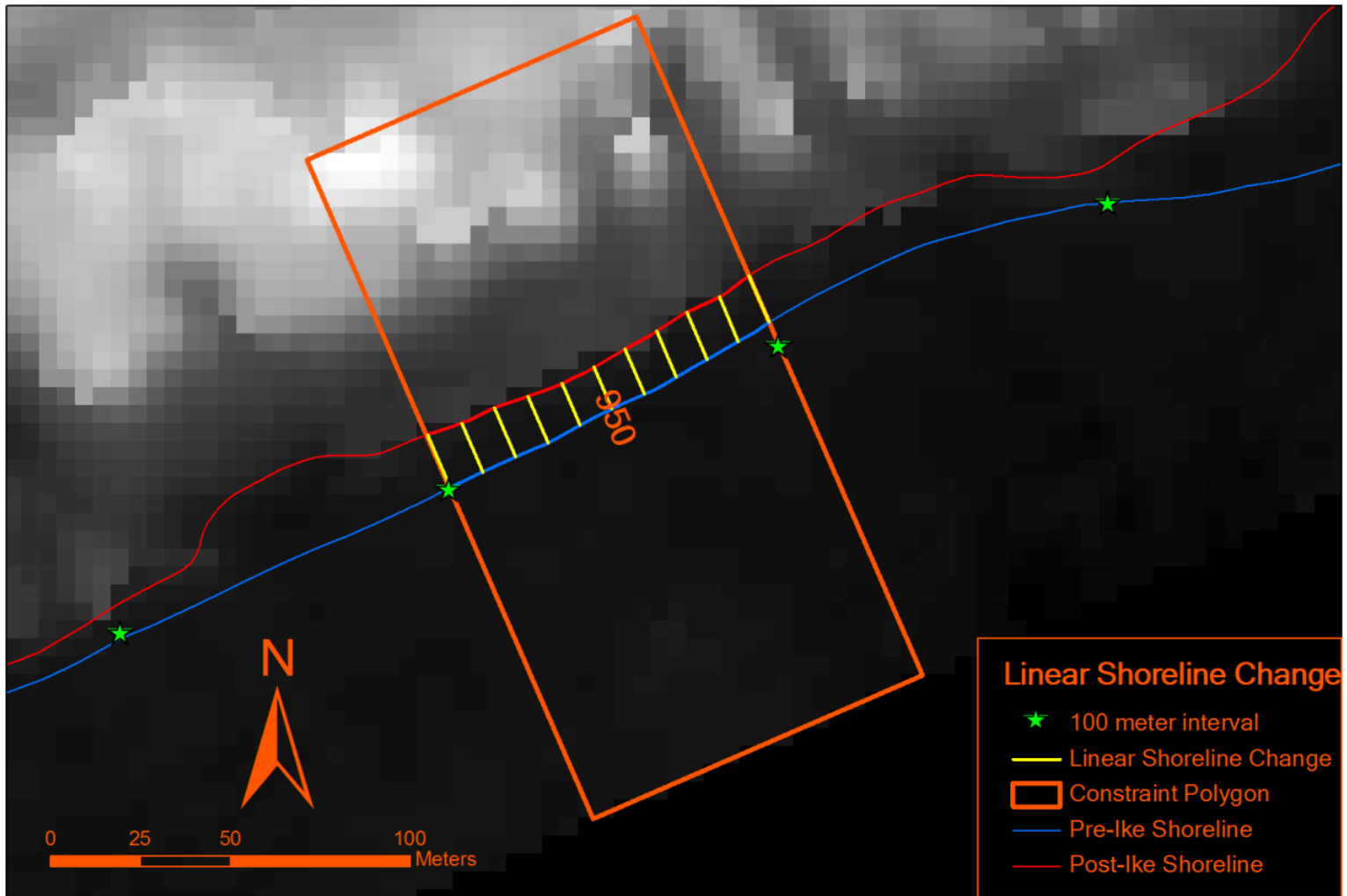


Figure 3.16. Generated linear shoreline change polylines between pre-Ike and post-Ike shorelines. Image in background is that of the USGS-acquired post Hurricane Ike LiDAR dataset near Rollover Pass.

Each cut or ‘piece’ of the buffer polygon is a separate feature. On average, the polygon datasets had about 1300 features within them. These features are then given names with the ArcGIS Desktop® Field Calculator using the command, ‘format([FID] + 1, “####”)’. This command took the numeric feature ID field, a field that is included with all shapefiles, added one to that numeric value, and translated the result to ASCII text in the ‘Name’ field. This resulted in names such as ‘1’ to ‘1300’.

It is possible to separate the constraint polygon dataset into individual polygon shapefiles that have the same name as each ‘name’ for the features previously with the Field Calculator ‘format’ command. With unique names, the ArcGIS® Desktop ‘Split’ command can output a shapefile for each feature that has a unique name. The result of this operation is a directory with many shapefiles that have names like ‘1.shp’ to ‘1300.shp’. The polygon constraints are then ready for 100 meter shoreline segment extraction.

Shoreline Segment Constraint

After all constraint polygon shapefiles are created, the next step is to ensure that both the base pre-storm shoreline and the target post-storm shoreline are facing the same direction. This step is necessary because all polylines features in the ArcView® shapefile scheme have directionality implicit (Price, 2006). To check that these shorelines are indeed going in the same direction, the ‘Modify Feature’ command in the ArcGIS® Desktop Editor extension is used. With this tool, it is possible to see all the constituent vertices in a polyline feature—much like what was illustrated in Figure 3.12.

By a simple visual inspection of the shoreline with the ‘Modify Feature’ extension active, one could identify which direction the shoreline is facing by noticing that the first or leading vertex on a polylines is symbolized as red and the rest are symbolized as green (Figure 3.17). This task is accomplished by ensuring that red vertex is on the same end of both base and target imagery.

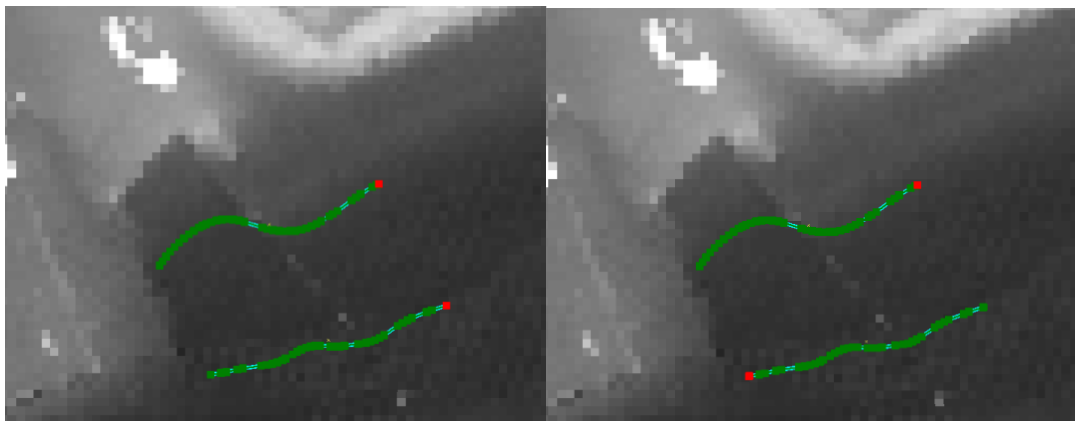


Figure 3.17. Correct orientation for both base and target shorelines (left), and incorrect orientation for both base and target shoreline (right). Image is of LiDAR baseline image taken in May of 2000.

After both shorelines are inspected for co-directionality, the shoreline segments need to be extracted using the constraint polygons. A python script, 'MassFeatClip' was implemented, Appendix A. The 'MassFeatClip' python script, when given the directory where the constraint polygons reside and the base and target shorelines for each storm event, will extract all of the 100 meter coastal segment shapefiles automatically and output them to a specified directory with the user-supplied name of the shoreline as a prefix and the name of the segment as a suffix. An example in the case of section 1000 of post Hurricane Ike shoreline would be 'PostIke_1000.shp'.

After all 100 meter shoreline segments have been extracted, a post-extraction shoreline segment validation must take place. The purpose of this validation is to check that extracted 100 meter shoreline datasets only have one shoreline segment feature per dataset. If more than one feature exists, the linear shoreline difference algorithm works in an unexpected manner.

This validation is done by inspecting the attribute tables of each shapefile segment. If more than one feature exists, a judgment is made with the goal that the shoreline will have the greatest chance of yielding reliable shoreline change data. Linear shoreline change data is judged as acceptable when it is normal or perpendicular to the centerline and the actual shore.

Linear Shoreline Change Analysis

When the shoreline segments have been validated, they are ready for shoreline change analysis. This analysis uses the ‘Coastal Analyst’ ArcGIS® extension (Arias 2003). This extension allows the user to construct a set of linear shoreline difference polylines, as shown in Figure 3.16. This shoreline change algorithm works by measuring the distance of the base pre-storm shoreline and taking note of the number of user-defined divisions are present in the shoreline.

For example, if the base shoreline is measured at 134 meters and the user specifies a 5 meter interval, then the algorithm will note twenty six 5 meter divisions. If the target post-storm shoreline is 143 meters, each division in that shoreline will be approximately 5.5 meters because the target shoreline distance is divided by the number of 10 meter intervals in the baseline—which was twenty six.

The result of this analysis is a personal geodatabase that contains a point feature dataset that contains locations of interval points along the base pre-storm shoreline and a polyline feature dataset that contains the linear distances between shorelines along with the angle upon which these lines were drawn. With the data from this algorithm, it is possible to model shoreline change in terms of the direction of change, but it is not possible to determine if this amount of change in a particular direction is erosion or accretion—which is why these linear shoreline change polylines will be classified as erosion or accretion with the aid of the area shoreline change polygons.

Area Shoreline Change Analysis

Shorelines can be analyzed in terms of the area that changed between pre-storm and post-storm images. Originally created by Arias (2003), the area shoreline change algorithm identifies areas between two shorelines at a beginning node, and then considers intersections between these shorelines as erosion or accretion.

The output of the area shoreline change procedure is a polygon shapefile that contains the type of shoreline change and the area eroded/accreted. It cannot be stressed enough that the user should inspect the datasets to see if the determination of erosion/accretion is accurate. For shorelines of different orientation or direction, it is possible that the algorithm could misclassify erosion as accretion or vice-versa. It is also noteworthy that the individual features in the polylines shoreline datasets should be isolated and have the area change analysis done on them separately. This algorithm cannot handle more than one polyline feature matched to one polyline feature predictably.

Linear Shoreline Change Classification

With linear shoreline change polylines and area shoreline change polygons, it is possible to classify the polylines as representing erosion or accretion. This is done by a 'Spatial Join' in ArcGIS® Desktop. A spatial join involves using a spatial criterion, in this case the intersect criterion, to determine which shoreline change polylines should be considered as erosion or accretion. Once the shoreline change polylines have been classified as erosion or accretion, the next task is to evaluate the linear shoreline change in each polyline as negative or positive. This is done by using a 'Select By Attribute' command in the attribute table of the shoreline change polyline dataset in question. Once properly selected, all shorelines considered as erosion are made negative by multiplying their linear shoreline change value by -1, and accretion values are unchanged. This procedure allows for summary statistics and pattern generation. The result of these operations is shown in Figure 3.18.

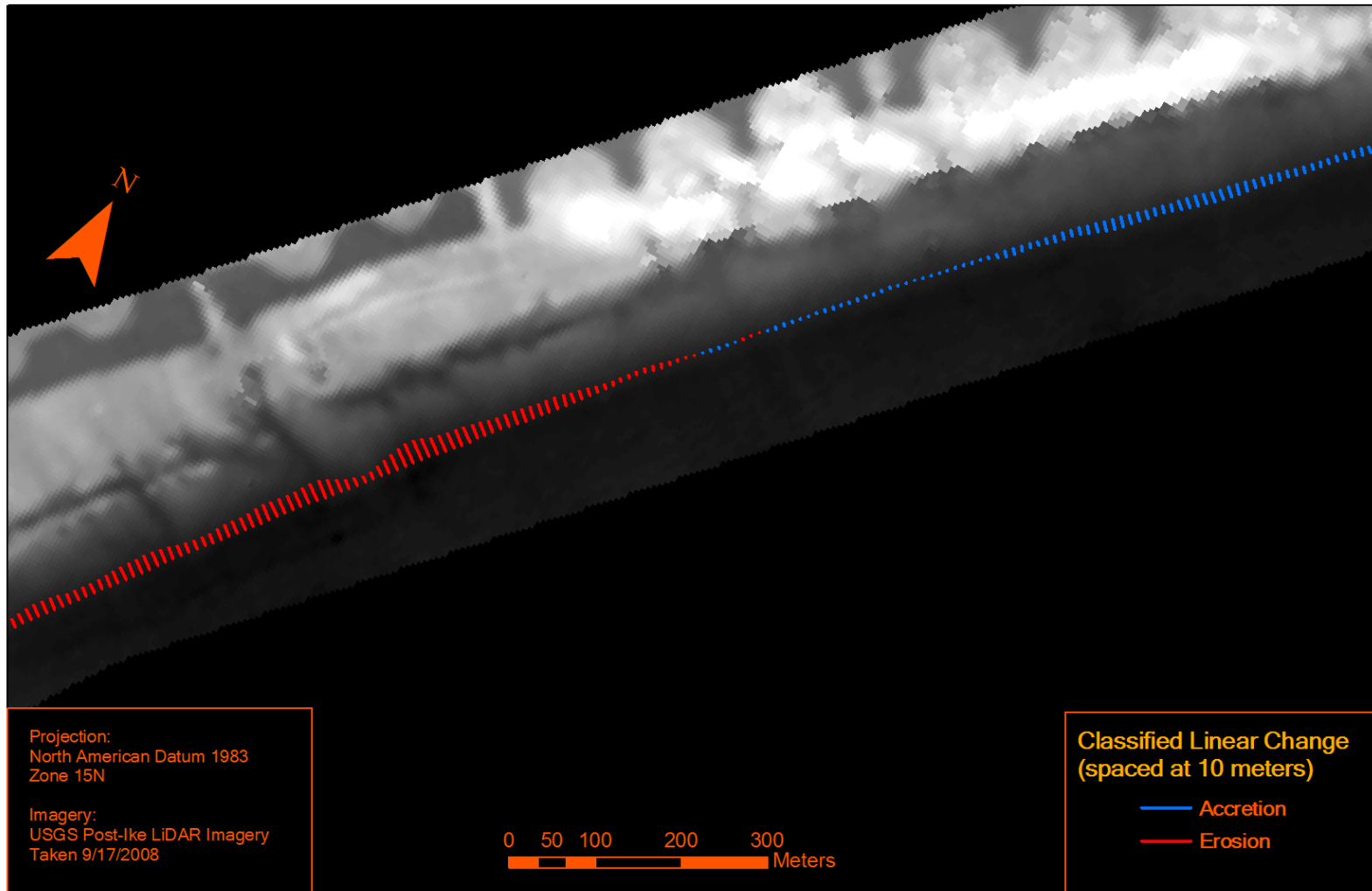


Figure 3.18. Classified linear shoreline change. This is taken at the distal end of Bolivar Peninsula in the Flake Quadrangle.

Volumetric Change Analysis

Volumetric Change Analysis is done using the ‘Coastal Morphology Analyst’ extension in ArcGIS® Desktop (Liu *et al.*, 2010). This extension allows the user to quantify volumetric change with sequential pre-storm and post-storm LiDAR surveys. This algorithm uses an object-oriented approach to discretize the continuous shoreline change into meaningful patches of erosion and accretion. By doing so, this algorithm can further inform coastal change measurements by attaching geometric, volumetric, and planimetric attributes to each of these patches (Liu *et al.*, 2010). Among these attributes are volumetric change, type of coastal change, along with summary statistics for all these patches of erosion and accretion for a LiDAR elevation change dataset (Liu *et al.*, 2010). In the past, cell-by-cell differencing was done and submitted as a final product for coastal change (Doran *et al.*, 2009; Gibeaut *et al.*, 2008). However, the method illustrated by Liu *et al.* (2010) allows the user to deduce patterns of erosion and accretion by using discrete coastal change patches.

Coastal Change Map

It is generally necessary to preprocess the imagery before analysis (Liu *et al.*, 2010). However, imagery used in this analysis has already been preprocessed ensuring that all datasets have the same map projection, and, that all datasets have been co-registered to each other (Liu *et al.*, 2011). This analytical approach begins by deriving a coastal change grid. A coastal change grid is a raster that shows a certain value denoting negative elevation change (erosion), positive elevation change (accretion), or no change beyond error. The user needs to specify the pre-storm base LiDAR dataset, the post-storm target LiDAR dataset, the error in these LiDAR datasets, and the multiplicative factor of the error. For these studies, the error is assumed to be 0.15 meters. Additionally, the error is multiplied by 2, since we are calculating a volume. An example of a coastal change map is shown in Figure 3.19.

Spurious Object Removal

The Spurious Object Removal procedure is identical to its counterpart in Shoreline Extraction. However, the threshold is different from that associated with shoreline extraction by two orders of magnitude for both the one-meter Tropical Storm Fay and Hurricane Rita data and the five-meter Hurricane Ike data. For both resolutions of data, the threshold is set at 6. This threshold removes all five pixel objects.

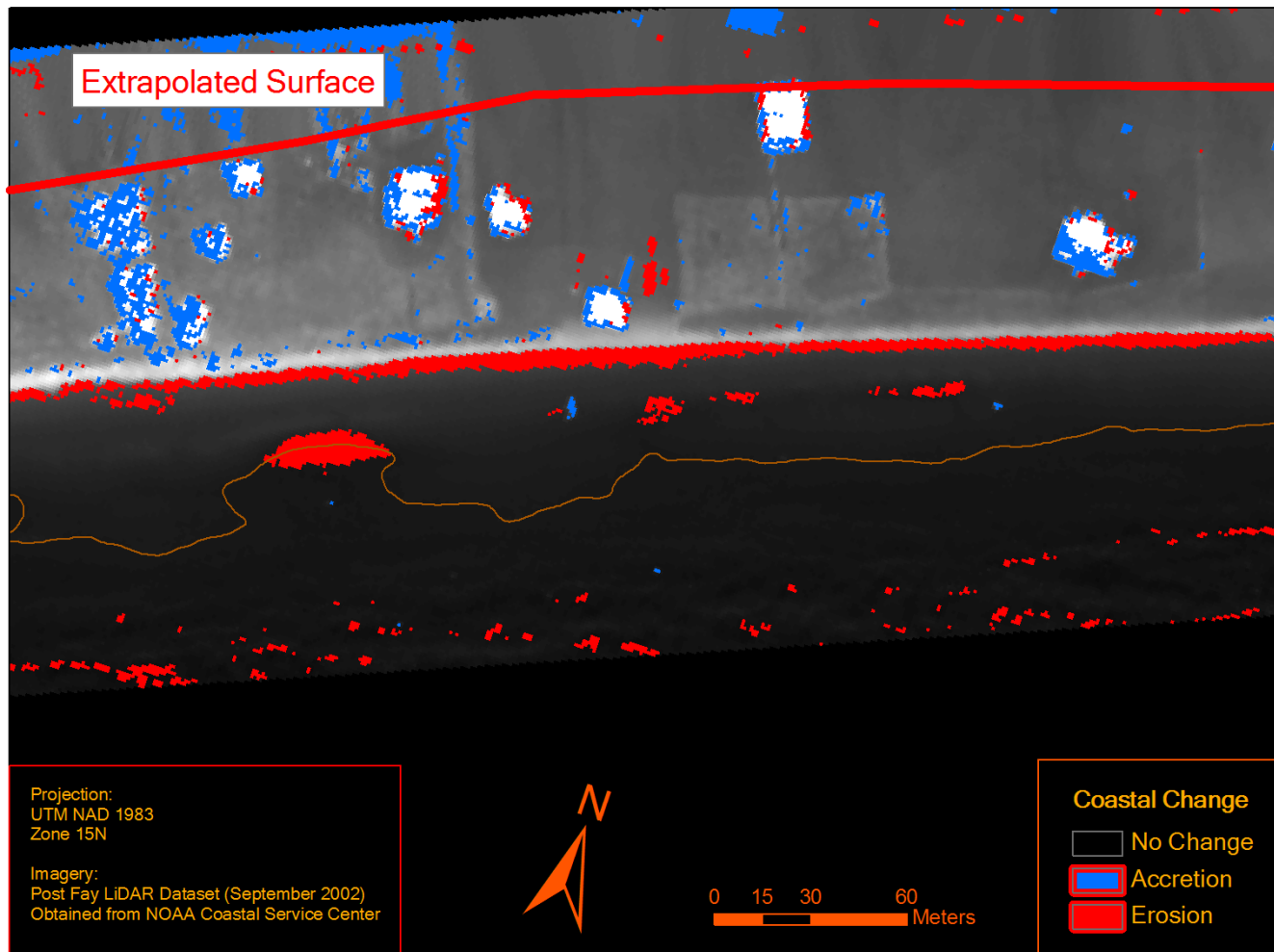


Figure 3.19. Hurricane Ike coastal change map with blue being accretion and red being erosion. Notice how there is an extrapolated surface. The pre-Hurricane Ike imagery was produced by the ArcGIS® IDW procedure, and the extrapolated surface is an artifact of that procedure. This resulted in error regarding the coastal change map.

Morphological Operations

In a manner similar to the Morphology Operator discussed in shoreline extraction, morphological operations serve to smooth out objects in the coastal change map. Just as in the past iteration of the Morphology operator for shoreline extraction, the morphological operations algorithm takes a series of commands that dictate which series of morphological operations it is to do. Similar to the past iteration, these commands are ‘detc’.

Object Identification

The first part of object identification is similar to the Spurious Object Removal procedure mentioned earlier for shoreline extraction. The only real difference between the first part of the Object Identification command and spurious object removal is the threshold value used. In the case of Object Identification, a threshold of 25 pixels was experimentally selected as a follow-up threshold value to try for the one-meter datasets considered. For the five-meter datasets, a threshold of 10 pixels was experimentally selected. The second part of object identification is unique to the Coastal Morphology Analyst. With this part of object identification, any object or patch of erosion or accretion larger than the threshold will be assigned a unique ID (Liu *et al.*, 2010). The exception to this rule is the background value. Individual patches of the background value are not given unique IDs.

For patches of erosion or accretion, the unique ID for each object will later be used by the volumetric and summary attributes commands within this extension to further inform these patches of erosion and accretion (Liu *et al.*, 2010). The unique patch

ID, change type, and volume eroded/accreted are the attributes of greatest concern for volumetric patterns in this study.

Vectorize Boundaries of Objects

The boundary detection portion of the volumetric change extraction procedure is much like the Land/Water object boundary tracing/vectorization portion of the shoreline extraction procedure. The same criterion is used to determine boundaries of erosion/accretion patches. With the input to this software routine being the unique ID raster that was the output in the last section, there is a twist to in the case of Coastal Morphology Analyst.

In the case of shoreline detection, boundary detection was only concerned with binary images of values '0' for water and '255' for land (Liu *et al.*, 2011). In the case of coastal morphology analyst, the values can have quite a range, dependent on the ID. The criterion for boundary detection is similar, barring this consideration. If one pixel of a different type than the focus, that pixel is considered a boundary pixel. All boundary pixels are then output to a boundary raster—much like the example in Figure 3.8. The other output is the vectorization of that boundary raster to yield a polygon shapefile that inherits the unique ID from the ID raster and elevation change type from the coastal change map, erosion or accretion (Liu *et al.*, 2011).

Compute Volumetric Attributes

This volumetric calculation routine takes three explicit raster dataset inputs and one implicit (not entered) raster dataset input. The three explicit raster dataset inputs are the pre-event DEM, post-even DEM, and the change raster. The change raster is nothing

more than the result of the pre-event DEM subtracted from the post-event DEM. The implicit input is the object raster.

The output consists of an attribute table with unique object IDs, and optional volumetric attributes. The attributes include average vertical change, standard deviation of vertical change, maximum vertical change, vertical change rate, volume change, and volume change rate (Liu *et al.*, 2010). Of interest for this work is average vertical change. From the object ID, vertical change type, and average vertical change, we could later deduce volume rates of erosion or accretion from pattern data.

Manual Corrections of Morphological Patches

As one could deduce from Figure 3.19, some features do not represent true erosion and accretion associated with the coastal change by secular conditions and storm conditions. These objects are removed manually, and inspected next to the Post-Storm LiDAR imagery. The product will be used in the upcoming methods to establish patterns of volumetric erosion and accretion.

Identification of Proper Spacing

To identify the proper spacing for these patterns and to understand the structure of the data, semivariogram analysis and fractal scaling range analysis were conducted. These analyses informed a proper spacing of the data for all three tropical cyclone impacts. Shifting window analysis was conducted with that spacing in order to identify areas of spatial sensitivity.

Semivariogram Analysis

To determine spatial characteristics of shoreline change data, a set of semivariograms were formed from equation 3.3, (Burt, Barber, and Rigby, 2009).

$$\gamma(d) = \frac{1}{2n(d)} \sum_{d_{ij}} (x_i - x_j)^2 \quad (3.3)$$

Semivariograms model the influence of space/distance on variance within a dataset. This is modeled as semivariance (ordinate) and lag distance (abscissa). Semivariance has two major components, the ‘sill’ and the ‘nugget variance’ (Curran, 1988). The ‘sill’ discusses that amount of variance that is spatially controlled, and the nugget discusses the amount of variance that is attributable to random error (Curran, 1988).

The item of interest from a semivariogram for the purpose of quantifying minimal spacing of data is the range. The range is a point on the x-distance axis that the sill is reached, and is commonly interpreted as the lag distance that corresponds to the maximum value on the semivariogram (Curran, 1988; Burt, Barber, and Rigby, 2009). Theoretically, the range is the lag distance where data no longer is spatially influenced by its neighbors (Curran, 1988).

Semivariograms can take on many characteristic shapes (Curran, 1988). One type of semivariogram is the periodic or hole-effect semivariogram (Pyrcz and Deutsch, 1978). This type of semivariogram often has a maximum value that exceeds the sill (Pyrcz and Deutsch, 1978). Often, these semivariograms oscillate around the sill value (Pyrcz and Deutsch, 1978). As a result, the range is often taken as being the lag distance

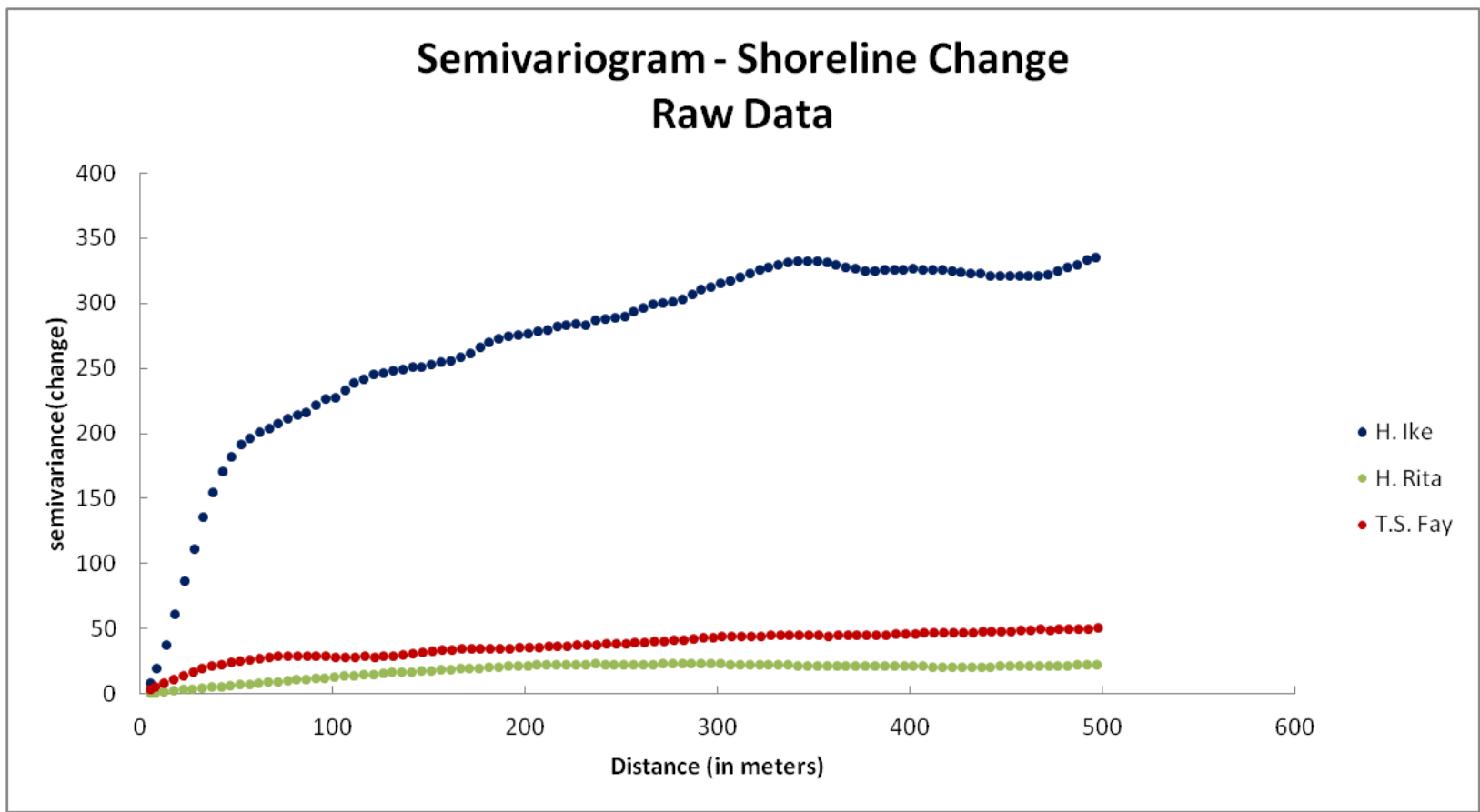


Figure 3.20. Semivariogram generated from raw shoreline change data from Hurricanes Ike, Rita, and Tropical Storm Fay.

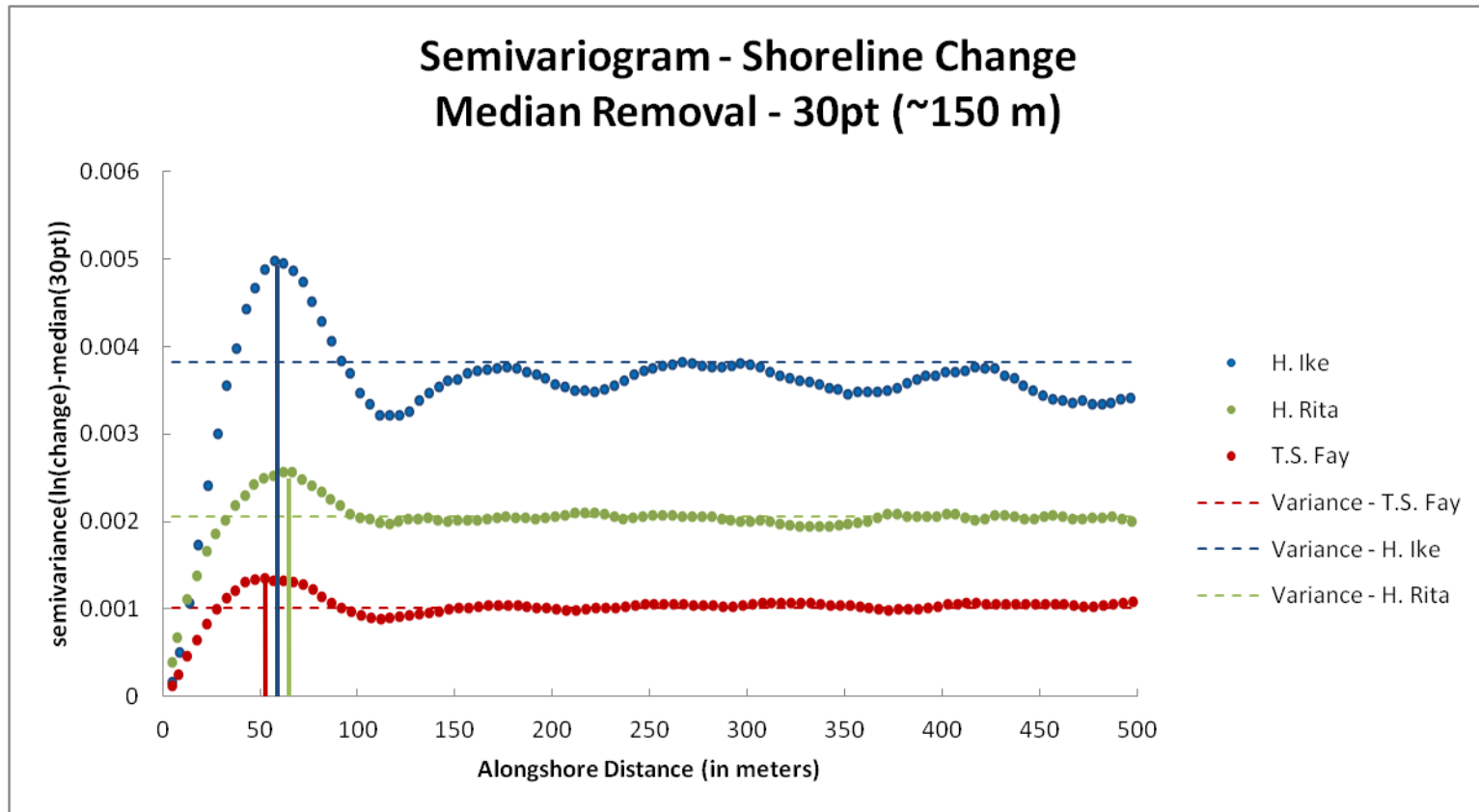


Figure 3.21. Semivariogram representing the 30 point running median residual from shoreline change data of Hurricanes Ike, Rita, and Tropical Storm Fay. Colored lines indicate interpreted mark interpreted ranges and maxima. Sample variances are represented in thin dashed lines.

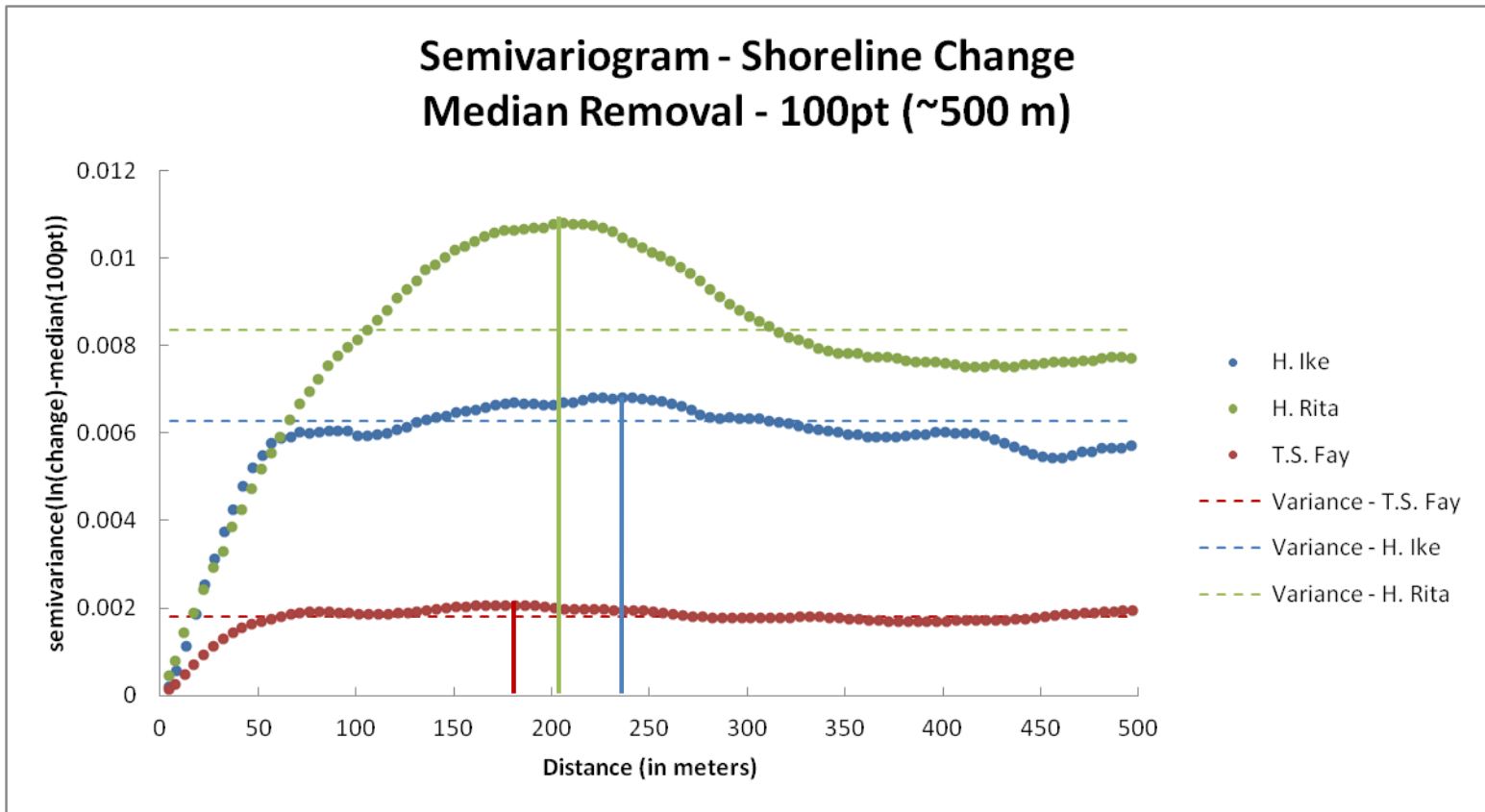


Figure 3.22. Semivariogram representing the 100 point running median residual from shoreline change data of Hurricanes Ike, Rita, and Tropical Storm Fay. Colored lines indicate interpreted mark interpreted ranges and maxima. Sample variances are represented in thin dashed lines.

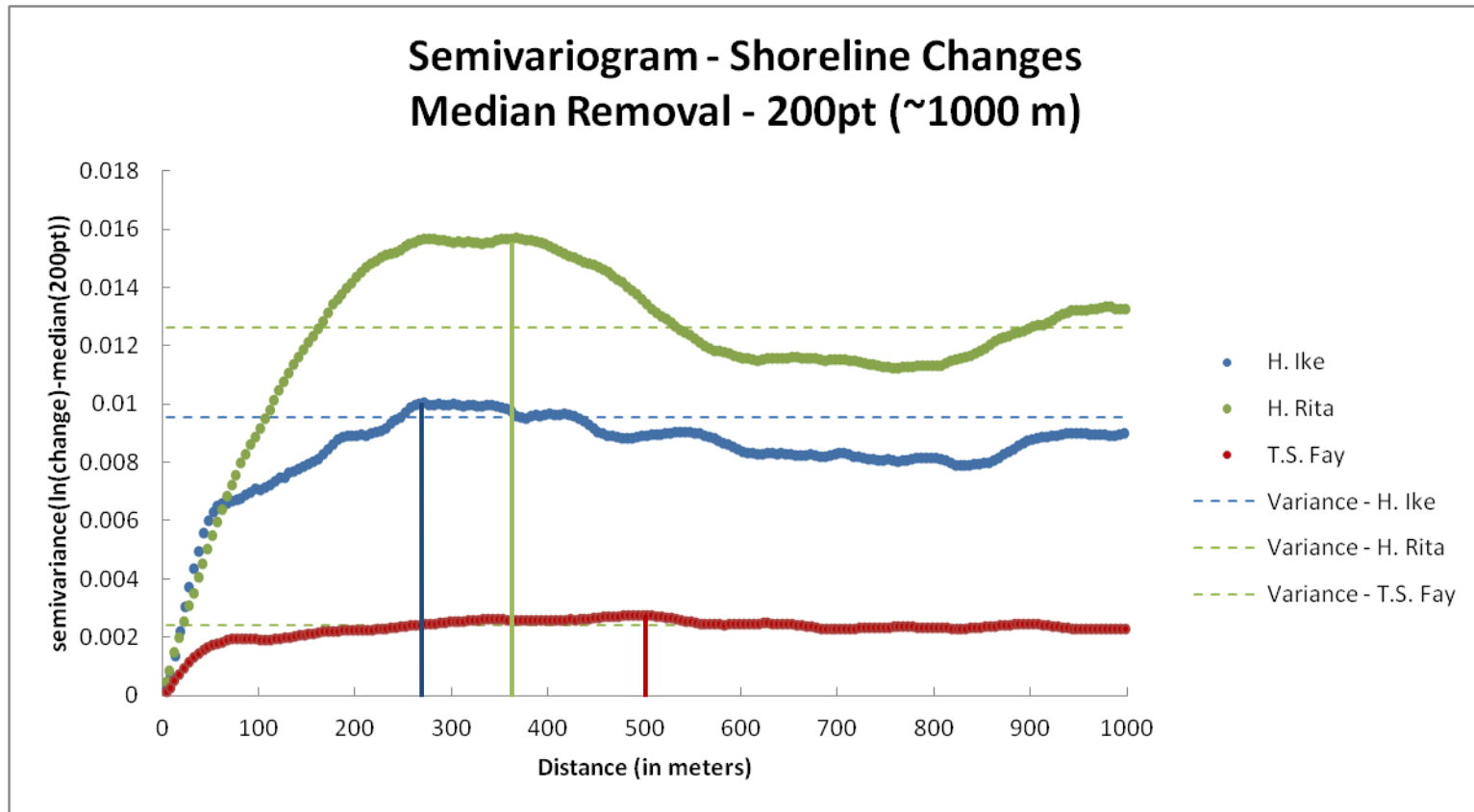


Figure 3.23. Semivariogram representing the 200 point running median residual from shoreline change data of Hurricanes Ike, Rita, and Tropical Storm Fay. Colored lines indicate interpreted mark interpreted ranges and maxima.

that corresponds to the top of the first period (Pyrzcz and Deutsch, 1978). Some semivariograms keep increasing in variance, and these semivariograms are often referred to as trended or unbound (Hamlett, Horton, and Cressie, 1986; Curran, 1988). It is possible to have hole-effect unbound semivariograms (Pyrzcz and Deutsch, 1978).

Initially, semivariograms were based on raw shoreline change data (Figure 3.20). In raw form, the data violate one of the two assertions in a semivariogram, and could arguably violate the other, Appendix E. These two assertions are the absence of a spatial trend (Hamlett, Horton, and Cressie, 1986; Dolan, Fenster, and Holme, 1992) and stationarity of the mean with respect to variance (Hamlett, Horton, and Cressie, 1986; Dolan, Fenster, and Holme, 1992). To remedy this, two steps were taken using a log transformation to dampen differences between extreme values in the dataset and trend removal by running median—as suggested by Hamlett, Horton, and Cressie (1986), Appendix E. It was observed in these data that there were extreme values present. To address this concern, a 1.5 interquartile range criteria (Ott and Longnecker, 2010) was implemented to omit outliers from the analysis. These outlier locations, in the case of Hurricane Ike, corresponded to areas where adjacent magnitudes of shoreline change had dramatic differences.

The residuals from removing the running median will be studied in semivariograms with a 30 point median window (150 m), a 100 point median window (500 m), and a 200 point median window (1000m), to see if the range changes dramatically as one changes window size (Figures 3.21, 3.22, 3.23, respectively). This variation in range is possible. This is because the greater the median window; the more

smoothing happens to the log-transformed shoreline changes. Thus, the more trend the residuals will have. It is noted that Dolan, Fenster, and Holme (1992) had difficulty in removing a trend via running mean. In light of these troubles, the work of Dolan, Fenster, and Holme (1992) advocated a semivariogram analysis with data transformed, but no trend removal.

Semivariogram lag spacing was roughly coincident to the data spacing (5m), and the lag search direction was alongshore. The total field length observed was 500 meters for the raw data, the 30 point, and the 100 point running median trial, and 1000 meters for the 200 point running median trial. These semivariograms are shown in Figures 3.21, 3.22, 3.23 for Hurricanes Rita, Ike, and Tropical Storm Fay.

For the 30 point running median, the results indicate that there are spatial controls on data points that are closer than 50-60 meters to each other. After observing results from the 100 point median removal (Figure 3.22) it was concluded that there is a change in range—57 meters to 271 meters for Hurricane Ike—depending on the median window being removed. The change in range is an indicator that the median removal procedure could cast inaccurate results.

Thus, a final set of semivariograms were created that were only given a logarithmic transformation with no trend removal (Dolan, Fenster, and Home, 1992) and a total observed field length of 1000 meters. Being that these semivariograms are based upon spatially trended data, these shoreline analyses do not reach a sample variance—an often-used surrogate for sill—within 500 meters, 1000 meters. In the case of Dolan, Fenster, and Holme (1992), they did not reach sample variance until a lag spacing of 8.5

kilometers. These results are not truly surprising, because Curran (1988) discussed the fact that trended or unbounded semivariograms may have a very large sill or never reach a sill value.

There are different levels of spatial control apparent in trended shoreline change semivariograms (Dolan, Fenster, and Holme, 1992). This was made apparent by the necessity of Dolan, Fenster, and Holme (1992) to use nested models in order to simulate the semivariance of shoreline change in their dataset to model ‘sills’ at 2.5 and 10.5 kilometers. The larger ‘sill’ was indicative of the true range.

To determine spacing from a trended semivariogram, the periodicity is observed instead of the range. This technique involves looking at the periodicity in the data, and adopting the first major peak outside the zone of very pronounced spatial dependence (Dolan, Fenster, and Holme, 1992), where the semivariance begins to level off, Figure 3.24.

Structurally, the semivariograms for Hurricane Rita had an easily interpretable periodic difference indicated in the 30, 100, and 200 point running median (Figures 3.21,3.22,3.23). The semivariograms for Hurricane Ike and Tropical Storm Fay have multiple scales of periodicity (Dolan, Fenster, and Holme, 1992) in all but the 30 point running median. This multi-scale periodic behavior could be because of the oscillating, continuous behavior of the different shoreline changes, Appendix C. It could also be because shorelines, objects that are notably fractal or multi-scale in nature (Mandelbrot, 1983), could possibly pass that attribute onto their residuals, shoreline changes. This multi-scale periodicity is even more apparent in the log-transformed

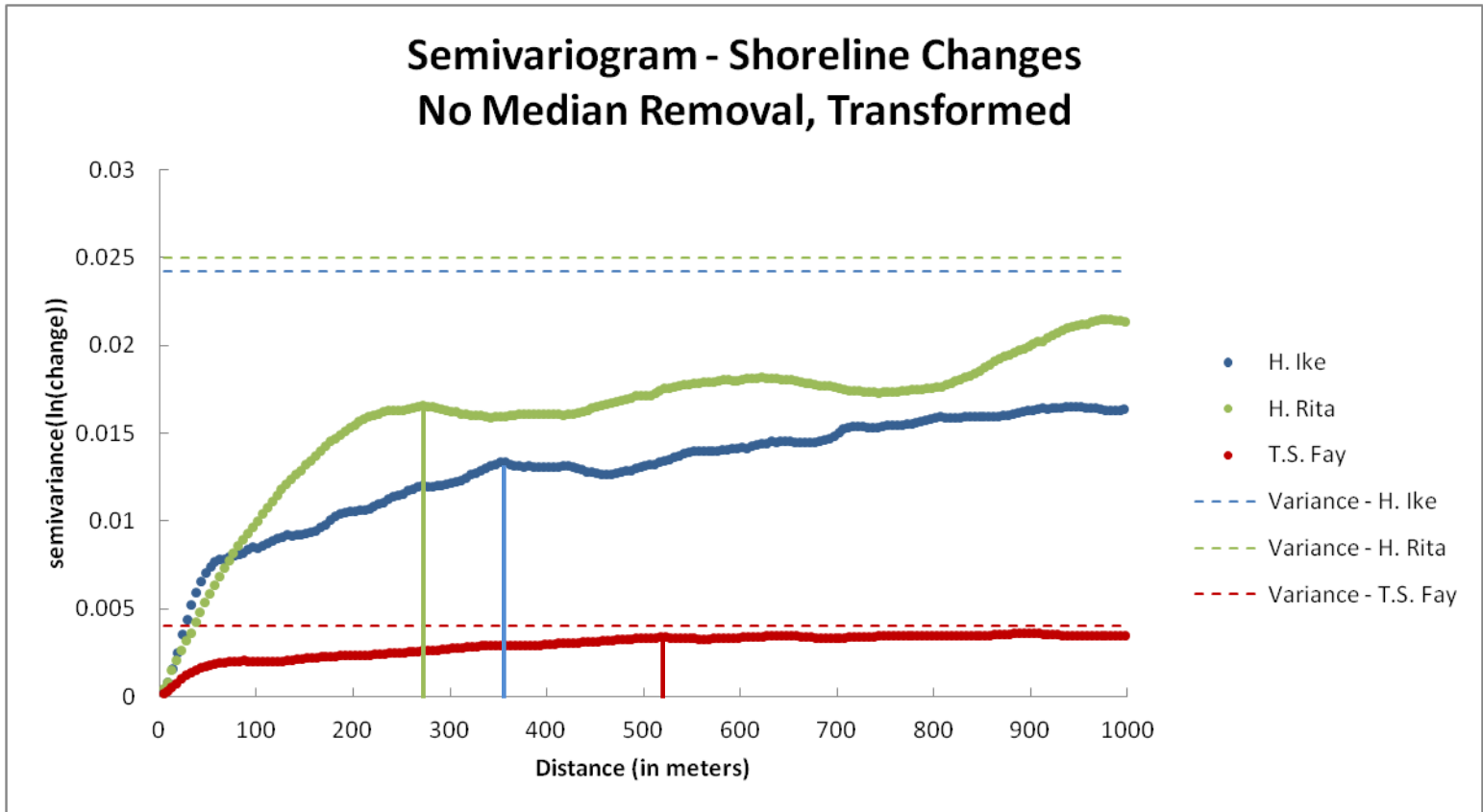


Figure 3.24. Trended semivariograms that have been transformed in a manner similar to that of Dolan, Fenster, and Holme (1992).

semivariograms (Figure 3.24). It was interpreted from the transformed semivariograms that Hurricane Ike has an initial periodicity at 356 meters, Hurricane Rita has an initial periodicity at 271 meters, and Tropical Storm Fay had a periodicity at 512 meters.

Results for all semivariogram analyses are summarized in Table 3.3.

Table 3.3. *Ranges obtained from semivariogram analyses.*

Storm	Raw (m)	150 meters (m)*	500 meters (m)*	1000 meters (m)*	Transformed (m)***
H. Ike	360	57	241	271	356
H. Rita	200	66	191	366	271
T.S. Fay	72**	52	180	497	512**

*Units represent unit width of running median window.

**Raw data resembles a trended semivariogram that has a very ambiguous sill.

***Data that was transformed but not detrended.

Fractal Scaling Range Analysis

With the ranges from semivariogram analysis exhibiting variety and multi-scale periodic behavior, a fractal scaling range analysis analogous to Stolum (1998) was conducted on a line that is generated from linear shoreline change. Specifically, linear shoreline change (y axis is positive for accretion and negative for erosion; x axis is alongshore the pre-storm shoreline) is represented by the line shapefile output from a software tool called 'EvalSLGen', Appendix A. Afterwards, a fractal dimension software tool was used to generate a Richardson plot (Shelberg, Moellering, and Lam, 1982; Mandelbrot, 1983) (Figures 3.25, 3.26, 3.27).

Richardson plots were then used to visualize the scaling behavior of these shoreline change impacts. Using Richardson plots, fractal scaling ranges can inform

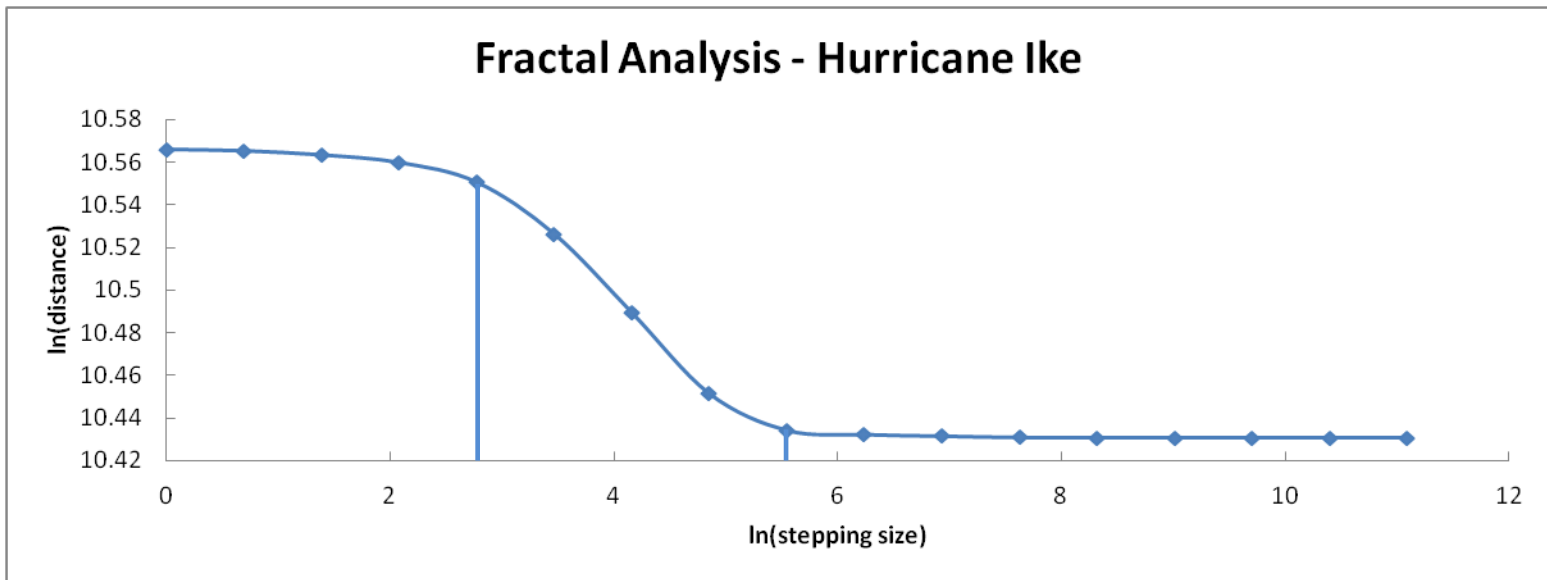


Figure 3.25. Fractal analysis for Hurricane Ike. Scaling range data presented in the graph is the transformation of $\ln(x)$. Physical values (in meters) are interpreted as $\exp(x')$. Therefore, the lower end of the scaling range will be interpreted as $\exp(2.77258872) = 16$ meters, and the higher end would be interpreted as $\exp(5.5451774) = 256$ meters. Fractal Dimension is estimated at 1.0444.

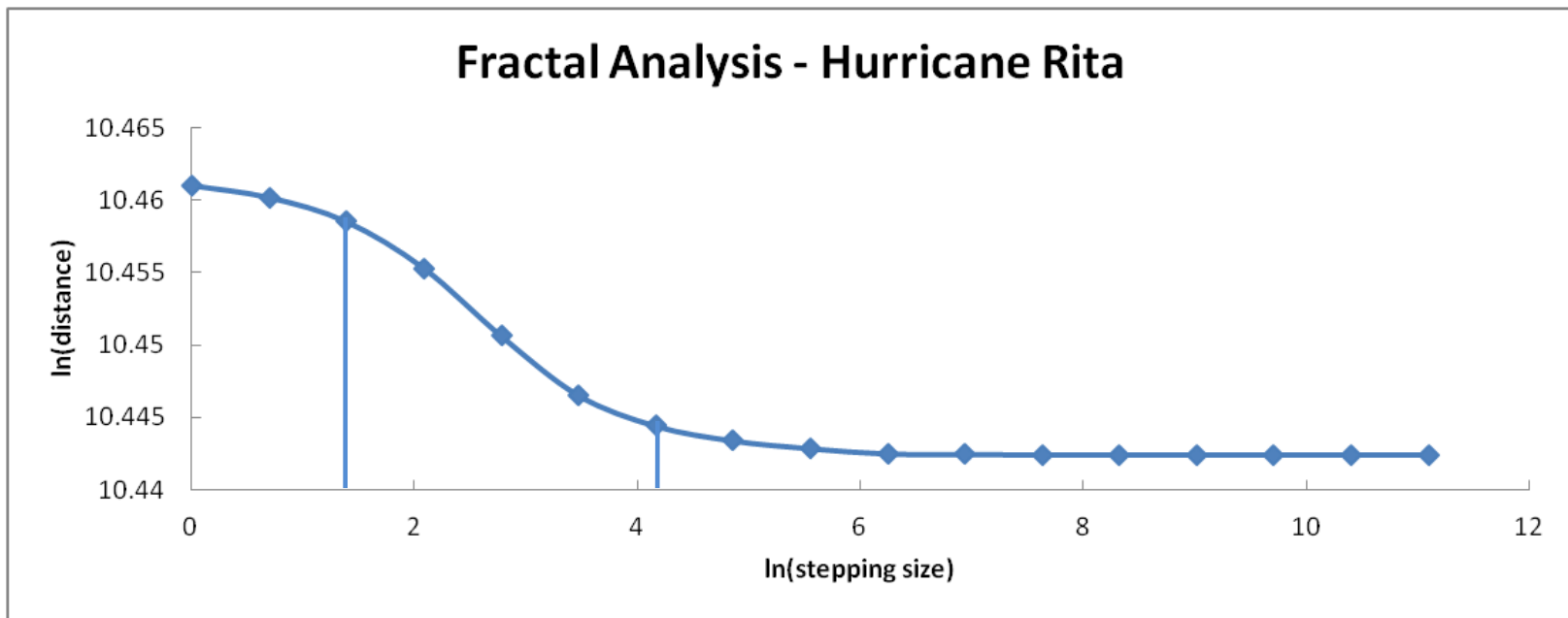


Figure 3.26. Fractal analysis for Hurricane Rita. Scaling range data presented in the graph is the transformation of $\ln(x)$. Physical values (in meters) are interpreted as $\exp(x')$. Therefore, the lower end of the scaling range will be interpreted as $\exp(1.38629436) = 4$ meters, and the higher end would be interpreted as $\exp(4.15888308) = 64$ meters. Fractal dimension is estimated at 1.0053.

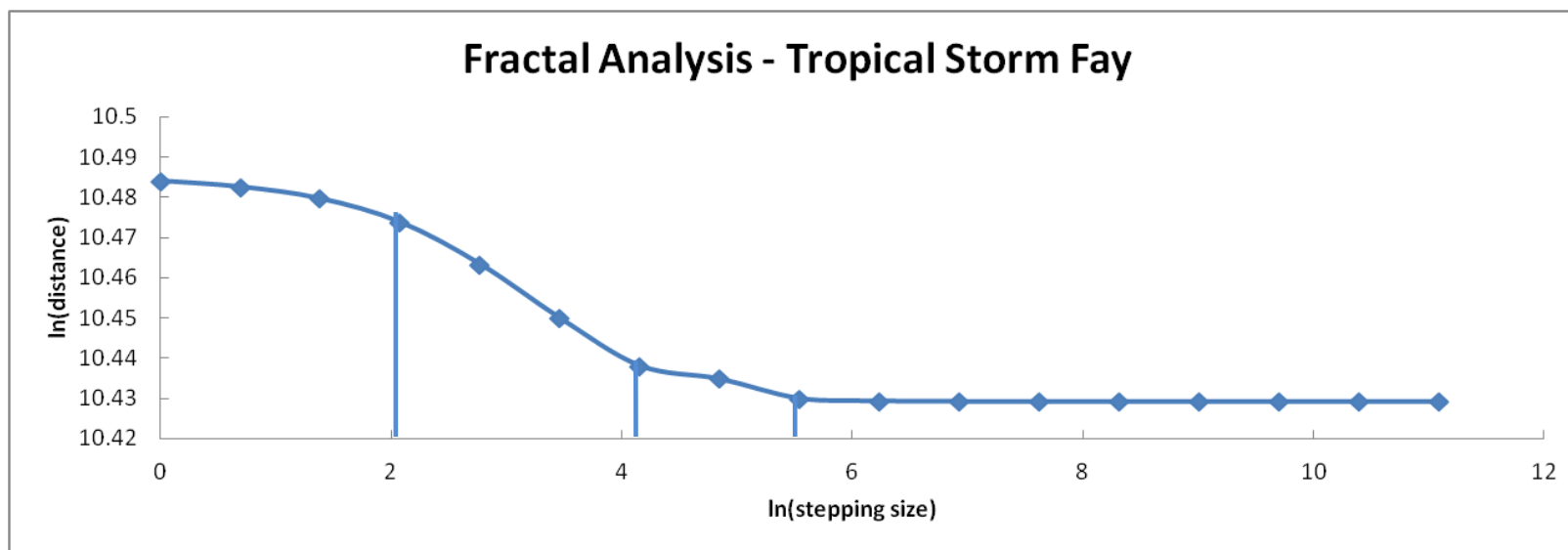


Figure 3.27. Fractal analysis for Tropical Storm Fay. Scaling range data presented in the graph is the transformation of $\ln(x)$. Physical values (in meters) are interpreted as $\exp(x')$. Therefore, the lower end of the scaling range will be interpreted as $\exp(2.079442) = 8$ meters, and the higher end would be interpreted as $\exp(4.15888308) = 64$ meters. However, it appears another scale of behavior is between 64 meters and $\exp(5.54177) = 256$ meters. The first scale has an estimated fractal dimension of 1.0174. The second fractal dimension is estimated at 1.0059.

researchers of the stepping size or spacing at which a linear feature is no longer sensitive (Stolum, 1998). Analysis of fractals via Richardson plots works by having a series of measured steps that increase after each iteration. As the stepping size increases, the total measured length of the feature being analyzed decreases (Mandelbrot, 1983). If the stepping size is too small, there is no decrease in the line length, and if it is too large, there is no further decrease. The stepping size that corresponds to the total measured line length on a Richardson plot that decreases to the point it cannot decrease anymore denotes the upper scaling range (Stolum, 1998). Results are shown in Figures 3.25, 3.26, and 3.27 for Hurricanes Ike, Rita, and Tropical Storm Fay, respectively. These plots are natural log-natural log transformed. The y-axis represents the distance of the alongshore shoreline change line, and the x-axis represents the stepping size.

The dataset representing shoreline change as a result of Hurricane Ike has a fractal scaling range that borders on 256 meters (Figure 3.24). Other shoreline storm impacts have a scaling range for which the upper value is bounded by 64 meters (Figures 3.25 and 3.26). However, impacts from Tropical Storm Fay also had another scaling range between 64 meters and 256 meters (Figure 3.26). Based on the semivariogram analyses and on the fractal scaling range analysis, a 500 meter spacing is the nearest round number (in the hundreds) that would be satisfactory to summarize the mesoscale effects of these three Tropical Cyclones.

Shifting Window Analysis

To consider how robust these analyses are, it is still necessary to understand the type and location of spatial sensitivity that is inherent in these patterns. To accomplish this task, a shifting window analysis was conducted, Figure 3.28. This analysis was carried out by using windows of 500 meters and shifting them toward the distal end of Bolivar Peninsula 125 meters and then 250 meters. Comparisons of results are made for Hurricane Ike in Figure 3.29, and areas that are spatially sensitive are identified in Figure 3.30. To demonstrate this, sensitivity, shoreline change averages from all spatial bins in each of the shifting window analyses from Hurricane Ike and Tropical Storm Fay are included in Figures 3.29 and 3.31.

Global spatial sensitivity is determined by counting 500 meter zones that change their character—from erosion to accretion, accretion to no change, etc. These changes in character are then totaled between the two moved windows, and then the dominant change type is noted as the color in the circle, and the less common zonal change type is shown to be the 2 point boundary around, (Figure 3.30).

Results show that the shoreline change impacts of Tropical Storm Fay had the most spatial sensitivity of 20 sensitive zones out of 67 total zones (Figures 3.30, 3.31). Second in place is Hurricane Rita at 12 sensitive zones out of 67 total zones (Figure 3.30). The least spatially sensitive is Hurricane Ike at 8 zones in total 67 zones (Figures 3.29, 3.30). This ranking is most likely determined by the average magnitude of shoreline change for each storm.

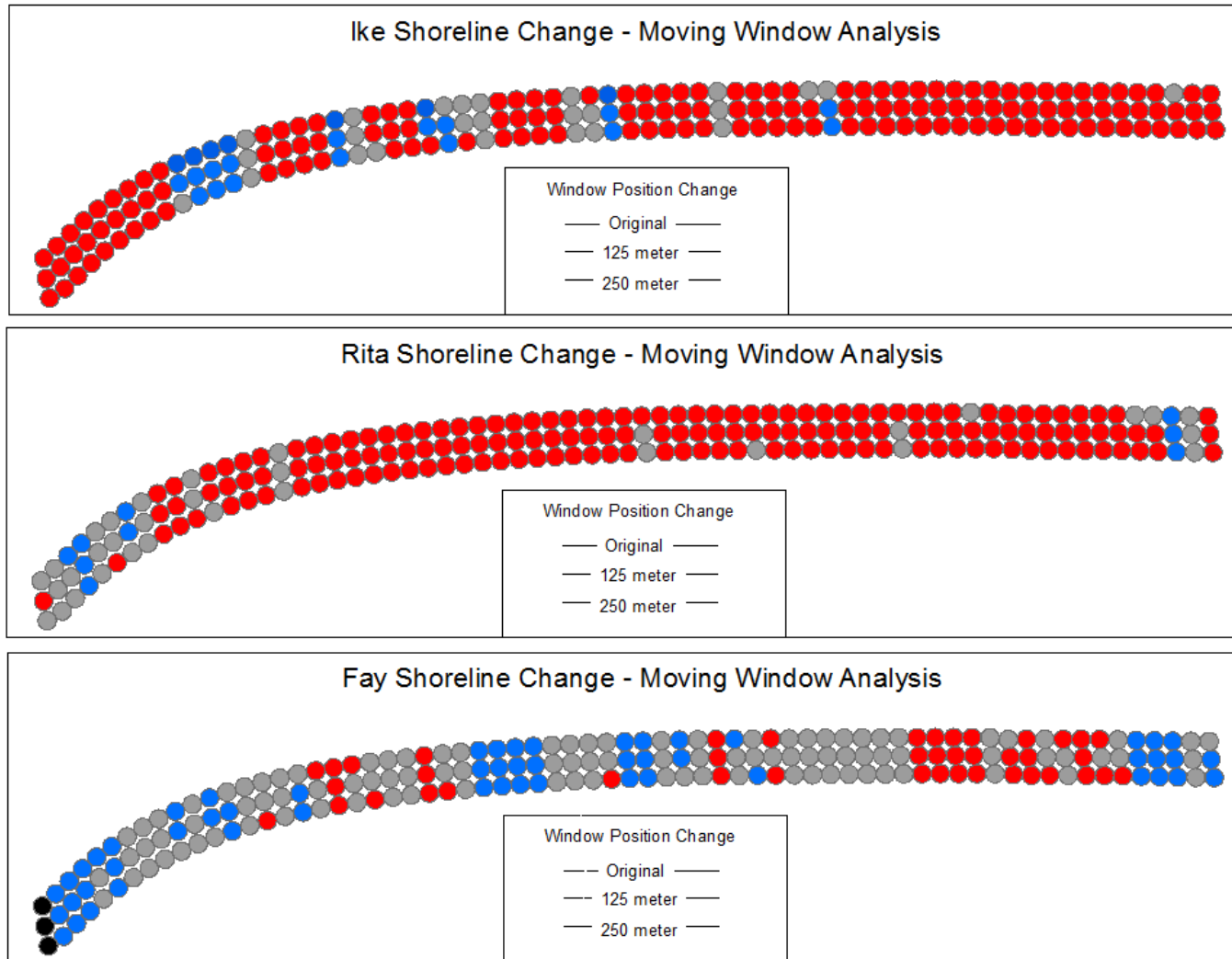


Figure 3.28. Shoreline change patterns derived from shifting window analysis. Red denotes erosion, blue denotes accretion, and grey denotes no change beyond error.

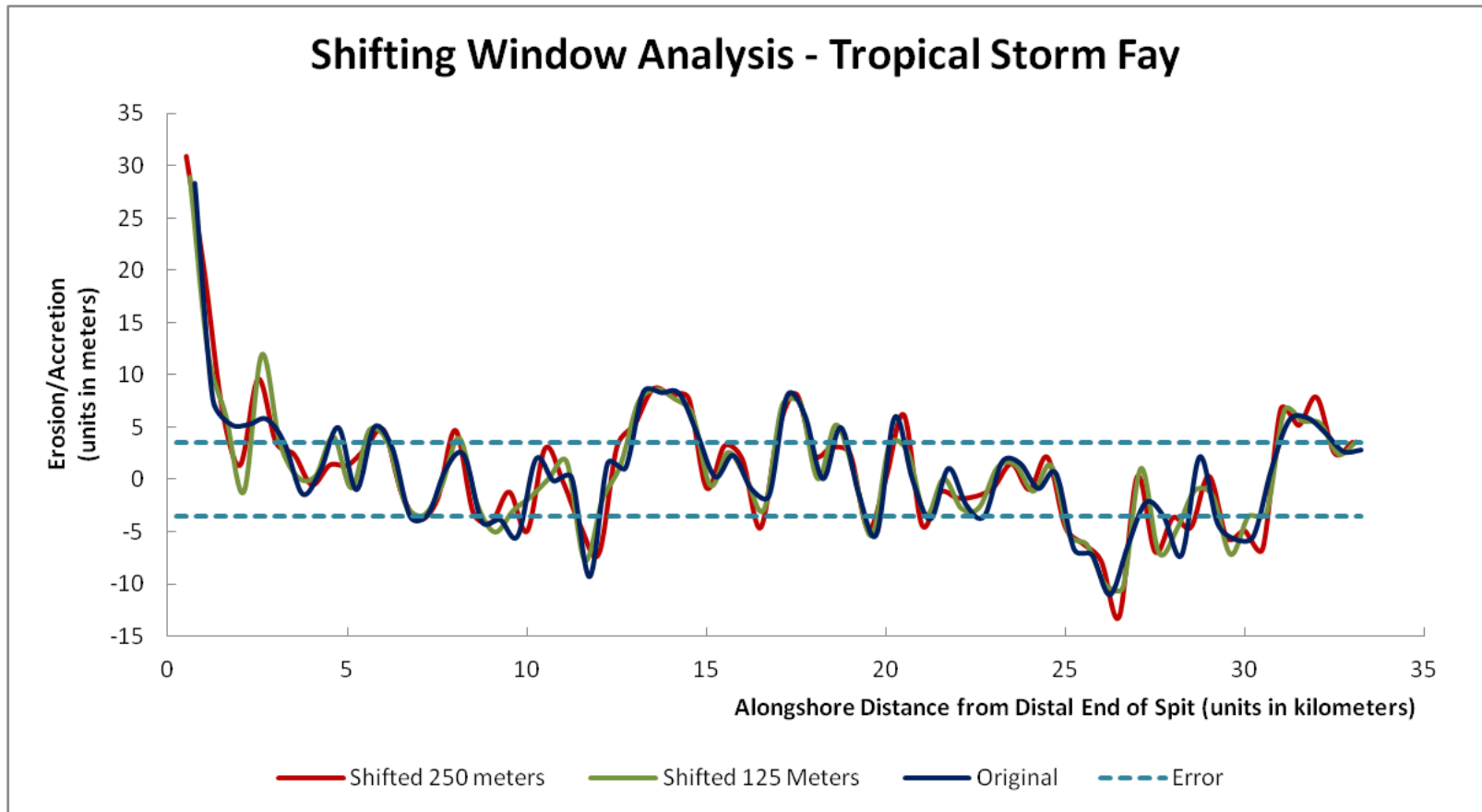


Figure 3.29. Results of shoreline change derived from the shifting window analysis of shoreline impacts from Tropical Storm Fay.

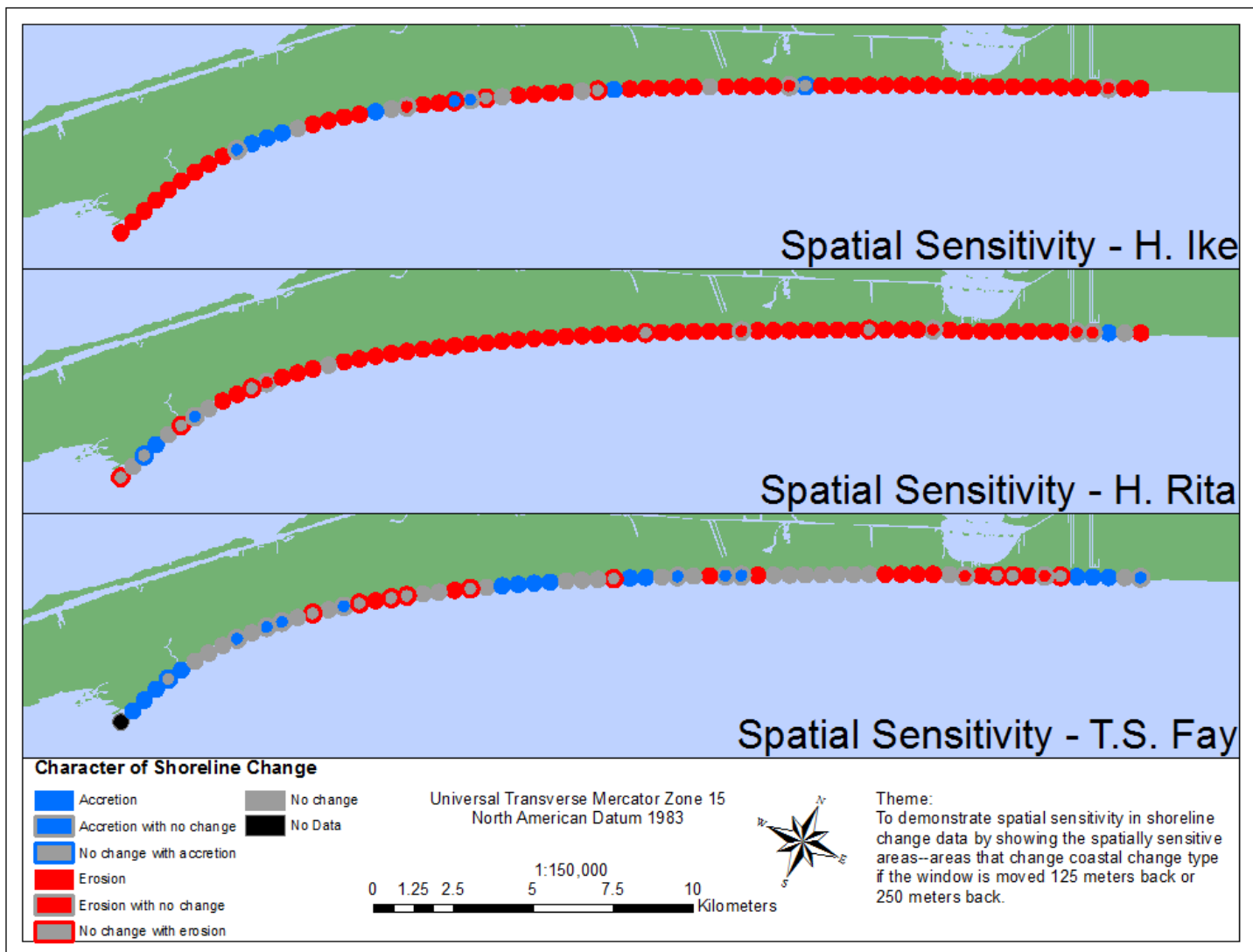


Figure 3.30. Spatially sensitive alongshore locations, as identified by the shifting window analysis.

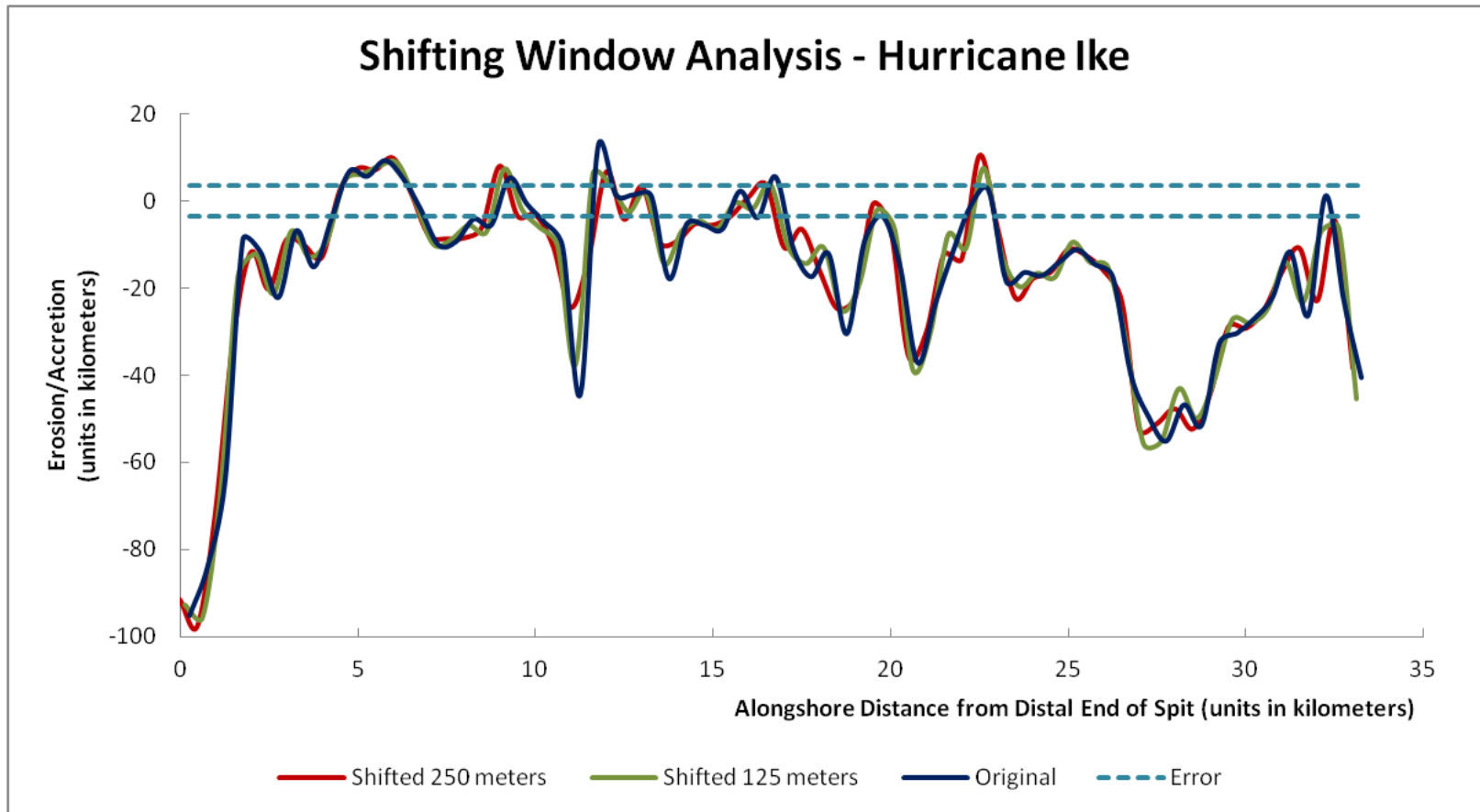


Figure 3.31 Results of shoreline change derived from the shifting window analysis of shoreline impacts from Hurricane Ike.

Figures 3.31 and 3.29 show the alongshore shoreline changes from the impacts of Tropical Storm Fay and Hurricane Ike. These figures seem to suggest that most of the character changes are because of the low shoreline change values that are close to the shoreline change error can be swayed into the region of error or out of the region of error. Figures 3.31 and 3.30 show the patterns, and they also seem to indicate that most sensitivity has to do with the “no change beyond error” threshold. In cases where there are extreme points, they can make an area that would normally be classified as ‘no change beyond error’ as in fact ‘erosion or accretion’. This implies that this sensitivity is linked to the threshold, and not the scale of storm impacts or spacing characteristics.

Spatial sensitivity for Hurricane Ike was greatest at the central portion of the spit—just a few kilometers updrift of the point of maximum curvature, twelve kilometers from the distal portion of the spit, Figure 3.28. The dominant type of zone in these sensitive areas is “No Change Beyond Error”, and they are often flanked by erosional zones. As for Tropical Storm Fay, the point of greatest sensitivity is at the point of maximum curvature—from ten to twelve kilometers from the distal end of the spit. In the case of Hurricane Ike, these points are mostly “No Change” and are flanked by erosive areas. Storm impacts for Tropical Storm Fay and Hurricane Ike show sensitivity that coincides with the smaller impacts—relative to impacts on other areas of the spit—on the area of maximum curvature or just updrift of it. For Hurricane Rita, most of the spatial sensitivity is in the most distal 4 kilometers of the spit. These areas of spatial sensitivity contain an equal mixture of “no change”, “accretion”, and erosion points (Figure 3.30).

Table 3.4. *Total 500 meter pattern bins that change character during shifting window analysis. Notice how the total is not additive.*

Storm	Changed in 125 meter shift	Changed in 250 meter shift	Total Incorrect
Hurricane Ike	6	8	9
Hurricane Rita	7	11	12
Tropical Storm Fay	11	18	20

Pattern Extraction

The following procedures are designed to abstract data output from coastal change algorithms and third party sources into patterns that are quantifiable. This involves decomposing data that results from 2D and 3D analyses into classes of erosion, accretion, and no change beyond error along the shore of Bolivar Peninsula. The procedures to extract patterns from shoreline change and volumetric change will be different and have their own unique challenges associated with them.

Linear Referencing for Pattern Extraction

Patterns have to be set to the same spatial reference in order to be compared. This is done by linear referencing via dynamic segmentation. To extract patterns, a standard centerline is established that represents the general shape and boundaries of the feature analyzed. The centerline is then turned into a route feature, and given an event table. The event table is established as beginning at 250 meters and with succeeding intervals of 500 meters, in a manner analogous to Figure 3.17. With a route and an event table, it is possible to make an event layer (Brennan and Harlow, 2004). As deduced in spacing analysis, this event layer will represent the point pattern of a 500 meter segment of the study area. With approximately 60 features, these points will represent erosion or

accretion in individual patterns, and a lineage of pattern change with pattern comparisons through route event overlay analysis.

Pattern Extraction from Previous Publications

A graph can be used to identify a pattern of erosion or accretion on a geomorphic body as long as the results have some means of relating to features on or attributes of the geomorphic feature in question. In the case of Bolivar Peninsula, Gibeaut, Gutierrez, and Hepner (2002) has a graph of the coastal volume change—deduced from beach profiles—caused by Tropical Storm Josephine. The graph has the names of landmarks and a characteristic distance. Thus, it is possible to deduce other features and to relate the erosion and accretion patterns to a trended route—as discussed earlier. This modified graph is shown in Figure 3.32.

Pattern Extraction from Shoreline Change

Extracting patterns from linear shoreline changes utilizes summary statistics for each of the event points mentioned in previous sections. In the first step, buffer proximity analysis is done to the event points at a radial distance of 250 meters. The results are circles that have a diameter of 500 meters.

Using a software tool, ‘ShapeStatCalc’, in Appendix A, these buffered regions will be used to select spatially coincident ‘chunks’ of linear shoreline changes and then compute an average from the selected values—negative values as erosion and positive values as accretion. This average is then judged as being erosive or accretive. Then, the average is judged as being within or outside of a threshold of positive or negative 3.58

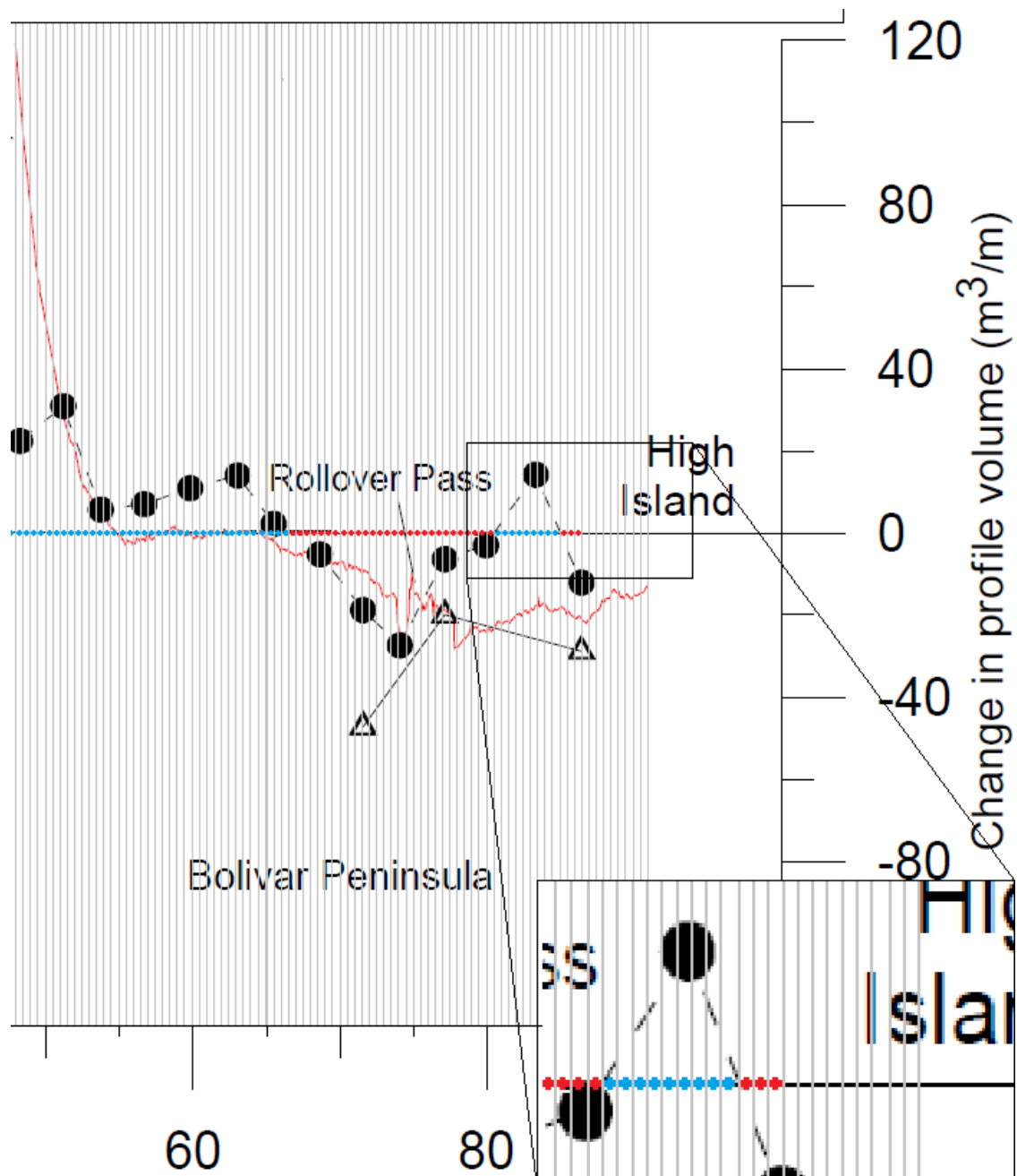


Figure 3.32. Pattern representation extracted from Figure 11 in Gibeaut, Gutierrez, and Hepner (2002). Magnified figure in lower right is intended to show individual blue points (accretion) and red points (erosion) deduced from volume change rates.

meters—as was derived from the error inherent in LiDAR for this study by Liu, Sherman, and Gu (2007).

The work of Liu, Sherman, and Gu (2007) involved a Monte Carlo error simulation procedure that determined the horizontal displacement error for a shoreline in the study area. Their answer was 1.79 meters. Following advice of Taylor (1997), this work simply doubles that figure—since it was quite difficult to separate the systematic versus random error in the vertical error of LiDAR elevation data found in Sallenger *et al.* (2003).

A positive average above 3.58 meters establishes a summary pattern of accretion at that event point on the shoreline, and a value below -3.58 meters is judged to be erosion. These steps are repeated for each point until all points either have a summary statistic that states erosion, accretion, or no change beyond error.

Pattern Extraction from Volumetric Change

The output of the volumetric change algorithm is an informed polygon shapefile of erosion and accretion patches. From these erosion and accretion patches and the representative LiDAR imagery, it is possible to generate quantifiable patterns of erosion and accretion.

With representative LiDAR imagery from the December 2008 dataset with resolution of one meter, the center of each pixel is converted to a point feature. These point features will be the discrete elements necessary to quantify erosion and accretion from patches—in much the same way as the shoreline change polylines were for

shoreline change. These point features are then combined with the erosion and accretion patches from the volumetric change analysis through a 'Location Join' with 'Intersect' criterion—an example is shown in Figure 3.33. This location join allows parameters from the volumetric analysis to be inherited by these points. Points that inherit no attributes are presumed to represent no change beyond error. These cells are also given the vertical change value of zero.

For the evaluation centerline route, an event table is drawn up that starts with a value of 500 meters and repeats an event for every 500 meters. This allows for the creation of evaluation polygons. From the resulting event layer, points that will make up the vertices for these polygons will be generated with the 'Buffer Points' software tool, Appendix A.

Two-Dimensional Pattern Extraction

For each storm event, it is presumed that there are different levels of erosive/accretive penetration into the barrier feature. Therefore, areas along the centerline of 0 to 40 meters seaward at 10 meter intervals, 0 to 100 meters landward at 10 meter intervals, and 100 to 300 meters at 50 meter intervals are given summary statistics of volumetric change points for each event. This will establish the extent of influence that the storm has at a sampling scale of 500 meters. The first class of observation areas cover 5000 cubic meters, and the second class will cover 25000 cubic meters.

A simple majority statistic will determine the area coverage of erosion/accretion at the particular observation area, and the mean vertical change will take magnitude of

Evaluation Features for Volumetric Pattern Analysis - Hurricane Ike

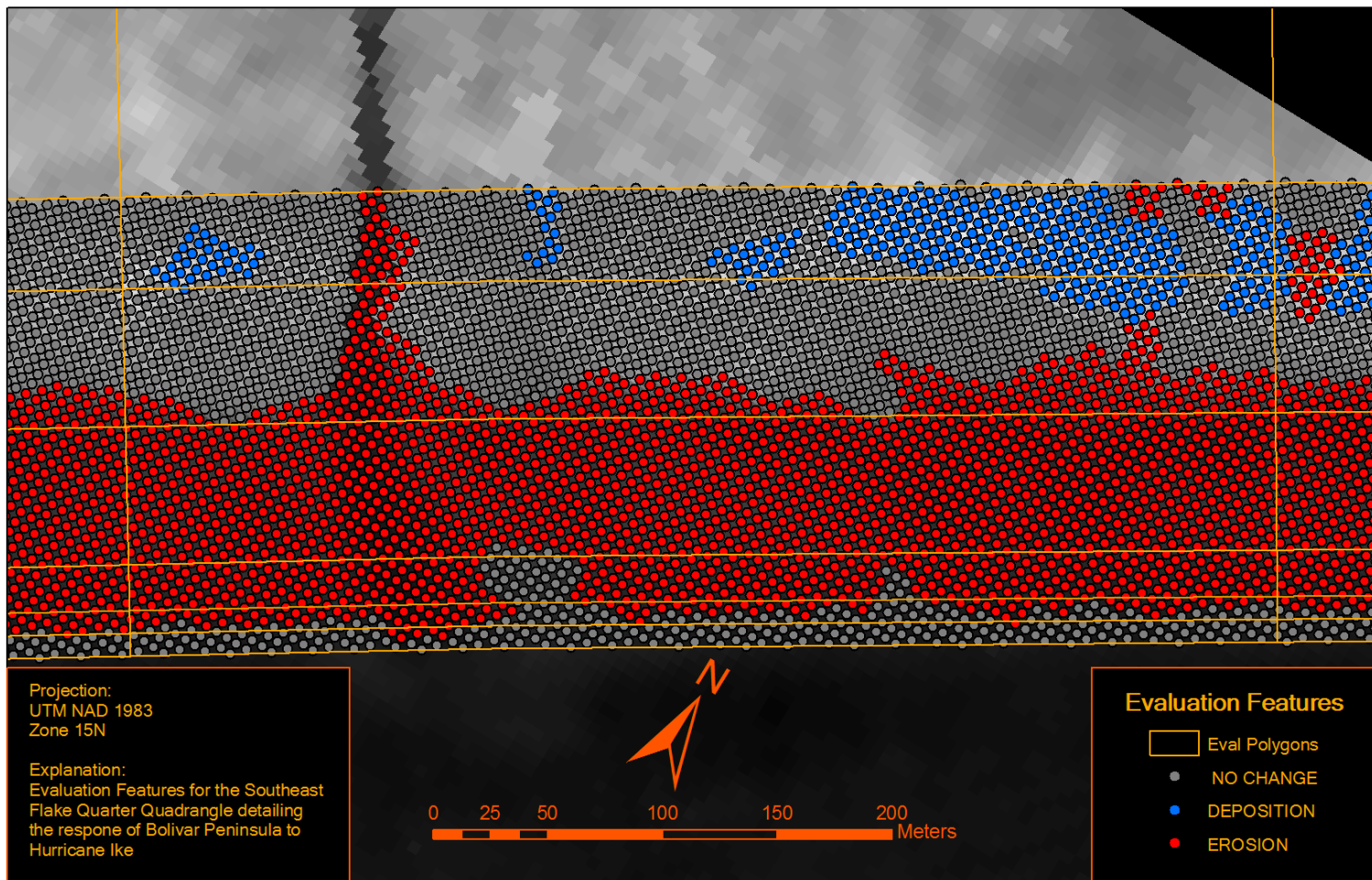


Figure 3.33. With points, it is possible to do summary statistics and counts in order to establish a pattern for tropical storm response and long term change.

erosion and accretion into account. These statistics and measures are calculated with the ArcGIS® Desktop ‘Dissolve’ function with the vertical change class as one parameter and the name of the observation area as the other. Depending on values from this dissolve operation, the output of these classifications will be “no change”, “erosion”, or “deposition” for each observation area. These text values are given numeric analogues such that "no change" = 0, "deposition" = 1, and "erosion" = 2.

Data resulting from these two calculations are combined via a logical ‘OR’ operation, and reclassified accordingly. To give an example, a value of ‘0’ "no change" is assigned to an area as a result of the the simple majority calculations and ‘1’ "deposition" is assigned as a result of the coastal change calculations. The ‘OR’ operation would take 0 and 1 and apply that logical operation to get a result of ‘1’. This same scenario is true for erosion as well.

One-Dimensional Pattern Extraction

To make two-dimensional patterns comparable to the volume change observations for Tropical Storm Josephine (Figure 3.32) the pattern needs to be turned into a one-dimensional volume change pattern. This is accomplished with the aid of a few observations. The first observation is that the volumes are calculated from beach profiles in Gibeaut, Gutierrez, and Hepner (2002). The second observation is that the average length from shoreline to monument is roughly 80 meters. From those observations, it is possible to create a bound upon which these observations can be made. So, 8 segments that span from the centerline to 80 meters landward of the centerline will be utilized as this measure.

The second measure is to calculate actual volume change from the number of points and mean change in each class of vertical displacement. This calculation is accomplished by equation 3.4.

$$V = DNR^2 + ENR^2. \quad (3.4)$$

‘V’ symbolizes net volume of erosion or accretion. ‘D’ and ‘E’ describes average vertical change from each class of deposition or erosion. ‘N’ details the number of pixels in each class, and ‘R’ describes the resolution of the points—in this case $R^2 = 25$ squared meters. A determination of the class will be made on the sign of ‘V’ after all calculations are made—with a negative value being erosion and positive being deposition.

Pattern Change Analysis

Pattern change analysis is done by a simple comparison using overlay analysis of the pattern features previously established. Using overlay analysis, the coastal change type, erosion or accretion, is documented for each storm or event. This makes it possible to compare one event to another and to look at difference or similarity for groups of events.

For shoreline change, the storms—with the exception of Tropical Storm Josephine—these storm events are compared to each other and evaluated for similarity/difference. In the case of volume change, 1D patterns are compared with each other to establish similarity/difference. 2D patterns for all storms are compared to each other and all together to establish similarity/difference.

CHAPTER IV

ANALYSIS OF STORM IMPACT PATTERNS

Shoreline Change Patterns

Alongshore shoreline change patterns are documented for Tropical Storm Fay and Hurricanes Rita and Ike. For both Hurricane Rita and Tropical Storm Fay, there was significant wave-generated noise in the data. This noise occurs when waves break on a very shallow and low gradient beach. These breaking waves register as false surfaces and interfere with the detection of the true beach surface. The result is significant confusion of where the shoreline actually could be. Often, it is necessary to use an alternative approach such as morphological operations, alongshore filtering of high elevation points, and visual interpretation. All of these techniques involve some degree of user interpretation and are subject to user error. Shoreline changes for each storm can be referenced in Appendix C.

Shoreline Change Pattern – Tropical Storm Fay

Overall, the pattern of shoreline change from Tropical Storm Fay appeared to reinforce the general pattern of accretion at the distal end of a spit and erosion being more prevalent at the narrow, proximal end (Figure 4.1). It is notable that there are large patches of shoreline change that do not register beyond error. These large patches appear to be rhythmic and separate patches of erosion and accretion. This area was also found to have the highest spatial sensitivity. The regions of Gilchrist and Caplen (near Rollover Pass) appear to be regions that have undergone coastal erosion. The Crystal Beach community also appears to be in an area marked by erosion. All zones considered, there

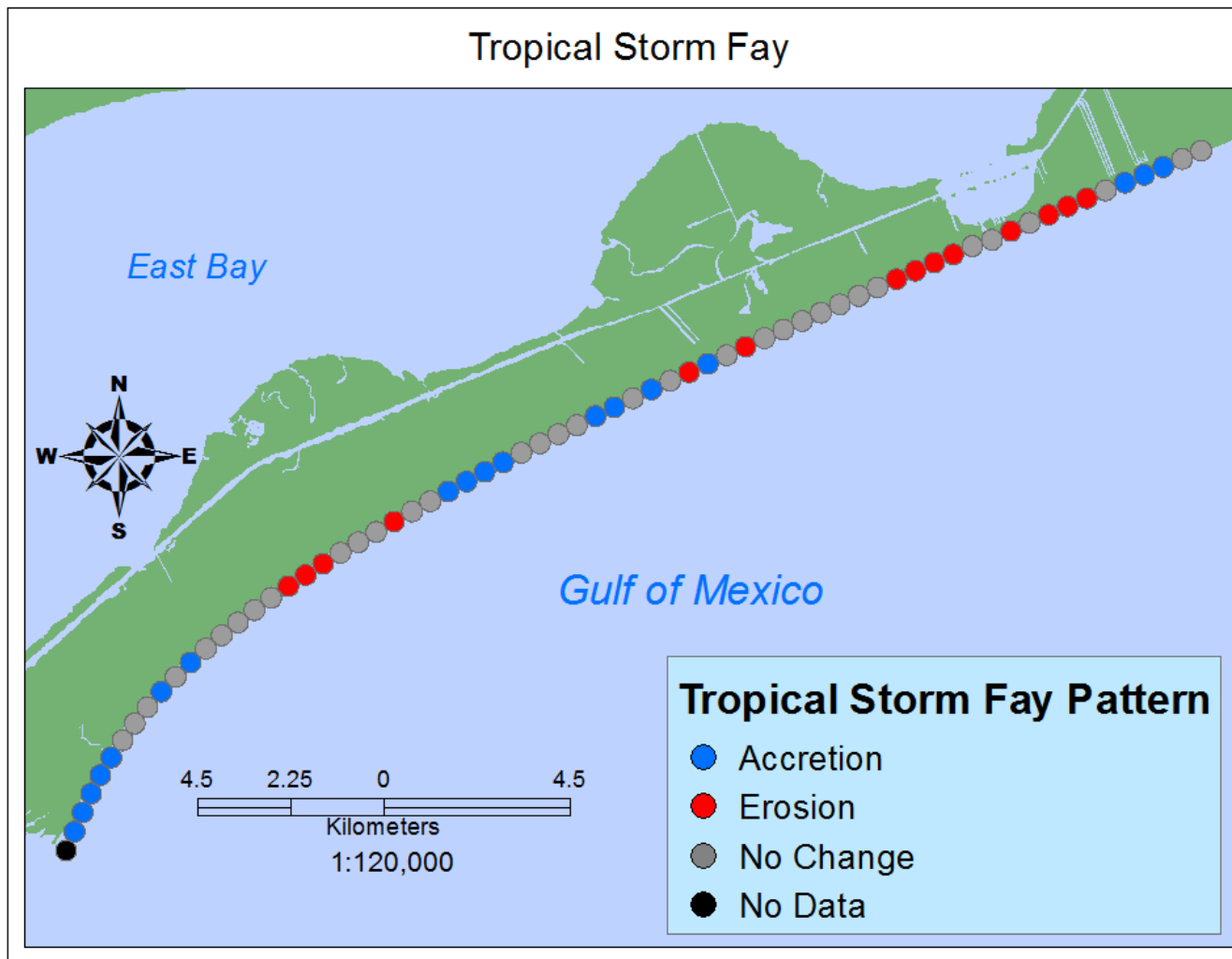


Figure 4.1. Pattern of shoreline erosion and accretion as a result of Tropical Storm Fay.

appears to be a periodic alternation of zones of erosion and accretion/no change that are attributable to Tropical Storm Fay.

Magnitudes of alongshore erosion and accretion for Tropical Storm Fay were similar to the long term shoreline change cited in Gibeaut, Gutierrez, and Hepner (2002). The similar traits are the larger accretive locations near the terminus of the spit and the higher erosion values near Rollover Pass—which is roughly at 27.5 kilometers from the proximal end of Bolivar Peninsula. However, this shoreline erosion was not nearly as stark as that suggested by Gibeaut, Gutierrez, and Hepner (2002). There is also a far greater oscillation—despite that oscillation being nearly all encapsulated within the error bars. Also of interest is a proximal region of accretion updrift 3 kilometers of Gilchrist, TX (Figure 4.2). This location is near Rollover Pass, and is characterized by very low-lying areas.

Shoreline Change Pattern – Hurricane Rita

Much of the post-Rita LiDAR dataset was affected by wave-generated noise. This distorted the shoreline's horizontal position. To help ameliorate this uncertainty, an alongshore ArcGIS® Desktop FocalMin procedure was used—as discussed in the previous chapter. After this procedure, it was still necessary to use excessive morphology operations in two different stages. This means that the erosion morphology operator was executed 15 times, then the object formation and removal command for land was executed with usual inputs, and finally the dilation command was executed 15 times. This resulted in a very blocky output that had to be generalized by manual editing.

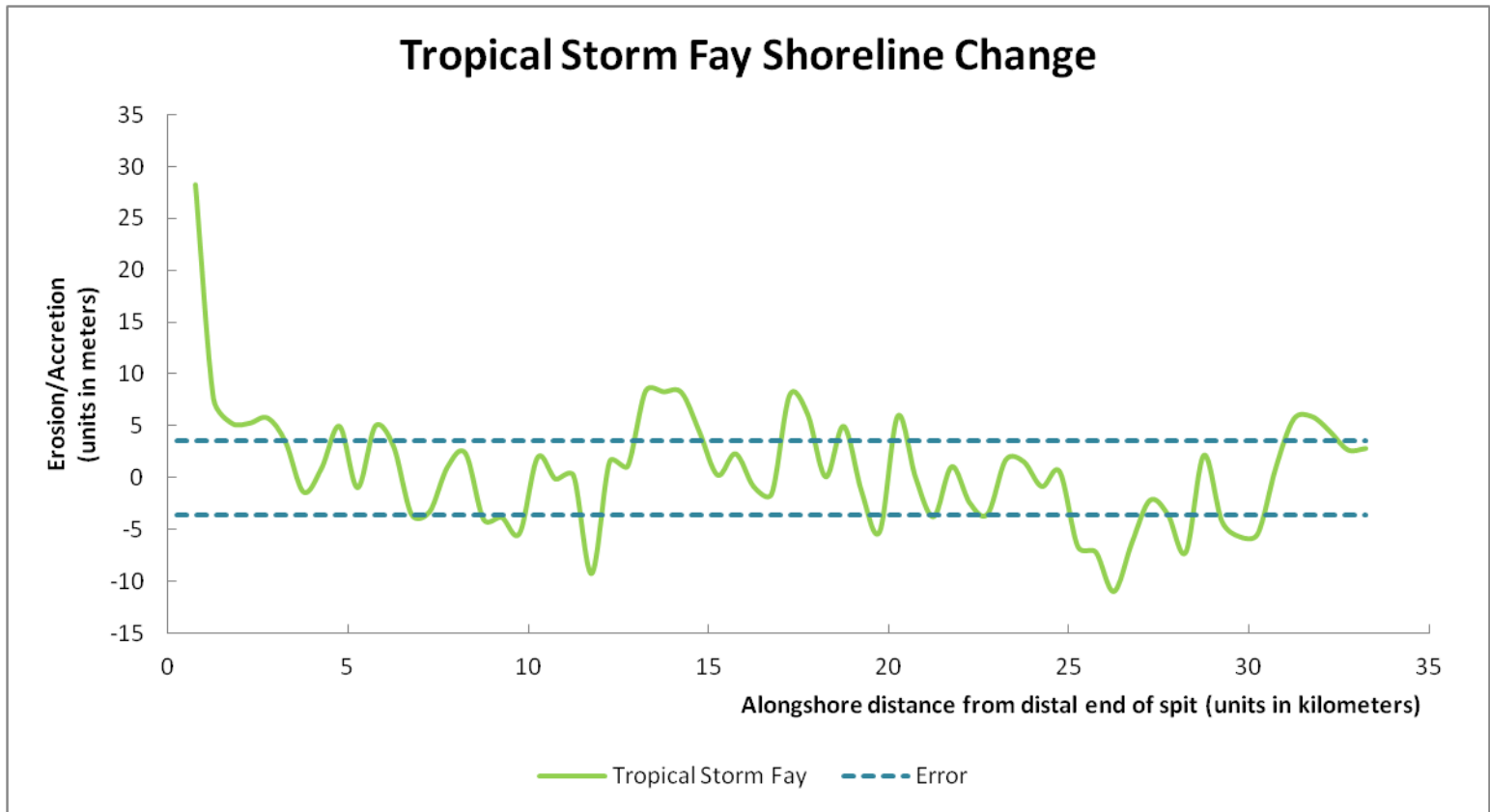


Figure 4.2. Detrended shoreline impacts from Tropical Storm Fay.

The shoreline change pattern established for Hurricane Rita is nearly all erosive—with small accretion patches at the distal end and one small accretionary zone near the eastern side of Rollover Pass (Figure 4.3), near the same region as there was accretion from Tropical Storm Fay. It should not be understated that strongly erosive character of this shoreline change could have been as a result of the uncertainty surrounding the post-Rita shoreline. Areas of no change were clustered around the distal end of the spit. There are also two zones—as opposed to alternating zones of erosion/accretion with Tropical Storm Fay and Hurricane Ike—of shoreline erosion/accretion for Hurricane Rita.

Magnitudes of shoreline change for Hurricane Rita has two major similarities with the long term shoreline change indicated by Gibeaut, Gutierrez, and Hepner (2002). The first similarity is the distal accretion—although the zone of distal accretion is quite small, and the second similarity is the erosive tendency near Rollover Pass. However, this shoreline change from Hurricane Rita does have a much more pronounced loss of sediment at the point of maximum curvature, 10-15 kilometers from the distal portion of the spit at 15 meters (Figure 4.4).

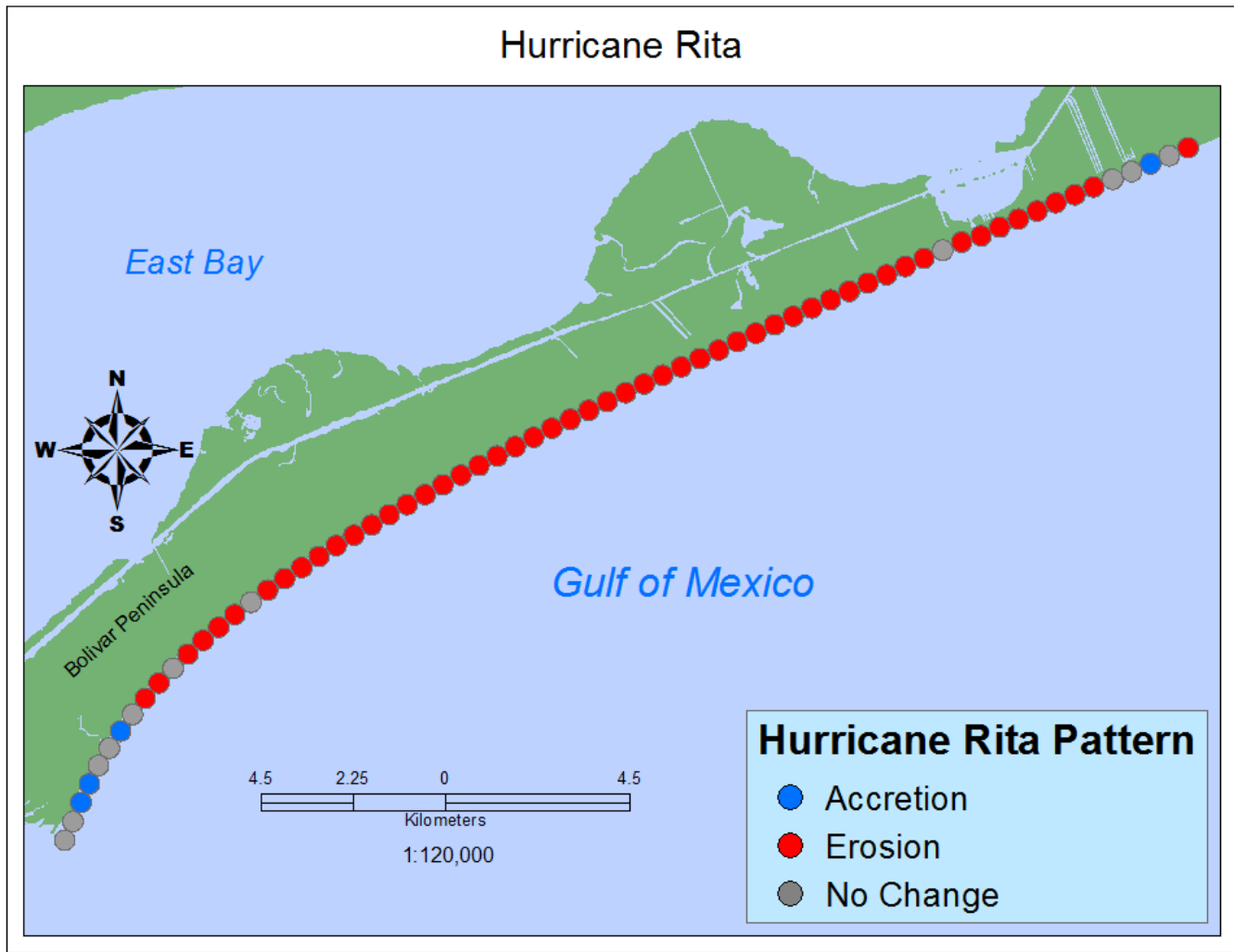


Figure 4.3. Pattern of shoreline erosion and accretion as a result of Hurricane Rita.

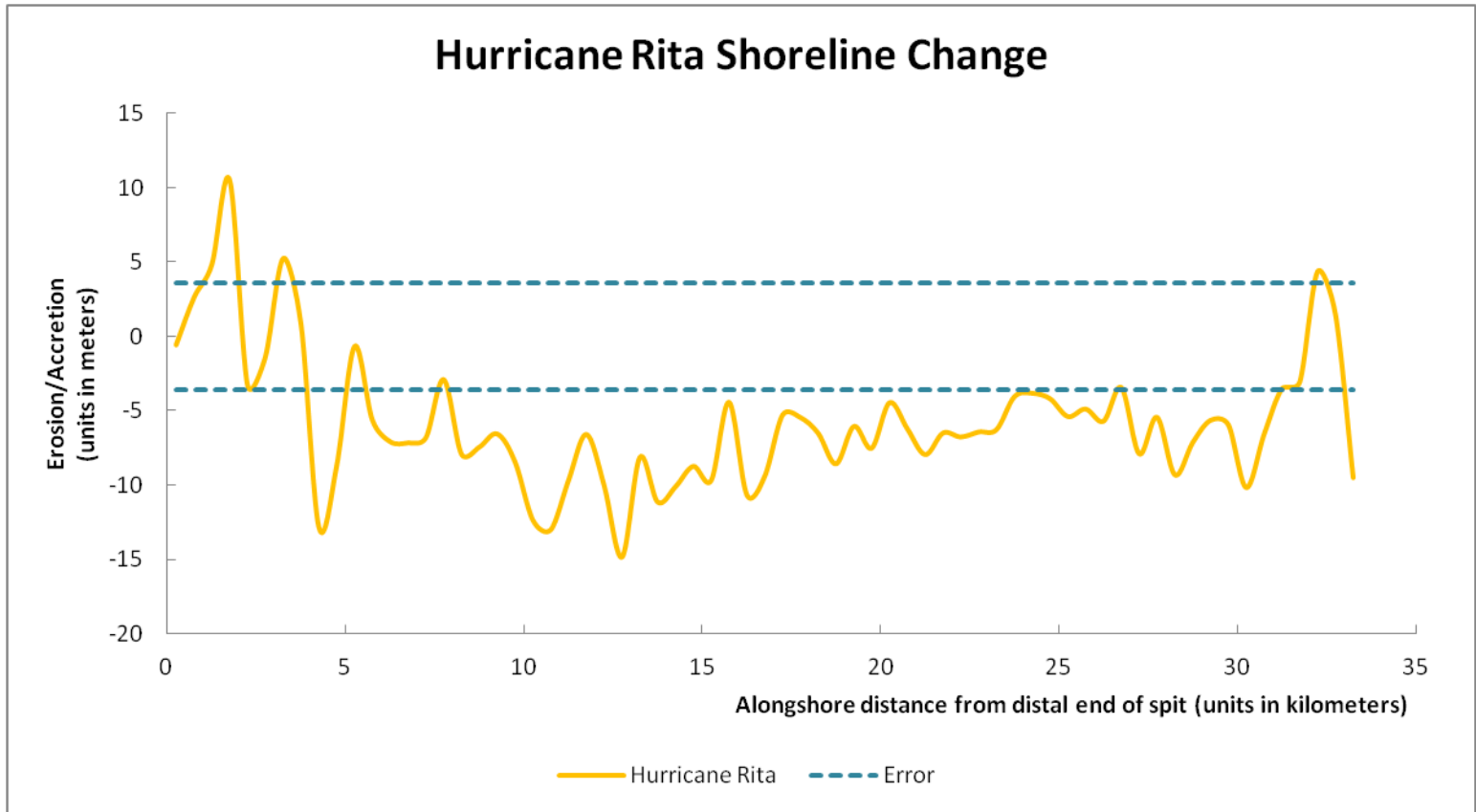


Figure 4.4. Detrended shoreline impacts from Hurricane Rita.

Shoreline Change Pattern – Hurricane Ike

Shorelines derived from post-Ike LiDAR imagery did not have the same problems as the other post-storm imagery. This is most likely because of the much larger magnitude of coastal change that Hurricane Ike brought to the North Texas coast. Like shoreline change from Hurricane Rita, the alongshore response was net erosive.

The shoreline change from Hurricane Ike defies the pattern commonly believed to be associated with barrier spits, accretion at the distal end and erosion at the proximal end. Hurricane Ike was erosive on the entire proximal portion of Bolivar Peninsula. With the shoreline changes from Hurricane Ike, the distal end of the spit eroded. Shoreline changes associated with Hurricane Ike exhibited a unique pattern with accretion at the part of the peninsula with most curvature 10-15 km from the distal end of the spit, but not the part most distal (Figure 4.5). The zones of accretion seem to match up with stream outlets (Carter, 1987) or large scours. It is also noteworthy to observe that areas of no change beyond error also coincide with these depositional or accretionary patches. Although the zones of accretion are far smaller than those of erosion, there does appear to be a sort of periodic nature to the zonation—especially in the zone of maximum curvature for the spit where zones of accretion vary from 5 to 10 meters.

Magnitudes of shoreline change for Ike are quite different from the shoreline response of the other two storms (Figure 4.6). Whereas there was accretion at the distal end of the spit between 30 and 10 meters for Tropical Storm Fay and Hurricane Rita, respectively, Hurricane Ike eroded more than 100 meters from the terminal end of Bolivar Peninsula.

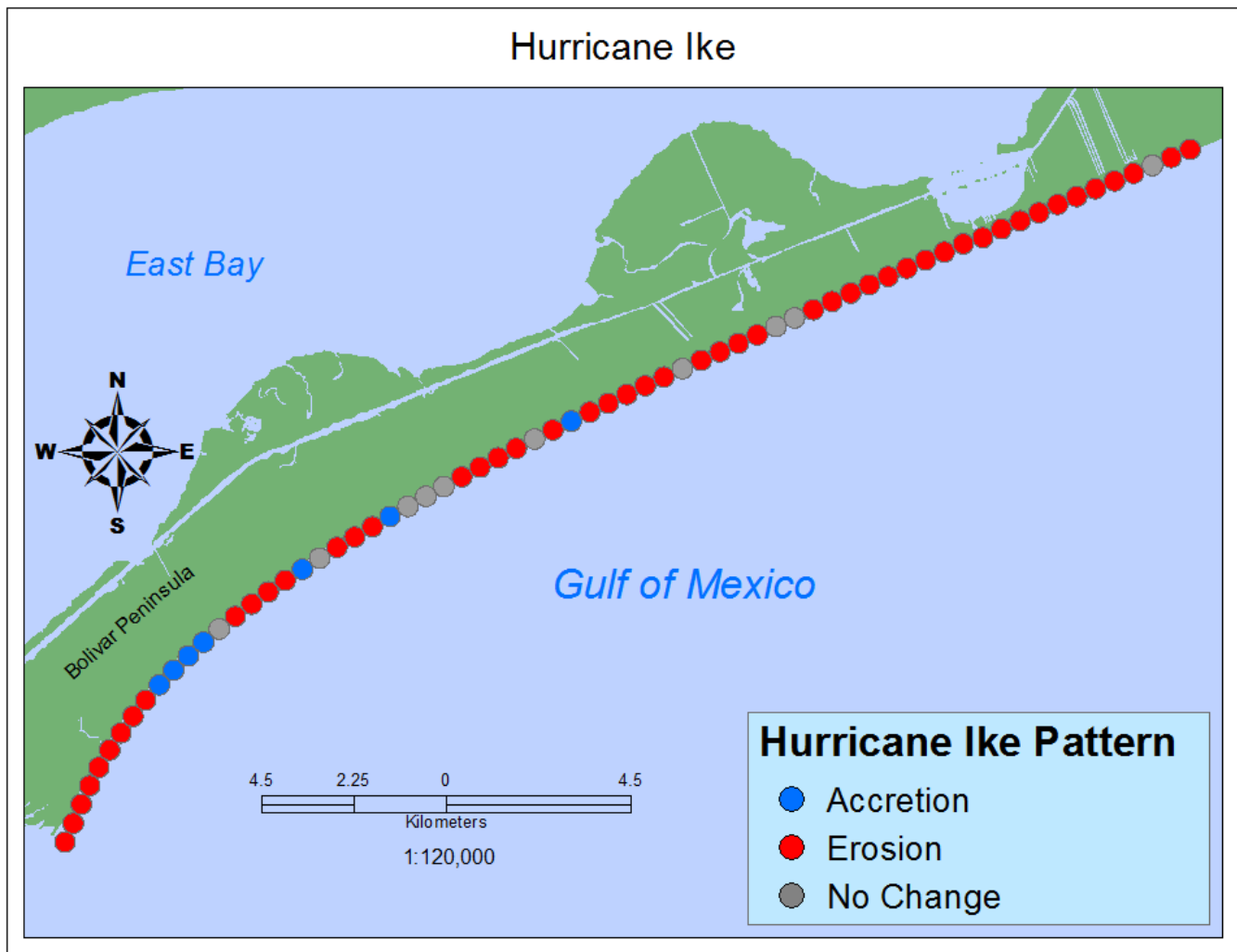


Figure 4.5. Pattern of shoreline erosion and accretion as a result of Hurricane Ike.

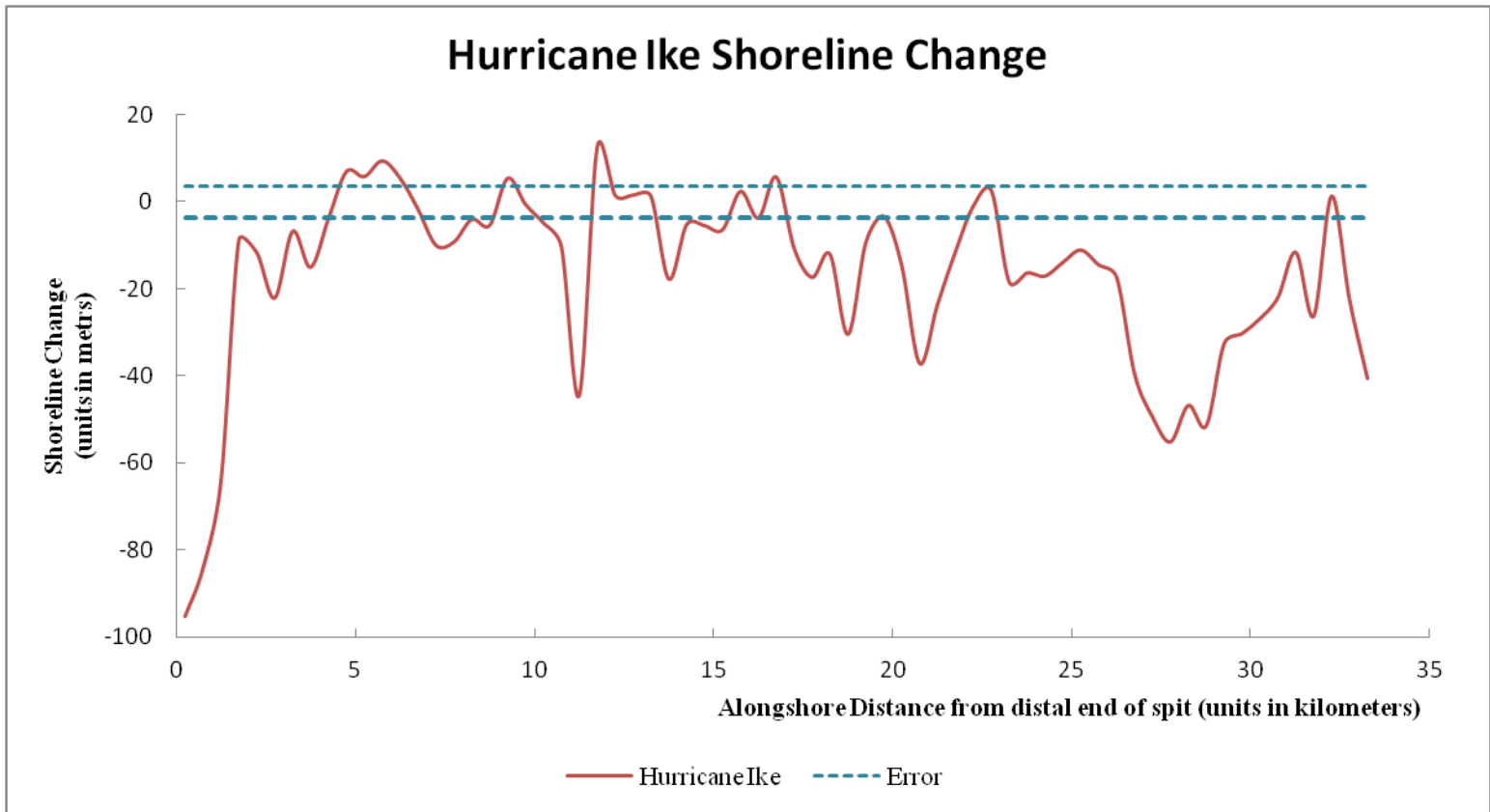


Figure 4.6. Detrended shoreline impacts from Hurricane Ike

There are similarities in the pronounced erosive trend at Rollover Pass to the response to Tropical Storm Fay, but the shoreline change is different in that aspect from Hurricane Rita. This is because the Rollover Pass shoreline erosion was much less pronounced in Rita, but is greatly emphasized from the impacts of Hurricane Ike. It is also noted that there is an island of accretion, but this accretion was considered no change because the accretion was within the error threshold of -3.58 meters to + 3.58 meters.

Volumetric Change Patterns

1D Volumetric Change Patterns

Alongshore trends of erosion and accretion in the subaerial zone were derived to make volume calculations compatible with the beach profile observations of Gibeaut, Gutierrez, and Hepner (2002) with respect to Tropical Storm Josephine. These alongshore patterns will be compared in the same manner as the alongshore shoreline change patterns. Magnitudes of volume change impacts are also included.

Point-discretized groups of erosion and accretion that extended 80 meters from the centerline were summed into groups of 500 meters—as to match one-dimensional shoreline change statistics. There is no ‘No Change’ volume change status for this analysis, since there was no such thing error involved in the assessments of Gibeaut, Gutierrez, and Hepner (2002).

Three storms, Tropical Storms Josephine and Fay, have a pattern of erosion and accretion. The two storms with higher intensities registered as all erosion in terms of trend. When comparisons are made, these two Hurricanes will be considered as one unit.

2D Volumetric Change Patterns

The purpose for 2D Volumetric change pattern analysis is to see how these storms behave in the sub-aerial zone in terms of berm erosion, foredune erosion, overwash, and comprehensive beach erosion/scarping. Patterns are generated with one dimension being the alongshore dimension, and the other dimension being the cross-shore dimension. Nominal values represent the type of change in the third dimension, the vertical dimension. There is observed variability alongshore and across the coastal barrier—as instructed by Figure 4.7. Knowing these facts, it is possible to further frame these storms in terms of their impacts as well as their intensity with the storm impact scale for barrier islands proposed by Sallenger (2000). Features can be linked to the maps-patterns below by referencing Appendix D.

Volumetric change from Hurricane Rita and Tropical Storm Fay primarily occurred on the beach face in the form of swash bar/berm erosion and minor accretion from dune impacts/overwash. From these storms, there was minimal dune impact, and no overwash in this pattern analysis was noted. Patches of accretion were thin and discontinuous, and they often removed in the process of generating a volumetric change shapefile with procedures specified in the last chapter. The presence or absence of geotubes are also noted. For the first sets of sections, A-D, D-G, G-J, and J-M, there are no geotubes present for both Tropical Storm Fay and Hurricane Rita. The last two sets of sections, M-P and P-S, include geotubes. For Hurricane Ike, there was extensive coastal erosion and complete destruction of dunes/geotubes. Coastal changes extended well past

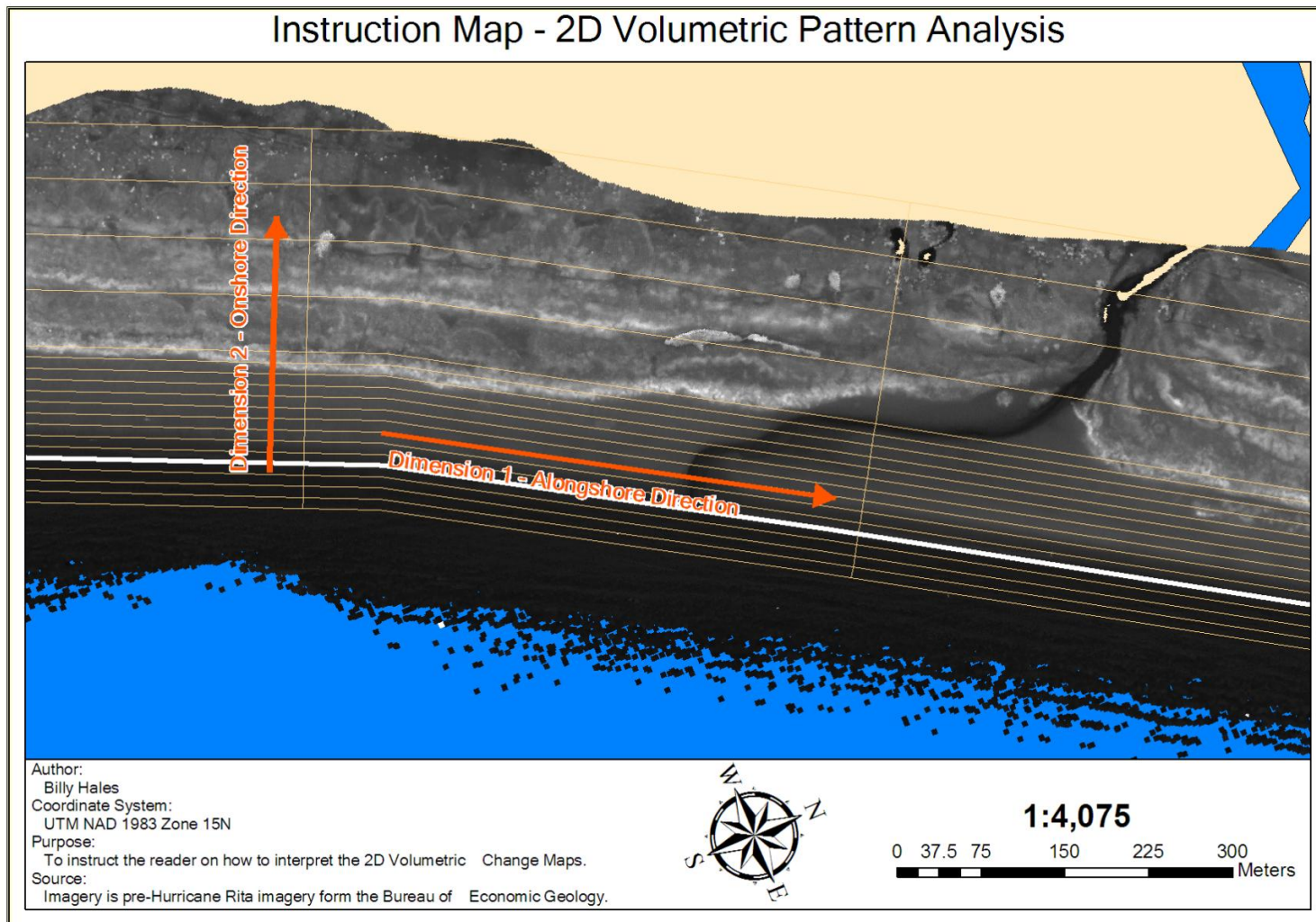


Figure 4.7. Instruction map that illustrates how to interpret 2D volumetric patterns.

100 meters from the shoreline, and there were notable patches of deposition landward of the coastal erosion.

1D Volume Change Patterns – Tropical Storm Josephine

Alongshore volumetric change patterns for Tropical Storm Josephine were derived from Figure 3.32. Through pixel-based analysis of this caption taken from Gibeaut, Gutierrez, and Hepner (2002), it is possible to get estimates that are accurate to +/- 1 meter from the profile observations that this figure was derived from. This analysis does not take into consideration error or estimation that was done by Gibeaut, Gutierrez, and Hepner (2002). It should also be cautioned that measurements in between are just interpolations, and that the stated accuracy cannot easily be commuted to those values. With that caveat in mind, Figure 4.8 details the alongshore pattern of volumetric erosion and accretion generated by Tropical Storm Josephine. In particular, it should be noted that nearly half the spit is in the accretion zone. Detrended alongshore volumetric change is also detailed in Figure 4.9.

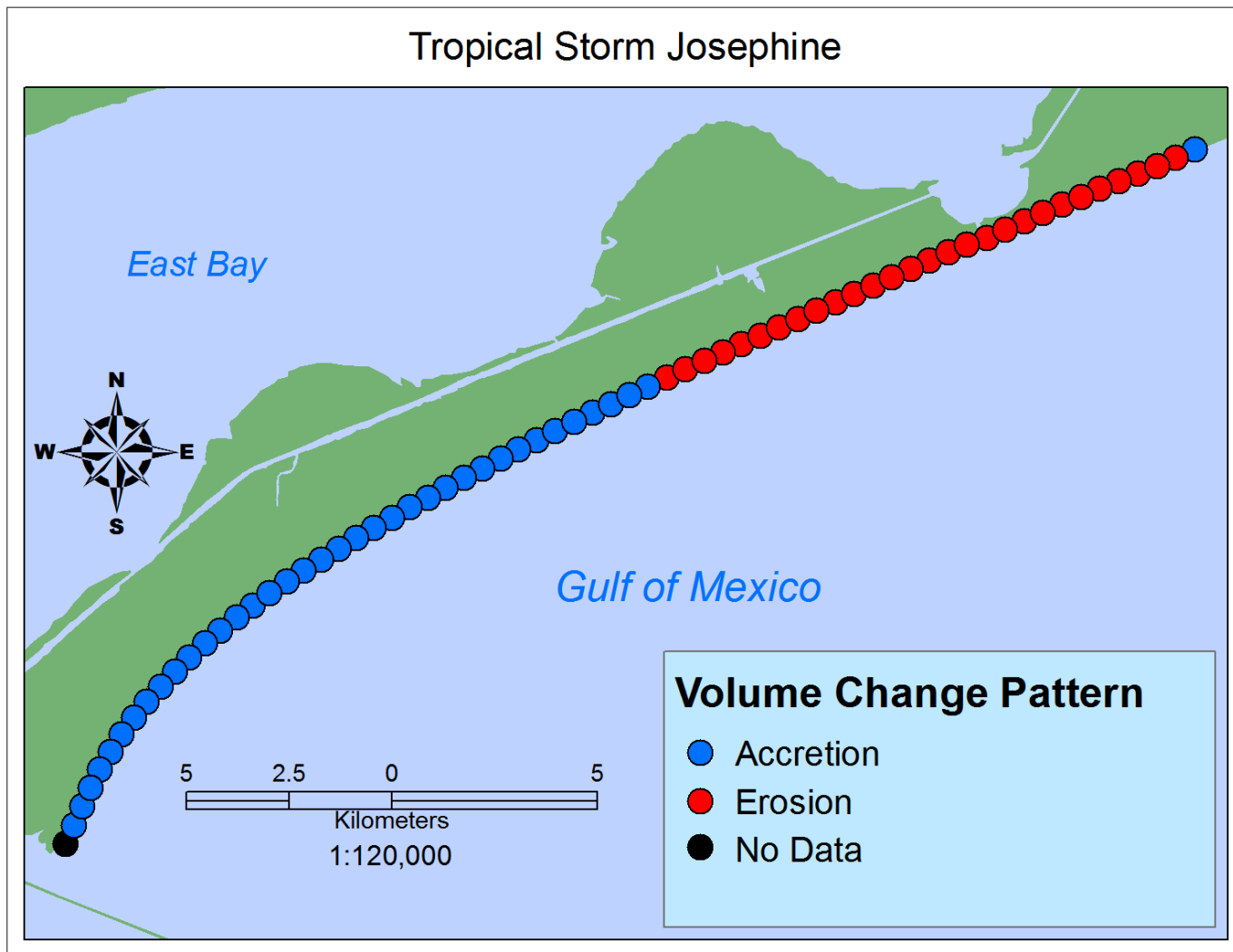


Figure 4.8. 1D alongshore volumetric pattern generated by Tropical Storm Josephine. Data were extracted from Gibeaut, Gutierrez, and Hepner (2002).

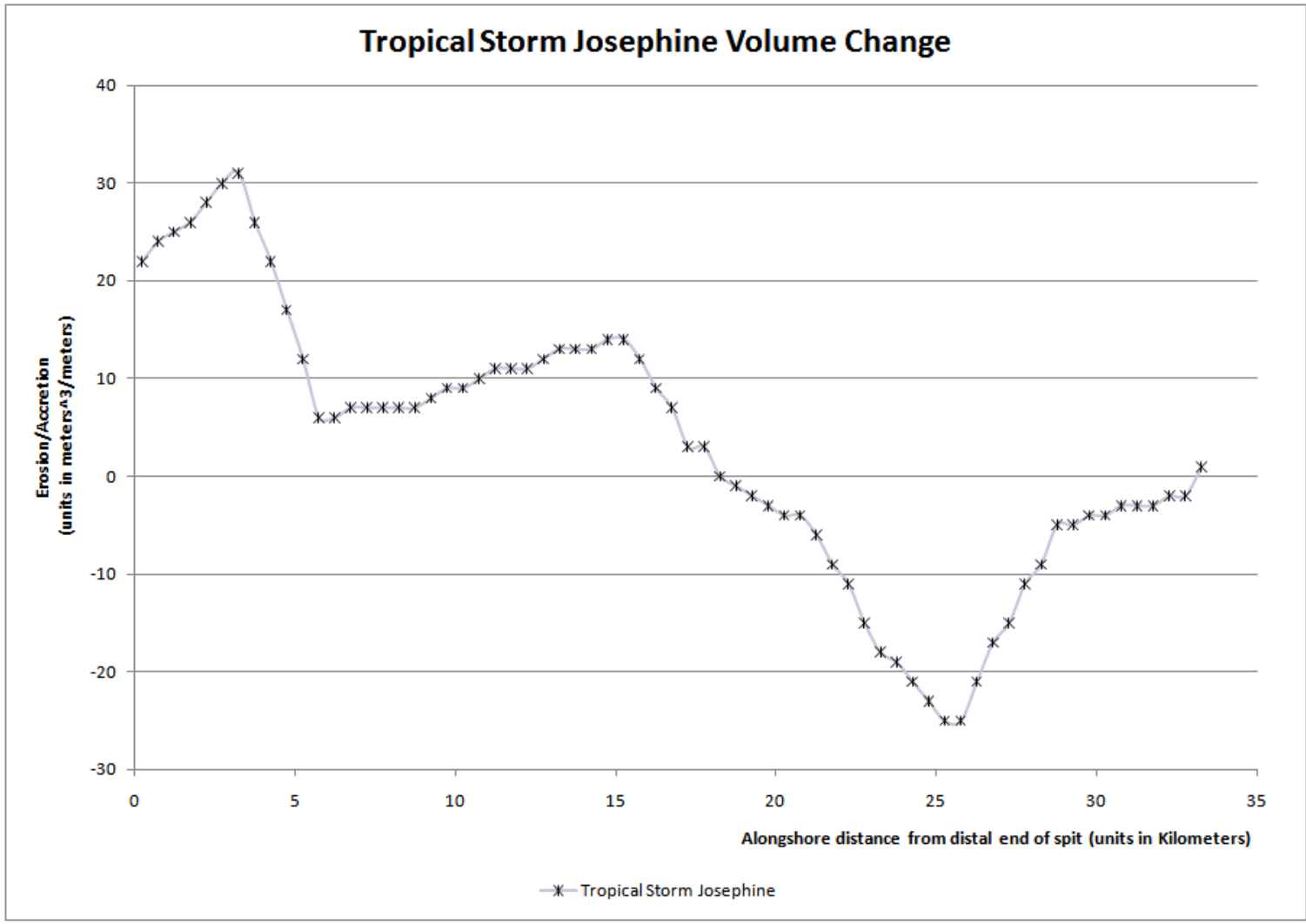


Figure 4.9. Detrended volumetric change for Tropical Storm Josephine, as derived from estimates from Gibeaut, Gutierrez, and Hepner (2002).

1D Volume Change Patterns – Tropical Storm Fay

The patterns of alongshore volume change from Tropical Storm Fay (Figure 4.10), show an alternating nature of erosion and accretion (Figure 4.11) that is similar, though more erosive, to the shoreline erosion and accretion associated with Tropical Storm Fay. An interesting observation is that this periodicity seems to end near Rollover Pass—as is also similar to the shoreline changes. It is important to note that these accretive trends may also be the result of the failure to separate backdune accretion from vegetation uncertainties—as was a difficulty noted in Claudino-Sales, Wang, and Horwitz (2010).

2D Volume Change Patterns – Tropical Storm Fay

The erosion and accretion patches associated with Tropical Storm Fay were binned into cells as mentioned in the last chapter (Figures 4.12-4.17). The patterns of erosion and accretion by Tropical Storm Fay register as “no change” beyond error throughout much of the study area. The cells that register as erosion are less common, and they are largely confined between 10 meters beyond the centerline and 40 meters beyond the centerline—with patches of erosion occurring most often between 20 to 30 meters beyond the centerline. Patches of accretion are very sparse and occur between 80 to 100 meters from the centerline at segment R-S (Figure 4.17). Erosion occurred most extensively at sections P-Q and Q-R (Figure 4.17) with near continuous cells of erosion indicated.

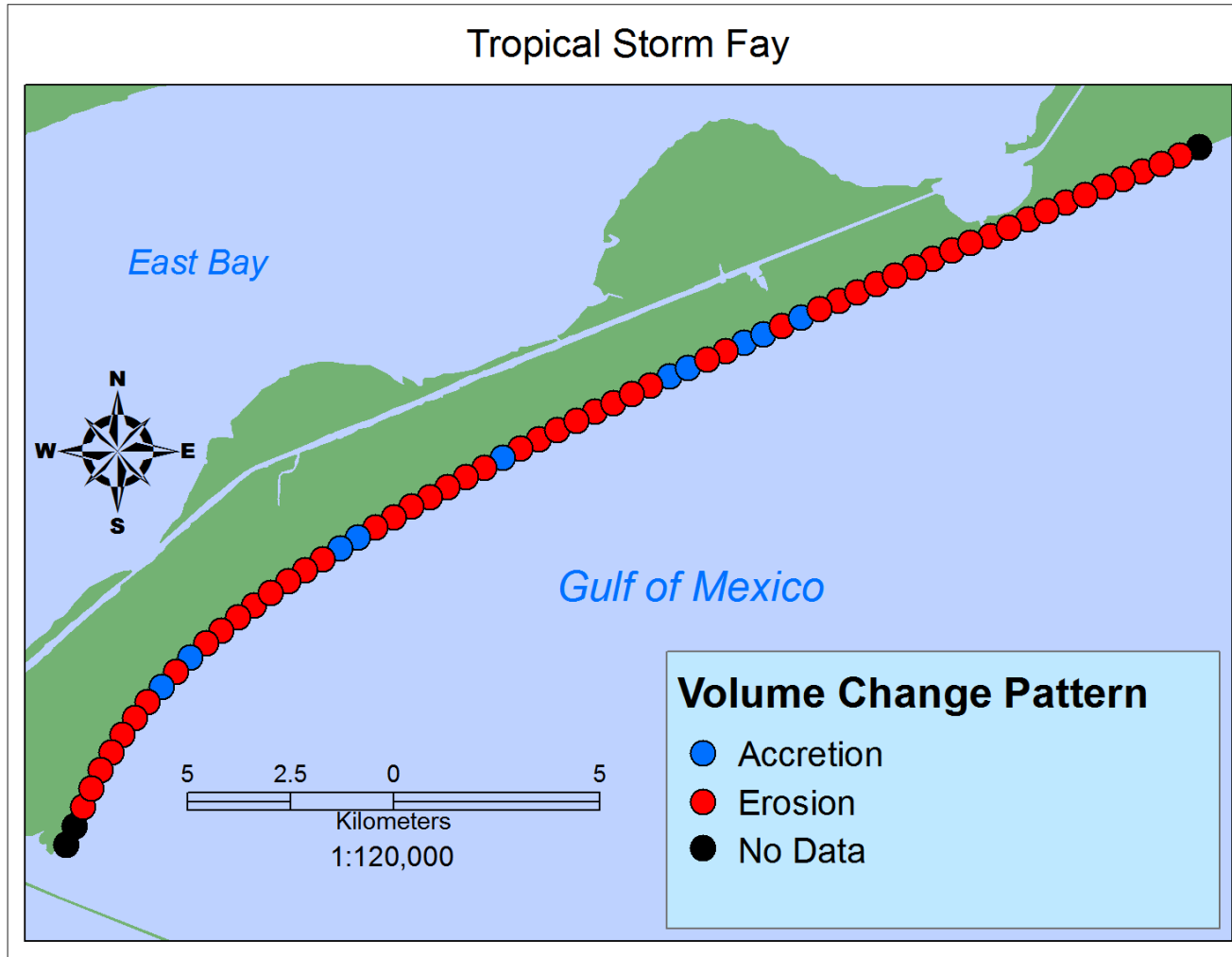


Figure 4.10. 1D alongshore volumetric pattern generated by Tropical Storm Fay. Derived from Bureau of Economic Geology LiDAR imagery.

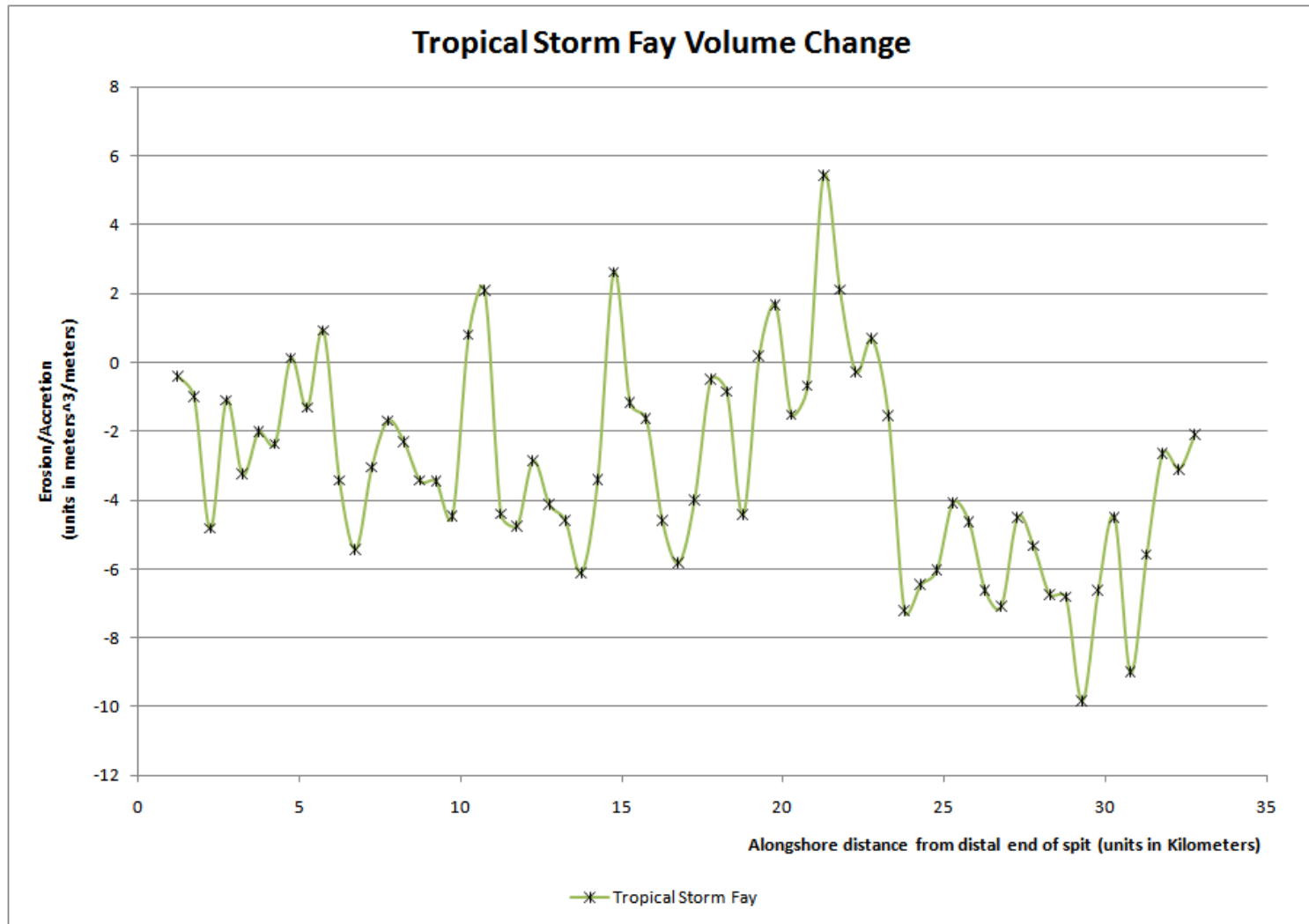


Figure 4.11. Detrended volumetric change for Tropical Storm Fay, as derived from values obtained by Coastal Morphology Analyst (Liu *et al.* 2010) and then derived as discussed in Chapter 3.

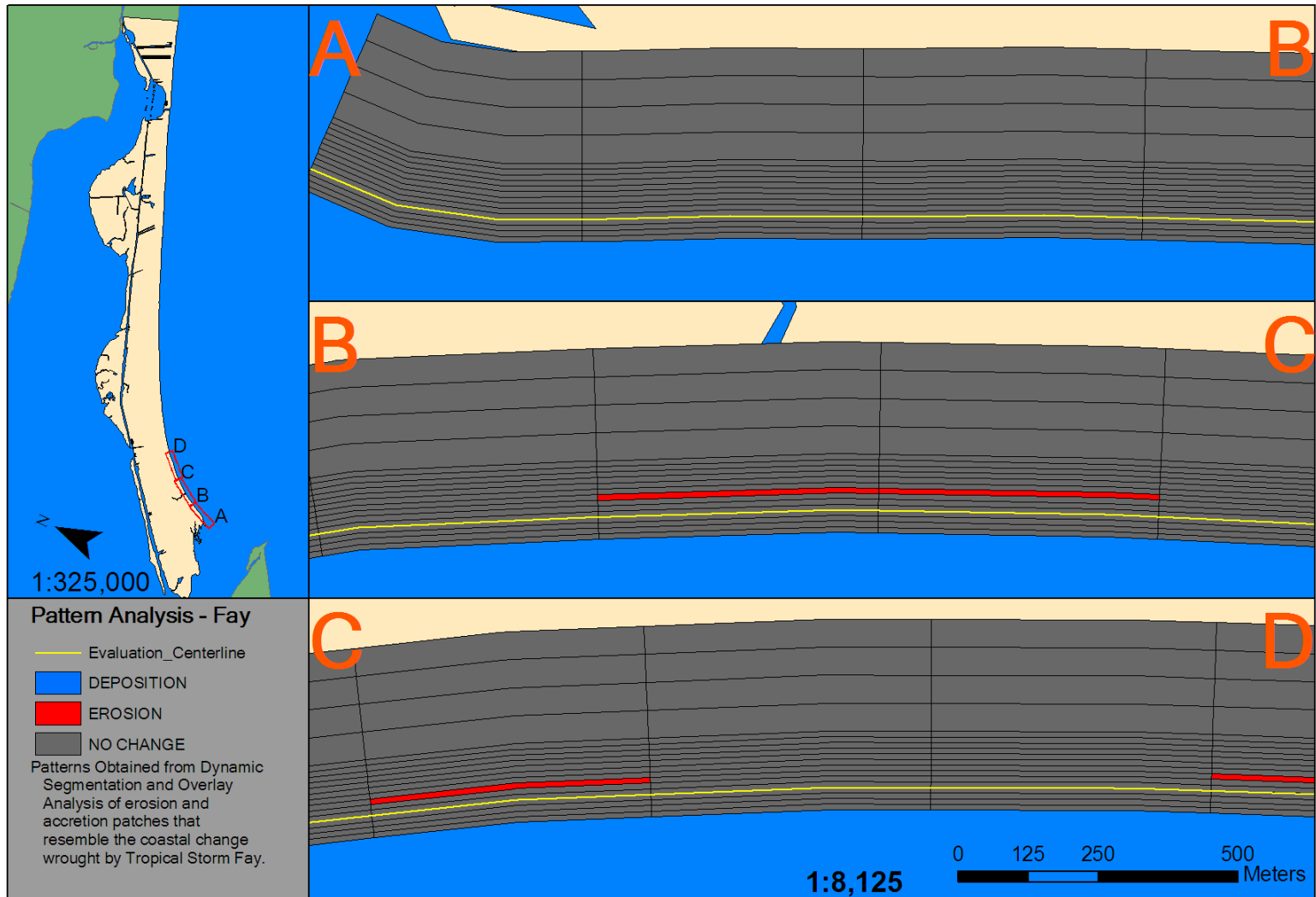


Figure 4.12. Sections A-D of 2D volumetric change patterns - Tropical Storm Fay.

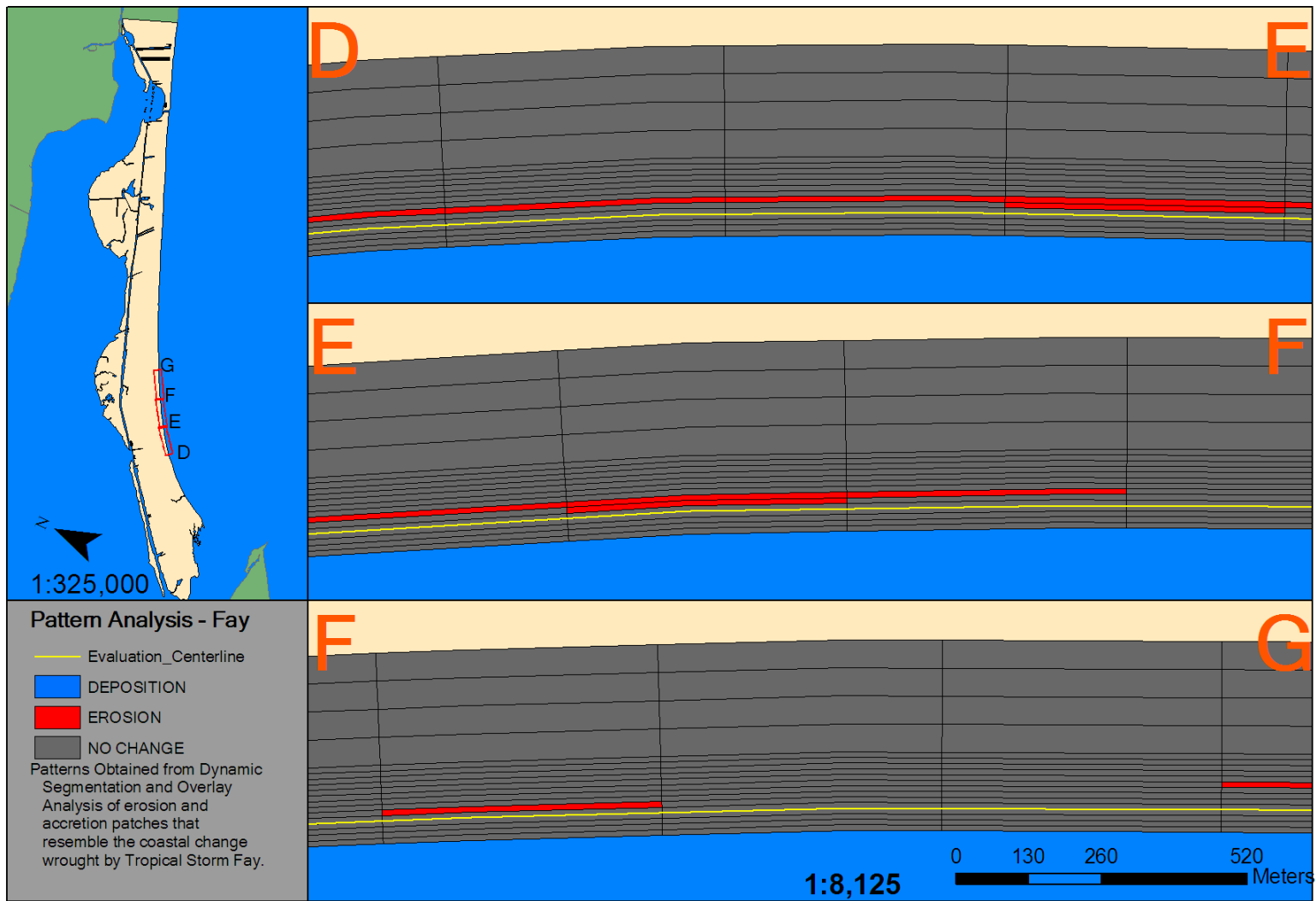


Figure 4.13. Sections D-G of 2D volumetric change patterns - Tropical Storm Fay.

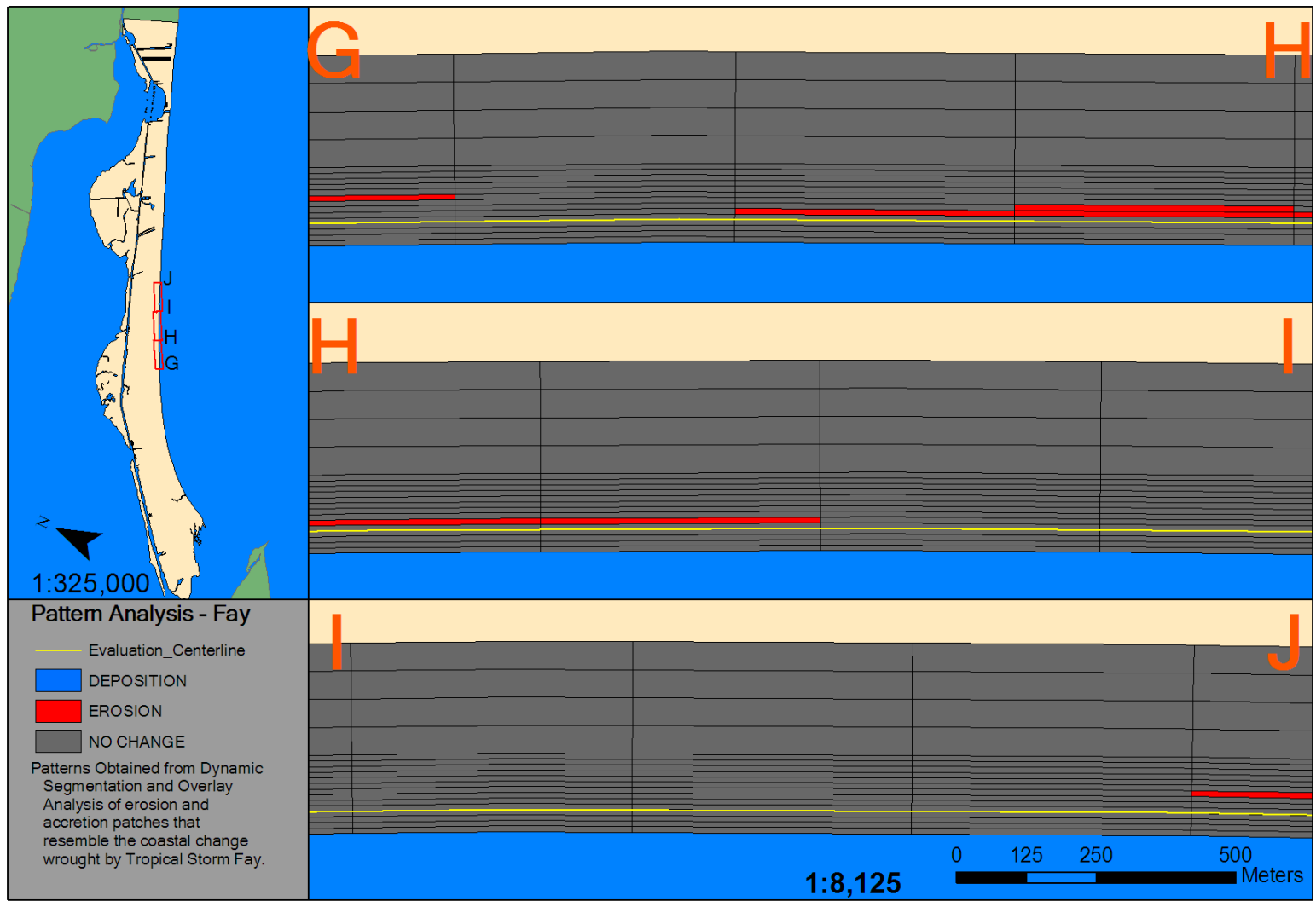


Figure 4.14. Sections G-J of 2D volumetric change patterns - Tropical Storm Fay.

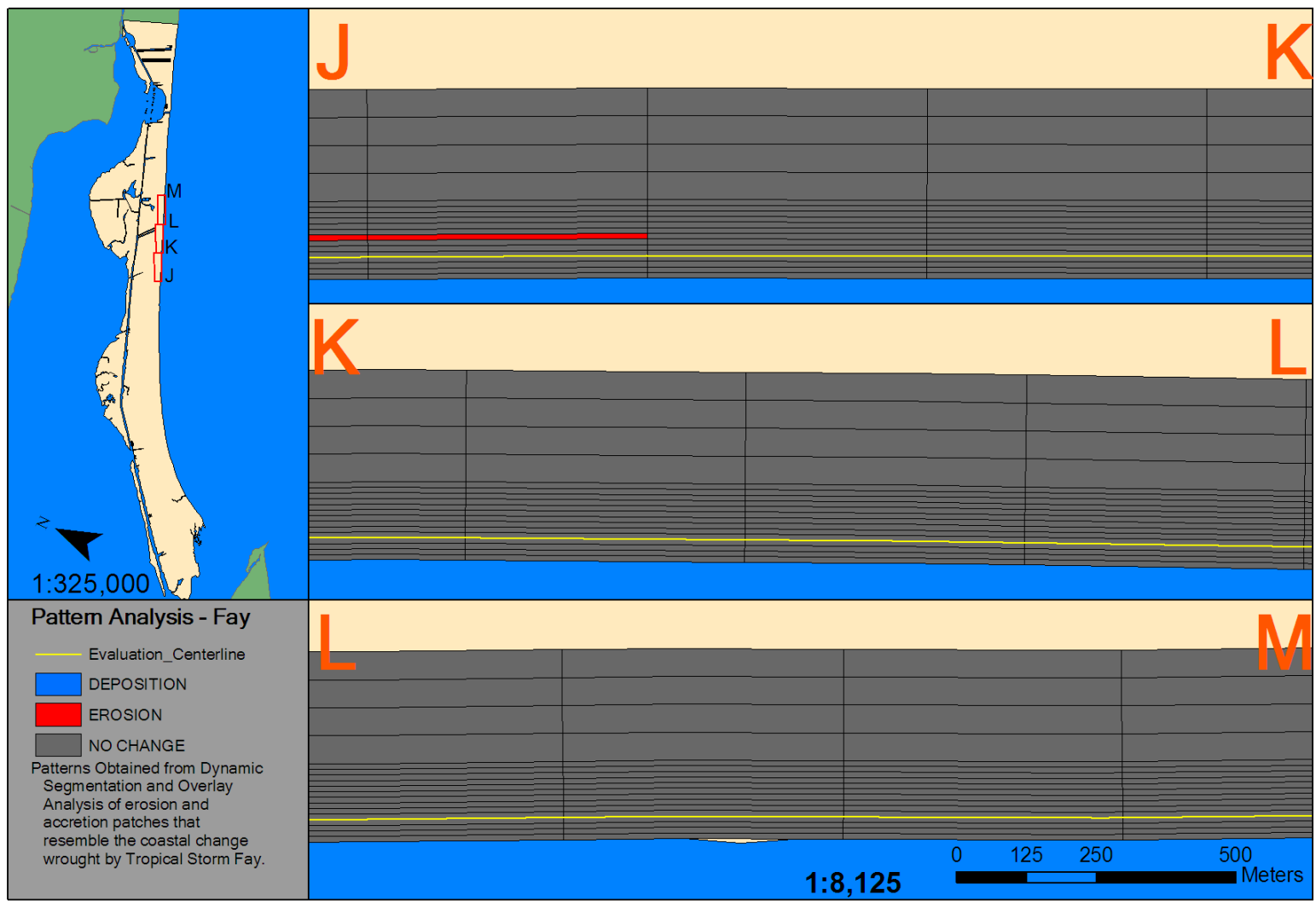


Figure 4.15. Sections J-M of 2D volumetric change patterns - Tropical Storm Fay.

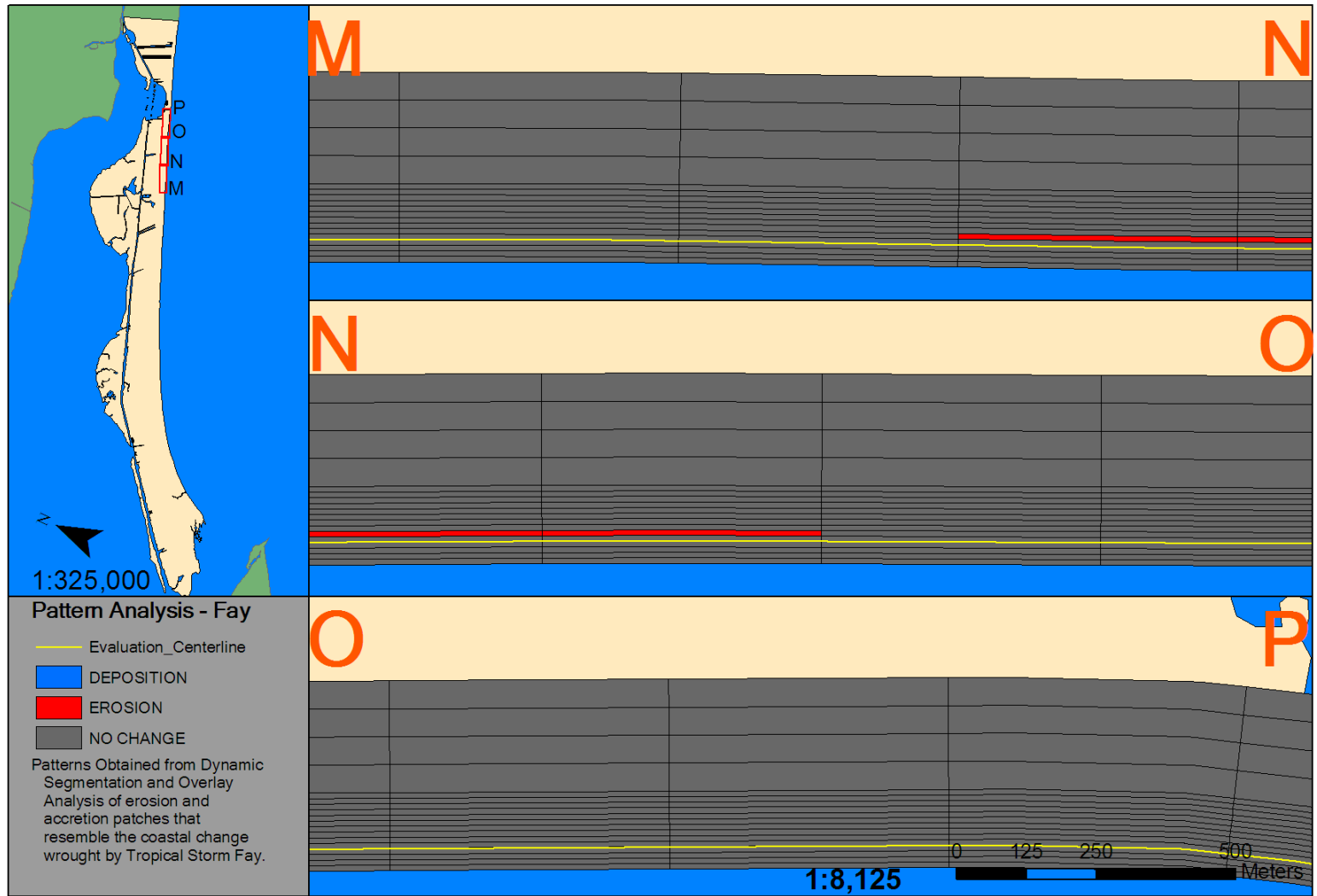


Figure 4.16. Sections M-P of 2D volumetric change patterns - Tropical Storm Fay.

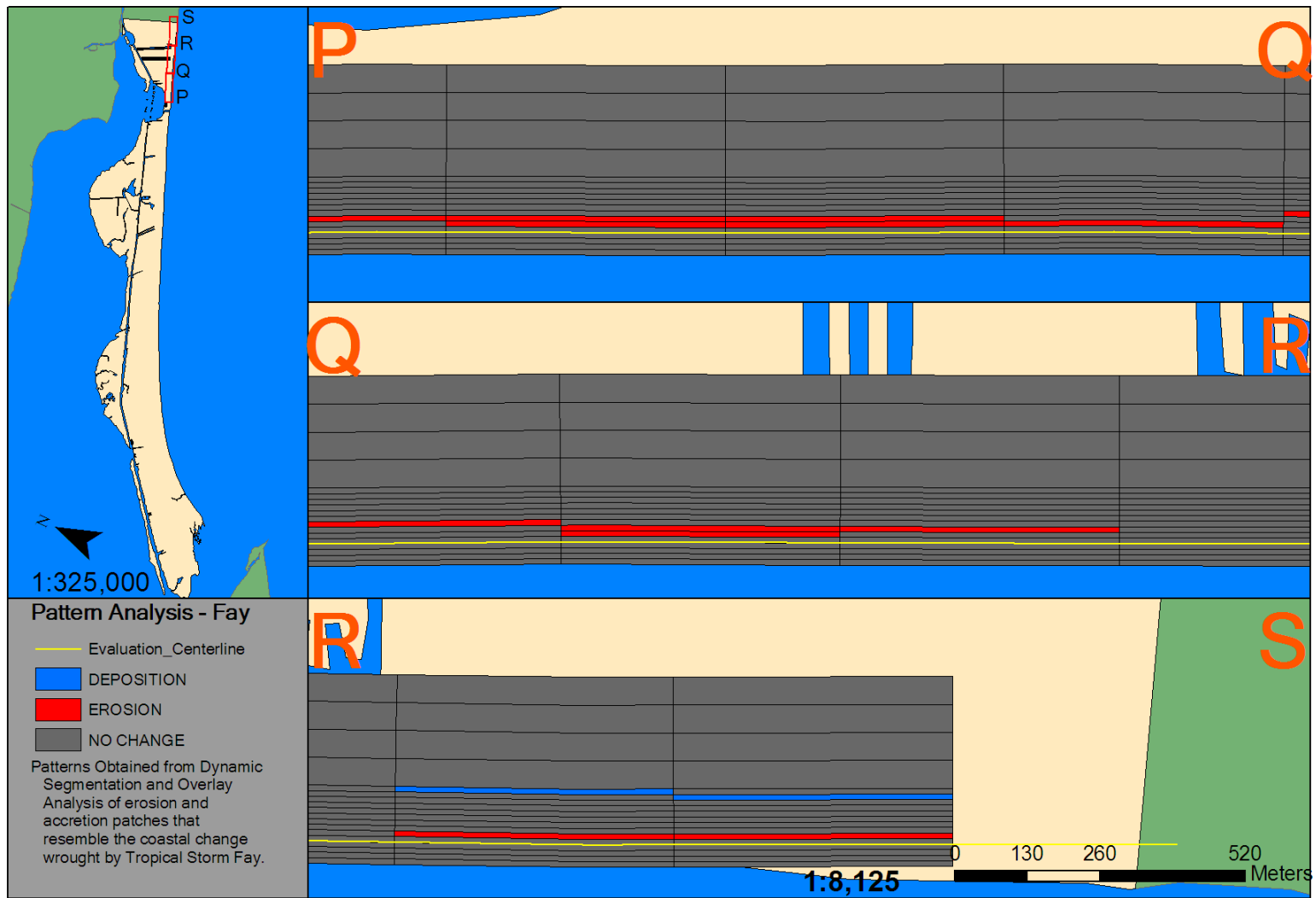


Figure 4.17. Sections P-S of 2D volumetric change patterns - Tropical Storm Fay.

1D Volume Change Patterns – Hurricanes Ike and Rita

Hurricanes Ike and Rita had a single trend of erosion for the entire length of the spit (Figure 4.18). However, the detrended volumetric impacts (Figure 4.19) shows that there is a change in the impacts from Tropical Storms Josephine and Fay. Instead, it appears as if there was greatest erosion at the distal end of the spit instead of accretion.

2D Volume Change Patterns – Hurricane Rita

Most of the effects of Hurricane Rita were on the beach face of Bolivar Peninsula with minor dune impacts—where dunes existed near the distal end and in parts of Caplen. Near the distal portion of Bolivar Peninsula (Figure 4.26) there was significant property development between time periods covered by the Pre-Rita LiDAR dataset and the Post-Rita LiDAR dataset. This means that if there were significant storm-driven changes past the dune line, they could not be separated from the changes brought forth by the property developments. Despite the human modifications, there was localized and small patches of accretion behind eroded foredune ridges (Figure 4.27).

Using the 2D pattern extraction method, the patterns generated by Hurricane Rita are not registerable as coastal change except for the distal segments and segments immediately to the southwest of Rollover Pass, as shown in Figures 4.20-4.25. In particular, sections A-B (Figure 4.20) had one 500m segment. Segments B-C and C-D, both on Figure 4.20, had nearly continuous erosion and accretion from 20 to 30 meters from the centerline with additional amounts of erosion from 30 to 40 meters of the centerline at segment B-C. Most of the berm erosion associated with Hurricane Rita occurred at the most distal portion of the spit, at segment B-C,C-D (Figure 4.20).

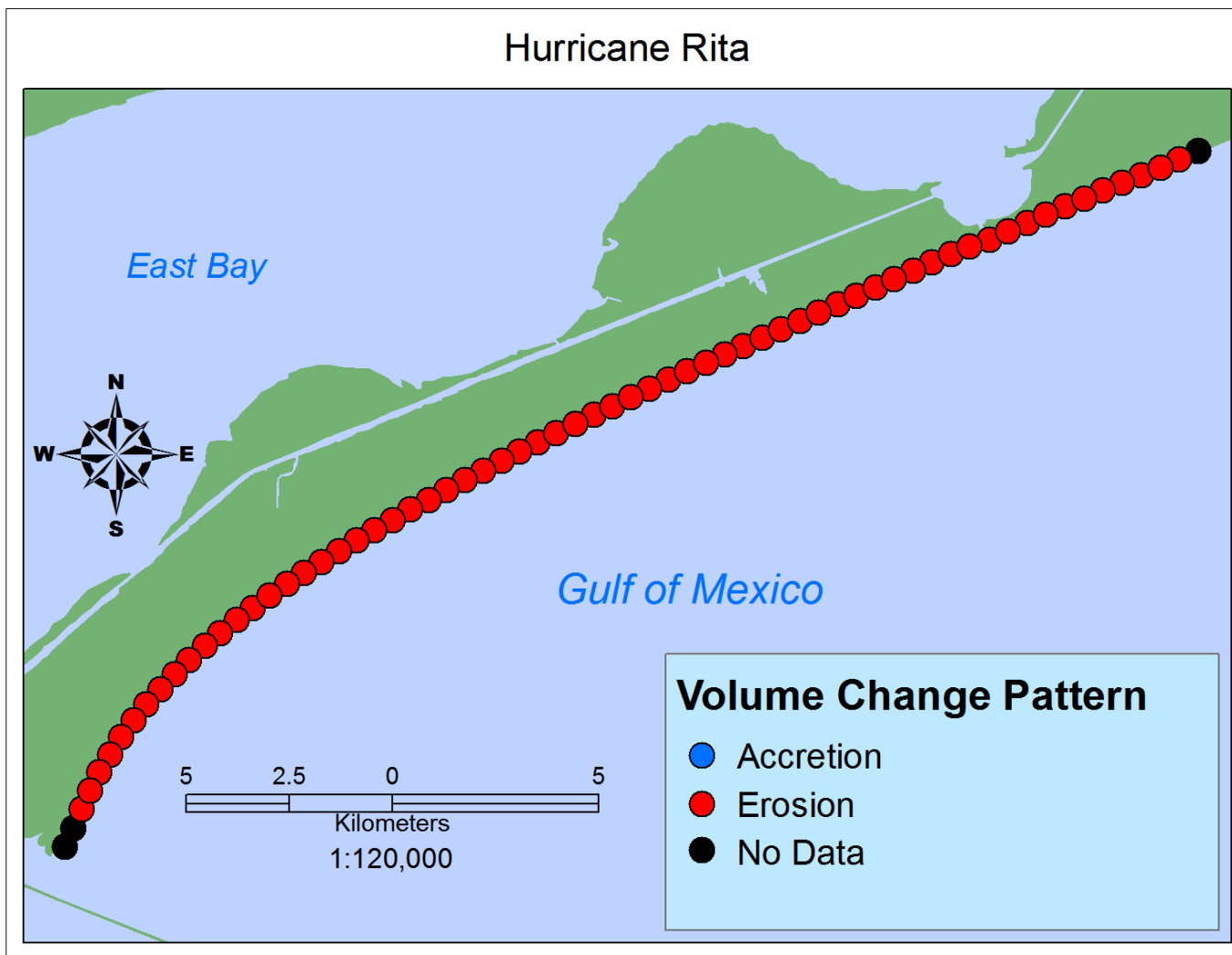


Figure 4.18. 1D alongshore volumetric pattern generated by Hurricane Rita. Derived from Bureau of Economic Geology LiDAR imagery.

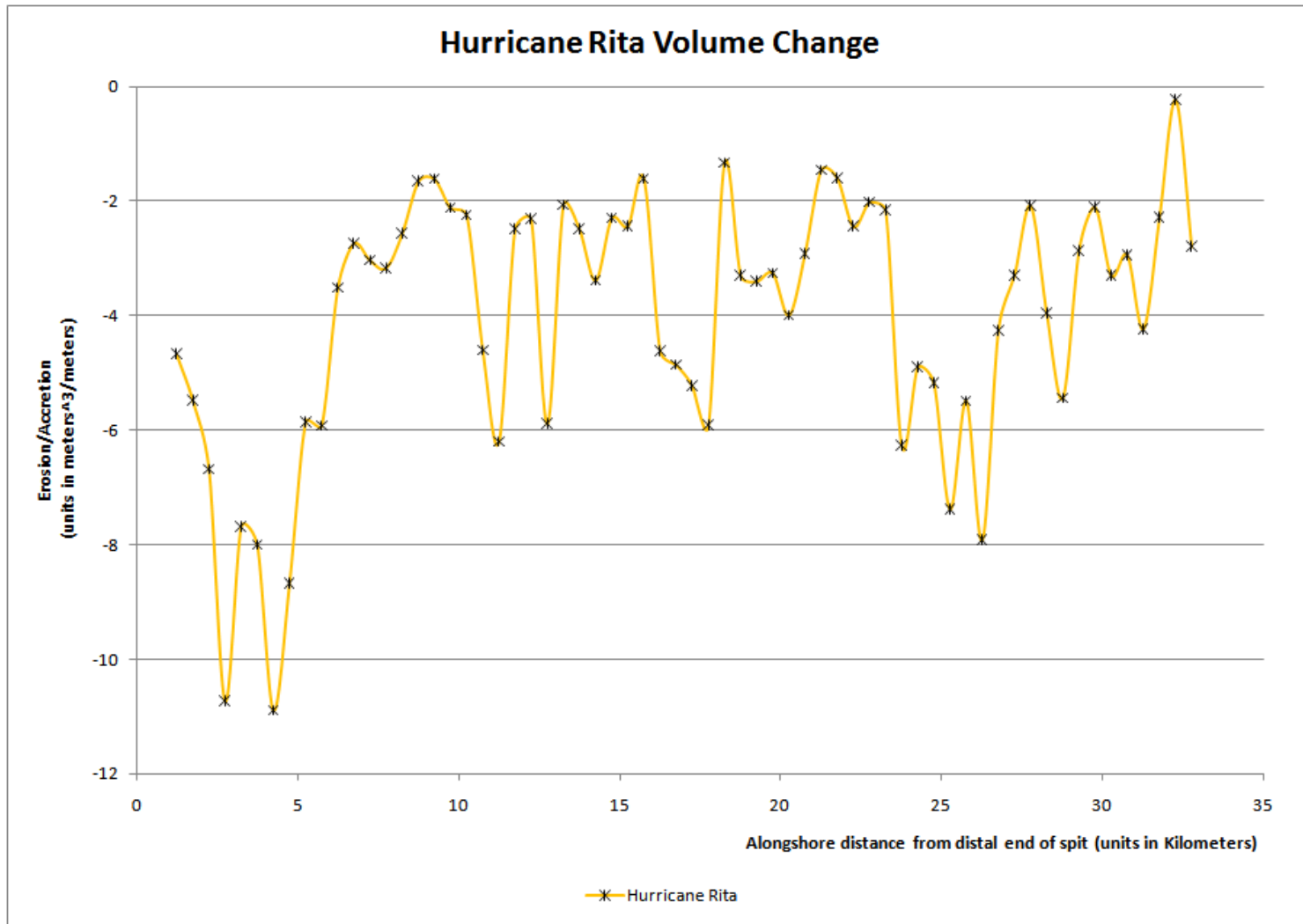


Figure 4.19. Detrended volumetric change for Hurricane Rita, as derived from values obtained by Coastal Morphology Analyst (Liu *et al.* 2010) and then derived as discussed in Chapter 3.

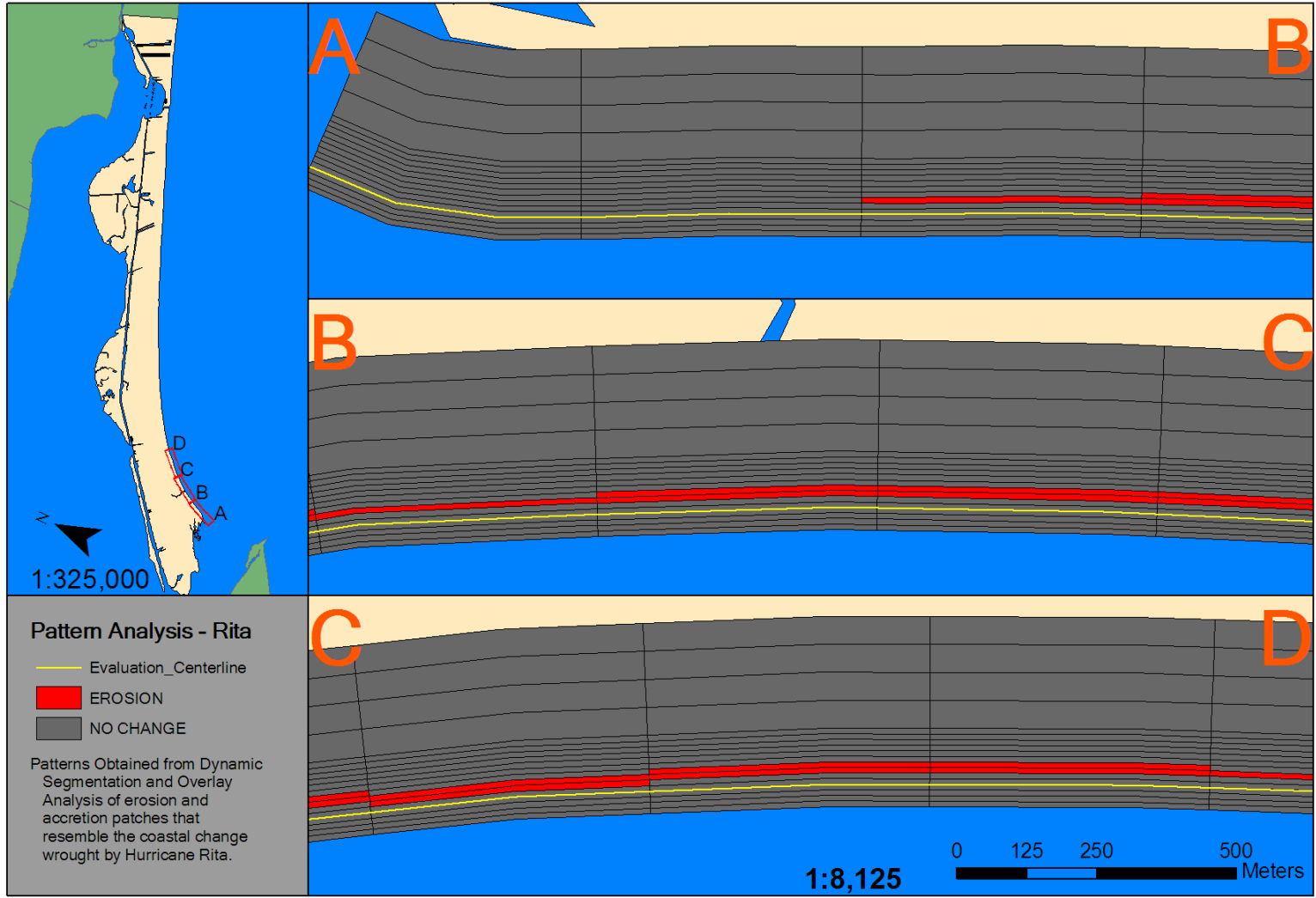


Figure 4.20. Sections A-D of 2D volumetric change patterns - Hurricane Rita.

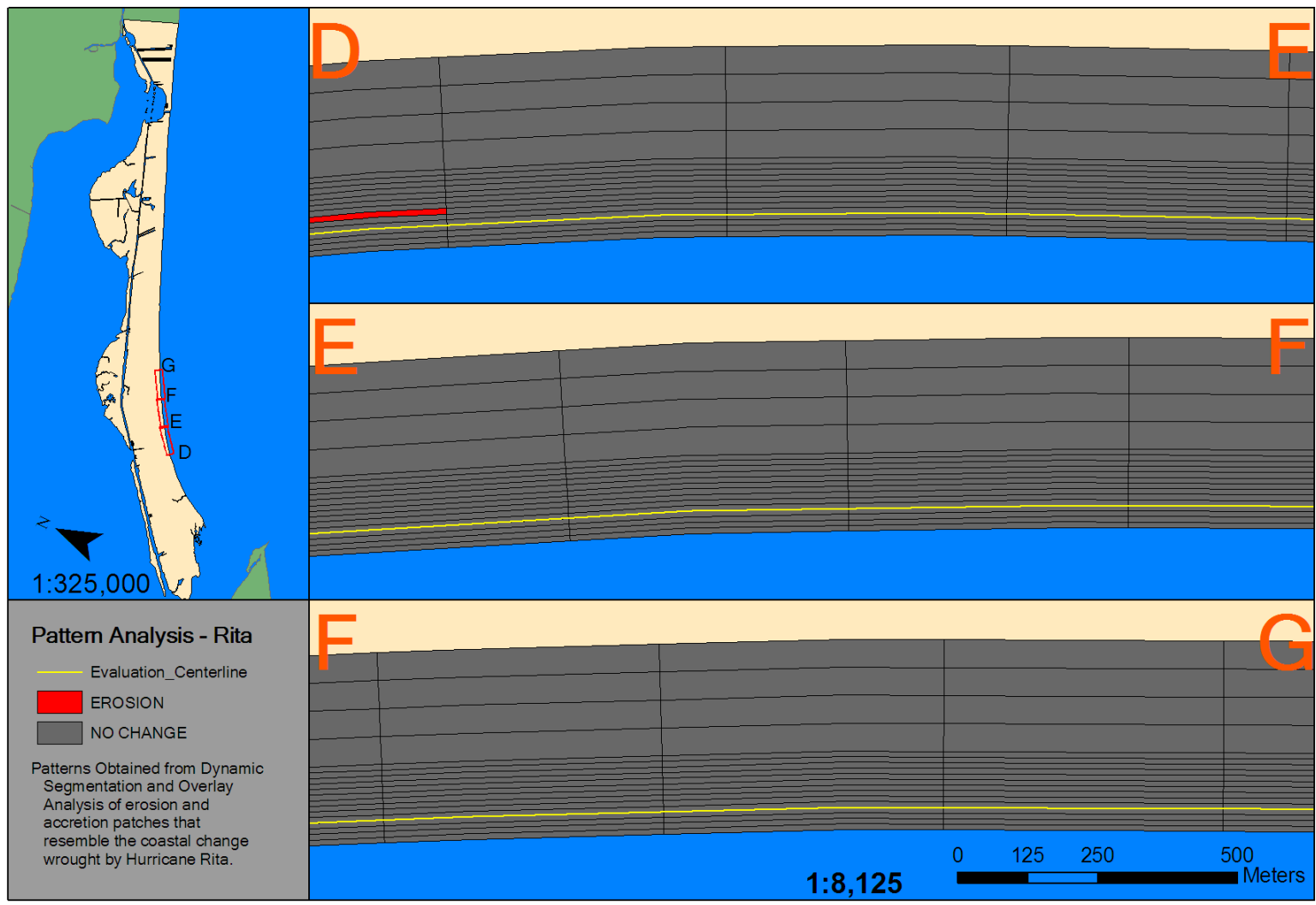


Figure 4.21. Sections D-G of 2D volumetric change patterns - Hurricane Rita.

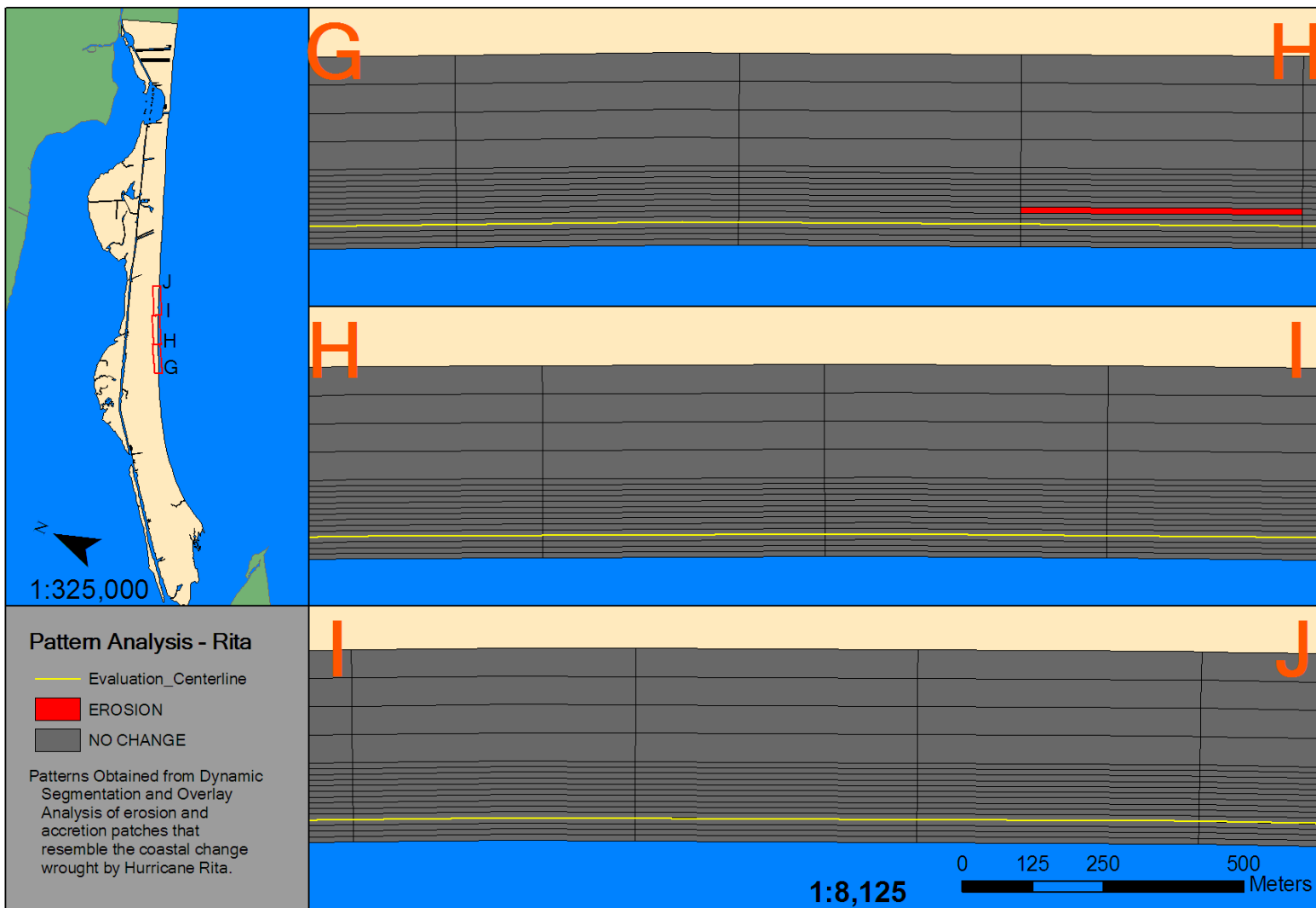


Figure 4.22. Sections G-J of 2D volumetric change patterns - Hurricane Rita.

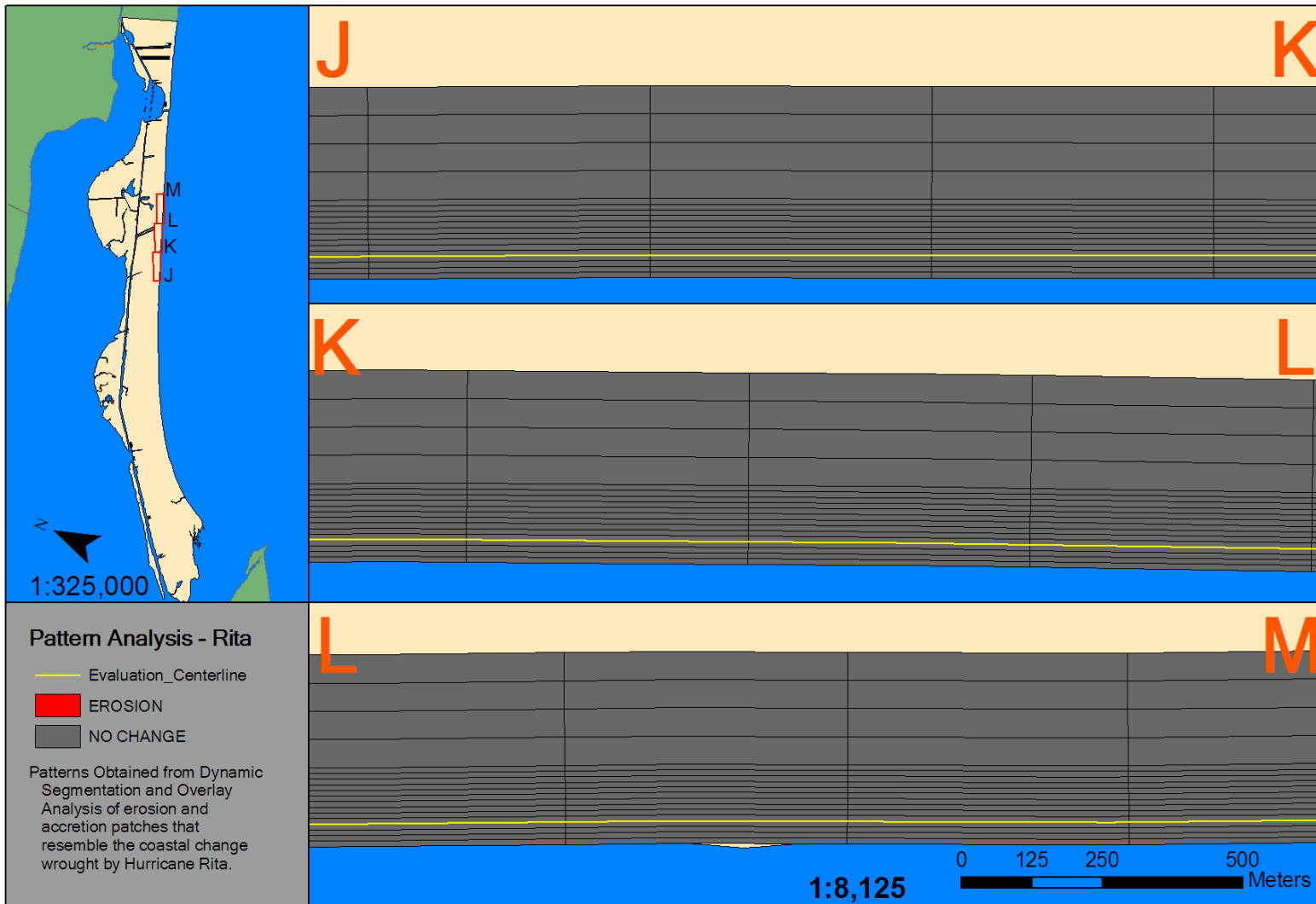


Figure 4.23. Sections J-M of 2D volumetric change patterns - Hurricane Rita.

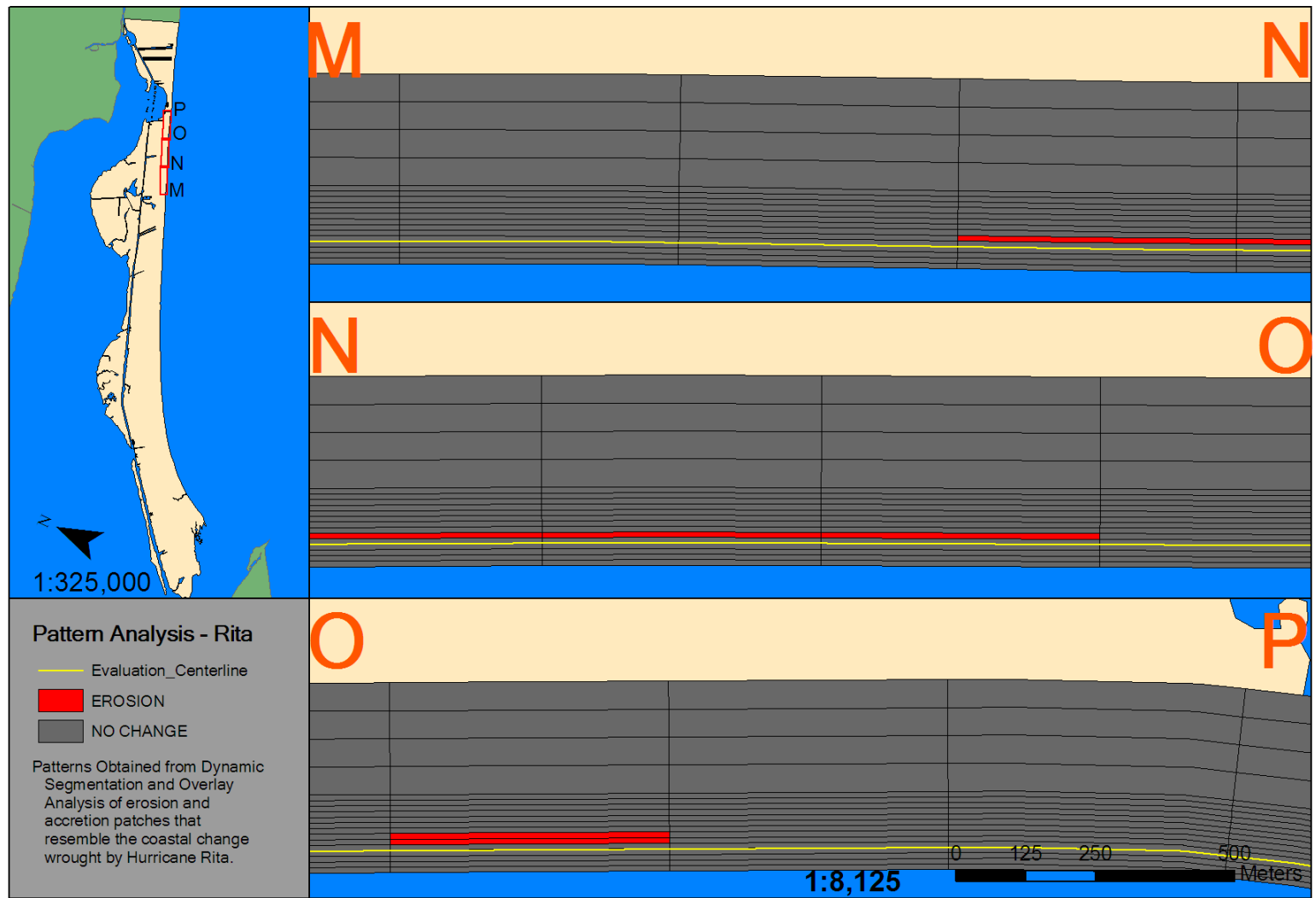


Figure 4.24. Sections M-P of 2D volumetric change patterns - Hurricane Rita.

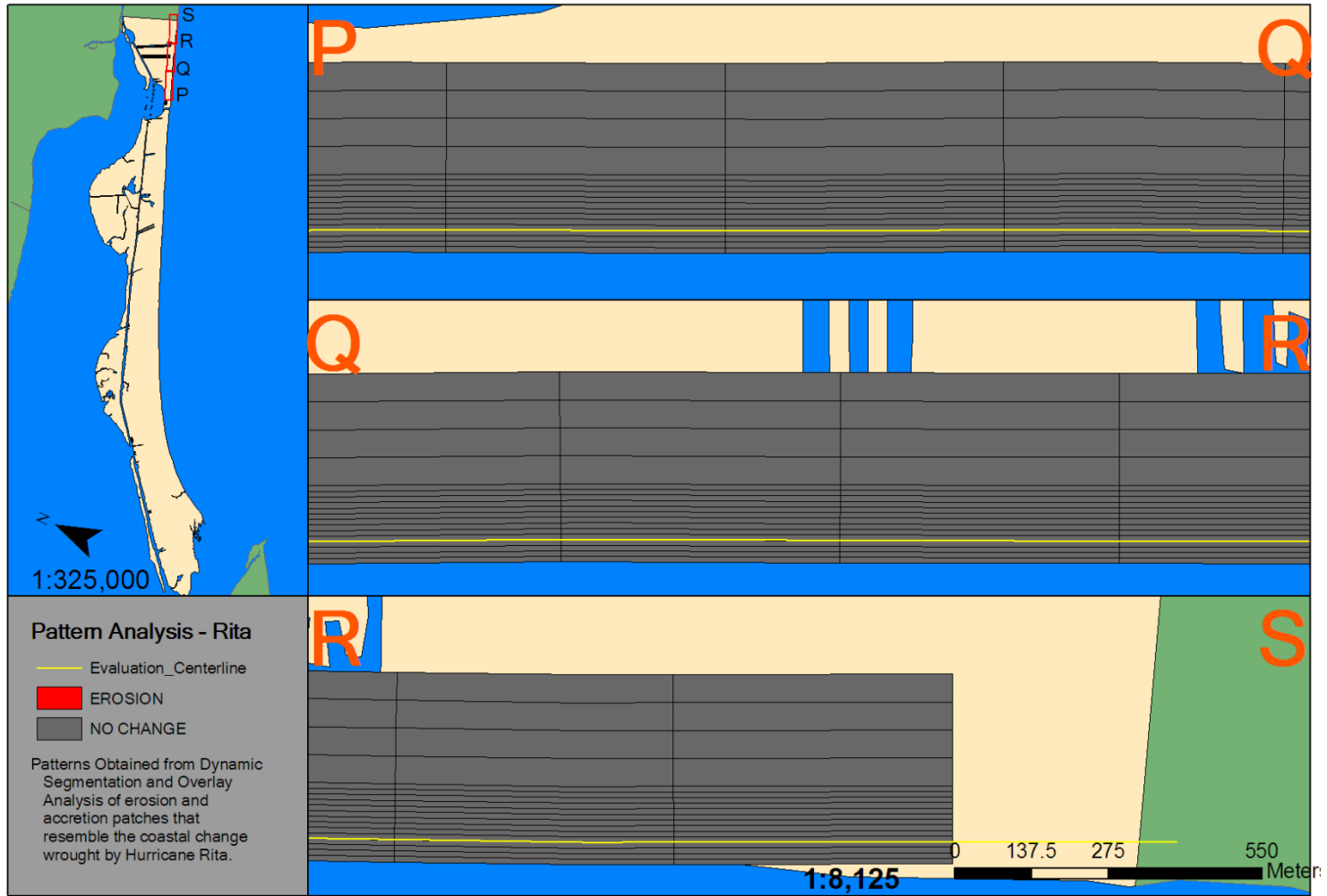


Figure 4.25. Sections P-S of 2D volumetric change patterns - Hurricane Rita.

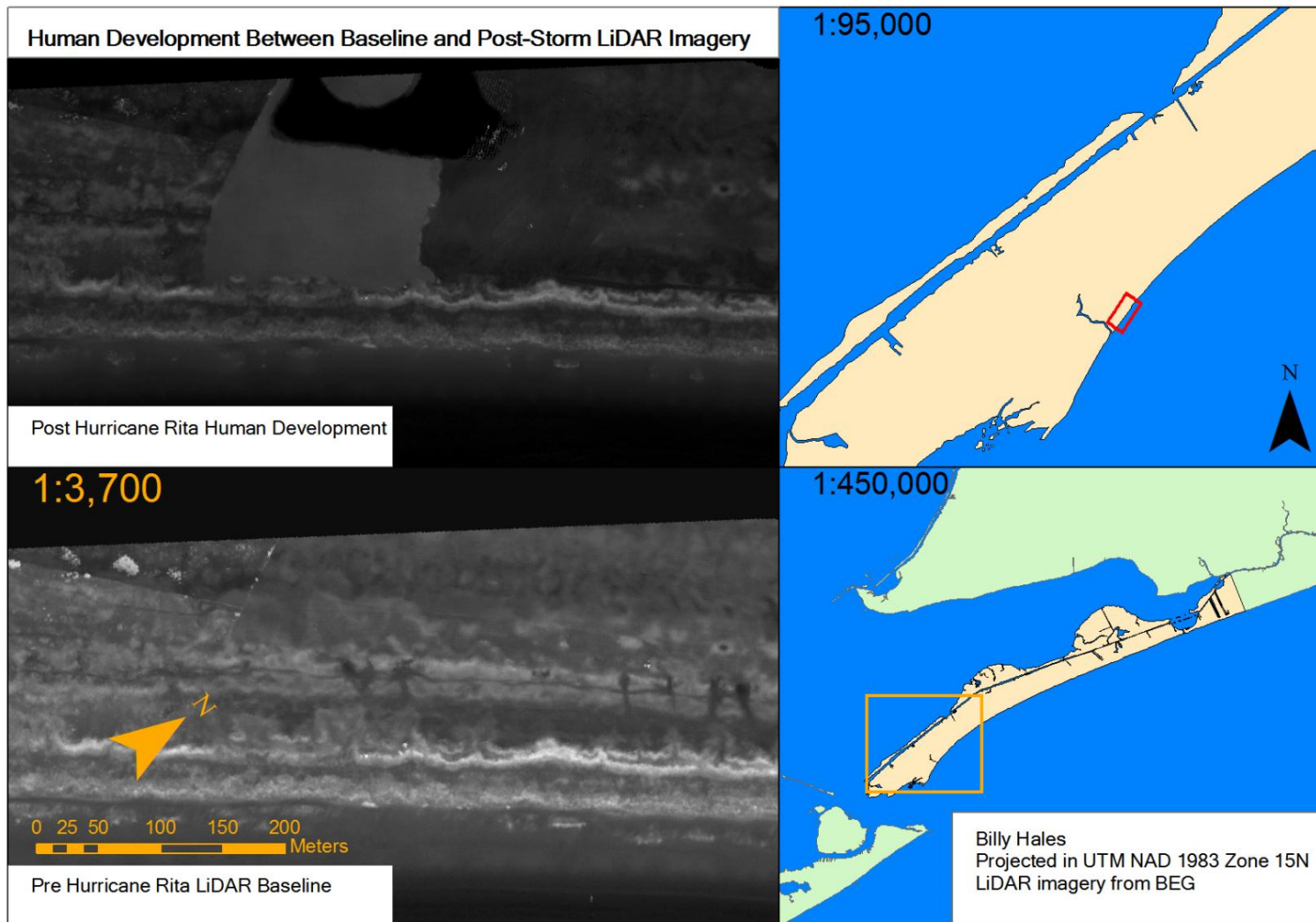


Figure 4.26. Human developments that have occurred between the pre and post-Rita LiDAR imagery.

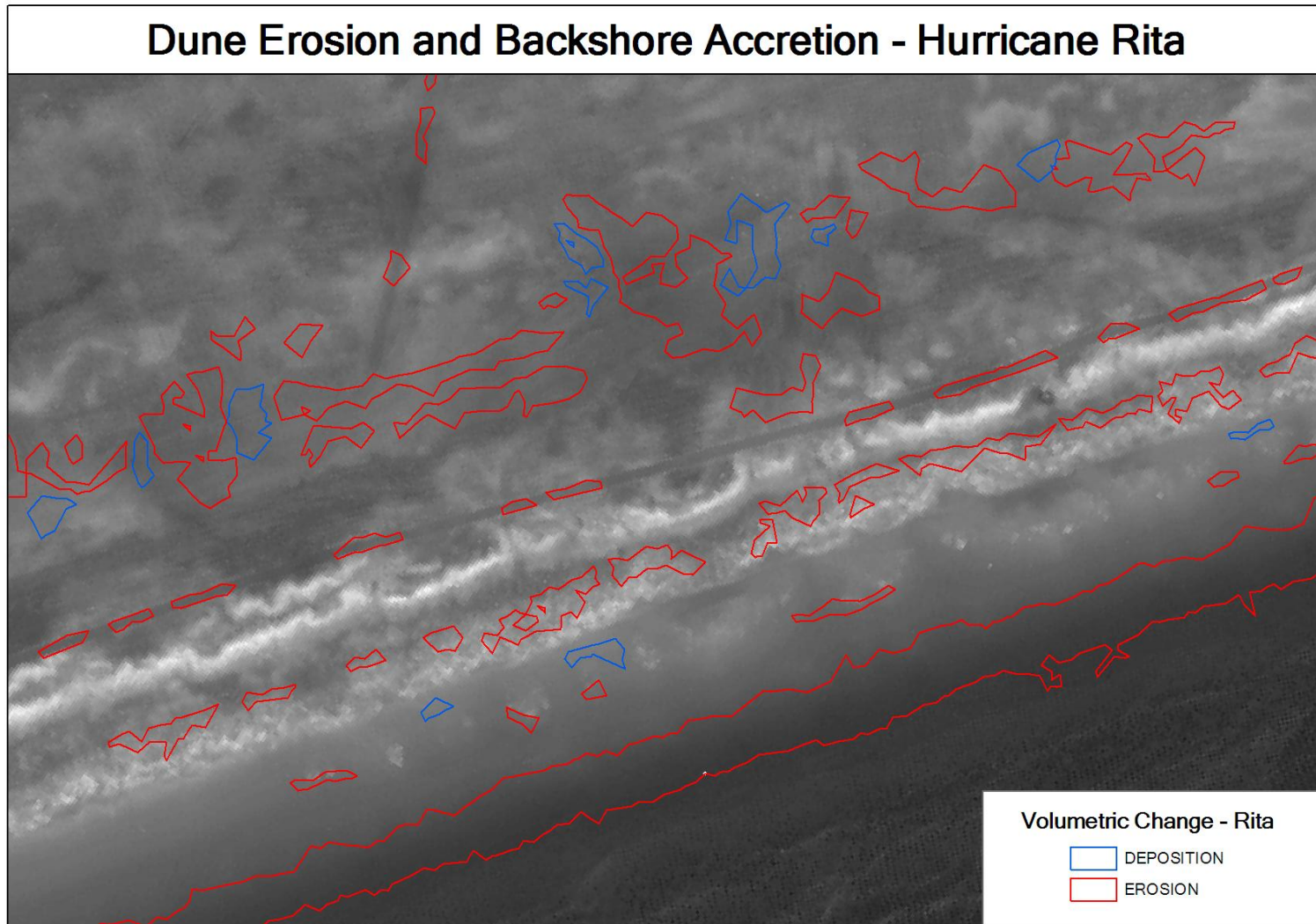


Figure 4.27. Localized areas of overwash from Hurricane Rita.

2D Volume Change Patterns - Hurricane Ike

The volume change of Bolivar Peninsula as a result of Hurricane Ike was tremendous. All over the spit, one could easily see that there were large areas of complete devastation from the storm (Figure 4.28). On Figures 4.29 and Figures 4.30-4.35, it is also shown how this data was interpreted as a pattern. Along with large volumes of sediment eroded, there were large scours that have been speculated to be from flow from the bay as Hurricane Ike went over East Bay (Potts, 2010).

For Hurricane Ike, erosion was between 150 and 200 meters landward of the centerline. Deposition was also recorded in sections E-F on Figure 4.31, I-J on Figure 4.33, N-P on Figure 4.34, and Q-R on Figure 4.35. These sections correspond to the area of maximum curvature—10-15 kilometers from the distal portion of the spit, and an area that is northeast of Rollover Pass. Areas of greatest erosive area spread were 200 meters landward of the centerline, and these are recorded in sections I-J and one small instance in section N-O on Figures 4.32 and 4.33, respectively. Section I-J is at the point where there is transition to the area of maximum curvature from the proximal straight-portion of the spit (Figure 4.32).

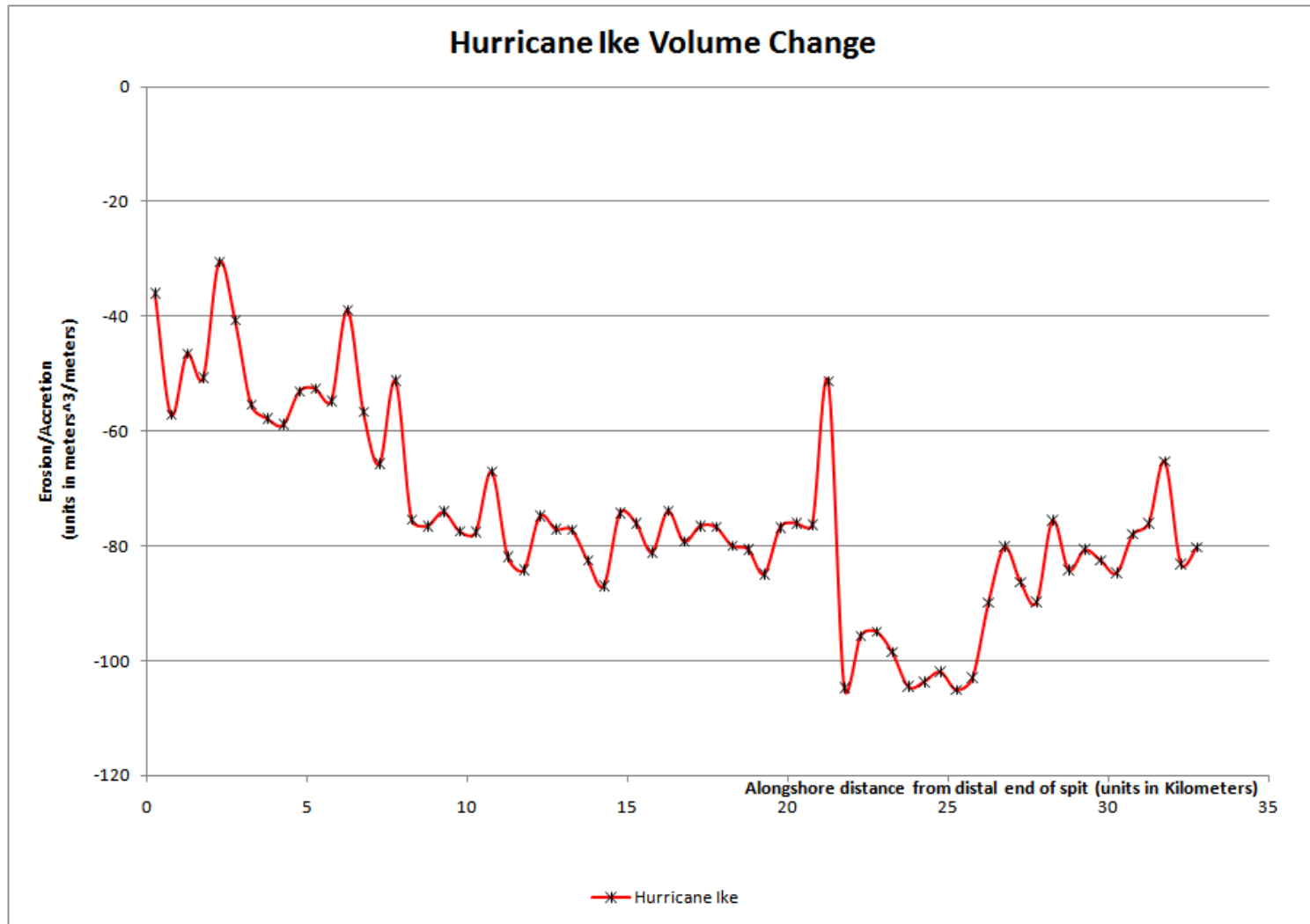


Figure 4.28. Detrended volumetric change for Hurricane Ike, as derived from values obtained by Coastal Morphology Analyst (Liu *et al.* 2010) and then derived as discussed in Chapter 3.

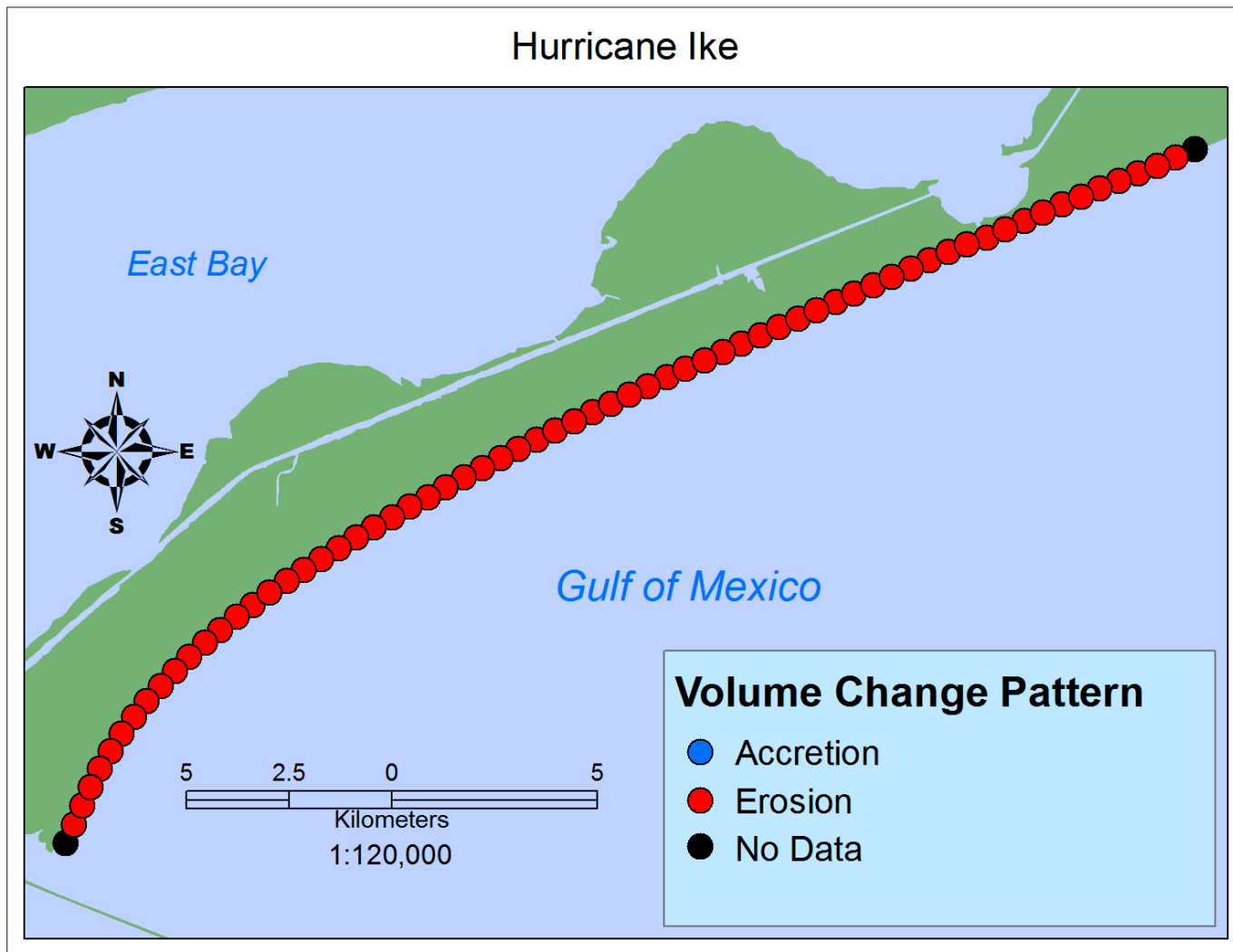


Figure 4.29. 1D alongshore volumetric pattern generated by Hurricane Ike. Derived from Bureau of Economic Geology and USGS LiDAR imagery.

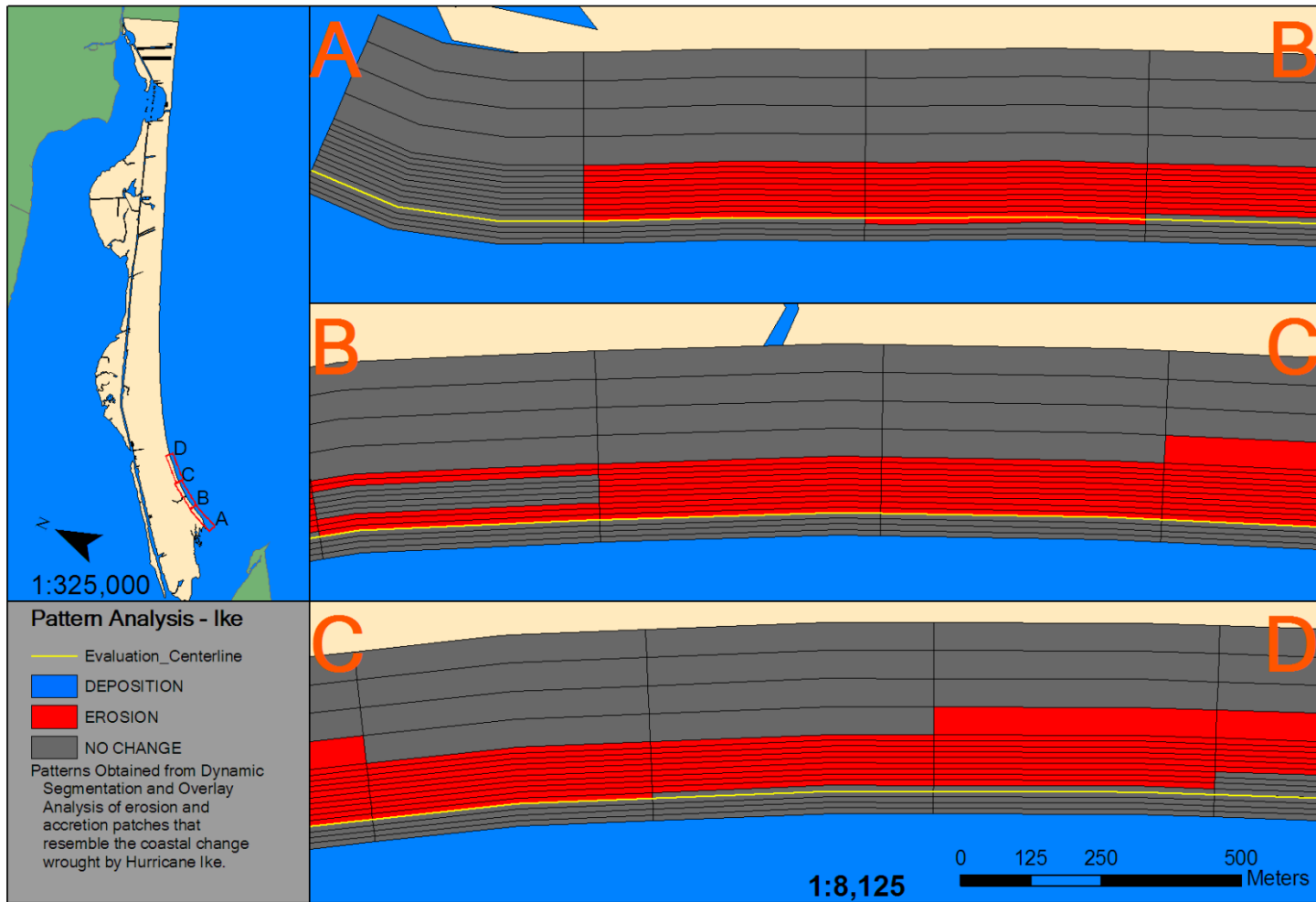


Figure 4.30. Sections A-D of 2D volumetric change patterns - Hurricane Ike.

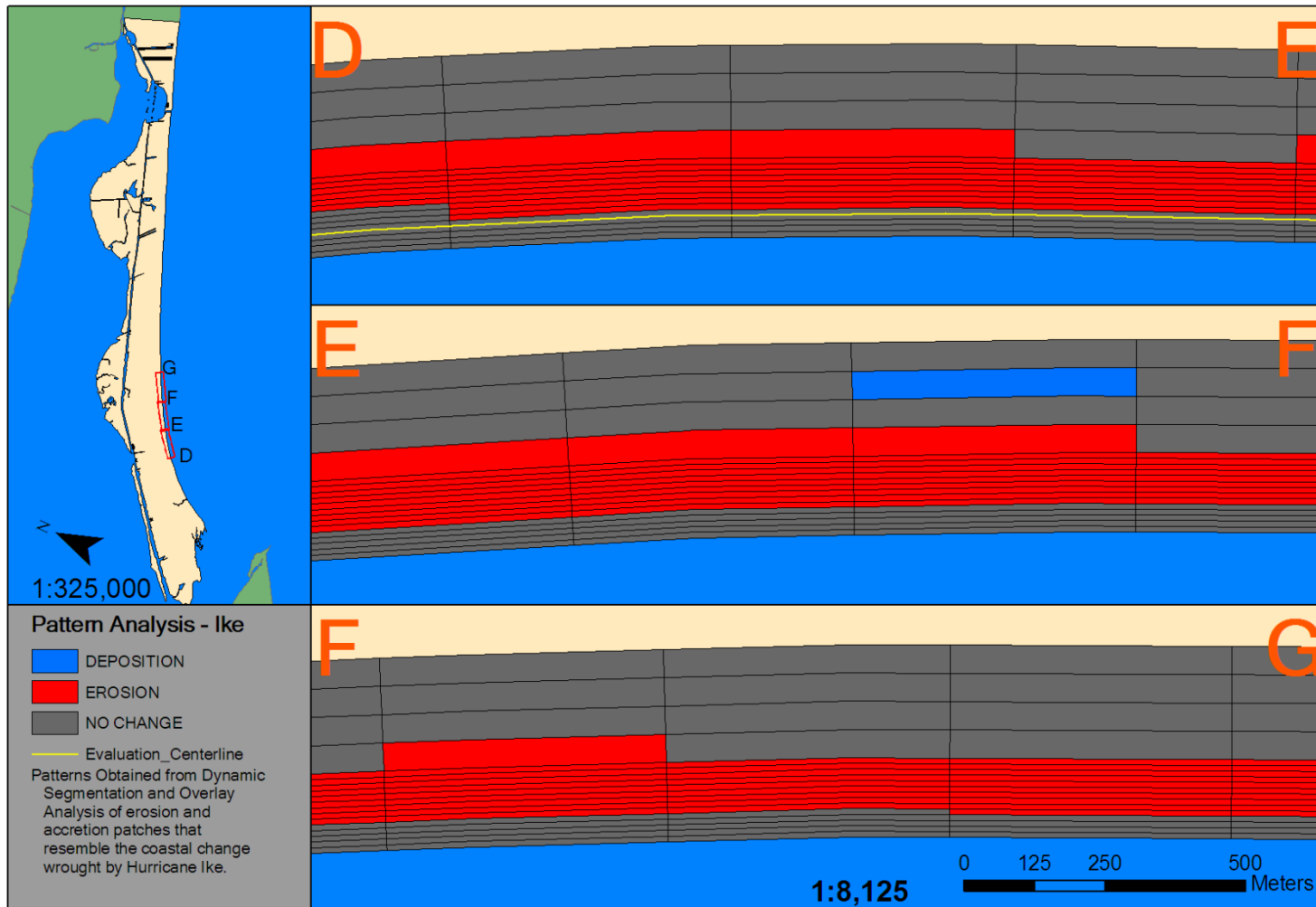


Figure 4.31. Sections D-F of 2D volumetric change patterns - Hurricane Ike.

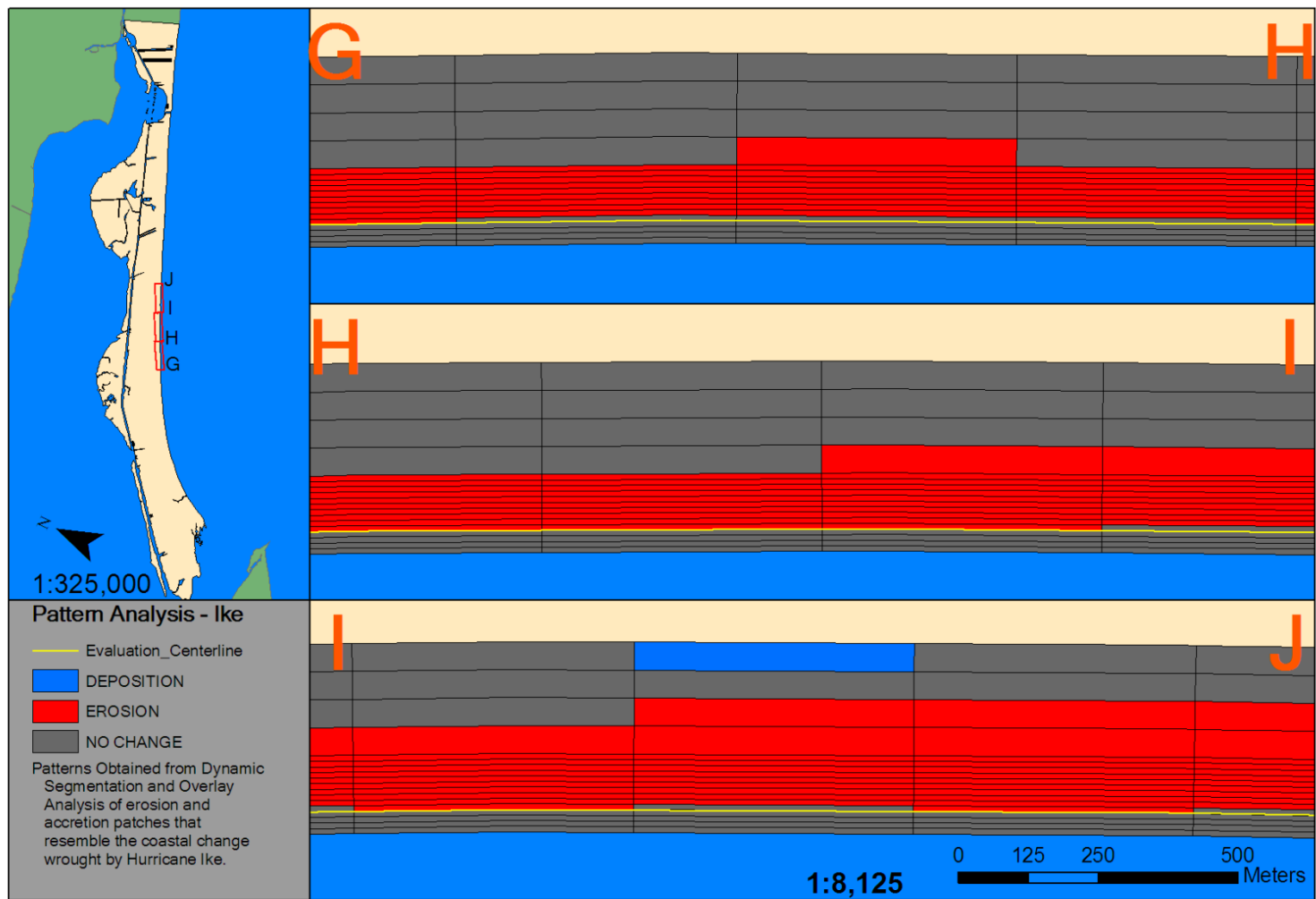


Figure 4.32. Sections G-J of 2D volumetric change patterns - Hurricane Ike.

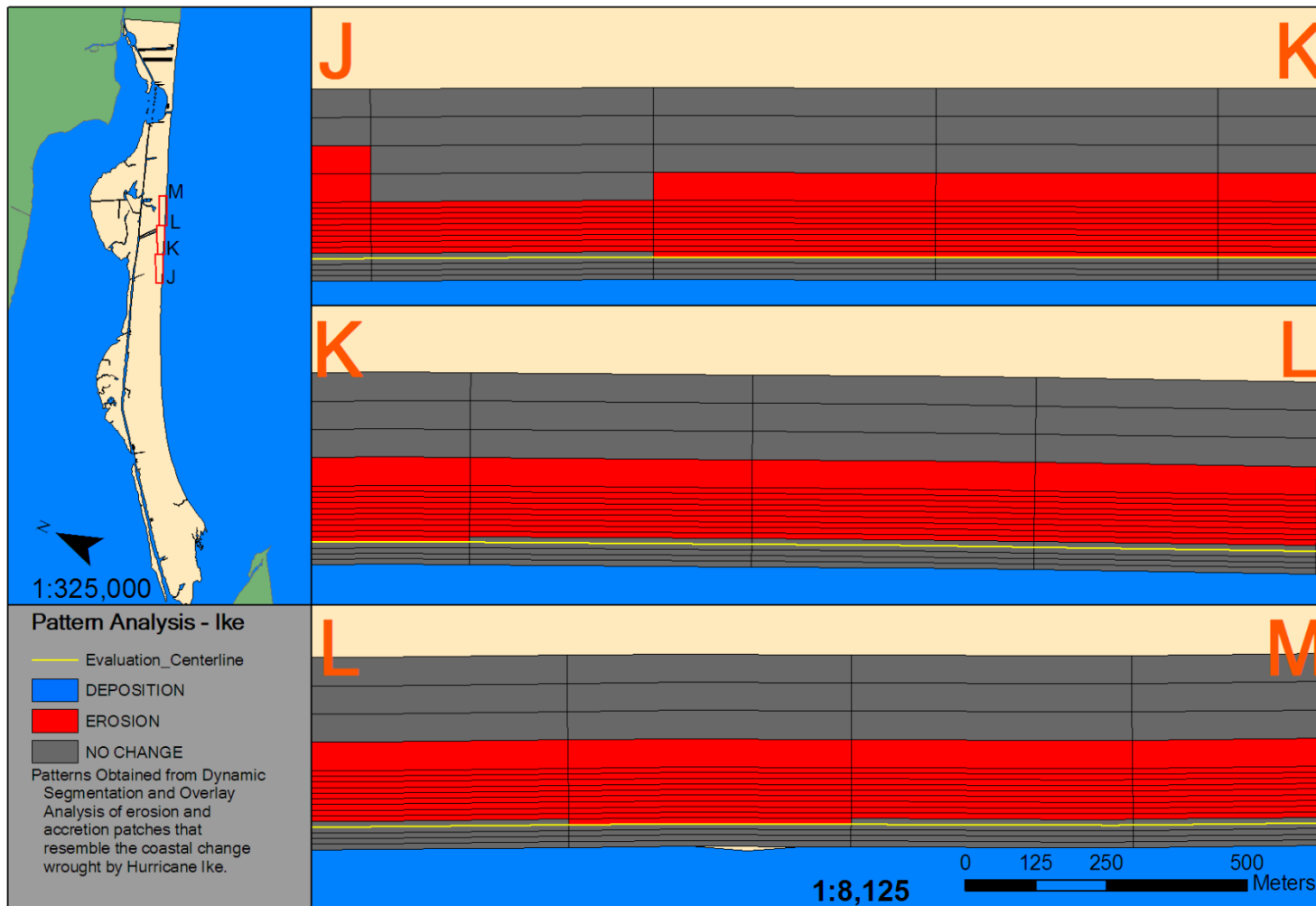


Figure 4.33. Sections J-M of 2D volumetric change patterns - Hurricane Ike.

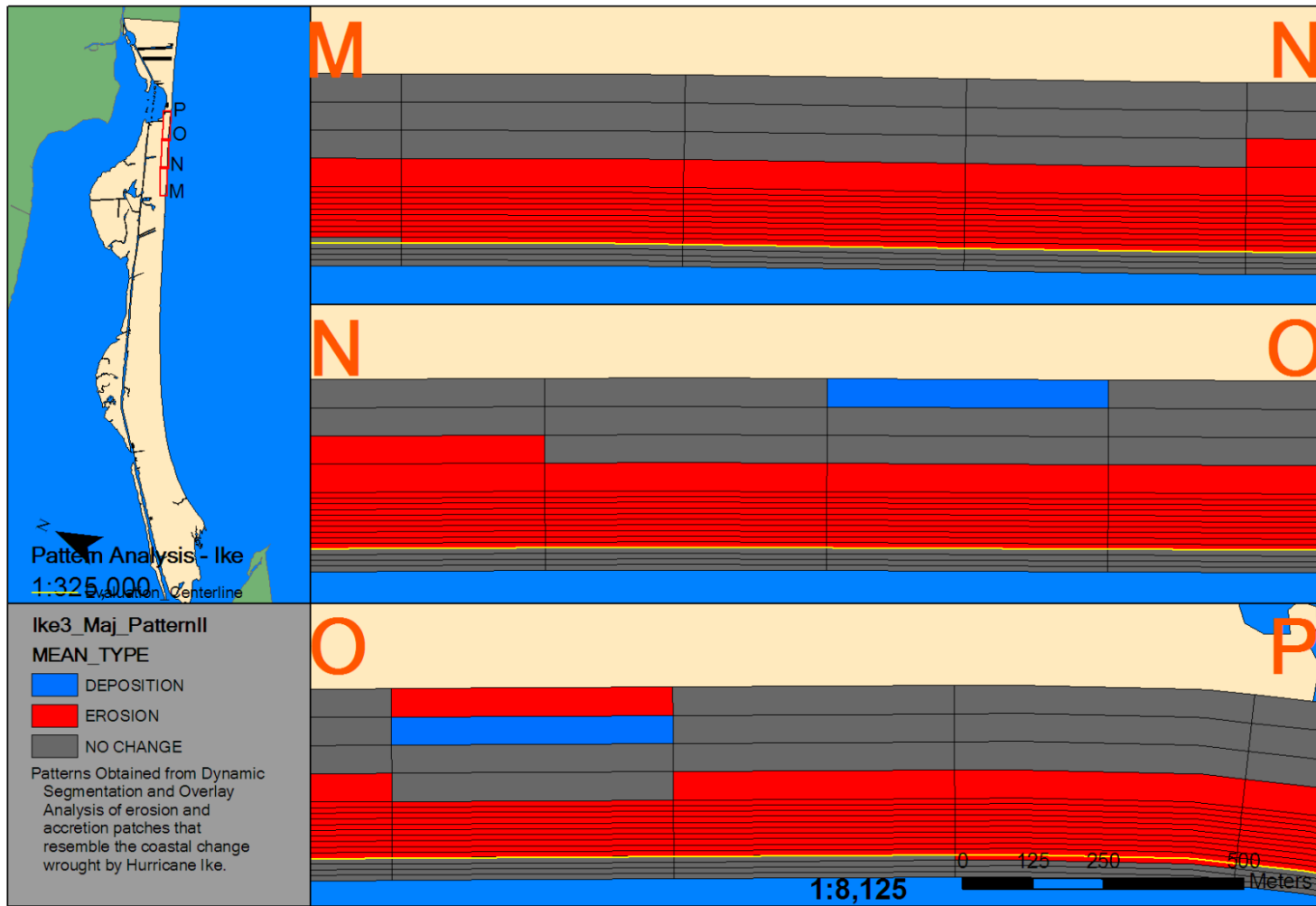


Figure 4.34. Sections M-P of 2D volumetric change patterns - Hurricane Ike.

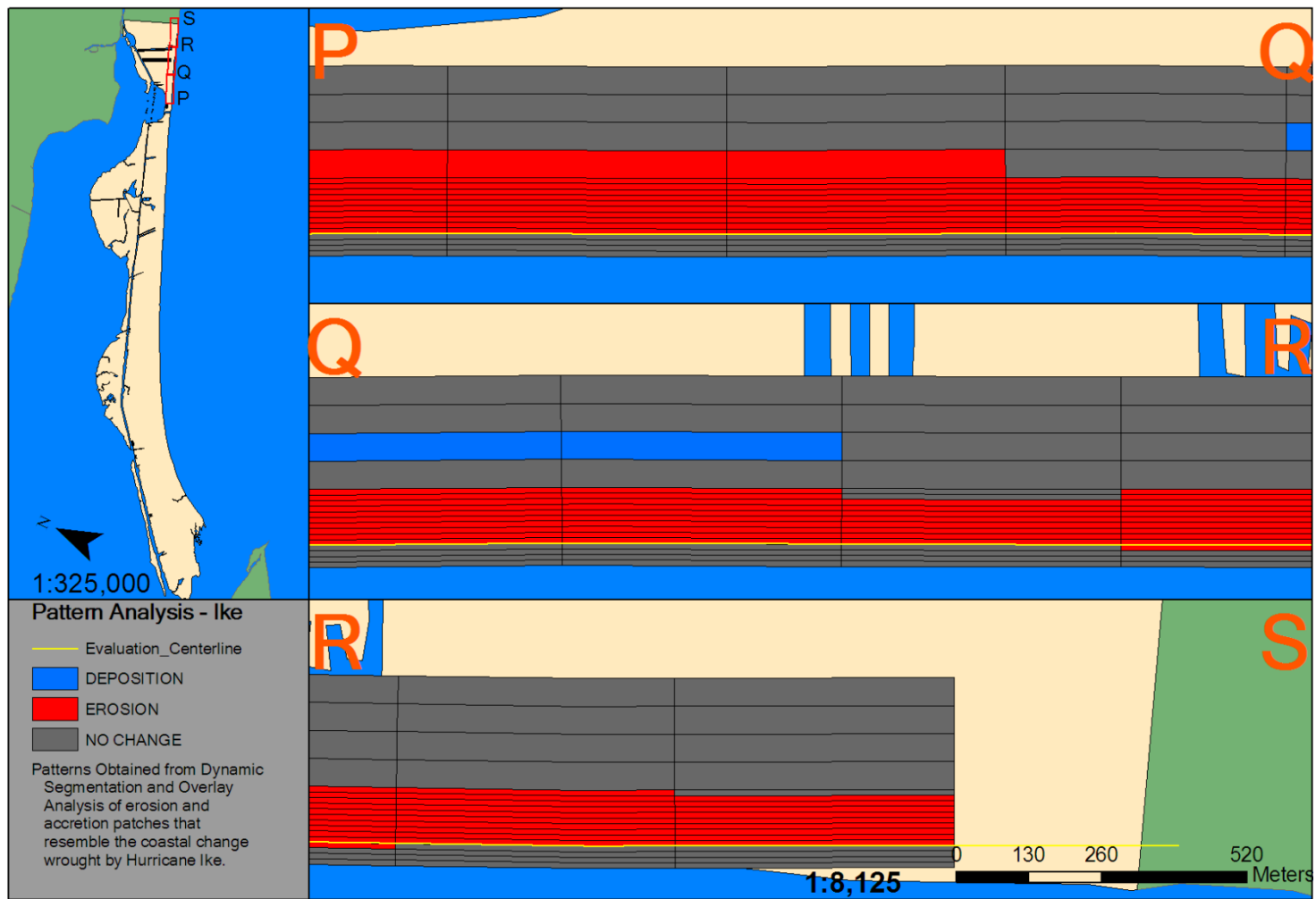


Figure 4.35. Sections P-S of 2D volumetric change patterns - Hurricane Ike.

Shoreline Change Pattern Comparisons

Pattern Comparison – Tropical Storm Fay to Hurricane Rita

Tropical Storm Fay and Hurricane Rita had patterns that were similar reflecting the blue colored points representing accretion on the distal end of the spit and the transition to groups of red dots on the proximal portion of the spit (Figure 4.36). However, it should be noted that all the yellow and peach points indicate a graduation from accretion/no change to erosion for much of the proximal portion of Bolivar Peninsula. Areas of erosion that are constant throughout both storms seem to have a preferred placement at Rollover Pass and at the transitional zone where shoreline curvature that is greater capitulates to a straight barrier feature near the proximal, connected end of the spit. Similarity was at 19 out of 66 cells similar, and most of them being 10 erosional cells near the prominent erosional zones mentioned earlier.

Pattern Comparison – Tropical Storm Fay to Hurricane Ike

Differences from the shoreline changes of Tropical Storm Fay to Hurricane Ike were more pronounced, as noticeable by fewer unchanged cells (Figure 4.37). There is also evidence of a northeast shift of the accretionary zone from the tip or distal end of the spit to the area of maximum curvature. It is also notable that areas of erosion near Rollover Pass remain similar between Tropical Storm Fay and Ike. This comparison had the least similarity with only 18 out of 66 cells similar. The largest and second-largest grouping of similar zones, four and three erosion zones, is within 3 miles of Rollover Pass (Figure 4.37).

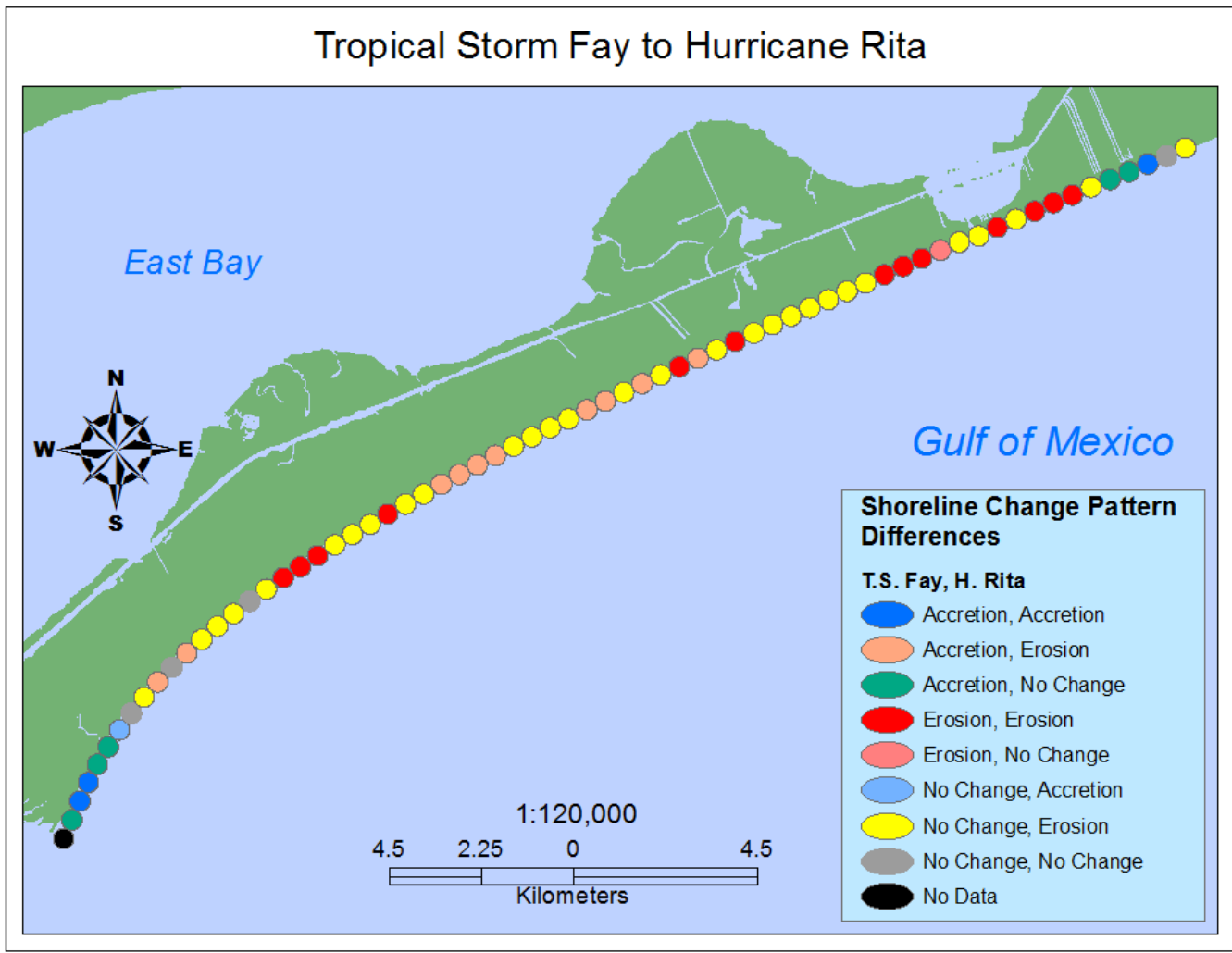


Figure 4.36. Alongshore shoreline change pattern comparison – Tropical Storm Fay to Hurricane Rita.

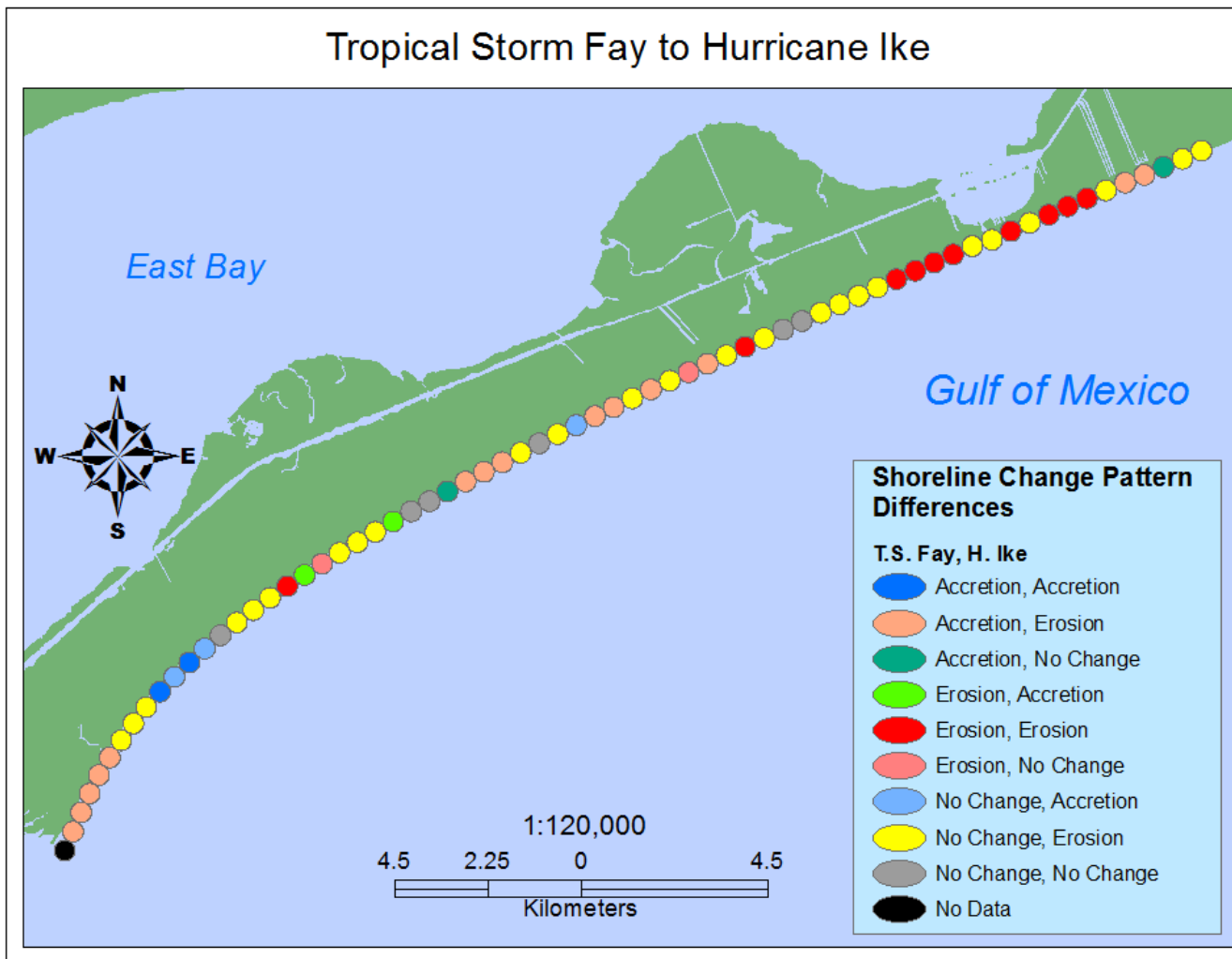


Figure 4.37. Alongshore shoreline change pattern comparison – Tropical Storm Fay to Hurricane Ike.

Pattern Comparison – Hurricane Rita to Hurricane Ike

Just as in the comparison between Fay and Rita, there is a shift of the no change/accretionary zone from the distal end of the spit to the area of highest curvature (Figure 4.38). Also note that the erosive zone that corresponds with Rollover Pass is still erosive when compared to Hurricane Ike. Patterns generated by Hurricane Ike and Hurricane Rita have the greatest amount of similarity via erosion, 37 out of 67. No similar unchanged accretion cells are present.

Pattern Comparison – All Storms

With all storms considered, there is approximately 13% similarity (Figure 4.39). This low number is largely because of differences in the locations of accretionary zones between the shoreline change impacts of Hurricane Ike and the other two storms in the distal portion of the spit, and the differences in the periodicity in these zones near the point of maximum curvature between Hurricane Rita and the other two storms.

Areas of similarity include one erosion zone near the transitional curvature zone toward the mid-point of the spit and the two groups of erosional zones near Rollover Pass. The area around Rollover Pass is erosive in all the storm impacts from about 3 kilometers from either side of the pass with four zones of no change beyond error in two zones that are separated by three erosive zones.

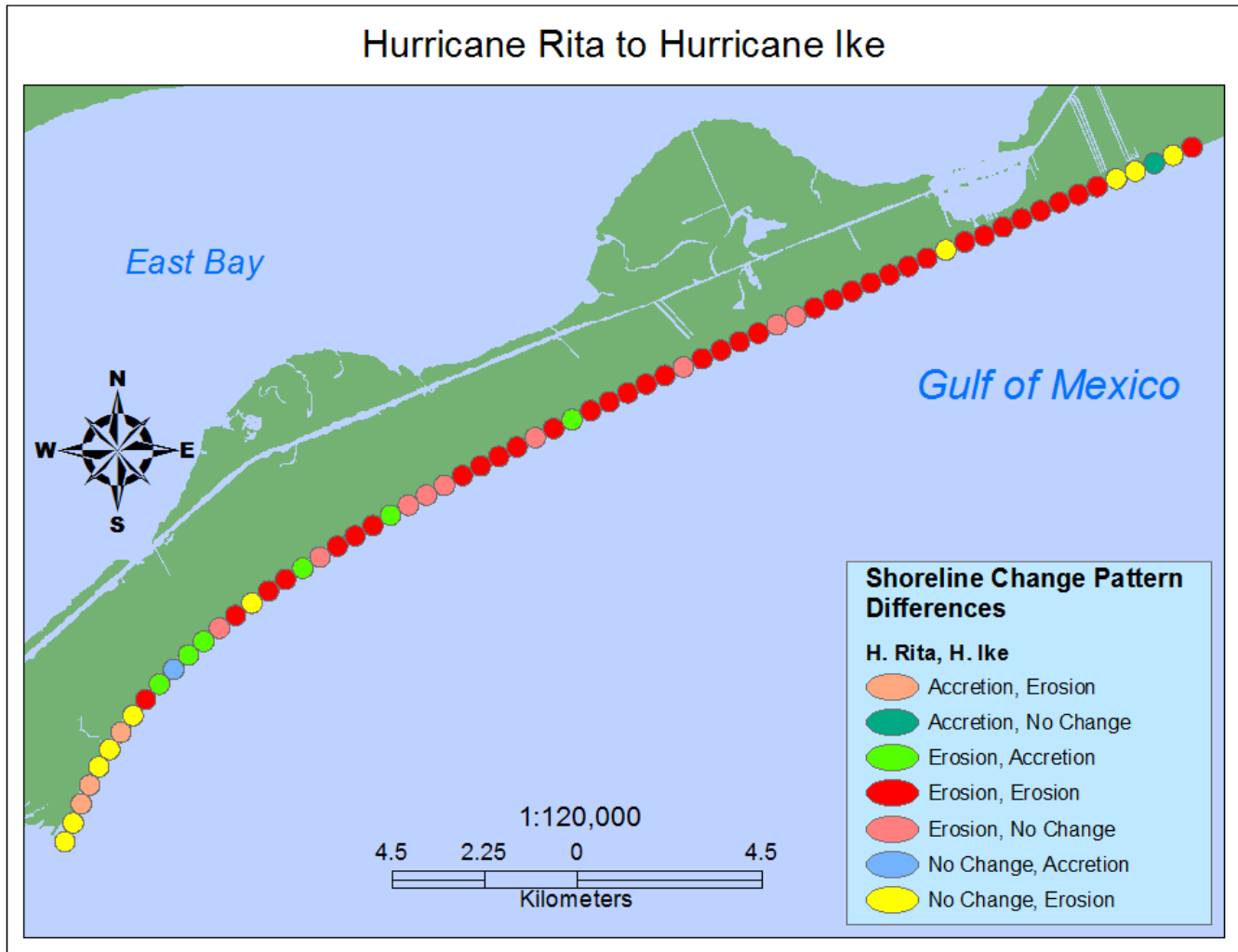


Figure 4.38. Alongshore shoreline change pattern comparison – Tropical Storm Fay to Hurricane Ike.

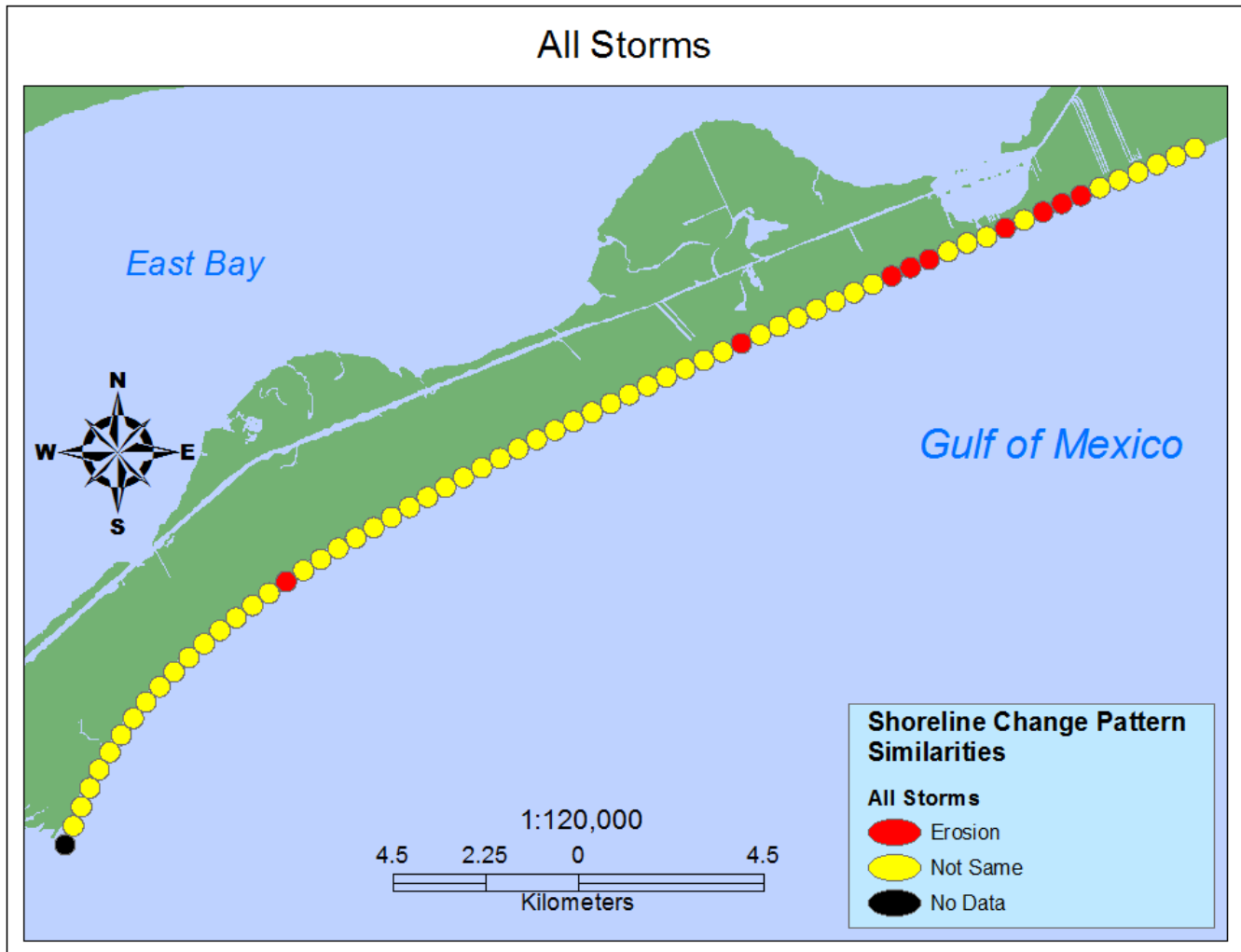


Figure 4.39. Alongshore shoreline change pattern comparison – all storms.

Volume Change Pattern Comparisons

ID Comparison – T.S. Josephine to T.S. Fay

Alongshore volumetric change for both Tropical Storms Josephine and Fay have variation within them. In general, both follow a distal accretion to proximal erosion pattern (Figure 4.40). However, the values for Tropical Storm Fay seem to be quite a bit more oscillatory and there is far more erosion than the impacts of Josephine. Josephine had more than half of the peninsula covered with accretion, and erosion at the proximal end of the spit. Although oscillatory, the accretive zones of Tropical Storm Fay impacts are further up the peninsula than those of Josephine.

In terms of detrended volumetric impacts, Tropical Storm Josephine had a far greater magnitude than Tropical Storm Fay (Figure 4.41). These results bring about many questions. In Gibeaut *et al.* (2008), Tropical Storm Fay had a longer duration of erosive conditions than did Tropical Storm Josephine. However, Josephine has much larger impacts than Tropical Storm Fay. The answer may be in the time period and in the methodology for acquiring these results. The method introduced by Liu *et al.* (2010) already factors out smaller results that fall within the error threshold specified by the user, 0.30 meters for this study. However, the results from Gibeaut, Gutierrez, and Hepner (2002) are gathered via beach profiles taken by emery rod and total station that have a vertical error of 0.02 meters (Gibeaut, Gutierrez, and Hepner 2002). This has a much smaller window of error, and introduces much more possible values that can be obtained from LiDAR vertical elevation change. The other variable is that Gibeaut, Gutierrez, and Hepner (2002)'s method assumes linear change between profiles. The

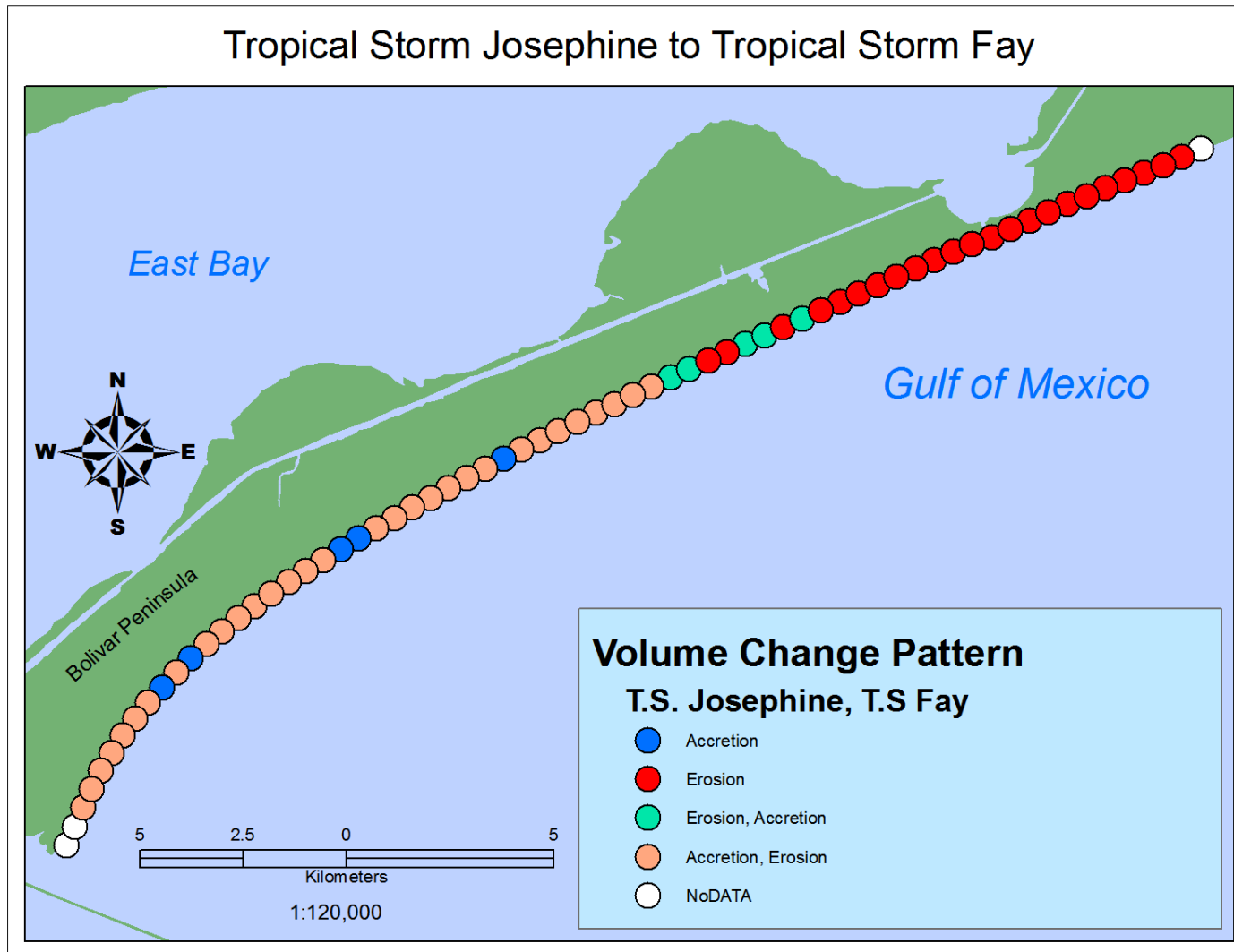


Figure 4.40. Alongshore volume pattern comparison – Tropical Storm Josephine to Tropical Storm Fay.

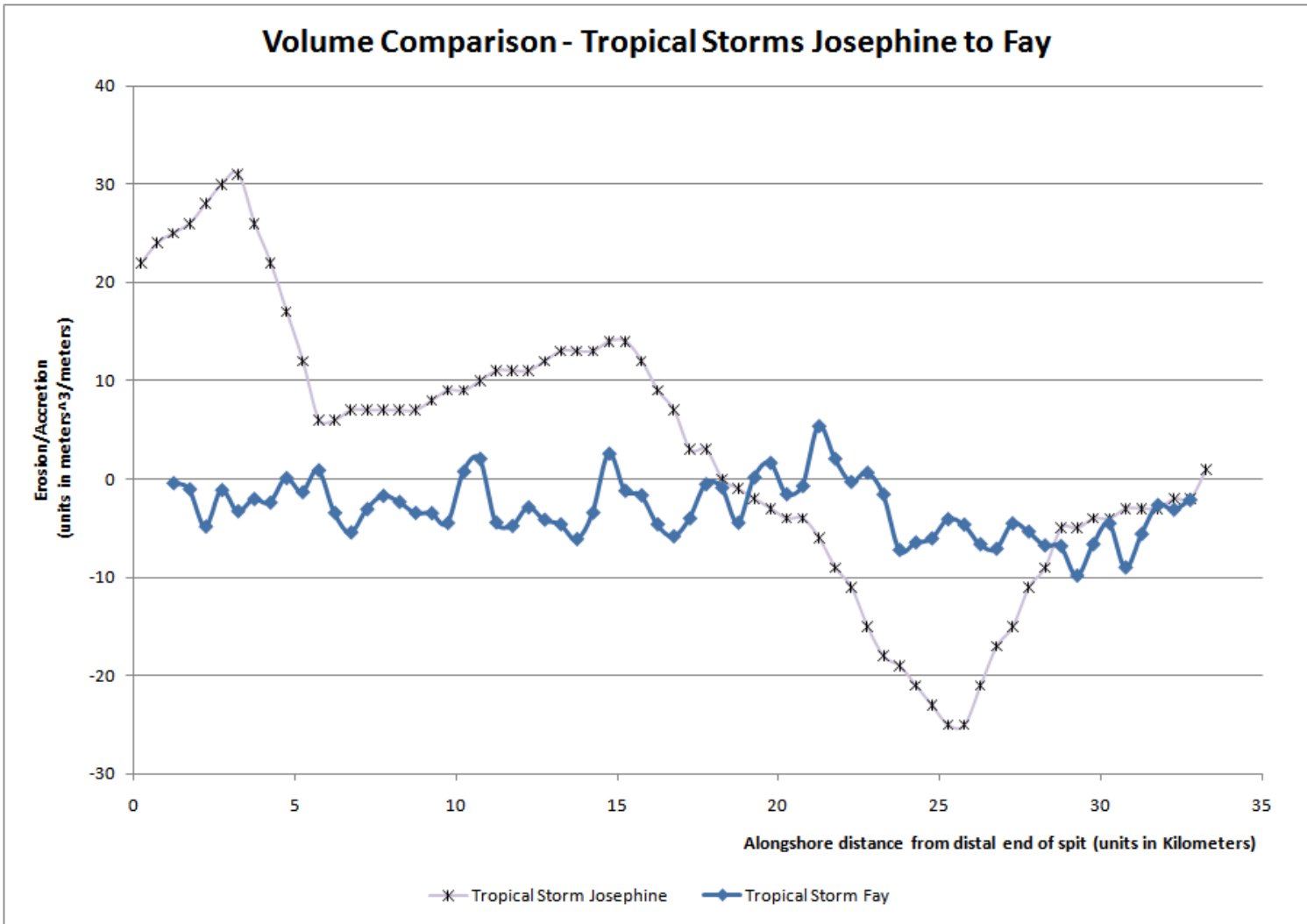


Figure 4.41. Comparison of detrended alongshore impacts from Tropical Storms Josephine and Fay.

final point is a temporal one. The results from Gibeaut, Gutierrez, and Hepner (2002) are obtained more than one year after Tropical Storm Josephine impacted the North Texas Coast. Given these considerations, results may be better seen as a comparison of post-storm trends to recovery trends.

1D Comparison – T.S. Josephine to H. Ike and H. Rita

Since the trend is all erosive for Hurricanes Ike and Rita, alongshore pattern comparisons will involve Tropical Storms Josephine and Hurricanes Rita and Ike—both classified as one pattern (Figure 4.42). Detrended impacts from Tropical Storm Josephine in comparison to Hurricane Rita show a stark decrease in magnitude from Josephine to Rita, and a change in trend. The distal end of the spit is greatly eroded as a result of Hurricane Rita—whereas the distal end is even more greatly accreted for Josephine (Figure 4.43).

Comparisons between the volumetric changes of Tropical Storm Josephine and Hurricane Ike are notable. It appears that both of the storms have a similar sediment distribution. If Hurricane Ike were offset upward by 80 meters³/meter, then it would be easy to make that observation. In terms of magnitude, Hurricane Ike has a greater disparity between the area of minimal erosion—the distal end of the spit, and the area of highest erosion—about 5 kilometers southwest of Rollover Pass (Figure 4.44).

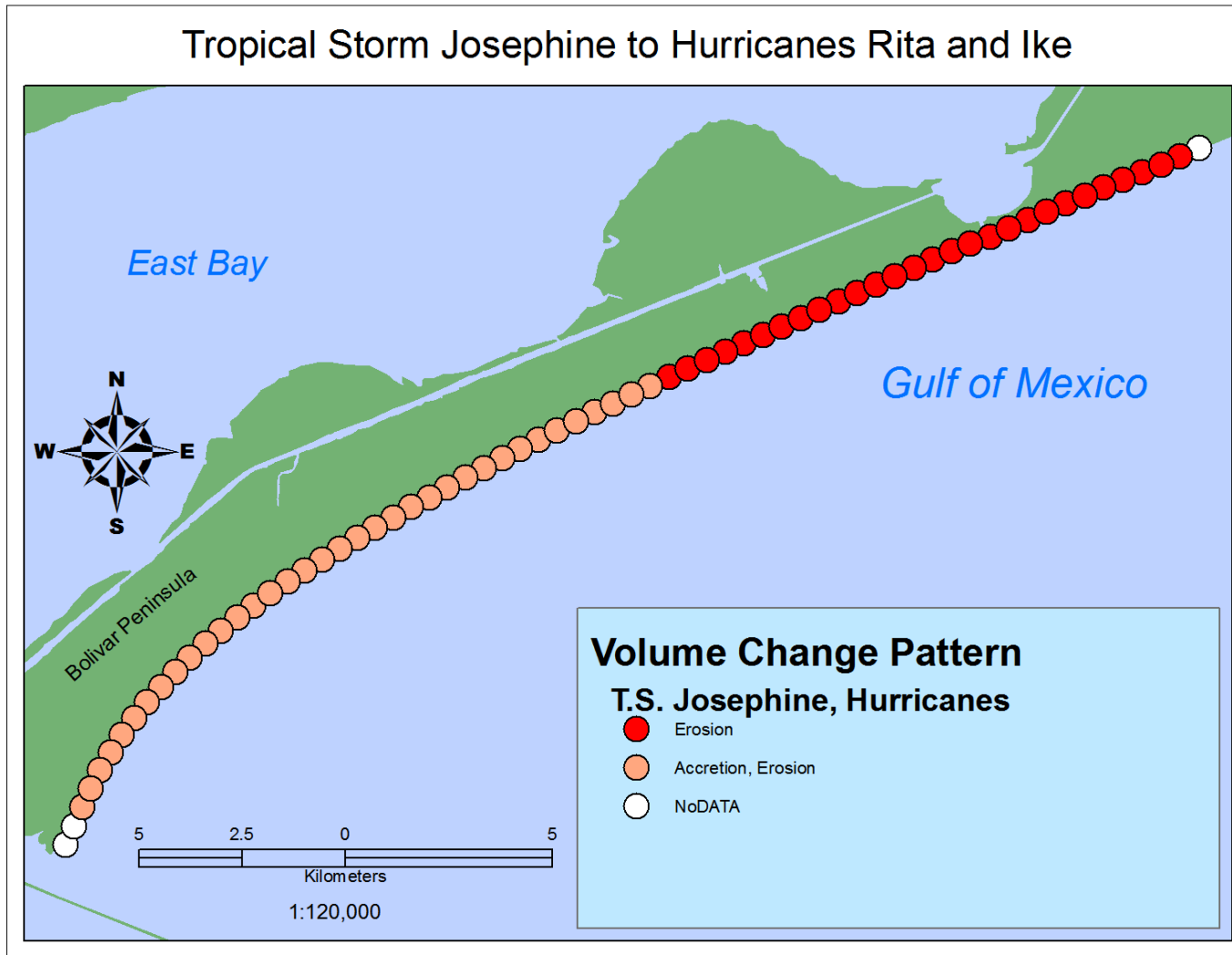


Figure 4.42. Alongshore volume pattern comparison – Tropical Storm Josephine to Hurricanes Rita and Ike.

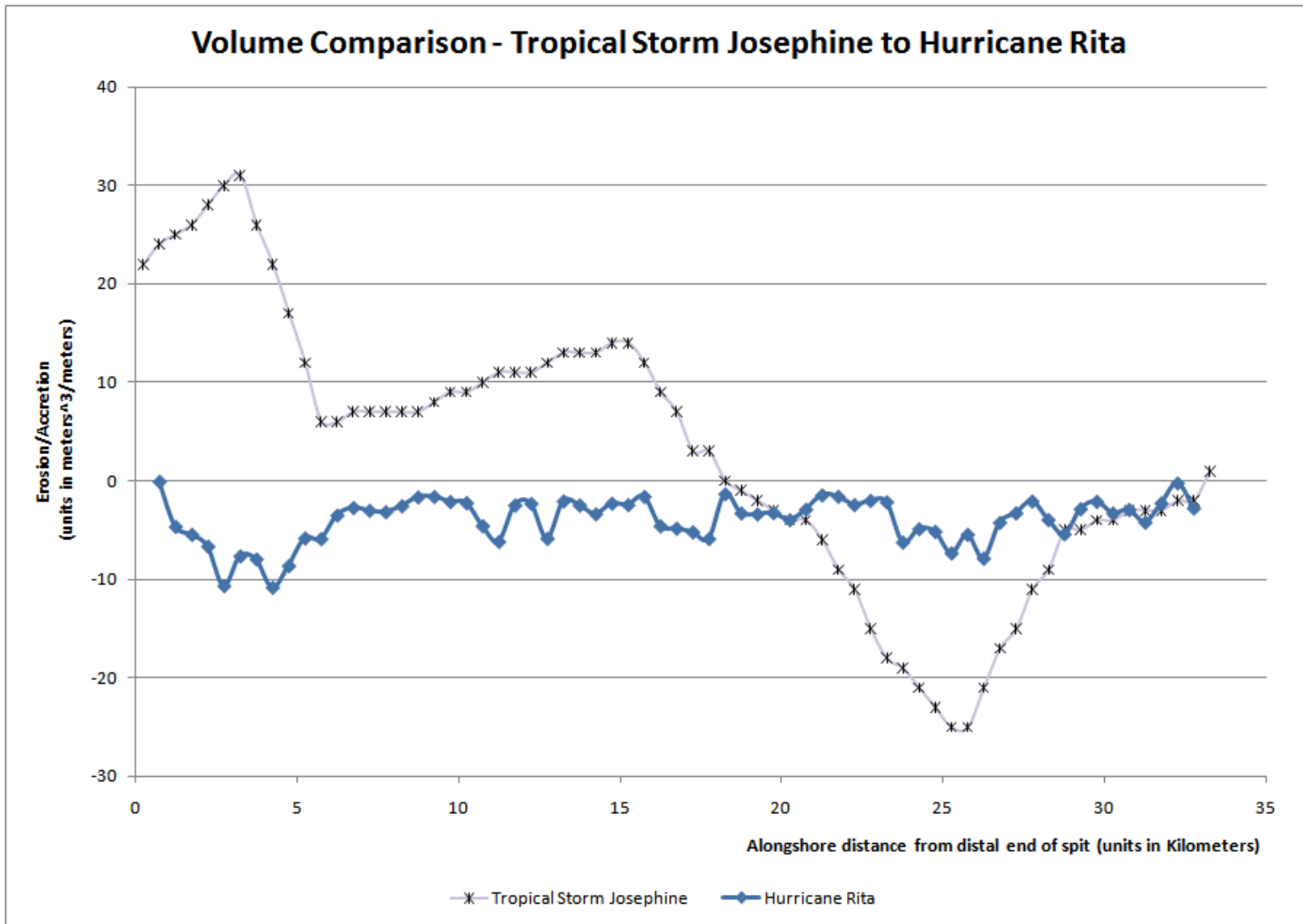


Figure 4.43. Comparison of detrended alongshore impacts from Tropical Storm Josephine and Hurricane Rita.

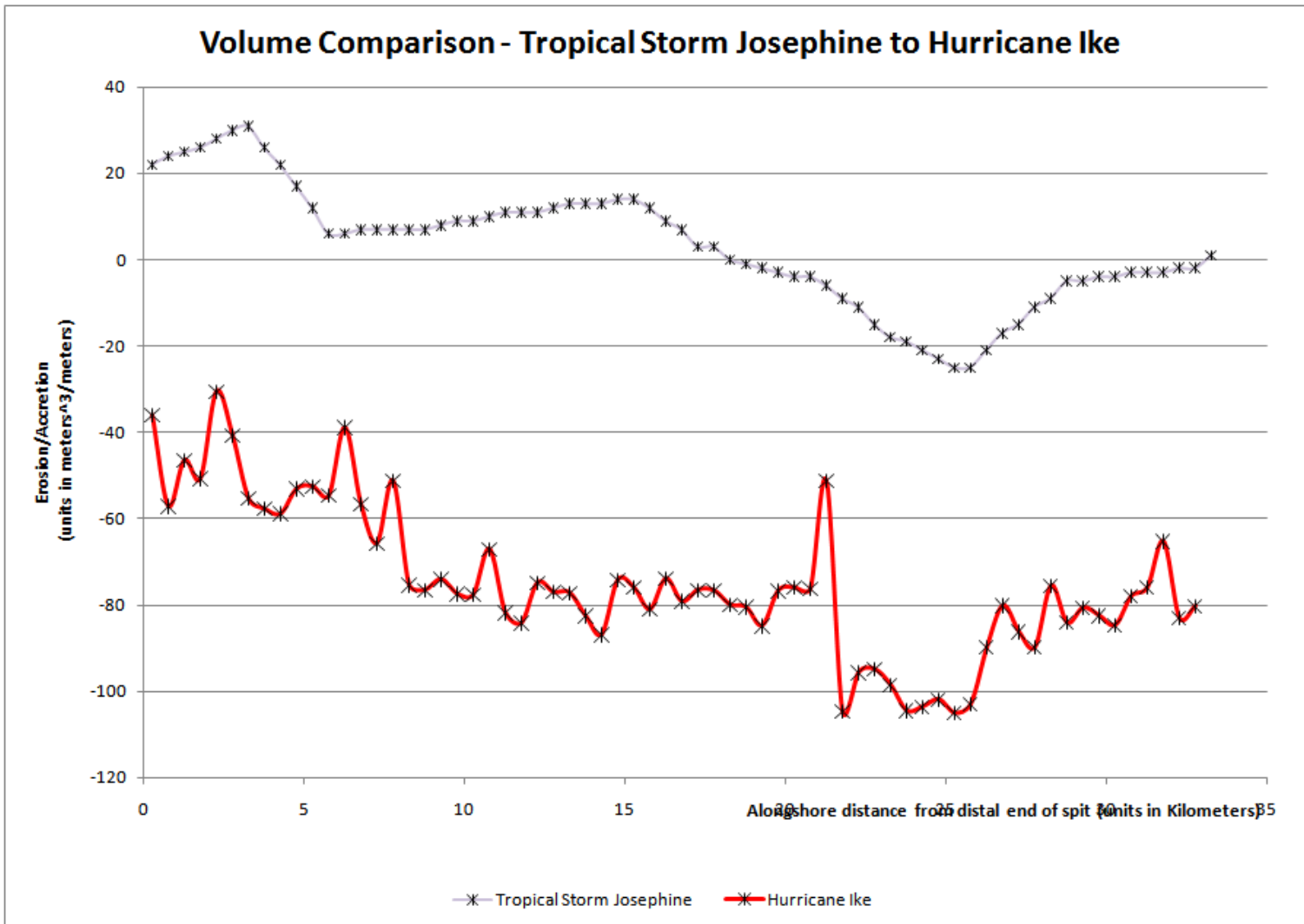


Figure 4.44. Comparison of detrended alongshore impacts from Tropical Storm Josephine and Hurricane Ike.

1D Comparison – T.S. Fay to H. Ike and H. Rita

Just as in the case of the 1D pattern comparison between Tropical Storm Josephine to Hurricanes Rita and Ike, this comparison (Figure 4.45) does not really demonstrate anything new. However, the comparison of detrended volumetric impacts between Tropical Storm Fay to Hurricanes Rita, (Figures 4.46 and 4.47), do yield interesting information. Comparisons between the volumetric impacts of Tropical Storm Fay and Hurricane Rita (Figure 4.46) indicate that impacts are similar in magnitude, phase, and in general trends. However, there is a marked difference in the areas of maximum erosion. For Tropical Storm Fay, the area of maximum erosion was near Rollover Pass, the proximal portion of the spit. However for Hurricane Rita, the area of greatest erosion was near the distal portion of the spit. Differences between the volumetric response of Tropical Storm Fay to Hurricane Ike vary greatly by amplitude and by offset—although the general trend is the same (Figure 4.47). Parts of the response of Tropical Storm Fay are in the accretionary zone, past the zero line, but these are only isolated patches, and could be related to error.

2D Comparison – T.S. Fay to H. Rita

Detection of erosive/accretive features for impacts of Tropical Storm Fay and Hurricane Rita is dependent on how continuous that feature is along the coast. Discontinuous and/or thin patterns of erosion/accretion are often undetected or discarded in the processing. The comparison of 2D volume change patterns for these two smaller storms reflect differences in the continuity of features for these two storms.

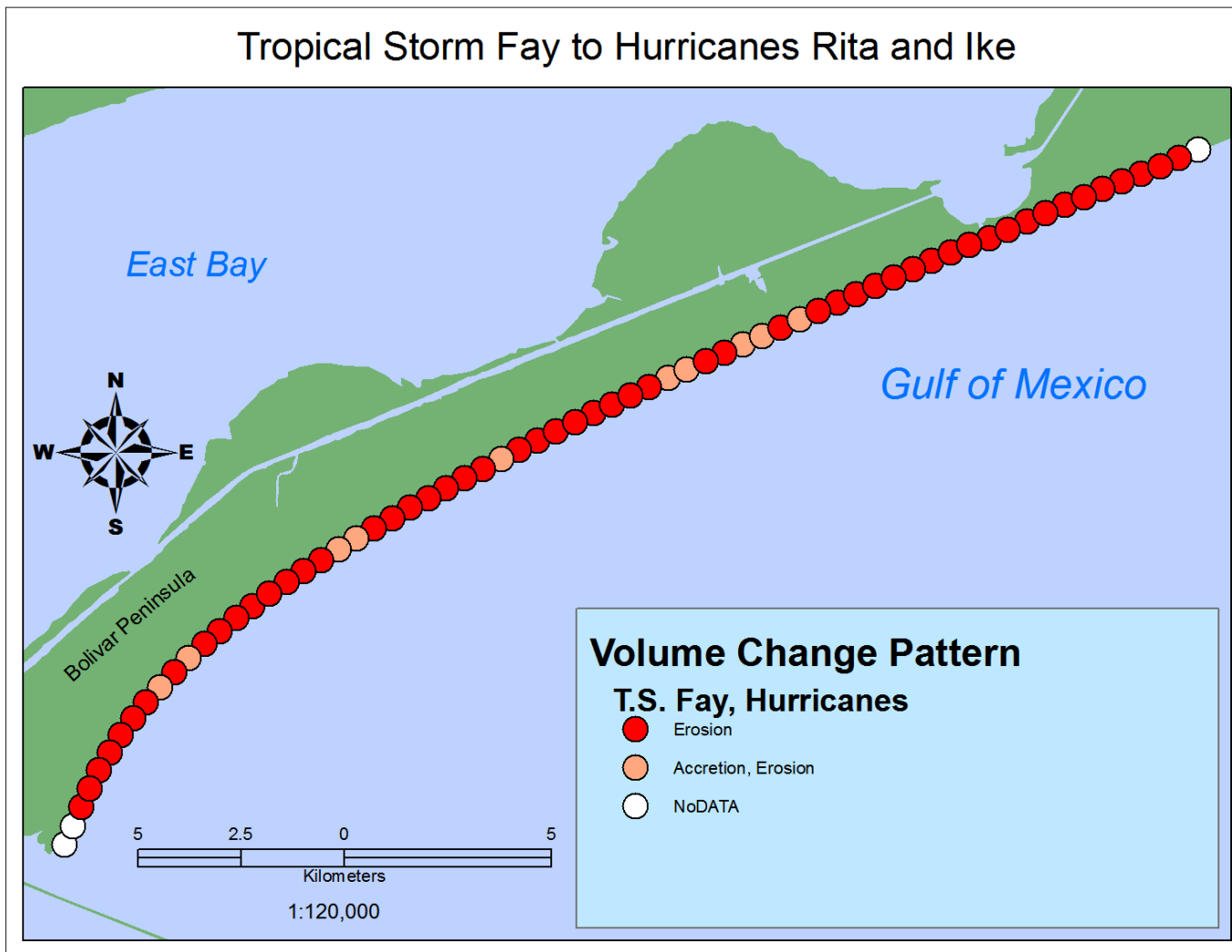


Figure 4.45. Alongshore volume pattern comparison – Tropical Storm Fay to Hurricanes Rita and Ike.

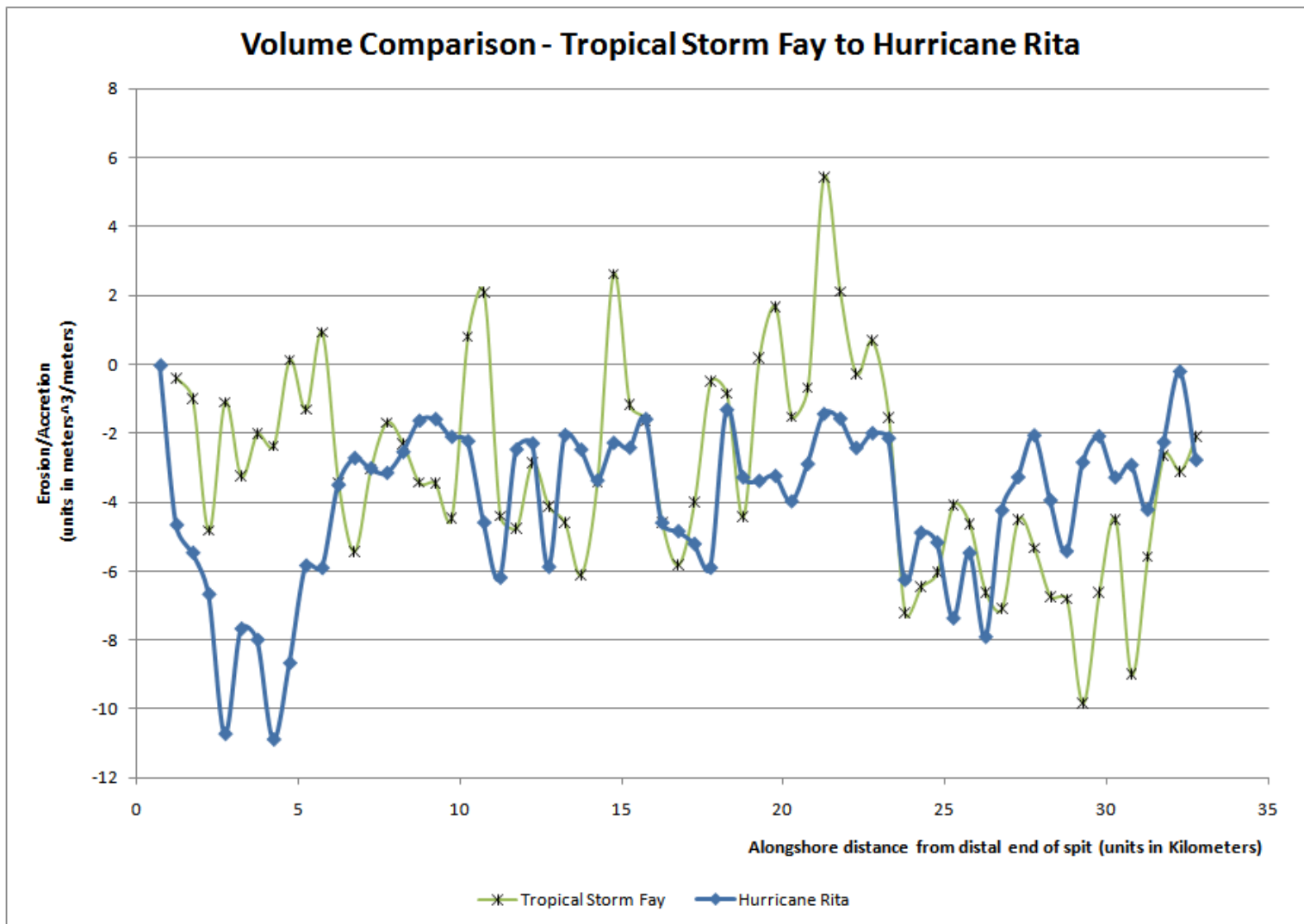


Figure 4.46. Comparison of detrended alongshore impacts from Tropical Storm Fay and Hurricane Rita.

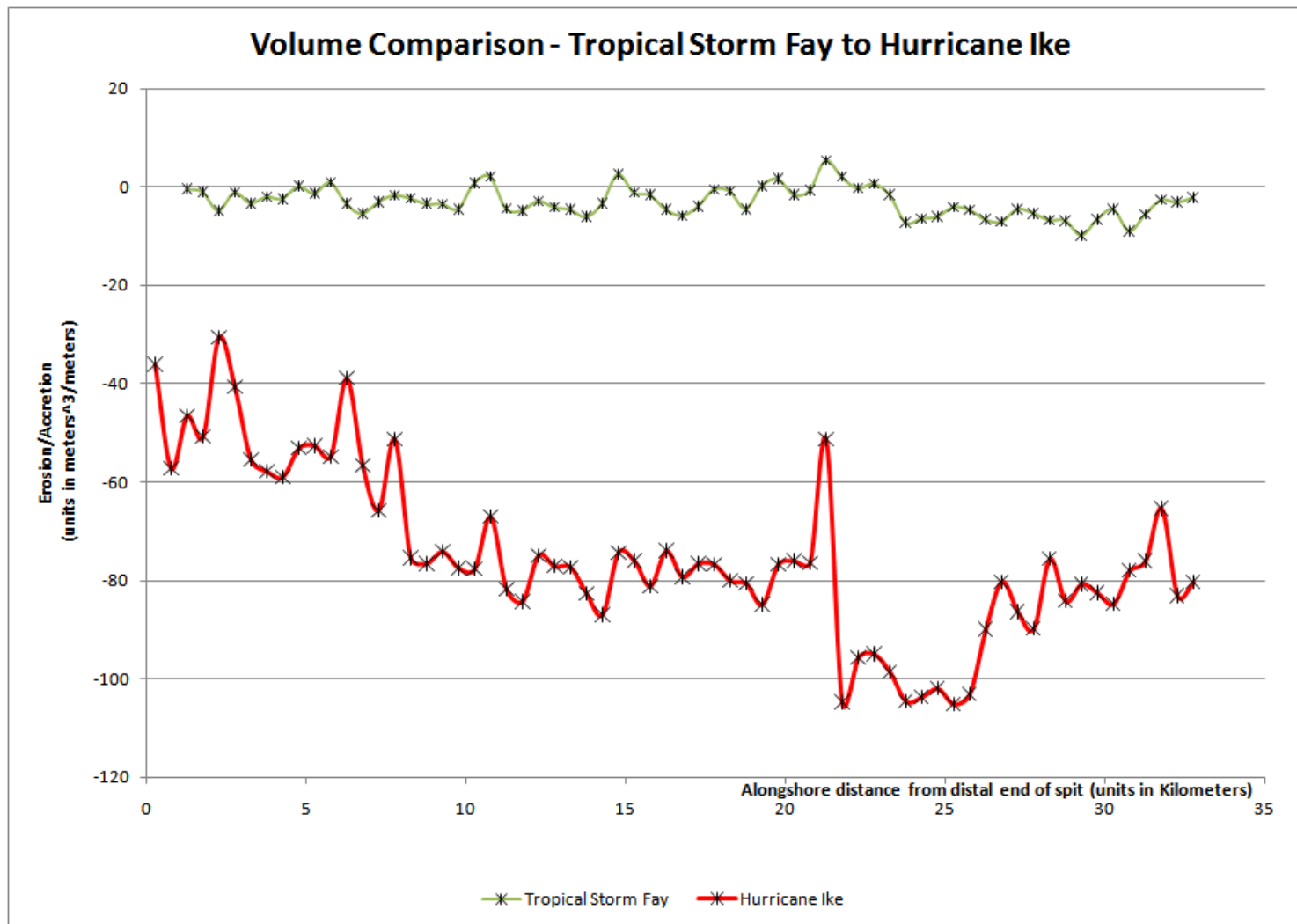


Figure 4.47. Comparison of detrended alongshore impacts from Tropical Storm Fay and Hurricane Ike.

The first sections of these comparisons, A-D on Figure 4.48, demonstrate the contrast between the noncontinuous versus continuous registration of erosion in the berm zone (1st through 3rd landward zone) and the seaward side of natural and anthropogenic foredune zone (8th through 10th landward zone near the distal end of the spit, and 4th through 5th landward zone near the center and proximal end). It should be noted that these are generalizations and local areas may have differences in zonation depending on the width of the beach and deviation of the shoreline from the centerline.

Hurricane Rita clearly had a more continuous coverage with respect to erosion at the distal end of the spit. Tropical Storm Fay appeared to have discontinuous registration of erosion at the foredune zone in sections B-C and C-D on Figure 4.48. For these zones, only berm erosion is detected with respect to both storms..

The middle two sets of sections, D-G on Figure 4.49 and G-J on Figure 4.50, depict the absence of any features of erosion from Hurricane Rita and the discontinuous presence of features from Tropical Storm Fay. There is some erosion of anthropogenic plots or rather the dunes formed seaward of these plots noted in between sections F-G on Figure 4.49 and G-H on Figure 4.50 and at the end of plot I-J, also on Figure 4.50, for Tropical Storm Fay. Aside from that, these zones are the only noted dune erosion up to this point from both storms.

The next set of sections, J-M on Figure 4.51, is largely unaffected by both storms. This is the last section without geotubes. The only impact noted for this section occurred with Tropical Storm Fay, and it is the continuation of the effect documented at the end of section I-J on Figure 4.50.

Section M-P, Figure 4.52, documents geotube erosion caused by Hurricane Rita. It should be noted that there are no impacts for the third and fourth landward zones—with the exception of section O-P on Figure 4.52. This lack of impacts is most likely because of the very narrow beaches in front of these geotubes—as also demonstrated in Gibeaut *et al.* (2002). There is a mixture of impacts documented in the first and second landward areas between berm erosion and geotube erosion. At section O-P, there is a suggestion of a failure of the geotube—as evidenced by erosion of land beyond it and an obvious scour pattern (Figure 4.52).

The last set of segments, P-S on Figure 4.53, document the complete lack of detected erosive impacts from Hurricane Rita and the presence of berm/geotube erosion from Tropical Storm Fay. The last segment, R-S on Figure 4.53, does not have a geotube, and it only underwent berm erosion. It should be noted that this beach appears noticeably wider than the geotubed beach as well (Gibeaut *et al.* 2002). For Tropical Storm Fay, there is deposition noted, although it is speculative as to whether this is an anomaly or not—since this deposition was immediately next to Highway 87.

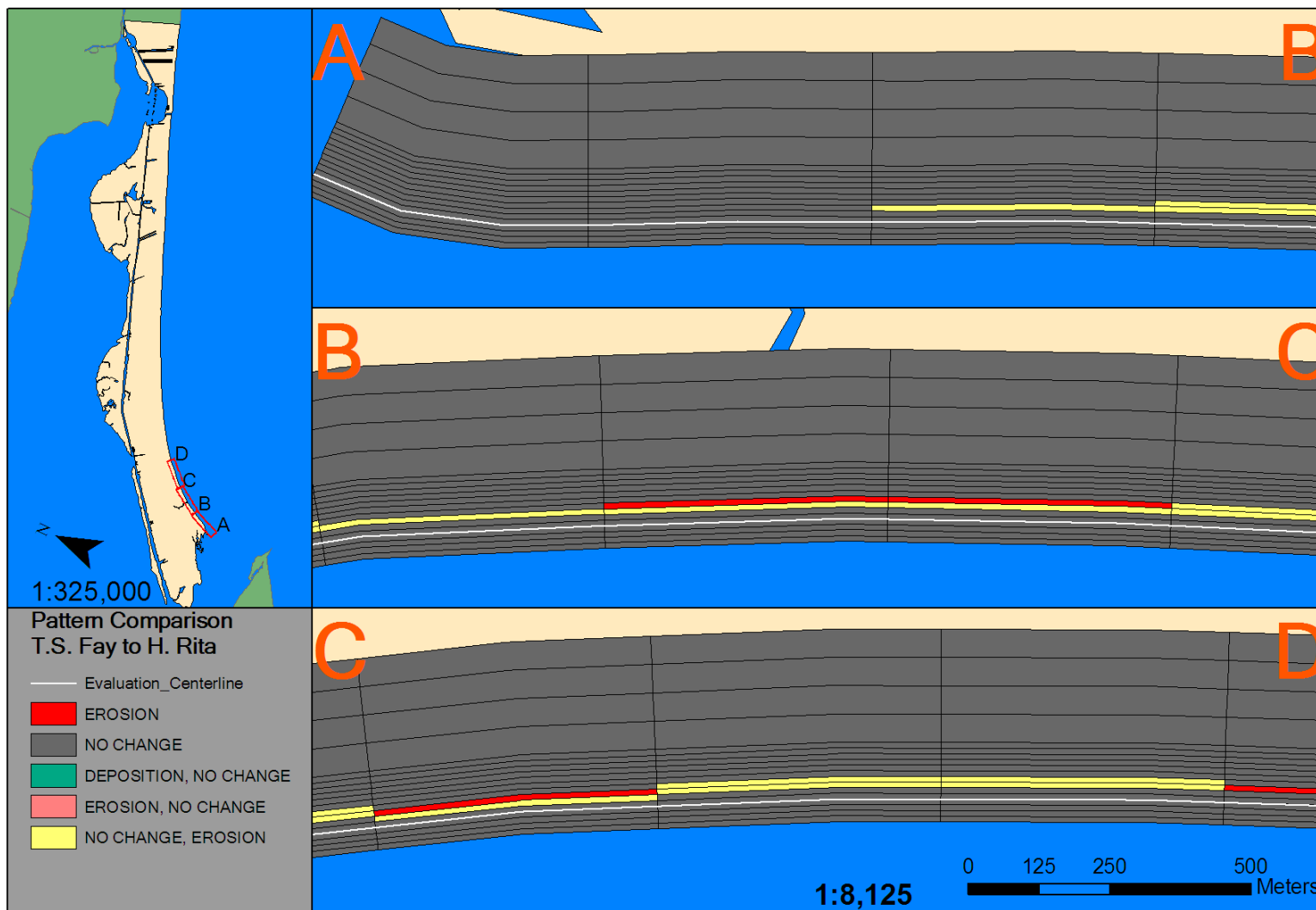


Figure 4.48. Sections A-D of 2D volumetric pattern comparison – Tropical Storm Fay to Hurricane Rita.

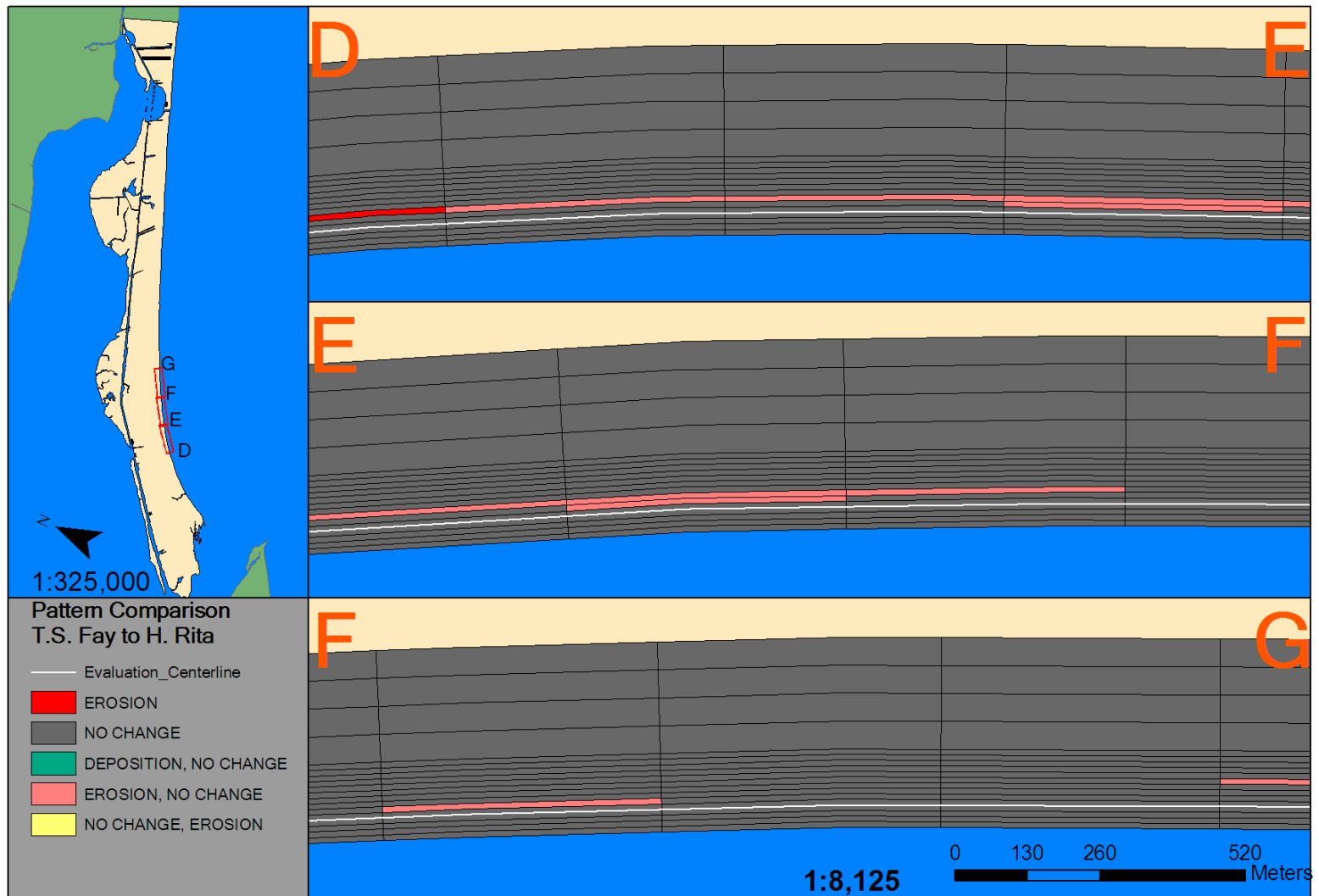


Figure 4.49. Sections D-G of 2D volumetric pattern comparison – Tropical Storm Fay to Hurricane Rita.

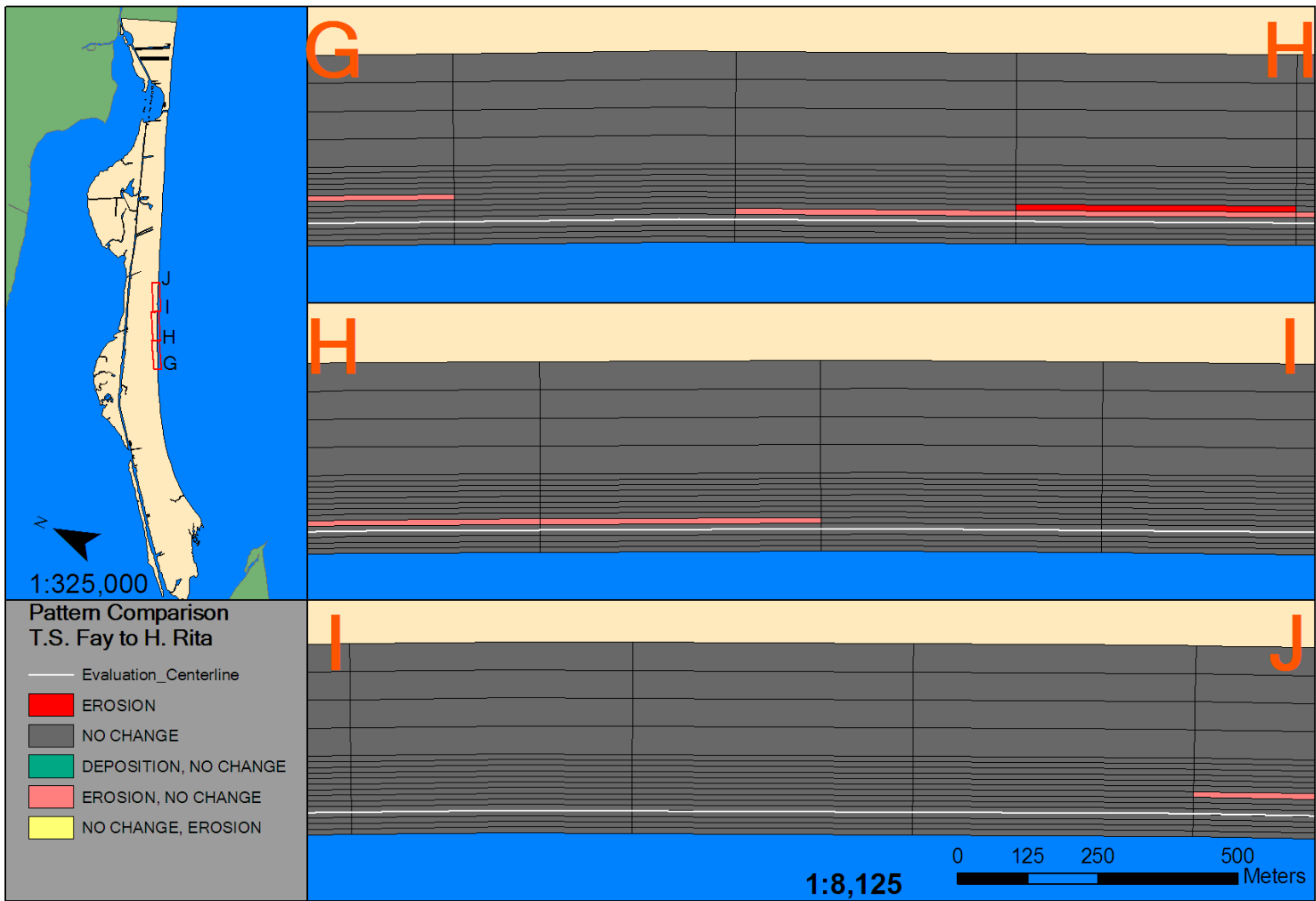


Figure 4.50. Sections G-J of 2D volumetric pattern comparison – Tropical Storm Fay to Hurricane Rita.

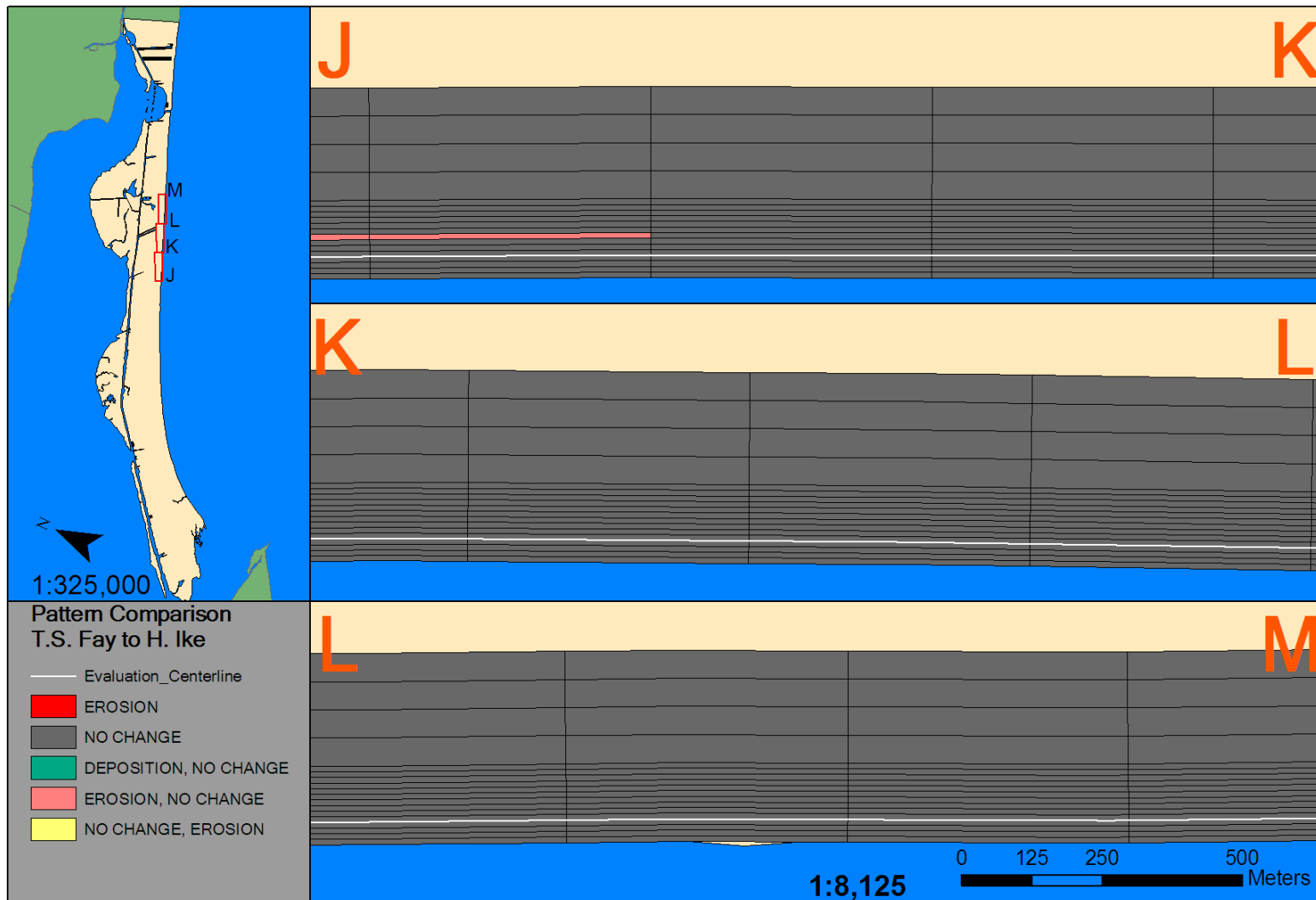


Figure 4.51. Sections J-M of 2D volumetric pattern comparison – Tropical Storm Fay to Hurricane Rita.

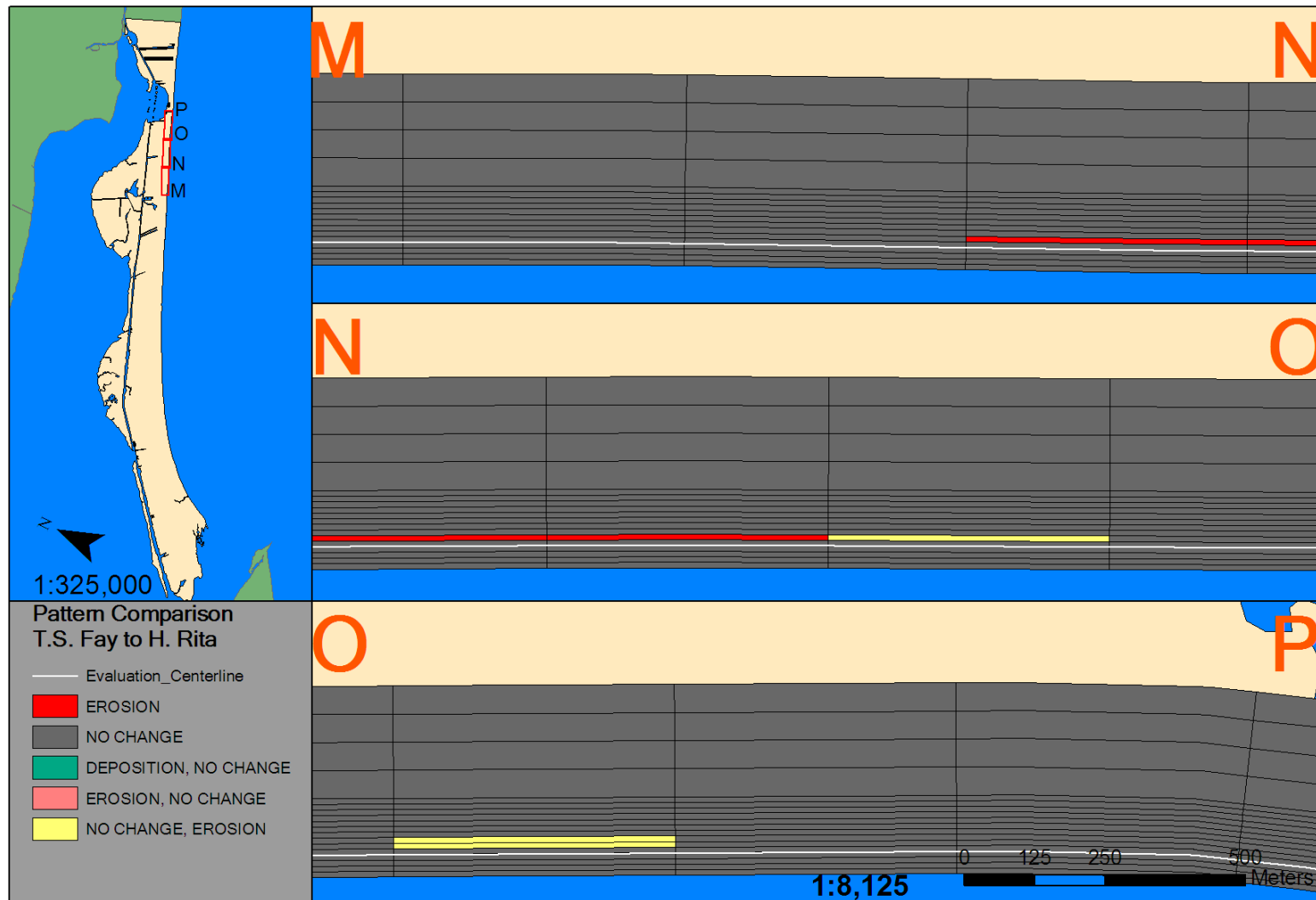


Figure 4.52. Sections M-P of 2D volumetric pattern comparison – Tropical Storm Fay to Hurricane Rita.

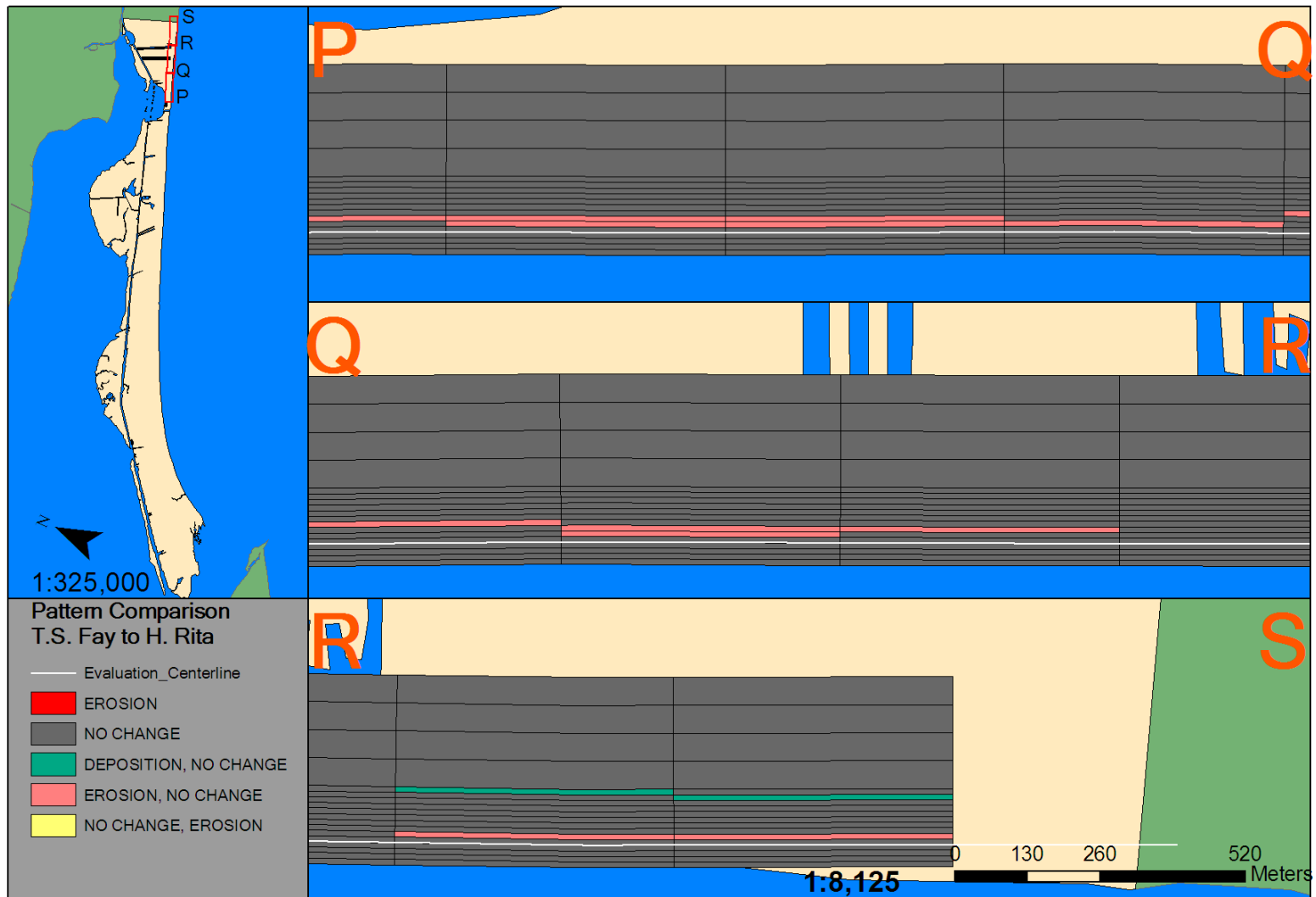


Figure 4.53. Sections P-S of 2D volumetric pattern comparison – Tropical Storm Fay to Hurricane Rita.

2D Comparison – T.S. Fay to H. Ike

The differences between the volumetric impacts of Tropical Storm Fay and Hurricane Ike is tremendous. Landward, there is very little similarity between Hurricane Ike and Tropical Storm Fay. In the first set of sections, A-D in Figure 4.54, there appears to be little correlation between the alongshore berm erosion caused by Tropical Storm Fay and the widespread coastal erosion from Hurricane Ike. However, there is discontinuous similarity in erosion character in sections B-C and C-D. The similarity in B-C seems to correspond to the presence of stream outlets.

The presence of stream outlets bound the continuous erosive impacts of sections D-E, and E-F in Figure 4.55. The next section does not have a stream outlet present from Tropical Storm Fay, but does have one present from the impacts of Hurricane Ike. The area coverage of Fay is discontinuous for this section, but the coverage/detection of erosion for the volumetric impacts of Ike is constant at 150 meters.

The next set of sections, G-J on Figure 4.56, present one of the largest landward extents of erosion from Hurricane Ike, which is 200 meters at section I-J. This section corresponds to a network of large scours that have occurred on Bolivar Peninsula. These scours correspond to Group 2 features as described in Potts (2010). This location of greatest areal extent of impact from Hurricane Ike does not have any correlation to the berm erosion from Tropical Storm Fay. However, it is noted that there are areas of berm erosion from Tropical Storm Fay immediately to the northeast (up the coast).

Sections J-M on Figure 4.57, aside from the area of similarity mentioned at the end of the last section, bears little similarity in impacts from Tropical Storm Fay and

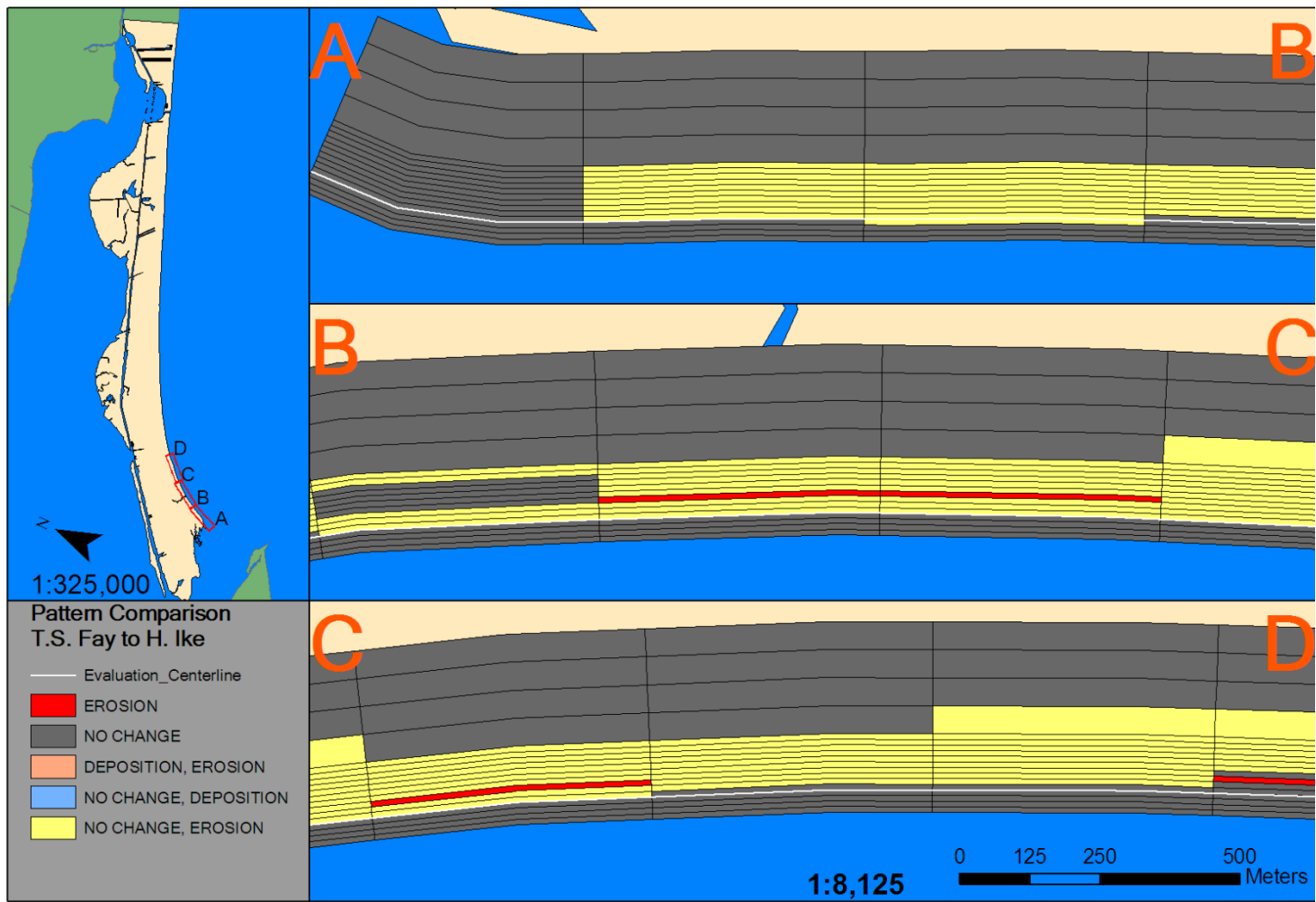


Figure 4.54. Sections A-D of 2D volumetric pattern comparison – Tropical Storm Fay to Hurricane Ike.

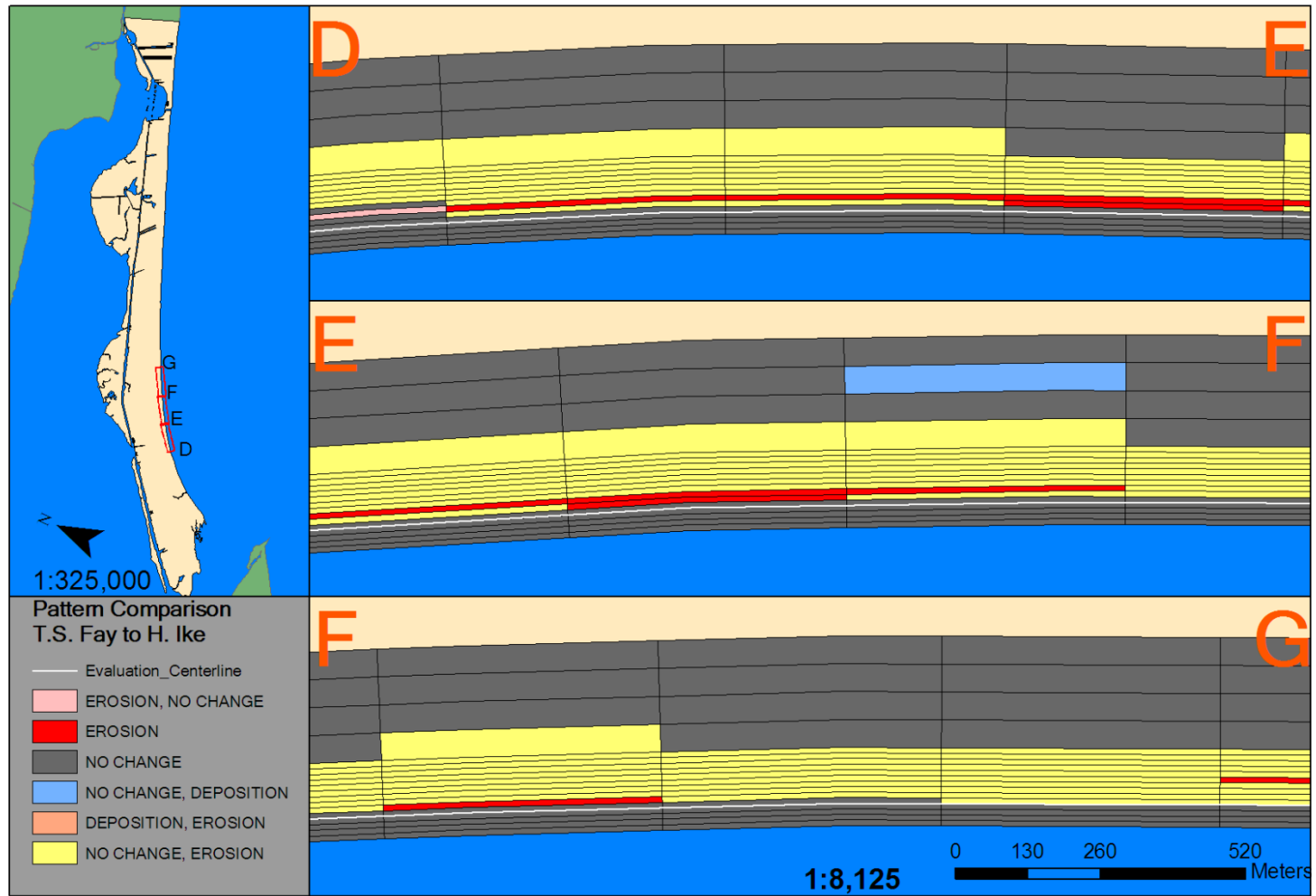


Figure 4.55. Sections D-G of 2D volumetric pattern comparison – Tropical Storm Fay to Hurricane Ike.

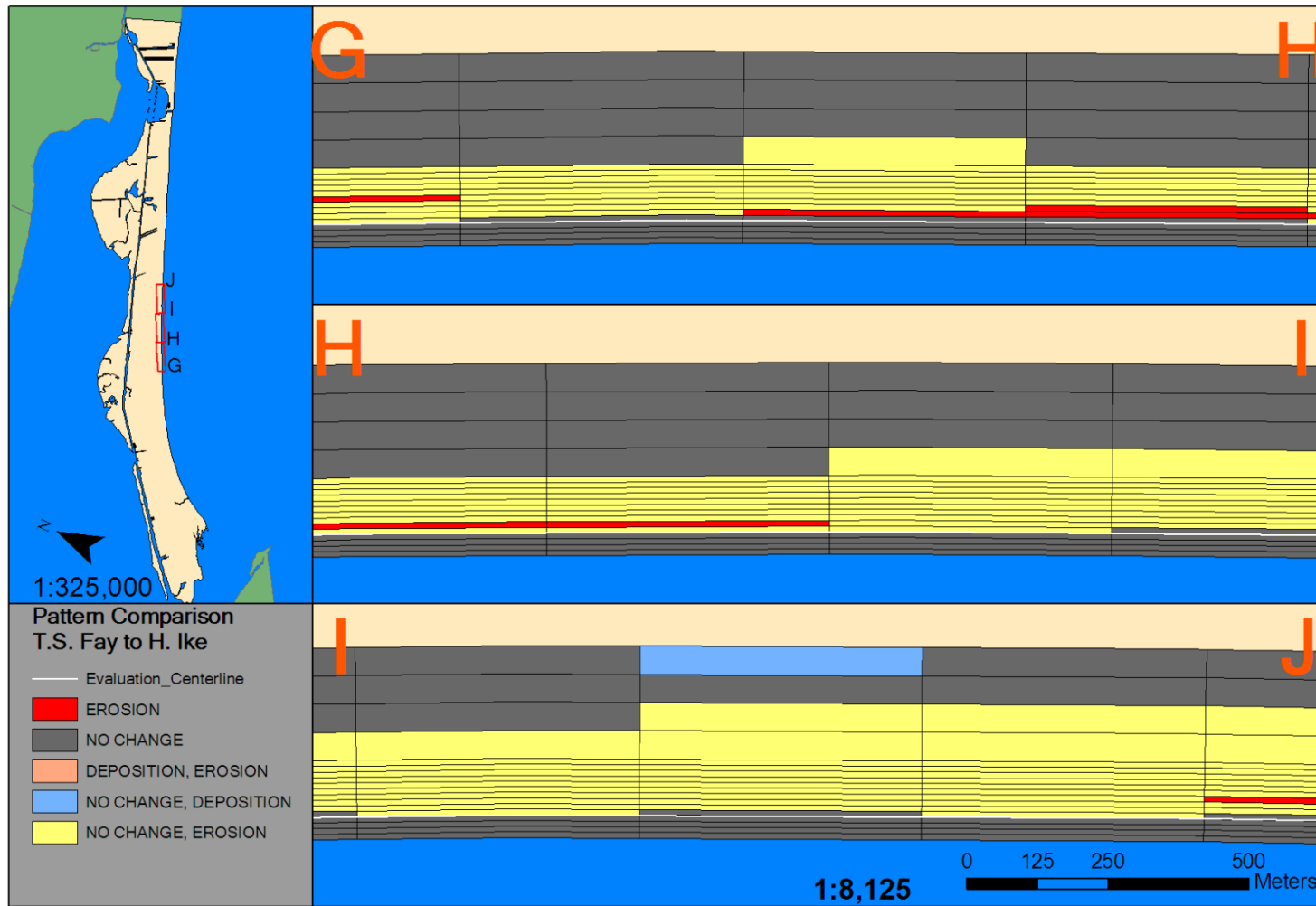


Figure 4.56. Sections G-J of 2D volumetric pattern comparison – Tropical Storm Fay to Hurricane Ike.

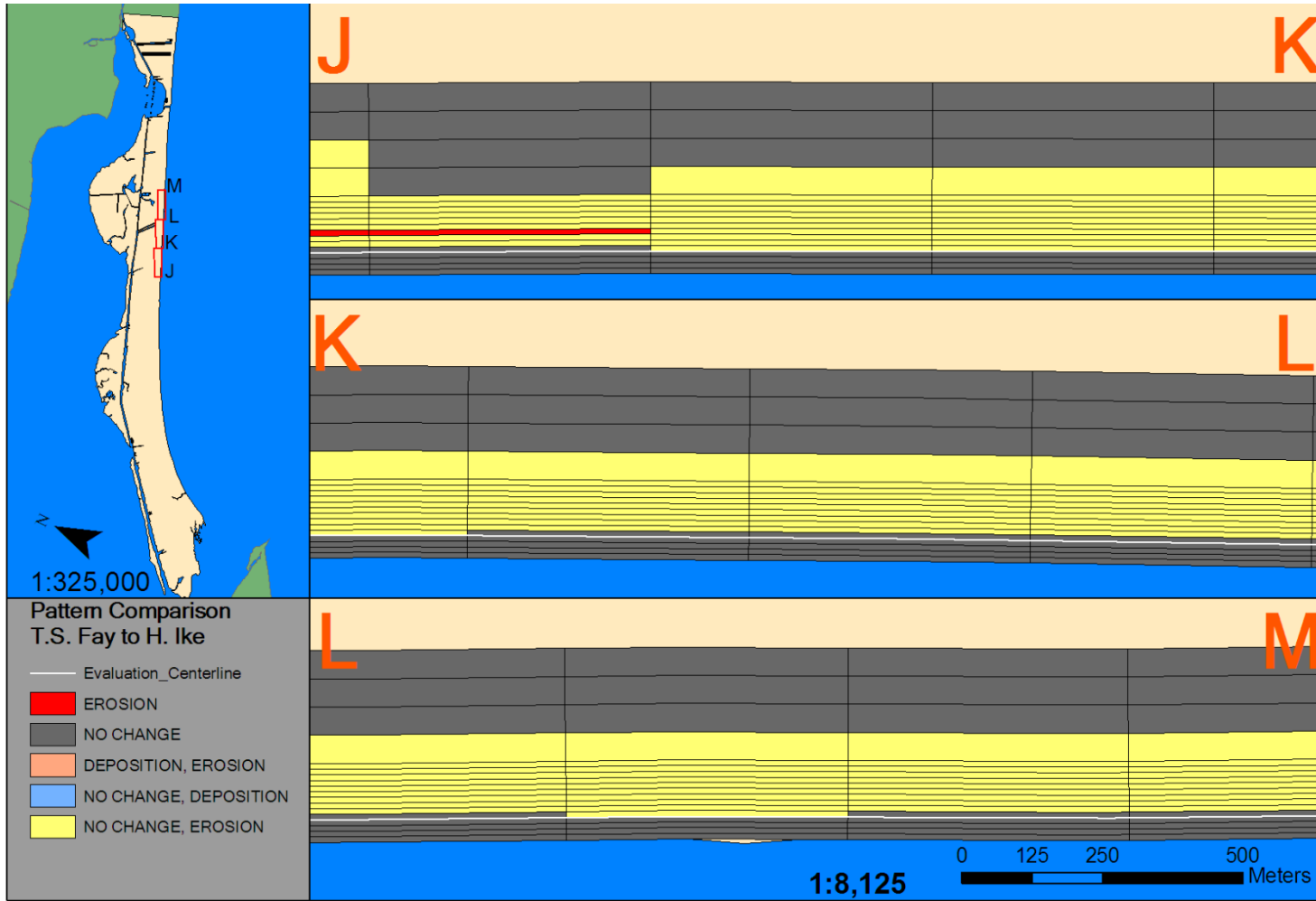


Figure 4.57. Sections J-M of 2D volumetric pattern comparison – Tropical Storm Fay to Hurricane Ike.

Hurricane Ike. It is noted, however, that this part of Bolivar Peninsula has a very small stream outlet and is consistent of houses—as for the time immediately after the impacts of Tropical Storm Fay.

At section M-P on Figure 4.58, there is one alongshore area of erosion that Tropical Storm Fay has in common with Hurricane Ike. Coming from the southwest, this area corresponds closely to the beginning of the geotube. For the next 1.5 kilometer, there is increased areal spread of erosion from Hurricane Ike and similarity with alongshore erosion. However, this similarity, terminates apparently from by virtue of the erosion pattern thinning substantially and losing area coverage.

The final set of sections, P-S on Figure 4.59, represents come of the most continuous patches of erosion for Tropical Storm Fay. In terms of area coverage, the coverage of erosion from Hurricane Ike appears to be reducing from 150 meters at section P-Q to 90 meters at section R-S.

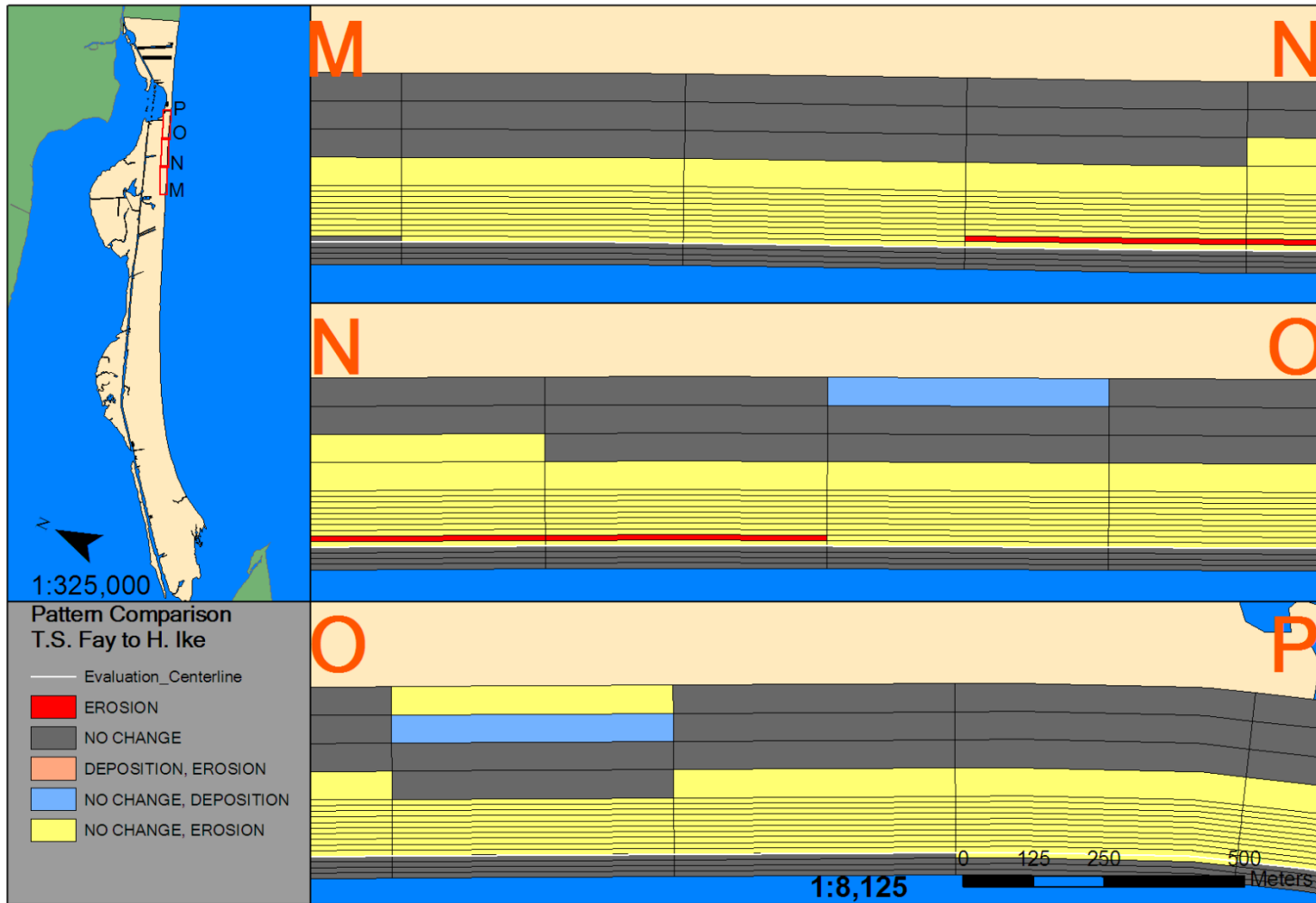


Figure 4.58. Sections M-P of 2D volumetric pattern comparison – Tropical Storm Fay to Hurricane Ike.

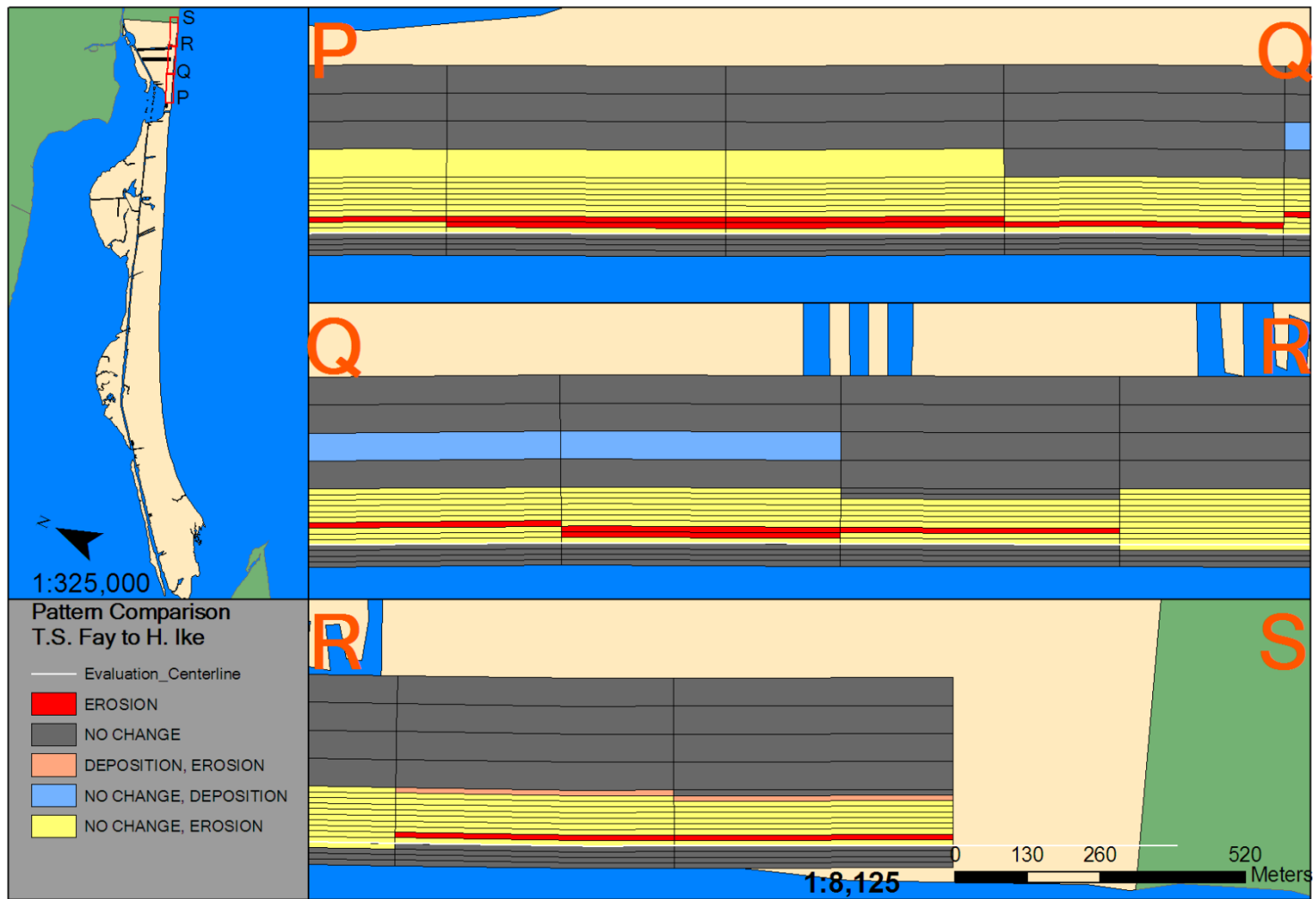


Figure 4.59. Sections P-S of 2D volumetric pattern comparison – Tropical Storm Fay to Hurricane Ike.

1D Pattern Change – Hurricane Rita to Hurricane Ike

Since both alongshore patterns generated by Hurricanes Rita and Ike only consisted of erosion, comparing them contributes little. However, there is merit in comparing detrended volumetric impacts of Hurricanes Rita and Ike. These comparisons (Figure 4.60) show that the volume change between Hurricanes Rita and Ike were out of phase and had a stark difference in amplitude. Interestingly enough, the period of volumetric change seems to be similar.

2D Pattern Change – Hurricane Rita to Hurricane Ike

For Bolivar Peninsula, the differences in alongshore erosion and accretion from Hurricane Rita to Hurricane Ike are greater than the differences between Tropical Storm Fay and Hurricane Ike. Three sets of sections, D-G, J-M and P-S in Figure 4.62, 4.64, and 4.66, bear no similarity with respect to erosion or accretion.

Section A-D (Figure 4.61) bears the greatest alongshore similarity in with the presence of erosional cells in both storms. In this section, as in the case of Tropical Storm Fay to Hurricane Ike, the common areas of erosion are bounded by stream outlets. In fact, the areas of the largest amounts of erosion and accretion are either adjacent or immediately in front of a stream outlet.

In sections G-J (Figure 4.63) there is only one area that is in common, and this area is directly northeast of a stream outlet. It is also interesting to note that this area is also one of the least impacted areas from Hurricane Ike, with detected erosion from 10 to 90 meters of inland erosion. This outlet also did not change course between the post-Rita

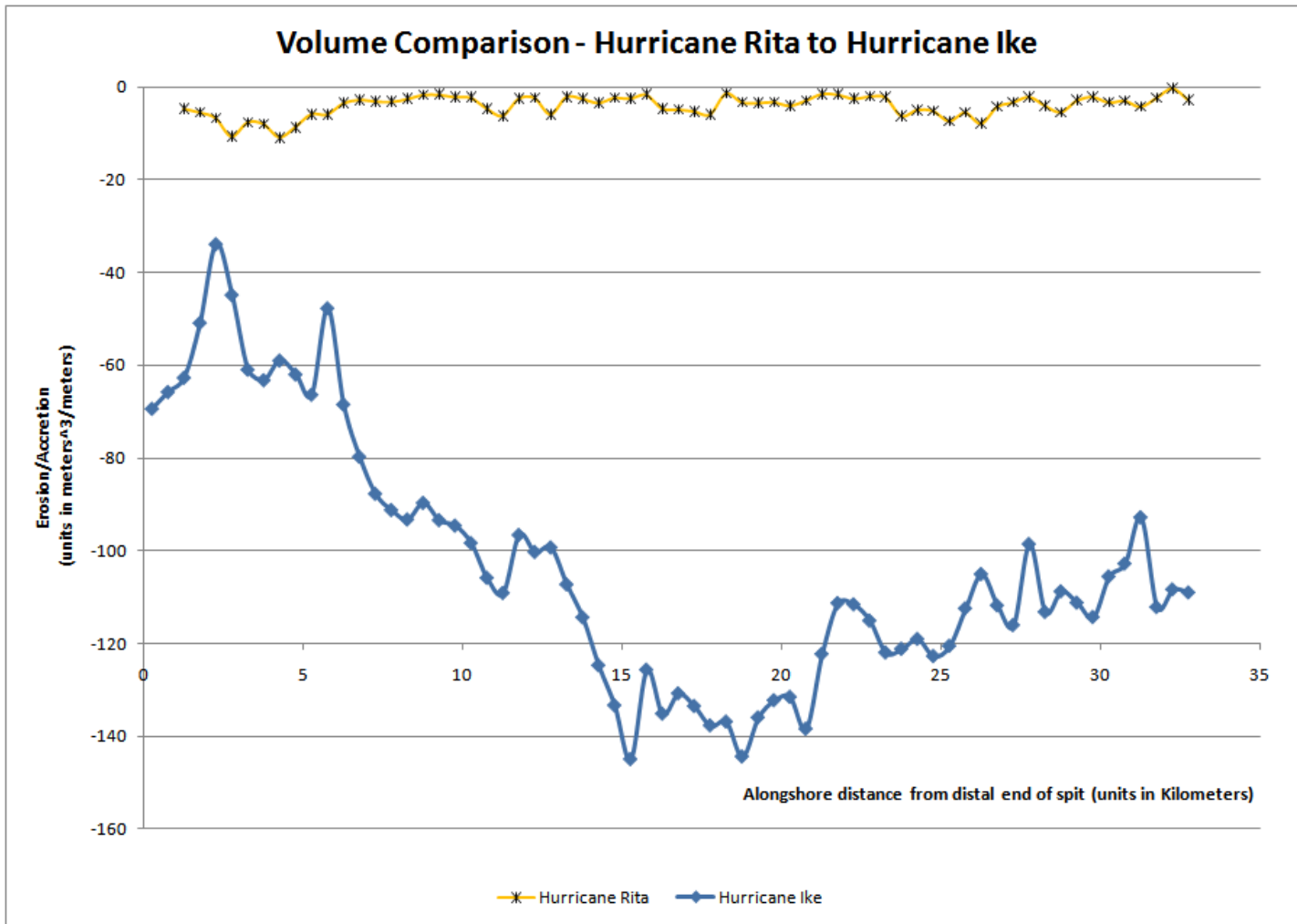


Figure 4.60. Comparison of detrended alongshore impacts from Hurricanes Ike and Rita.

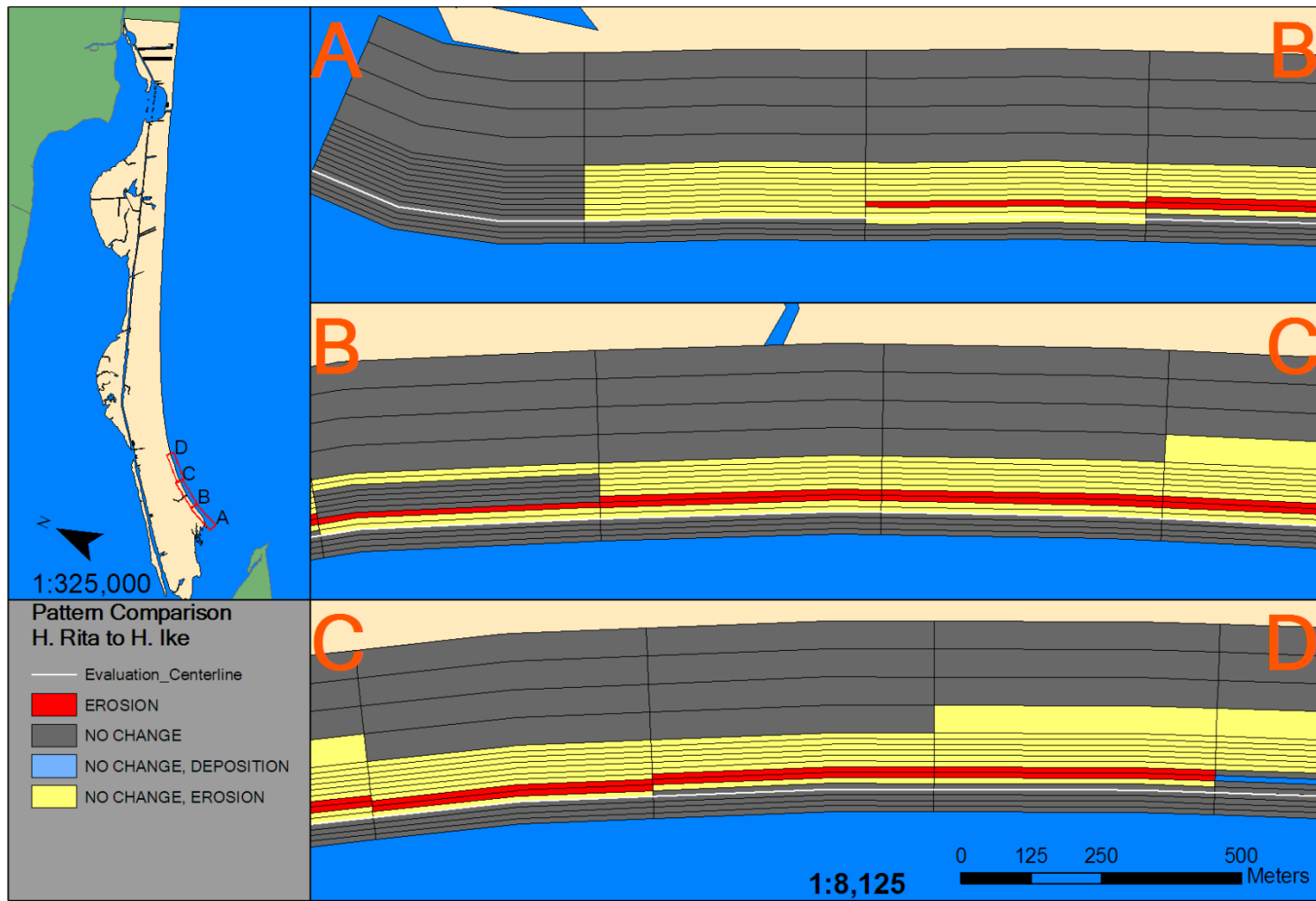


Figure 4.61. Sections A-D of 2D volumetric pattern comparison – Hurricane Rita to Hurricane Ike.

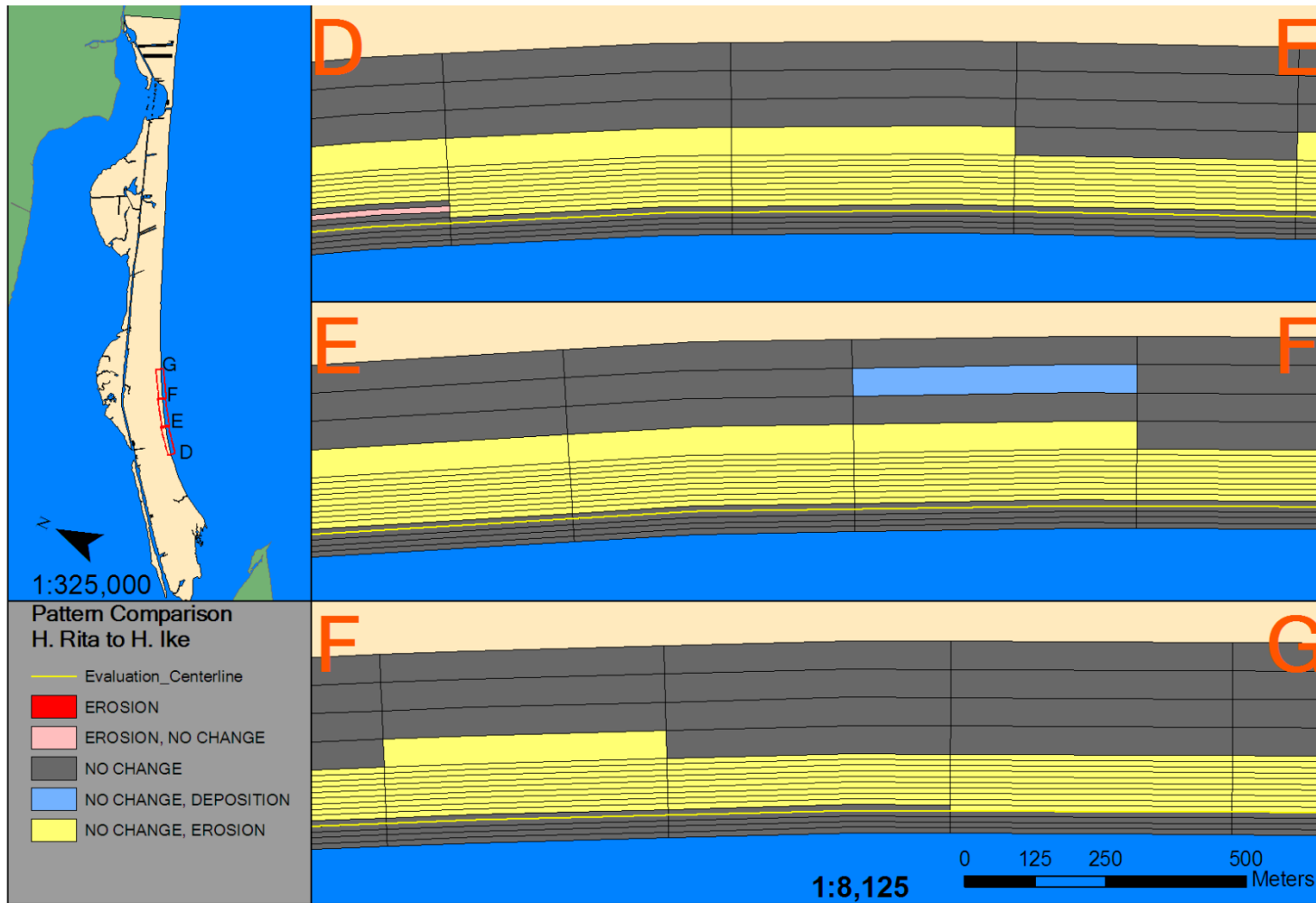


Figure 4.62. Sections D-G of 2D volumetric pattern comparison – Hurricane Rita to Hurricane Ike.

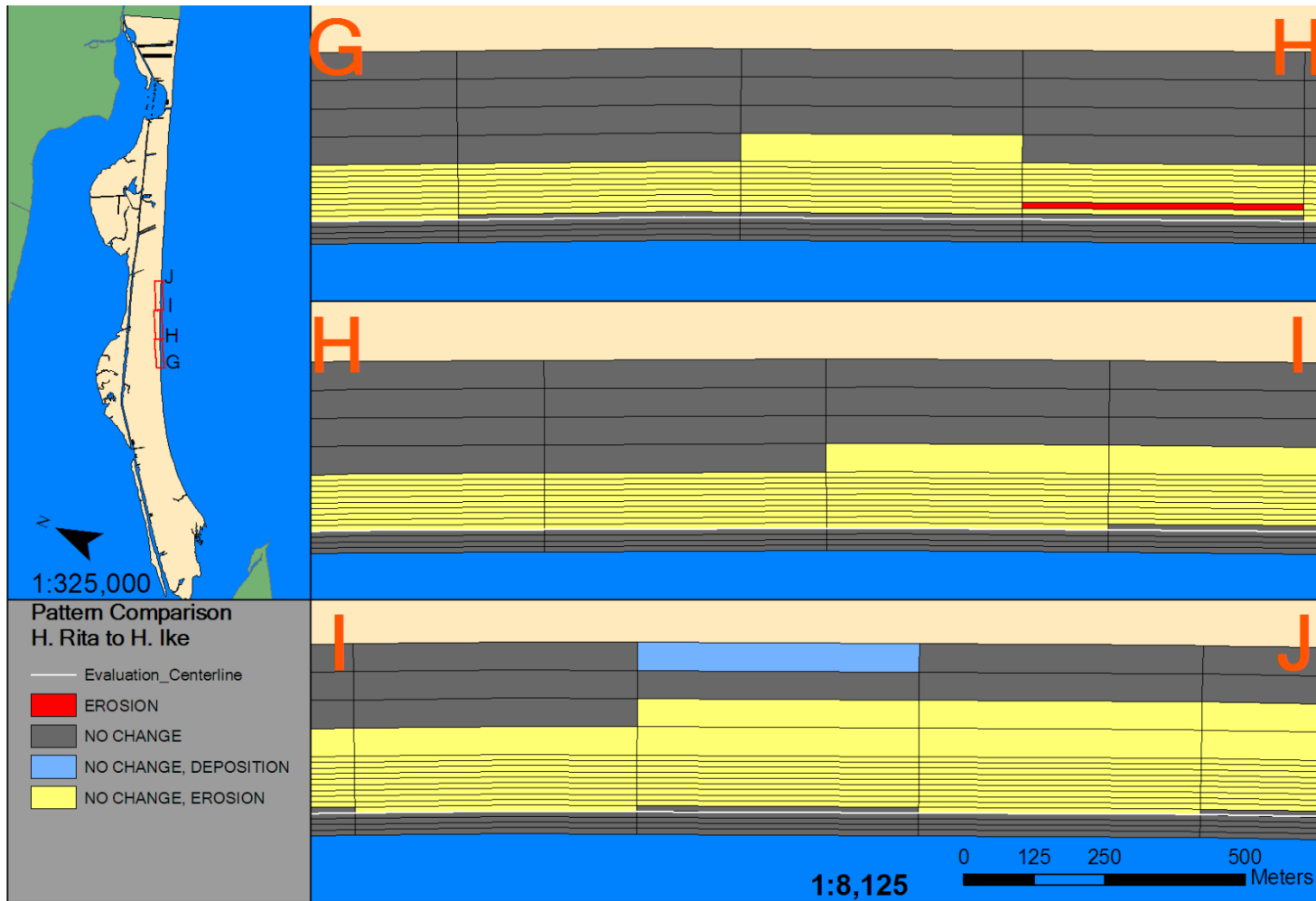


Figure 4.63. Sections G-J of 2D volumetric pattern comparison – Hurricane Rita to Hurricane Ike.

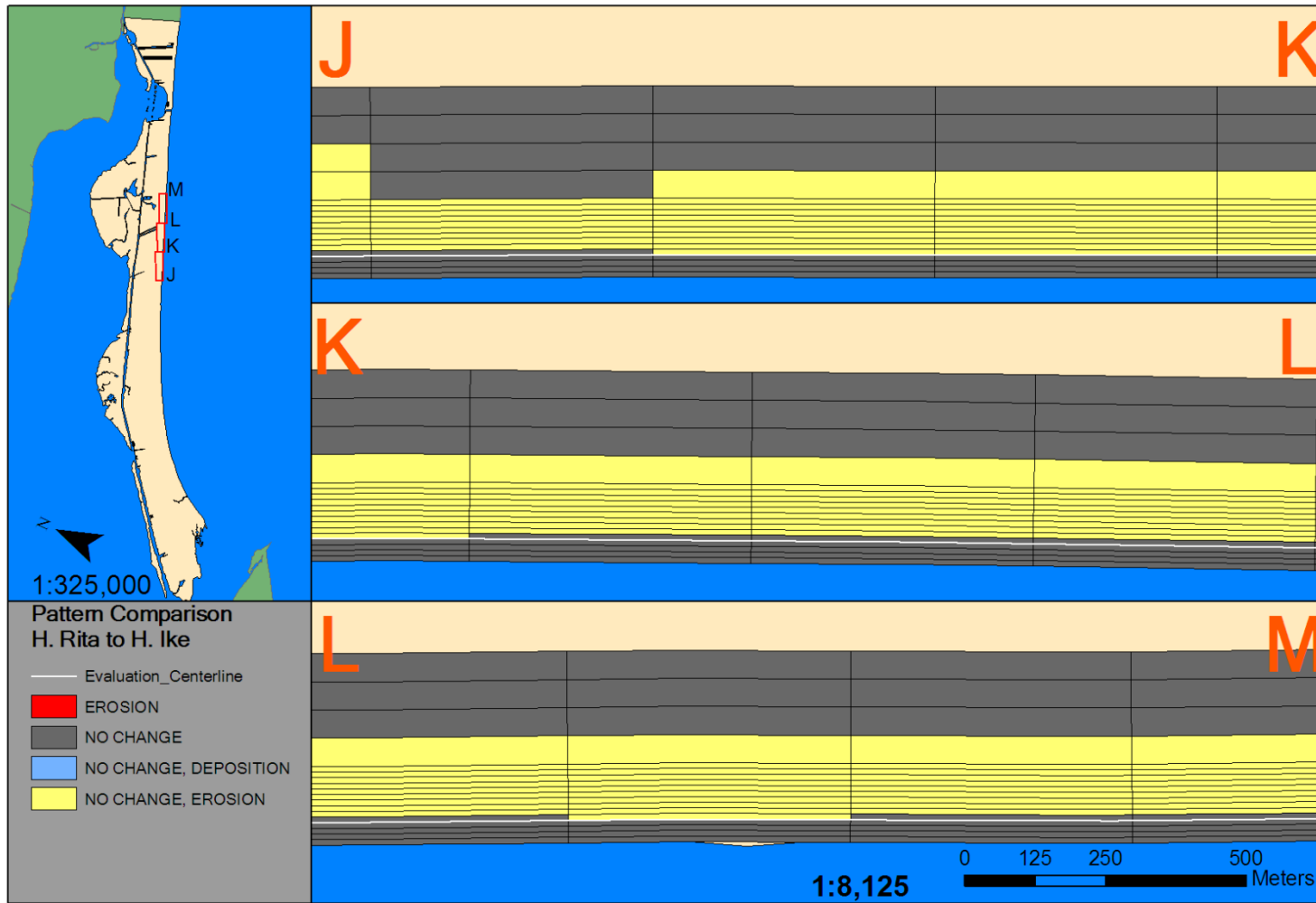


Figure 4.64. Sections J-M of 2D volumetric pattern comparison – Hurricane Rita to Hurricane Ike.

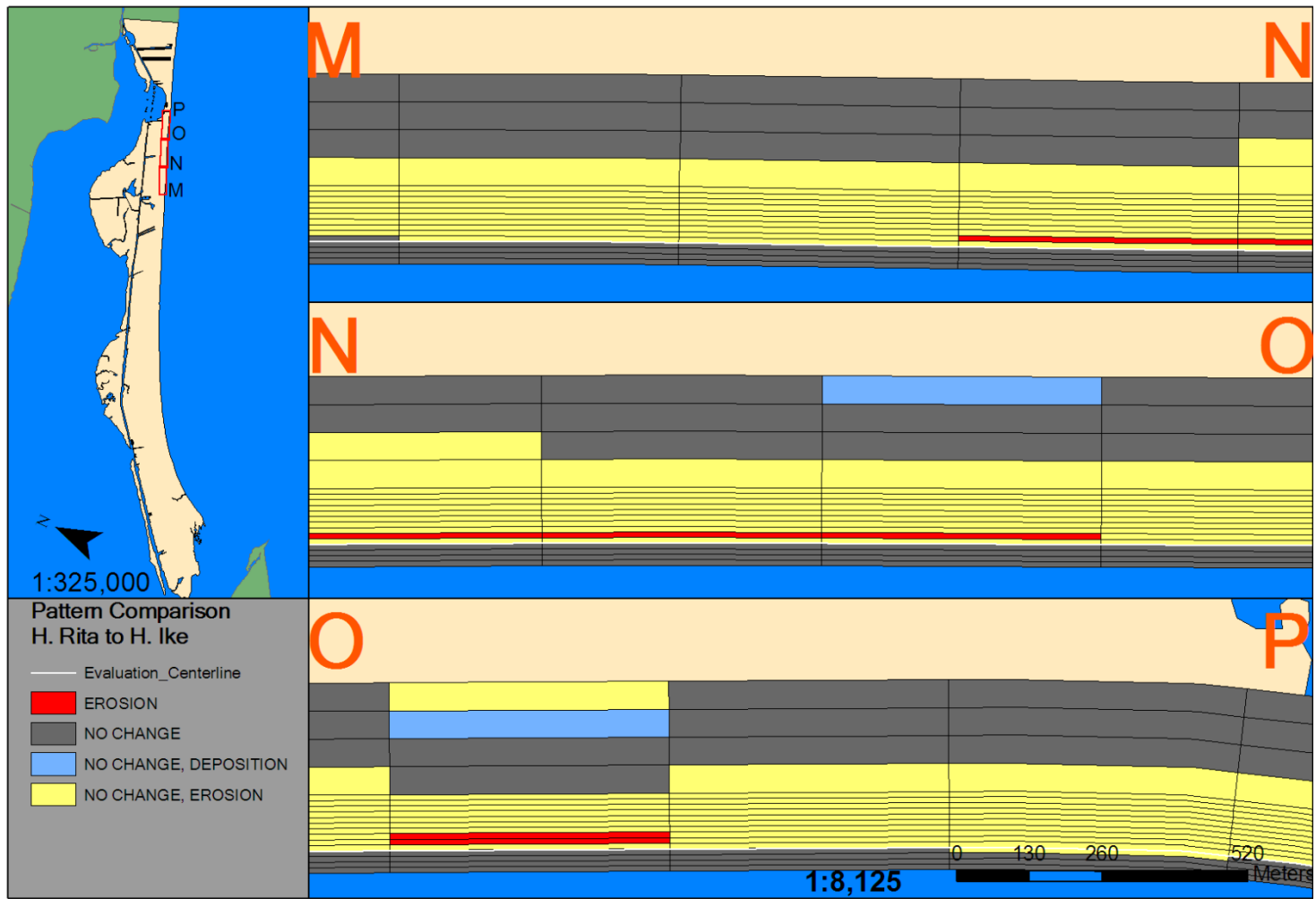


Figure 4.65. Sections M-P of 2D volumetric pattern comparison – Hurricane Rita to Hurricane Ike.

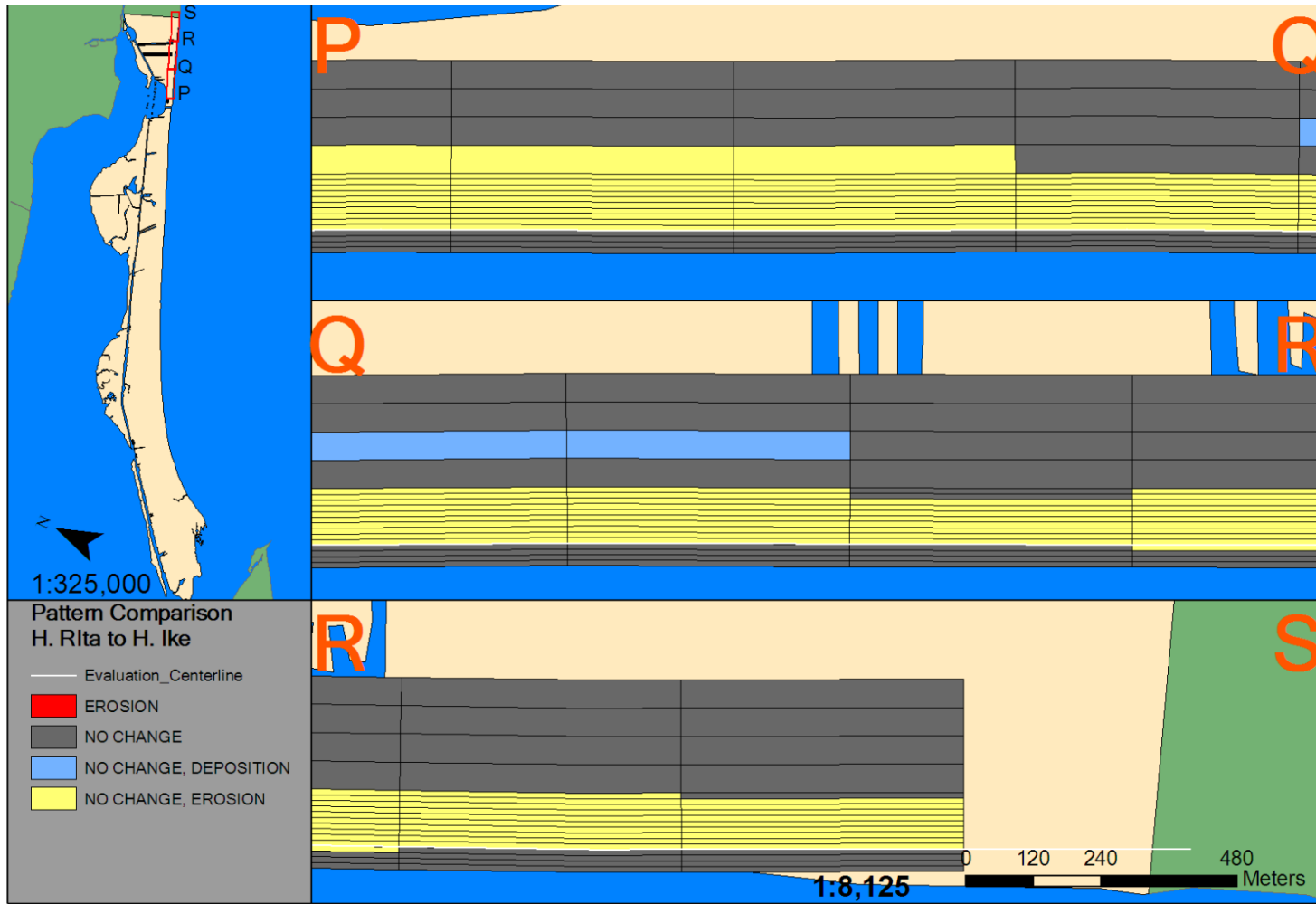


Figure 4.66. Sections P-S of 2D volumetric pattern comparison – Hurricane Rita to Hurricane Ike.

and post-Ike LiDAR imagery acquisition dates. The only major change is that the outlet widened and protruded seaward.

Sections M-P (Figure 4.65) have several zones of erosion that are similar alongshore between Hurricanes Rita and Ike. Both of these zones represent failure of the geotubes along this shore of Caplen. The longer segment is thinner and represents less erosion in terms of landward extent. The shorter segment represents failure in terms of greater landward extent and there appears to be more extensive damage to the geotube as well. The area of greater geotube damage also represents diminished area extent of erosion from Hurricane Ike.

2D Pattern Similarity – All Storms

The relative abundance of yellow symbology in Figures 4.67-4.72 demonstrate that these storms have little in common when considered altogether. There are alongshore similarities of impacts from these storms, however. As for Hurricane Rita patterns, this analysis is restricted to looking at elements where there are similarities of patterns. Therefore, sections J-M and P-S will be omitted, (Figures 4.68, 4.70, and 4.72).

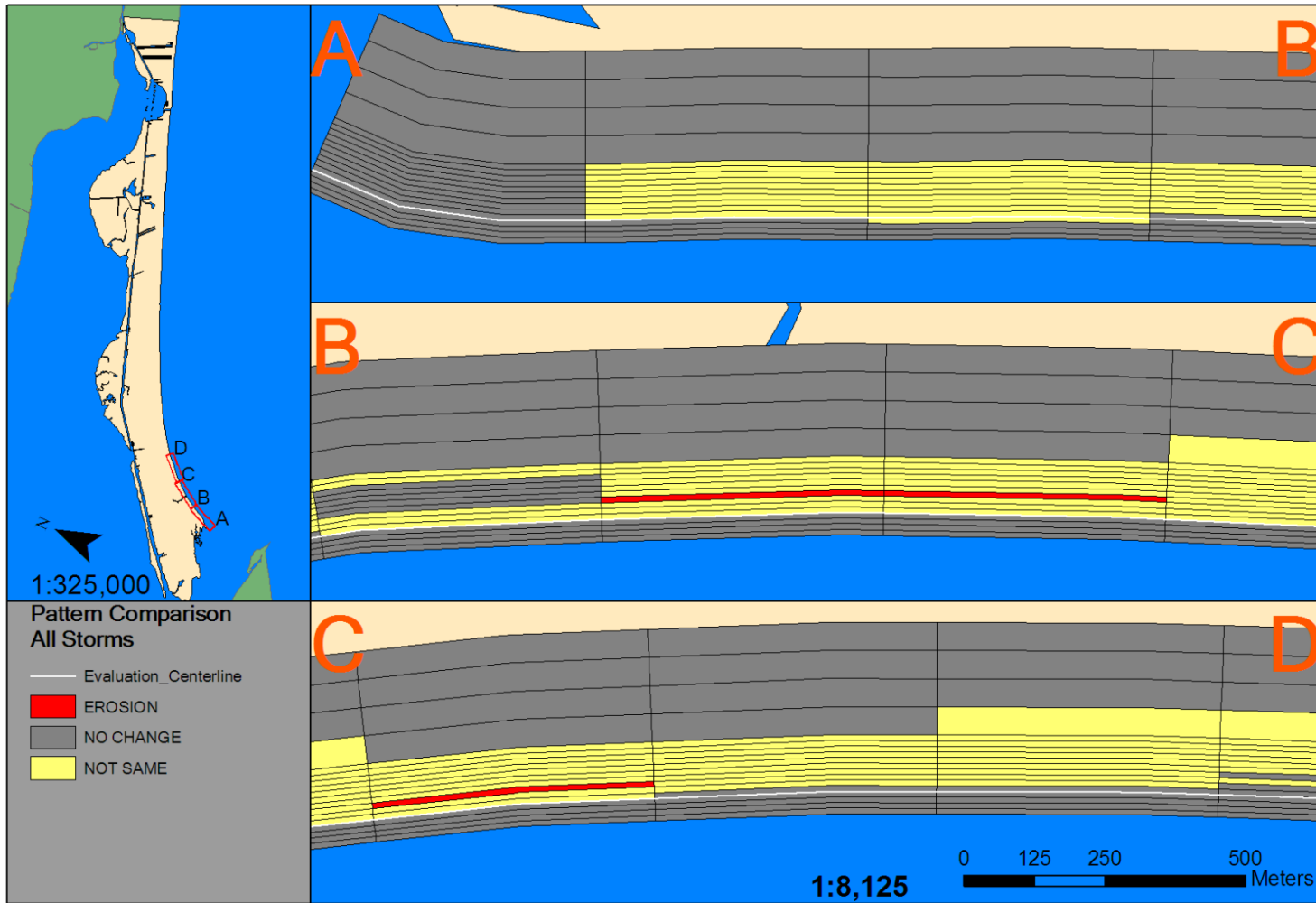


Figure 4.67. Sections A-D of 2D volumetric pattern comparison – all storms.

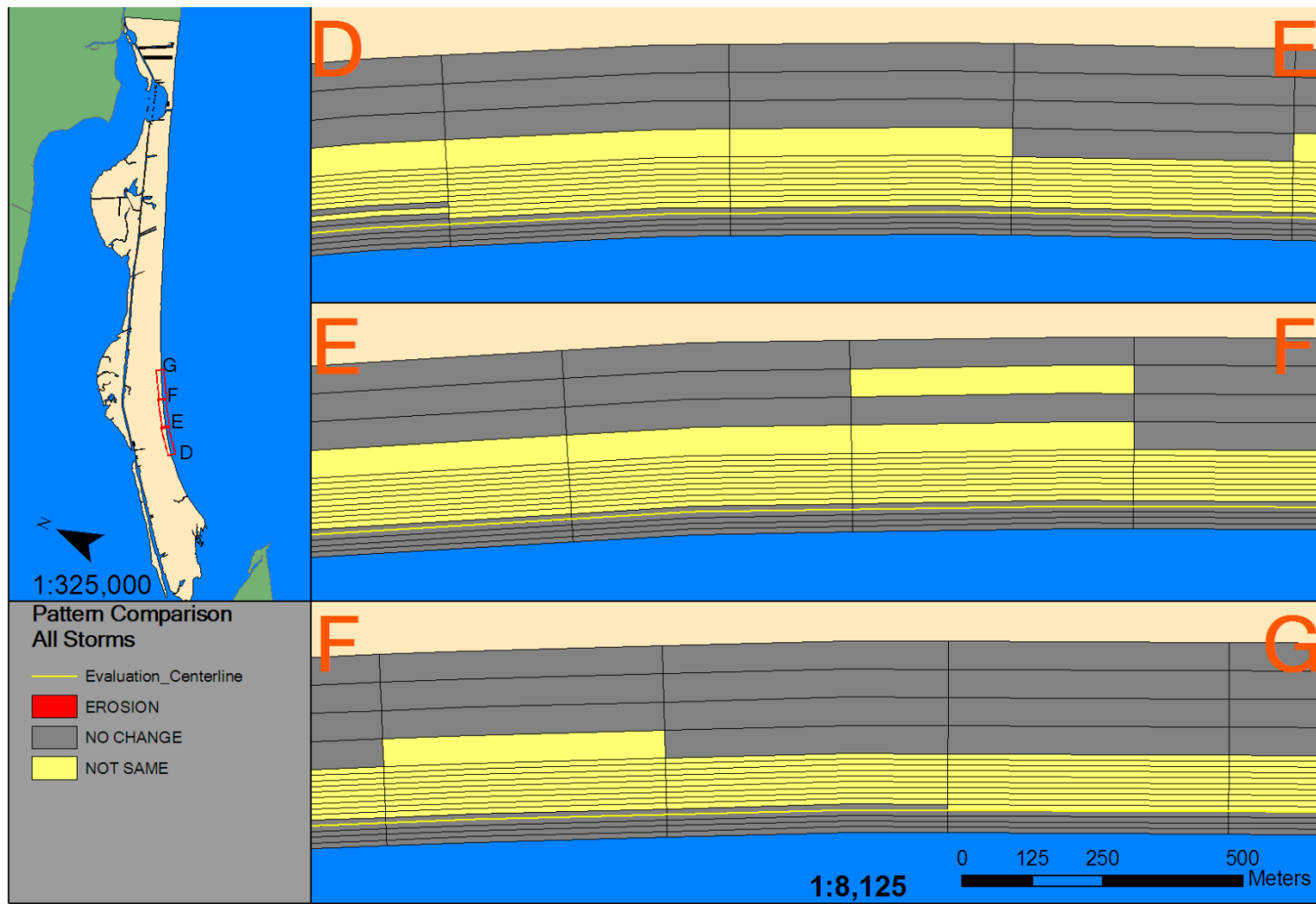


Figure 4.68. Sections D-G of 2D volumetric pattern comparison – all storms

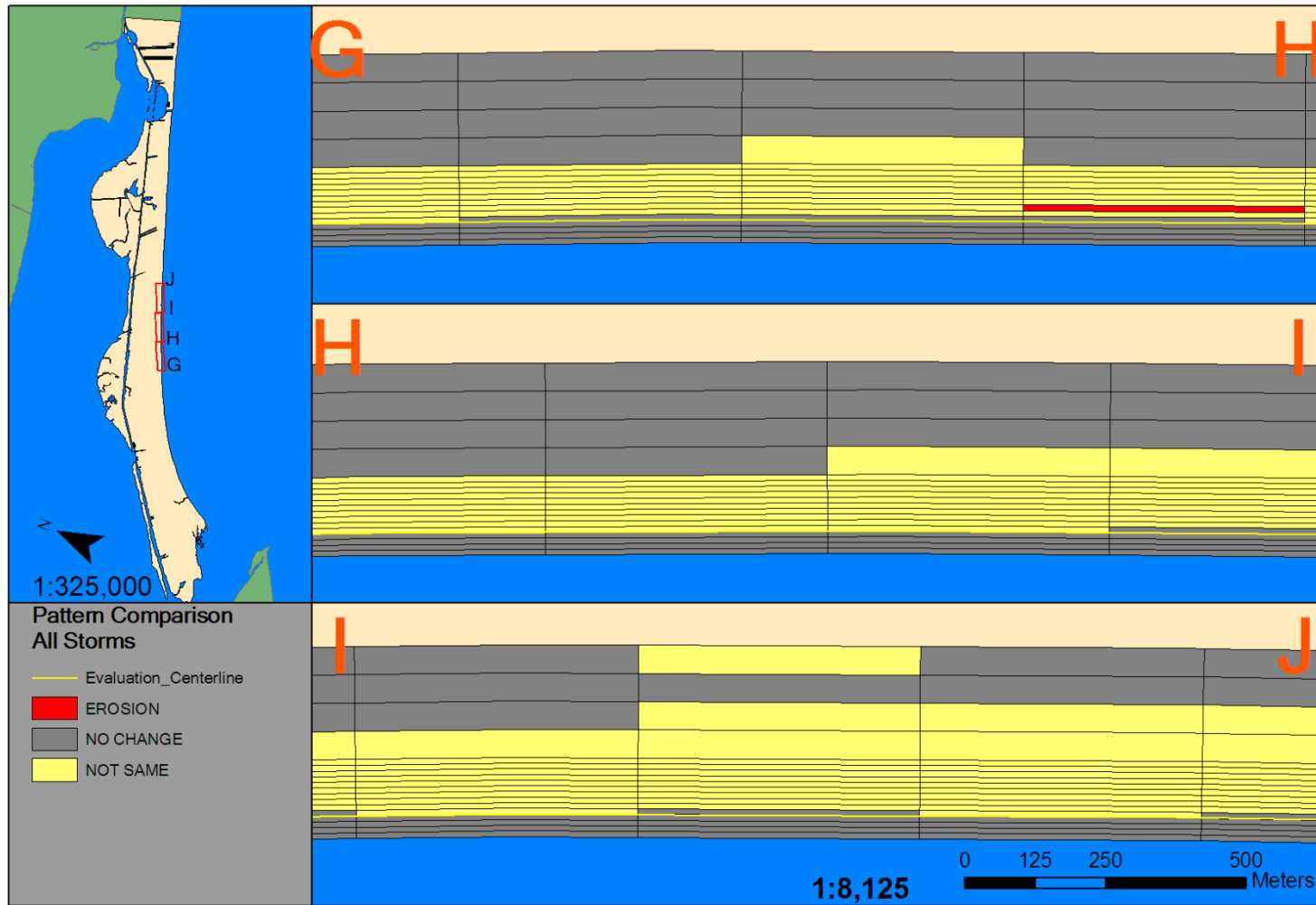


Figure 4.69. Sections G-J of 2D volumetric pattern comparison – all storms.

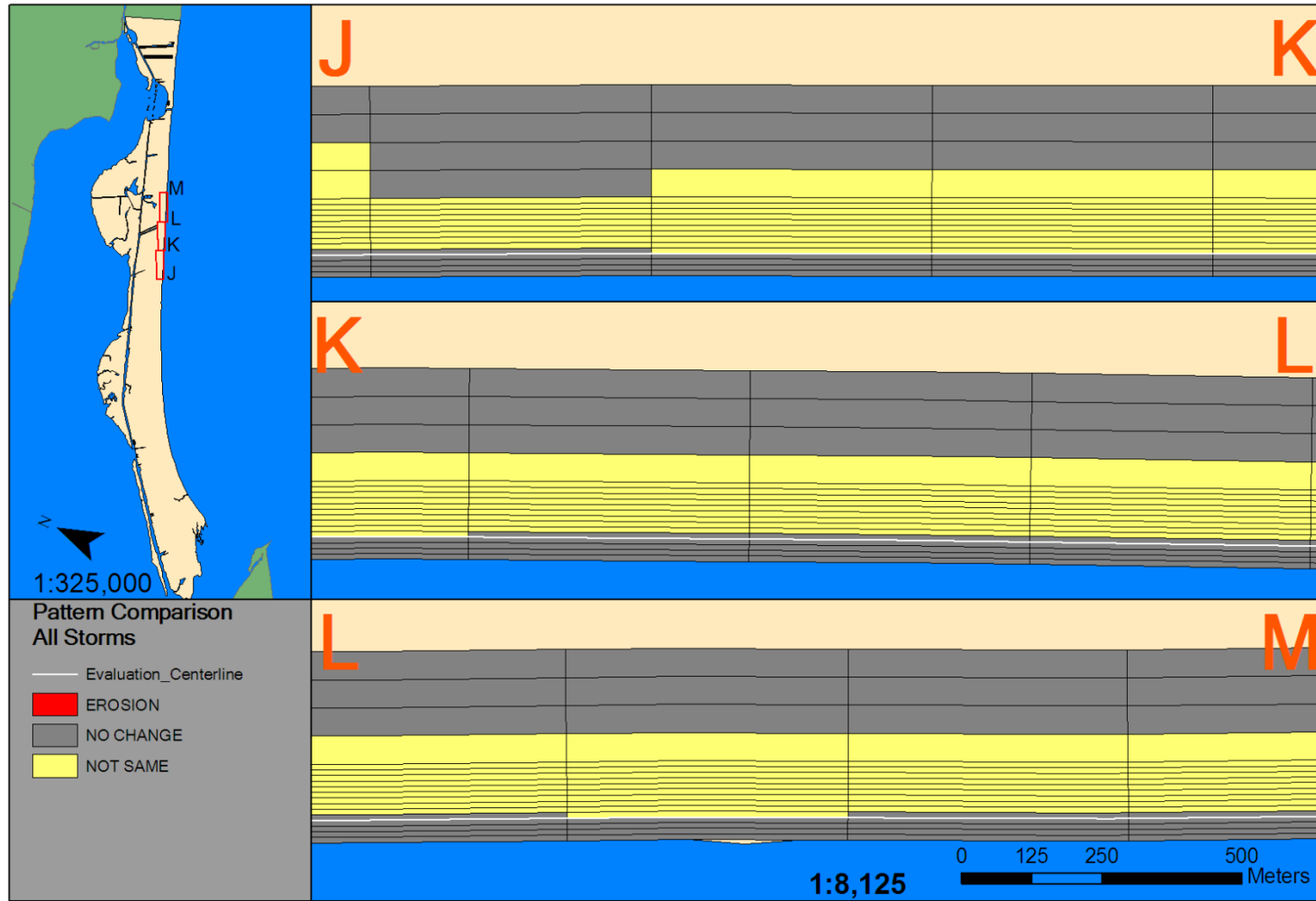


Figure 4.70. Sections J-M of 2D volumetric pattern comparison – all storms

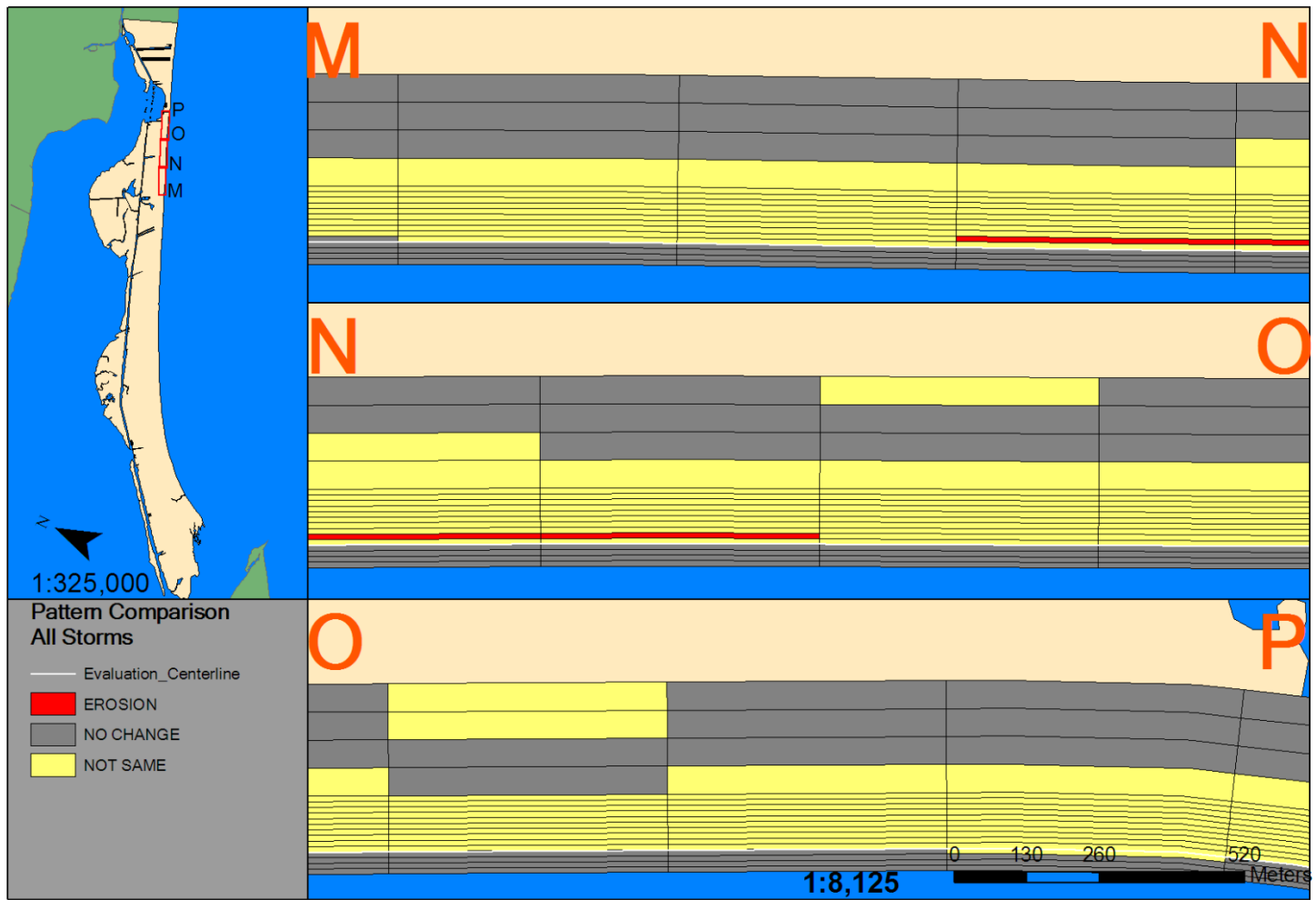


Figure 4.71. Sections M-P of 2D volumetric pattern comparison – all storms

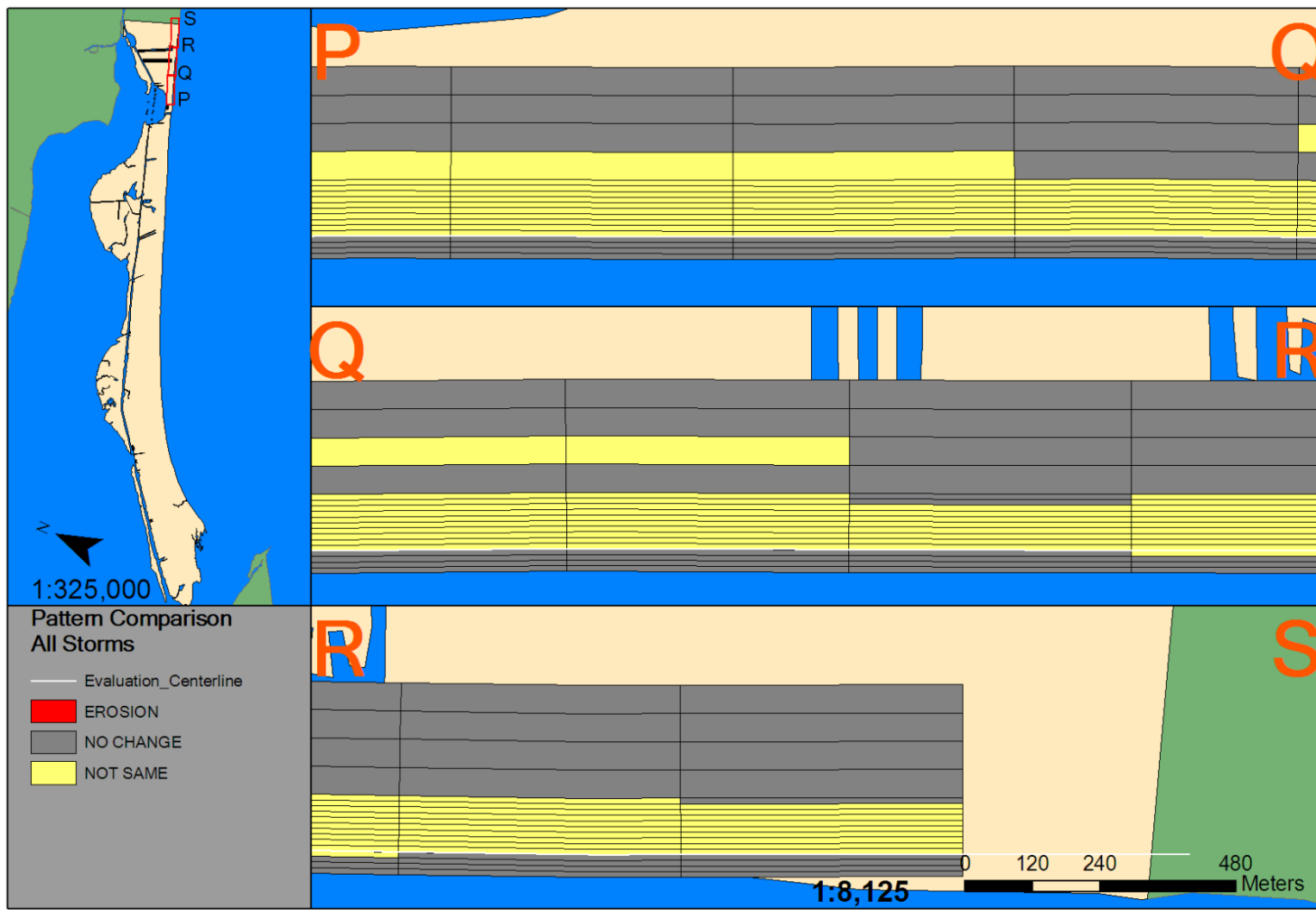


Figure 4.72. Sections P-S of 2D volumetric pattern comparison – all storms

For the first set of sections, common areas of erosion seem to be related to stream outlets. For Hurricanes Ike and Rita, these three sets of erosion featured in Figures 4.67 and 4.69 were all connected and bound by stream outlets. In fact, both of the bounding areas of common erosion in this section are immediately updrift or northeast of a stream outlet. At sections G-J in Figure 4.70, there is one single area of common erosion in section G-H. This area is also immediately updrift of a stream outlet. At sections M-P (Figure 4.72) a large common alongshore zone of erosion coincides with a series of geotube failures along the coast.

Impacts Derived From 2D Volumetric Change Patterns

Impacts in terms of erosion and accretion can be derived from these 2D volumetric change patterns. Table 4.1 shows that there is definitely a stark difference between those impacts of Tropical Storm Fay and Rita as compared to those of Hurricane Ike.

Table 4.1. Values of erosion and accretion extracted from 2D Volumetric Patterns of Hurricanes Ike, Rita and Tropical Storm Fay.

Storm	Erosion	Accretion
Tropical Storm Fay	148000 cubic meters	101539 cubic meters
Hurricane Rita	161131 cubic meters	10003 cubic meters
Hurricane Ike	4038138 cubic meters	443275 cubic meters

CHAPTER V

DISCUSSION

Visual interpretation of shoreline patterns has been used in previous works (Morton 1997; Gibeaut, Gutierrez, and Hepner, 2002; Dolan, Fenster, and Morton, 2002). Other studies involved studying beach volumetric change (Gibeaut, Gutierrez, and Hepner, 2002; Doran *et al.* 2009). Some studies used methods that attempted to abstract raster LiDAR beach changes as polylines (shoreline change) and polygons (volumetric change) (Liu *et al.*, 2010; Liu *et al.* 2011). This study extracts spatial patterns out of these changes, in the form of 1D alongshore shoreline and volumetric change and 2D volumetric change.

Shoreline Change Patterns

Shoreline change patterns for Tropical Storm Fay and Hurricane Rita, Figure 5.1, have a general trend of accretion at the most distal portion of the spit and erosion on the rest of the spit. This is in general agreement with the long term shoreline change from Gibeaut, Gutierrez, and Hepner (2002) in Figure 5.2, works like those of Morton (1983, 1997) and McBride, Byrnes, and Hiland (1995) and classic literature (Gilbert , 1890). However, Hurricane Ike did not register this same pattern. Hurricane Ike registered accretion zones at the area of 10 to 12 kilometers from the distal portion of the spit on Bolivar Peninsula, as shown in Figure 4.5 and significant erosion at the distal end of the spit (Figure 4.6).

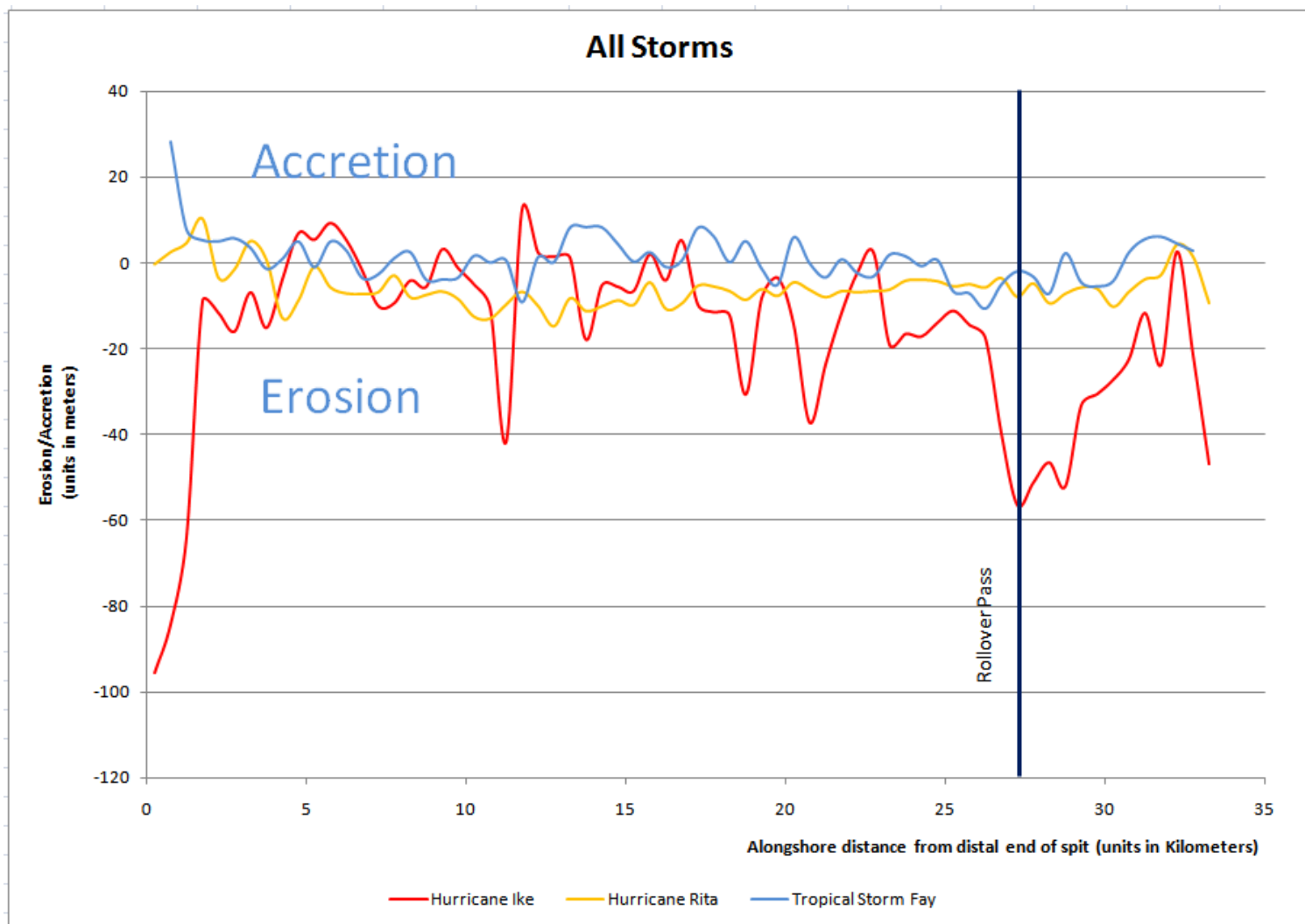


Figure 5.1. Alongshore shoreline erosion from Tropical Storm Fay and Hurricanes Ike and Rita.

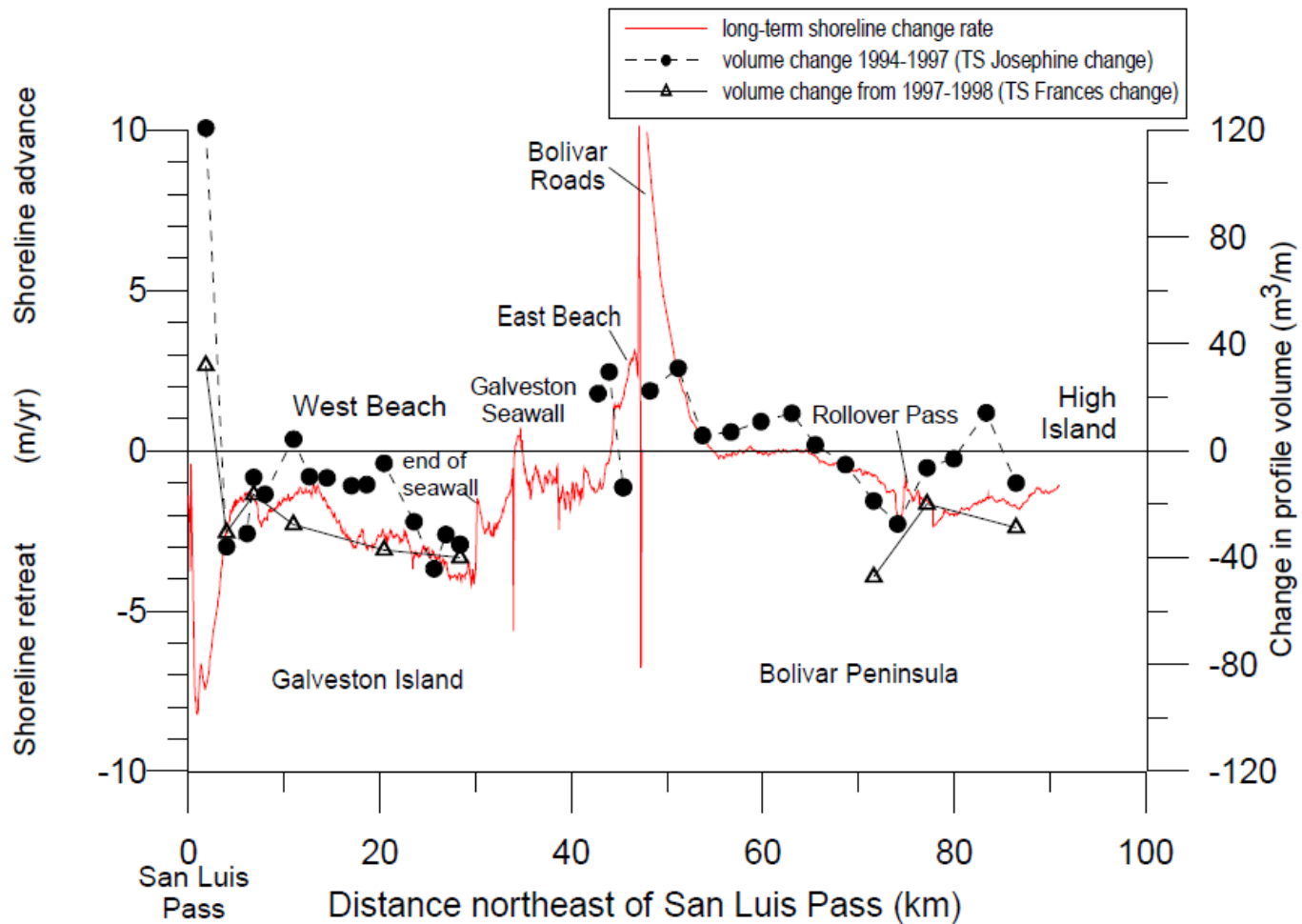


Figure 11. Comparison of long-term shoreline change and profile volume change caused by Tropical Storms Josephine (September 1994 to November 1997) and Frances (November 1997 to September 1998).

Figure 5.2. Caption of alongshore trends in volumetric change from Tropical Storm Josephine compared to long-term shoreline change (Gibeaut, Gutierrez, and Hepner, 2002)

In terms of the character or type of coastal change, shoreline change patterns were erosive on all storm events for areas surrounding Rollover Pass. This is consistent with the conclusions by Bales and Holley (1989) and Prather and Sorenson (1972), and adds an observation to the findings of Dolan and Fenster (1996). Bales and Holley (1989) and Prather and Sorenson (1972) found that the inlet was trapping significant amounts of sediment, and they speculated that this sediment was taken from the beaches nearby the inlet. Dolan and Fenster (1996) did a study of inlets and found that inlets have the ability to cause shoreline change up to several kilometers around that inlet. This same trend is found in Figure 5.2 for long-term shoreline change.

The results from this study indicate that shoreline change for Hurricane Rita was nearly all erosive—with the exception of a small 5 kilometer region of accretion/no change at the distal end of Bolivar Peninsula. Hurricane Ike had several smaller areas of no change/accretion at the point 10 to 15 kilometers from the distal end of the spit—different from Hurricane Rita. However, there were still large regions of erosion at the proximal end of the spit—similar to Hurricane Rita. For Tropical Storm Fay (Figure 4.1), it is evident that there is also a zone of alternating no/change accretion, but it brackets much of the distal portion of the spit. The treatment of the most distal five kilometer portion of the spit is similar, but greater than Hurricane Rita's impacts. As for Hurricane Ike, the broad region of interspersed zones of accretion/no change is similar to that of Tropical Storm Fay. These observations imply that the shoreline impact of Tropical Storm Fay has a factor in common with Hurricanes Rita and Ike, and that

Hurricane Rita has a different factor in common with Tropical Storm Fay and Hurricane Ike.

Information from the National Weather Service (Berg, 2009, Knabb *et al.*, 2006; Stewart, 2003) shows that Hurricane Ike and Tropical Storm Fay made landfall on the right hand side of the storm and differ by intensity and distance from the study area, (Table 2.1). This data also shows that the Hurricanes Rita and Ike had a similar intensity at landfall of wind speeds at 115 miles per hour for Hurricane Rita (Knabb *et al.*, 2006) and 110 miles per hour for Hurricane Ike (Berg, 2009). However, the major difference is that one storm, Ike, was not even 5 miles away, Rita, made landfall 60 miles to the northeast and hit with the left hand side of the storm.

Volumetric Change Patterns

One-dimensional volumetric changes were entirely erosive in the case of Hurricanes Ike and Rita. In the case of 2D volumetric change for Tropical Storm Fay and Hurricane Rita, erosion was detected on the berm in many locations and on foredunes in select areas—like Crystal Beach, an area with human development has taken place behind the foredunes. Human development does appear to be a contributing factor with these coastal changes—especially in the case of Caplen and Rollover Pass. Results such as these can be related back to Gibeaut *et al.* (2002) and Morton (2002). Furthermore, these patches of erosion appear to be modulated by stream outlets (Carter, *et al.*, 1987) and geotubes (Gibeaut *et al.* 2002), particularly the geotubes in front of Caplen.

It has been shown in these results that stream outlets seem to correlate with shoreline change and berm erosion (Figure 5.3). The behavior of these stream outlets as a response to coastal storms is quite dynamic, and could also be partly determined by bay responses to a storm, as discussed in relation to geotubes and Hurricane Ike by Potts (2010) and Carter *et al.* (1987). For Tropical Storm Fay, the shoreline advanced in front of these outlets, and the shoreline retreated as a result of the impact of Hurricane Rita. This behavior is demonstrated in Figure 5.4. It was also noticed in the 2D volumetric pattern comparisons for Tropical Storm Fay and Hurricane Rita that patterns of erosion in the analysis areas were seemingly always detected as erosion updrift of a stream outlet. It is easily observable that outlets play a role in the geomorphic evolution of a barrier spit by changing the sediment supply dynamic (Carter *et al.*, 1987).

As for geotubes, Gibeaut *et al.* (2002) and Gibeaut *et al.* (2008) discussed geotube failures as a damage statistic following the impacts of tropical storms. Additionally, there was discussion by McLellan and Lee (2009) regarding speculations about the effects these damages had on the coast of Bolivar Peninsula. From LiDAR imagery (Figure 5.5) it is obvious that damages to geotubes in front of Caplen did cause a back-tube scarping as a result of Tropical Storm Fay and Hurricane Rita. The majority of these geotubes were completely destroyed by Hurricane Ike.

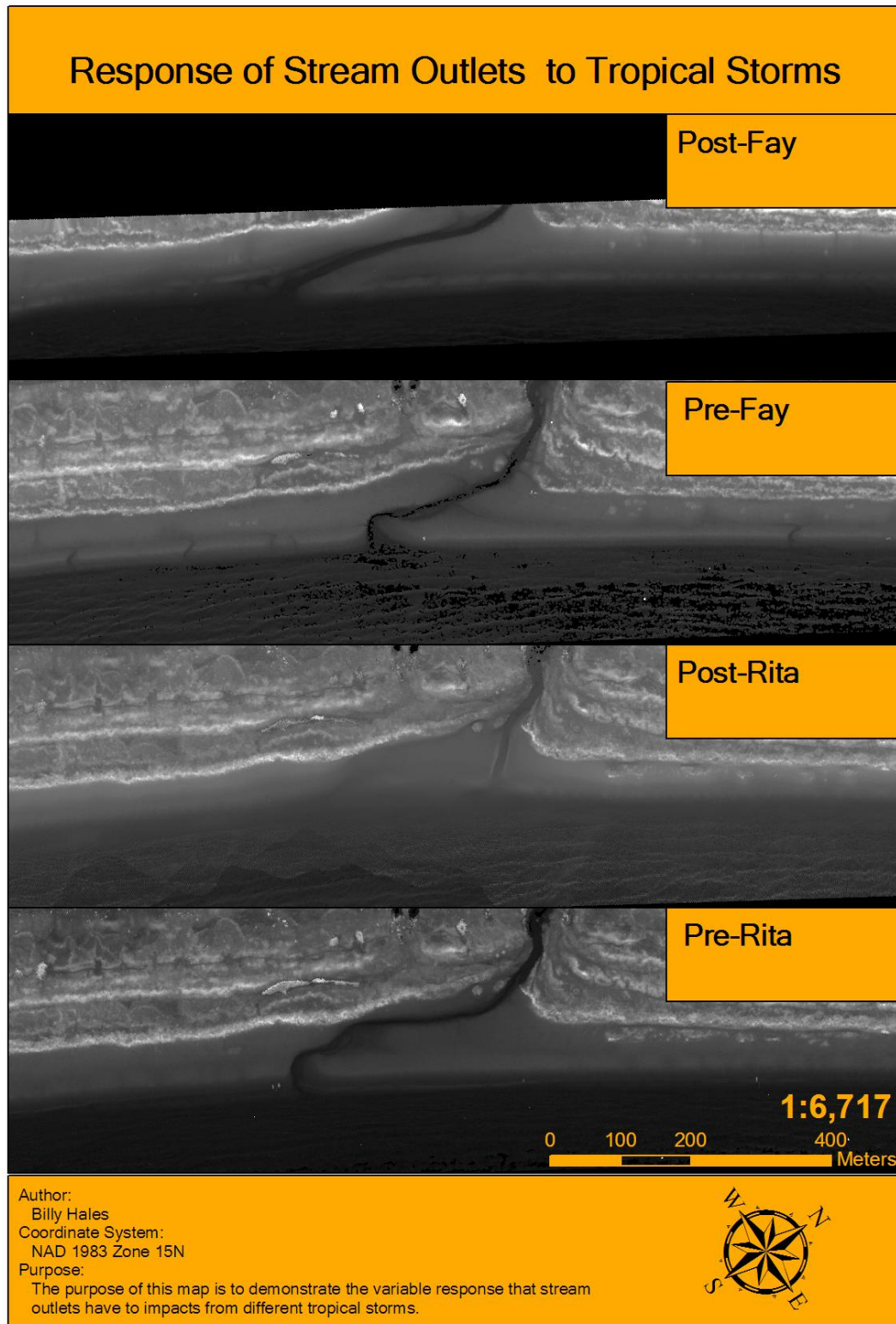


Figure 5.3. Details of how a stream outlet changes in shape and how the shoreline accretes as a result of Tropical Storm Fay and erodes from Hurricane Rita

Stream Outlet Variability - Bolivar Peninsula

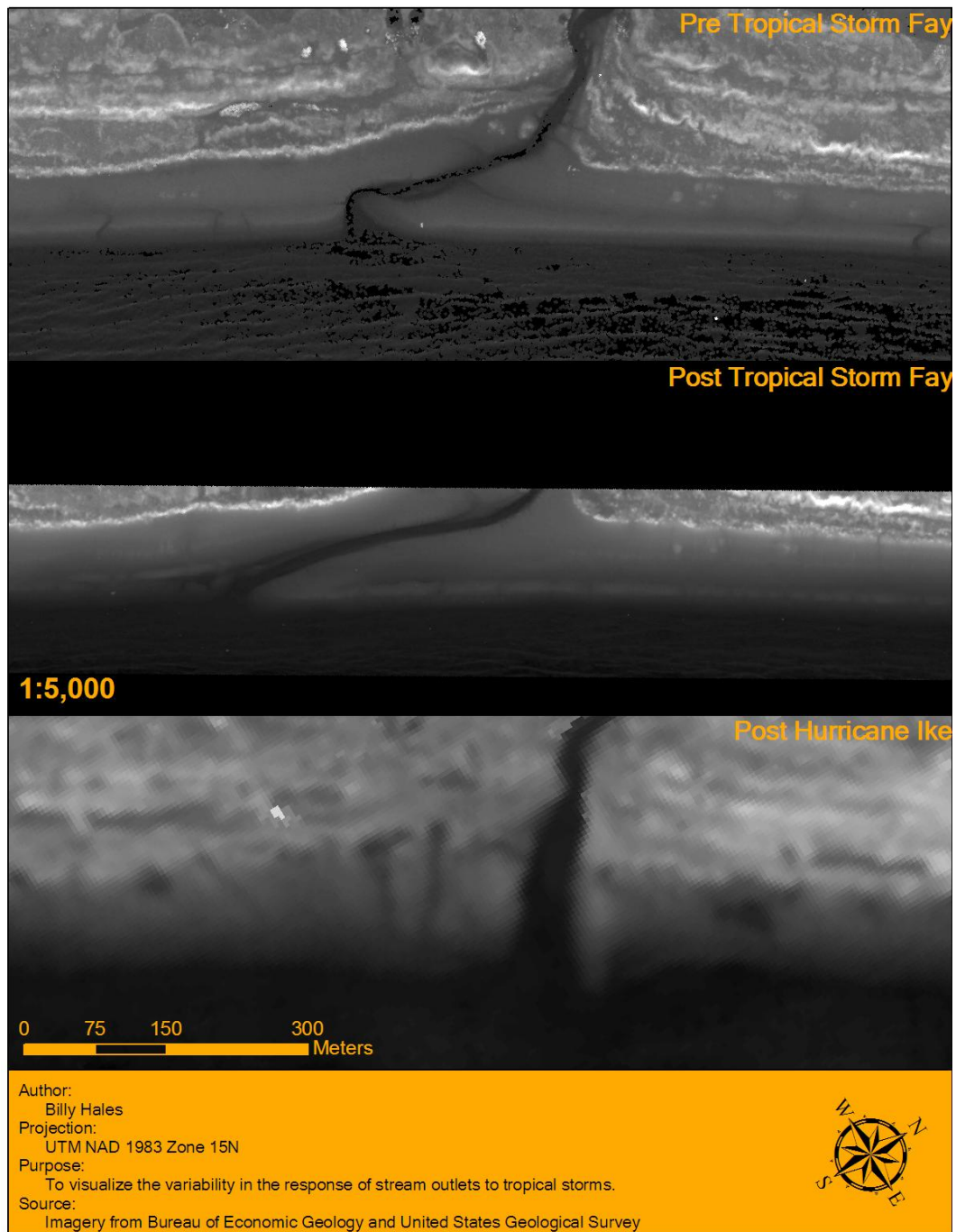


Figure 5.4. Three images of before Tropical Storm Fay, after Tropical Storm Fay, and after Hurricane Ike to demonstrate the stream outlets are highly dynamic environments.

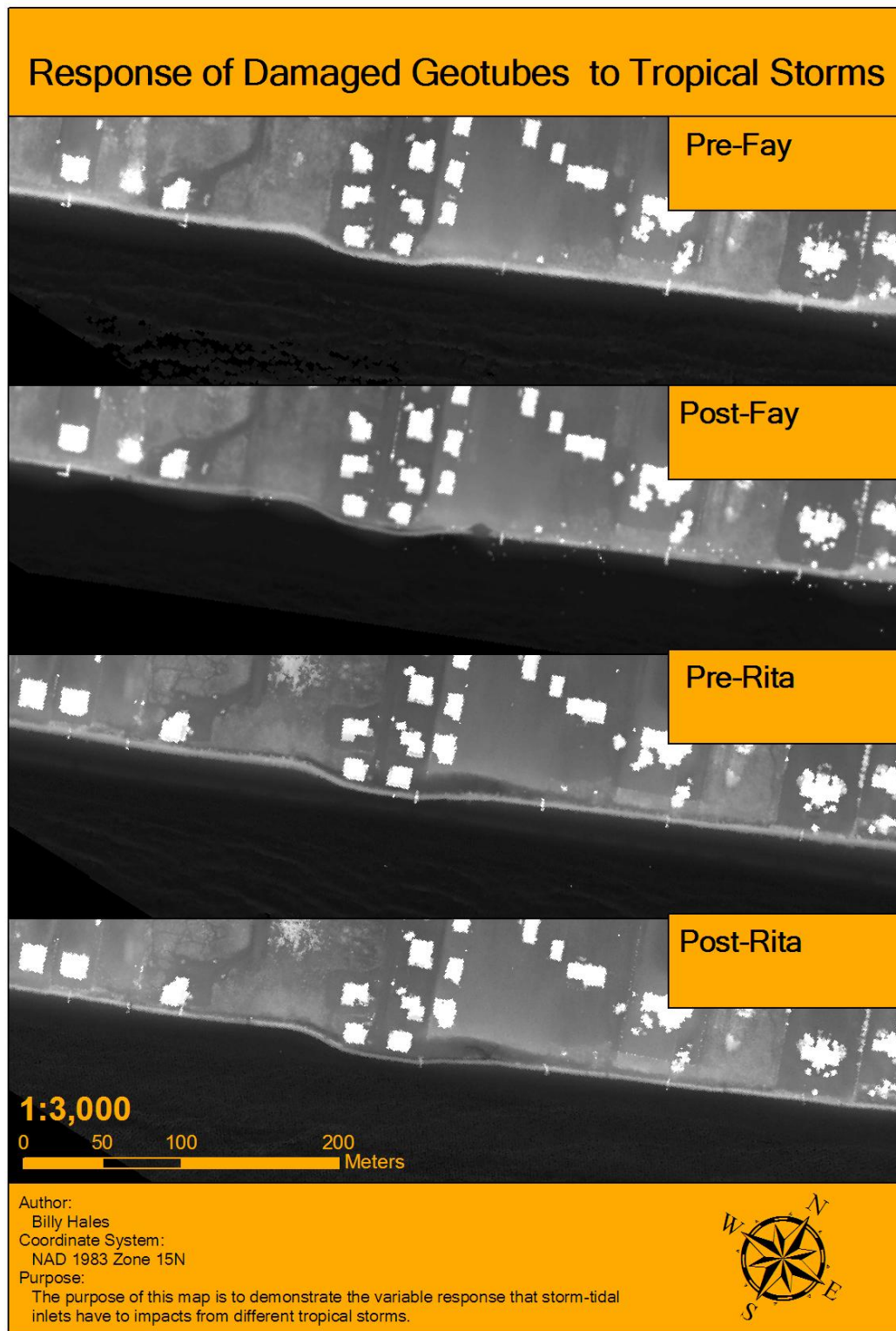


Figure 5.5. Details of how damages on the geotube from Tropical Storm Fay and Hurricane Rita caused a back-scarring and even scour patterns from Hurricane Rita.

Comparisons between the 2D volumetric patterns of Tropical Storm Fay and Hurricane Rita to the patterns of Hurricane Ike provide for quite stark differences, (Figures 4.55-4.60). Overall, Hurricane Ike shows a pattern of beach erosion and scarping that span up to 100 meters landward of the centerline with scours that can go up to 200 meters (Figure 5.6).

One dimensional results were primarily used to make data comparable to those results obtained for the time period that bracketed the impacts of Tropical Storm Josephine (Figure 5.7). This measure allows the ignoring of overland penetration and impact regimes in favor of alongshore trends—similar to those of shoreline change pattern analysis. The alongshore volumetric change given by Tropical Storm Josephine is distinctly different than that pattern given by the other three storms. This may be because of the result of recovery processes that occurred afterward—since there was an appreciable amount of time (one year) between profile measurement and storm occurrence (Gibeaut, Gutierrez, and Hepner (2002)). Given that these profiles were taken one year after the impact of the storm, separating storm response from storm recovery is not possible. It may be more informative to compare the former three storms to the impact-recovery of Josephine for the purposes of recovery on a barrier feature.

As for Hurricanes Ike and Rita, the alongshore pattern registered as entirely erosive. The one dimensional volumetric change patterns near the distal portion of the spit for Tropical Storm Fay seem to demonstrate an oscillatory nature that has a generally less erosive trend and a slight accretive trend at the distal portion of the spit, but these results may be because of the failure to separate dune erosion/accretion from

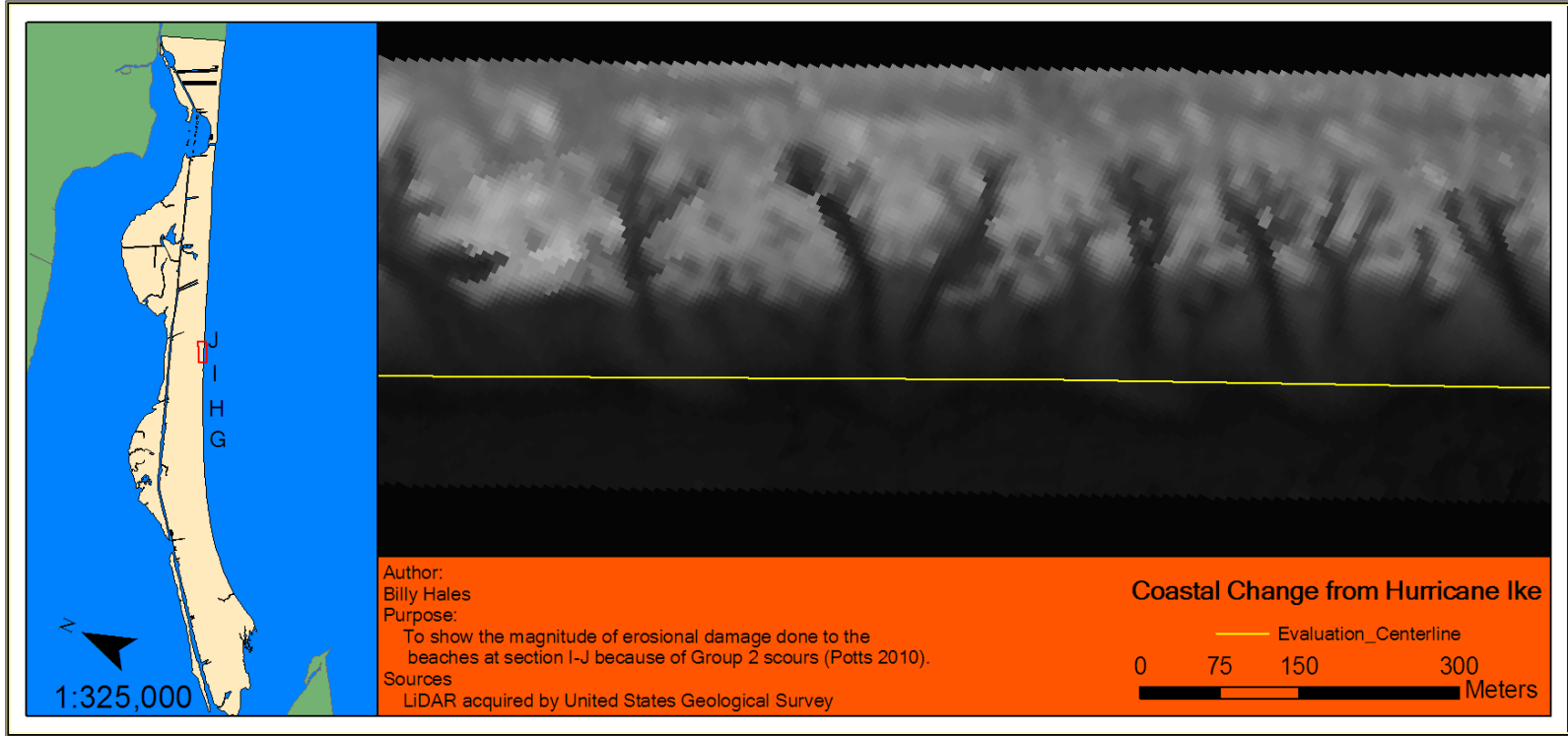


Figure 5.6. Detail of extreme beach change as a result of Hurricane Ike.

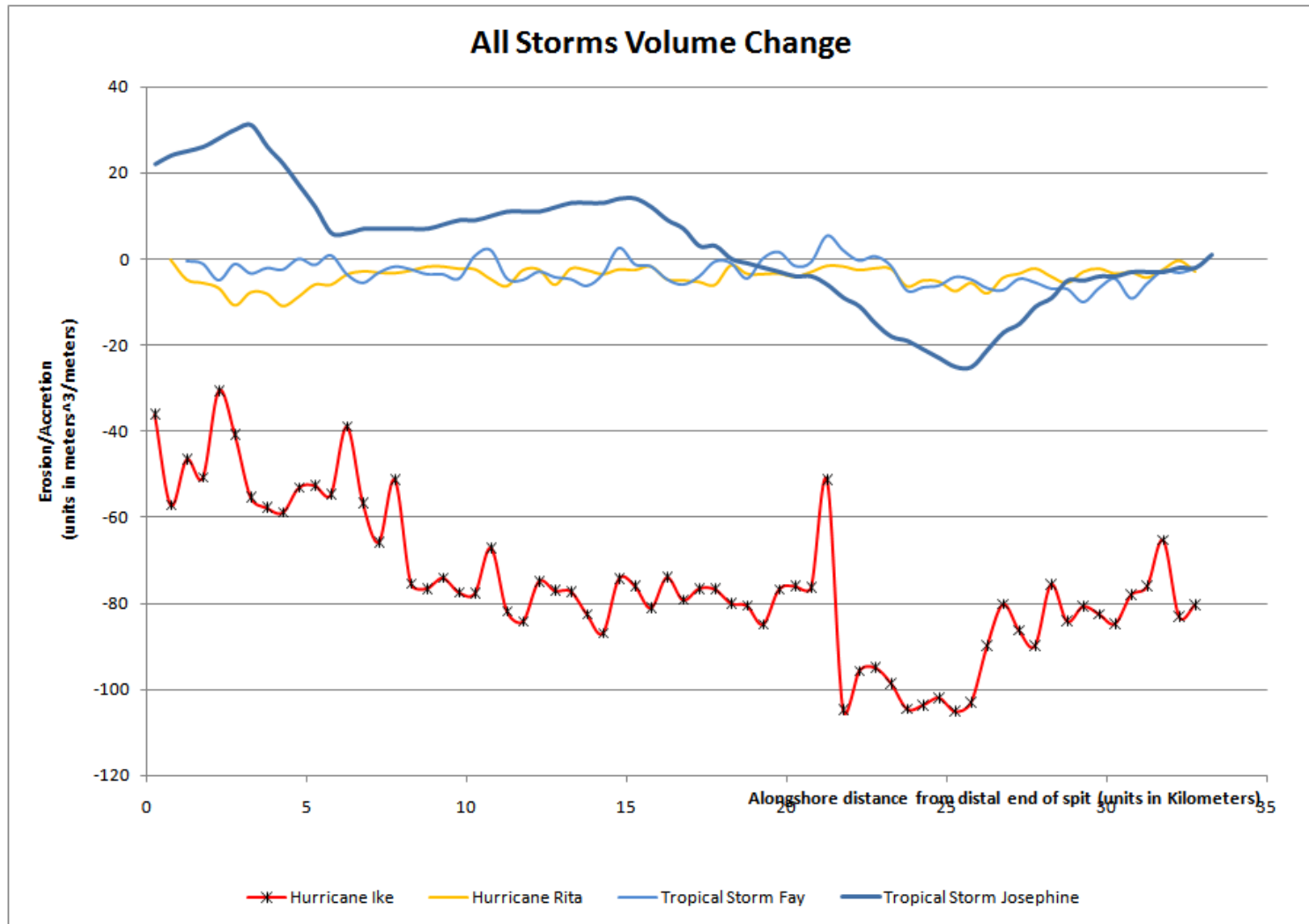


Figure 5.7. All alongshore trends from 1D volumetric change analysis.

vegetation, in a manner similar to the dilemma faced by Claudino-Sales, Wang, and Horwitz (2010). Volumetric change analysis and classification of backdune accretion/erosion was inconclusive on several areas, and the data was unaltered as a result. The net result is that the alongshore accretion values of Tropical Storm Fay may be confused with the ‘accretion’ involved with growth of vegetation or alignment/datum issues—since the profiles of dune features have a high cross-shore angle. Therefore, it is possible that Tropical Storm Fay is entirely erosive like the other two storms.

The detrended volumetric impacts of Hurricane Ike show a large amount of erosion between 15 and 20 kilometers from the distal portion of the spit. This area is bounded close to the mid-point of the spit. The distal portion of the spit is generally less erosive as one is progressing towards than the middle of the spit. At 27.5 kilometers from the distal portion of the spit—which is roughly where Rollover Pass is located, there is a slight lessening of the erosion, but not much when compared to the lesser amount on the distal portion of the spit. This alongshore volumetric trend agrees with volume calculations of Doran *et al.* (2009). However, the area of maximum erosion and the amount of erosion for the proximal portion of the spit is in contradiction. However, this discrepancy would be explained by the extent of the imagery analyzed. It should be known that Doran *et al.* (2009) used beach profiles that extended from the pre-storm dune base and the pre-storm shoreline. Volumetric analysis in this study does not include just the beach, but also includes the area 300 meters from the centerline. This was done to make the data comparable to those results from Gibeaut, Gutierrez, and Hepner (2002) in the case of Tropical Storm Josephine. Another factor could be the presence of

structures in the pre-storm LiDAR imagery. These structures have potential to bias the mean and it could be that heavily populated areas such as Gilchrist and Crystal Beach have a biased amount of erosion associated with them—although efforts like those Potts (2010) were taken to reduce that factor.

Synthesis

All of these storms were different in terms of distance away from the study area, the Saffir–Simpson Hurricane Wind scale on landfall, and the side of the storm that study area experienced. Tropical Storm Fay made landfall near Matagorda Peninsula about 150 miles to the southwest. In general, the impact of Tropical Storm Fay was greater than that of Hurricane Rita in terms subaerial erosion/accretion, but less in terms of shoreline erosion. This could be explained by the very strong longshore currents that were heading southwest as a result of the wind/wave intensities and directions caused by Hurricane Rita (Gibeaut *et al.* 2008) (Figure 2.13).

Factors that contribute to this dichotomy between shoreline and subaerial responses to Tropical Storm Fay and Hurricane Rita are the duration of elevated wave-wind conditions and extreme wave-wind conditions (Gibeaut *et al.* 2008). Hurricane Rita was a Saffir-Simpson Hurricane Wind Scale Class 3 Hurricane that had an extreme surge-wave condition that was greater than that of Tropical Storm Fay, although Fay had a longer duration of elevated surge-wave conditions (Gibeaut *et al.* 2008). As for Hurricane Rita, the combination of high storm surge and large waves of roughly 4 meters with prevailing winds and waves heading in a southwesterly direction before landfall and low storm surge and smaller waves and lower wind speeds with waves and

wind heading in a northeasterly direction after landfall (Gibeaut *et al.* 2008; NDBC 2011; DNR 2008) was thought to add up to a large erosive potential and sediment transport in the southwesterly direction about 24 hours before the landfall of Hurricane Rita.

In terms of classification, the results from the 2D Volumetric Pattern comparisons suggest that Tropical Storm Fay and Hurricane Rita were in the swash regime on most of the peninsula and in the collision regime on other parts (Sallenger, 2000). In order for the collision regime to occur, dunes had to be present and there had to be measured damage of the dunes from storm overwash processes (Sallenger, 2000). This occurred primarily on the distal and recurved portion of the spit—as this portion has higher relict dune ridges at the proximal end and smaller foredune ridges near the recurved zone. It should be noted that many of these dunes have been compromised by developments that build behind them and have roads that breach them (Figure 4.14).

Just as in works like those of Claudino-Sales, Wang, and Horwitz (2010), there was considerable difficulty in determining erosion or accretion at the back dune area—so small amounts of overwash can be difficult to separate from changes in and error associated with dune vegetation. This unmixing of the two was based on air photo analysis, just as had to be done in Claudino-Sales, Wang, and Horwitz (2010).

Since it takes nearly a foot of sediment, 0.30 meters, to register as accretion or erosion by virtue of the error threshold, there should be visible evidence of sediment at a given area. If the area in question had vegetation present and did not have any indication of sediment encroachment, then the accretion signature was considered to be a false

positive. At the end of this process, it was shown that there are very few detectable levels of accretion in the 2D volumetric patterns from Tropical Storm Fay and Hurricane Rita. Therefore, these patterns can only support an impact regime of swash (level 1) or collision (level 2), and not overwash (level 3) (Sallenger, 2000).

However, Hurricane Ike results do have overwash present. With the signature of accretion in 25000 square meter evaluation cells, accretion from Hurricane Ike is certainly extreme or is widespread. Considering that these cells are more than 100 meters from the centerline, this would certainly put Hurricane Ike the overwash regime.

Based on observations from East, Turco, and Mason (2008) and Potts (2010) (Figure 2.16), it is also obvious that much of the barrier—especially those areas with low-lying elevation near the proximal part of Bolivar Peninsula—underwent the inundation regime (level 4) of coastal impact (Sallenger, 2000). The erosive impact that is depicted by morphological patches from this study show a volumetric erosion that far exceeds values from the analyses of other storms (Table 4.1).

The study shows that trends in subaerial volumetric change do not follow the same patterns and trends as shoreline change for some storms. Although there were common linear trends observable in the cases of Tropical Storm Fay, the trends for Hurricanes Rita and Ike are different. It is quite obvious that a barrier spit response to a storm is as much storm-dependent as it is geomorphically dependant. In fact, volume change with Hurricane Rita showed an alongshore trend in erosion and accretion that was nearly opposite of the trend of accretion at the distal end and erosion at the proximal

end. This could have something to do with the wind pattern anomaly found in Figure 2.13.

The final solution may be summarized with a phrase that the author has heard his advisor state, “sand is stupid”. To elaborate, he makes the statement that sand obeys the law of physics, and these geomorphic/storm-driven traits can be broken down into component physical parts—like wind directions and speeds and waves (Ashton, Murray, and Littlewood, 2007; King and McCullagh, 1971; Kraus, 1999). These are physical forcing agents associated with the storm, and should behave in a predictable manner given that we know the geometry and composition of the feature in question, Bolivar Peninsula.

This work shows that there is not a single scalable and controlling geomorphic factor for the response of a barrier spit to tropical storms. This is not contradictory to such works as (Fenster, Dolan, and Morton, 2002), but shows the processes are simply different. It does not state an independence or dependence on the long term evolution from storm effects.

CHAPTER VI

SUMMARY AND CONCLUSIONS

Summary

This study focuses on Bolivar Peninsula, TX. In this study, impacts of tropical storms are measured through LiDAR elevations. Using analyses that gather 2D shoreline differences and 3D volumetric differences from pre-storm and post-storm LiDAR elevations, this study derives patterns of erosion and accretion for each storm.

Tropical Storms are important factors in the evolution of coastal barriers (Fenster, Dolan, and Morton, 2002). Major factors that contribute to the impact of a storm are distance from landfall or greatest impact from study area, orientation of storm at landfall (Simpson and Reihl, 1981), duration of storm (Gibeaut *et al.*, 2008), and maximum wind speeds (Saffir Simpson Team, 2010). This study looks at four tropical cyclones, Tropical Storms Josephine and Fay and Hurricanes Rita and Ike. On 6 October 1996, Tropical Storm Josephine approached the Texas coast and was around 300 miles from the study area, impacted the study area with its left side, lasted for 79 hours above a threshold defining meaningful shoreline impact (Gibeaut *et al.*, 2008), and had sustained winds of 15.1 meters per second at the study area. On 7 September 2002, Tropical Storm Fay made landfall near Matagorda Peninsula, TX and was around 150 miles from the study area, impacted the area with its right side, lasted for 81 hours above a threshold defining meaningful shoreline impact (Gibeaut *et al.*, 2008), and had sustained winds of 14.4 meters per second at the study area during landfall. Hurricane Rita impacted the Texas and Louisiana coast just east of Sabine Pass on 24 September 2005, and was

around 60 miles from the study area, impacted the area with its left side, lasted for 17 hours above a threshold defining meaningful shoreline impact (Gibeaut *et al.*, 2008), and had sustained winds of 26 meters per second at the study area during landfall (DNR, 2008). Hurricane Ike made landfall within five miles of the study area on 13 September 2008, impacted the study area with its right side, and had sustained winds at the TCOON Rollover Pass Station of 26.2 meters per second three hours before landfall (DNR, 2008).

Methods consist of three major phases. These phases are to identify and quantify coastal change into 2D shore-normal shoreline change vectors and 3D volumetric change patches, to abstract 1D alongshore and 2D cross-shore patterns from these 2D and 3D phenomena, to analyze these patterns for differences and similarities.

In the first phase, the first step is to acquire shorelines from pre and post-storm LiDAR imagery. The next step was to acquire shoreline change vectors from these shorelines, and the final step is to classify differences as erosion and accretion.

Before the second phase could begin, there was need to look at the spatial characteristics of the data, and determine proper spacing. After a spacing of 500 meters is obtained, the second phase involves obtaining patterns from the two different types of phenomena, shoreline change and volumetric change. This is first done by setting up the alongshore divisions. The next step is to extract patterns from data obtained in the first phase.

The last phase involves using overlay analysis to see which areas alongshore and cross-shore had similar trends of erosion, accretion, or no change. Shoreline changes for all storms were compared with each other for differences and all storms together for similarity. Then 2D volumetric analyses of all storms were compared with each other for differences and altogether for similarity. Alongshore patterns of volumetric changes were compared in all storms to each other for differences.

Conclusions

Based on knowledge acquired and the results from the methods discussed, this study concludes

- 1. Tropical storm impacts on coastal barrier spits do have unique patterns of shoreline and volume change.***

To follow a phrase discussed in section 5.3, different tropical storms have differing factors that contribute to their impacts on coastal barriers. It all comes down to differences in directions and speeds of fluid movement. These storms have some factors that are similar, and some that are different. This is why patterns are unique for each storm.

- 2. For an individual storm, shoreline retreat/advance does not necessarily correlate to erosion/accretion in the subaerial zone.***

Tropical Storm Fay had an alternating sequence of accretion and erosion nearly until the mid-point of the spit. The volumetric alongshore trend shows similar details, but please keep in mind that these values may be swayed by erroneous vertical change values caused by backdune vegetation. In short, many

of these small spikes that register as accretion may not be truly accretion.

Hurricane Rita was a nearly complete erosive pattern for shoreline change, although the volumetric change showed all erosion, the trend is far different. The trend shows that Bolivar Peninsula was eroded greatest at about 2 kilometers from the distal end of the peninsula. As for Hurricane Rita, shoreline change values near proximal end of the peninsula could be the result of a sensitivity issue. In terms of shoreline change, profile measurements from Hurricane Rita show that the beach was flattened even more so after the storm impact. This flattening caused great sensitivity in the shoreline change results as opposed to volumetric change. In short, this means that a small quantity of 3D volumetric change can result in large quantity of 1D shoreline change. This finding should come as no surprise, since high water levels and wave action caused by storms do generally erode and flatten the subaerial portion of a beach profile (Komar, 1983).

As for Hurricane Ike, the shoreline change and volumetric change patterns were different. Small and accretionary shoreline changes occur 5 kilometers from the distal portion of the spit. This is contrast with the entirely erosive volumetric change.

3. *Rollover Pass introduces greater sensitivity to shoreline and volumetric erosion.*

The information out of this work suggests, for all patterns, that change in volume and shoreline is greatest—for all three storms—near Rollover Pass. This finding is consistent with the findings of Fenster and Dolan (1996).

4. *Shoreline change is a multi-frequency phenomena*

Analysis of shoreline change with semivariograms and fractal scaling ranges shows that there are multifrequency and multiscale characteristics in shoreline change. This is in agreement with the works of Dolan, Fenster, and Holme (1992). This study adds to the works of Dolan, Fenster, and Holme (1992) because conclusions were drawn from the sampling of shoreline changes at 5m instead of 50m, as they have done.

5. *LiDAR data can be an alternative to and a supplement to traditional beach profile-based analyses.*

With the flexibility in using abstracted patterns, it could be possible to do research into storms that had an occurrence before the advent of LiDAR for coastal storm research. In particular, this study used a Figure that had volumetric change documented for the time bracketed the impacts of Tropical Storm Josephine.

6. *2D volumetric change patterns produced from this methodology can be used to distinguish swash and collision from inundation, as in Sallenger (2000) and Stockdon et al. (2007).*

Although this approach relies on elevation values to work, this approach would inform the geomorphologist as to erosion on the berm (swash regime) as shown in Appendix C for Tropical Storm Fay and Hurricane Rita, sections A-D, D-G for Hurricane Rita and sections D-G, G-J for Tropical Storm Fay, erosion on the foredune on the beach side (collision regime) as shown for stream outlets and natural dune fields in Appendix C for Tropical Storm Fay and Hurricane Rita, sections M-P, P-S on Tropical Storm Fay and sections J-M for Hurricane Rita, extensive erosion of the dune and deposition in the backdune area (overwash regime), and extensive beach erosion/scarping along with deposition several hundred meters to several kilometers inland (inundation) as shown in Appendix C for Hurricane Ike, all sections. There is also several orders of magnitude difference in the volume of erosion and accretion involving Tropical Storm Fay and Hurricane Rita compared to Hurricane Ike, Table 4.1.

Future Work

One issue that is recurrent in these LiDAR-based analyses is the difficulty in getting more precise instrumentation and in actually deducing constrained error parameters. Sallenger *et al.* (2003) demonstrate an error of 0.15 meters for LiDAR measurements. However, they acknowledged a systematic component and a non-systematic component. With that consideration in mind for elevation change, it would be improper to add these values in quadrature (Taylor, 1997). Estimates of LiDAR error for these LiDAR datasets often take place on very flat areas such as parking lots and roads. Standardization in LiDAR processing and error analysis would be a good first step. With constrained error that is appropriate for each type of land cover, it would be possible to have more informed coastal change measurements.

A valuable endeavor that could extend this work would be to extract patterns for storms that have similar factors, and see if these storms have similar impacts. A more comprehensive analysis of storms that have similar attributes would allow the researcher to begin to form relationships that are testable and demonstrate repeatability. That would be a step towards a prescriptive solution to coastal storm impact awareness—rather than descriptive. It would also be useful to apply this same pattern-modeling paradigm to storm recovery to determine of the recovery from impacts of different tropical cyclones reinforce or are in contrary to the long-term evolution of a barrier spit. With a prescriptive solution to storm impacts and a better understanding of the recovery process, we can then fully answer the question of whether tropical cyclones ultimately have a similar impact barrier spits.

LITERATURE CITED

- Anderson, J.B., 2007. *The Formation and Future of the Upper Texas Coast*. College Station: Texas A&M University Press, 163p.
- Arias, C.A., 2003. Spatio-Temporal Analysis of Texas Shoreline Changes Using GIS Technique. College Station, Texas: Texas A&M University, Master's thesis, 79p.
- Ashton, A. D.; Murray, A.B., and Littlewood, R., 2007. The Response of spit shapes to wave-angle climates. *In: Kraus, N.C. and Rosati, J.D., (eds.), Coastal Sediments '07* (New Orleans, Louisiana), pp. 351-363.
- Bales, J. D. and Holley, E. R., 1989. Sand transport in texas tidal inlet. *Journal of Waterway, Port, Coastal, and Ocean Engineering*, 115, 427-443.
- Barnes, R.J., 1991. The variogram sill and the sample variance. *Mathematical Geology*. 23(4), 673-678.
- Berg, R. 2009. Tropical Cyclone Report: Hurricane Ike
http://www.nhc.noaa.gov/pdf/TCR-AL092008_Ike_3May10.pdf
 (accessed August 14, 2011)
- Brennan, P. and Harlow, M., 2004. *ArcGIS 9: Linear Referencing*. Redlands, CA: ESRI Press, 164p.
- Burt, J. E.; Barber, G.M., and Rigby, D. L., 2009. *Elementary Statistics for Geographers*. New York, New York: The Guilford Press, 653p.
- Carter, R.W.G; Johnston, T.W.; McKenna, J.; Orford, J.D., 1987. Sea-level, sediment supply and coastal changes: examples from the coast of Ireland. *Progress in Oceanography*, 18, 79-101.
- Claudino-Sales, V.; Wang, P., and Horwitz, M., 2010. Effect of Hurricane Ivan on coastal dunes of Santa Rosa Barrier Island, Florida: Characterized on the basis of pre and post storm LiDAR surveys. *Journal of Coastal Research*, 26(3), 470-484.
- Curran, P.J., 1988. The semivariogram in remote sensing: An introduction. *Remote Sensing of Environment*, 24, 493-507.
- Davidson-Arnott, R.G. 2010. *Introduction to Coastal Processes and Geomorphology*. Cambridge, United Kingdom: Cambridge University Press, 442p.

- Demers, M.N. 2005. *Fundamentals of Geographic Information Systems*. John Wiley & Sons, Inc, 468p.
- DNR (Division of Nearshore Research), 2008. Texas Coastal Ocean Observation Network. <http://lighthouse.tamucc.edu/TCOON/HomePage> (accessed August 14, 2011).
- Dolan, R.; Fenster, M.S. and Holme, S.J., 1992. Spatial analysis of shoreline recession and accretion. *Journal of Coastal Research*, 8(2), 263-285
- Doran, K.; Plant, N.; Stockdon, H.; Sallenger, A. and Serafin, K., 2009. Hurricane Ike: Observations and Analysis of Coastal Change. U.S. Geological Survey, Open-File Report 2009-1061, 43p.
- Dorst, N., 2004. Why Do Hurricane Force Winds Start at 64 knots? <http://www.aoml.noaa.gov/hrd/tcfaq/D10.html> (accessed August 8, 2011).
- ESRI (Environmental Systems Research Institute), 2010. ArcGIS Desktop Help 9.2 - Smooth Line. http://webhelp.esri.com/arcgisdesktop/9.2/index.cfm?TopicName=smooth_line_%28data_management%29 (accessed June 23, 2011).
- East, J.W.; Turco, M.J., and Mason, R.R., 2008. Monitoring Inland Storm Surge and Flooding from Hurricane Ike in Texas and Louisiana, September 2008. U.S. Geological Survey, Open-File Report 2008-1365, 34p.
- Evans, O. 1942 The origin of spits, bars, and related structures. *The Journal of Geology*, 50, 846-865.
- Fenster, M. S. and Dolan, R., 1996. Assessing the impact of tidal inlets on adjacent barrier island shorelines. *Journal of Coastal Research*, 12(1), 294-310.
- Fenster, M. S.; Dolan, R., and Morton, R.A., 2002. Coastal storms and shoreline change: signal or noise? *Journal of Coastal Research*, 17(3), 714-720.
- Fisher, J. J., 1968. Barrier island formation: discussion. *Geological Society of America Bulletin*, 79, 1421-1426.
- Gibeaut, J.; Gutierrez, R., and Hepner, T., 2002. Threshold conditions for episodic beach erosion along the Southeast Texas coast. *Gulf Coast Association of Geological Societies Transactions*, 52, 323-335.

- Gibeaut, J.; Hepner, T.; Waldinger, R.; Andrews, J.; Smyth, R., and Gutierrez, R., 2002. Geotubes Along the Gulf Shoreline of the Upper Texas Coast: Observations During 2001. Texas Coastal Coordinating Council, 33p.
- Gibeaut, J.; Hepner, T.; Andrews, J.; Gutierrez, R., and Smyth, B., 2008. Hurricane Rita Impacts on the Texas Shoreline. Texas General Land Office, 26 p.
- Gilbert, G.K., 1890. *Lake Bonneville*. Washington, DC: Government Printing Office, 566p.
- Gutierrez, R.; Gibeaut, J.C.; Smyth, R.C.; Hepner, T.; Andrews J.R.; Weed, C.; Gutelius, W., and Mastin, M., 2001. Precise airborne LiDAR surveying for coastal research and geohazards applications. *International Archives of Photogrammetry and Remote Sensing*, 34, 185-192.
- Hamlett, J.M.; Horton, R. and Cressie, N.A.C., 1986. Resistant and exploratory techniques for use in semivariogram analyses. *Soil Science of America Journal*, 50, 868-875.
- Houser, C.; Hapke, C., and Hamilton, S., 2008. Controls on coastal dune morphology, shoreline erosion, and barrier island response to extreme storms. *Geomorphology*, 100, 223-240.
- Hoyt, J. H., 1967. Barrier island formation. *Bulletin of the Geological Society of America*, 78, 1125-1136.
- Islam, T; Merrell, W; Seitz, W, and Harriss, R., 2009. Origin, distribution, and timing of Texas hurricanes: 1851-2006. *Natural Hazards Review*, 10(4), 136-144.
- Jensen, J.R., 2005. *Introductory Digital Image Processing*. Upper Saddle River, New Jersey: Pearson-Prentice Hall, 526p.
- Jensen, J. R., 2007. *Remote Sensing of the Environment An Earth Resource Perspective*. Upper Saddle River, New Jersey: Pearson-Prentice Hall, 592p.
- Johnson, D., 1919. *Shore Processes and Shoreline Development*. New York, New York: John Wiley & Sons, 584p.
- King, C. and McCullagh, M., 1971. A simulation model of a complex recurved spit. *The Journal of Geology*, 79, 22-37.
- Knabb, R.D.; Brown, D.P., and Rhome, J.R., 2006. Tropical Cyclone Report Hurricane Rita. http://www.nhc.noaa.gov/pdf/TCR-AL182005_Rita.pdf (accessed August 14, 2011).

- Komar, P.D., 1983. Beach processes and erosion – An introduction. *In: Komar, P.D. (ed.), Handbook of Coastal Processes and Erosion*. Boca Raton, Florida: CRC Press, pp. 7.
- Kraus, N. 1999. Analytical model of spit evolution at inlets. *In: Coastal Sediments '99* (Long Island, New York), pp. 1739-1754.
- Leatherman, S. P.; Rice, T.E., and Goldsmith, V., 1982. Virginia barrier island configuration: a reappraisal. *Science*, 215(4530), 285-287.
- LeBlanc, R. and Hodgson, W., 1959. Origin and development of the Texas shoreline. *Gulf Coast Association of Geological Societies Transactions*, 9, 197-220.
- Li, R.; Liu, J.K., and Felus, Y., 2001. Spatial modeling and analysis for shoreline change detection and coastal erosion monitoring. *Marine Geodesy*, 24, 1-12.
- Liu, H.X.; Wang, L.; Tang, S.J., and Jezek, K. (accepted) Robust multi-scale image matching for deriving ice surface velocity field from sequential satellite images. *Transactions on Geoscience and Remote Sensing*.
- Liu, H.X.; Wang, L.; Sherman, D.J., and Wu, Q., and Su, H., 2011. Algorithmic foundation and software tools for extracting shoreline features from remote sensing imagery and LiDAR data. *Journal of Geographic Information System*, 3, 99-119.
- Liu, H.X.; Wang, L.; Sherman, D.; Gao, Y., and Wu, Q., 2010. An object-based conceptual framework and computational method for representing and analyzing coastal morphological changes. *International Journal of Geographical Information Science*, 24(7), 1015-1041.
- Liu, H.X.; Sherman, D., and Gu, S.G., 2007. Automated extraction of shorelines from airborne light detection and ranging data and accuracy assessment based on Monte Carlo simulation. *Journal of Coastal Research*, 23(6), 1359-1369.
- Longshore, D., 2008. *Encyclopedia of Hurricanes, Typhoons, and Cyclones*. New York, New York: Facts on File, 468p.
- Mandelbrot, B.B., *The Fractal Geometry of Nature*. New York, New York: W.H. Freeman and Company, 468p.
- McBride, R. A., Byrnes, M.R., and Hiland, M.W., 1995. Geomorphic response-type model for barrier coastlines: a regional perspective. *Marine Geology*, 126, 143-159.

- McLellan, N. and Lee, J., 2009. Post-Hurricane Ike ground observations on the Bolivar Peninsula, Texas. *Shore & Beach*, 77, 24-29.
- Morang, A. 2006. North Texas Sediment Budget: Sabine Pass to San Luis Pass ERDC/CHL TR-06-17. U.S. Army Corps of Engineers, Engineering Research and Development Center, 68p.
- Morton, R.A., 1975. Shoreline Changes Between Sabine Pass and Bolivar Roads, An Analysis of Historical Changes of the Texas Gulf Shoreline. Bureau of Economic Geology, Geological Circular 75-6, 46p.
- Morton, R.A., 1983. Selecting a site. *In*: Morton, R.A.; Pilkey, O.H. Jr.; Pilkey, O.H. Sr., and Neal, W.J. (eds.), *Living with the Texas Shore*. Durham, NC:Duke University Press, pp 39-114.
- Morton, R.A., 1997. Gulf shoreline movement Sabine Pass and the Brazos River, Texas: 1974 to 1996. Bureau of Economic Geology, Geological Circular 97-3, 46p.
- Morton, R.A., 2002. Factors controlling storm impacts on coastal barriers and beaches - a preliminary basis for near real-time forecasting. *Journal of Coastal Research*, 18 (3), 486-501.
- Morton, R.A.; Paine, J.G., and Blum, M.D., 2000. Responses of stable bay-margin and barrier-island systems to holocene sea-level highstands, Western Gulf of Mexico. *Journal of Sedimentary Research*, 70(3), 478-490.
- Morton, R.A. and Sallenger, A.H., 2003. Morphological impacts of extreme storms on sandy beaches and barriers. *Journal of Coastal Research*, 19(3), 560-573.
- NDBC (National Data Buoy Center), 2011. Station 42035. http://www.ndbc.noaa.gov/station_page.php?station=42035 (accessed August 12, 2011).
- NDBC (National Data Buoy Center), 2002. What Averaging Procedures Are Performed on the Wind Measurements? <http://www.ndbc.noaa.gov/wndav.shtml> (accessed August 8, 2011).
- NOAA (National Oceanic and Atmospheric Administration), 2011. Galveston Pleasure Pier, TX Data Retrieval. <http://tidesandcurrents.noaa.gov> (accessed August 14, 2011).

- Oertel, G. F., 1985. The barrier island system. *Marine Geology*, 63(1), 1-18
- Ott, R.L. and Longnecker, M., 2010. *An Introduction to Statistical Methods and Data Analysis*. Belmont, California: Brooks/Cole, 1273p.
- Otvos, E., 2001. Assumed Holocene highstands, Gulf of Mexico: Basic issues of sedimentary and landform criteria: discussion. *Journal of Sedimentary Research*, 71, 645.
- Pasch, R.J., 1997. Preliminary Report: Tropical Storm Josephine.
<http://www.nhc.noaa.gov/1996josephin.html> (accessed September 4, 2011)
- Potts, M. K., 2010. Forms and Distributions of Hurricane Ike Backflow and Scour Features: Bolivar Peninsula, Texas. College Station, Texas: Texas A&M University, Master's thesis, 180p.
- Prather, S. and Sorensen, R., 1972. *An Investigation of Rollover Pass, Bolivar Peninsula, Texas. Sea Grant Publication No. TAMU-SG-72-202*. College Station, Texas: Texas A&M University Press, 126p.
- Price, M., 2006. *Mastering ArcGIS*. New York, New York: McGraw-Hill, 609p.
- Pyrz, M.J. and Deutsch, C.V., 1978. The whole story on the hole effect. *Environmental Engineering*, 18, 1-16.
- Rodriguez, A. B.; Anderson, J.B.; Siringan, F.P., and Taviani, M., 2004. Holocene evolution of the east Texas coast and inner continental shelf: Along-strike variability in coastal retreat rates. *Journal of Sedimentary Research*, 74, 405-421.
- Saffir-Simpson Team, 2012. The Saffir-Simpson Hurricane Wind Scale.
<http://www.nhc.noaa.gov/sshws.shtml> (accessed March 2, 2012).
- Sallenger, A. H., 2000. Storm impact scale for barrier islands. *Journal of Coastal Research*, 16(3), 890-895.
- Sallenger, A. H.; Krabill, W.; Swift, R., and Brock, J., 2001. Quantifying hurricane-induced coastal changes using topographic lidar. In: Hanson, H. and Larson, M. (eds.), *Coastal Dynamics '01* (Lund, Sweden), pp. 1007-1016.

- Sallenger, A.H.; Krabill, W.B.; Swift, R.N.; Brock, J.; List, J.; Hansen, M., Holman, R.A.; Manizade, S.; Sontag, J.; Meredith, A.; Morgan, K.; Yunkel, J. K.; Frederick, E. B., and Stockdon, H., 2003. Evaluation of airborne topographic lidar for quantifying beach changes. *Journal of Coastal Research*, 19(1), 125-133.
- Sargent, F.E.; Bottin, R.R., 1989. Case Histories of Corps Breakwater and Jetty Structures. Waterways Experiment Station, Corps of Engineers, Technical Report REMR-CO-3, 53p.
- Schwartz, M. L., 1971. The multiple causality of barrier islands. *The Journal of Geology*, 79, 91-94.
- Shepard, F. P.; Phleger F.B., and van Andel, T.H., 1960. *Recent Sediments, Northwest Gulf of Mexico*. Tulsa, Oklahoma: American Association of Petroleum Geologists, 394p.
- Shelberg M.C.; Moellering, H. and Lam, N.S., 1982. Measuring the fractal dimensions of empirical cartographic curves. In: *Proceedings Fifth International Symposium on Computer-Assisted Cartography* (Crystal City, Virginia), pp. 481-490.
- Simpson, R.H. and Riehl, J., 1981. *The Hurricane & Its Impact*. Baton Rouge, Louisiana: Louisiana State University Press, 398p.
- Stewart, S.R., 2003. Tropical Cyclone Report: Tropical Storm Fay.
<http://www.nhc.noaa.gov/2002fay.shtml> (accessed on September 4, 2011)
- Stockdon, H. F.; Sallenger, A.H.; Holman, R.A., and Howd, P.A., 2007. A simple model for the spatially-variable coastal response to hurricanes. *Marine Geology*, 238, 1-20.
- Stolum, H.H., 1998. Planform geometry and dynamics of meandering rivers. *Geological Society of America Bulletin*, 110(11), 1485-1498.
- Taylor, J.R., 1997. *An Introduction to Error Analysis*. Sausalito, California: University Science Books, 327p.
- Wallace, D. J.; Anderson, J.B., and Fernández, R.A., 2010. Transgressive ravinement versus depth of closure: a geological perspective from the Upper Texas Coast. *Journal of Coastal Research*, 26(6), 1057-1067.

- Wang, P.; Ebersole, B., and Smith, E., 2002. Longshore Sand Transport—Initial Results from Large-Scale Sediment Transport Facility. Coastal and Hydraulics Laboratory Technical Note CHETN-II-46. U.S. Army Engineer Research and Development Center, 11p.
- Wehr, A. and Lohr, U., 1999. Airborne laser scanning - an introduction and overview. *ISPRS Journal of Photogrammetry and Remote Sensing*, 54, 68-82.

APPENDIX A
SOURCE CODE

```

#Vario
#Author: Billy. U. Hales
#Input Variables:
# "Workspace" As Workspace
# "Table or Shapefile" As Table
# "Results File" As File
# "Lag Distance" As String
# "Field Name" As String
#Output:
# One LARGE DBF file containing all distances/variances
# One DBF file for each lag up to 500/1000 meters
# One CSV file with semivariogram variances versus lags.
#Platform: ArcGIS Desktop (ArcINFO) 10.0
#Description:
# This script implements an algorithm featured in
# Burt, Barber, and Rigby (2009) to calculate a semivariogram
# from the user-specified field. The "MEAS" field is used
# to calculate distance.
# Additional documentation and reference used:
# http://help.arcgis.com/en/arcgisdesktop/10.0/help/

#Boilerplate
import arcpy, os, sys, string, math

#Initializes input variables
ws = arcpy.GetParameterAsText(0)
tb = arcpy.GetParameterAsText(1)
resultsfile = arcpy.GetParameterAsText(2)
lagdist = arcpy.GetParameterAsText(3)
fname = arcpy.GetParameterAsText(4)

#Initializes environmental parameters
arcpy.env.workspace = ws
arcpy.env.overwriteOutput = True

#Seperates input table name from direcotry and appends
# _vario.dbf to the end of the file name.
tbvario = tb.split("\\")[-1].split(".")[0] + "_vario.dbf"

#Initialzes layer with same name as newly-named table
lyr = tbvario.split(".")[0] + "lyr"
arcpy.AddMessage(tbvario)

```

```

#Creates table named in previous code block and
# and adds 2 fields, DIST and SD.
arcpy.CreateTable_management(ws,tbvario,"#", "#")
arcpy.AddField_management(tbvario,"DIST","double")
arcpy.AddField_management(tbvario,"SD","double")

#Counts all the features in the user input
# shapefile/table
total = arcpy.GetCount_management(tb).getOutput(0)

#Opens Cursors (Edit Session)
rowsI = arcpy.InsertCursor(tbvario)
rowsS1 = arcpy.SearchCursor(tb)

#Begins comparing first item to other items in table, and
# then outputs variances to "SD" and distances to "DIST"
# in the large DBF file.
i = 0
j = 0
for rowS1 in rowsS1:
    arcpy.AddMessage("Evaluating item number " + str(i + 1) + " of " + total)

#The second searchcursor allows for the algorithm to compare the
# current object to other objects, only does ONE comparison
# per object, if statement assures that.
rowsS2 = arcpy.SearchCursor(tb)
j = 0
for rowS2 in rowsS2:
    if j < i + 1:
        j = j + 1
        continue
#Calculation of variance and distance
else:
    rowI = rowsI.newRow()
    rowI.SD = math.pow((rowS1.getValue(fname) - rowS2.getValue(fname)),2)
    rowI.DIST = math.fabs(rowS1.MEAS - rowS2.MEAS)
    rowsI.insertRow(rowI)
del rowS2, rowsS2
i = i + 1

del rowI, rowS1
del rowsI, rowsS1

```

```

#Second phase of semivariogram, this is where algorithm seperates big DBF
# file into bins (lags). Then takes average distance and variance
# and outptus to results file.
writefile = open(resultsfile, 'a')

i = int(lagdist)
writefile.write("Lag, Avg_Dist, Avg_Sqd_Diff, Variogram\n")

#Implements hard-coded analysis distance. It is 1000 meters in this instance
while i <= 1000:

    arcpy.MakeTableView_management(ws + "\\ " + tbvario,lyr," \"DIST\" > " + \
                                   str(i - int(lagdist)) + " AND \"DIST\" <= " + \
                                   str(i),"#", "#")
    arcpy.CopyRows_management(lyr,lyr.split("lyr")[0] + "_" + str(i) + ".dbf")
    sumSD = 0
    sumDIST = 0
    j = 0
    arcpy.AddMessage("Making " + lyr.split("lyr")[0] + "_" + str(i) + ".dbf")
    rowsCSV = arcpy.SearchCursor(lyr.split("lyr")[0] + "_" + str(i) + ".dbf")
    for rowCSV in rowsCSV:
        sumSD = sumSD + rowCSV.SD
        sumDIST = sumDIST + rowCSV.DIST
        j = j + 1
    del rowCSV, rowsCSV
    writefile.write("%s,%1.6f,%1.6f,%1.6f\n" % (str(i), sumDIST / j, sumSD / j, (sumSD\
                                                / (2*j))))
    i = i + int(lagdist)

writefile.close()

```

```

#Buffer_Points
#Author: Billy U. Hales
#Input Variables:
# "Workspace" As Workspace
# "Route Feature" As Shapefile
# "Output Root Name" As String
# "Interval Length" As String
#Output:
# Polyline Shapefile
#Platform: ArcGIS Desktop (ArcINFO) 10.0
#Description:
# This script outputs a polyline shapefile that intersects a given route feature
# at right angles at a given interval, "Interval Length". This output is
# then used to cut a buffered polygon shapefile into x number of pieces at the
# user-specified interval length or width parallel to the route feature. Part of this
# code uses material from an ESRI help forum entitled,
# "creating polyline shapefile from XY coordinate excel table". It is
# currently—as of 8-22-2011--be found at...
# http://forums.esri.com/Thread.asp?c=93&f=1149&t=286041
# Additional documentation and referenced used:
# http://help.arcgis.com/en/arcgisdesktop/10.0/help/

#Please Note:
# This source code listing uses general python rules for explicit line continuation.
# This was done to make the code easier to read. In short, backslash ‘\’ characters
# are used and put in after the fact. If code does not run directly copied out of this
# appendix, chances are the problem is with the backslashes and the tabs after
# them. Some statements could not be explicitly continued—such as text strings.

#Boilerplate
import arcpy, os, sys, string, math

#Input Variables
ws = arcpy.GetParameterAsText(0)
rt = arcpy.GetParameterAsText(1)
name = arcpy.GetParameterAsText(2)
int_length = arcpy.GetParameterAsText(3)

#Input Processing
sr = arcpy.Describe(rt).spatialReference
arcpy.env.workspace = ws
arcpy.env.overwriteOutput = True
rt = rt.split("\\")[-1]

```

```

#Defining output files
tb = name + "_tb" + int_length + ".dbf"
lyr = name + "_evt" + int_length
sf = name + "_evt" + int_length + ".shp"
sfsort = name + "_evt" + int_length + "_sorted.shp"
#For final result, polyline shapefile.
lineArray = arcpy.Array()
vectorPnt = arcpy.Point()

#Needed Trigonometric Functions to Calculate Location of Buffere Points.
codeblock = """def calcAngle(initVal,isX,isComp,angle,distance):
    if isComp == True:
        if isX == True:
            if angle < 180:
                return initVal + distance * math.cos((angle + 180.0) * (math.pi/180.0))
            else:
                return initVal + distance * math.cos((angle - 180.0) * (math.pi/180.0))
        else:
            if angle < 180:
                return initVal + distance * math.sin((angle + 180.0) * (math.pi/180.0))
            else:
                return initVal + distance * math.sin((angle - 180.0) * (math.pi/180.0))
    else:
        if isX == True:
            return initVal + distance * math.cos(angle * (math.pi/180.0))
        else:
            return initVal + distance * math.sin(angle * (math.pi/180.0))"""

#Creating Source Table for Point Route Event Layer
arcpy.CreateTable_management(ws,tb)
arcpy.AddField_management(tb,"NAME","text","5")
arcpy.AddField_management(tb,"MDIST","double")
arcpy.AddField_management(tb,"RID","text")

```

```

#Populating Table with Name(Index), MDIST(Distance), RID(RouteID) until 33400,
# length of polyline route feature
rows = arcpy.InsertCursor(tb)
seg_length = 0
i = 1
while seg_length < 33400:
    row = rows.newRow()
    row.NAME = str(i)
    row.MDIST = seg_length
    row.RID = "1"
    seg_length = seg_length + long(int_length)
    i = i + 1
    rows.insertRow(row)

del row, rows
#Making route event layer with table just created
arcpy.MakeRouteEventLayer_lr(rt,"Name",tb,"RID POINT MDIST",\
lyr,"#","#","ANGLE_FIELD","NORMAL","#","#","POINT")

#Turning temporary event layer into shapefile
arcpy.CopyFeatures_management(lyr,sf)

#Adding coordinate fields and coordinates of each node for the perpendicular lines
arcpy.AddField_management(sf,"XPT","double")
arcpy.AddField_management(sf,"YPT","double")
arcpy.AddField_management(sf,"XLNONE","double")
arcpy.AddField_management(sf,"YLNONE","double")
arcpy.AddField_management(sf,"XLNTWO","double")
arcpy.AddField_management(sf,"YLNTWO","double")

#Using the python equivalent of "Calculate Geometry" to coordinates for event layer
# points.
arcpy.CalculateField_management(sf,"XPT","float(!SHAPE.centroid!.split(\" \")[0]),\
"PYTHON")
arcpy.CalculateField_management(sf,"YPT","float(!SHAPE.centroid!.split(\" \")[1]),\
"PYTHON")

```

```

#With given point coordinates of route event layer, calculating coordinates of points at
# the end of the extending lines at 400 meters
arcpy.CalculateField_management(sf,"XLNONE","calcAngle(!XPT!,True,False,\
!LOC_ANGLE!,400.0)","PYTHON",codeblock)
arcpy.CalculateField_management(sf,"YLNONE","calcAngle(!YPT!,False,False,\
!LOC_ANGLE!,400.0)","PYTHON",codeblock)
arcpy.CalculateField_management(sf,"XLNTWO","calcAngle(!XPT!,True,True,\
!LOC_ANGLE!,400.0)","PYTHON",codeblock)
arcpy.CalculateField_management(sf,"YLNTWO","calcAngle(!YPT!,False,True,\
!LOC_ANGLE!,400.0)","PYTHON",codeblock)

#Creating base of new shapefile.
arcpy.CreateFeatureclass_management(ws,sf.split(".")[0] + \
"_ln.shp","POLYLINE","#","DISABLED","DISABLED",sr)

#Populating new shapefile with end nodes and declaring them lines.
curI = arcpy.InsertCursor(sf.split(".")[0] + "_ln.shp")
curS = arcpy.SearchCursor(sf)
for rowS in curS:
    rowI = curI.newRow()
    vectorPnt.X = rowS.XLNONE
    vectorPnt.Y = rowS.YLNONE
    lineArray.add(vectorPnt)
    vectorPnt.X = rowS.XLNTWO
    vectorPnt.Y = rowS.YLNTWO
    lineArray.add(vectorPnt)
    rowI.shape = lineArray
    curI.insertRow(rowI)
    lineArray.removeAll()

#Saves progress by releasing editing handles
del rowI, rowS
del curI, curS

#Sorting all points so that they start at the western side of Bolivar Peninsula first.
#Useful for future operations
arcpy.Sort_management(sf,sfsort,[["MDIST","ASCENDING"]])
arcpy.Delete_management(sf)
arcpy.Rename_management(sfsort,sf)

```

```

#LAS_Process
#Author: Billy U. Hales
#Input Variables:
# "Input Workspace" As Workspace
# "Output Workspace" As Workspace
#Output:
# Multipoint Shapefiles that represent vectorized that represent the 3D point cloud
# found in a LiDAR dataset.
#Platform: ArcGIS Desktop (ArcINFO) 9.3.1
#Description:
# This python algorithm uses the Windows API to get a file directory from the
# specified input workspace. The algorithm then iterates through that list of files
# and filters out only "*.LAS" files.
# After that, a separate list is created with just the LAS binary LiDAR files.
# With all LAS binary files, the algorithm uses the LASToMultipoint method
# in the geoprocessing library to convert all LAS binary files to multipoint
# shapefiles and then write the results to the output workspace.
# Additional documentation and reference used:
# http://webhelp.esri.com/arcgisdesktop/9.3/
#Please Note:
# This source code listing uses general python rules for explicit line continuation.
# This was done to make the code easier to read. In short, backslash '\ ' characters
# are used and put in after the fact. If code does not run directly copied out of this
# appendix, chances are the problem is with the backslashes and the tabs after
# them. Some statements could not be explicitly continued—such as text strings.

#Boilerplate - Imports necessary libraries and creates a geoprocessing environment
import sys, string, os, arcgisscripting
gp = arcgisscripting.create()

#Specify the location for the new shapefile.
gp.Workspace = sys.argv[1]
outWorkspace = sys.argv[2]

#Uses the LISTDIR method in the OS library to list all files within the specified
# directory, and then establishes a blank list, L!, to append all "*.LAS" files
dirlist = os.listdir(gp.Workspace)
L1 = []

```

```

#Iterates through list created by LISTDIR method and filters out only "*.LAS" files
# and then outputs those to the L1 list.
for x in dirlist:
    if x[-4:] == ".las":
        L1.append(x)

#Iterates through the L1 list and performs the LASToMultipoint geoprocessing
# method to convert LAS binary files to multipoint shapefiles. Those shapefiles
# are then output with the same name as the LAS binary file to an output directory.
for y in L1:
    gp.AddMessage("Reading " + y)
    gp.LASToMultipoint_3d(y, outWorkspace + "\\\" + y[0:-4] + ".shp", \
        "0.25", "#", "ANY_RETURNS", "#",
        "C:\\Program Files\\ArcGIS\\Coordinate Systems\\" + \
        "Projected Coordinate Systems\\UTM\\NAD 1983\\" + \
        "NAD 1983 UTM Zone 15N.prj", "las", "1")
    gp.AddMessage("Completed " + y[0:-4] + ".shp")

```

```

#IDW_Process
#Author: Billy U. Hales
#Input Variables:
# "Input Workspace" As Workspace
# "Output Workspace" As Workspace
#Output:
# Rasters that represent IDW-interpolated surfaces or Digital Elevation Models
# from multipoint feature classes that represent the 3D point cloud from a LiDAR
# dataset.
#Platform: ArcGIS Desktop (ArcINFO) 9.3.1
#Description:
# This algorithm uses a method to scroll through and get a count of all feature
# classes in the input workspace. This algorithm uses a technique outlined in the
# ESRI Code Snippets collection to operate on the non-iterable python list of all
# features that is obtained through the ListFeatureClasses method in the ArcGIS
# Desktop 9.x geoprocessor library.
# As this algorithm scrolls through the list, it builds a count and then uses the
# IDW_3D geoprocessor method to generate
# a raster from each multipoint feature class in that directory. Current
# algorithm expects that all features be multipoint feature classes obtained
# from LiDAR LAS files.
# This algorithm assumes shapefile names are of format
# abcd_abcd_abcd.shp
# Additional documentation and reference used:
# http://webhelp.esri.com/arcgisdesktop/9.3/

#Please Note:
# This source code listing uses general python rules for explicit line continuation.
# This was done to make the code easier to read. In short, backslash '\ ' characters
# are used and put in after the fact. If code does not run directly copied out of this
# appendix, chances are the problem is with the backslashes and the tabs after
# them.

#Boilerplate - Imports necessary libraries and creates a geoprocessing environment.
import sys, string, os, arcgisscripting
gp = arcgisscripting.create()

#Establishes input variables
gp.Workspace = sys.argv[1]
outWorkSpace = sys.argv[2]

```

```

#Establishes List of Point Features
myDataList = gp.ListFeatureClasses("*","point")
myDataItem = myDataList.next()
a = 1

#Uses technique to scroll through non-iterable list and get count of point feature classes.
while myDataItem:
    a = a + 1
    myDataItem = myDataList.next()

#Resets list index for next scroll operation
myDataList.reset()

#Uses technique to scroll through non-iterable list to display data operation, item, and
# time. Then it actually does the IDW processing and lists the results in the output
# with finish time.
myDataItem = myDataList.next()
b = 1
while myDataItem:
    F1 = myDataItem.split("_")
    gp.AddMessage("Processing " + myDataItem)
    gp.Idw_3d(myDataItem,"Shape",outWorkSpace + "\\ " + "s" + F1[0] + F1[1] + \
        F1[2][0:-4],1,1,"FIXED 1.5 3",)
    gp.AddMessage("Generated " + "s" + F1[0] + F1[1] + F1[2][0:-4] + " " + \
        + " [" + str(b) + "/" + str(a) + "]")
    myDataItem = myDataList.next()
    b = b + 1

#Deletes lists so that system can properly get back to its previous state.
del myDataItem
del myDataList

```

```

# LiDARDiffPy
#Author: Billy U. Hales, Jr.
#Input Variables:
# "LiDAR PIF" As Shapefile
# "Input Param File" As File
#Example File Input:
# E:\clp_122008\freesw,E:\clp_082005\freesw,E:\Registration\PreRitatoIke,freesw
# E:\clp_122008\freese,E:\clp_082005\freese,E:\Registration\PreRitatoIke,freese
# E:\clp_122008\freene,E:\clp_082005\freene,E:\Registration\PreRitatoIke,freene
#Output:
# Clipped difference rasters that represent the difference between a baseline and
# target LiDAR-derived DEM that correspond to locations of pseudo invariant
# features.
# Raster attribute tables for all the clipped attribute rasters.
#Platform: ArcGIS Desktop (ArcINFO) 9.3.1
#Description:
# This algorithm was based off of an equivalent ModelBuilder application
# developed with the same name. This python script takes a shapefile containing
# pseudo invariant features and an input parameter file as input. Inputs from the
# parameter file are delimited by commas and ordered as Reference LiDAR
# Dataset, Comparative LiDAR Dataset, Output Directory, and root output file
# name. From those inputs and the shapefile representing pseudo invariant features,
# the reference and comparative LiDAR-derived DEMs are clipped to the extent of
# the PIFs, then the results of the clipping of the comparative LiDAR-derived
# DEM are subtracted from the results of the clipping of the reference LiDAR-
# derived DEM. The output is then saved to a directory specified in the input
# parameter file. Given the file input example above, this directory would be
# E:\Registration\PreRitatoIke.
# This source code was adapted from ModelBuilder code in ArcINFO Desktop v9.3.1.
#Please Note:
# This source code listing uses general python rules for explicit line continuation.
# This was done to make the code easier to read. In short, backslash '\` characters
# are used and put in after the fact. If code does not run directly copied out of this
# appendix, chances are the problem is with the backslashes and the tabs after
# them.

#Boilerplate - Imports necessary libraries and creates a geoprocessing environment.
import sys, string, os, arcgisscripting
gp = arcgisscripting.create()

```

```

#Explicitly sets the scratch workspace. This is where intermediate results go.
gp.scratchWorkspace = "E:\\Scratch"
#Prepares the parameter file for extraction.
fileName = sys.argv[2]
myFile = open(fileName,'r')
fileData = myFile.read()
records = fileData.split("\n")

#Predefined and ModelBuilder-Generated Variables
O1 = "%scratchworkspace%\O1"
O2 = "%scratchworkspace%\O2"
Times_Output = "%scratchworkspace%\O4"
One_Million = "1000000"
Int_Output = "%scratchworkspace%\O5"
Select_All = "\"Count\" IS NOT NULL"
Overwrite = "true"

#Extracts parameters from the parameter file for each quadrangle
for x in records:
    recordData = x.split(',')
    Lidar_PIF = sys.argv[1]
    RefLiDAR = recordData[0]
    Clip_Ref_Geometry = "true"
    CmpLiDAR = recordData[1]
    Clip_Cmp_Geometry = "true"
    LiDARDir = recordData[2]
    LiDARTabDir = "tables\\"
    LiDARRoot = recordData[3]
    LiDARDiff = LiDARDir + "\\\" + LiDARRoot + ".df"
    Output_Table__end_file_name_with__dbf_ = LiDARDir + "\\\" + LiDARTabDir + \
        LiDARRoot + ".dbf"

#Defines the bounding coordinates of the baseline LiDAR Digital Elevation Model
envelopeR = str(gp.GetRasterProperties(RefLiDAR, "LEFT")) + " " + \
    str(gp.GetRasterProperties(RefLiDAR, "BOTTOM")) + " " + \
    str(gp.GetRasterProperties(RefLiDAR, "RIGHT")) + " " + \
    str(gp.GetRasterProperties(RefLiDAR, "TOP"))

```

```

#Clips the portions of the baseline LiDAR-derived DEM that coincide with pseudo
# invariant features.
try:
    gp.Clip_management(RefLiDAR, envelopeR, O1, Lidar_PIF, "", \
                       Clip_Ref_Geometry)
    gp.AddMessage(RefLiDAR + " clipped successfully")
except:
    gp.GetMessages()
    gp.AddMessage(RefLiDAR + " has no PIFs! Next!")
    continue

#Defines the bounding coordinates of the target LiDAR Digital Elevation Model
envelopeR = str(gp.GetRasterProperties(CmpLiDAR, "LEFT")) + " " + \
            str(gp.GetRasterProperties(CmpLiDAR, "BOTTOM")) + " " + \
            str(gp.GetRasterProperties(CmpLiDAR, "RIGHT")) + " " + \
            str(gp.GetRasterProperties(CmpLiDAR, "TOP"))

#Clips the portions of the target LiDAR-derived DEM that coincide with pseudo
# invariant features.
try:
    gp.Clip_management(CmpLiDAR, envelopeR, O2, Lidar_PIF, "#", \
                       Clip_Cmp_Geometry)
    gp.AddMessage(CmpLiDAR + " clipped successfully")
except:
    gp.AddMessage(CmpLiDAR + " has no PIFs! Next!")
    continue

#Subtracts the clipped target LiDAR DEM from the baseline LiDAR DEM.
gp.Minus_sa(O1, O2, LiDARDiff)

#These steps are necessary to turn a 32-bit floating point raster into a format that can
# support an attribute table in the ArcGIS Desktop environment. This couple of
# methods multiplies the raster by 1,000,000 and then turns it into an integer. This
# process is reversed later in LiDARStatCalc in order to retrieve actual floating
# point statistical values.
gp.Times_sa(LiDARDiff, One_Million, Times_Output)
gp.Int_sa(Times_Output, Int_Output)

#Builds the raster attribute table. This is essential for histogram statistical analysis done
# later with the LiDARStatCalc procedure.
gp.BuildRasterAttributeTable_management(Int_Output, Overwrite)

```

```
#Generates the actual table and stores it in the directory specified in the parameter file.  
gp.TableSelect_analysis(Int_Output, Output_Table__end_file_name_with__dbf_,  
                        Select_All)  
gp.AddMessage(LiDARDiff + " table created successfully")  
  
#Deletes all intermediate data from the scratch workspace  
gp.delete_management(O1)  
gp.delete_management(O2)  
gp.delete_management(Times_Output)  
gp.delete_management(Int_Output)
```

```

#LiDARStatCalc
#Author: Billy U. Hales, Jr.
#Input Variables:
# "Input Directory" As Workspace
# "Output File Name" As File
#Output:
# Comma separated values file containing histogram statistics from a DEM raster.
#Platform: ArcGIS Desktop (ArcINFO) 9.3.1
#Description:
# This algorithm uses the windows API to list all command seperated values
# (CSV) files that do not begin with a 'd' in a given directory. This
# algorithm then establishes an output csv file that calculates and displays
# and tabularizes all of the given histogram-based statistics such as the
# 2.5 percentage threshold values (left and right of histogram),
# and the remaining amounts for each statistic.
# Additional documentation and reference used:
# http://webhelp.esri.com/arcgisdesktop/9.3/
#Please Note:
# This source code listing uses general python rules for explicit line continuation.
# This was done to make the code easier to read. In short, backslash '\` characters
# are used and put in after the fact. If code does not run directly copied out of this
# appendix, chances are the problem is with the backslashes and the tabs after
# them.

#Boilerplate - Imports necessary libraries and creates a geoprocessing environment
import sys, string, os, arcgisscripting
gp = arcgisscripting.create()

#Establishes input directory and output file name
DirName = sys.argv[1]
outfileName = sys.argv[2]

#Uses the windows API to crawl through the input directory name to get
# a list of ALL files in directory
dirlist = os.listdir(DirName)

```

```

#Uses list generated from the DIRLIST method in the Operating System library
# to parse out only files that do NOT begin with a d and files that are ending
# in "*.csv".
L1 = []
for x in dirlist:
    if x[-4:] == ".csv" and x[0] <> "d":
        L1.append(x)
for x in L1:
    gp.addmessage(x)
#Uses a crude error identification routine that stops execution if there are
# comma separated values files (CSV).
if len(L1) == 0:
    gp.addmessage("No comma separated values files exist")
    sys.exit(1)

#Opens output file for appending (writing+reading) and writes first row of
# text labels.
writeFile = open(outfileName,'a')
writeFile.write("Quad Name,Total,Threshold,Lower Cut Value,Lower Cut " + \
                "Remaining Value, Lower Cut Remaining Amount," + \
                "Higher Cut Value, Higher Cut Remaining Value, " + \
                "Higher Cut Remaining Amount\n")

#Opens a file in the directory that meets that aforementioned criteria and
# establishes the top line of that file (text and labels).
#Afterward, all data are read, and parsed by newline characters to establish
# records.
for a in L1:
    myFile = open(DirName + "\\\" + a, 'r')
    FirstLine = myFile.readline()
    myData = myFile.read()
    myRecords = myData.split("\n")

#Fix implemented that corrects an issue in Microsoft Excel that generates a
# last line of null (0) length.
if len(myRecords[-1]) == 0:
    del myRecords[-1]

#Iterates through all bins in the histogram that is detailed in this comma separated
# values file to get the total count of pixels analyzed for each file coverage.
total = 0
for b in myRecords:
    dataElement = b.split(',')
    total = total + int(dataElement[1])

```

```

#Based on total pixel amount, the threshold (or ideal size) of each side or tail
# of the histogram.
    threshold = total * 0.025

#Prepares quad name and outputs that with the total and threshold pixel counts
    a = a.replace('.csv', '')
    fileItems = a.split("\\")
    writeFile.write("%s,%0.6f,%0.6f," % (fileItems[-1],total,threshold))
#Crawls down through records and speculatively adds the next value in hope of
# obtaining the value corresponds to the lower threshold amount of pixels. This
# value and the "remaining value"--or value corresponding to a bin that has not
# been fully removed.
    d = 0
    for c in myRecords:
        dataElement = c.split(',')
        if (d + int(dataElement[1])) > threshold:
            upper_threshValue = prev_dE
            rem_upper_threshValue = float(dataElement[0])/1000000
            break
        else:
            d = d + int(dataElement[1])
            prev_dE = float(dataElement[0])/1000000

#Writes down the lower value (left-hand-side) of the histogram and the remaining
# value along with the remaining amount of pixels at that remaining value.
    writeFile.write("%0.6f,%0.6f,%0.6f," % \
                    (upper_threshValue,rem_upper_threshValue,threshold - d))
    prev_dE = 0

#Establishes a reversed list from the aforementioned list.
    f = 0
    myRecords.reverse()

```

```
#Crawls up through the records and speculatively adds the next value in hope
# of finding the greater threshold (right-hand-side) on the side of the histogram.
for e in myRecords:
    dataElement = e.split(',')
    if (f + int(dataElement[1])) > threshold:
        lower_threshValue = prev_dE
        rem_lower_threshValue = float(dataElement[0])/1000000
        break
    else:
        f = f + int(dataElement[1])
        prev_dE = float(dataElement[0])/1000000

#Writes down the upper value (right-hand-side) of the histogram and the remaining
# value along with the remaining amount of pixels at that remaining value.
writeFile.write("%0.6f,%0.6f,%0.6f\n" % \
                (lower_threshValue,rem_lower_threshValue,threshold - f))

#Closes and commits all writes for all files involved in editing.
myFile.close()
writeFile.close()
```

```

# LiDARMaskPy
#Author: Billy U. Hales, Jr.
#Input Variables:
#  "Param File" As File
#  "Workspace" As Workspace
#  "ASCII Remap File" As File
#Output:
#  Mask files that represent values cut from the right and left tail of the histogram.
#  Corrected Difference rasters with upper and lower 2.5% of values removed--right
#  and left tails of histogram.
#Platform: ArcGIS Desktop (ArcINFO) 9.3.1
#Description:
#  This algorithm was based off of an equivalent ModelBuilder application
#  developed with the same name. This python script takes a comma separated
#  values file that contains the output from the LiDARStatCalc python routine as
#  input. From that file, this algorithm uses the threshold values to generate mask
#  files that represent the most extreme upper and lower 2.5% of values. This
#  algorithm then uses these mask files to cut out the extreme values—leaving a
#  corrected difference raster.
#  Additional documentation and reference used:
#  http://webhelp.esri.com/arcgisdesktop/9.3/

#Please Note:
#  This source code listing uses general python rules for explicit line continuation.
#  This was done to make the code easier to read. In short, backslash '\ characters
#  are used and put in after the fact. If code does not run directly copied out of this
#  appendix, chances are the problem is with the backslashes and the tabs after
#  them.

#Boilerplate - Imports necessary libraries and then creates a geoprocessing environment
import sys, string, os, arcgisscripting
gp = arcgisscripting.create()

#Explicitly sets the scratch workspace for all operations. This is where intermediate
#  files go.
gp.scratchWorkspace = "E:\\Scratch"

#Establishes input parameter file.
myfileName = sys.argv[1]

```

```

#Begins to set up parameter file for extraction.
myinputFile = open(myfileName,'r')
myinputFile.readline()
myfileData = myinputFile.read()
mycsvRows = myfileData.split('\n')

#Sets the option to change values not mentioned in the ASCII remap file to NoDATA. In
# a binary image, this condition should never have to happen, but is set to account
# for the possibility of this happening.
Change_missing_values_to_NoData = "true"

#Extracts the parameters from the parameter file.
for x in mycsvRows:
    mydataElements = x.split(',')
    myDirectory = sys.argv[2]
    Input_Raster = myDirectory + '\\ + mydataElements[0] + ".df"
    Preserve_Greater_Than__Constant_ = mydataElements[3]
    Preserve_Less_Than__Constant_ = mydataElements[6]
    Mask = myDirectory + '\\ + mydataElements[0] + ".msk"
    Corrected_Mask = myDirectory + '\\ + mydataElements[0] + ".cmask"
    Input_ASCII_remap_file = sys.argv[3]
    Corrected_Difference = myDirectory + '\\ + mydataElements[0] + ".cdf"
    LessThan = myDirectory + '\\ + mydataElements[0] + ".l"
    MoreThan = myDirectory + '\\ + mydataElements[0] + ".h"

#Uses the Less Than method in the Spatial Analyst extension to retrieve the mask that
# represents the lower 2.5% of extreme values from alpha trimmed means.
gp.LessThan_sa(Input_Raster, Preserve_Less_Than__Constant_, LessThan)

#Uses the Greater Than method in the Spatial Analyst extension to retrieve the mask that
# represents the lower 2.5% of extreme values from alpha trimmed means.
gp.GreaterThan_sa(Input_Raster, Preserve_Greater_Than__Constant_, MoreThan)

#Combines both masks to get the final extraction mask.
gp.BitwiseAnd_sa(LessThan, MoreThan, Mask)

#Reclassifies the mask to a format that is workable or the ExtractByMask
# method.
gp.ReclassByASCIIFile_sa(Mask, Input_ASCII_remap_file, \
                          Corrected_Mask, Change_missing_values_to_NoData)

#Extracts the corrected difference files using the reclassified mask and the
# difference rasters.
gp.ExtractByMask_sa(Input_Raster, Corrected_Mask, Corrected_Difference)

```

```

#MassFeatClip
#Author: Billy U. Hales, Jr.
#Input Variables:
# "Clipping Workspace" As Workspace
# "Output Workspace" As Workspace
# "Shoreline One" As Shapefile
# "Shoreline Two" As Shapefile
# "Shoreline One Prefix" As AnyValue
# "Shoreline Two Prefix" As AnyValue
#Output:
# Clipped Shorelines that are within the bounds of the clipping polygons
# specified in the "clipping workspace algorithm.
#Platform: ArcGIS Desktop (ArcINFO) 9.3.1
#Description:
# This algorithm will take one shoreline, like shoreline_122008.shp and
# assigns it a user-defined prefix such as Post3Ike_ . The algorithm will
# then clip this shoreline and name it with the given prefix and the name
# of the clipping polygon. If the polygon were named 500, then the name
# of the newly clipped shoreline would be Post3Ike_500.
# Additional documentation and reference used:
# http://webhelp.esri.com/arcgisdesktop/9.3/
#Please Note:
# This source code listing uses general python rules for explicit line continuation.
# This was done to make the code easier to read. In short, backslash '\ ' characters
# are used and put in after the fact. If code does not run directly copied out of this
# appendix, chances are the problem is with the backslashes and the tabs after
# them. Some statements could not be explicitly continued—such as text strings.

#Boilerplate
import sys, string, os, arcgisscripting
gp = arcgisscripting.create()

#Input Variables Defined
clippingWorkspace = sys.argv[1]
destWorkspace = sys.argv[2]
shorelineOne = sys.argv[3]
shorelineTwo = sys.argv[4]
shorelineOneSuffix = sys.argv[5]
shorelineTwoSuffix = sys.argv[6]

#Sets main workspace to clipping workspace
gp.Workspace = clippingWorkspace

```

```
#Obtains a list of all polygons in main workspace
myDataList = gp.ListFeatureClasses("*","POLYGON")
myDataItem = myDataList.next()

#Establishes a separate list of all polygons to make the list iterable.
L1 = []
while myDataItem:
    L1.append(myDataItem)
    myDataItem = myDataList.next()

#Clips both shoreline one and shoreline two with the same polygon and names
#    them appropriately.
for x in L1:
    gp.clip_analysis(shorelineOne,x,destWorkspace + "\\\" + \
                    shorelineOneSuffix + x)
    gp.AddMessage("Clipped " + shorelineOneSuffix + x)
    gp.clip_analysis(shorelineTwo,x,destWorkspace + "\\\" + \
                    shorelineTwoSuffix + x)
    gp.AddMessage("Clipped " + shorelineTwoSuffix + x)

#Deletes data structures so that no output resources are locked.
del myDataItem, myDataList
```

```
#Parser
#Author: Billy U. Hales, Jr.
#Input Variables:
# "Shapefile" As Shapefile
# "Distance" As String
#Output:
# Corrected Shapefile
#Platform: ArcGIS Desktop (ArcINFO) 10.0
#Description:
# This algorithm corrects a bug in the shoreline segmentation procedure
# that may result in closely spaced linear shoreline differences.
# This bug is corrected by comparison of the MEAS fields in a polyline
# shapefile or table and eliminates features that are less than
# dist/2 meters
# away from their neighbor. Please note that this algorithm expects the shapefile to be
# sorted according to the MEAS field in ascending order.
# Additional documentation and reference used:
# http://help.arcgis.com/en/arcgisdesktop/10.0/help/

#Please Note:
# This source code listing uses general python rules for explicit line continuation.
# This was done to make the code easier to read. In short, backslash '\ ' characters
# are used and put in after the fact. If code does not run directly copied out of this
# appendix, chances are the problem is with the backslashes and the tabs after
# them. Some statements could not be explicitly continued—such as text strings.

#Boilerplate
import arcpy, os, string

#Input parameters
sf = arcpy.GetParameterAsText(0)
dist = arcpy.GetParameterAsText(1)

#Sets up evaluation criteria
evalCriteria = float(dist) / 2.0

#Sets up distance field
arcpy.AddField_management(sf, "DISTANCE", "DOUBLE", 12, 10)
```

```

#Populates distance field with distance between MEAS fields
i = 0
prevMeas = 0.0
rows = arcpy.UpdateCursor(sf)
for row in rows:
    if i == 0:
        prvMeas = row.MEAS
        row.DISTANCE = row.MEAS - prvMeas
        rows.updateRow(row)
        i = i + 1
    else:
        row.DISTANCE = row.MEAS - prvMeas
        rows.updateRow(row)
        prvMeas = row.MEAS
        i = i + 1

prevDist = 0.0
i = 0
del row, rows

#Now that DISTANCE field is populated, runs evaluation criteria and deletes values that
# exceed that criteria.
rows = arcpy.UpdateCursor(sf)
for row in rows:
    if row.DISTANCE < evalCriteria:
        prevDist = row.DISTANCE
        if i == 0:
            continue
        arcpy.AddMessage("Eliminated Line Number " + str(i) + \
            " with a paltry distance of " + str(row.DISTANCE))
        rows.deleteRow(row)
        i = i + 1
    else:
        row.DISTANCE = row.DISTANCE + prevDist
        prevDist = 0.0
        rows.updateRow(row)
        if row.DISTANCE < evalCriteria:
            arcpy.AddMessage("Eliminated Line Number " + str(i) + \
                " with a paltry distance of " + str(row.DISTANCE))
            rows.deleteRow(row)
        i = i + 1
del row, rows

```

```

#EvalSLGen
#Author: Billy U. Hales, Jr.
#Input Variables
# "Workspace" As Workspace
# "XY DBASE Table" As Table
# "Output Shapefile" As Shapefile
# "Coordinate System" As Coordinate System
#Output:
#Line shapefile that resembles erosion and accretion on a pre-storm
# shoreline, based off of the classified erosion and accretion values.
#Platform: ArcGIS Desktop (ArcINFO) 9.3.1
#Description:
#This algorithm takes ordered points from a DBASE file and connects
# them to generate a line that represents the shoreline change
# as a result of a Tropical Cyclone. The source code for this
# python script was adapted from "faulty" source
# code taken from the Archived ESRI Forum Post entitled,
# "creating polyline shapefile from XY coordinate excel table". It is
# currently--as of publication--be found at...
# http://forums.esri.com/Thread.asp?c=93&f=1149&t=286041
# Additional documentation and reference used:
# http://webhelp.esri.com/arcgisdesktop/9.3/

import sys, string, os, arcgisscripting
gp = arcgisscripting.create()
gp.Overwriteoutput = 1

#Establishes input variables
inWorkspace = sys.argv[1]
sourceXY = sys.argv[2]
outfilename = sys.argv[3]
coordsys = sys.argv[4]

gp.Workspace = inWorkspace

outfiledesc = outfilename.split('\')
outfile = outfiledesc[-1]

gp.CreateFeatureclass(inWorkspace + "\\", outfile, "POLYLINE")
gp.defineprojection(outfile, coordsys)

#Open a cursor to insert rows into the shapefile.
cur = gp.InsertCursor(inWorkspace + "\\" + outfile)

```

```

#Create an Array and Point object.
lineArray = gp.CreateObject("Array")
pnt = gp.CreateObject("Point")

#Open a cursor on the table of XY coordinates to read from.
rows = gp.SearchCursor(sourceXY)

#Reset the cursor to the top.
row = rows.Next()

#Loop through each record in the table of point pairs..
while row:

#Get the first set of coordinates for the first point.
    pnt.x = row.GetValue("MEAS")
    pnt.y = row.GetValue("EVALEA")

    lineArray.add(pnt)

#Go to next row in table.
    row = rows.Next()

#After both matching points are defined in terms of coordinates,
# the next step is to set the InsertCursor to the desired location
# of the shapefile. Then we use that InsertCursor method to commit
# the coordiantes in the line data structure to the polyline feature
# class.

feat = cur.NewRow()
feat.shape = lineArray
cur.InsertRow(feat)
lineArray.RemoveAll()

#Delete aforementioned data structures from memory so that shapefile is
# able to be used.
del cur, row, rows

```

APPENDIX B
STATISTICS

Table B.1: Mean differences in elevation PIFs on imagery compared to 12-2008 BEG dataset.

Quad Name	08-2002	09-2002	08-2005	10-2005	7-2006	9-2008
free_sw	---	-0.031414	-0.219255	-0.1888143	-0.153050	---
free_se	---	-0.021677	-0.279468	-0.215577	-0.268970	---
Free_ne	0.230013	-0.013274	0.051589	0.036148	0.049090	0.263964
see_cp_nw	0.168423	-0.064137	0.052279	0.038212	0.006756	0.278582
cp_sw	0.163111	-0.041831	0.077956	0.040502	0.002050	0.312130
cp_se	0.172723	-0.103243	0.060320	0.031849	0.050749	0.309043
cp_ne	0.099342	---	0.064050	0.035697	0.042161	---
slp_nw	-0.031442	-0.142664	0.094048	0.007325	0.082040	0.199422
si_sw	---	-0.146561	0.091517	0.004951	0.053568	---
si_se	-0.003019	0.433782	0.100165	0.023114	-0.035551	0.242472
lc_sw	---	-0.109345	0.058292	0.048284	0.086536	0.280588
lc_nw	-0.004851	-0.155217	0.062043	0.043627	-0.064477	0.305202
lc_ne	0.092642	-0.146759	0.121029	0.088151	-0.168817	0.330490
see_g_nw	0.054843	-0.157477	0.152297	0.063724	-0.026897	0.284209
gal_sw	0.066005	-0.179054	0.137164	0.063142	-0.010404	0.233935
gal_se	0.078221	-0.145434	0.155615	0.077150	0.020067	0.261485
gal_ne	0.125602	---	---	0.116821	0.096143	0.334174
tj_nw	0.060534	---	0.152500	0.075116	-0.026199	0.198523
flk_sw	0.010484	-0.014963	0.024737	-0.000385	-0.005305	0.282320
flk_se	0.015896	-0.040758	0.036163	0.008796	0.002949	0.118875
flk_ne	-0.016125	0.017234	0.034336	0.028516	0.005374	0.100475
cap_nw	0.050017	-0.050778	0.033642	-0.009780	-0.009895	0.275559
cap_ne	0.108004	-0.059463	0.105832	0.042925	0.083318	0.270541
fp_se	0.122479	-0.004734	0.083765	0.090213	0.109509	0.287605
hi_sw	0.075801	0.032085	0.081094	0.079388	0.081097	0.357042
hi_se	0.054054	0.072127	0.086089	0.068491	0.089377	---
ml_sw	0.015249	-0.042410	---	---	-0.498773	---
ml_nw	---	0.098778	---	---	---	---
ml_ne	---	0.0130756	---	---	---	---
sosl_nw	---	-0.048922	---	---	---	---
sl_se	---	0.4337821	---	---	---	---
cl_sw	---	-0.041831	0.113482	0.067202	0.157505	---
cl_se	---	0.123936	0.106328	0.079557	0.022342	---
sp_sw	---	0.0059989	---	---	---	---

Table B.2: Length of Quadrangles

Quad Name	Quad Length (m)
free_sw	7563
free_se	1920
Free_ne	6631
see_cp_nw	3186
cp_sw	4777
cp_se	6354
cp_ne	1387
slp_nw	8468
si_sw	302
si_se	7448
lc_sw	4324
lc_nw	3023
lc_ne	7358
see_g_nw	2090
gal_sw	5140
gal_se	6656
gal_ne	1045
tj_nw	7414
flk_sw	6503
flk_se	3128
flk_ne	4057
cap_nw	6767
cap_ne	4478
fp_se	2185
hi_sw	6597
hi_se	6584
ml_sw	2214
ml_nw	4374
ml_ne	6639
sosl_nw	6044
sl_se	6602
cl_sw	6426
cl_se	6186
sp_sw	6057

Table B.3: Number of Pixels to derive means in Table B.1

Quad Name	08-2002	09-2002	08-2005	10-2005	7-2006	9-2008
free_sw	---	491	2806	7736	1905	---
free_se	---	479	1631	2662	1977	---
Free_ne	4334	3308	6536	13485	5655	143
see_cp_nw	9794	1839	9259	9054	6003	90
cp_sw	18744	5380	20231	20231	18948	418
cp_se	6589	6096	8690	8690	6838	272
cp_ne	3871	---	3547	4997	2995	---
slp_nw	23259	3944	11175	11175	10441	332
si_sw	---	1978	1031	1031	767	---
si_se	12172	11363	17171	17171	16785	130
lc_sw	10935	2030	12489	12489	11777	380
lc_nw	14117	882	9001	9001	8052	203
lc_ne	41329	3144	21967	25797	17772	676
see_g_nw	13264	7933	14837	14837	13330	282
gal_sw	29688	2070	33152	33152	30189	1137
gal_se	44634	3951	38612	41702	41635	1073
gal_ne	18413	---	---	3454	11289	412
tj_nw	9286	---	867	2028	6060	230
flk_sw	14972	578	6396	10759	5416	209
flk_se	6291	1616	2254	3601	2219	50
flk_ne	11595	2497	2756	7372	2539	105
cap_nw	37883	9075	3859	6605	4025	141
cap_ne	26888	2003	17910	24504	15436	415
fp_se	18277	516	19846	19846	18951	749
hi_sw	46029	21201	50339	50339	47123	1503
hi_se	29750	20862	33102	33102	30280	---
ml_sw	1880	239	2166	2166	1525	---
ml_nw	---	492	---	---	---	---
ml_ne	---	368	---	---	---	---
sosl_nw	---	234	---	---	---	---
sl_se	---	1330	---	---	---	---
cl_sw	---	5066	11822	11822	11765	---
cl_se	---	460	19772	20881	19028	---
sp_sw	---	101	---	---	---	---

Table B.4: Final solutions calculated from statistical analysis using PIFs.

Dataset	Offset (m)
08-2002	0.070123
09-2002	0.087981
08-2005	0.080262
10-2005	0.041286
07-2006	0.014078
09-2008	0.273732

APPENDIX C
SHORELINE CHANGES

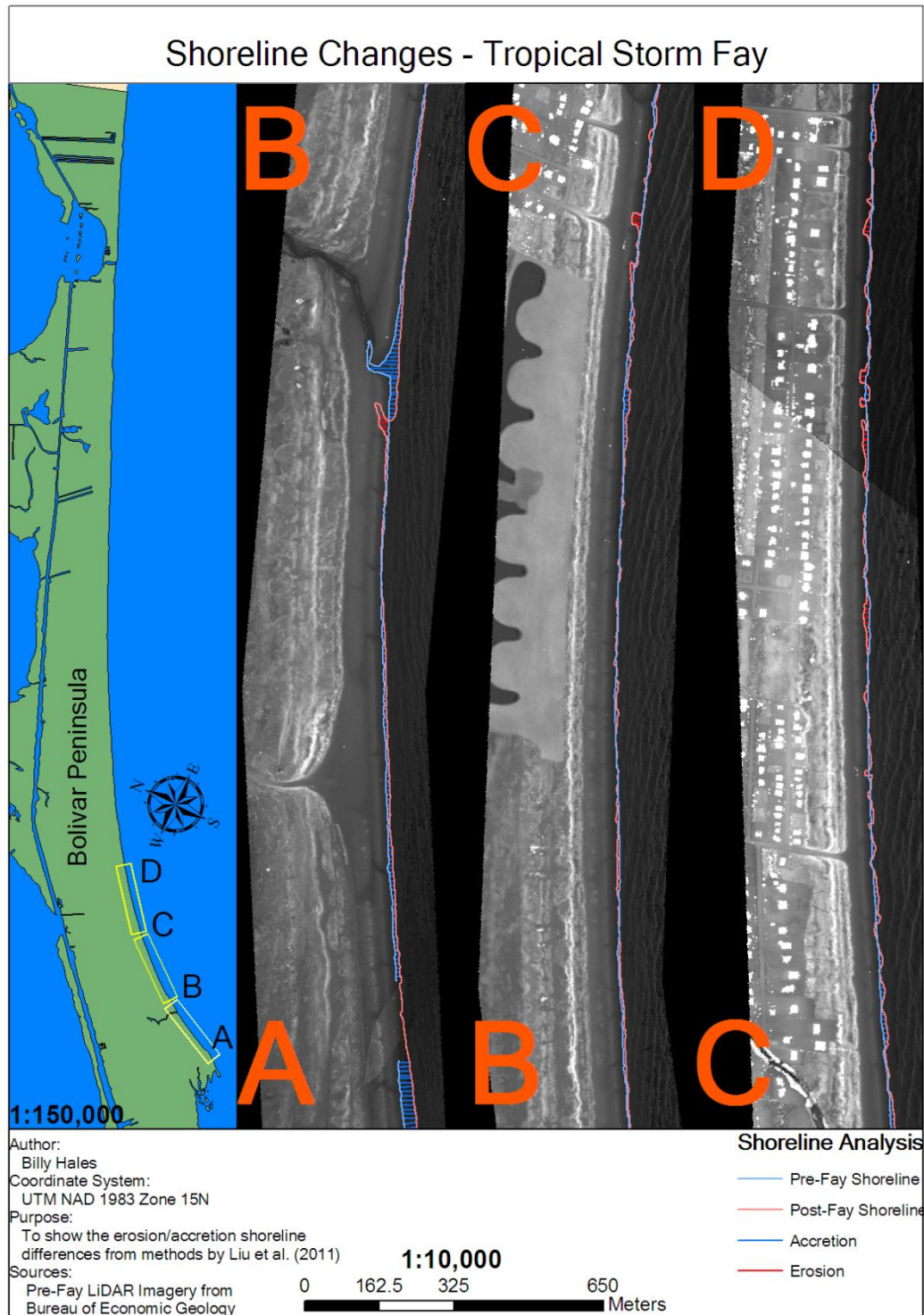


Figure C.1. Section 1/5 of 1:10000 scale shoreline changes - Tropical Storm Fay

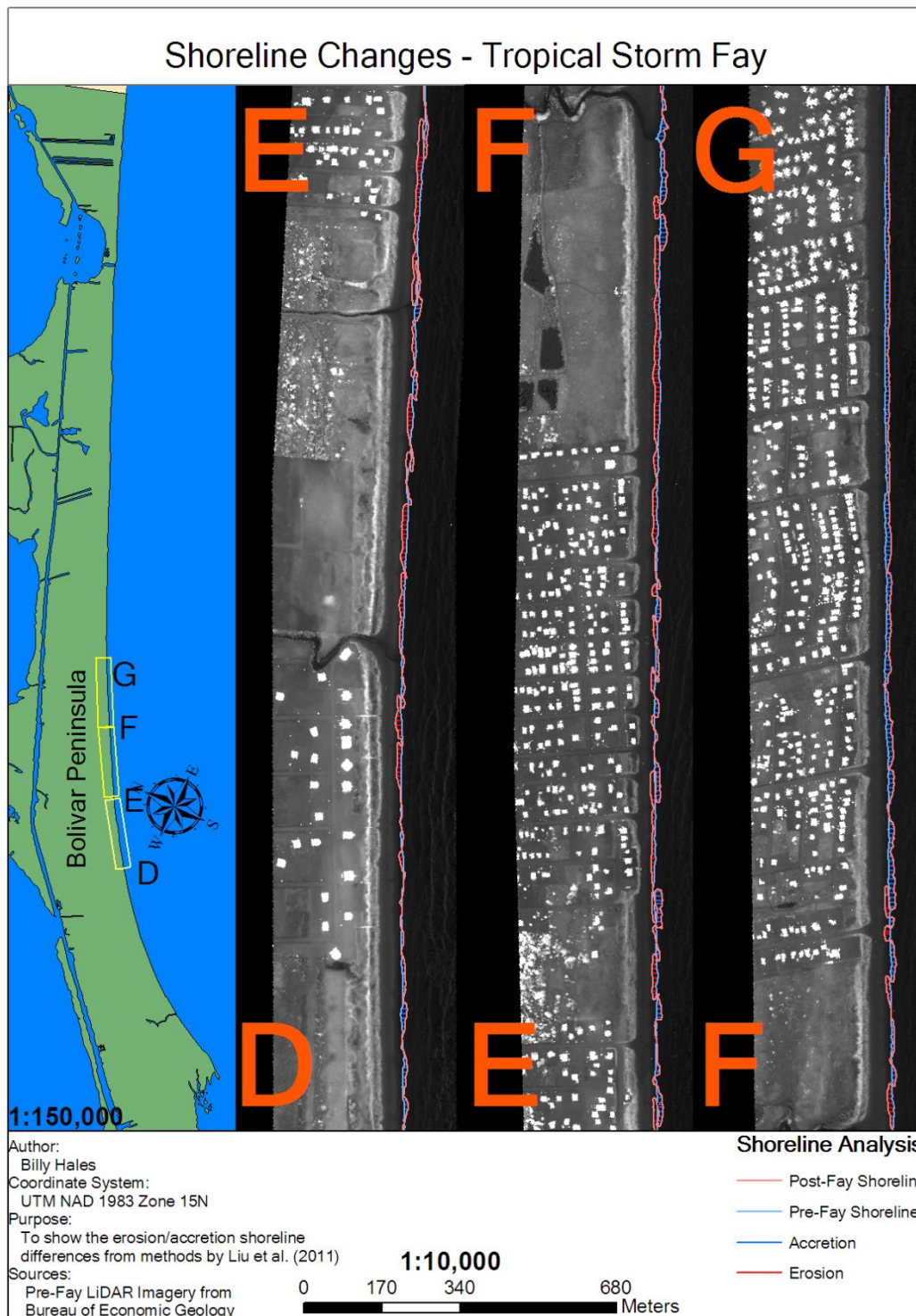


Figure C.2. Section 2/5 of 1:10000 scale shoreline changes - Tropical Storm Fay

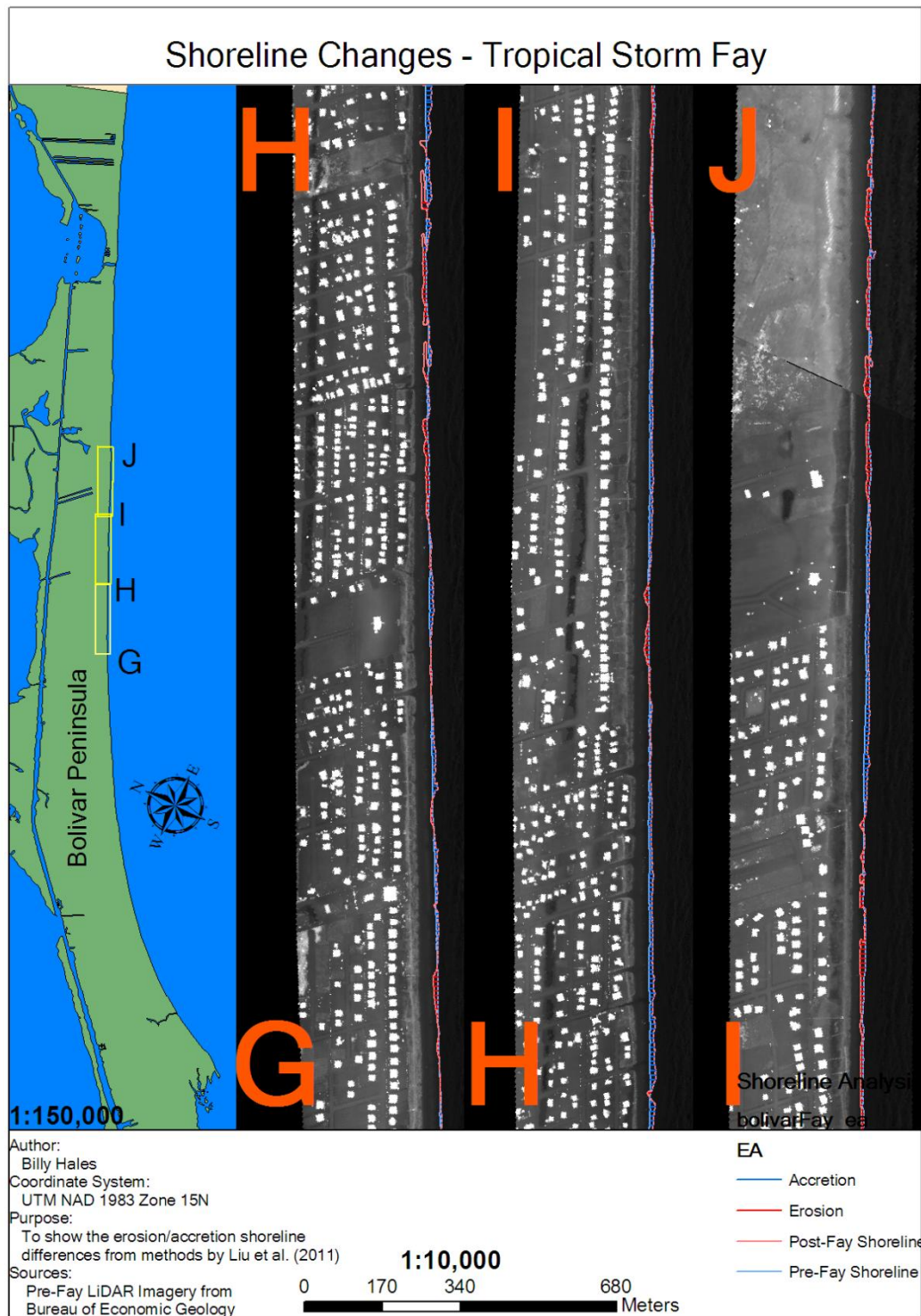


Figure C.3. Section 3/5 of 1:10000 scale shoreline changes - Tropical Storm Fay

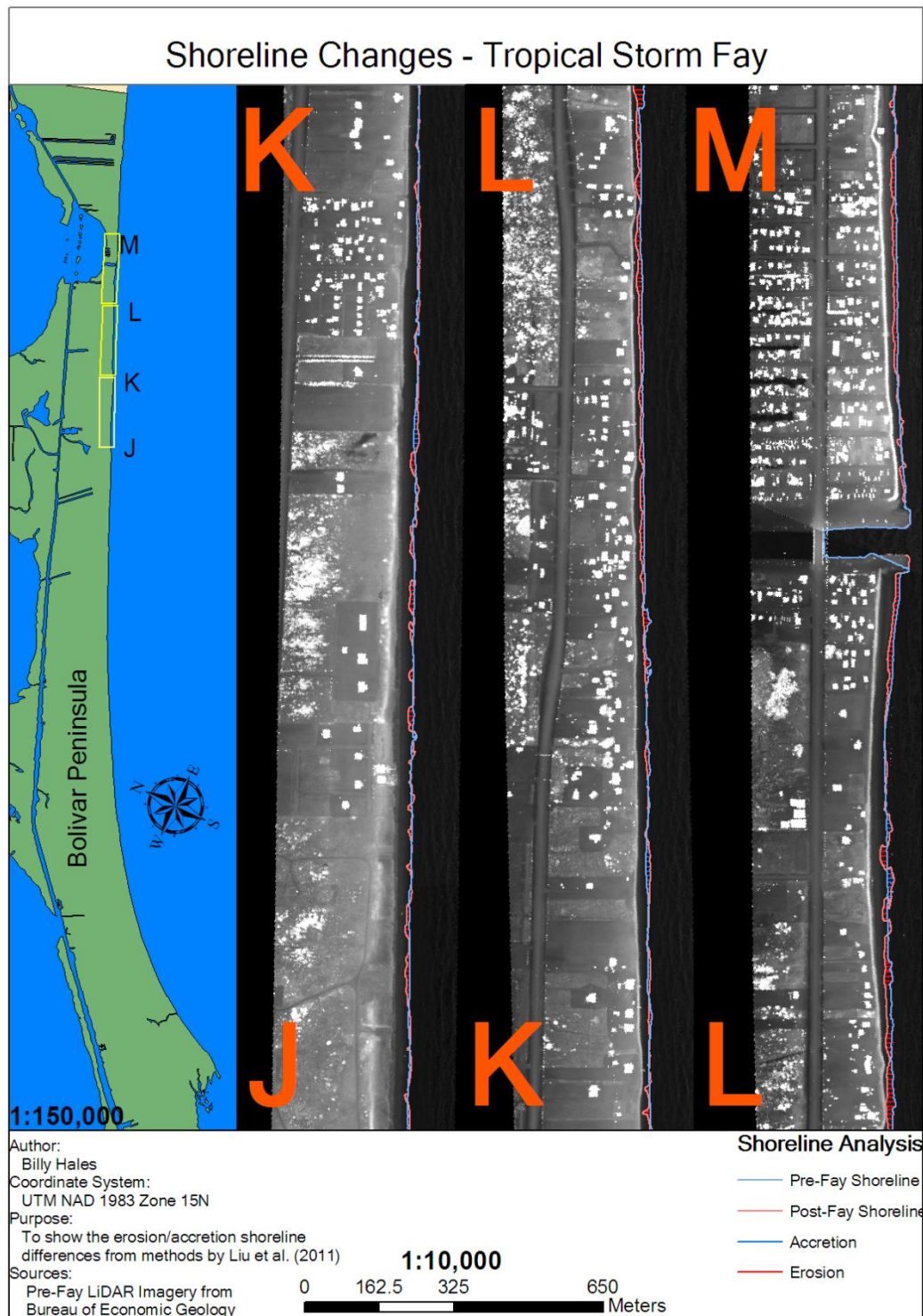


Figure C.4. Section 4/5 of 1:10000 scale shoreline changes - Tropical Storm Fay

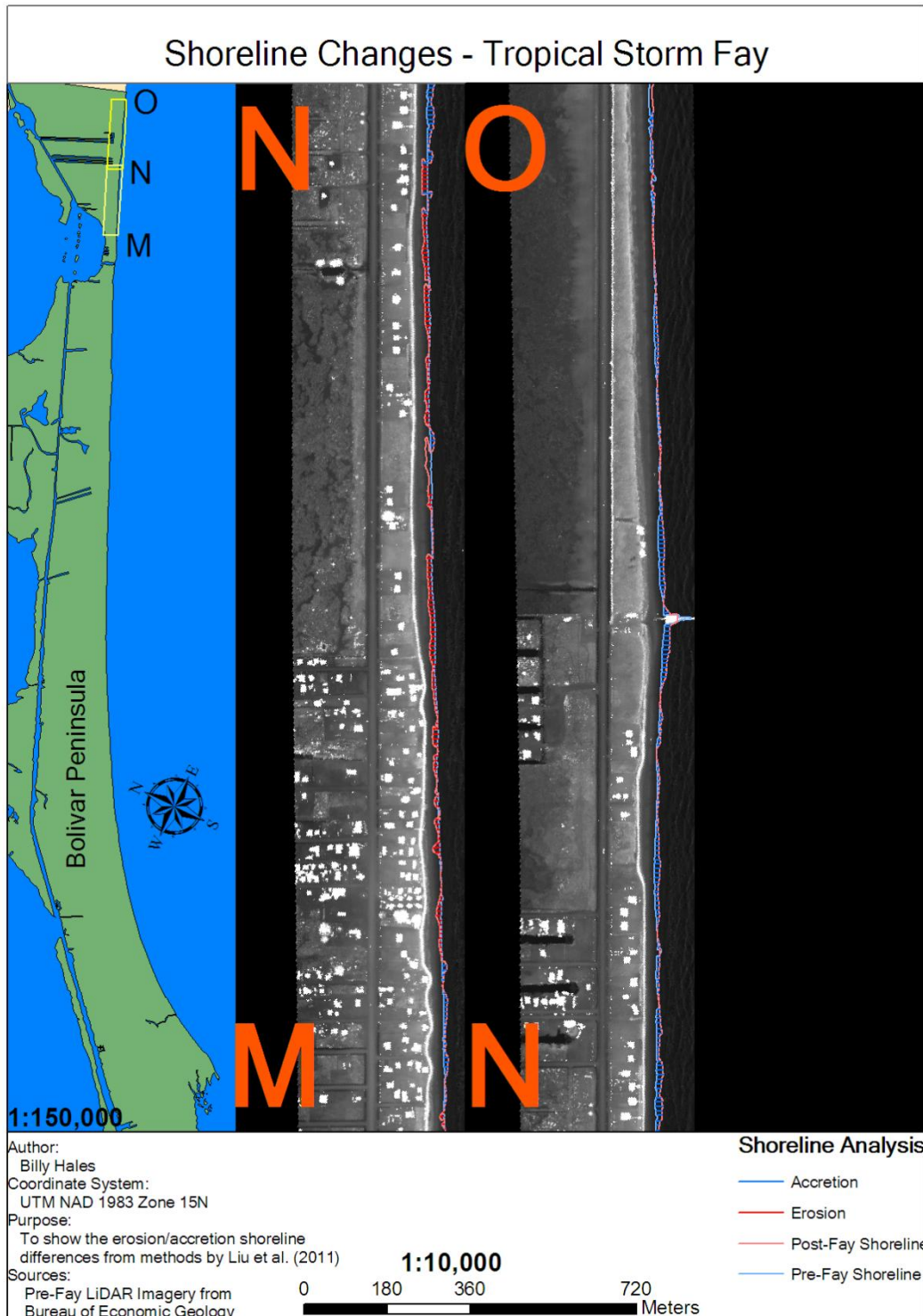


Figure C.5. Section 5/5 of 1:10000 scale shoreline changes - Tropical Storm Fay

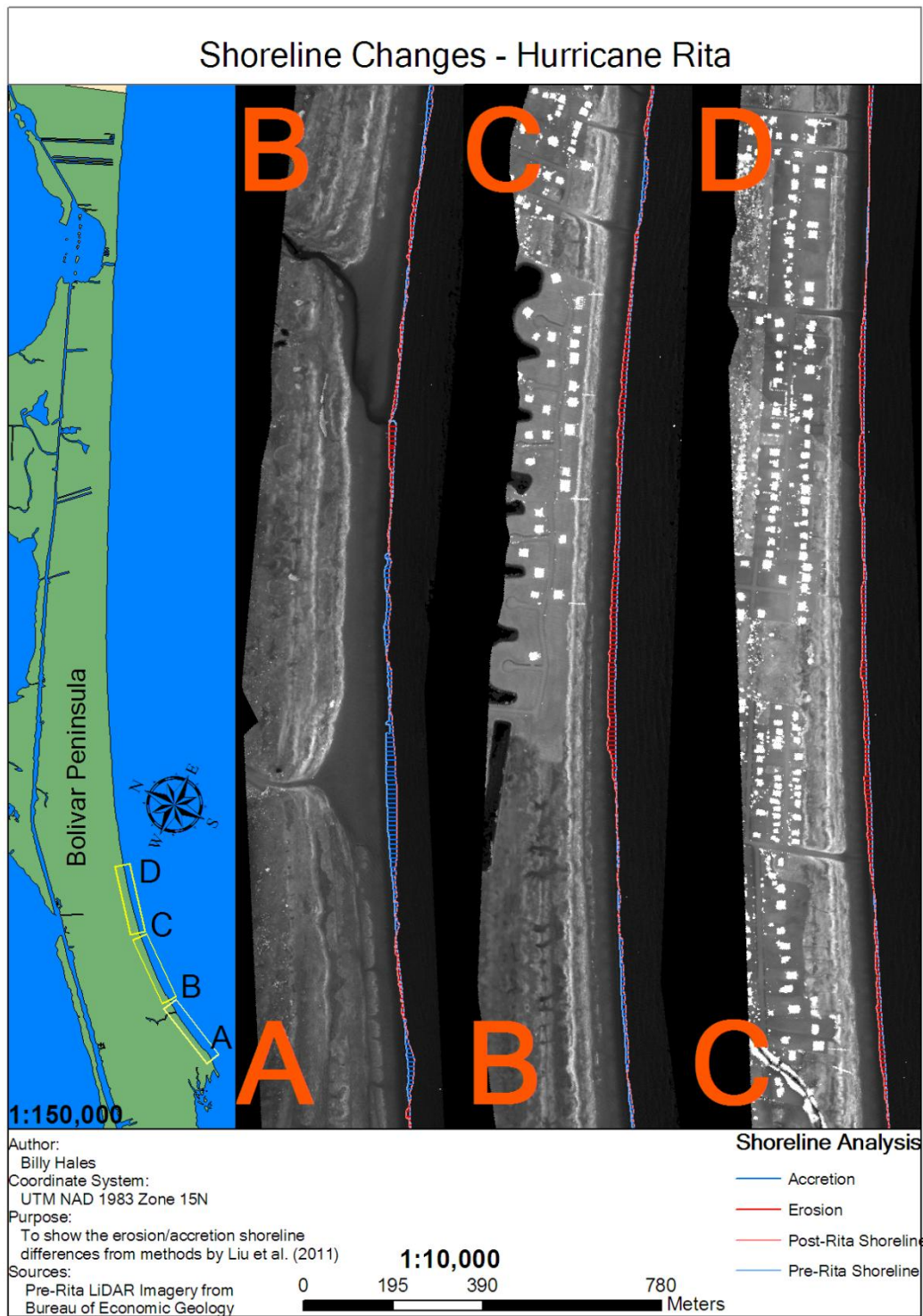


Figure C.6. Section 1/5 of 1:10000 scale shoreline changes - Hurricane Rita

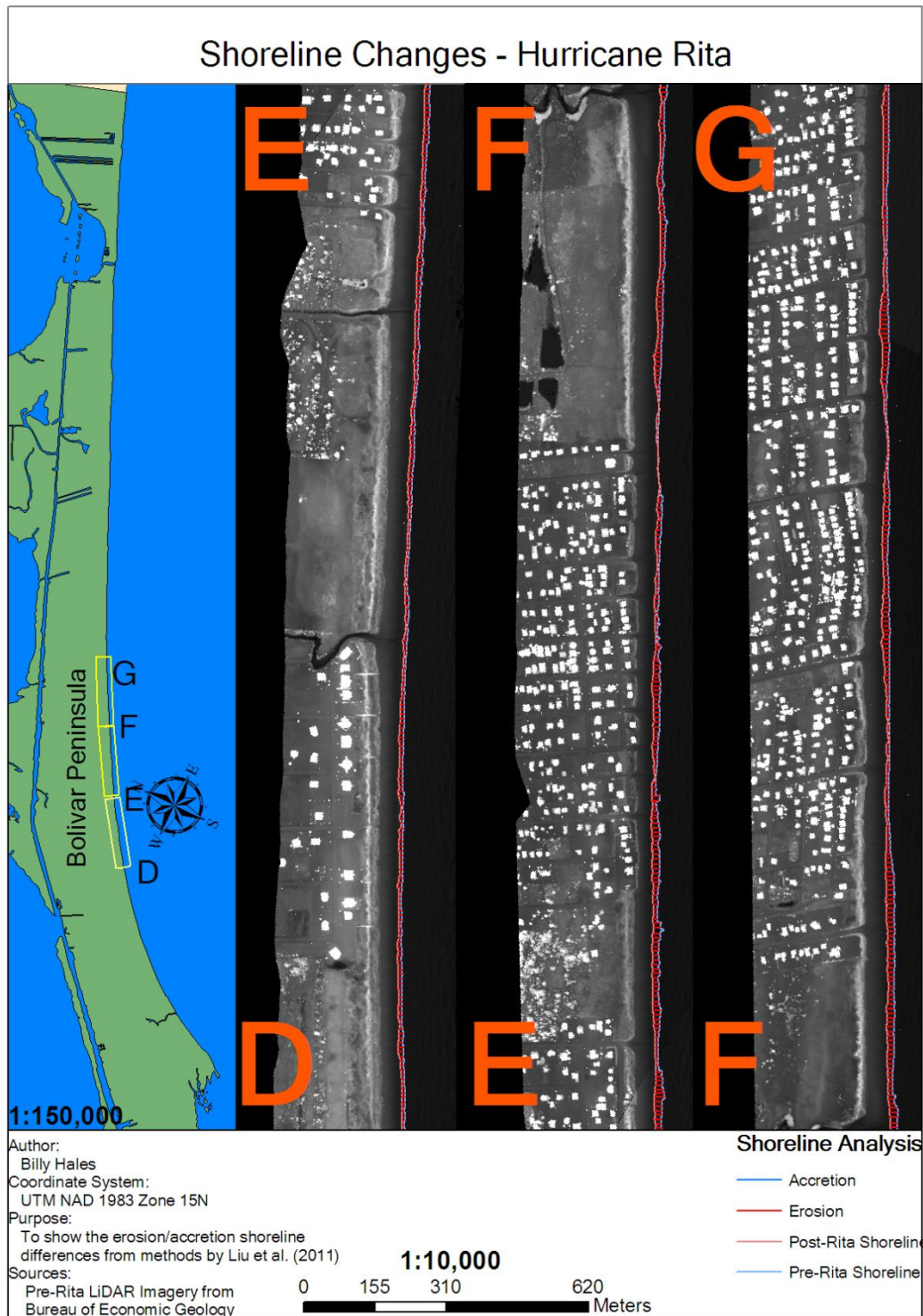


Figure C.7. Section 2/5 of 1:10000 scale shoreline changes - Hurricane Rita

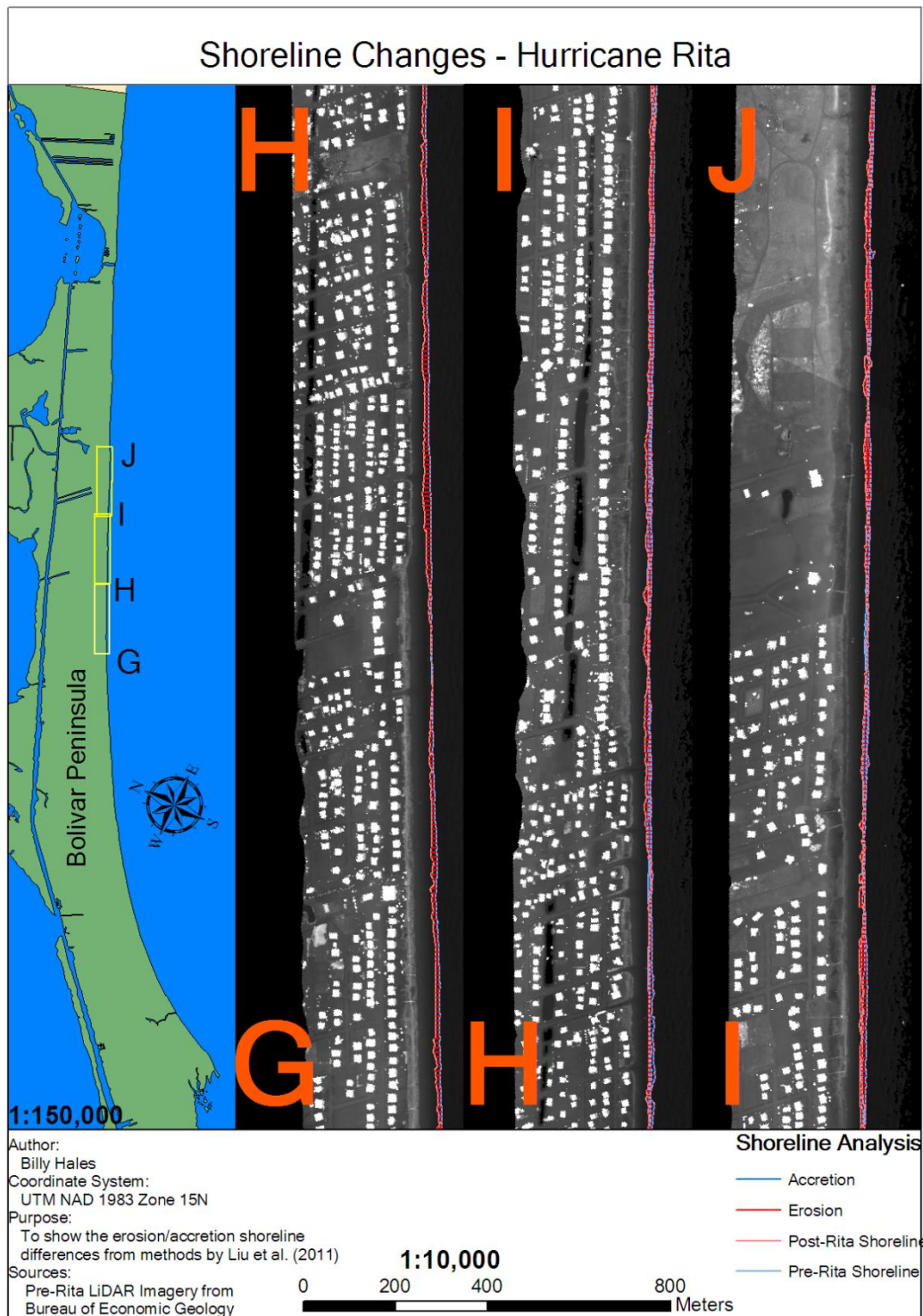


Figure C.8. Section 3/5 of 1:10000 scale shoreline changes - Hurricane Rita

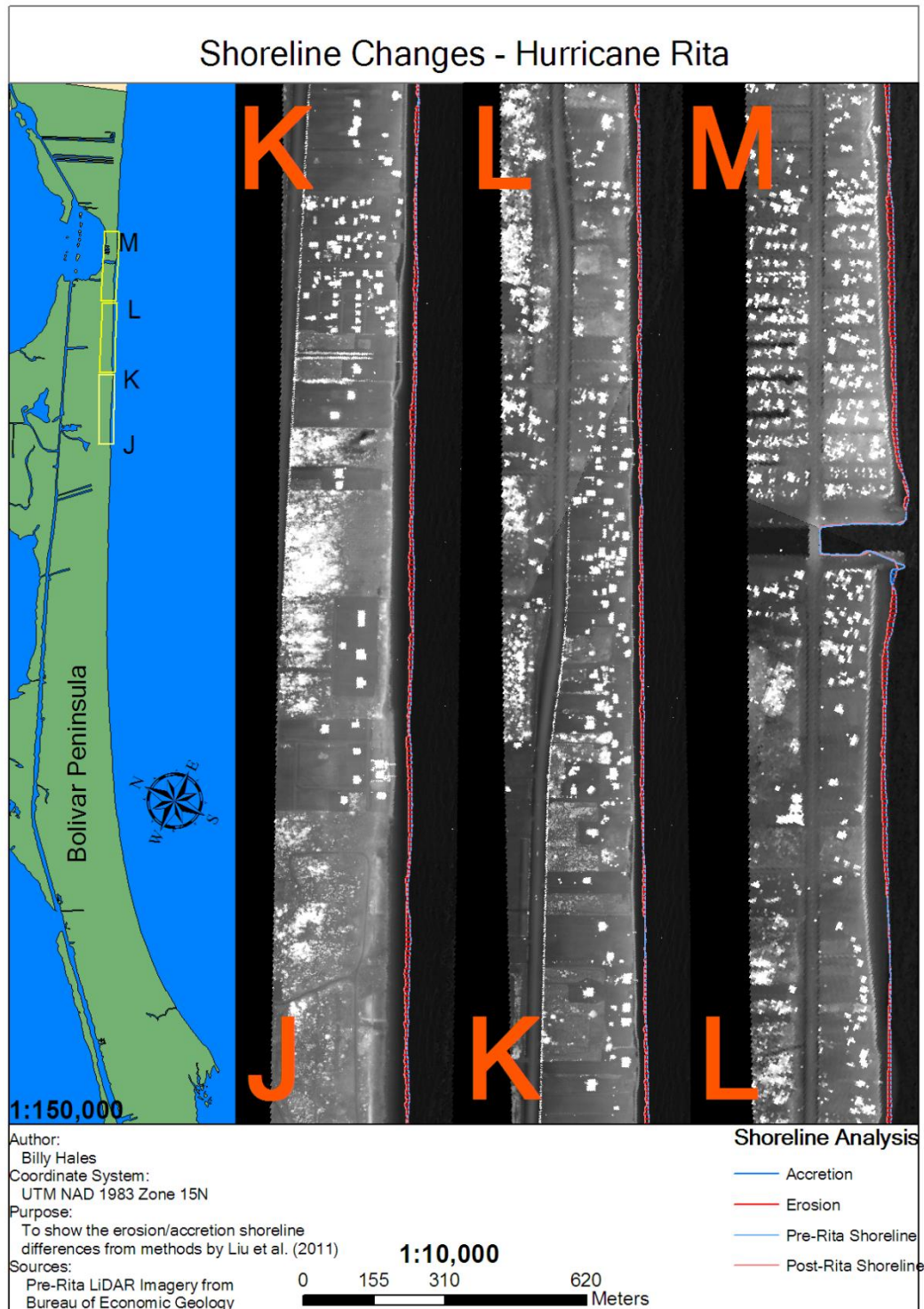


Figure C.9. Section 4/5 of 1:10000 scale shoreline changes - Hurricane Rita.

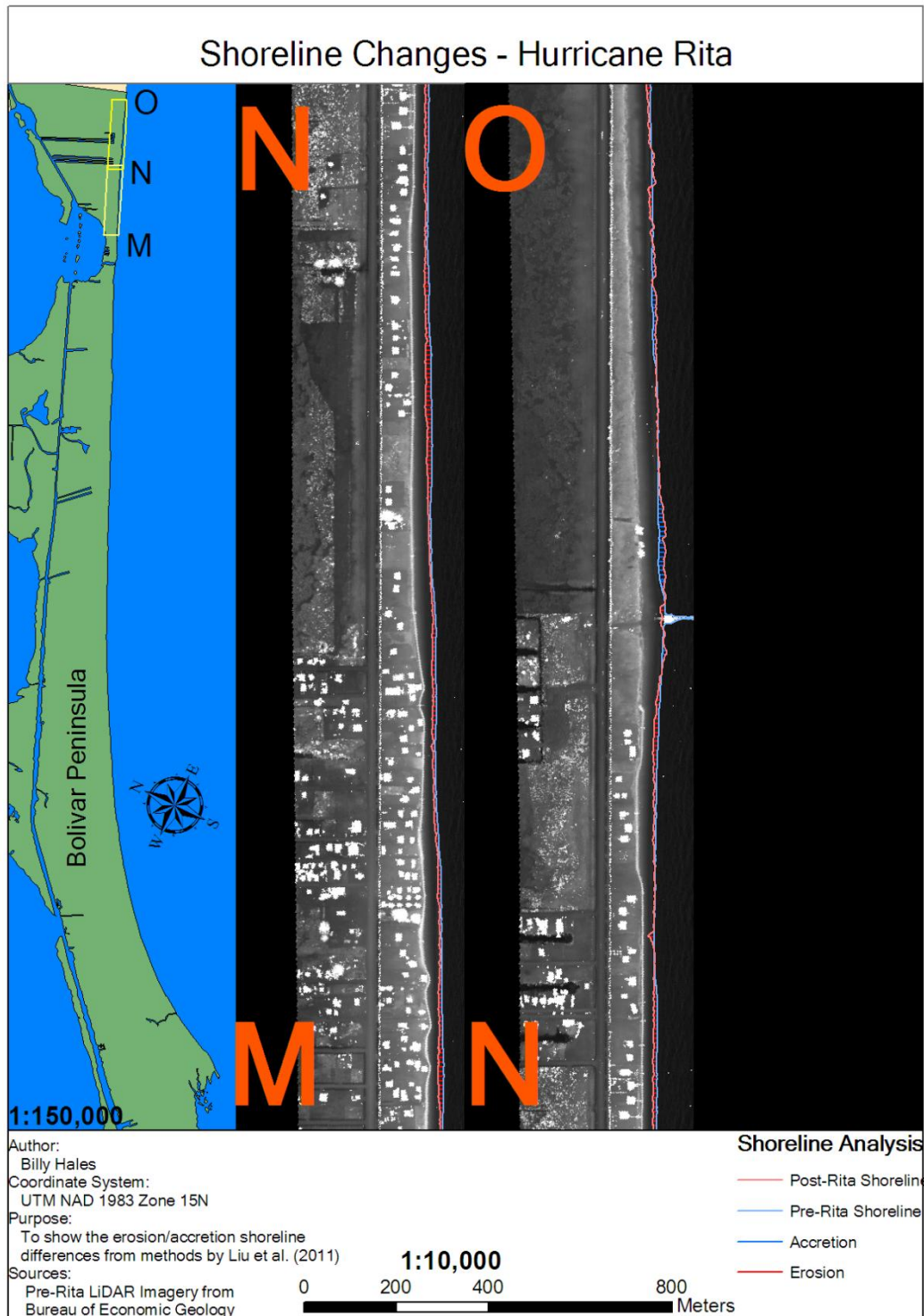


Figure C.10. Section 5/5 of 1:10000 scale shoreline changes - Hurricane Rita.

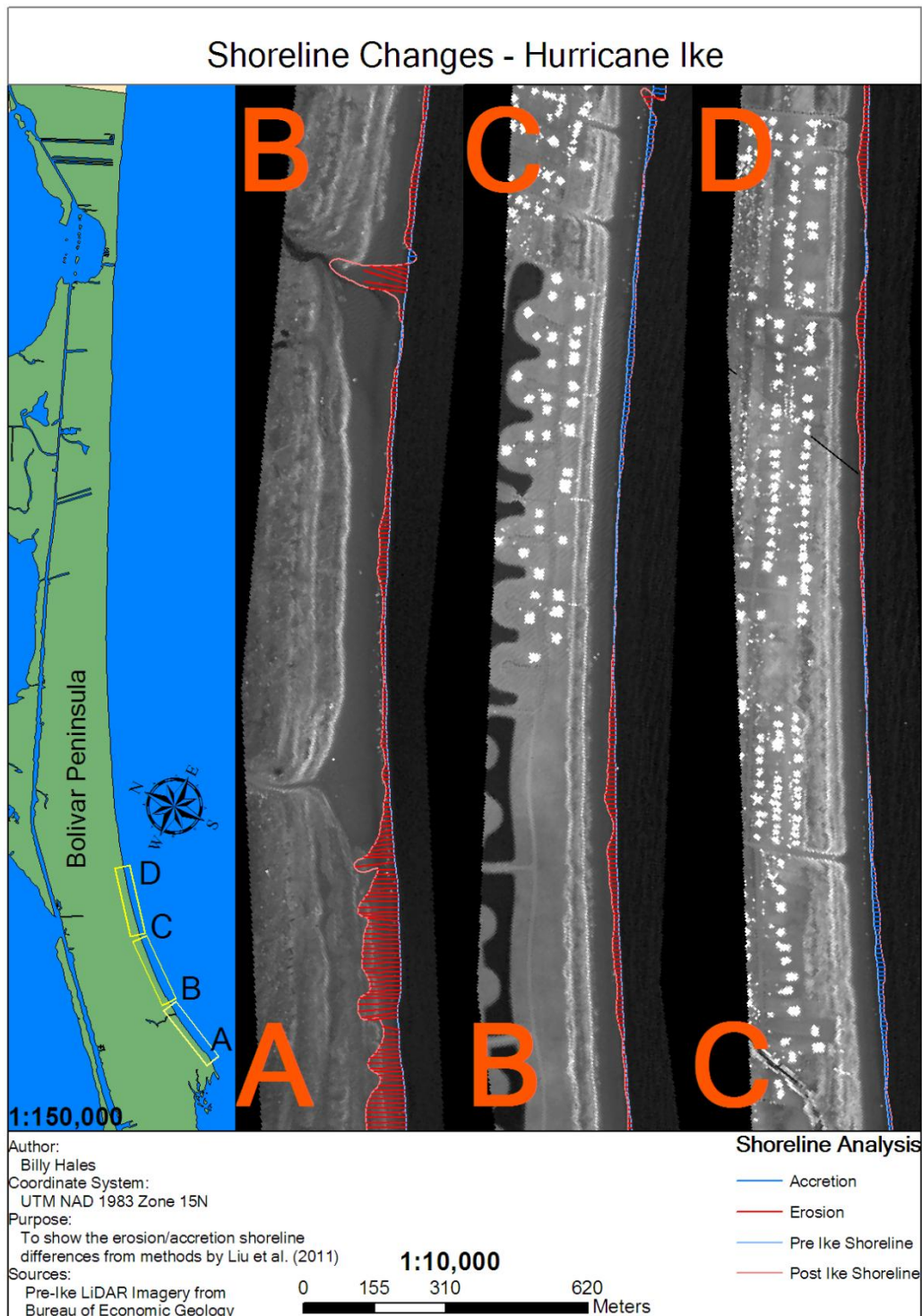


Figure C.11. Section 1/5 of 1:10000 scale shoreline changes - Hurricane Ike.

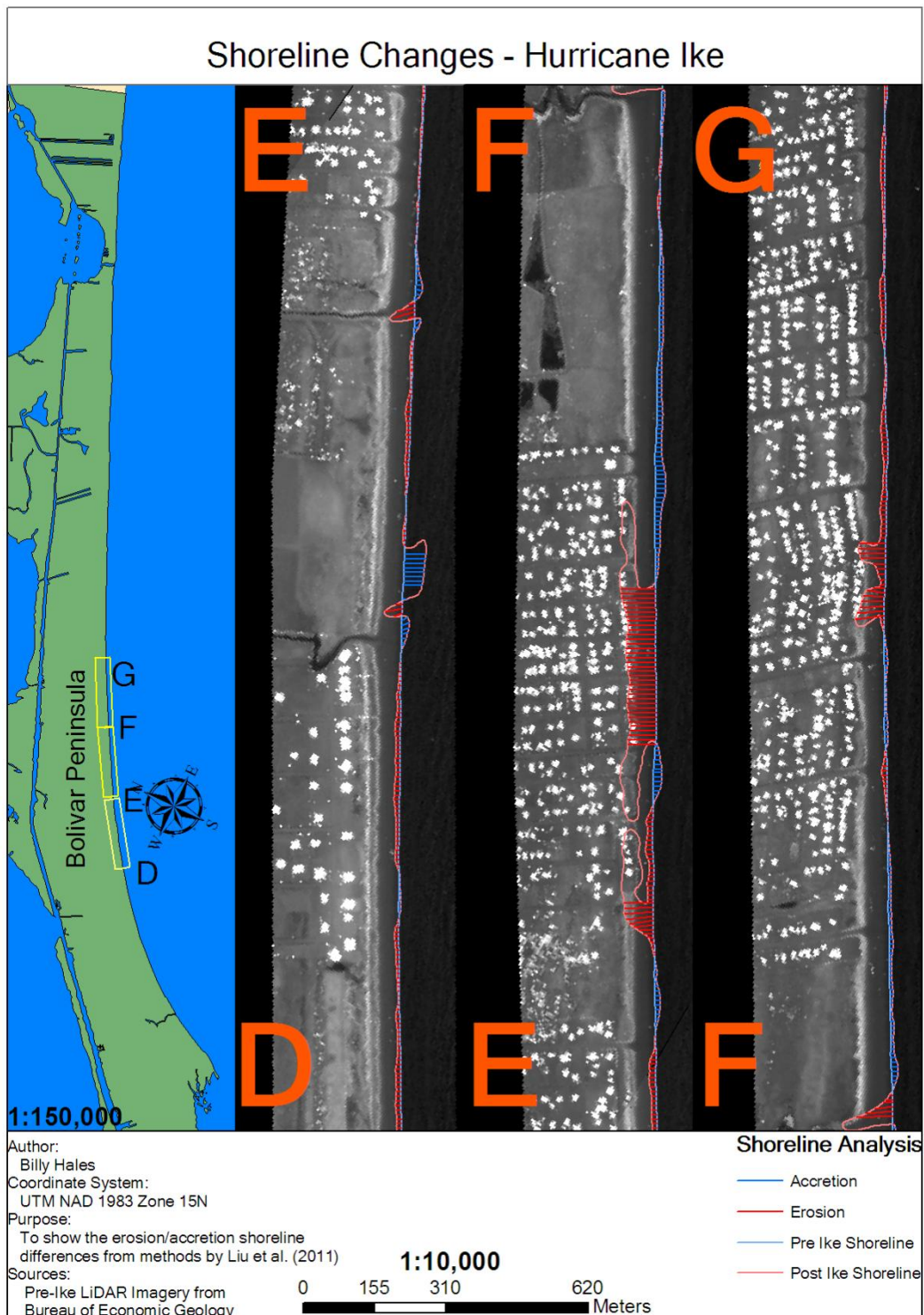


Figure C.12. Section 2/5 of 1:10000 scale shoreline changes - Hurricane Ike.

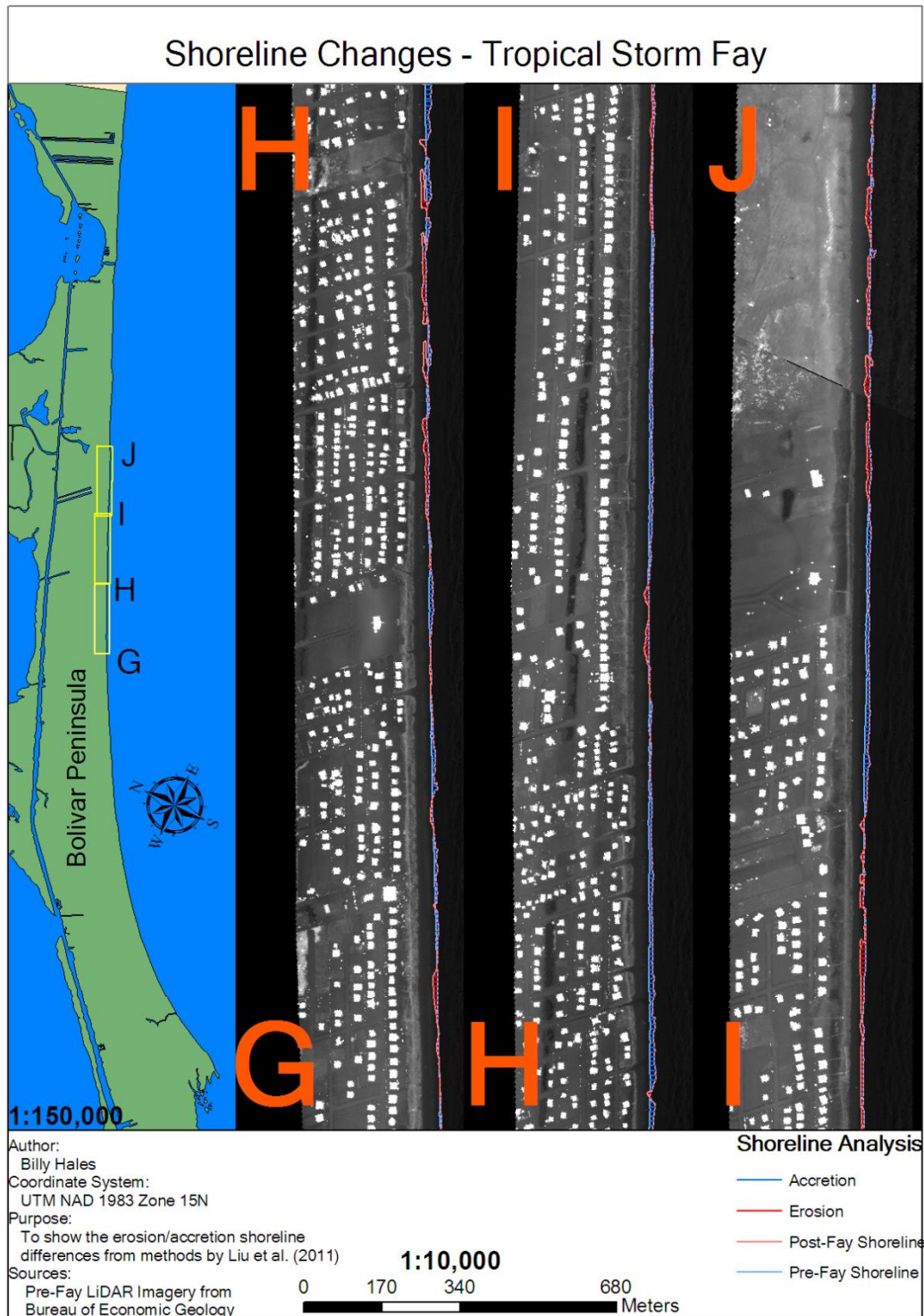


Figure C.13. Section 3/5 of 1:10000 scale shoreline changes - Hurricane Ike.

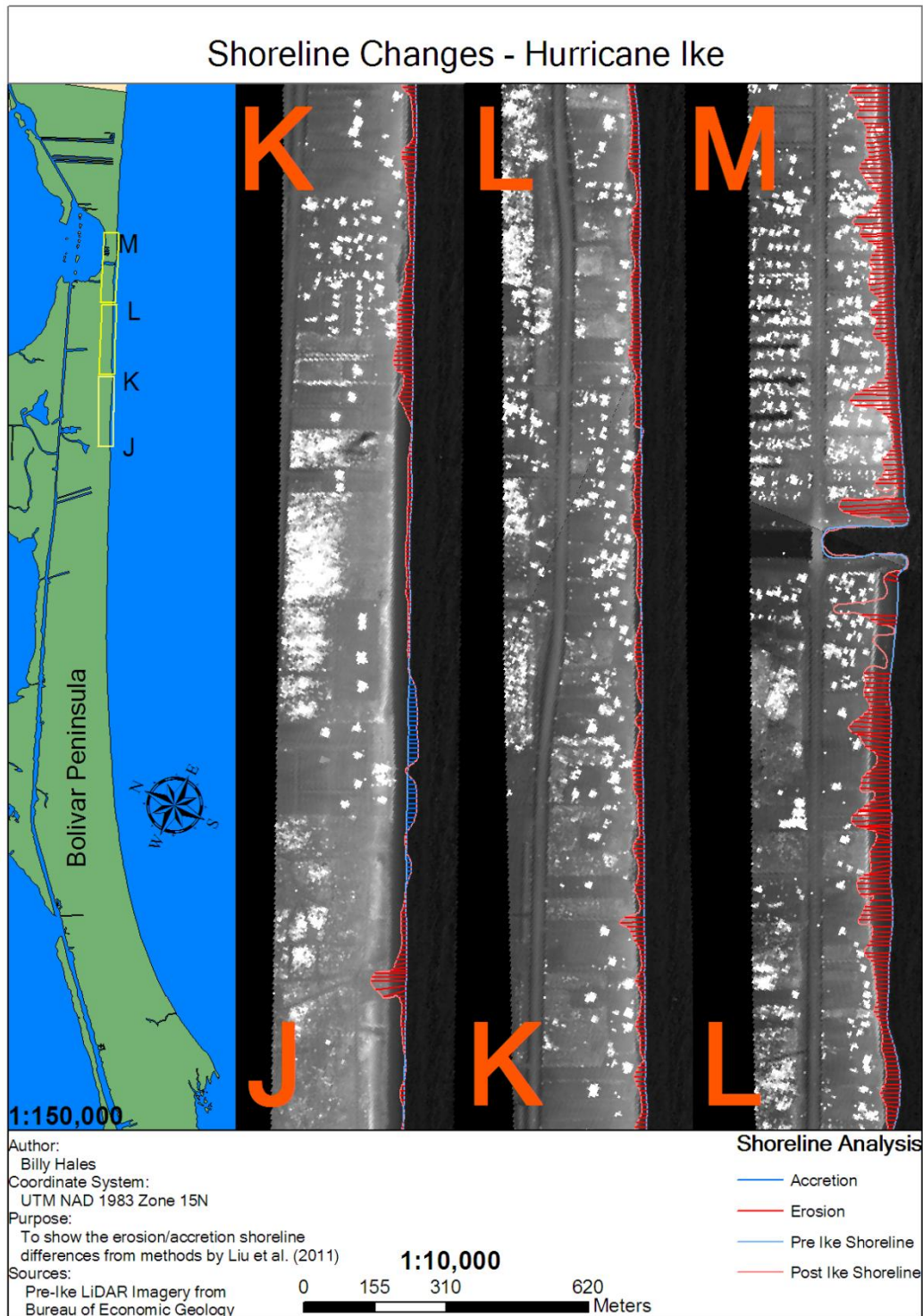


Figure C.14. Section 4/5 of 1:10000 scale shoreline changes - Hurricane Ike.

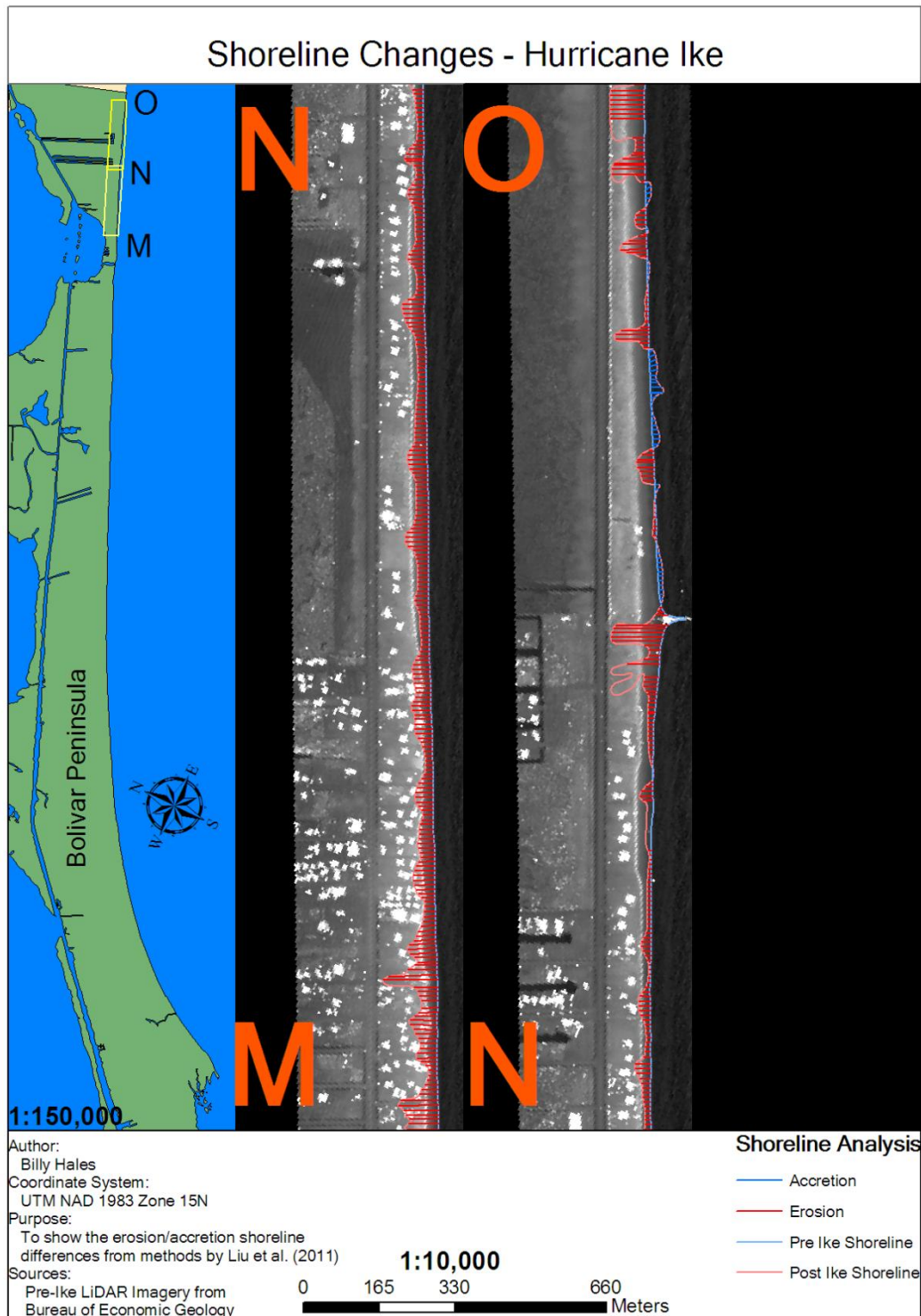


Figure C.15. Section 5/5 of 1:10000 scale shoreline changes - Hurricane Ike.

APPENDIX D
VOLUME CHANGES

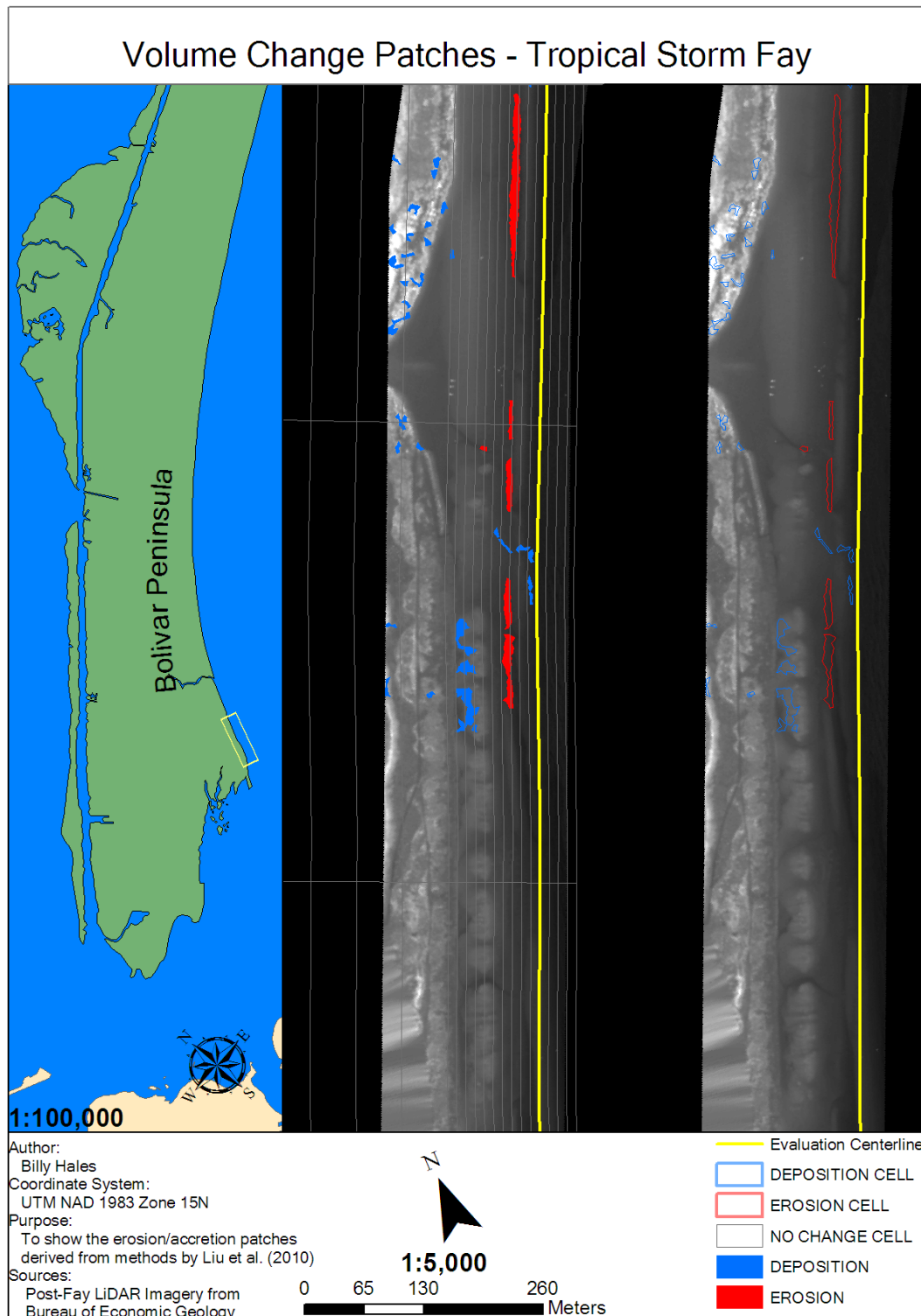


Figure D.1. Tropical Storm Fay section 1/28 of 1:5000 scale volumetric changes. Corresponds to A-B on Figure 4.12.

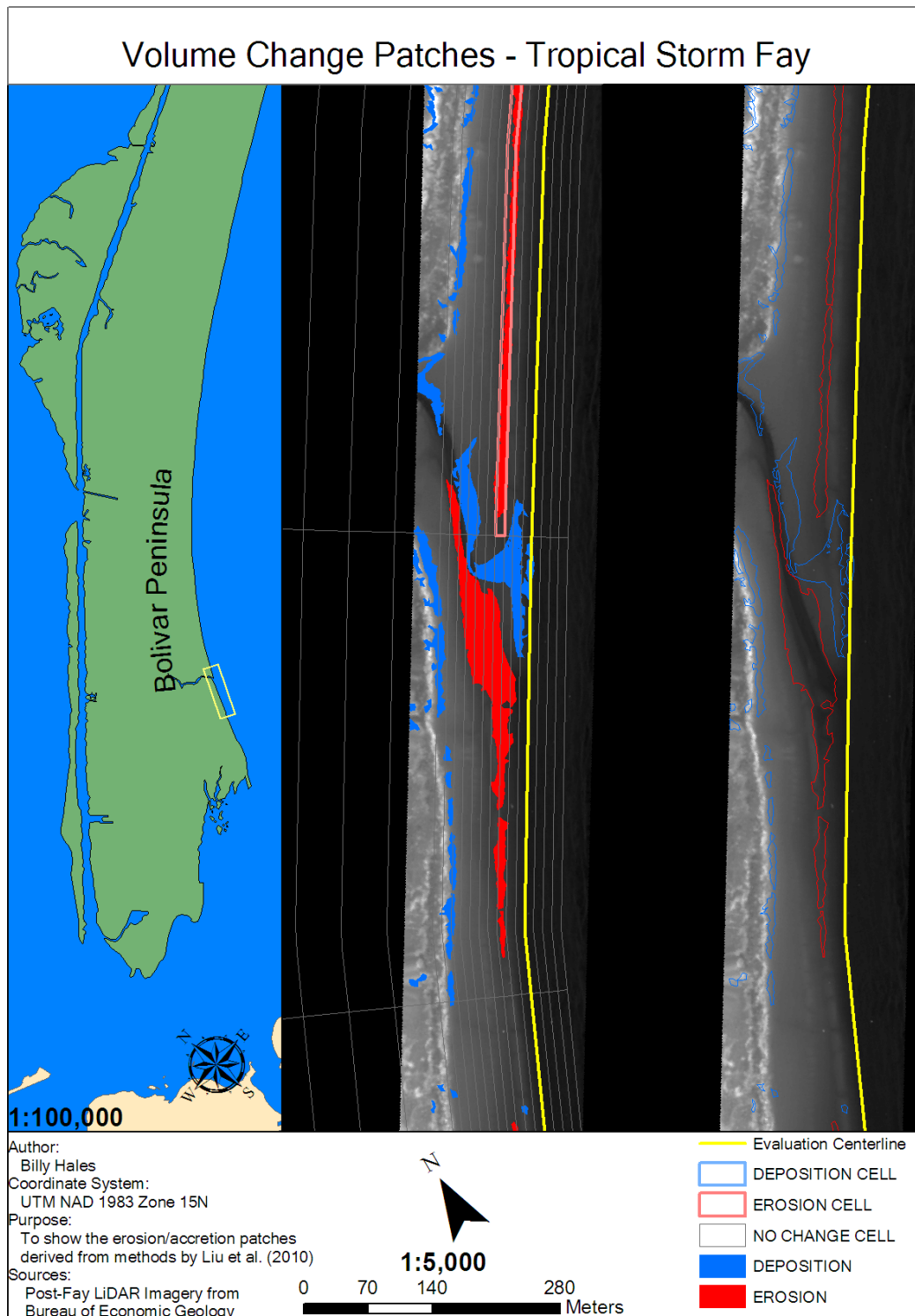


Figure D.2. Tropical Storm Fay section 2/28 of 1:5000 scale volumetric changes. Corresponds to A-B,B-C on Figure 4.12.

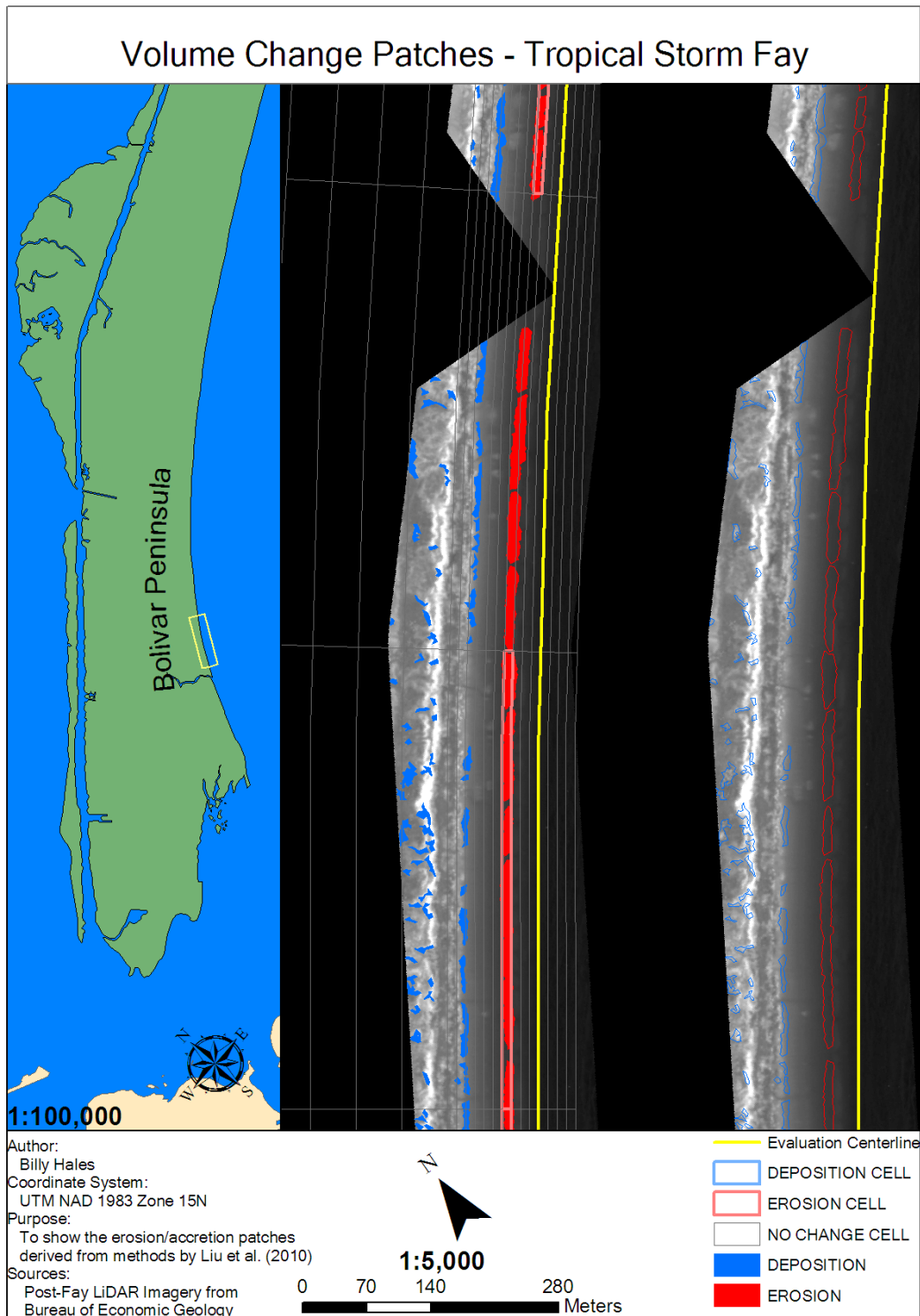


Figure D.3. Tropical Storm Fay section 3/28 of 1:5000 scale volumetric changes. Corresponds to B-C,C-D on Figure 4.12.

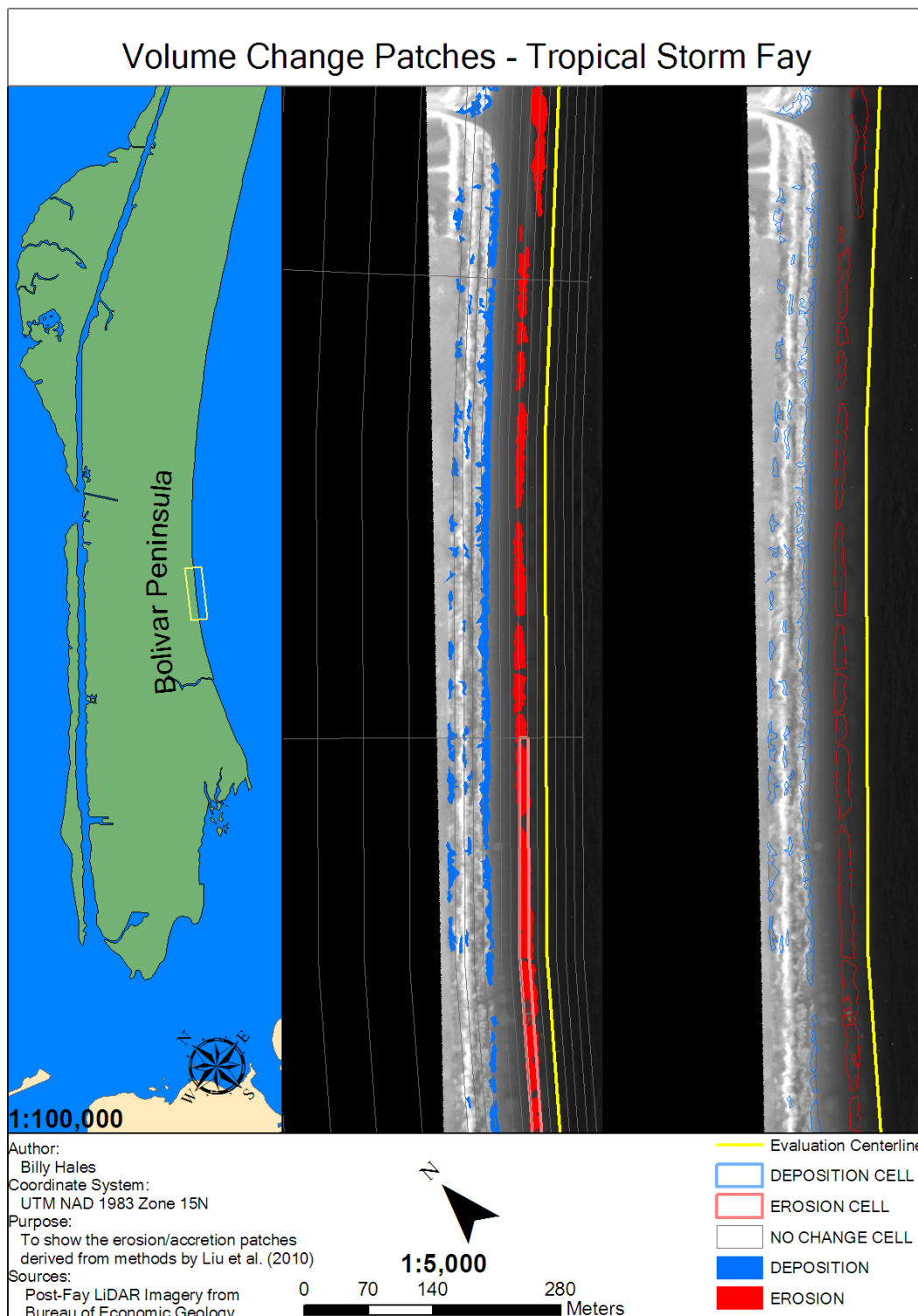


Figure D.4. Tropical Storm Fay section 4/28 of 1:5000 scale volumetric changes. Corresponds to C-D on Figure 4.12.

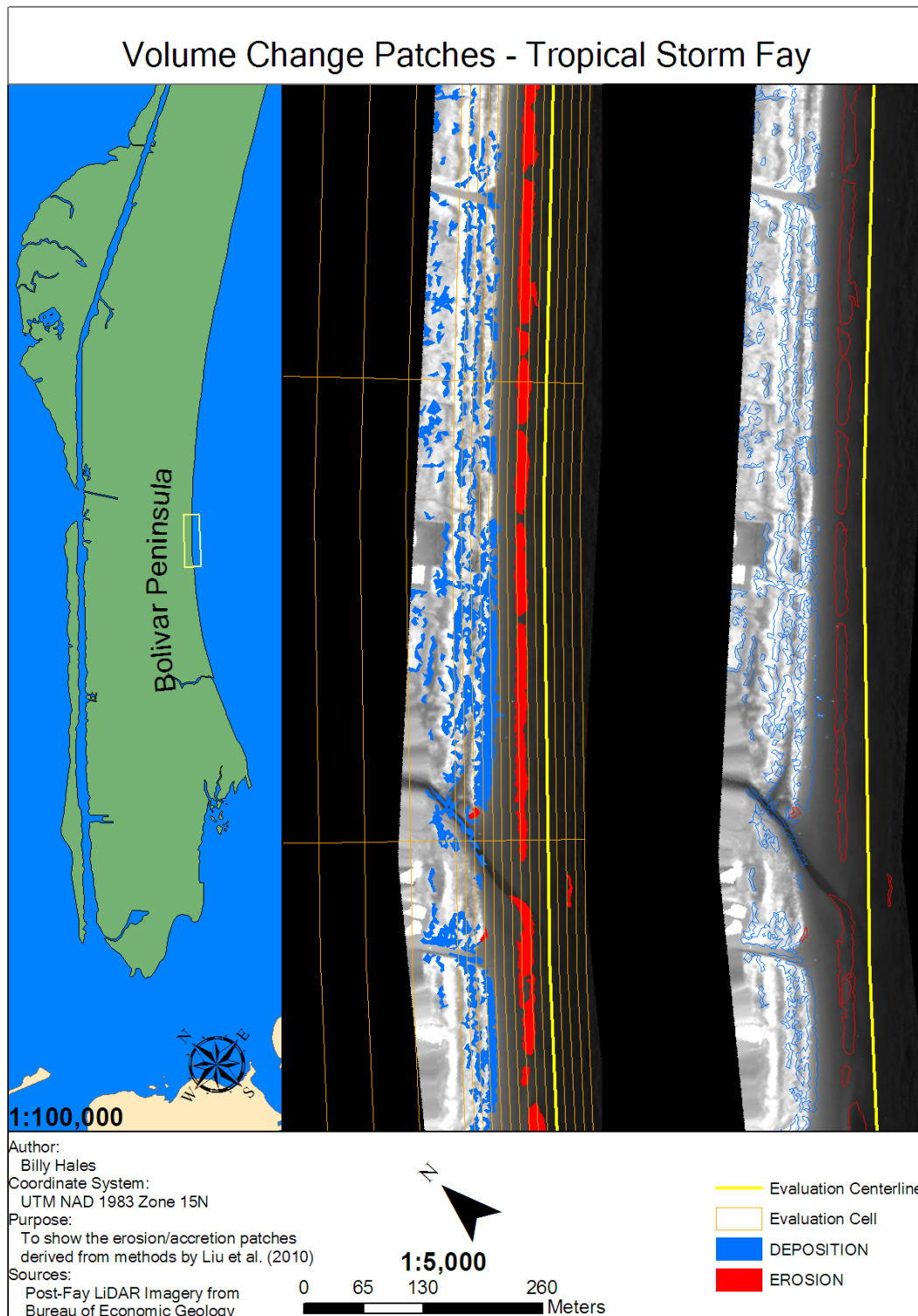


Figure D.5. Tropical Storm Fay section 5/28 of 1:5000 scale volumetric changes. Corresponds to C-D,D-E on Figures 4.12, 4.13.

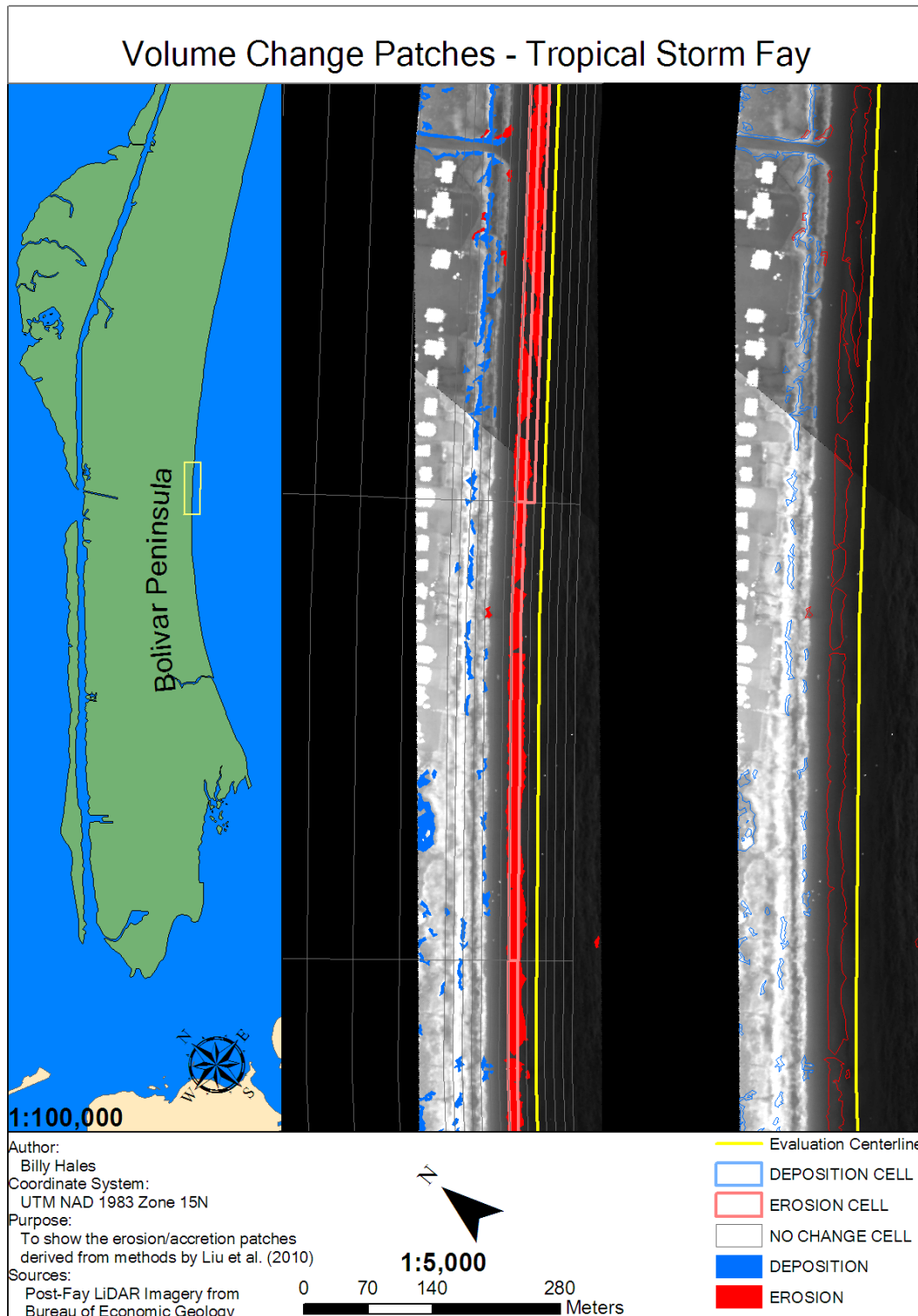


Figure D.6. Tropical Storm Fay section 6/28 of 1:5000 scale volumetric changes. Corresponds to D-E on Figure 4.13.

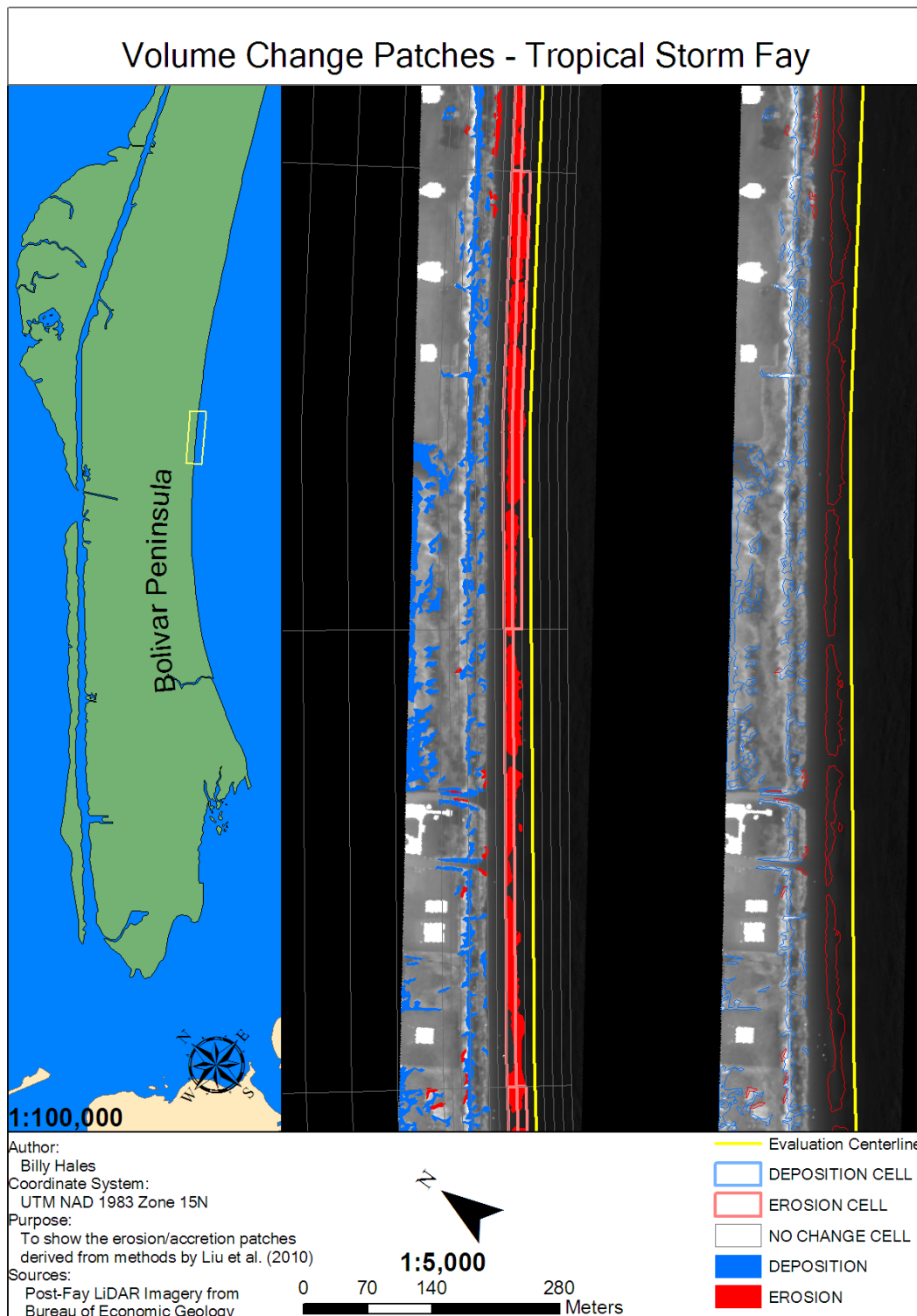


Figure D.7. Tropical Storm Fay section 7/28 of 1:5000 scale volumetric changes. Corresponds to E-F on Figure 4.13.

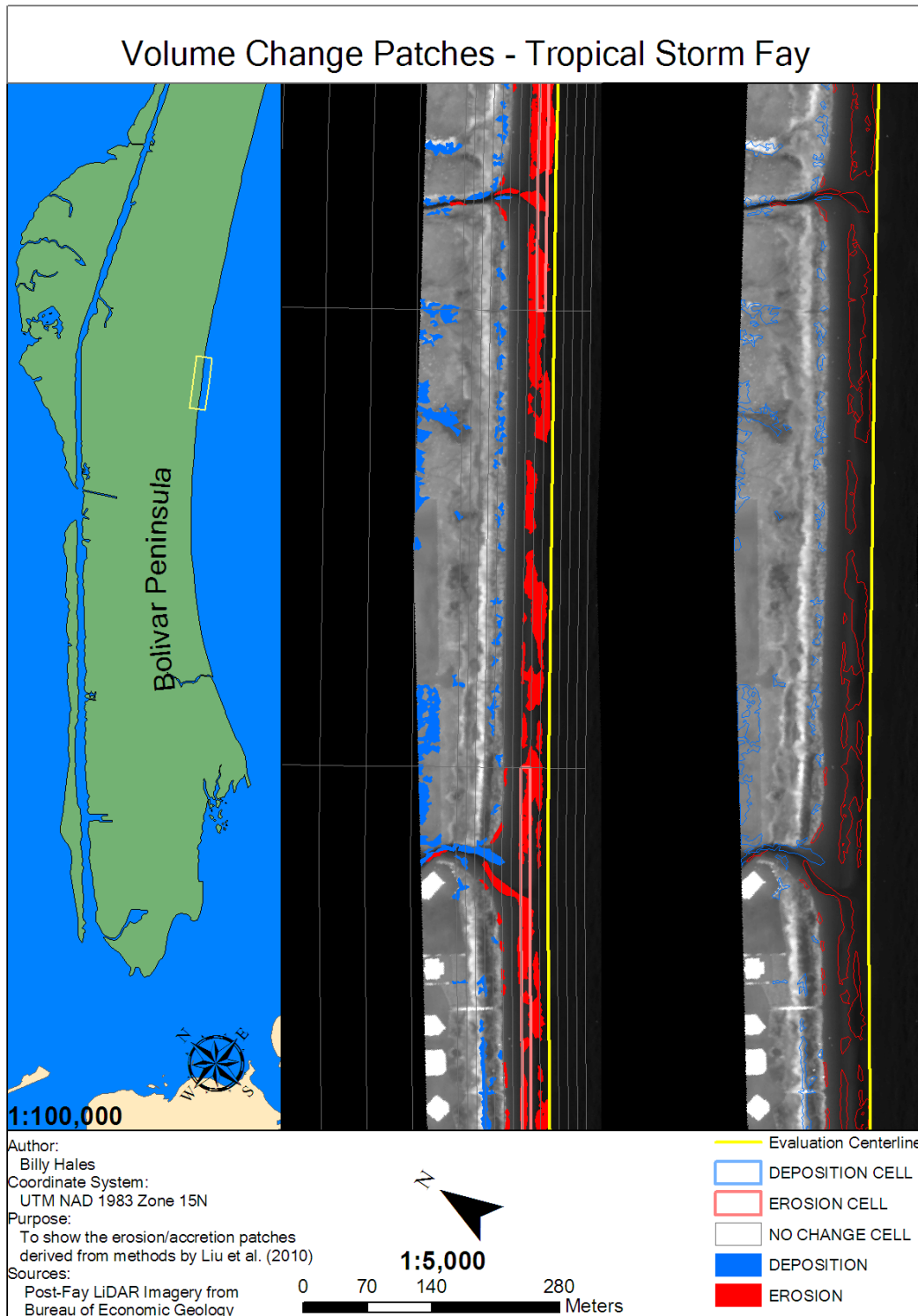


Figure D.8. Tropical Storm Fay section 8/28 of 1:5,000 scale volumetric changes. Corresponds to E-F,F-G on Figure 4.13.

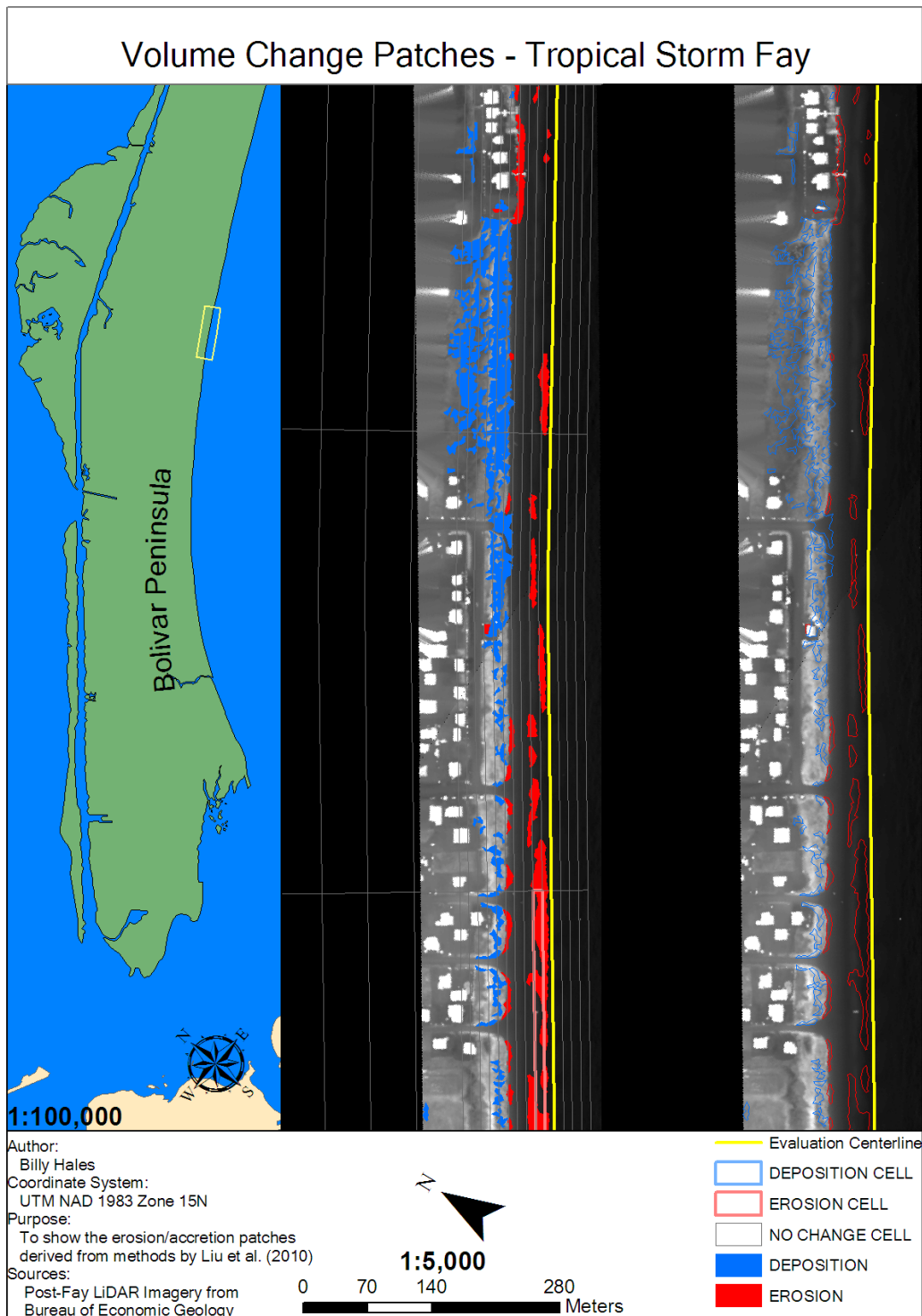


Figure D.9. Tropical Storm Fay section 9/28 of 1:5000 scale volumetric changes. Corresponds to F-G on Figure 4.13.

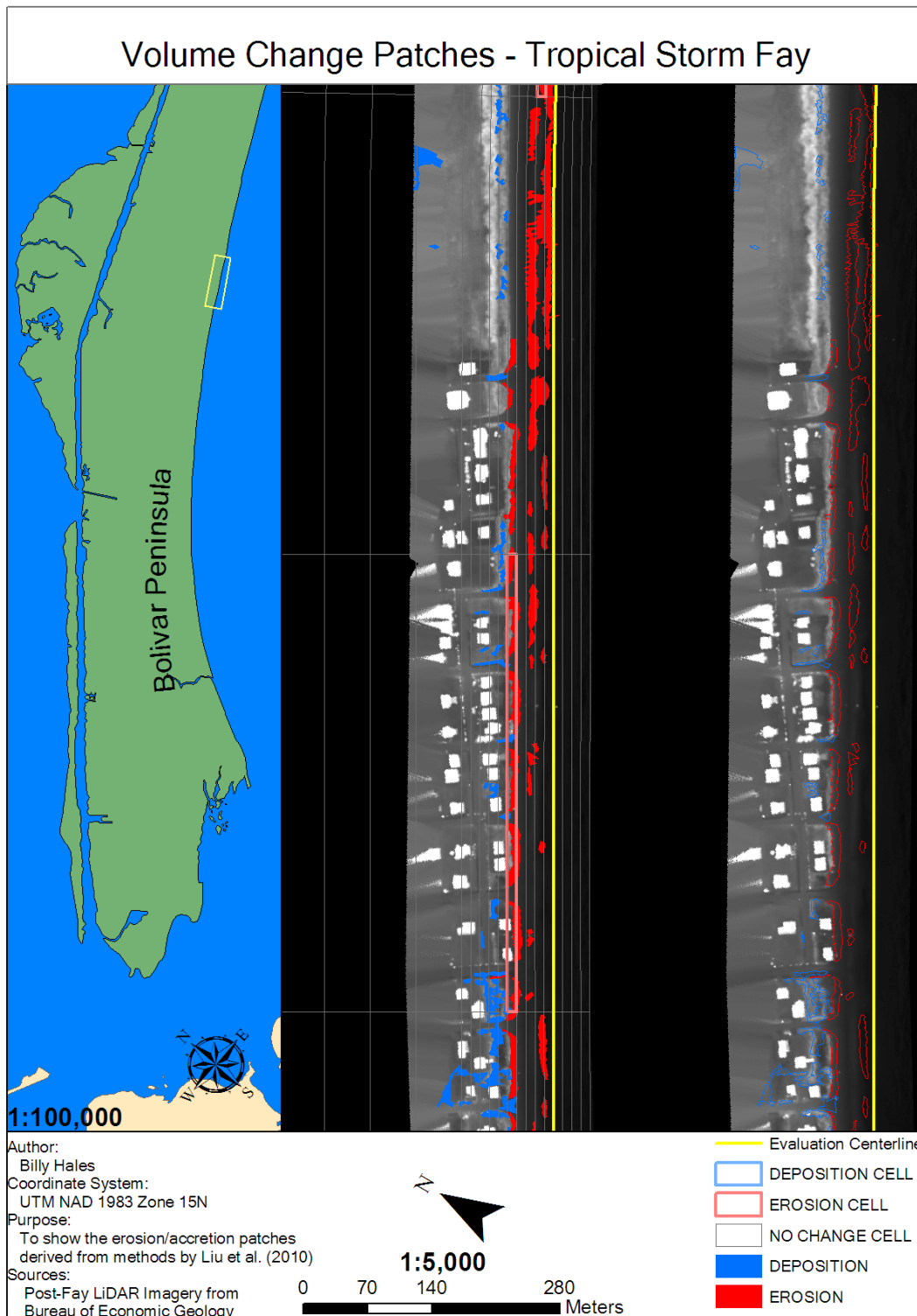


Figure D.10. Tropical Storm Fay section 10/28 of 1:5000 scale volumetric changes. Corresponds to F-G,G-H on Figures 4.13 and 4.14.

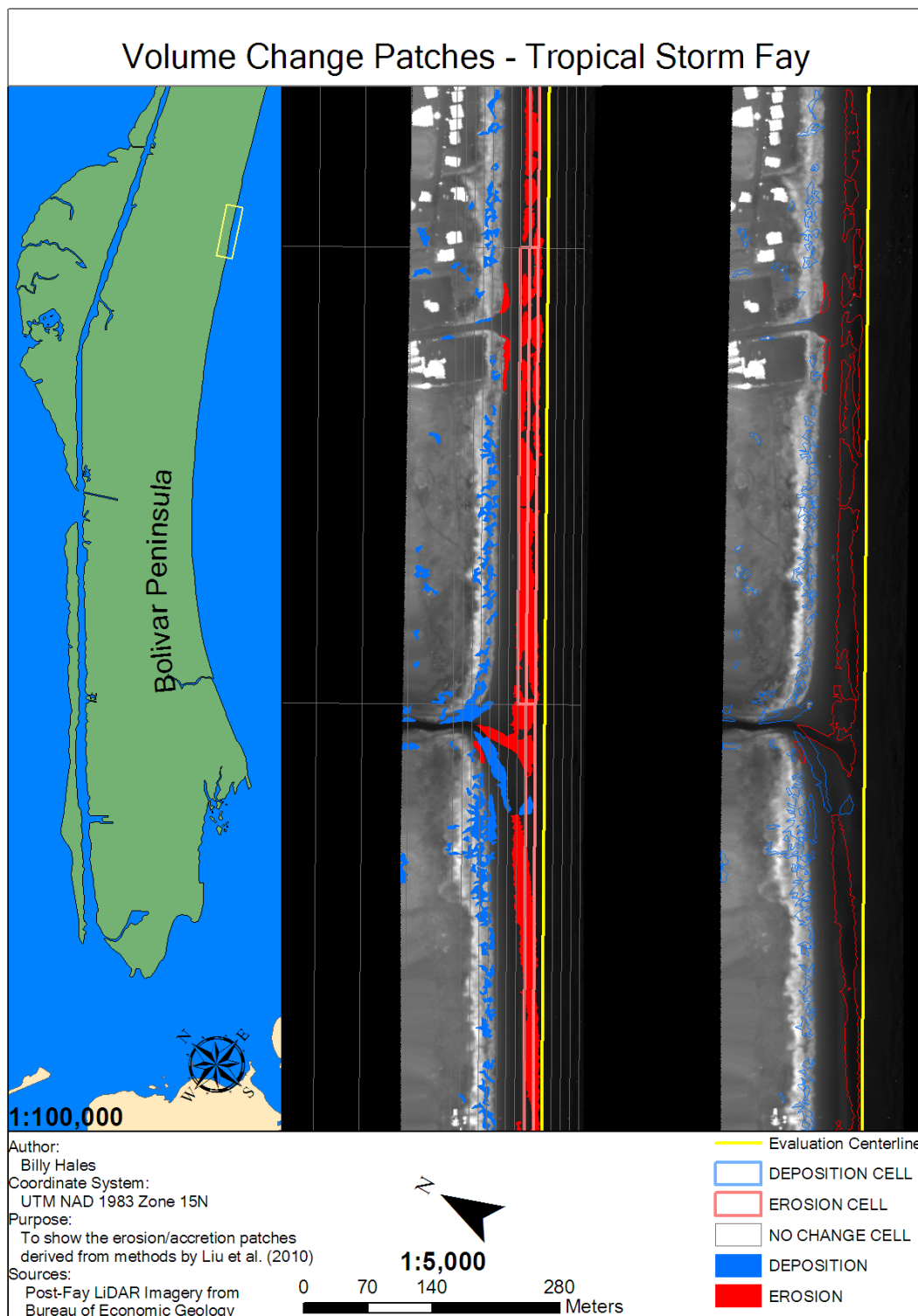


Figure D.11. Tropical Storm Fay section 11/28 of 1:5000 scale volumetric changes. Corresponds to G-H on Figure 4.14.

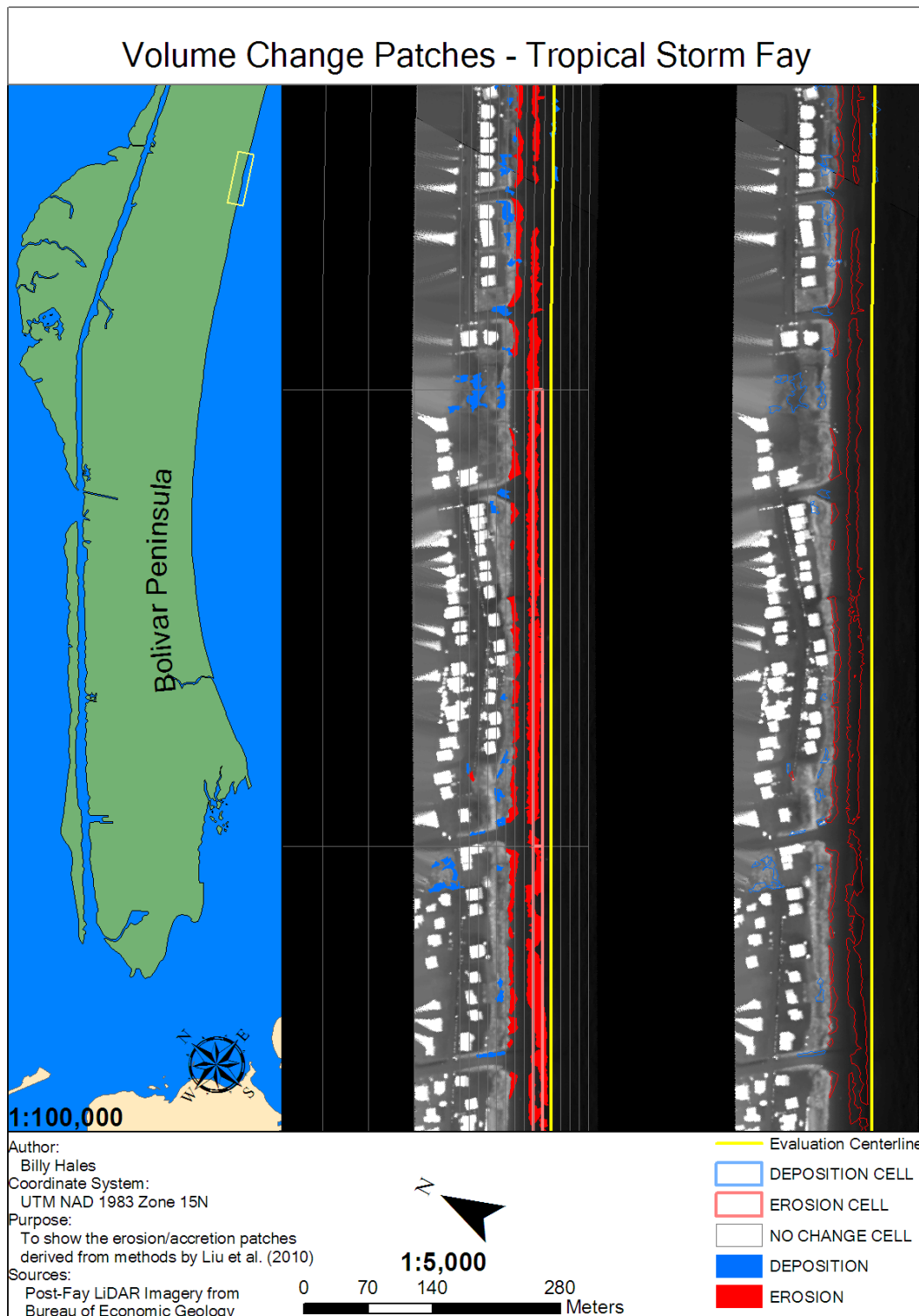


Figure D.12. Tropical Storm Fay section 12/28 of 1:5000 scale volumetric changes. Corresponds to H-I on Figure 4.14.

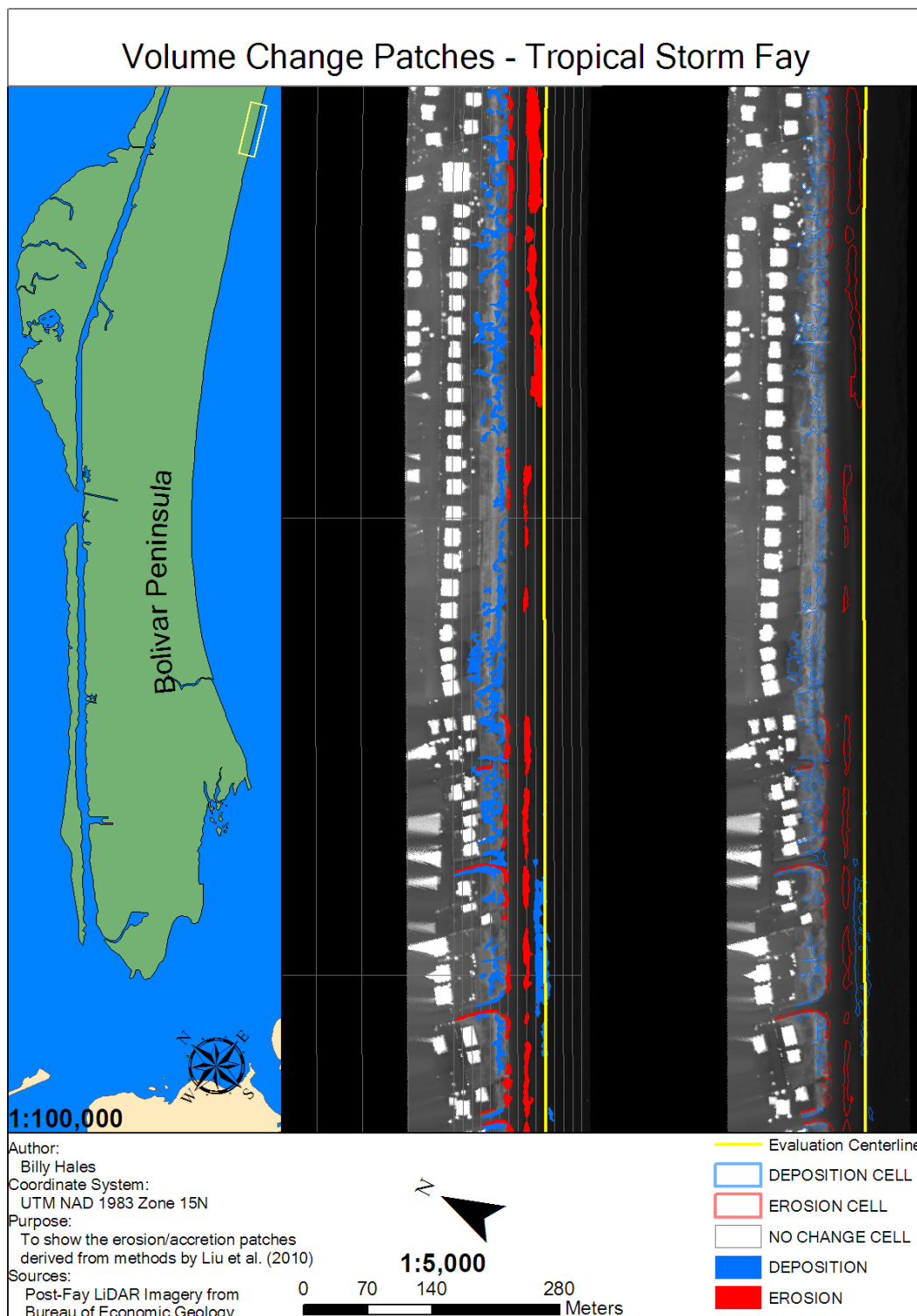


Figure D.13. Tropical Storm Fay section 13/28 of 1:5000 scale volumetric changes. Corresponds to H-I,I-J on Figure 4.14.

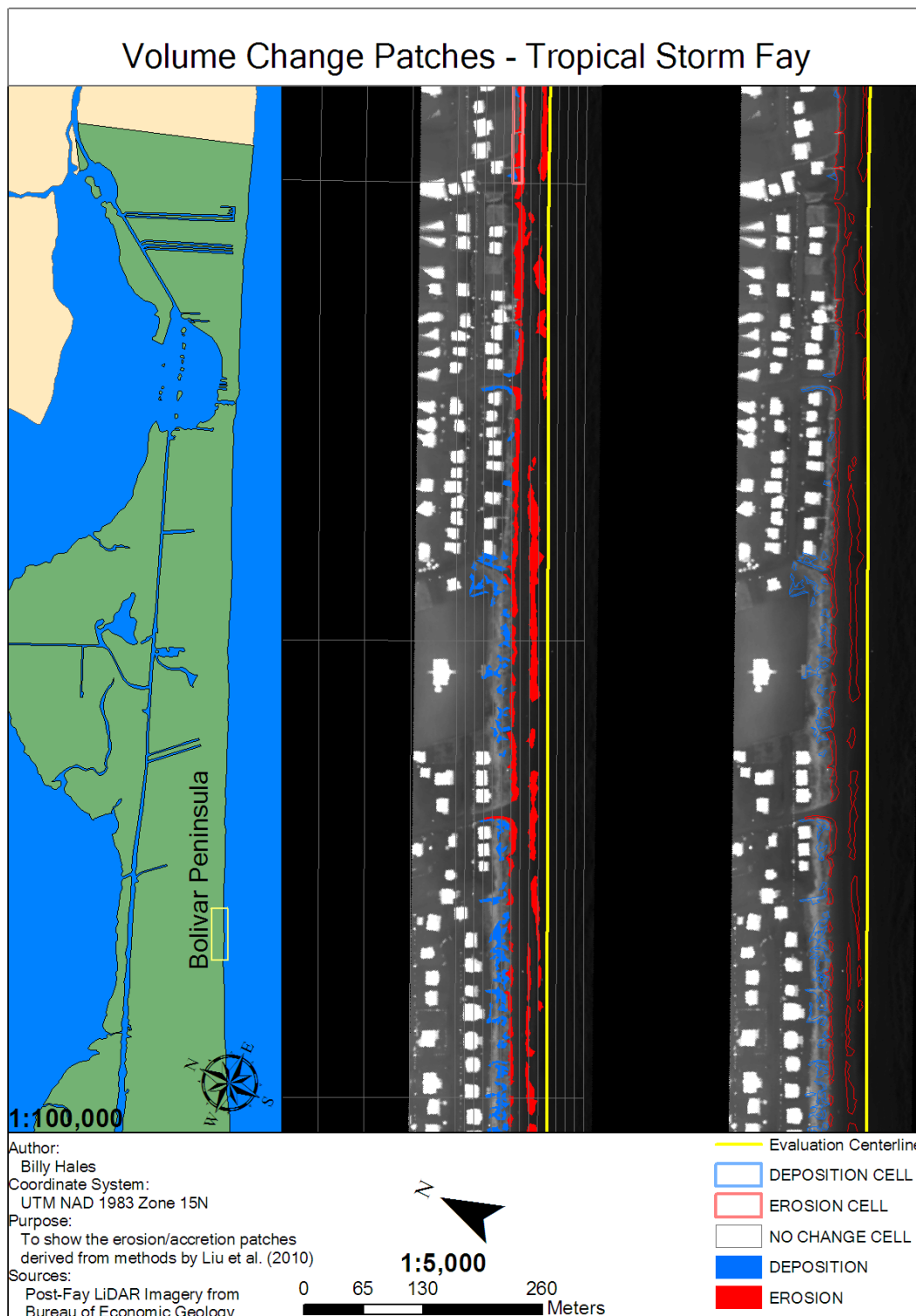


Figure D.14. Tropical Storm Fay section 14/28 of 1:5000 scale volumetric changes. Corresponds to I-J on Figure 4.14.

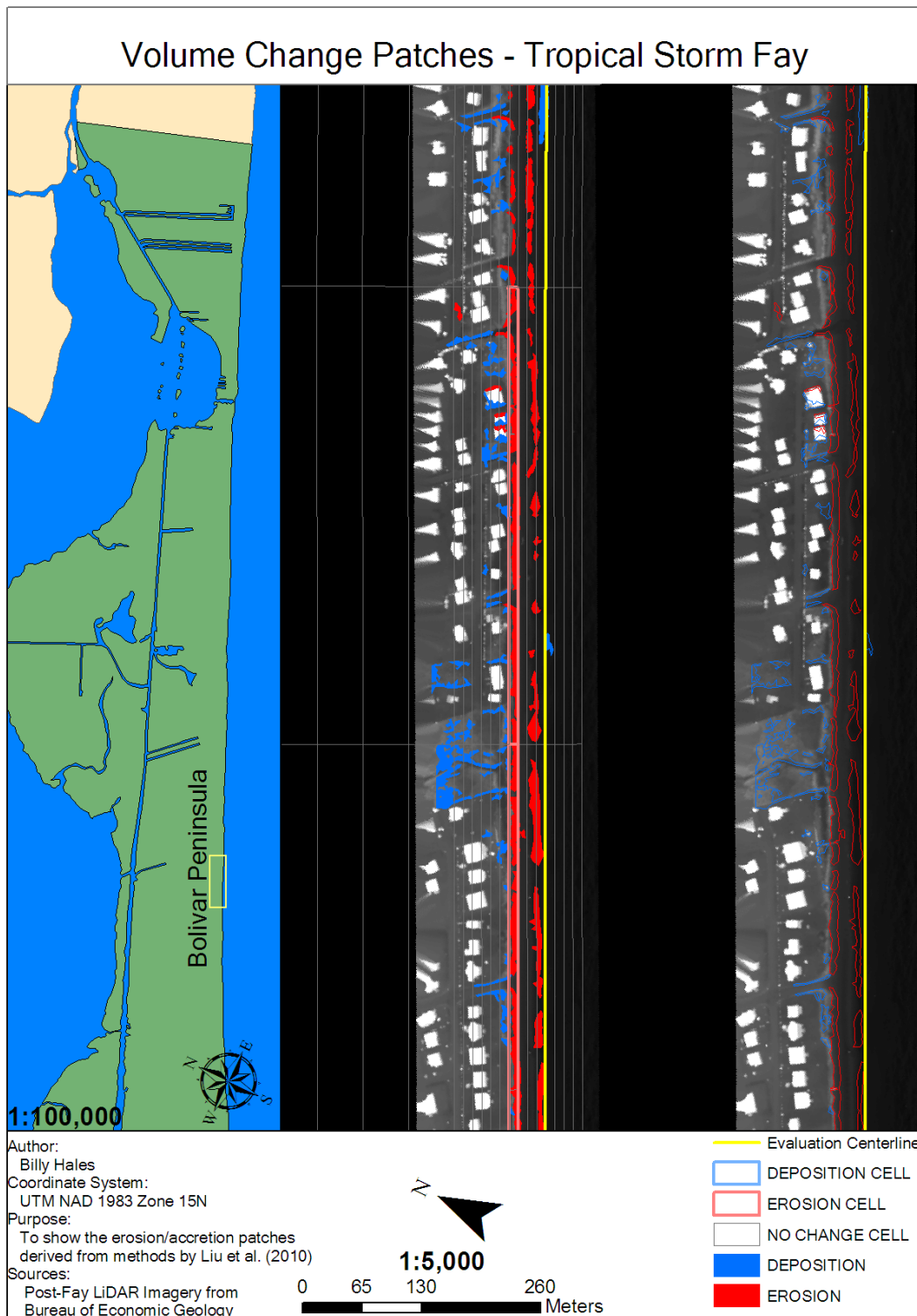


Figure D.15. Tropical Storm Fay section 15/28 of 1:5000 scale volumetric changes. Corresponds to J-K on Figure 4.15.

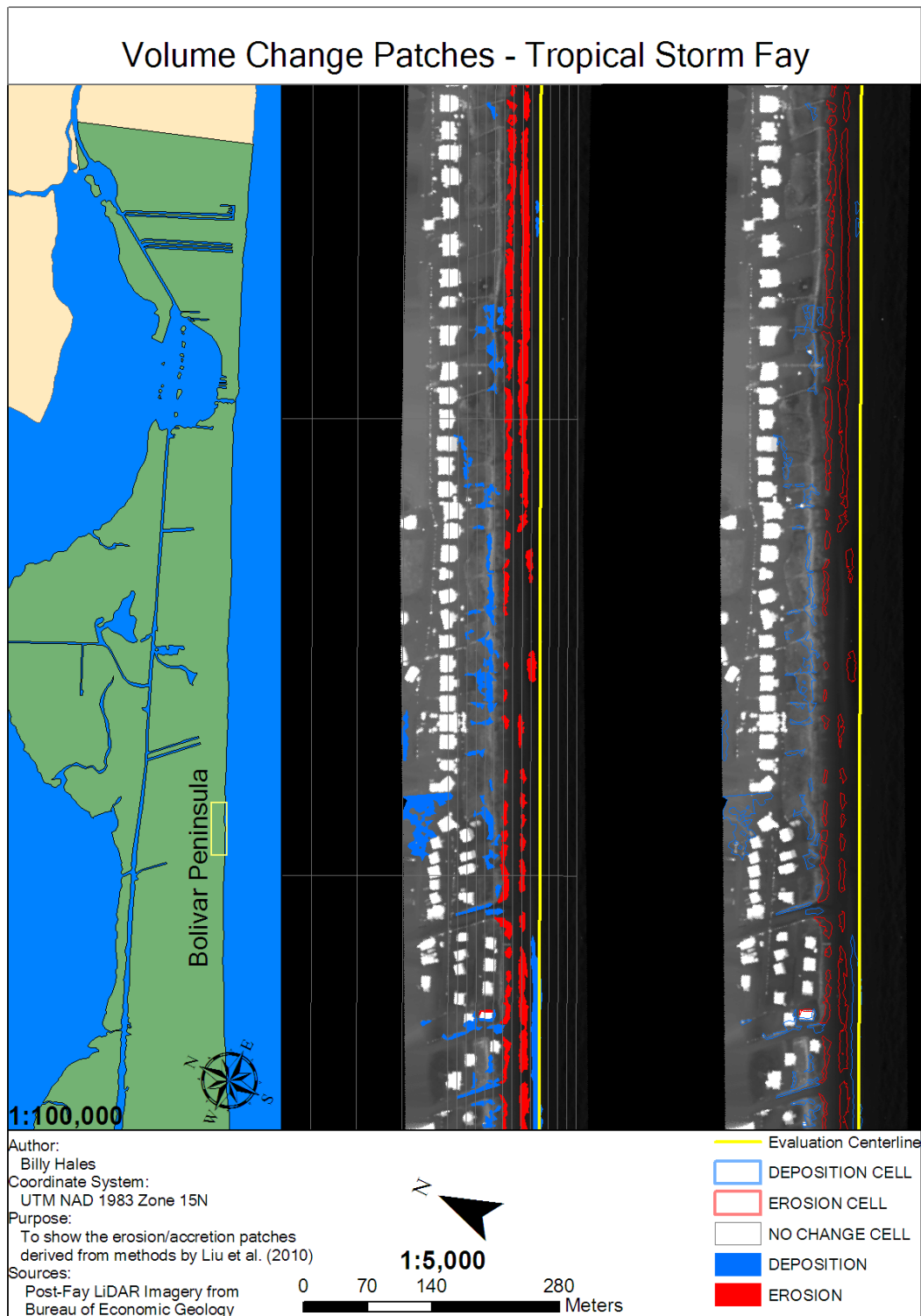


Figure D.16. Tropical Storm Fay section 16/28 of 1:5000 scale volumetric changes. Corresponds to J-K,K-L on Figure 4.15.

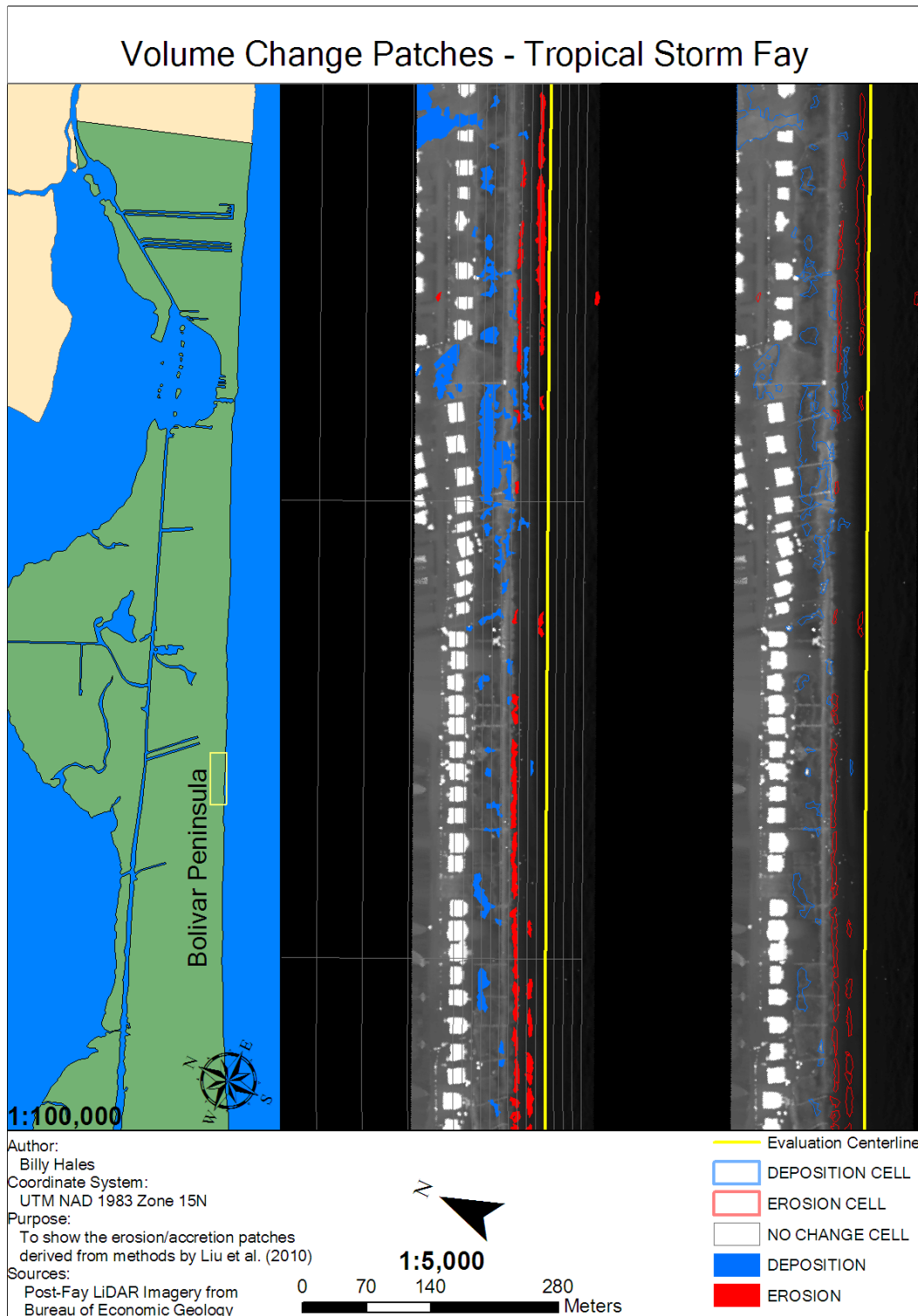


Figure D.17. Tropical Storm Fay section 17/28 of 1:5000 scale volumetric changes. Corresponds to K-L on Figure 4.15.

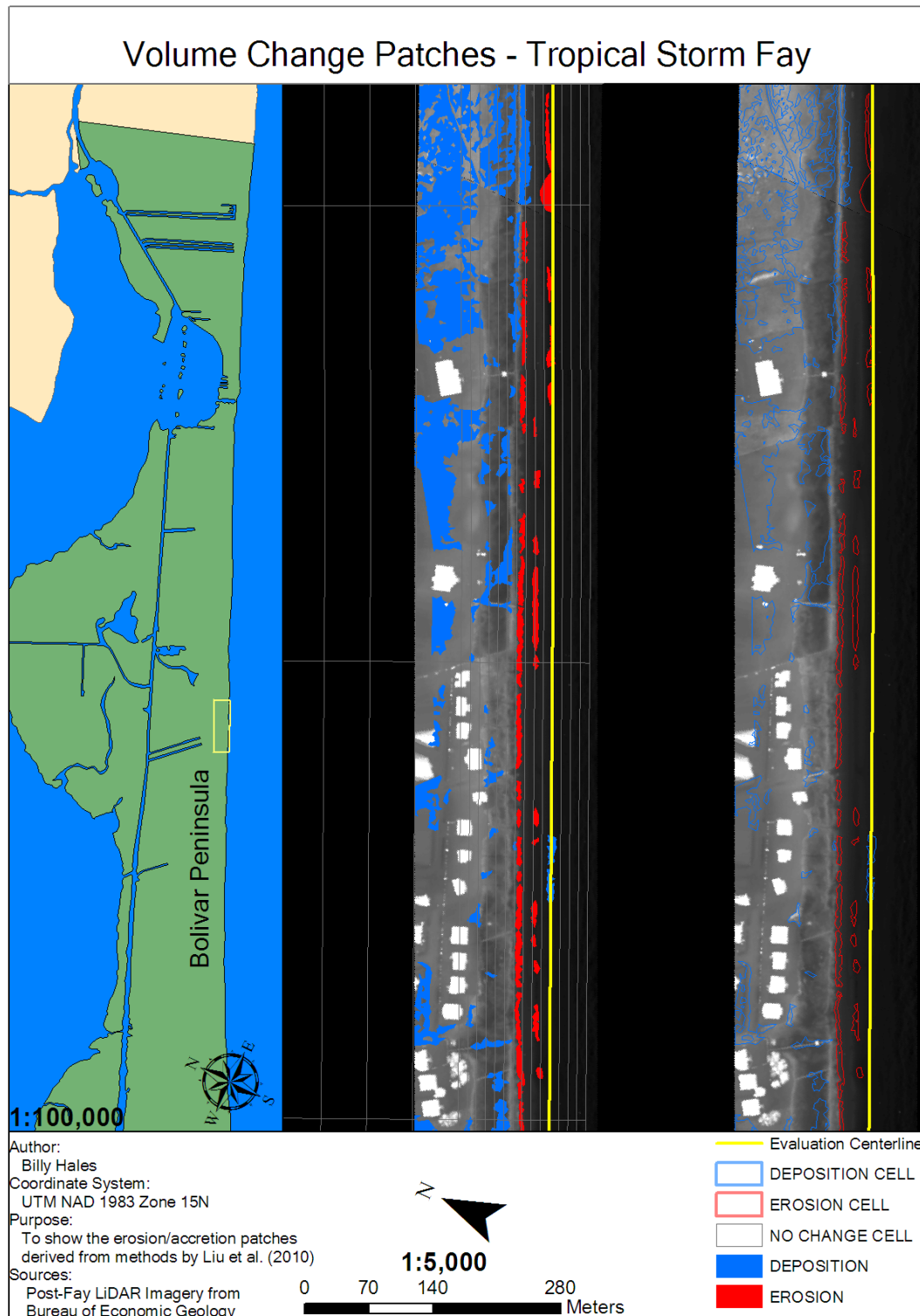


Figure D.18. Tropical Storm Fay section 18/28 of 1:5000 scale volumetric changes. Corresponds to K-L,L-M on Figure 4.15.

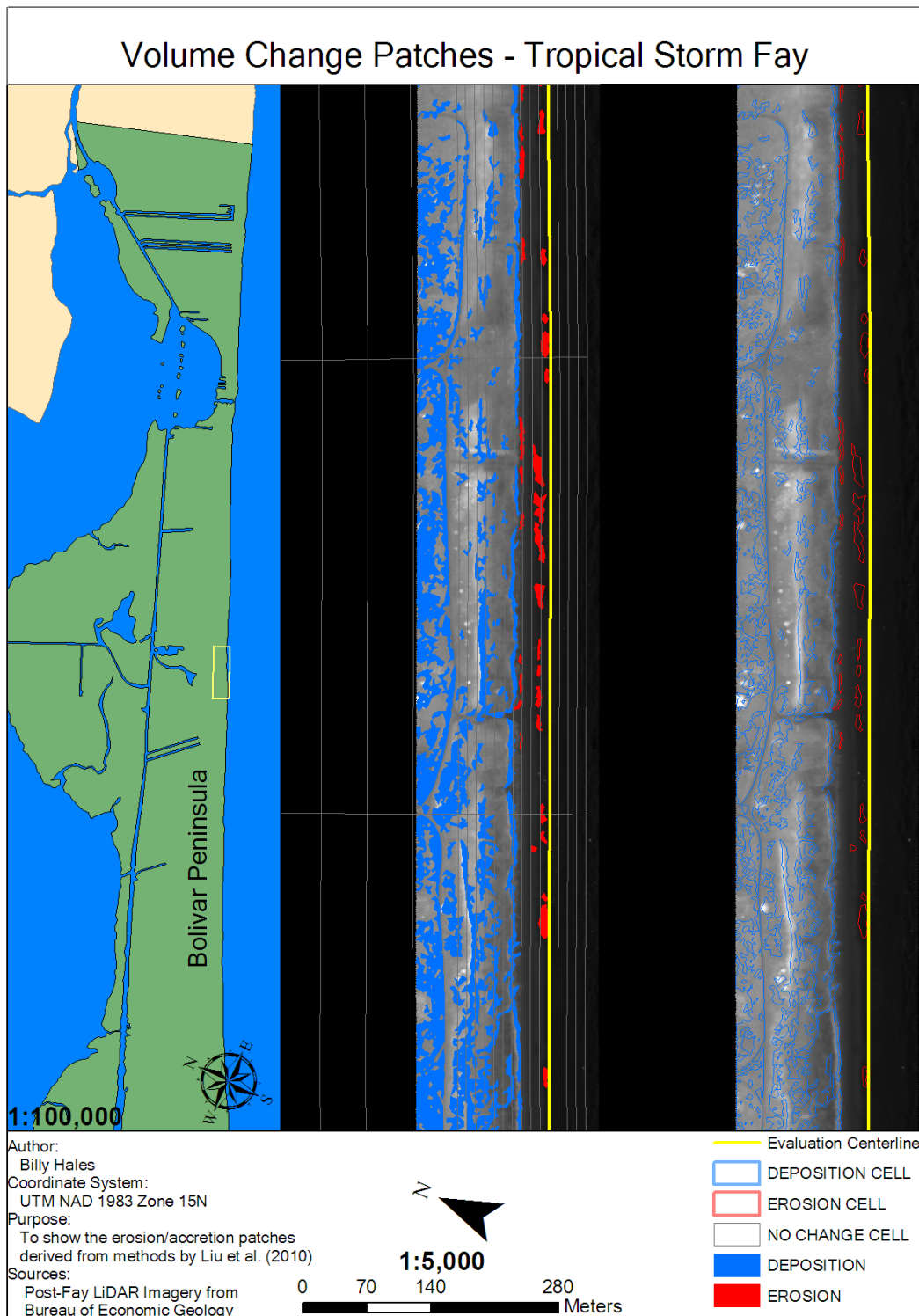


Figure D.19. Tropical Storm Fay section 19/28 of 1:5000 scale volumetric changes. Corresponds to L-M on Figure 4.15.

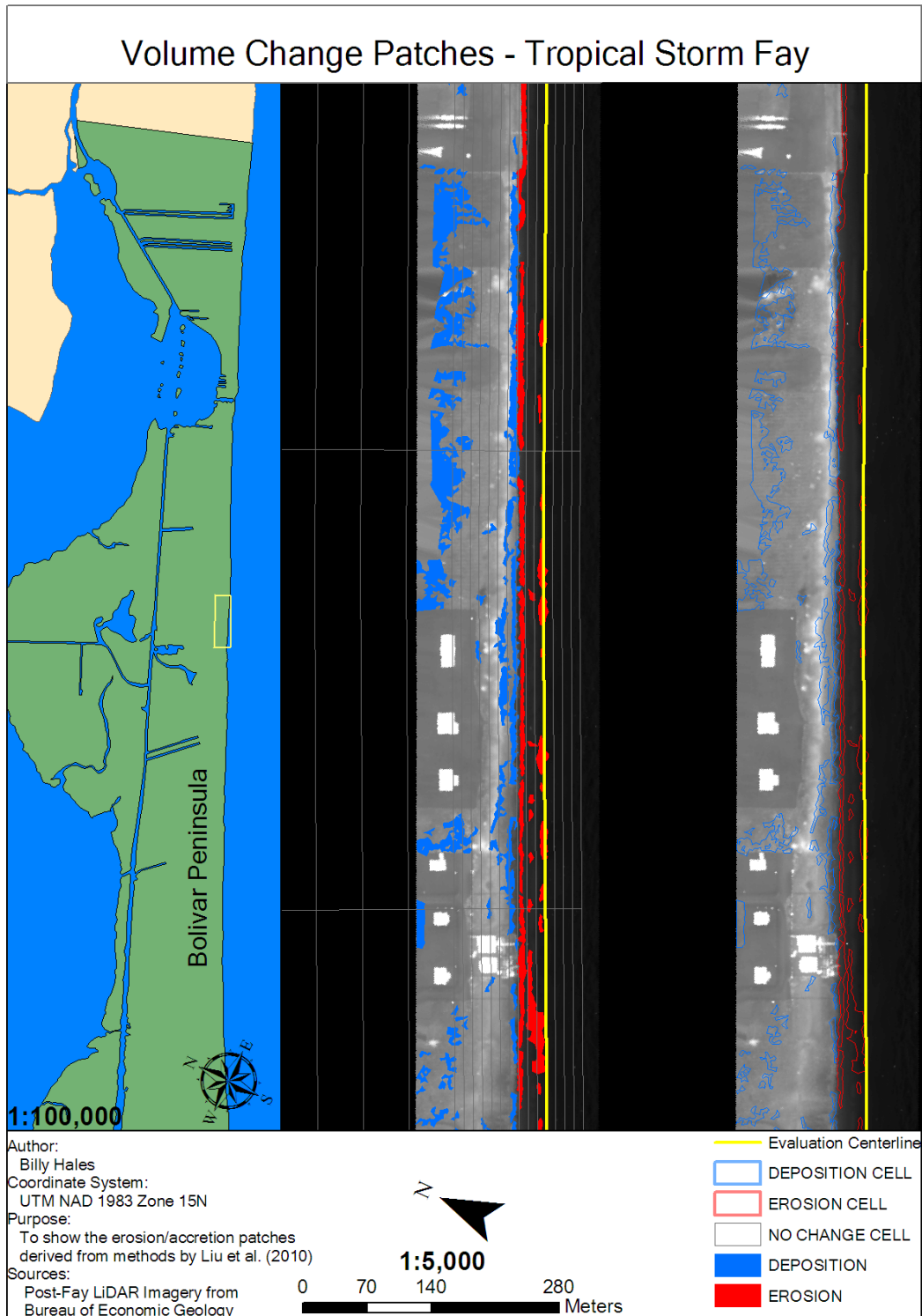


Figure D.20. Tropical Storm Fay section 20/28 of 1:5000 scale volumetric changes. Corresponds to L-M,M-N on Figure 4.16.

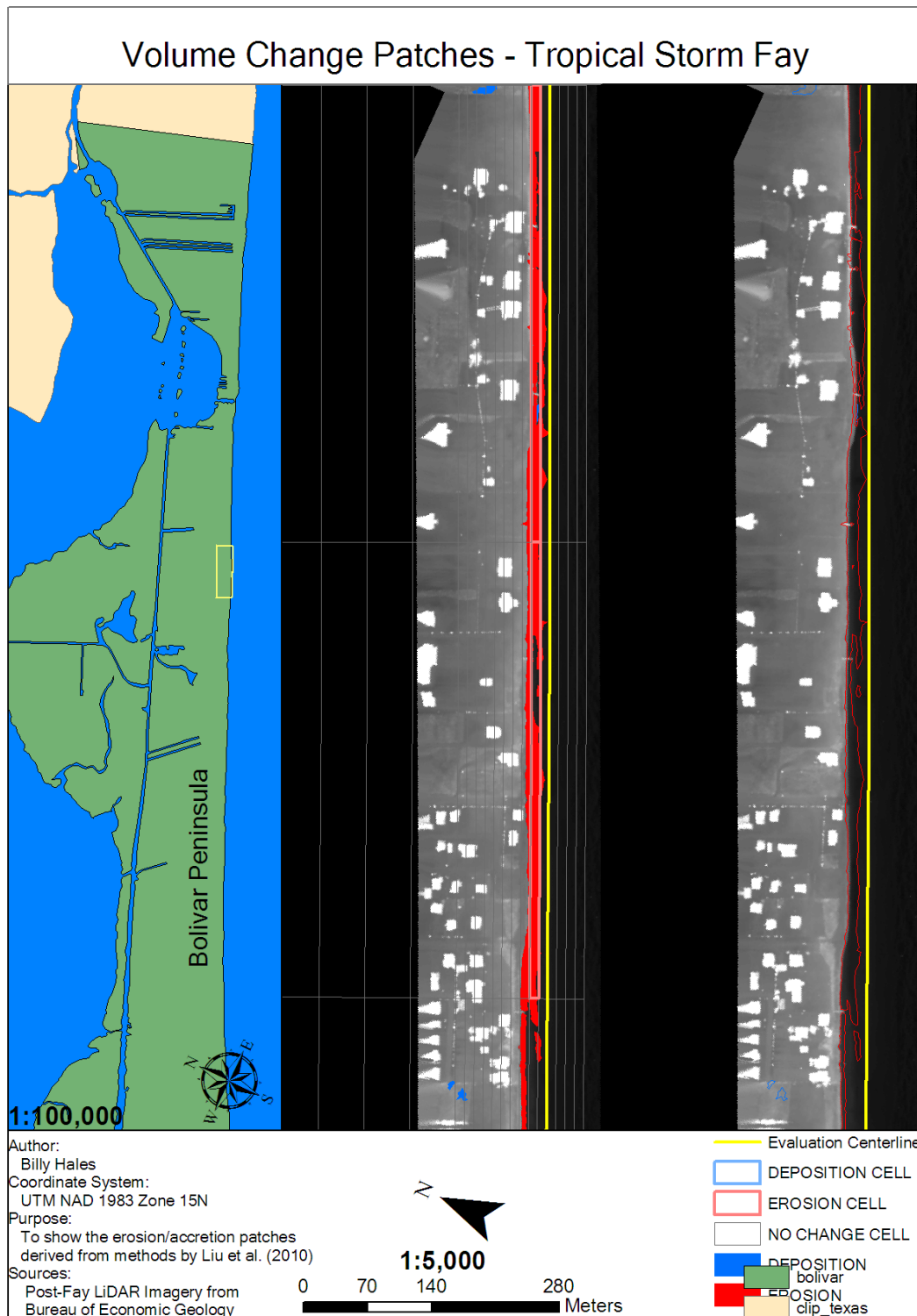


Figure D.21. Tropical Storm Fay section 21/28 of 1:5000 scale volumetric changes. Corresponds to M-N,N-O on Figure 4.16.

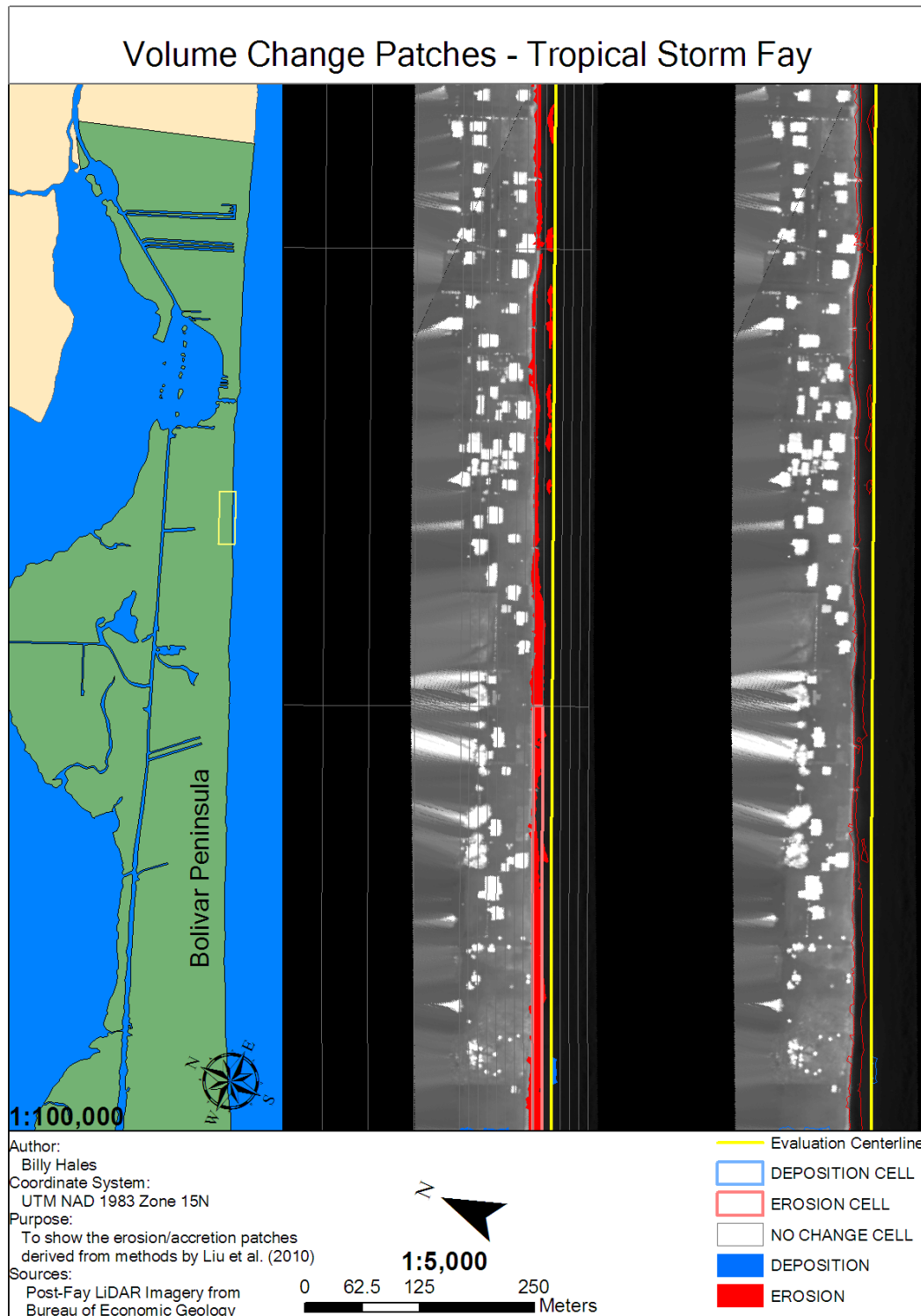


Figure D.22. Tropical Storm Fay section 22/28 of 1:5000 scale volumetric changes. Corresponds to N-O on Figure 4.16.

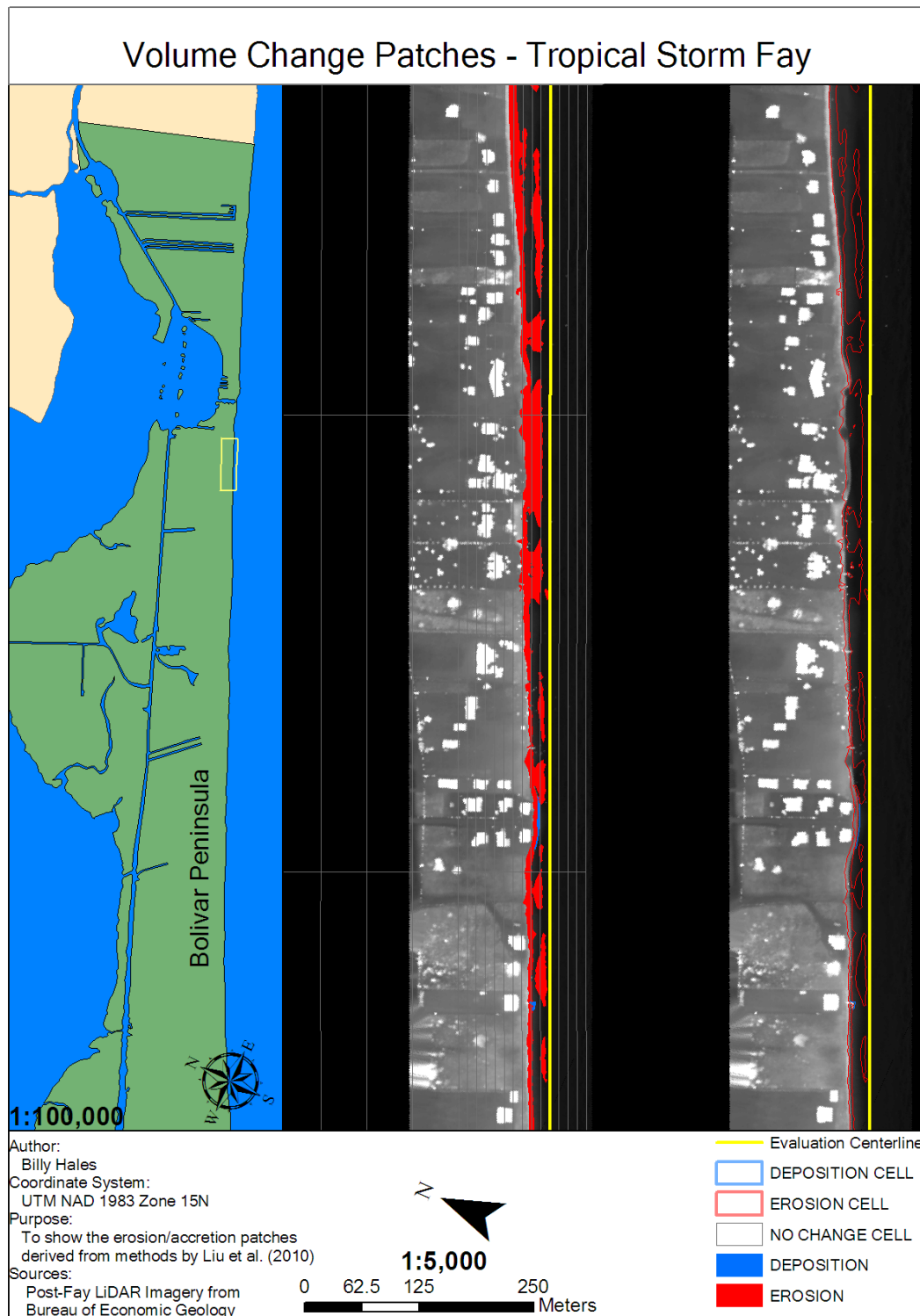


Figure D.23. Tropical Storm Fay section 23/28 of 1:5000 scale volumetric changes. Corresponds to O-P on Figure 4.16.

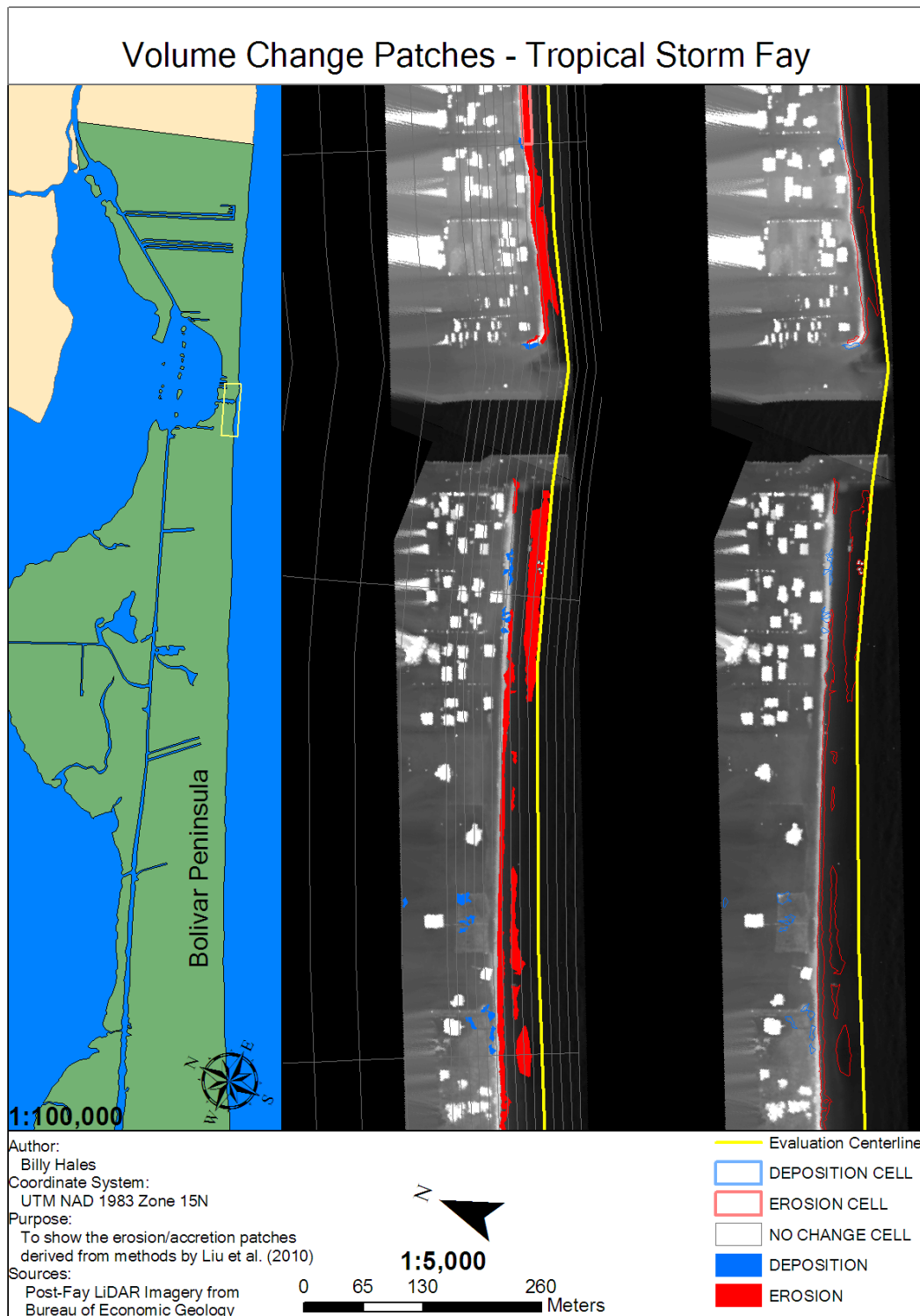


Figure D.24. Tropical Storm Fay section 24/28 of 1:5000 scale volumetric changes. Corresponds to O-P,P-Q on Figures 4.16 and 4.17.

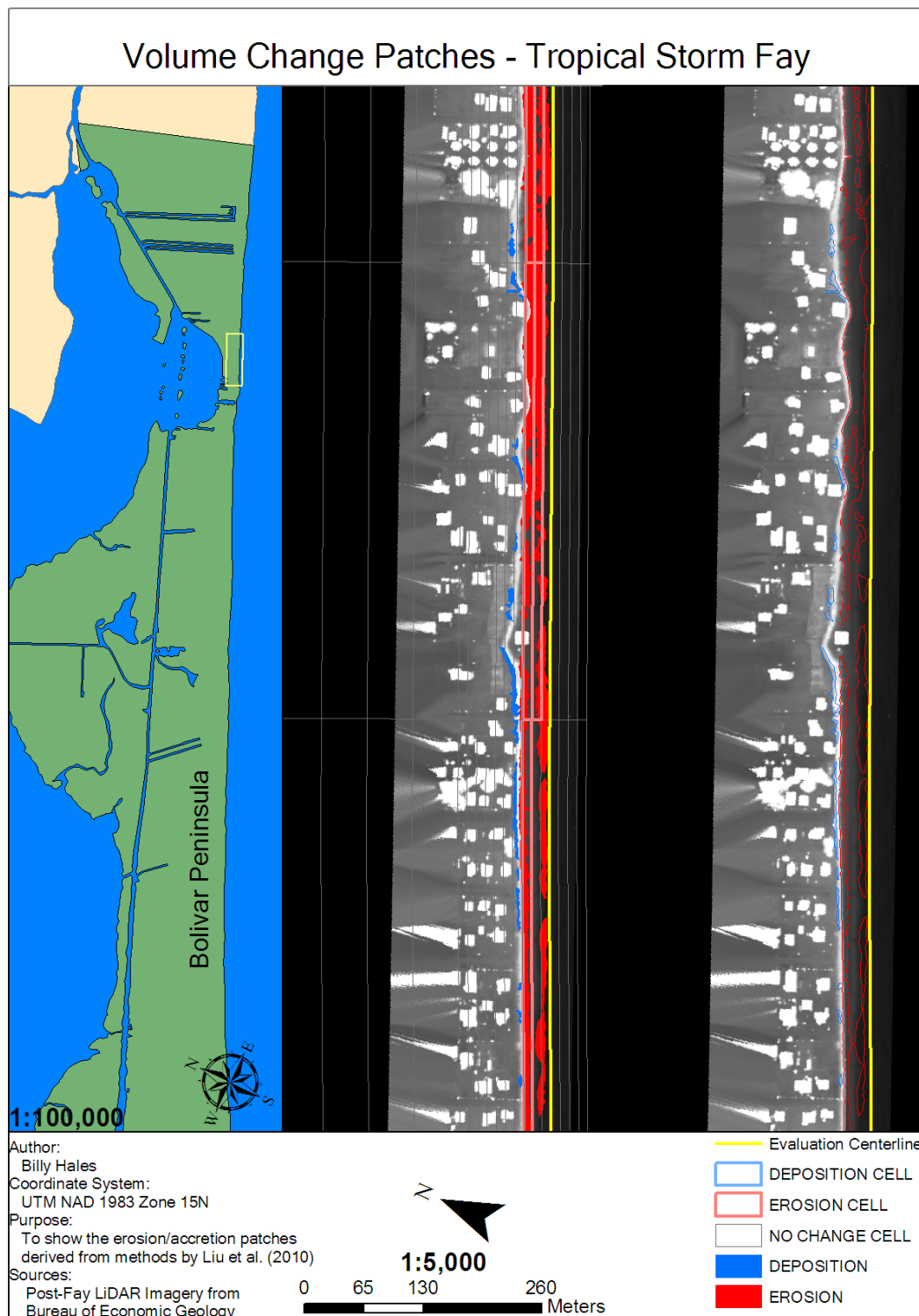


Figure D.25. Tropical Storm Fay section 25/28 of 1:5000 scale volumetric changes. Corresponds to P-O on Figure 4.17.

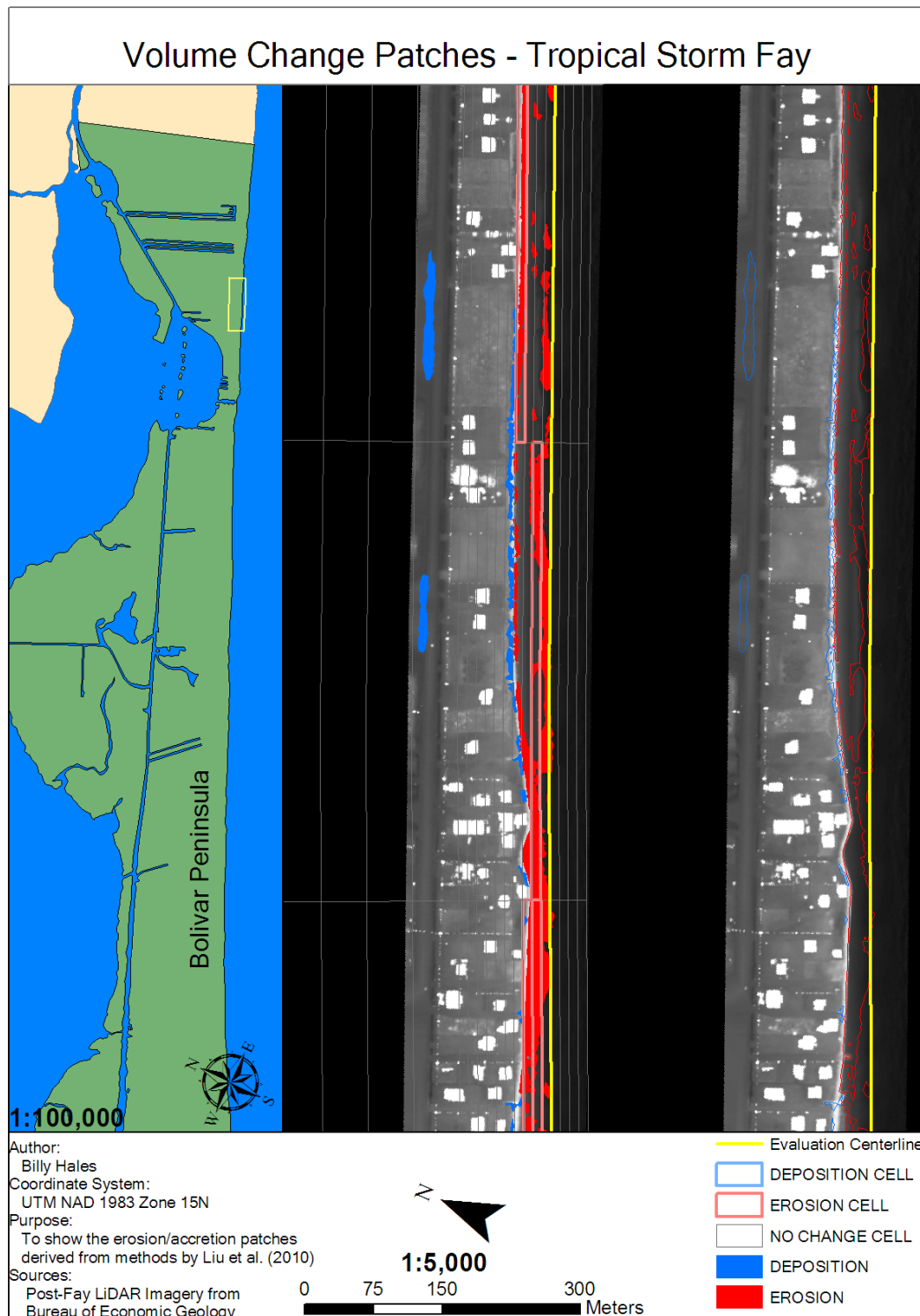


Figure D.26. Tropical Storm Fay section 26/28 of 1:5000 scale volumetric changes. Corresponds to P-Q,Q-R on Figure 4.17.

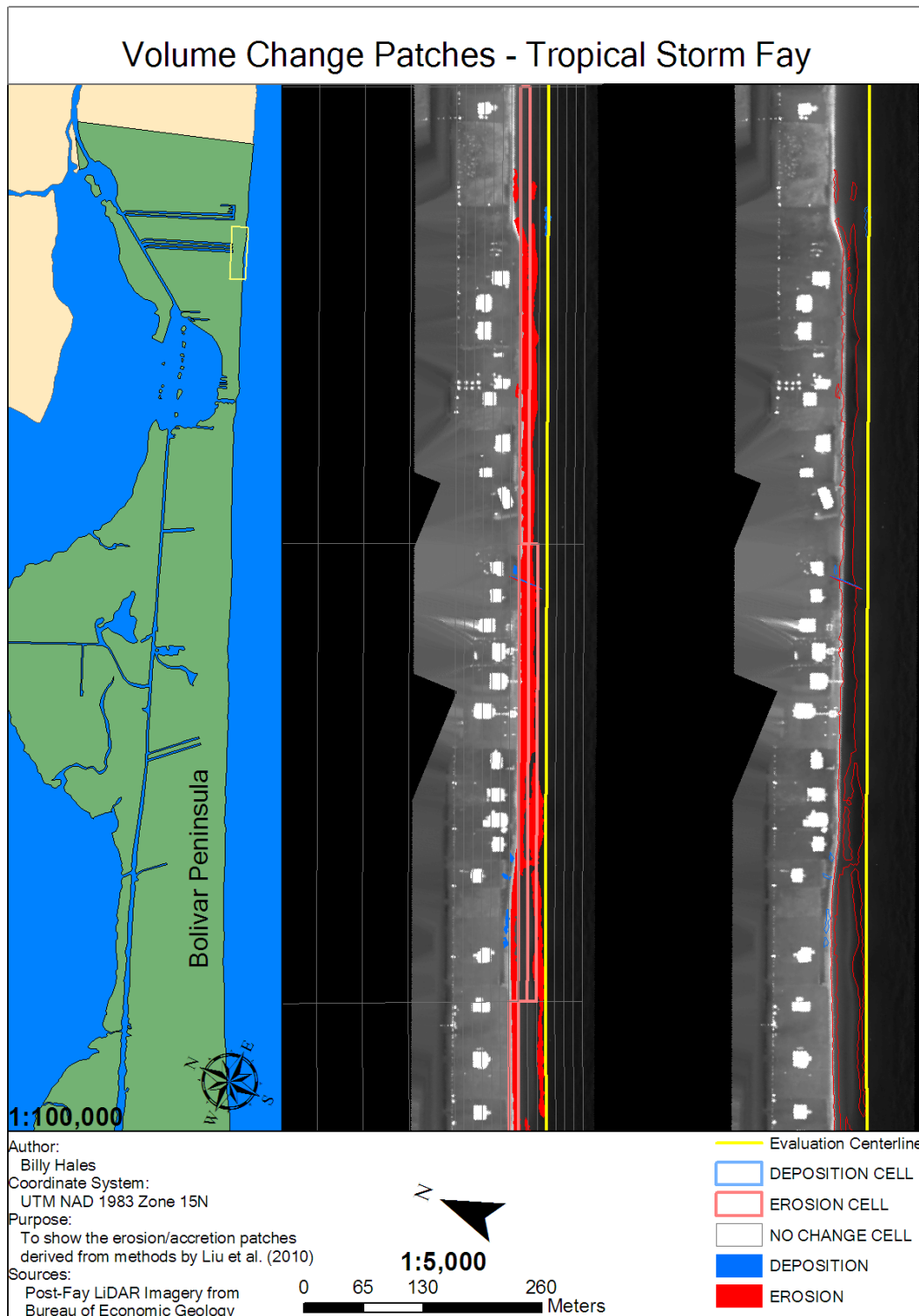


Figure D.27. Tropical Storm Fay section 27/28 of 1:5000 scale volumetric changes. Corresponds to Q-R on Figure 4.17.

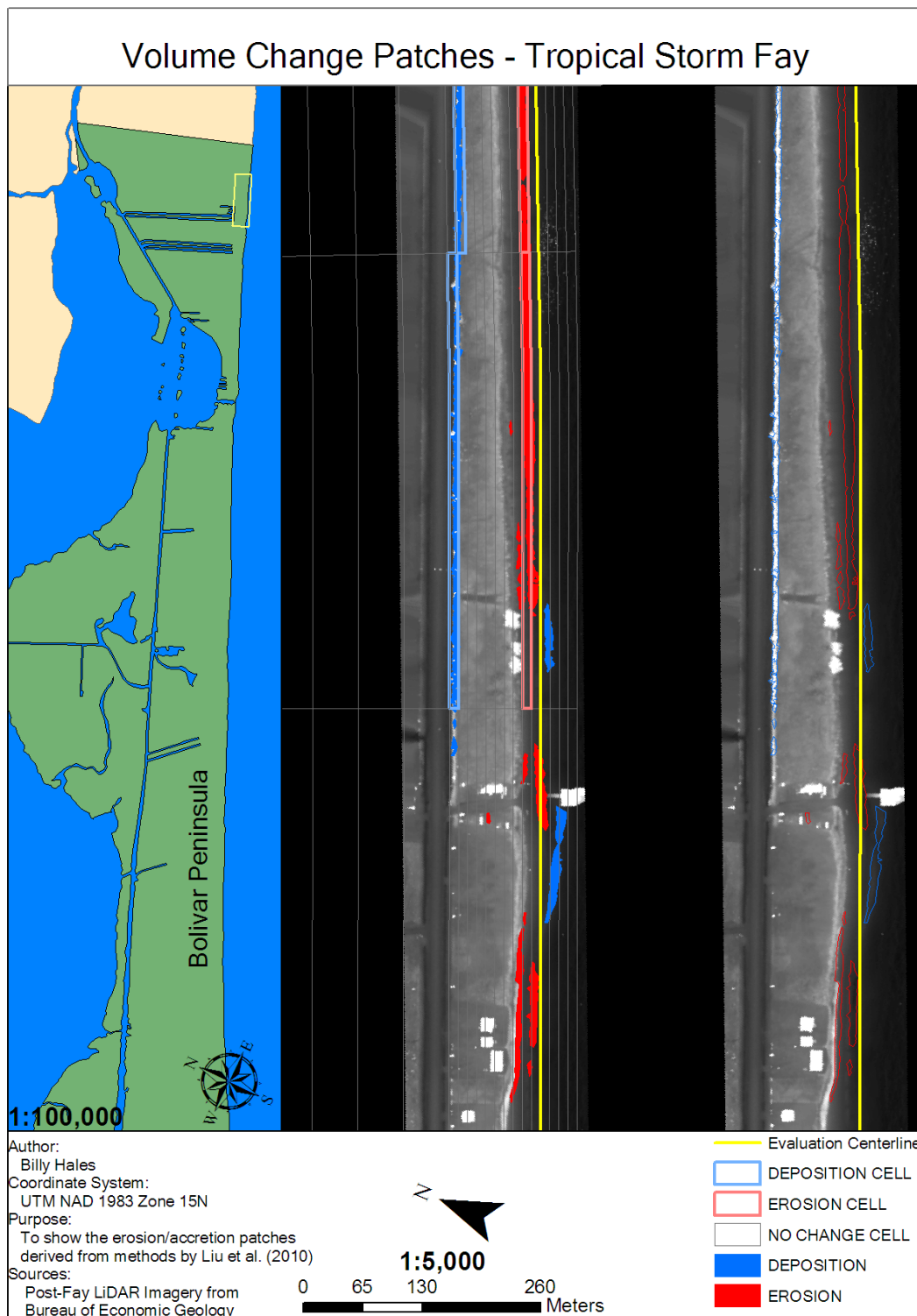


Figure D.28. Tropical Storm Fay section 28/28 of 1:5000 scale volumetric changes. Corresponds to Q-R,R-S on Figure 4.17.

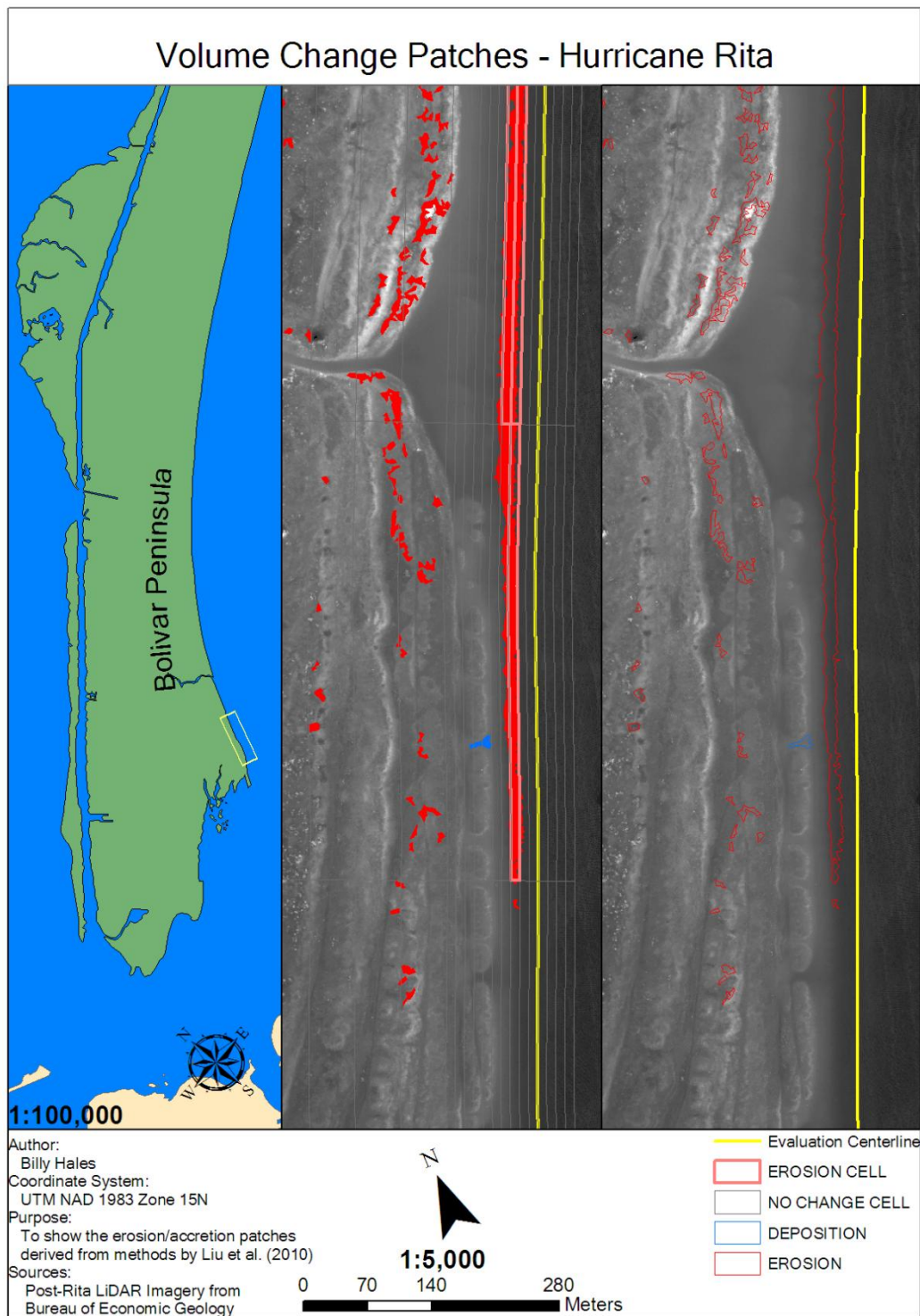


Figure D.29. Hurricane Rita section 1/28 of 1:5000 scale volumetric changes. Corresponds to A-B on Figure 4.23.

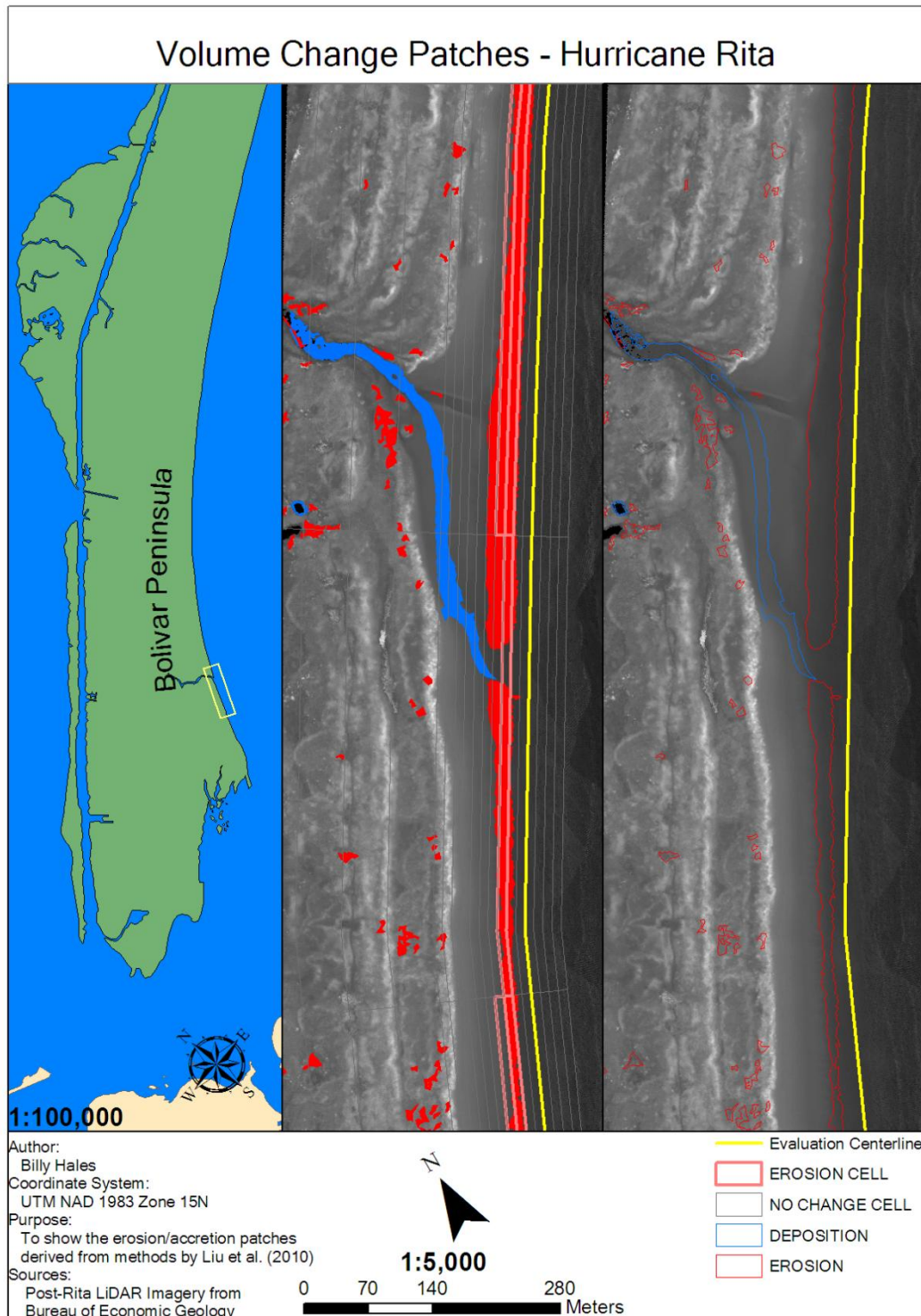


Figure D.30. Hurricane Rita section 2/28 of 1:5000 scale volumetric changes. Corresponds to A-B,B-C on Figure 4.23.

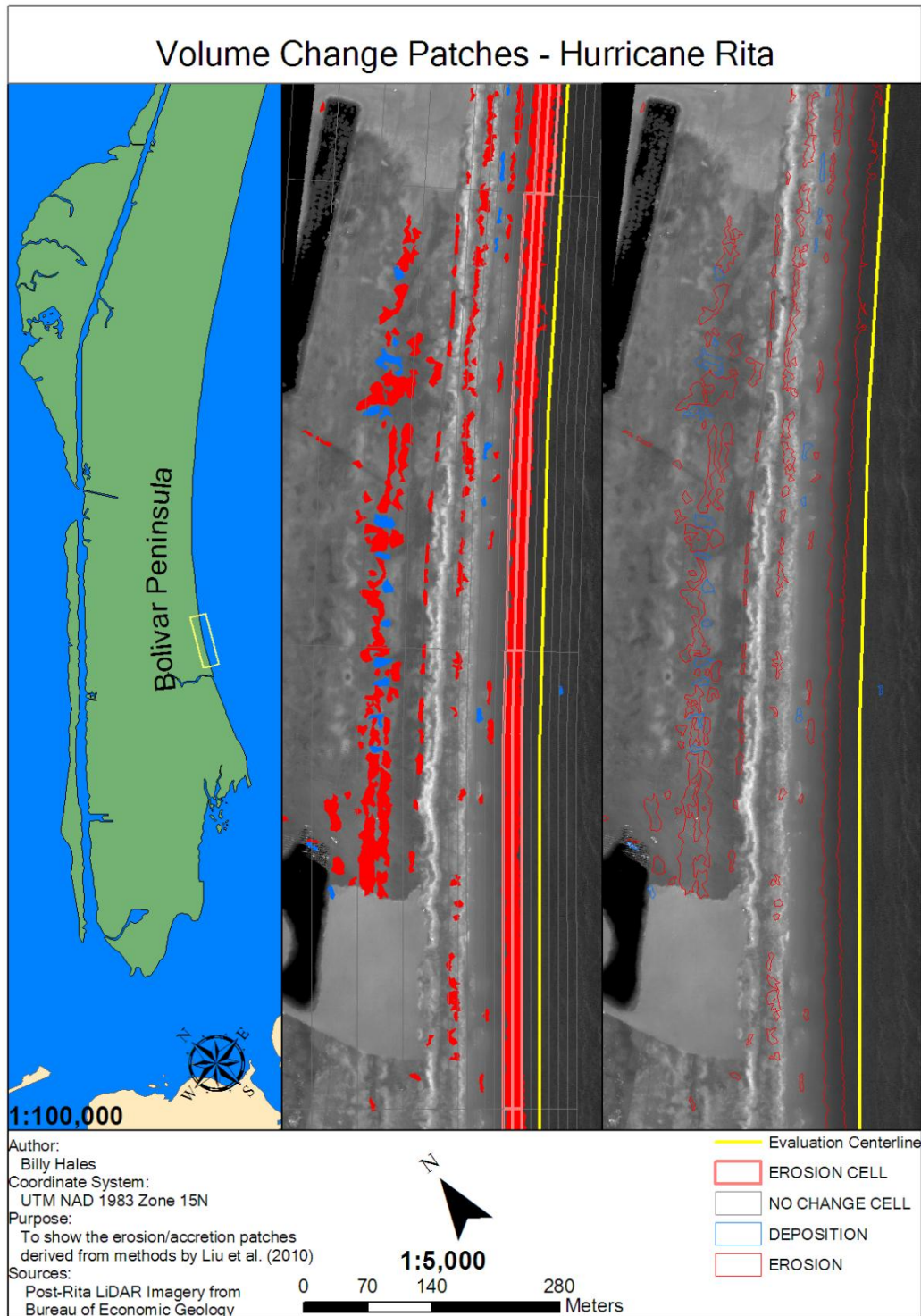


Figure D.31. Hurricane Rita section 3/28 of 1:5000 scale output from coastal morphology analyst. Corresponds to B-C,C-D on Figure 4.23.

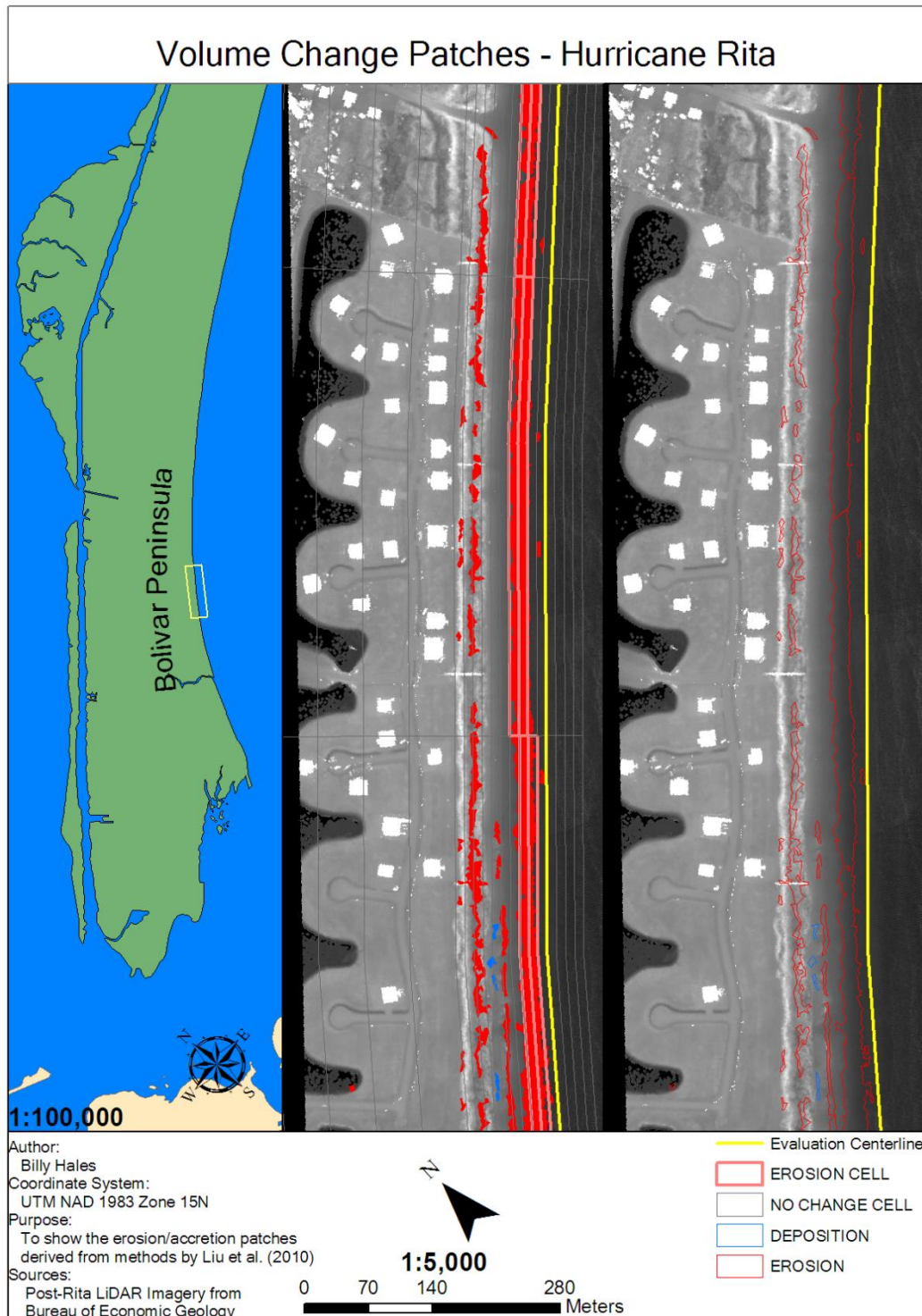


Figure D.32. Hurricane Rita section 4/28 of 1:5000 scale output from coastal morphology analyst. Corresponds to C-D on Figure 4.23.

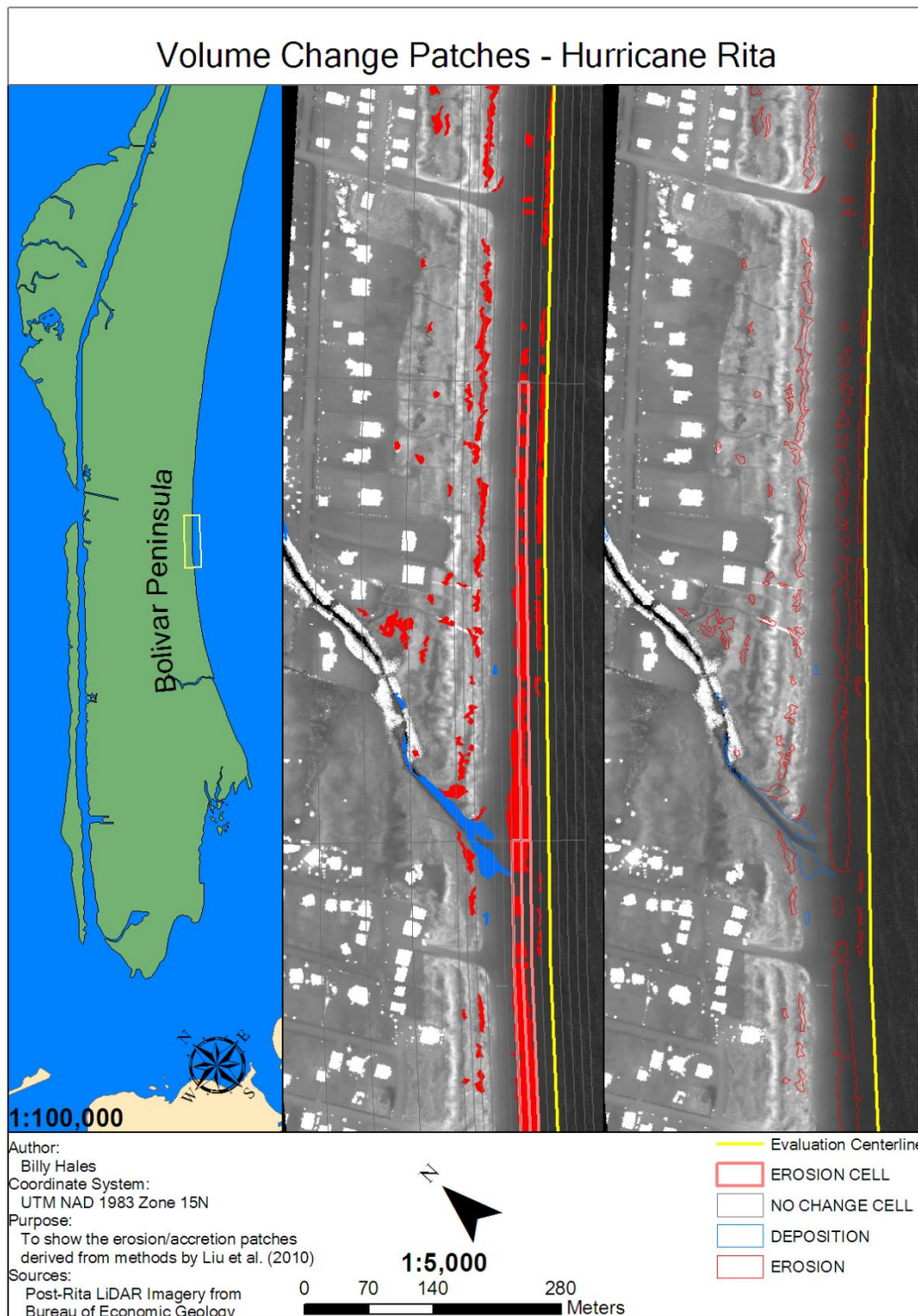


Figure D.33. Hurricane Rita section 5/28 of 1:5000 scale volumetric changes. Corresponds to C-D,D-E on Figures 4.23 and 4.24.

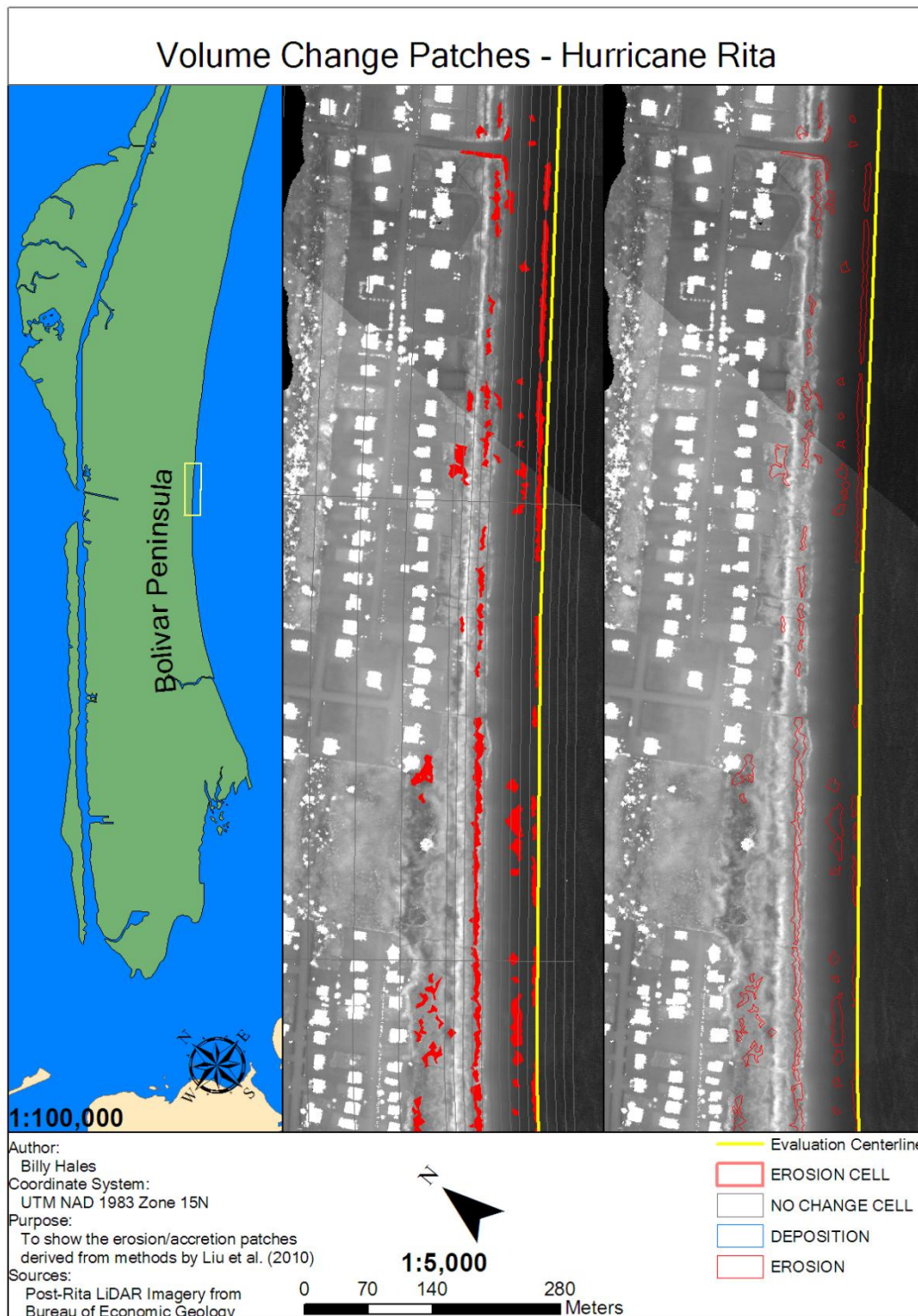


Figure D.34. Hurricane Rita section 6/28 of 1:5000 scale volumetric changes. Corresponds to D-E on Figure 4.24.

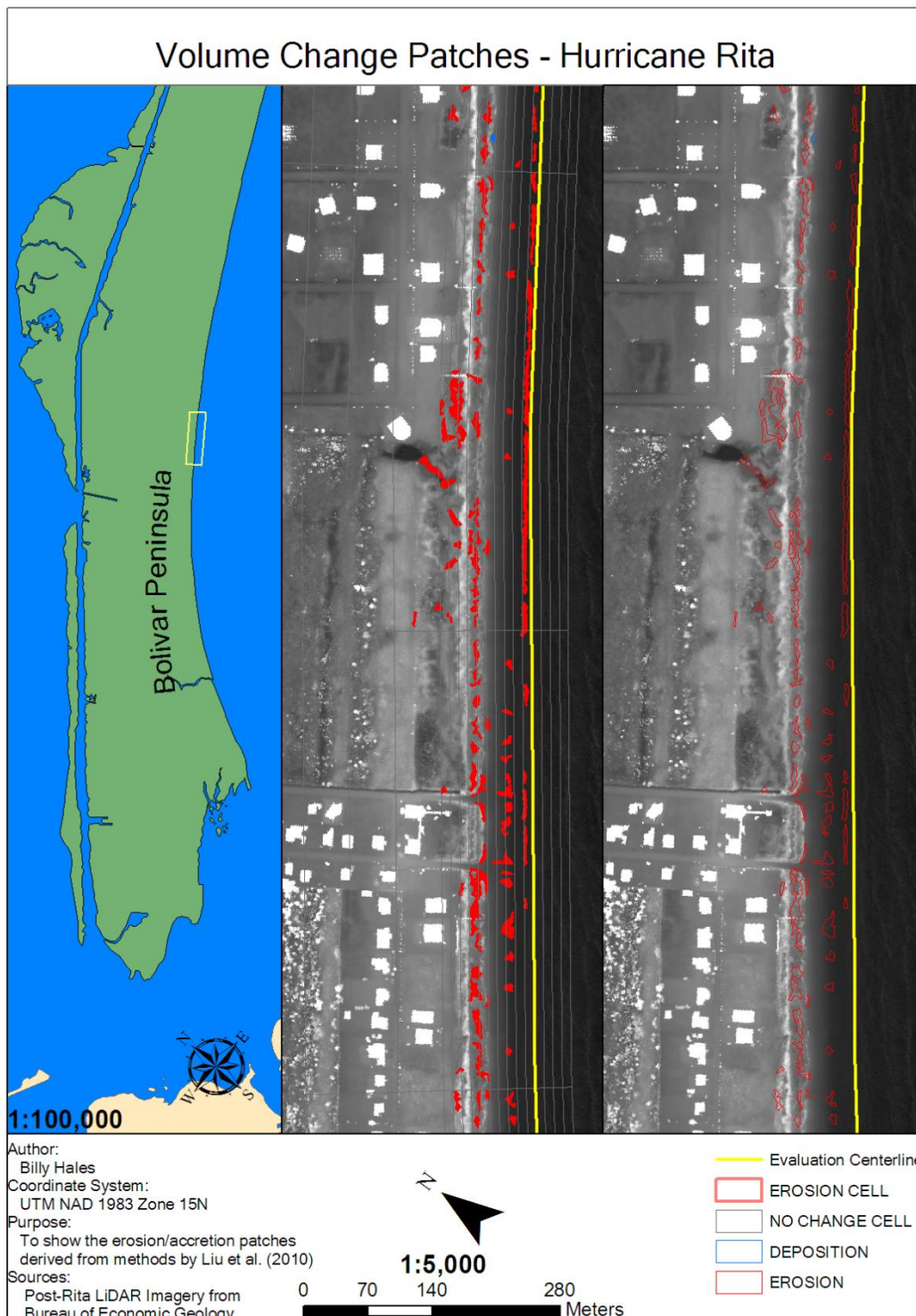


Figure D.35. Hurricane Rita section 7/28 of 1:5000 scale volumetric changes. Corresponds to E-F on Figure 4.24.

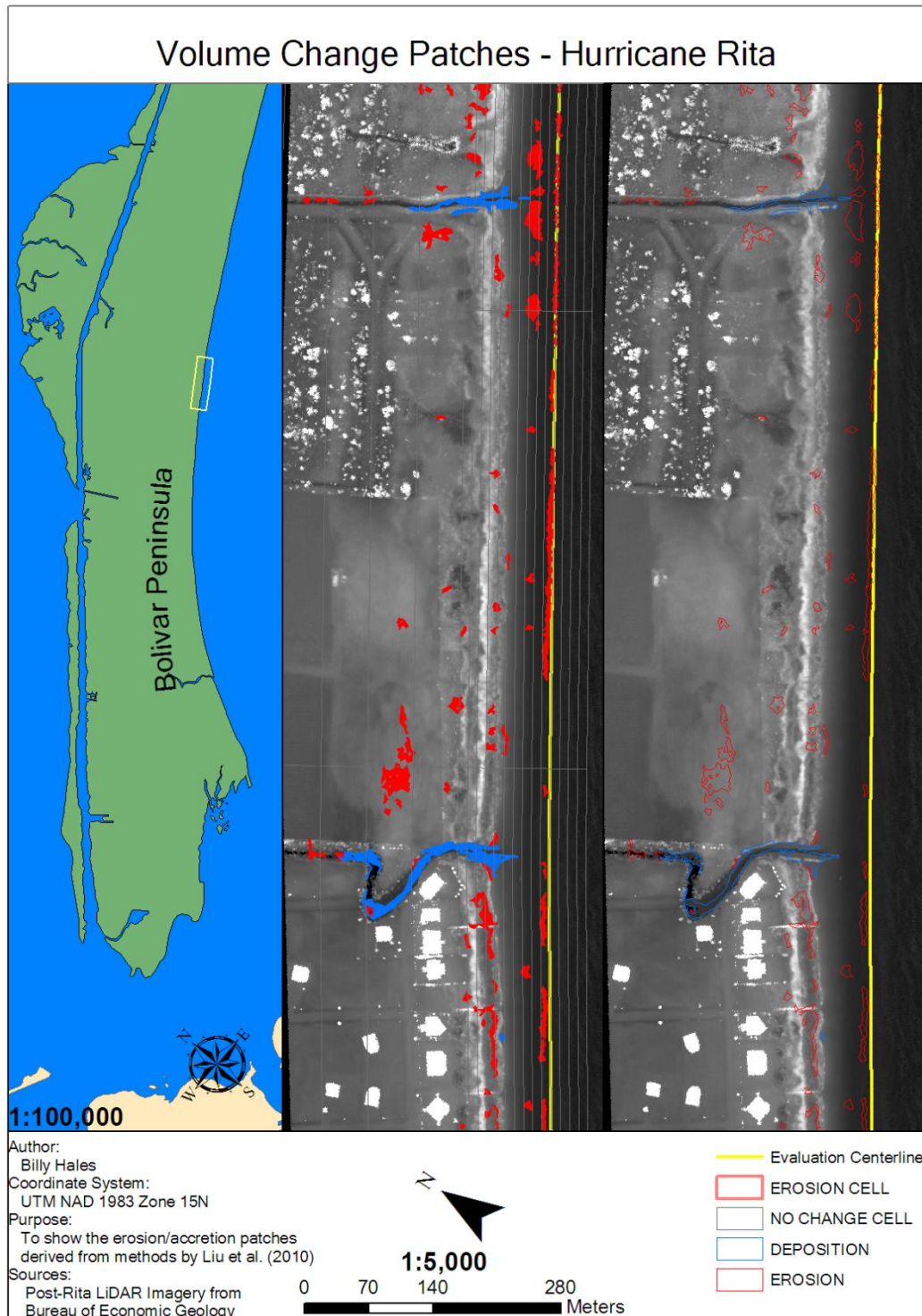


Figure D.36. Hurricane Rita section 8/28 of 1:5000 scale volumetric changes. Corresponds to E-F,F-G on Figure 4.24.

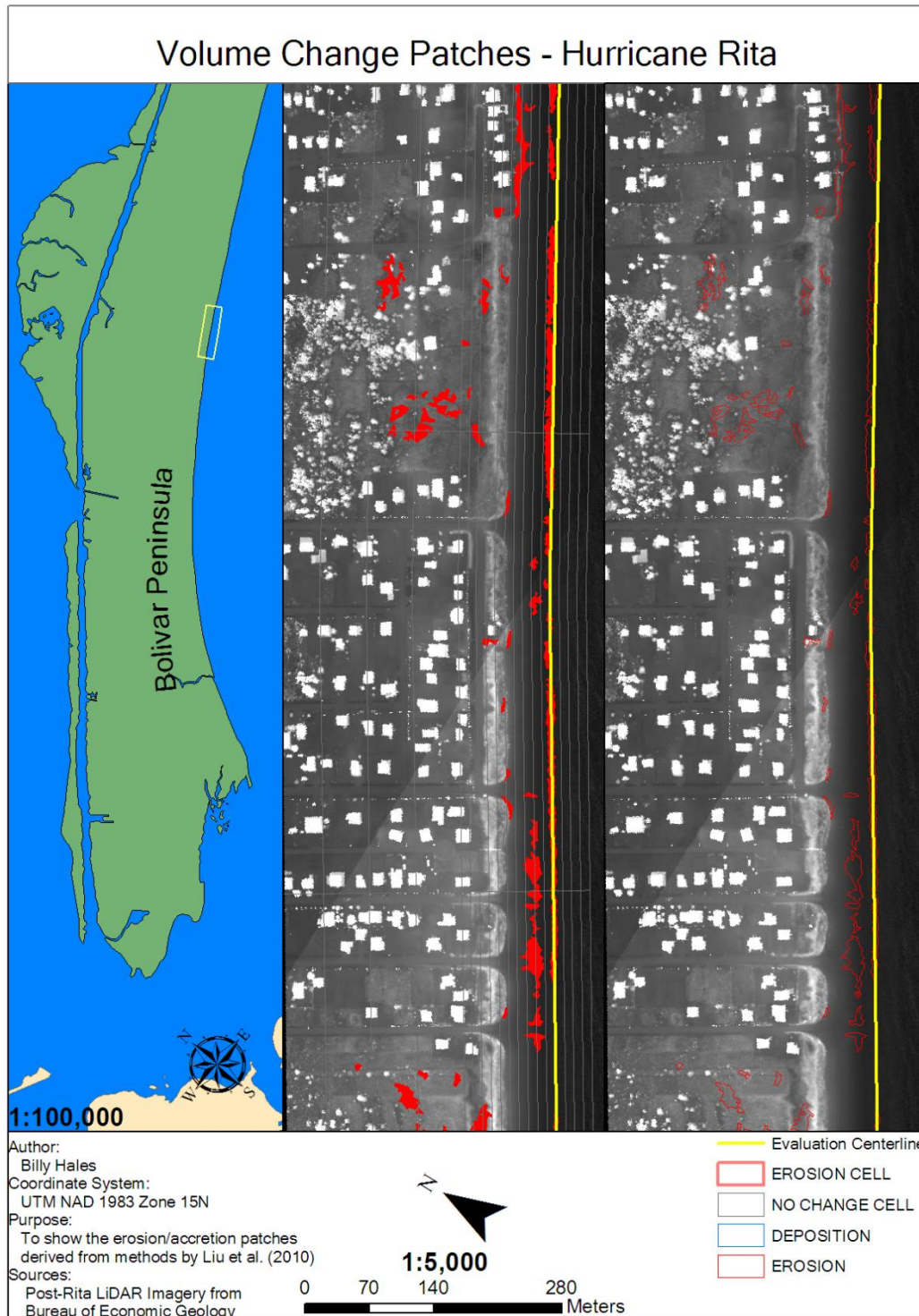


Figure D.37. Hurricane Rita section 9/28 of 1:5000 scale volumetric changes. Corresponds to F-G on Figure 4.24.

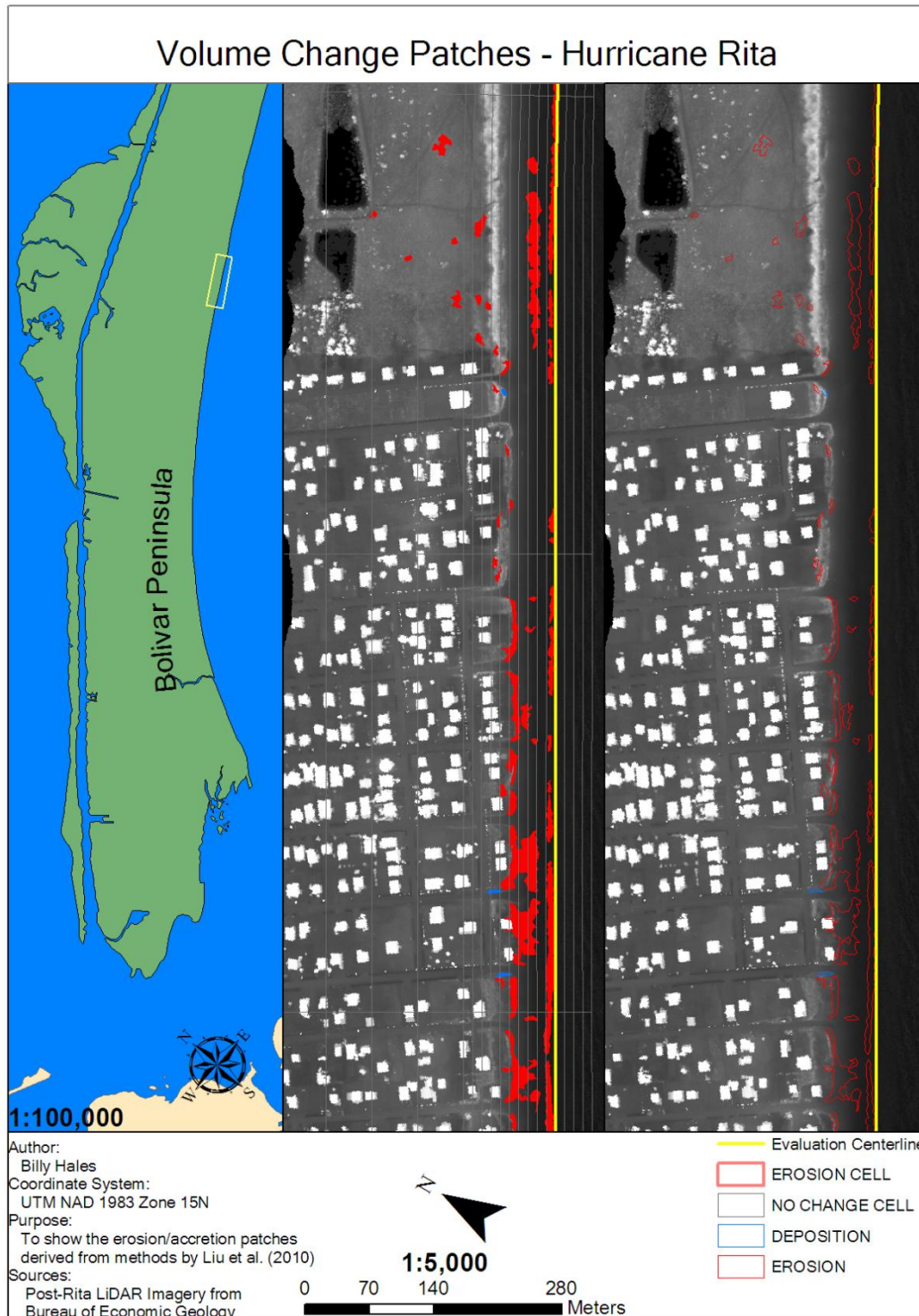


Figure D.38. Hurricane Rita section 10/28 of 1:5000 scale volumetric changes. Corresponds to F-G,G-H on Figures 4.24 and 4.25.

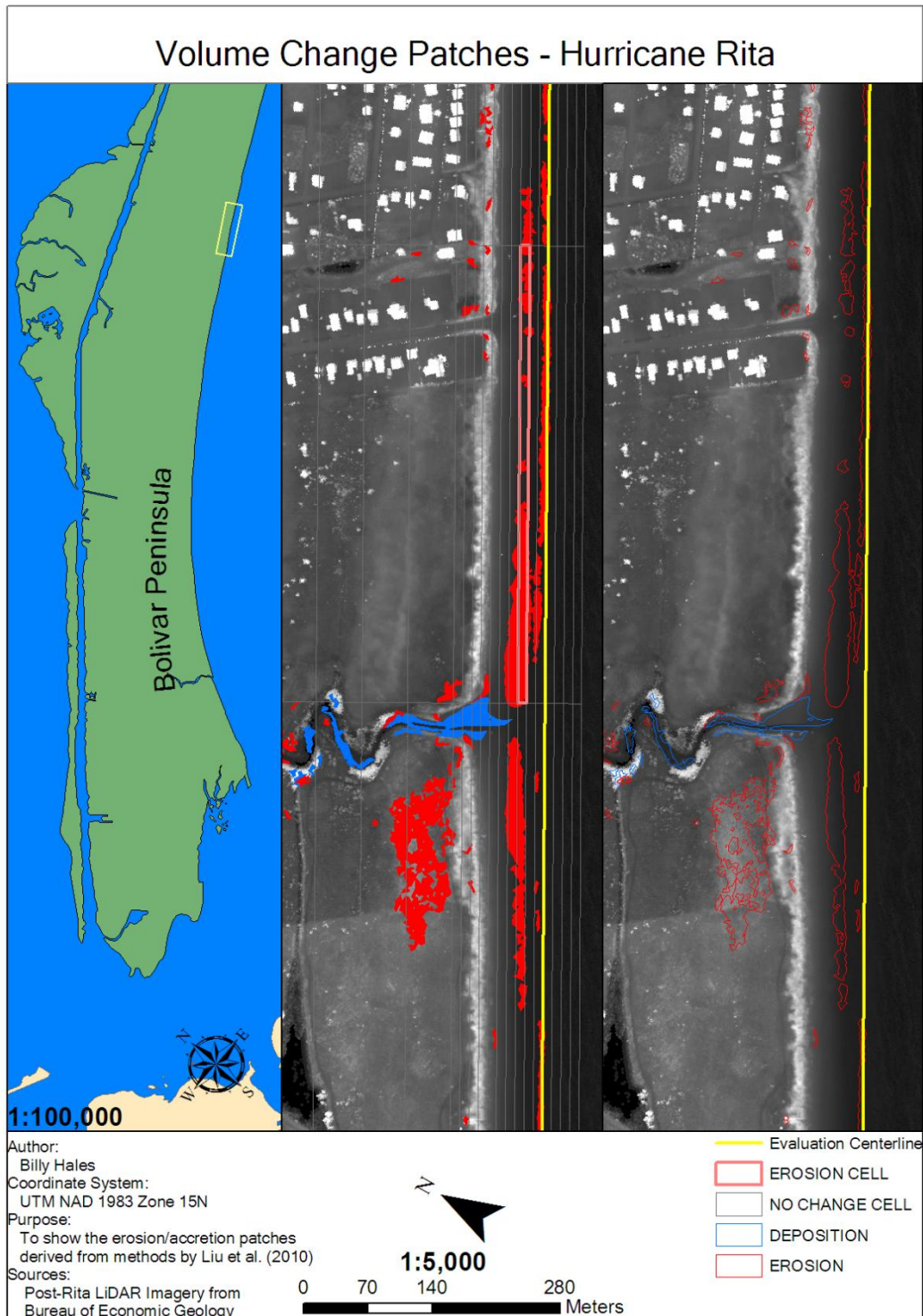


Figure D.39. Hurricane Rita section 11/28 of 1:5000 scale volumetric changes. Corresponds to G-H on Figure 4.25.



Figure D.40. Hurricane Rita section 12/28 of 1:5000 scale volumetric changes. Corresponds to H-I on Figure 4.25.

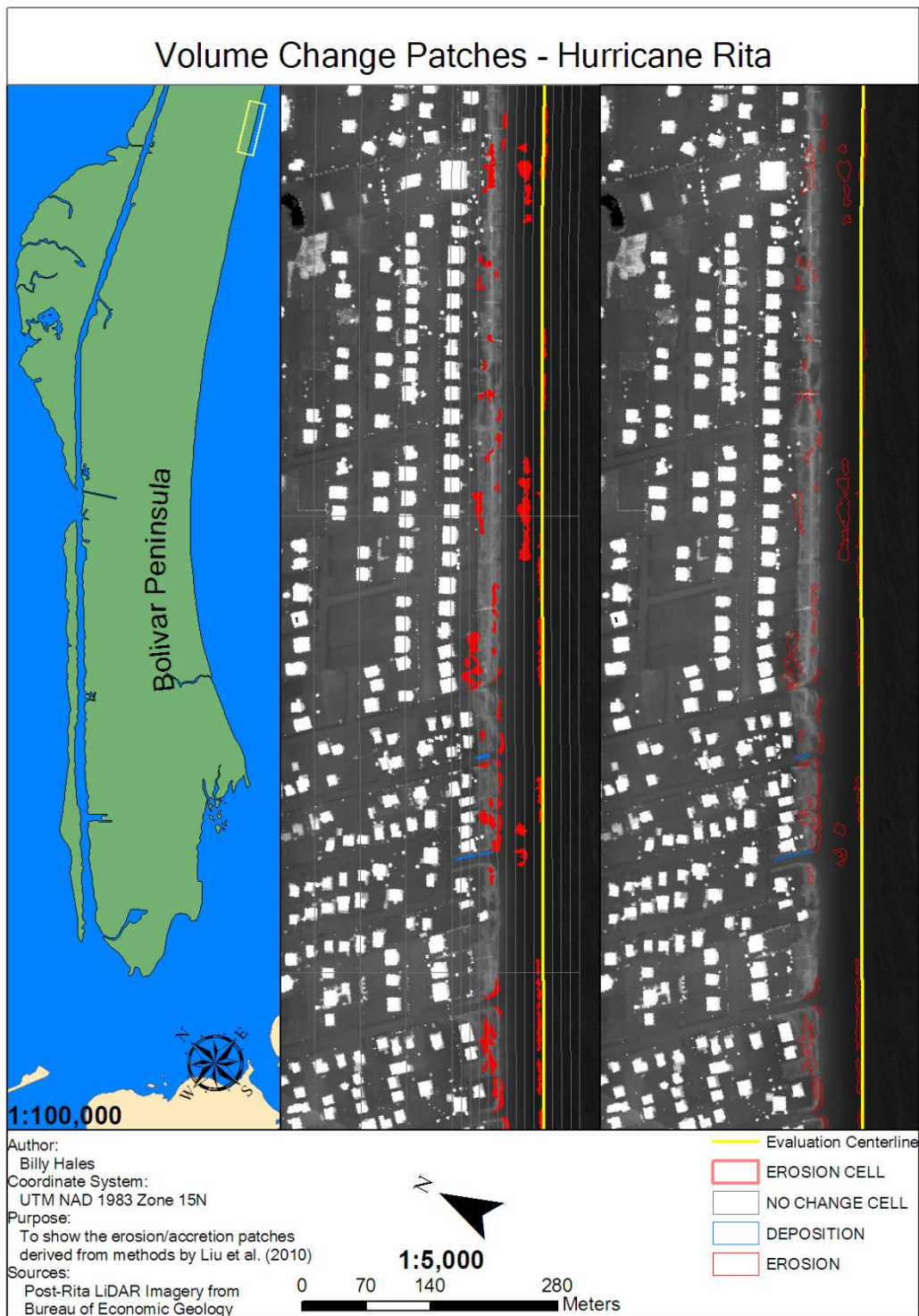


Figure D.41. Hurricane Rita section 13/28 of 1:5000 scale volumetric changes. Corresponds to H-I,I-J on Figure 4.25.

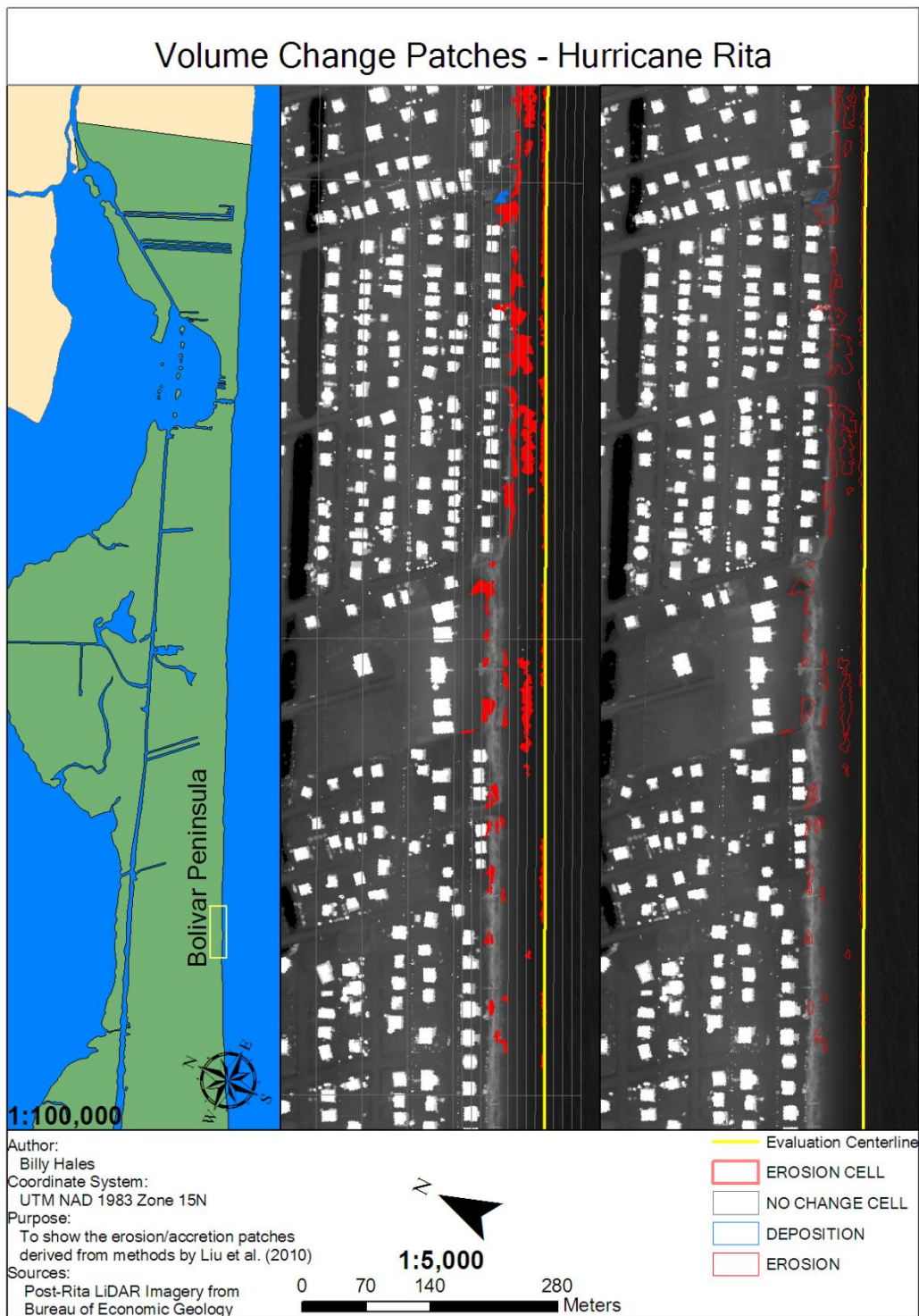


Figure D.42. Hurricane Rita section 14/28 of 1:5000 scale volumetric changes. Corresponds to I-J on Figure 4.25.

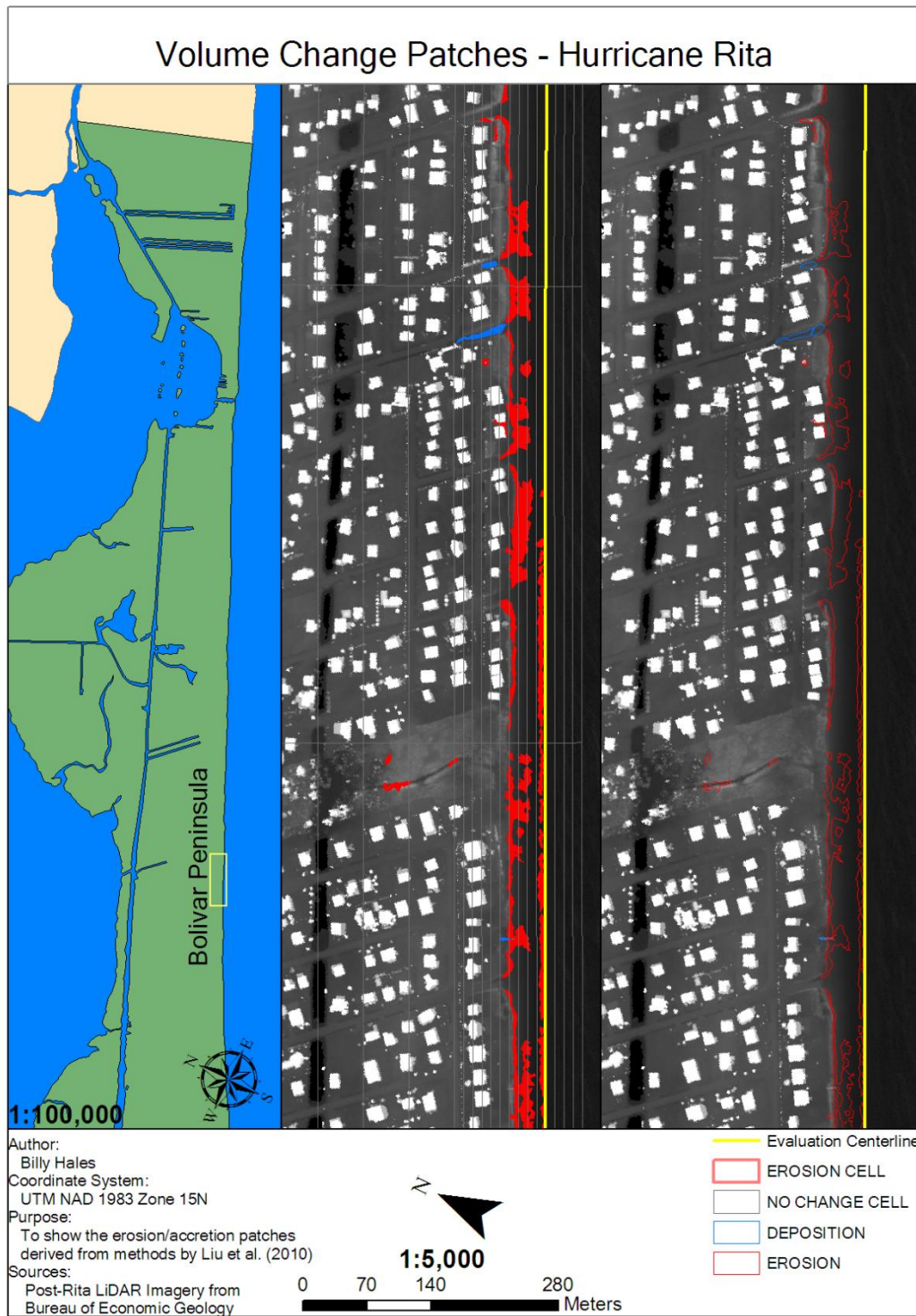


Figure D.43. Hurricane Rita section 15/28 of 1:5000 scale volumetric changes. Corresponds to J-K on Figure 4.26.

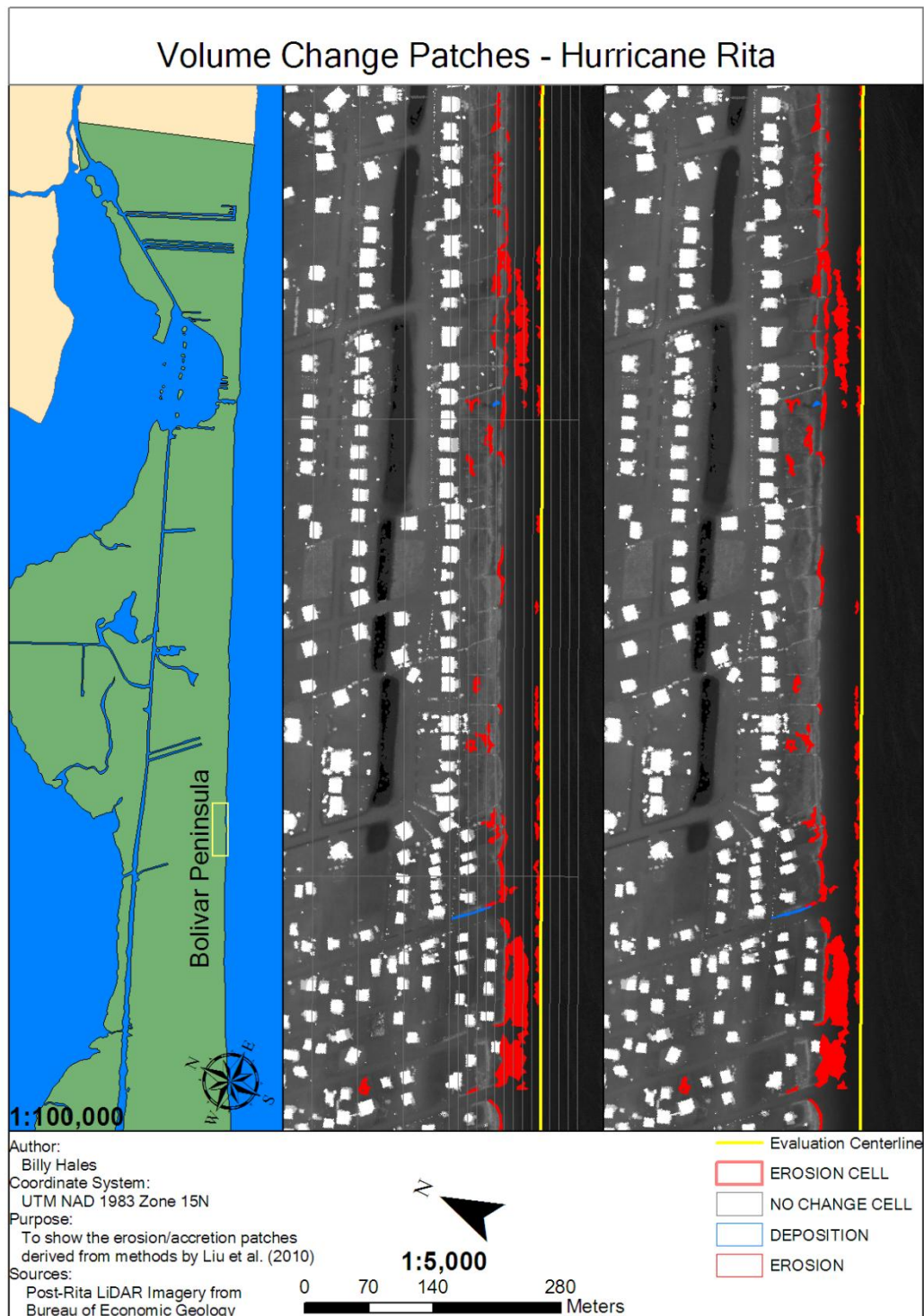


Figure D.44. Hurricane Rita section 16/28 of 1:5000 scale volumetric changes. Corresponds to J-K,K-L on Figure 4.26.

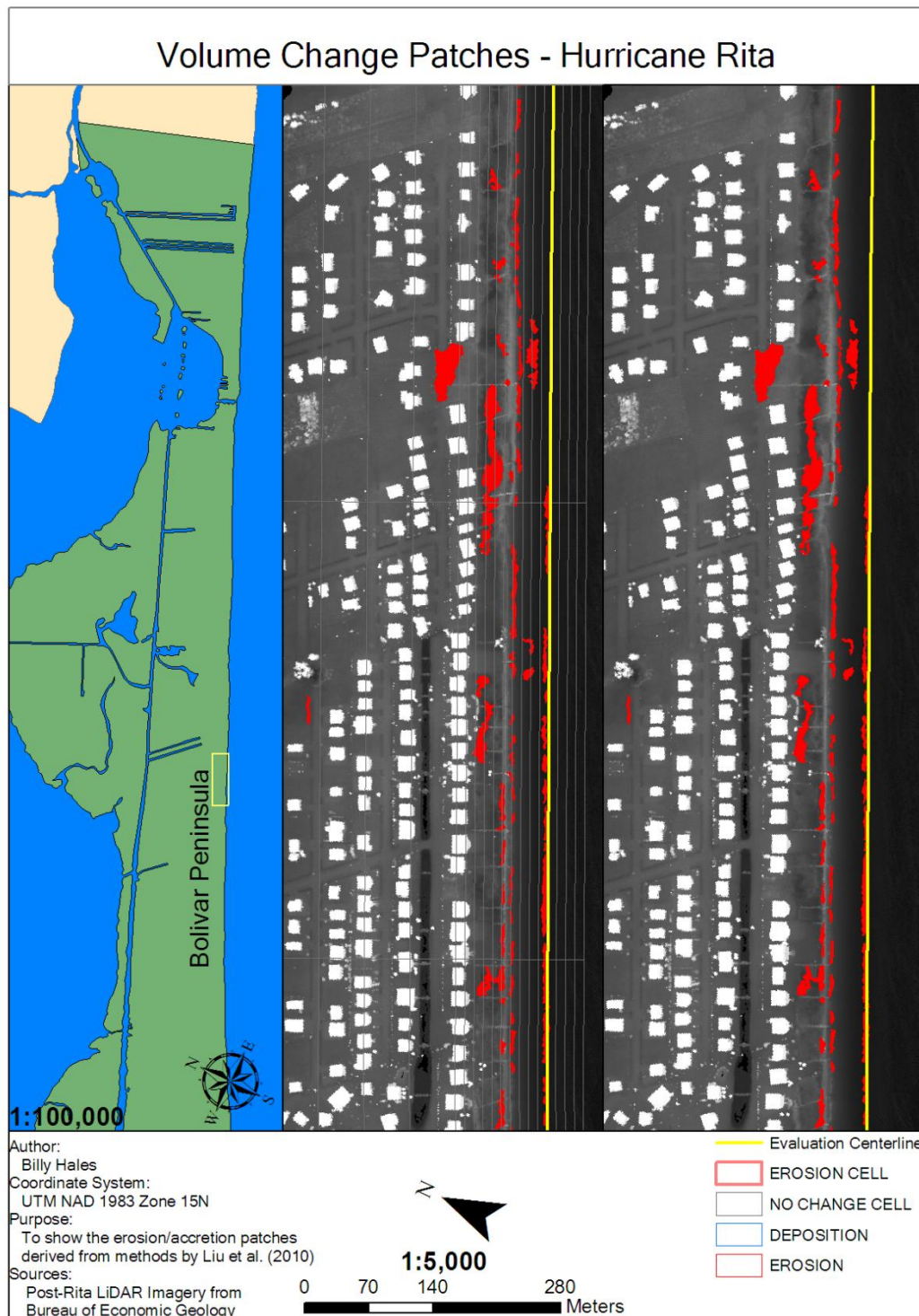


Figure D.45. Hurricane Rita section 17/28 of 1:5000 scale volumetric changes. Corresponds to K-L on Figure 4.26.

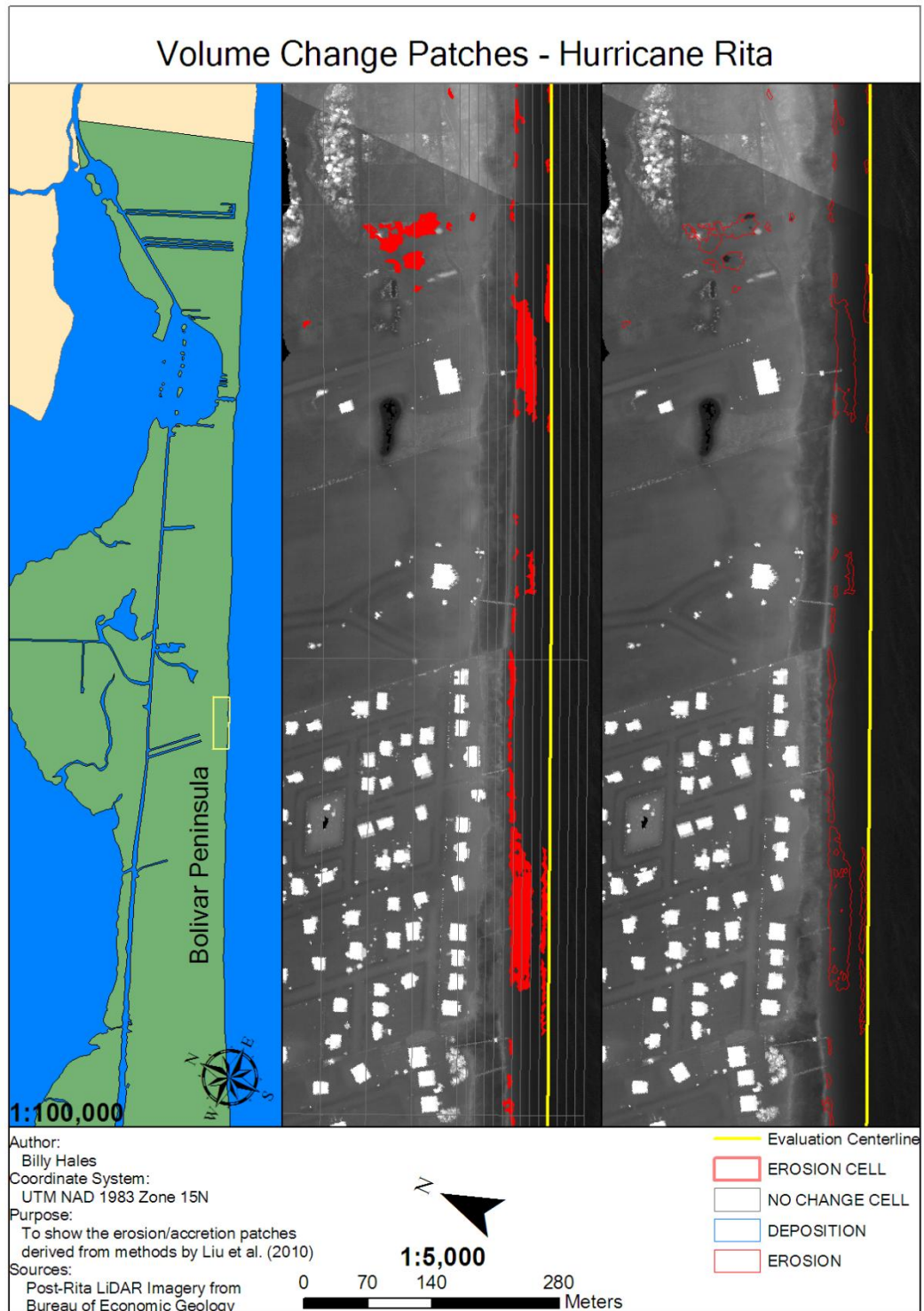


Figure D.46. Hurricane Rita section 18/28 of 1:5000 scale volumetric changes. Corresponds to K-L,L-M on Figure 4.26.

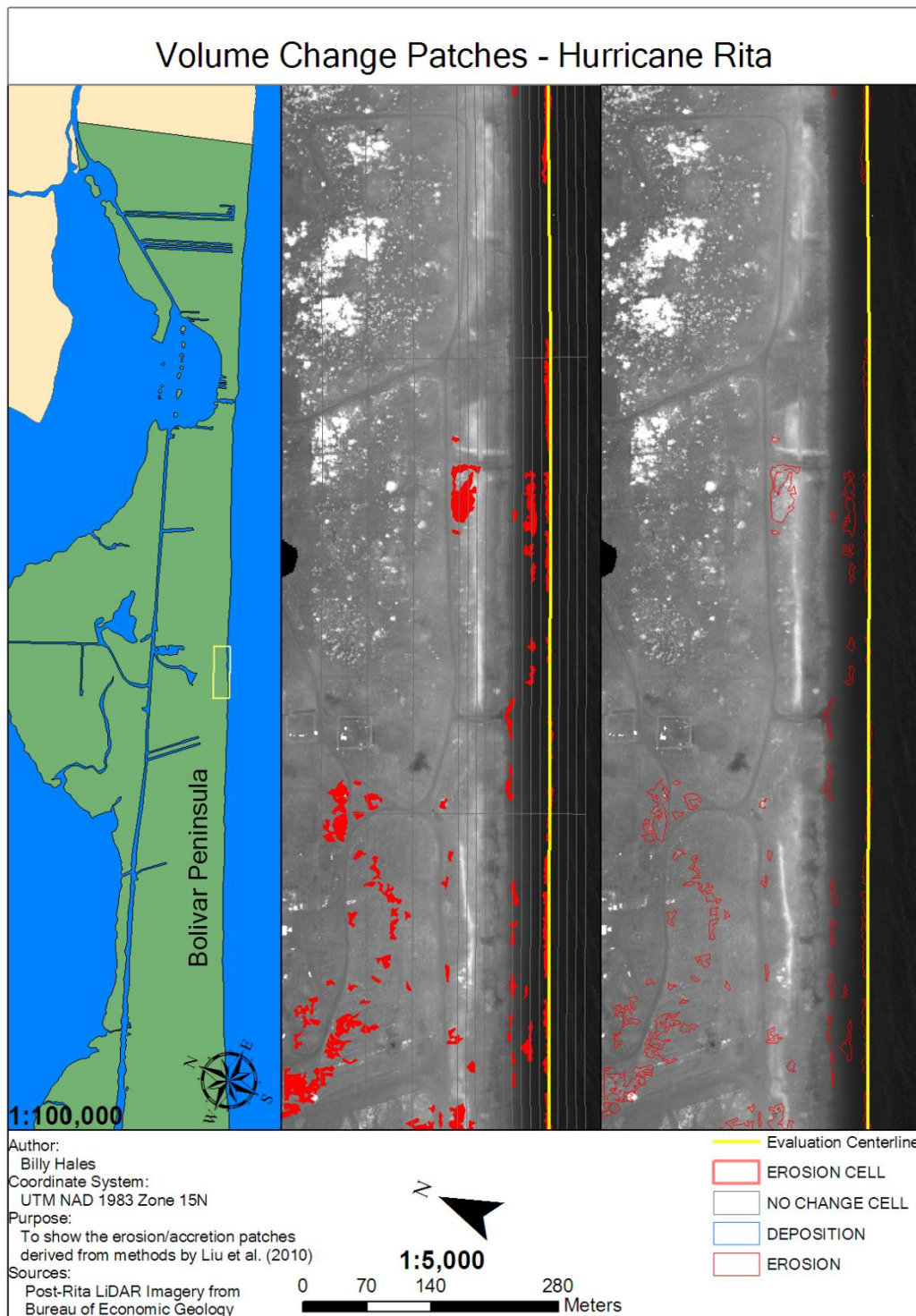


Figure D.47. Hurricane Rita section 19/28 of 1:5000 scale volumetric changes. Corresponds to L-M on Figure 4.26.

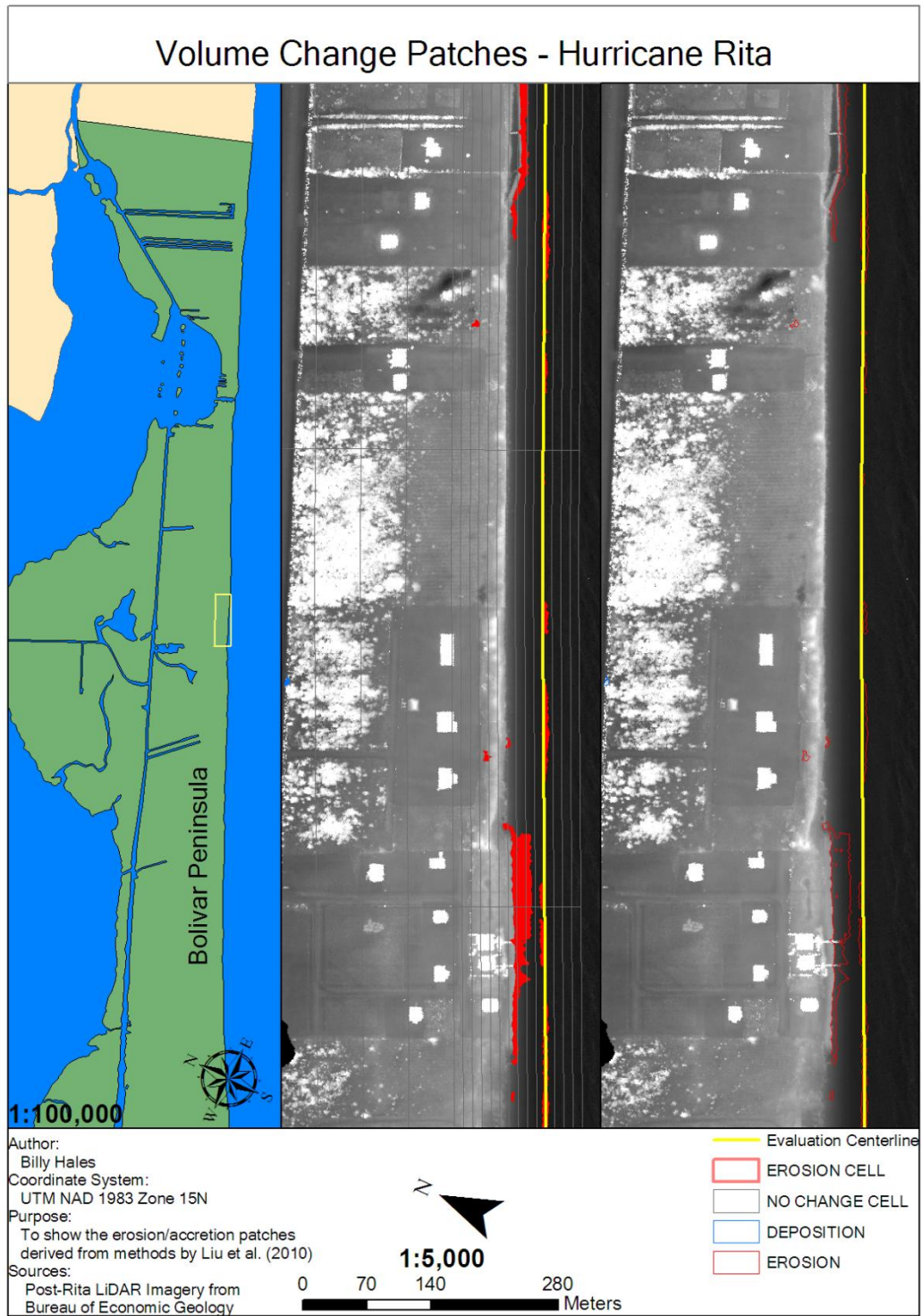


Figure D.48. Hurricane Rita section 20/28 of 1:5000 scale volumetric changes. Corresponds to L-M,M-N on Figure 4.27.

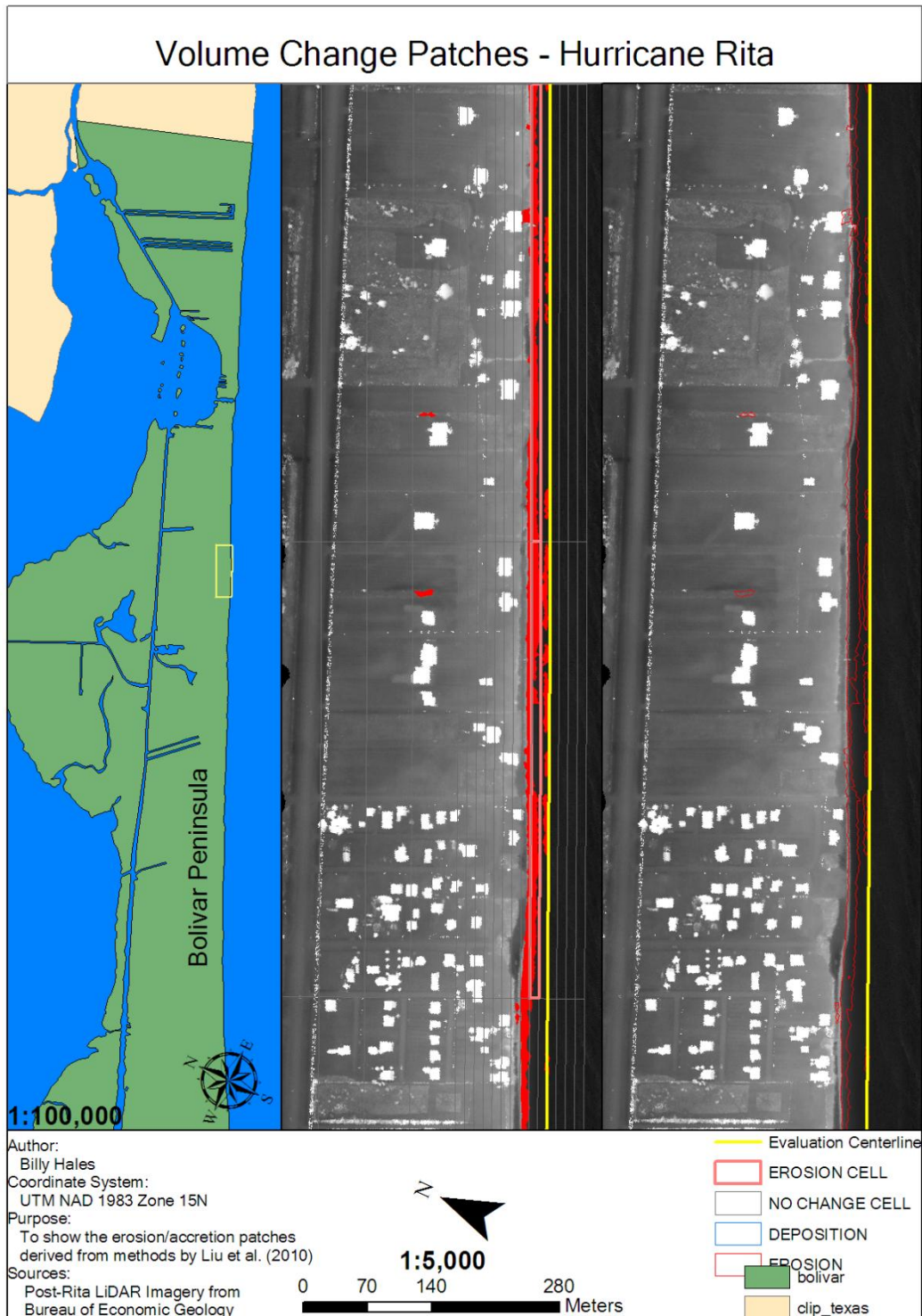


Figure D.49. Section 21/28 of 1:5000 scale output from coastal morphology analyst. Corresponds to M-N,N-O on Figure 4.27.

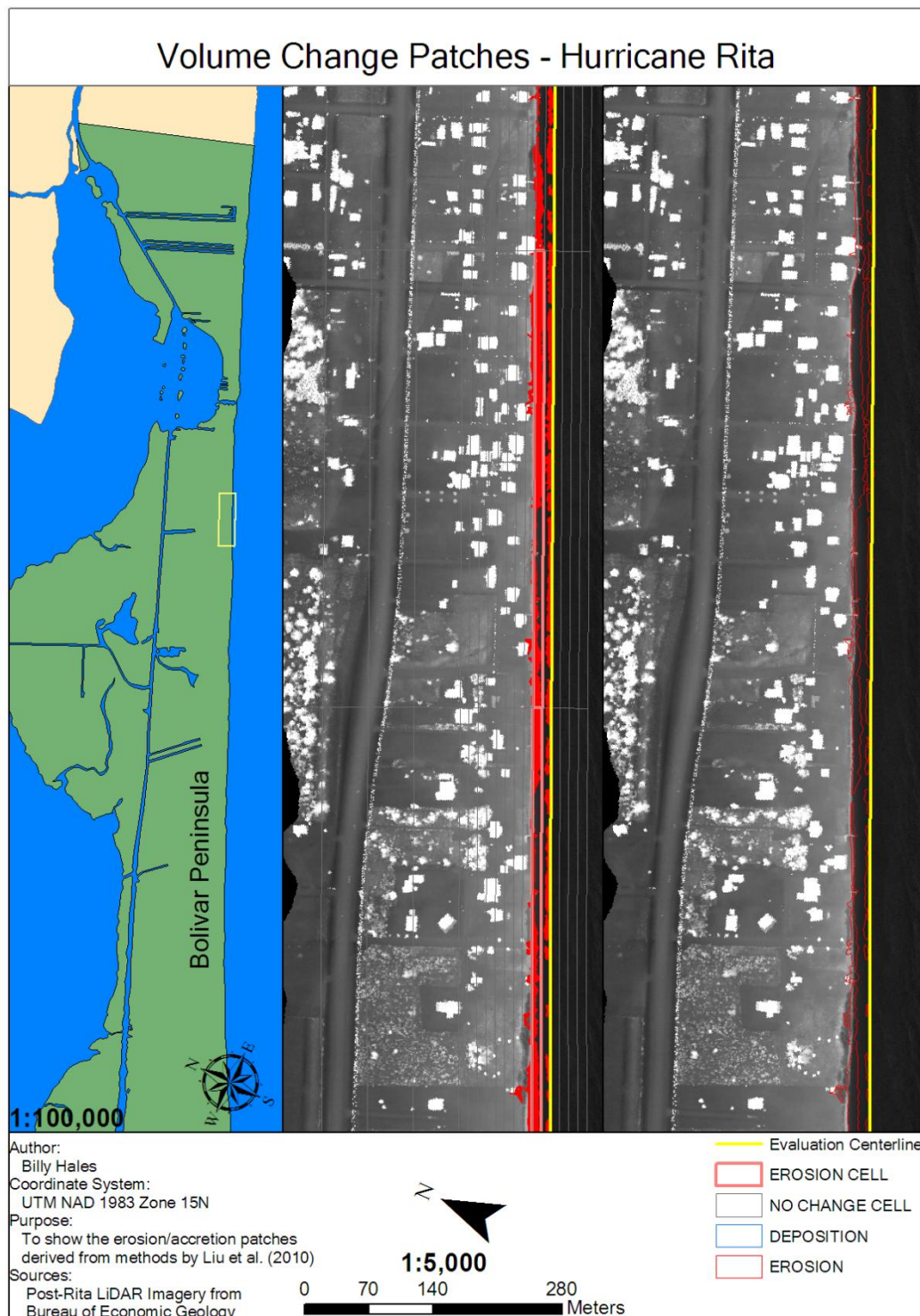


Figure D.50. Section 22/28 of 1:5000 scale output from coastal morphology analyst. Corresponds to N-O on Figure 4.27.

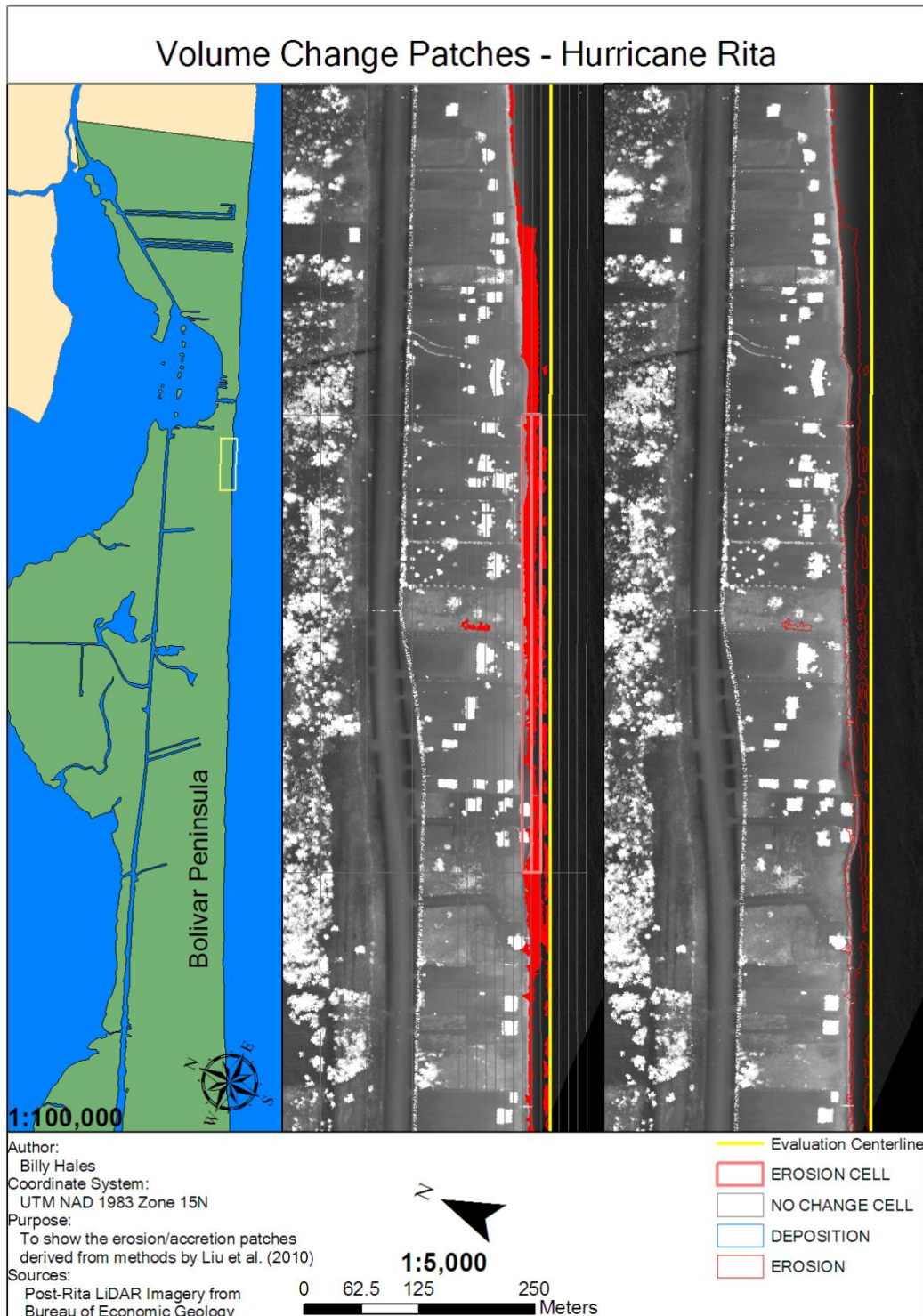


Figure D.51: Section 23/28 of 1:5000 scale output from coastal morphology analyst. Corresponds to O-P on Figure 4.27.

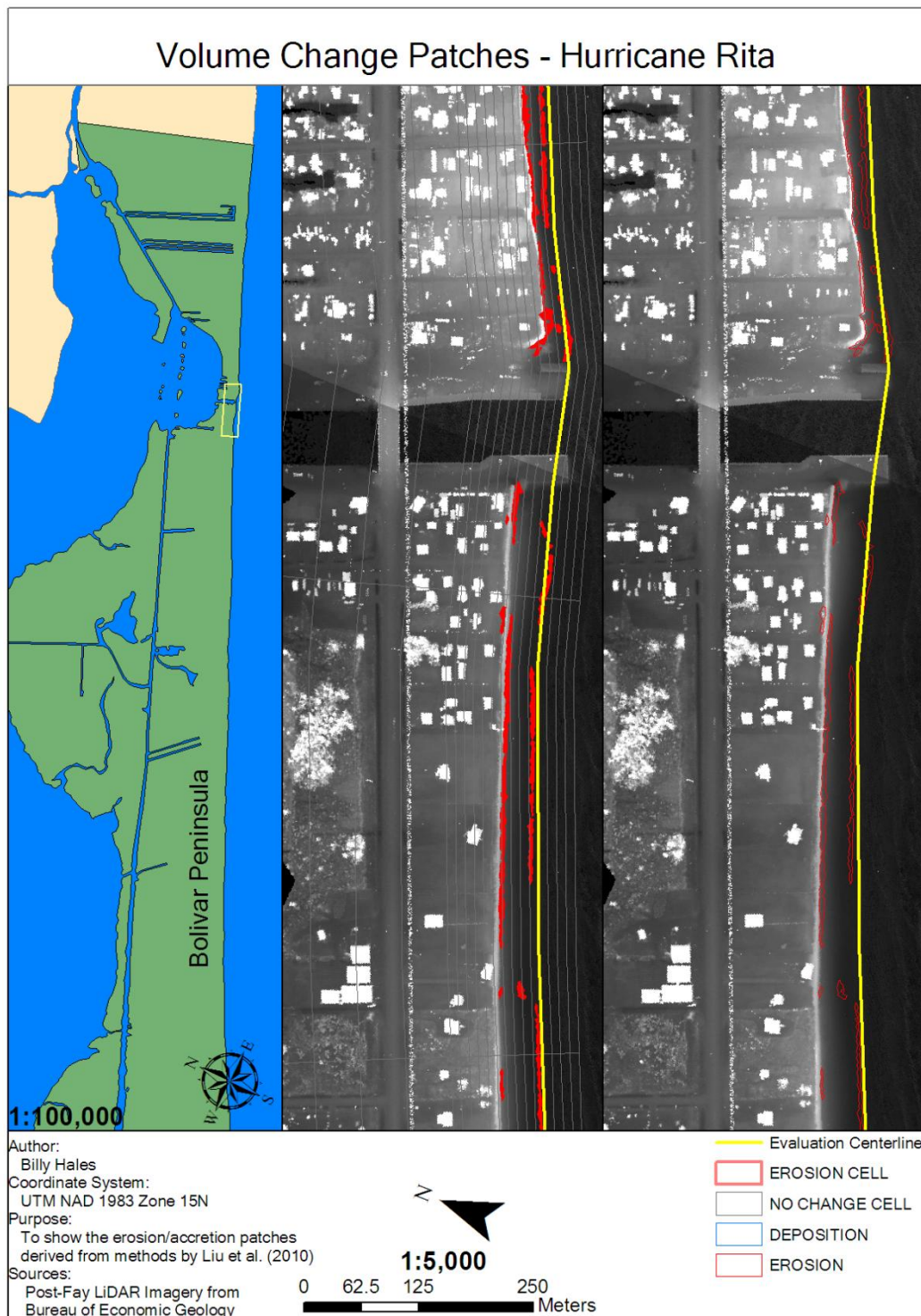


Figure D.52: Section 24/28 of 1:5000 scale output from coastal morphology analyst. Corresponds to O-P,P-Q on Figures 4.27 and 4.28.

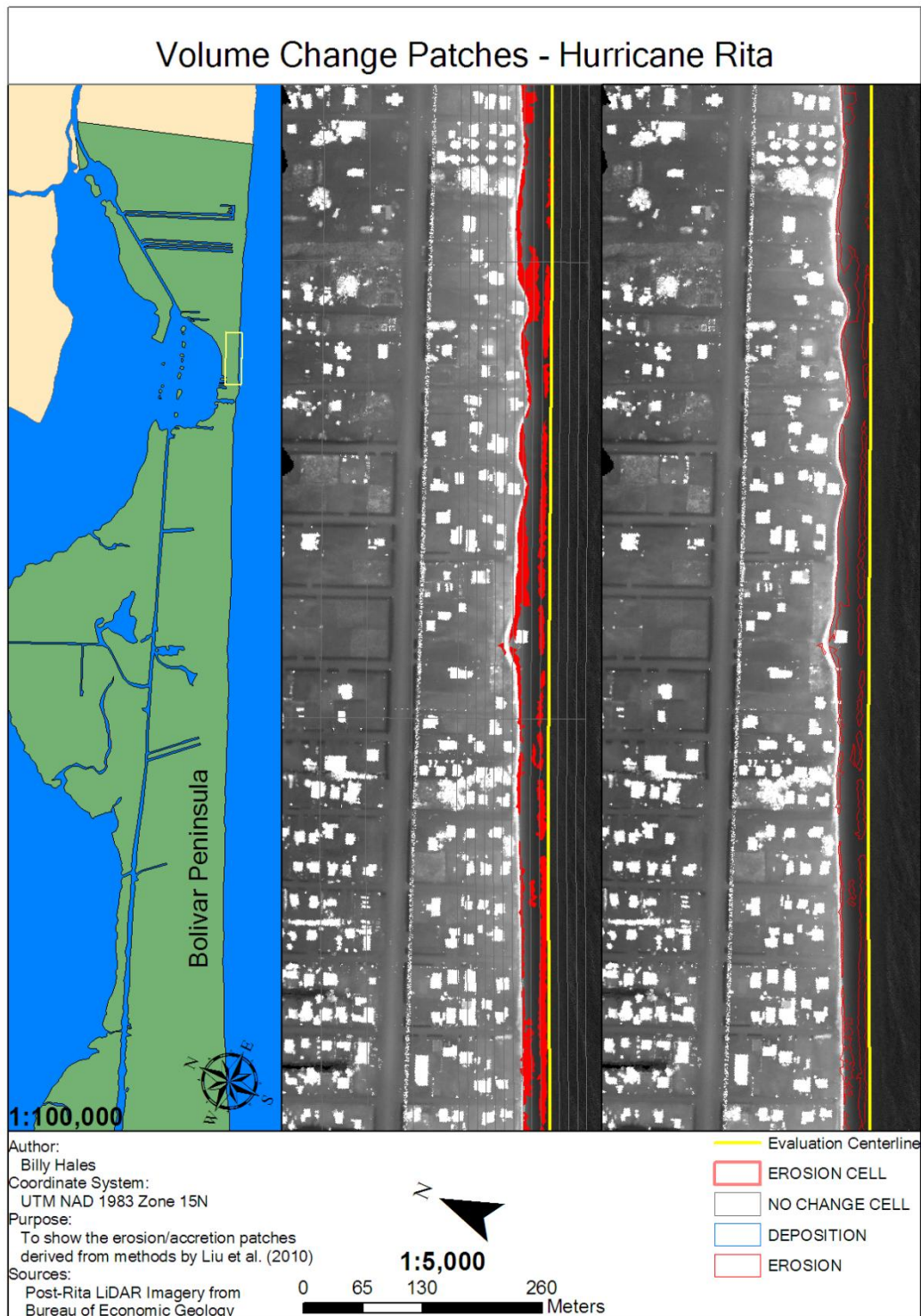


Figure D.53. Hurricane Rita section 25/28 of 1:5000 scale volumetric changes. Corresponds to P-O on Figure 4.28.

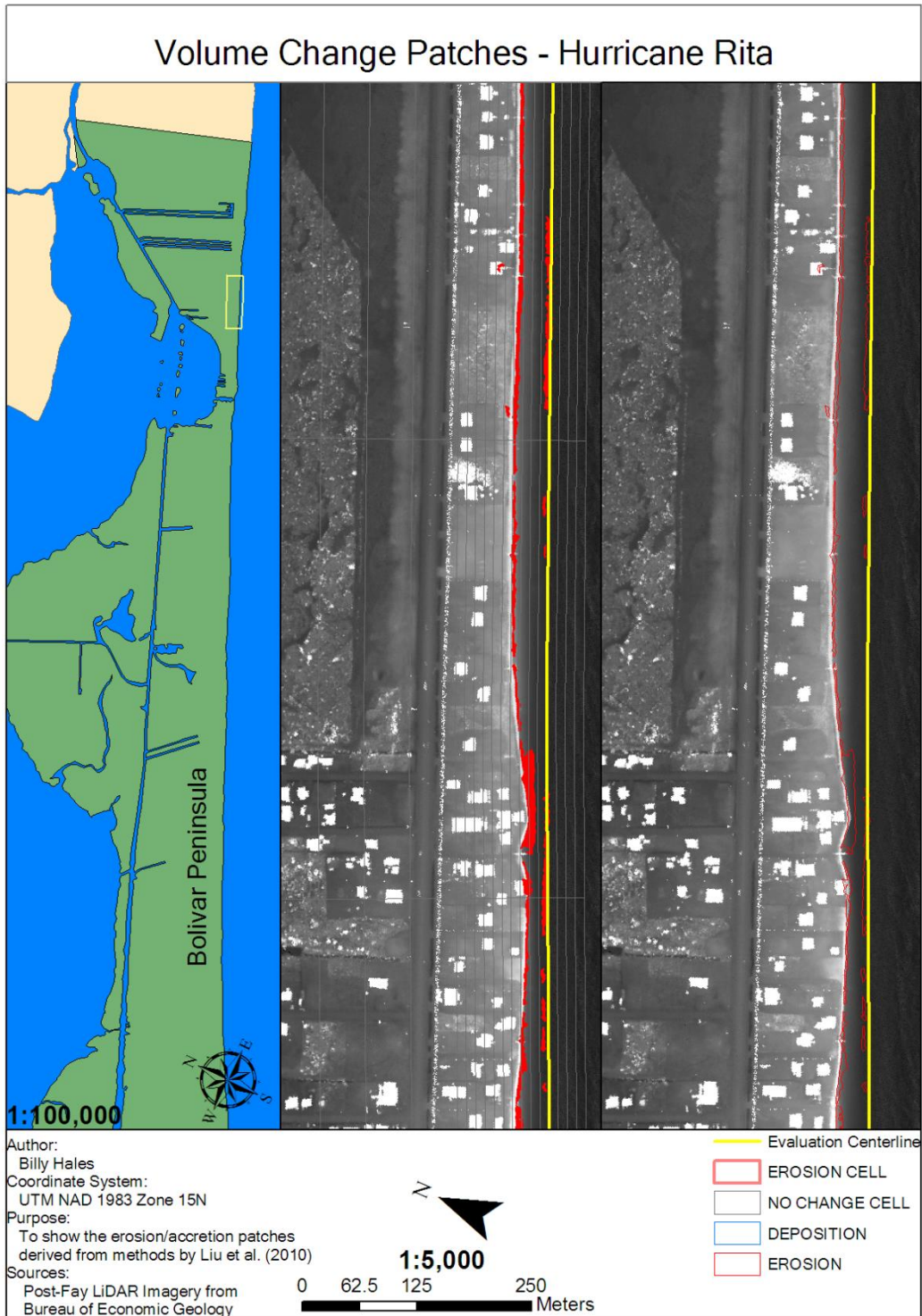


Figure D.54. Hurricane Rita section 26/28 of 1:5000 scale volumetric changes. Corresponds to P-Q,Q-R on Figure 4.28.

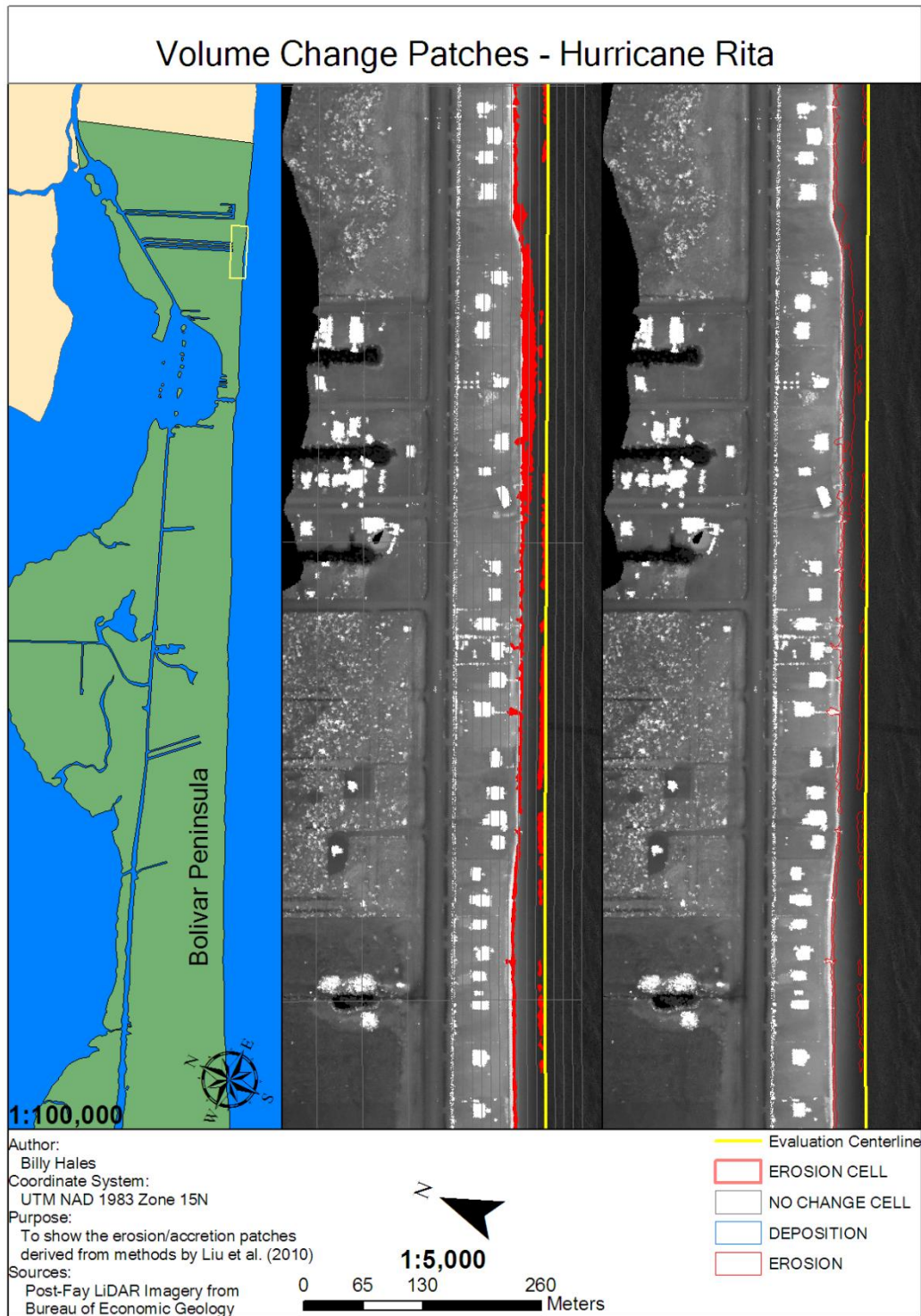


Figure D.55. Hurricane Rita section 27/28 of 1:5000 scale volumetric changes. Corresponds to Q-R on Figure 4.28.

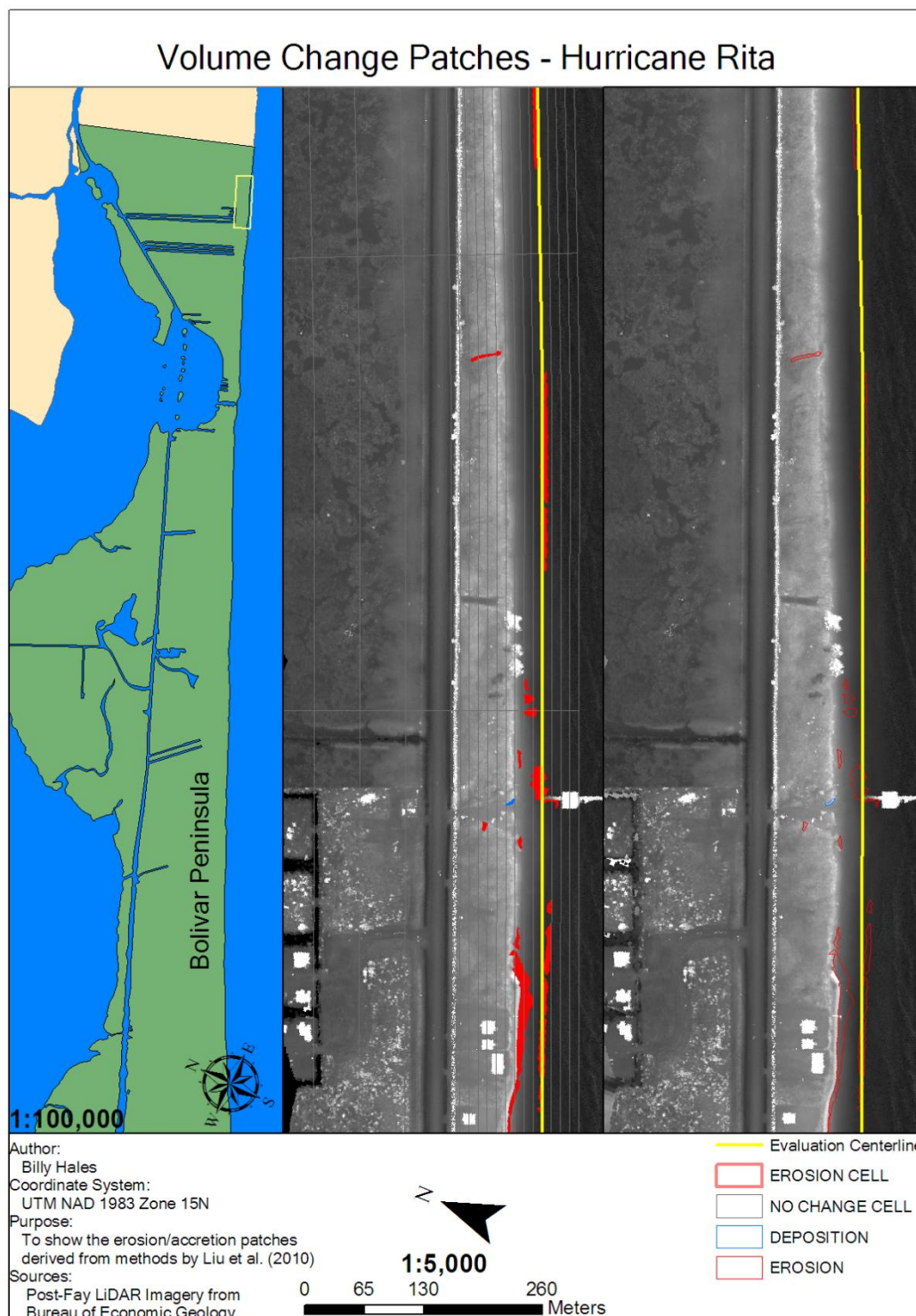


Figure D.56. Hurricane Rita section 28/28 of 1:5000 scale volumetric changes. Corresponds to Q-R,R-S on Figure 4.28.

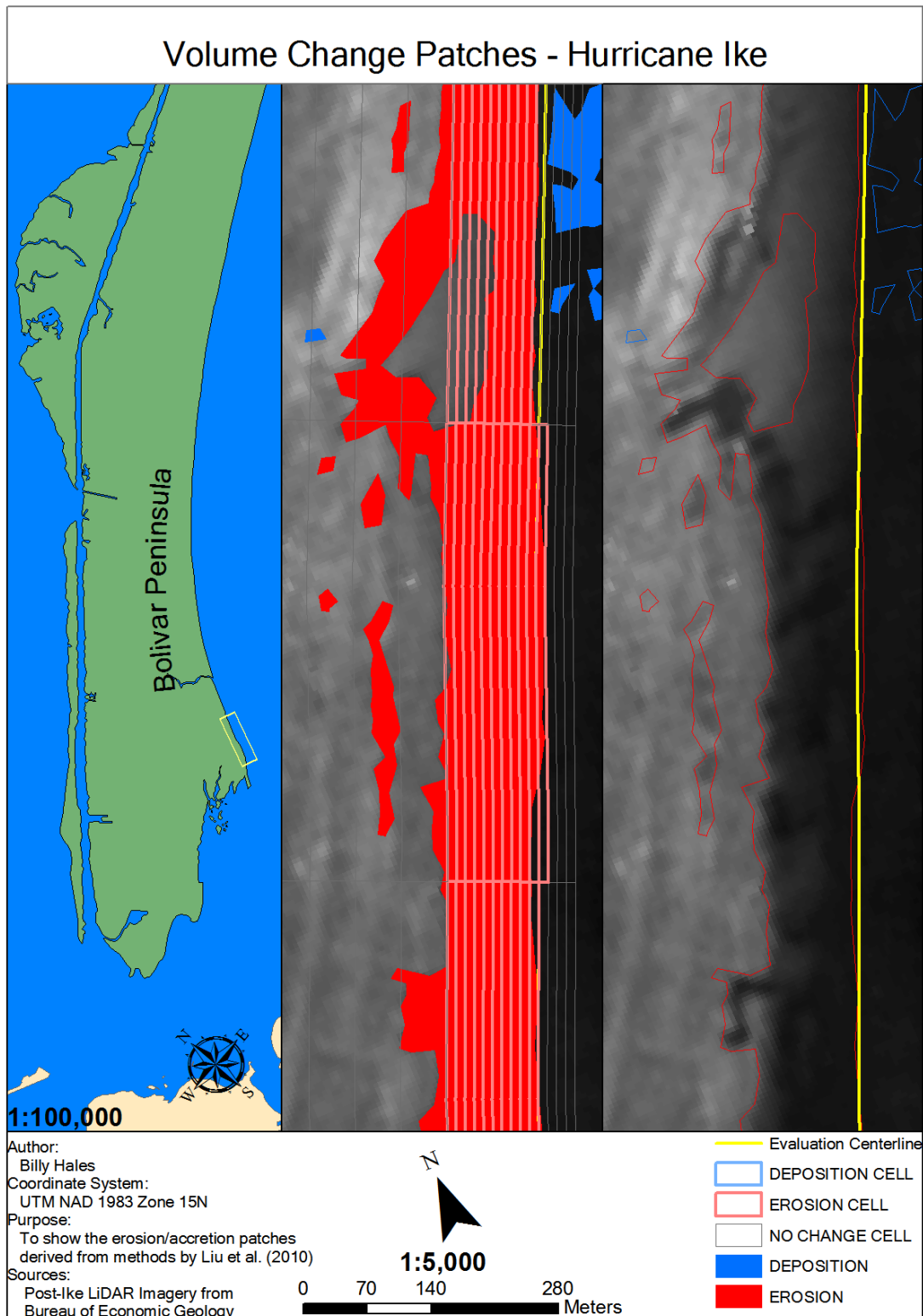


Figure D.57. Hurricane Ike section 1/28 of 1:5000 scale volumetric changes. Corresponds to A-B on Figure 4.31.

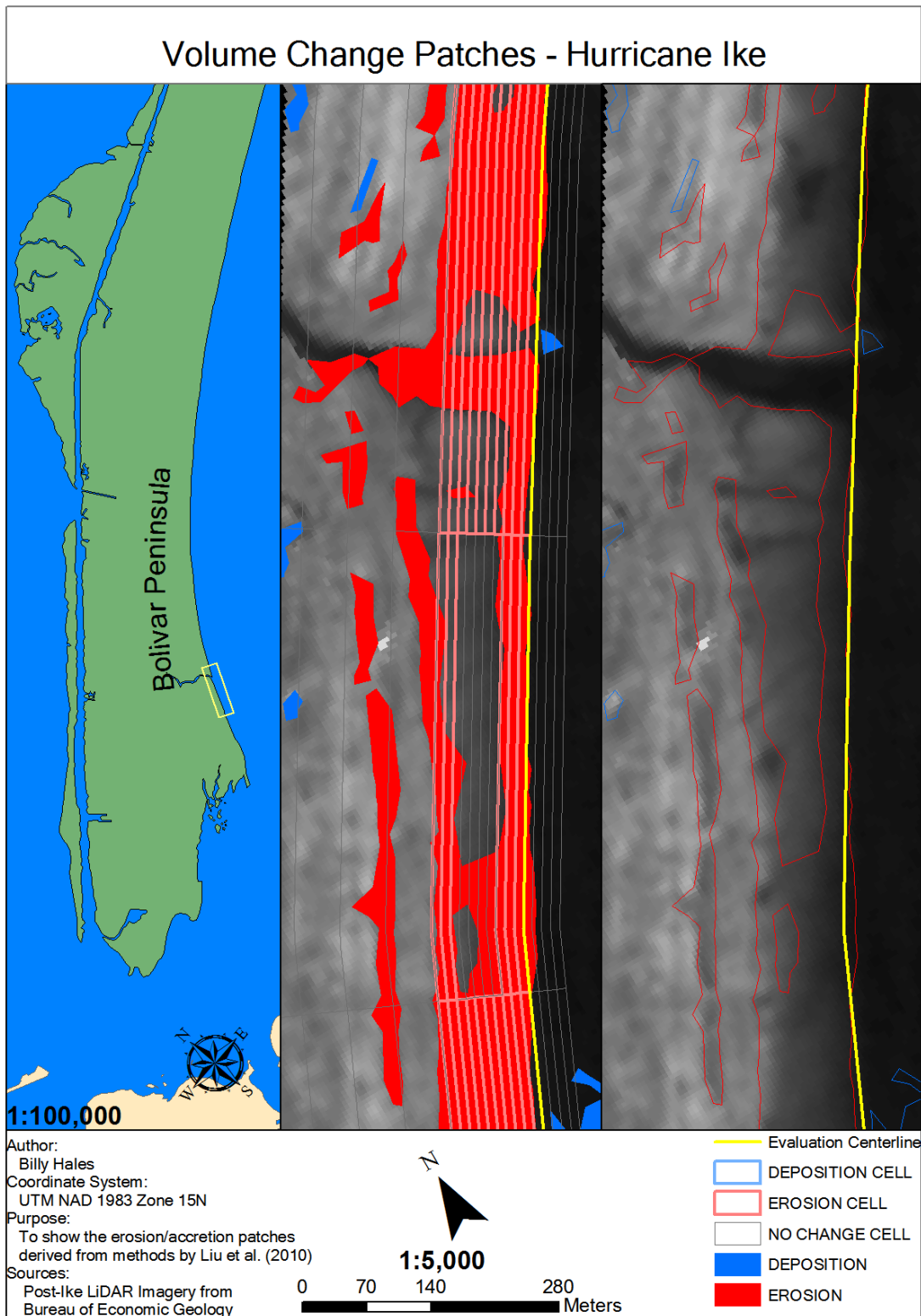


Figure D.58. Hurricane Ike section 2/28 of 1:5000 scale volumetric changes. Corresponds to A-B,B-C on Figure 4.31.

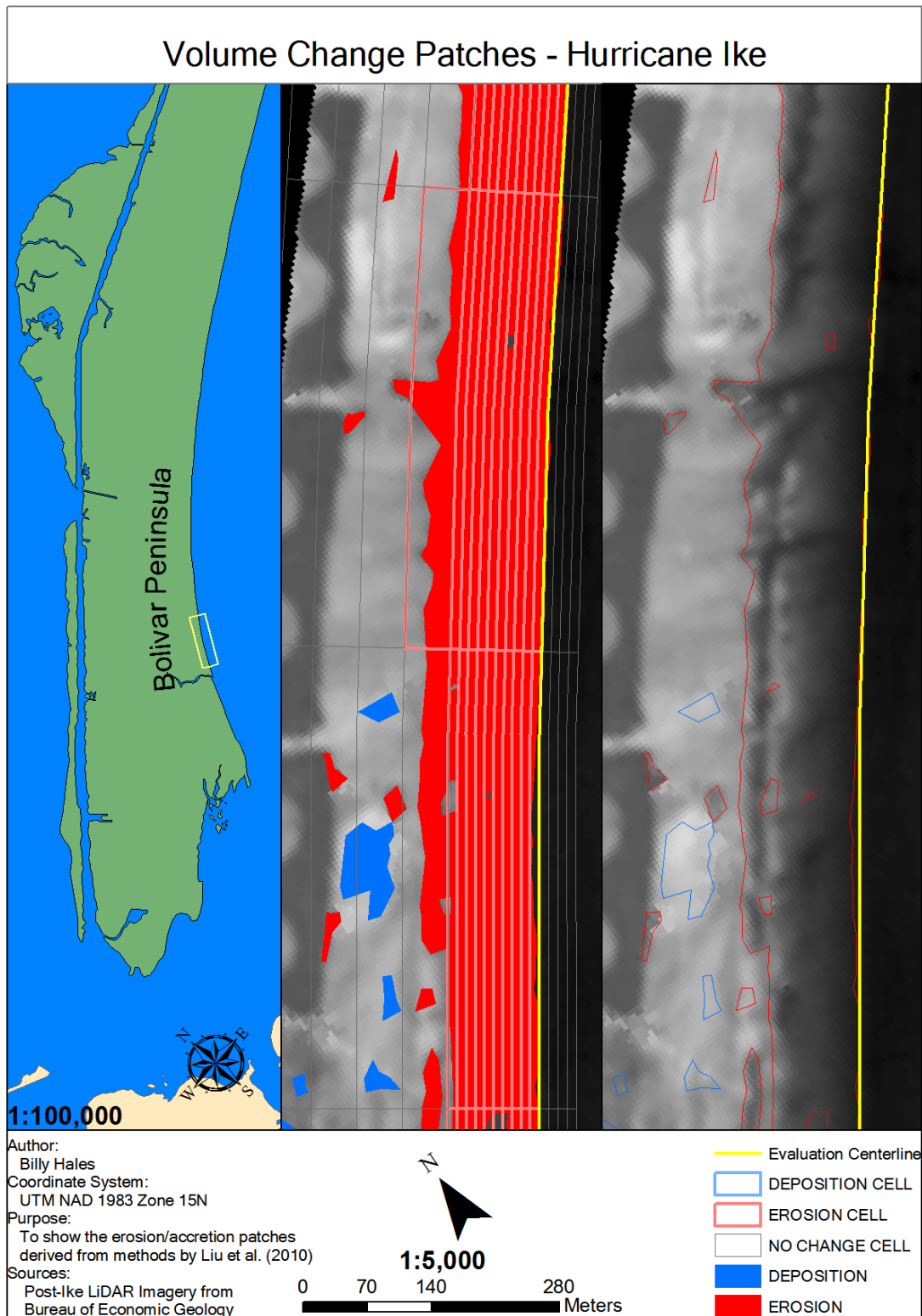


Figure D.59. Hurricane Ike section 3/28 of 1:5000 scale volumetric changes. Corresponds to B-C,C-D on Figure 4.31.

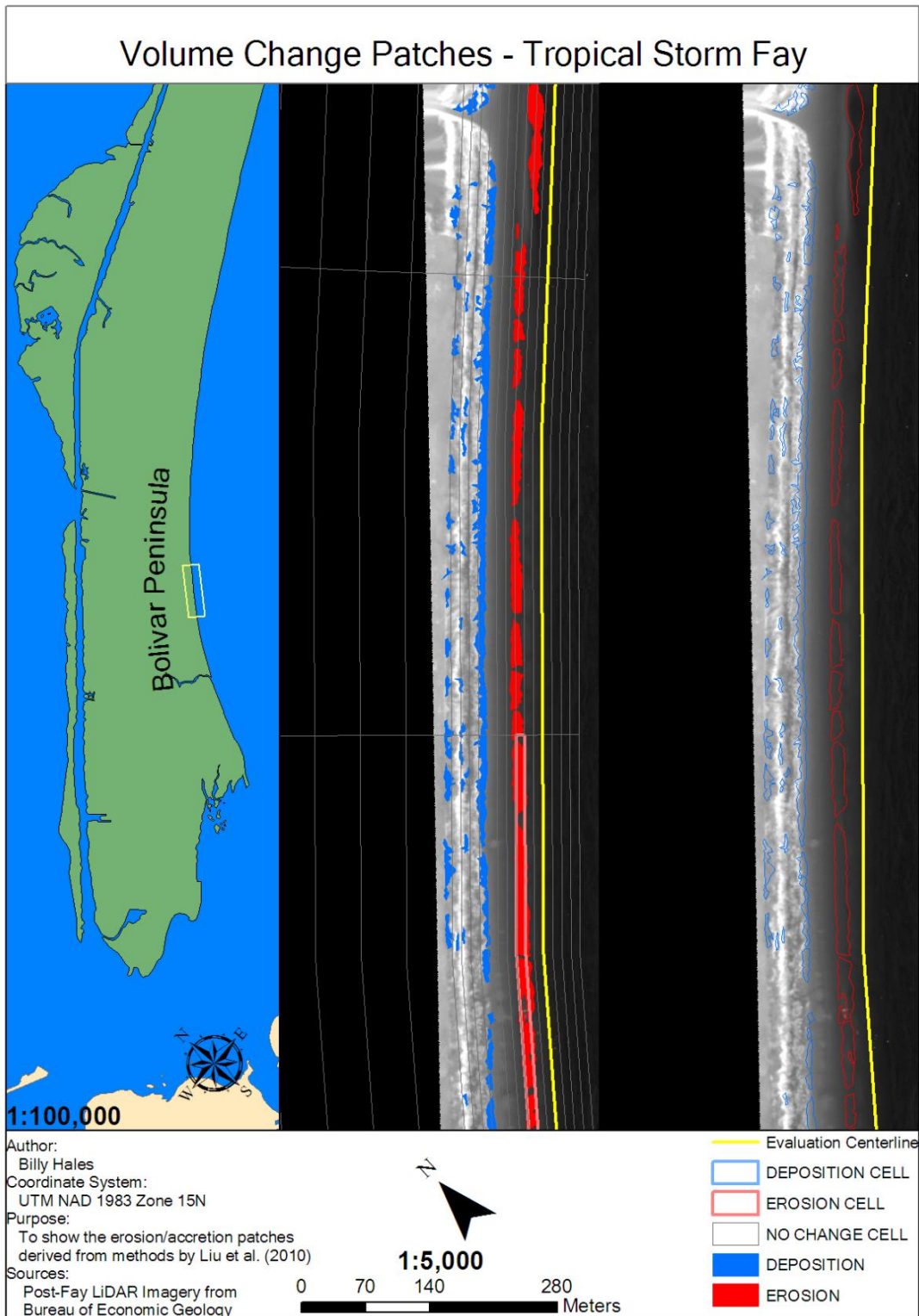


Figure D.60. Hurricane Ike section 4/28 of 1:5000 scale volumetric changes. Corresponds to C-D on Figure 4.31.

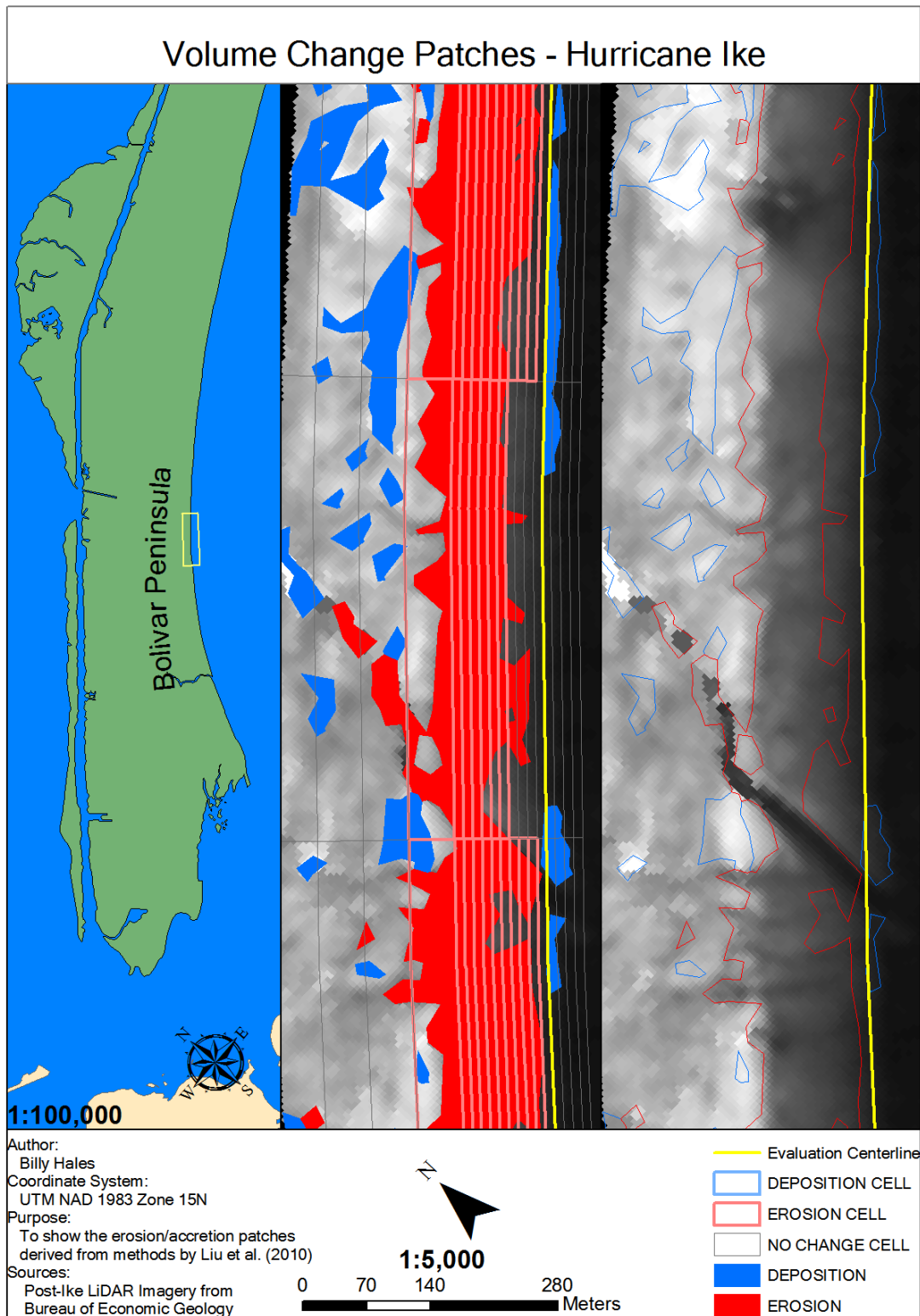


Figure D.61. Hurricane Ike section 5/28 of 1:5000 scale volumetric changes. Corresponds to C-D, D-E on Figures 4.31 and 4.32.

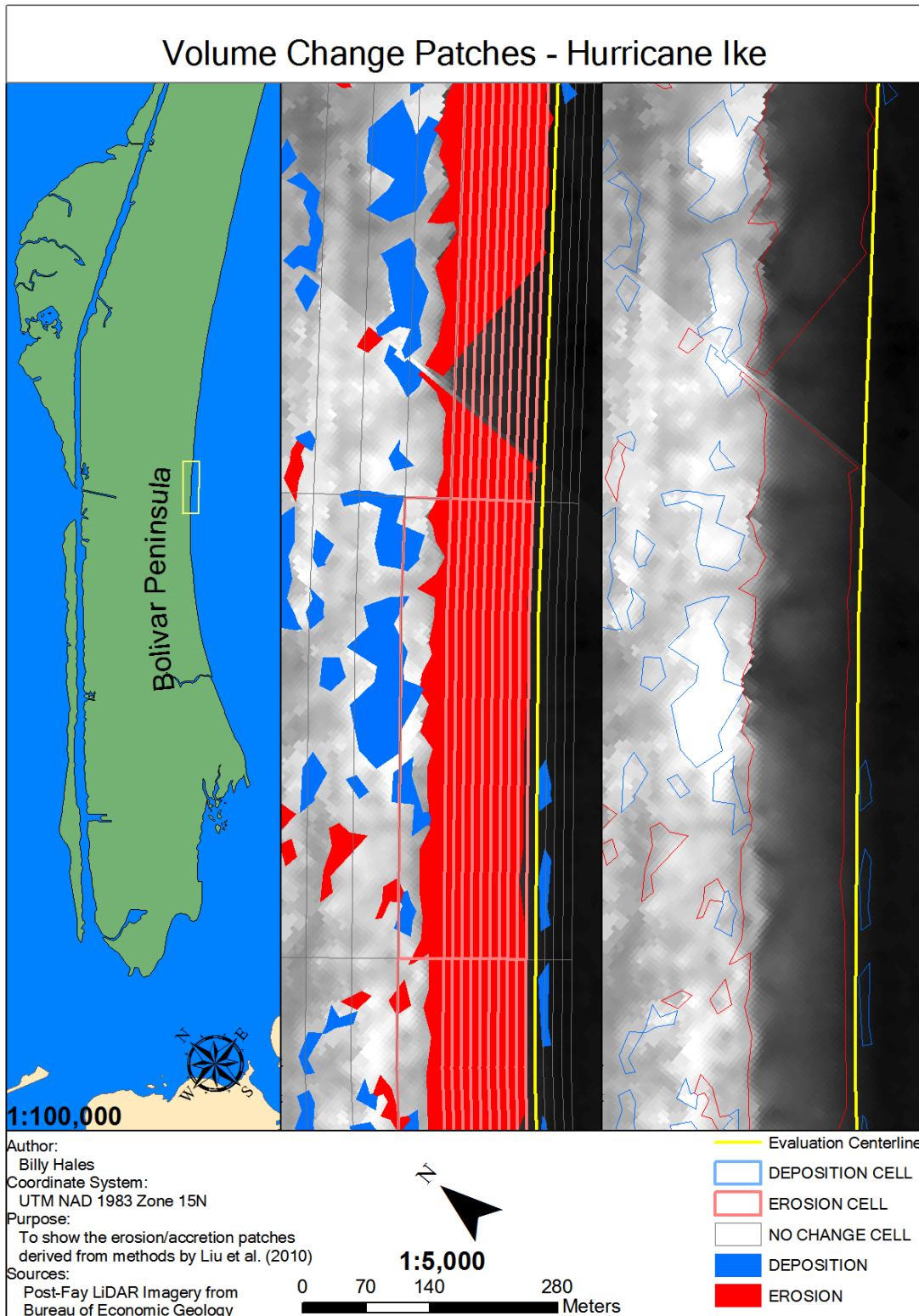


Figure D.62. Hurricane Ike section 6/28 of 1:5000 scale volumetric changes. Corresponds to D-E on Figure 4.32.

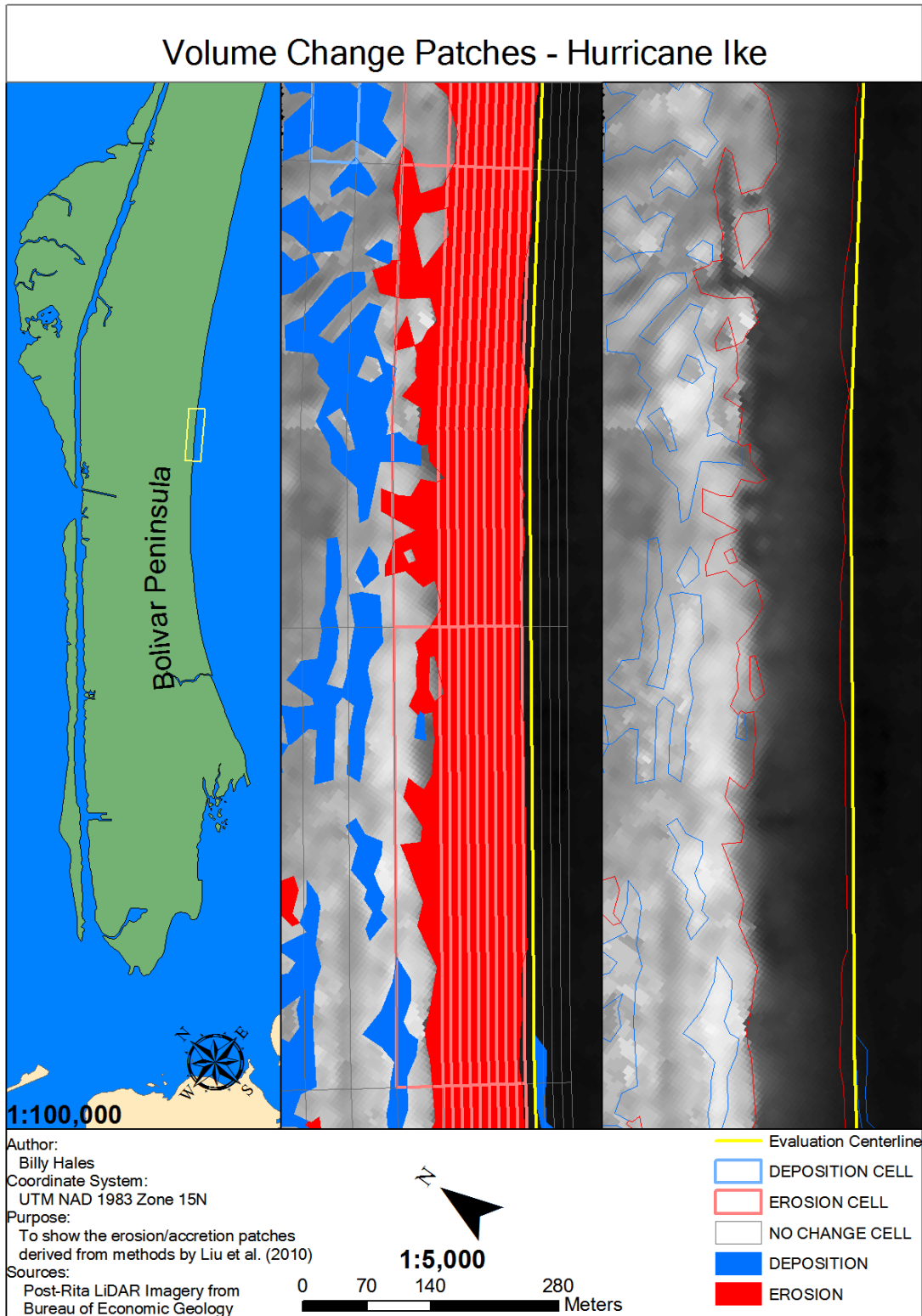


Figure D.63. Hurricane Ike section 7/28 of 1:5000 scale volumetric changes. Corresponds to E-F on Figure 4.32.

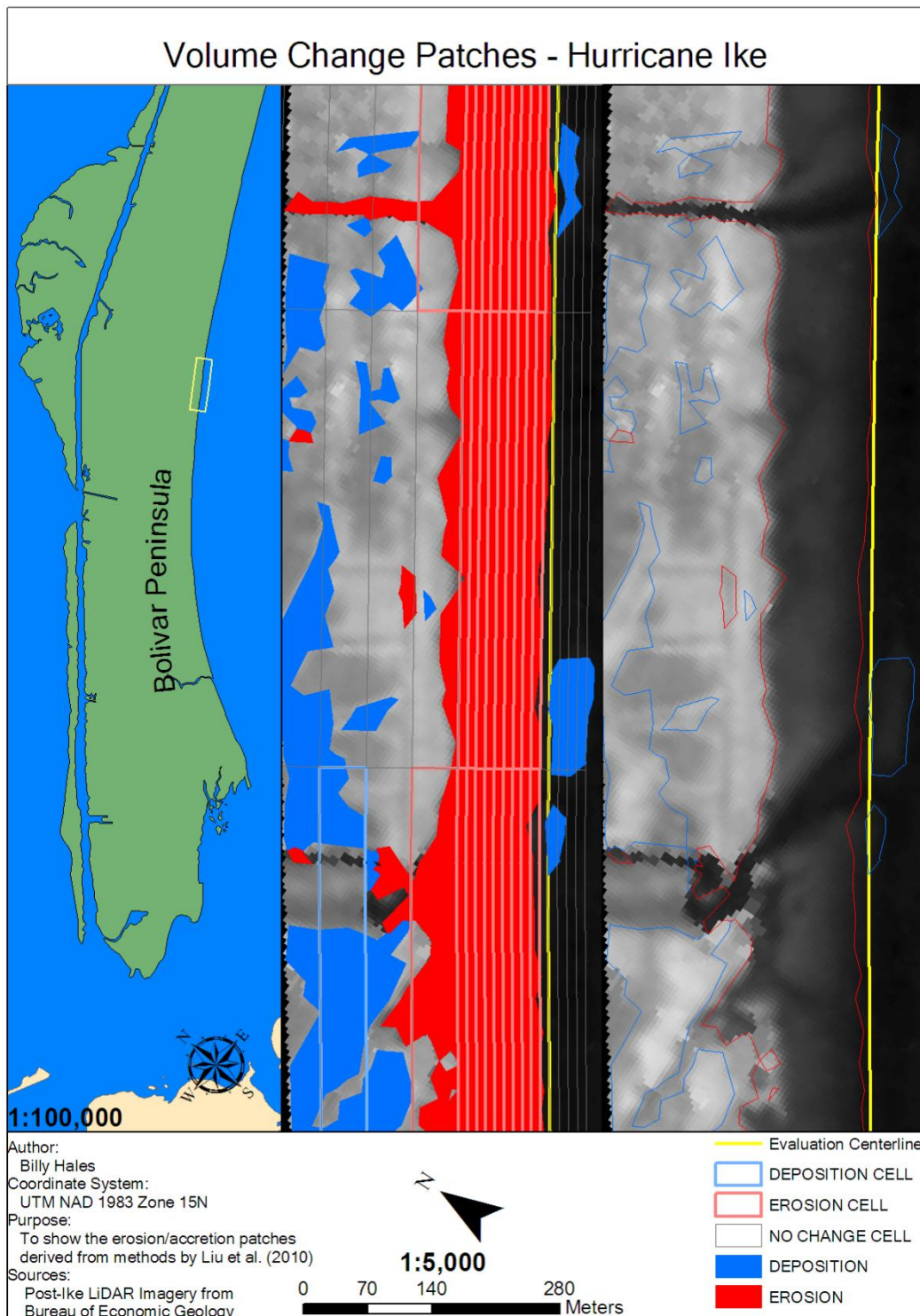


Figure D.64. Hurricane Ike section 8/28 of 1:5000 scale volumetric changes. Corresponds to E-F, F-G on Figure 4.32.

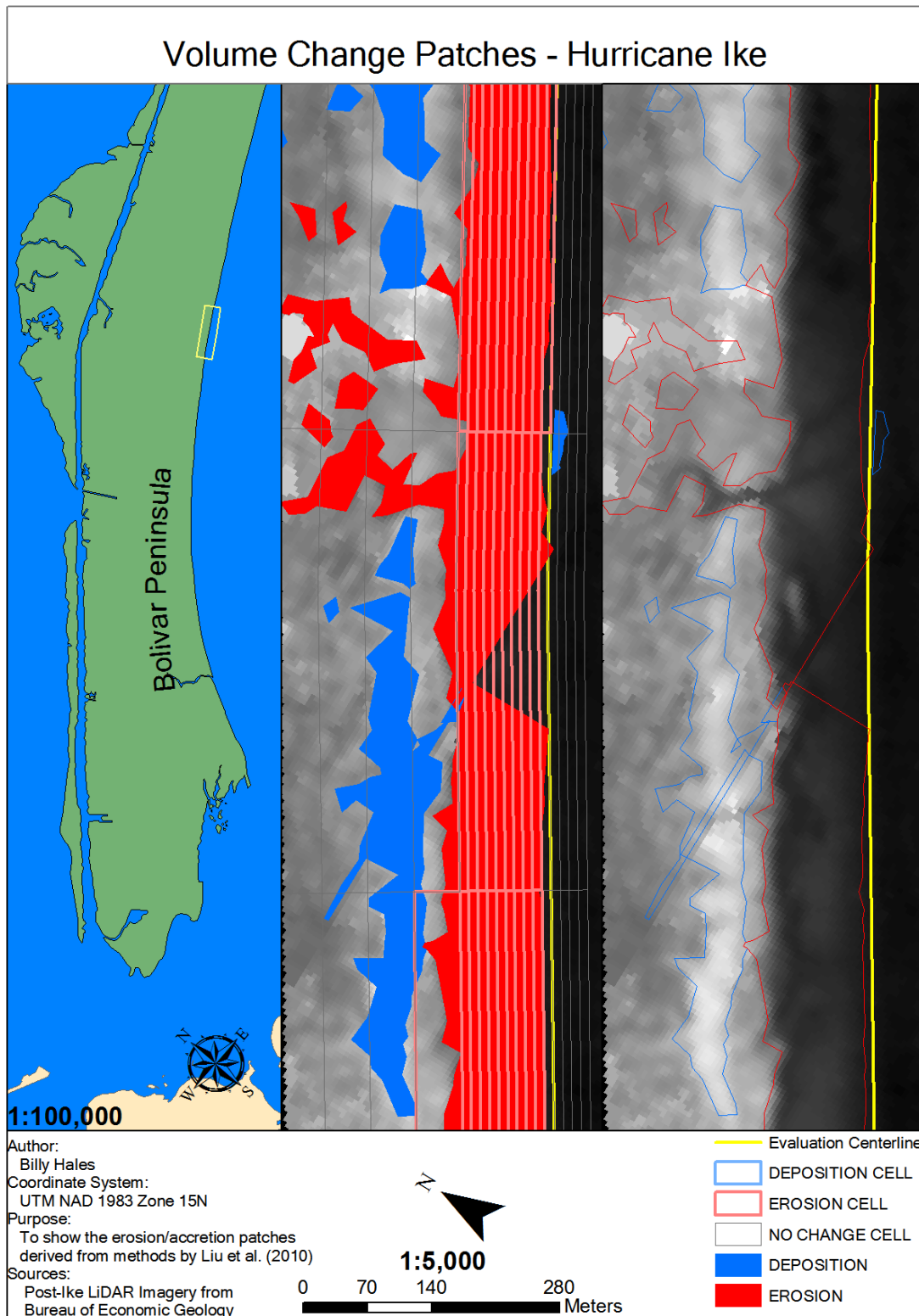


Figure D.65. Hurricane Ike section 9/28 of 1:5000 scale volumetric changes. Corresponds to F-G on Figure 4.32.

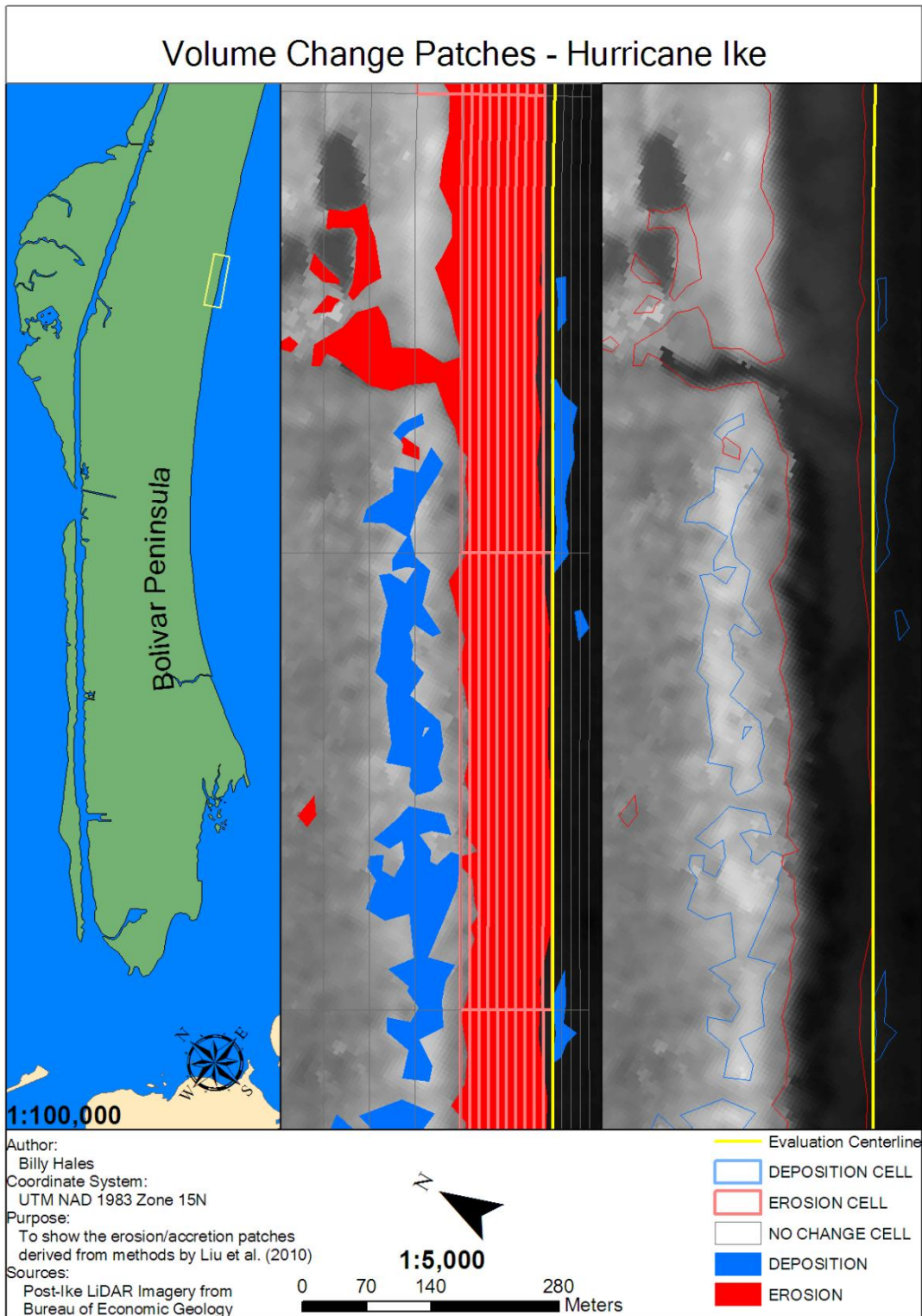


Figure D.66. Hurricane Ike section 10/28 of 1:5000 scale volumetric changes. Corresponds to F-G, G-H on Figures 4.32 and 4.33.

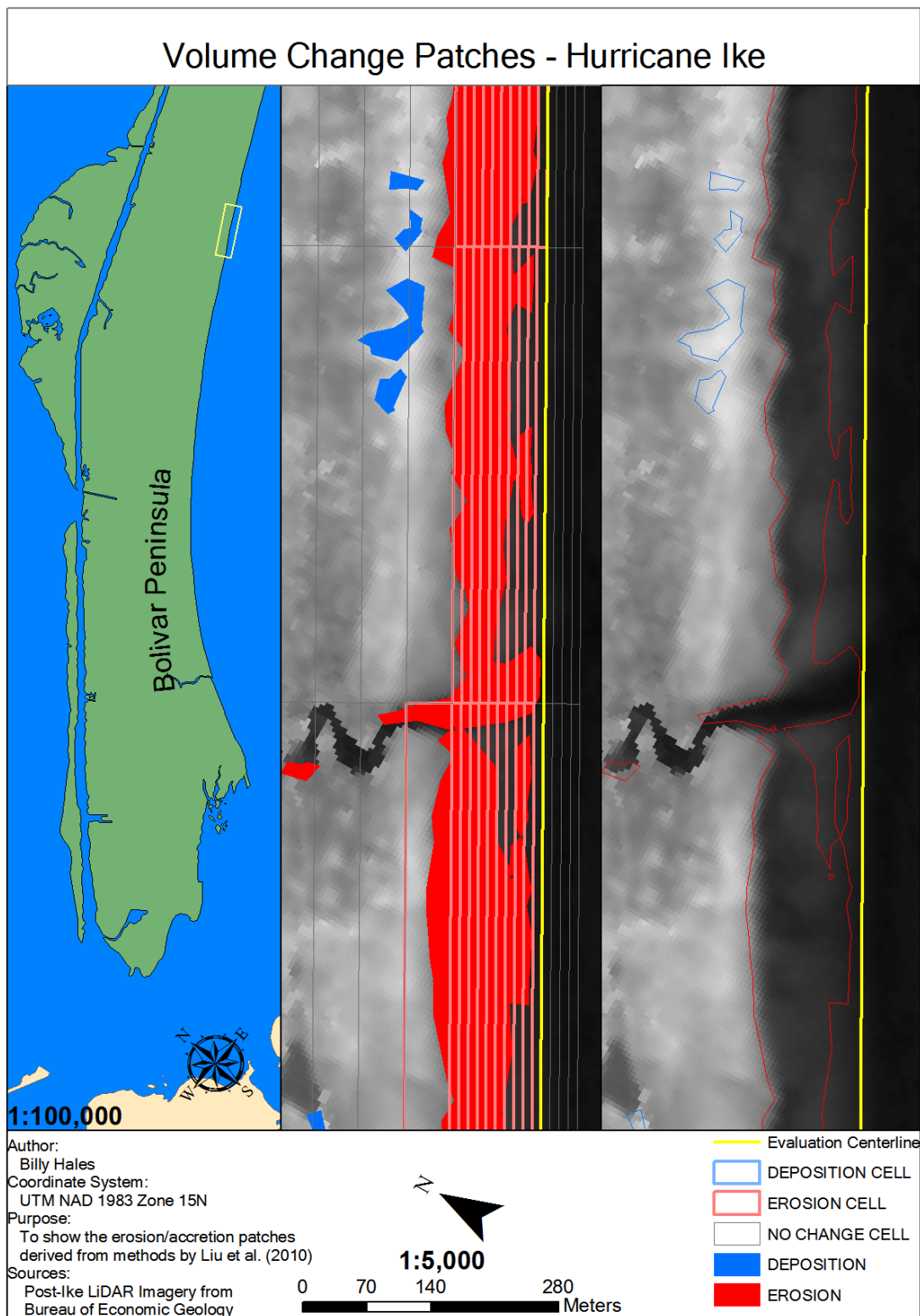


Figure D.67. Hurricane Ike section 11/28 of 1:5000 scale volumetric changes. Corresponds to G-H on Figure 4.33.

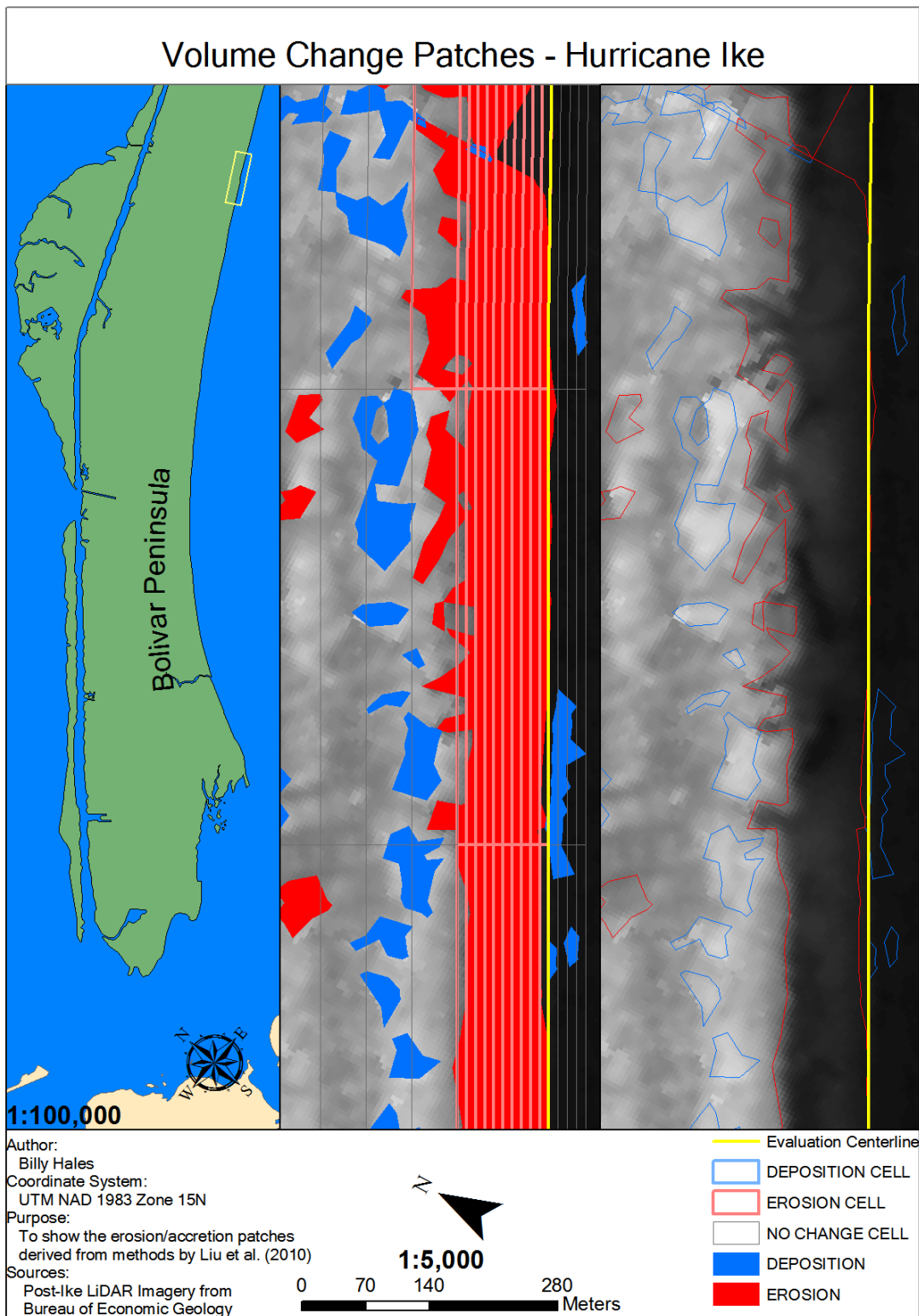


Figure D.68. Hurricane Ike section 12/28 of 1:5000 scale volumetric changes. Corresponds to H-I on Figure 4.33.

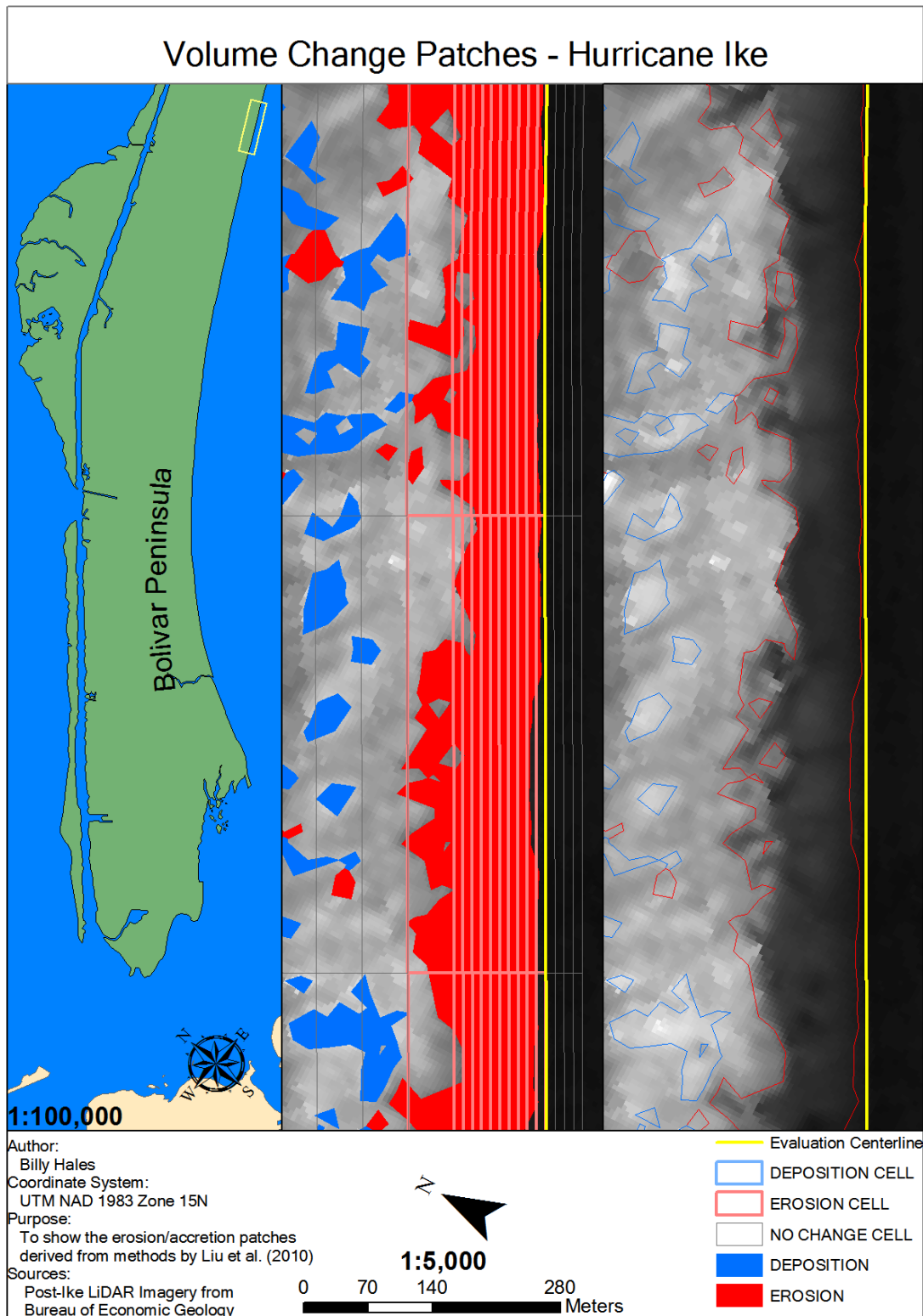


Figure D.69. Hurricane Ike section 13/28 of 1:5000 scale volumetric changes. Corresponds to H-I,I-I-J on Figure 4.33.

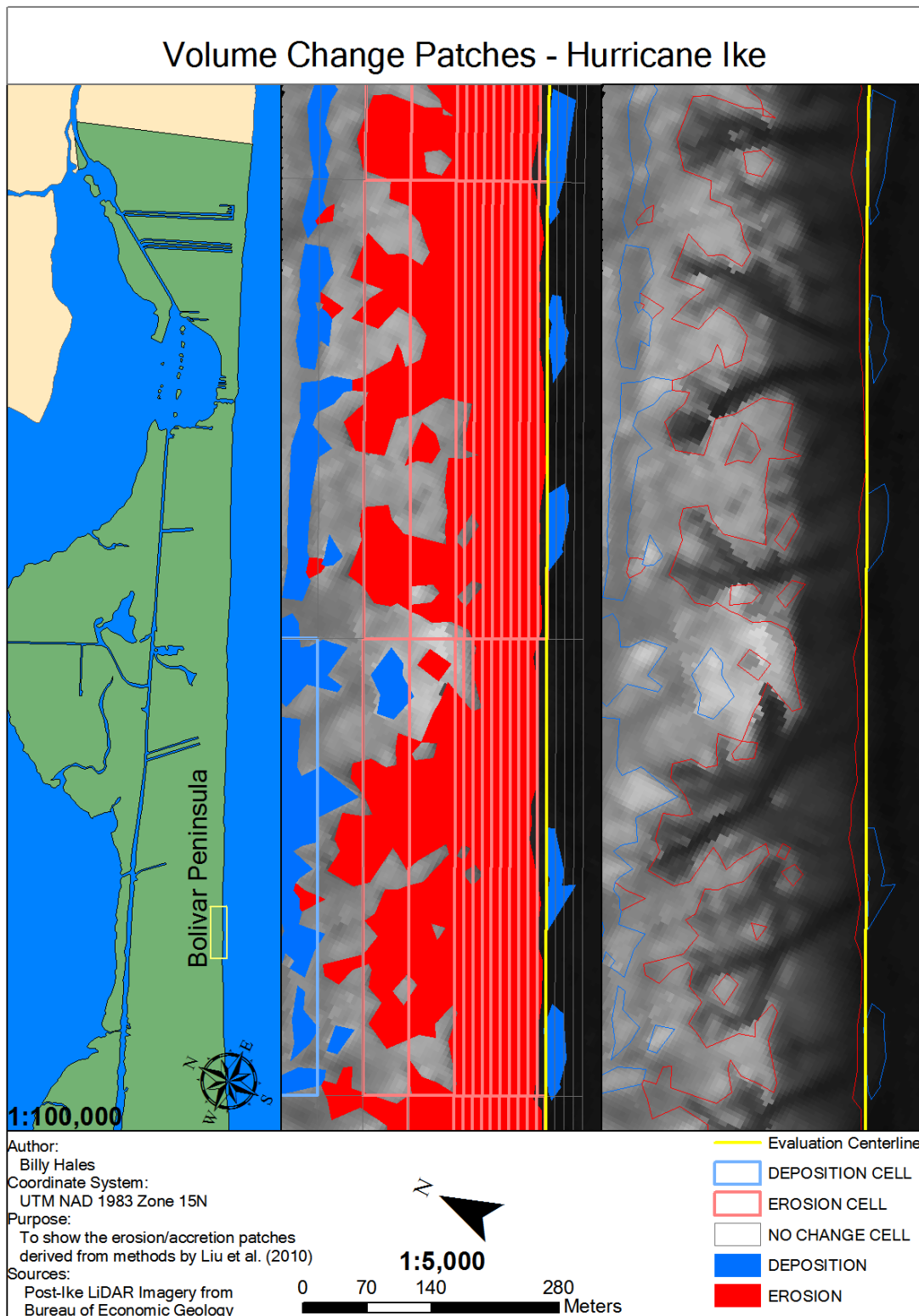


Figure D.70. Hurricane Ike section 14/28 of 1:5000 scale volumetric changes. Corresponds to I-J on Figure 4.33.

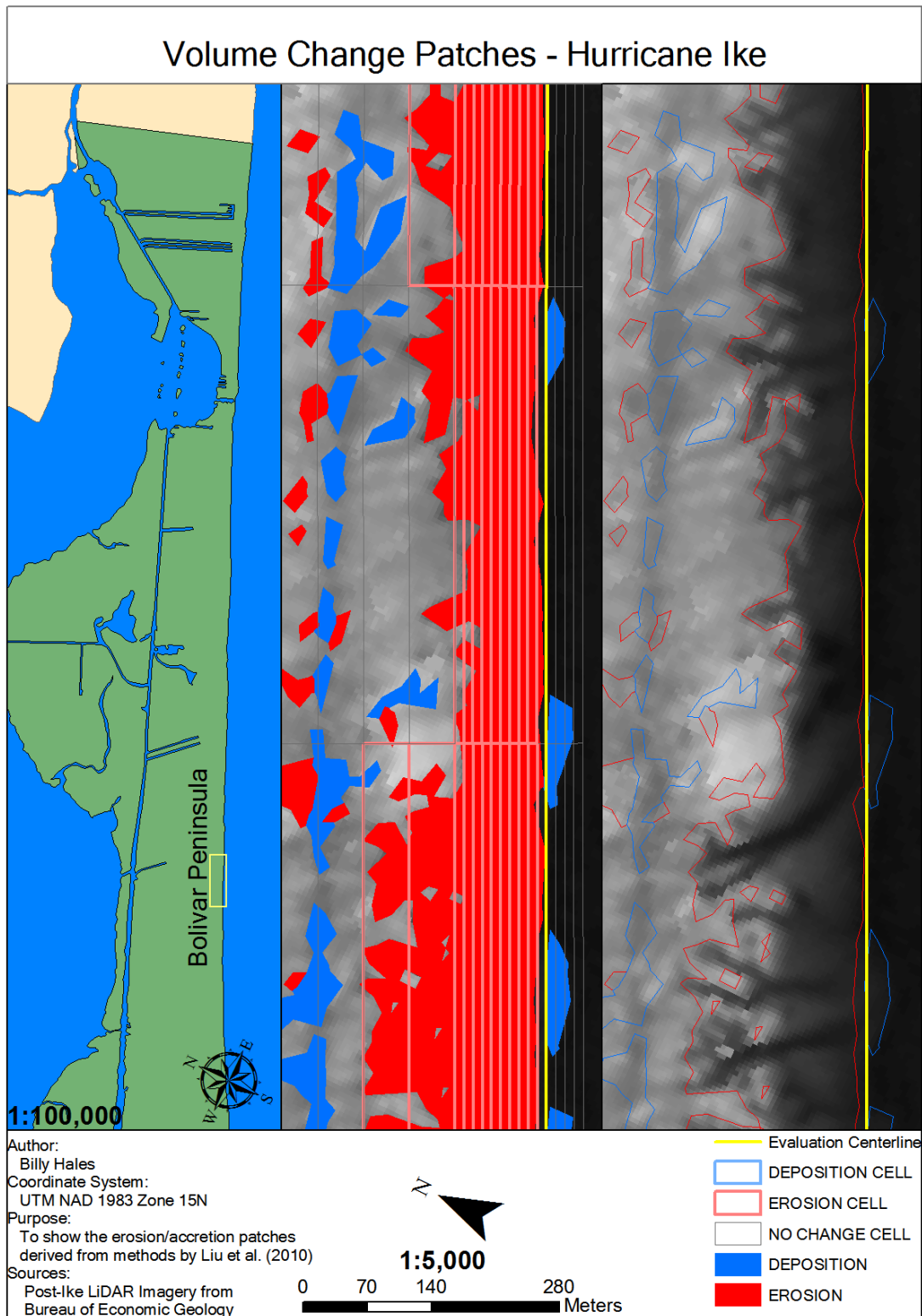


Figure D.71. Hurricane Ike section 15/28 of 1:5000 scale volumetric changes. Corresponds to J-K on Figure 4.34.

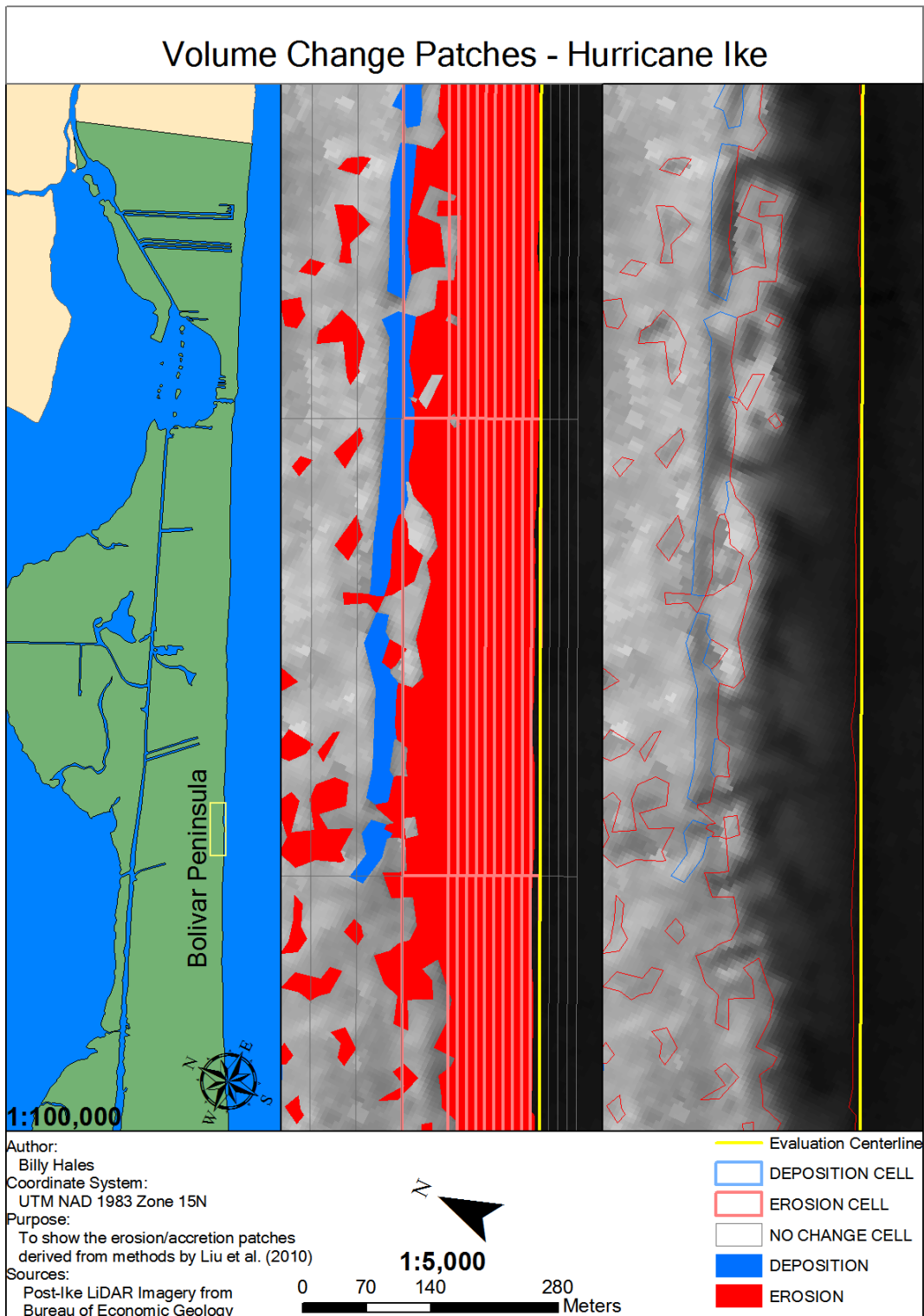


Figure D.72. Hurricane Ike section 16/28 of 1:5000 scale volumetric changes. Corresponds to J-K, K-L on Figure 4.34.

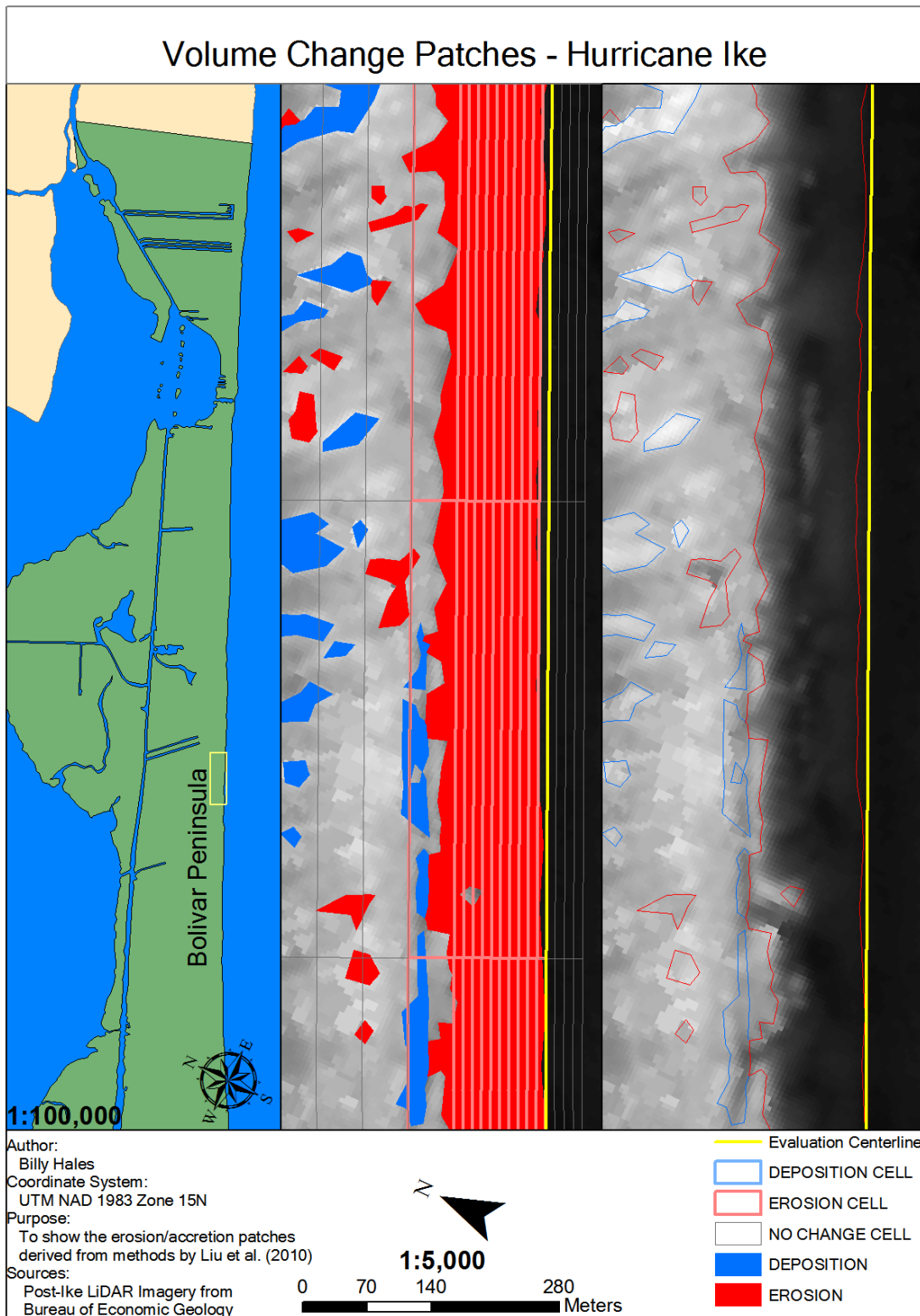


Figure D.73: Hurricane Ike section 17/28 of 1:5000 scale volumetric changes. Corresponds to K-L on Figure 4.34.

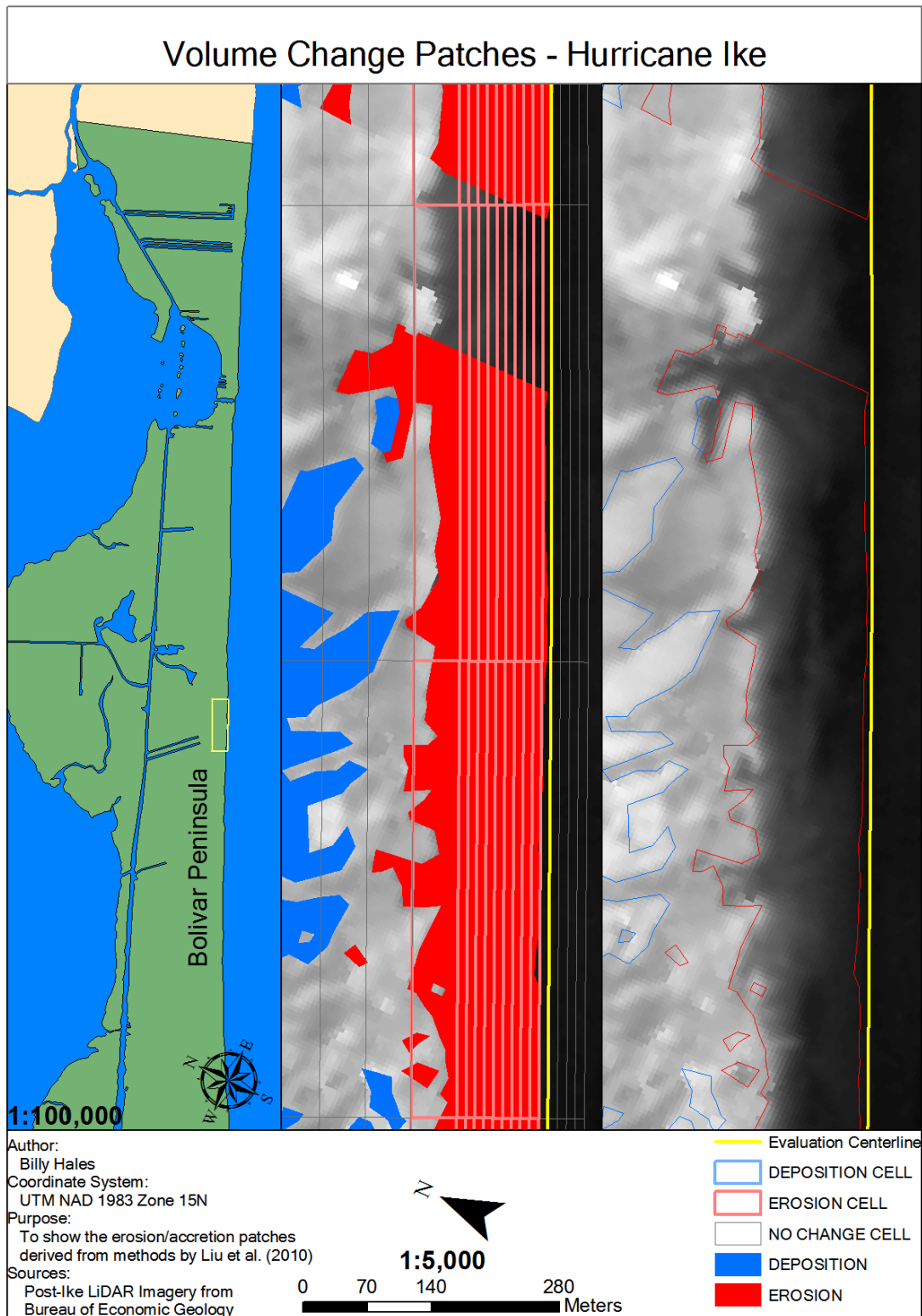


Figure D.74: Hurricane Ike section 18/28 of 1:5000 scale volumetric changes. Corresponds to K-L, L-M on Figure 4.34.

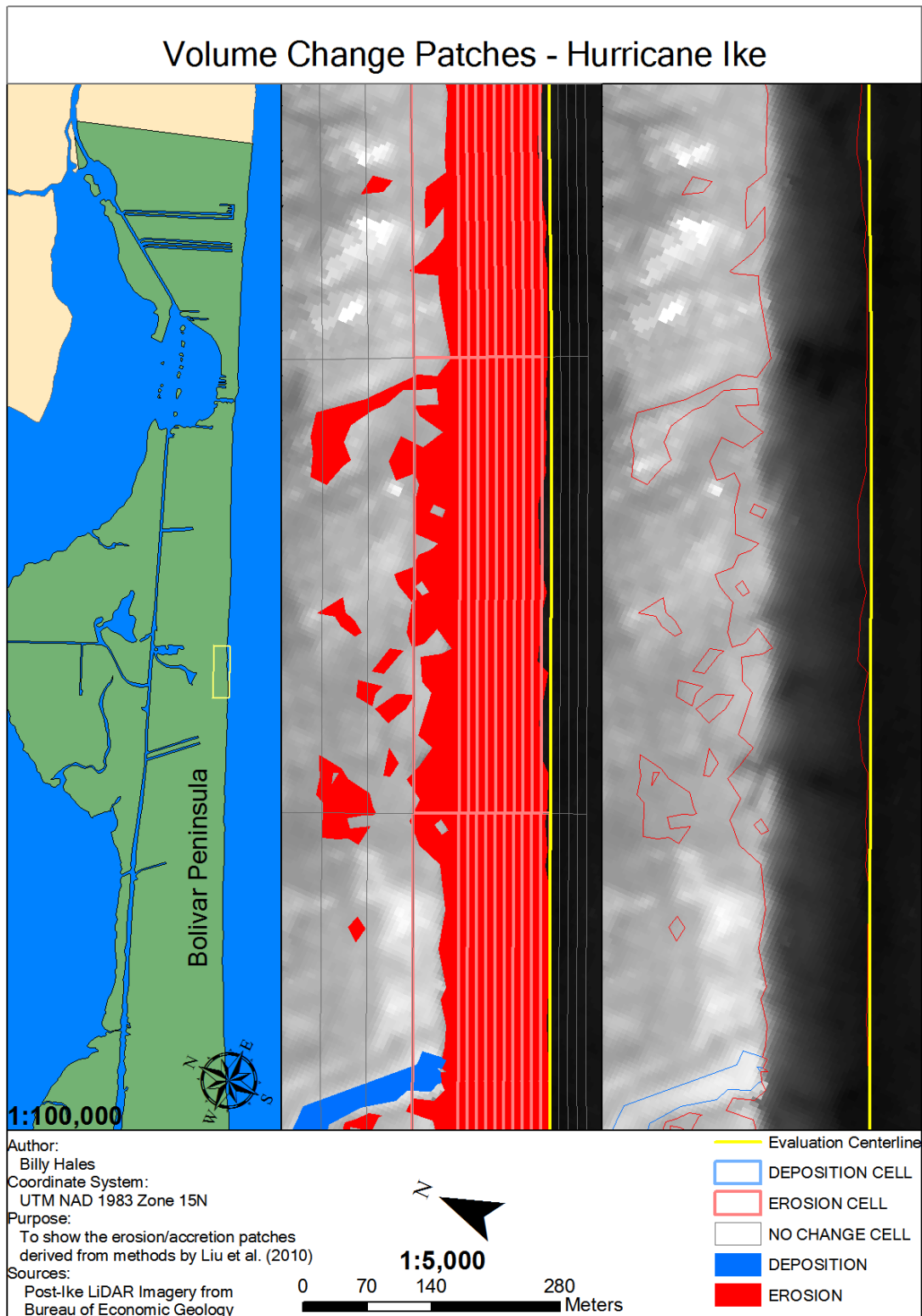


Figure D.75. Hurricane Ike section 19/28 of 1:5000 scale volumetric changes. Corresponds to L-M on Figure 4.34.

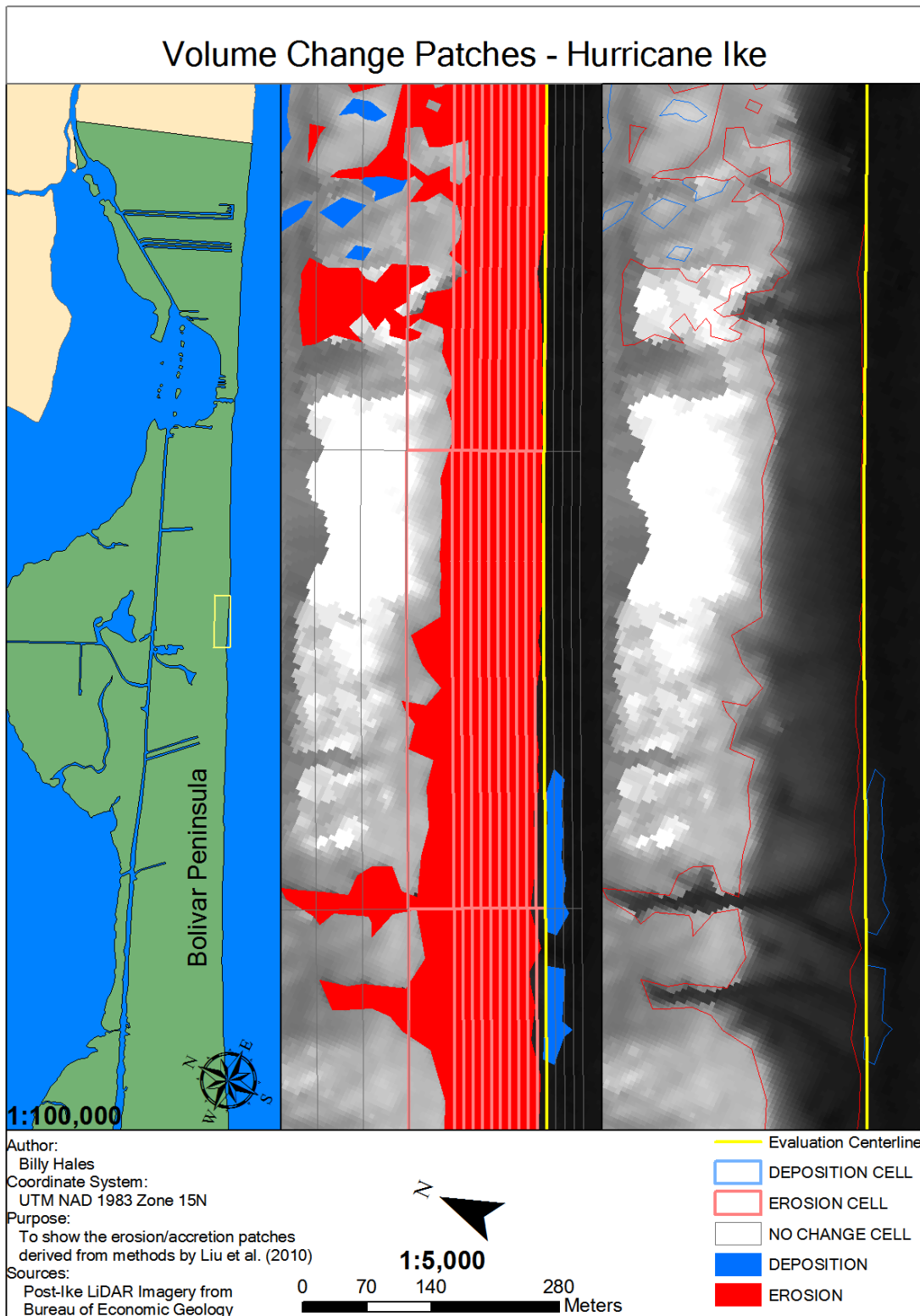


Figure D.76. Hurricane Ike section 20/28 of 1:5000 scale volumetric changes. Corresponds to L-M, M-N on Figure 4.35.

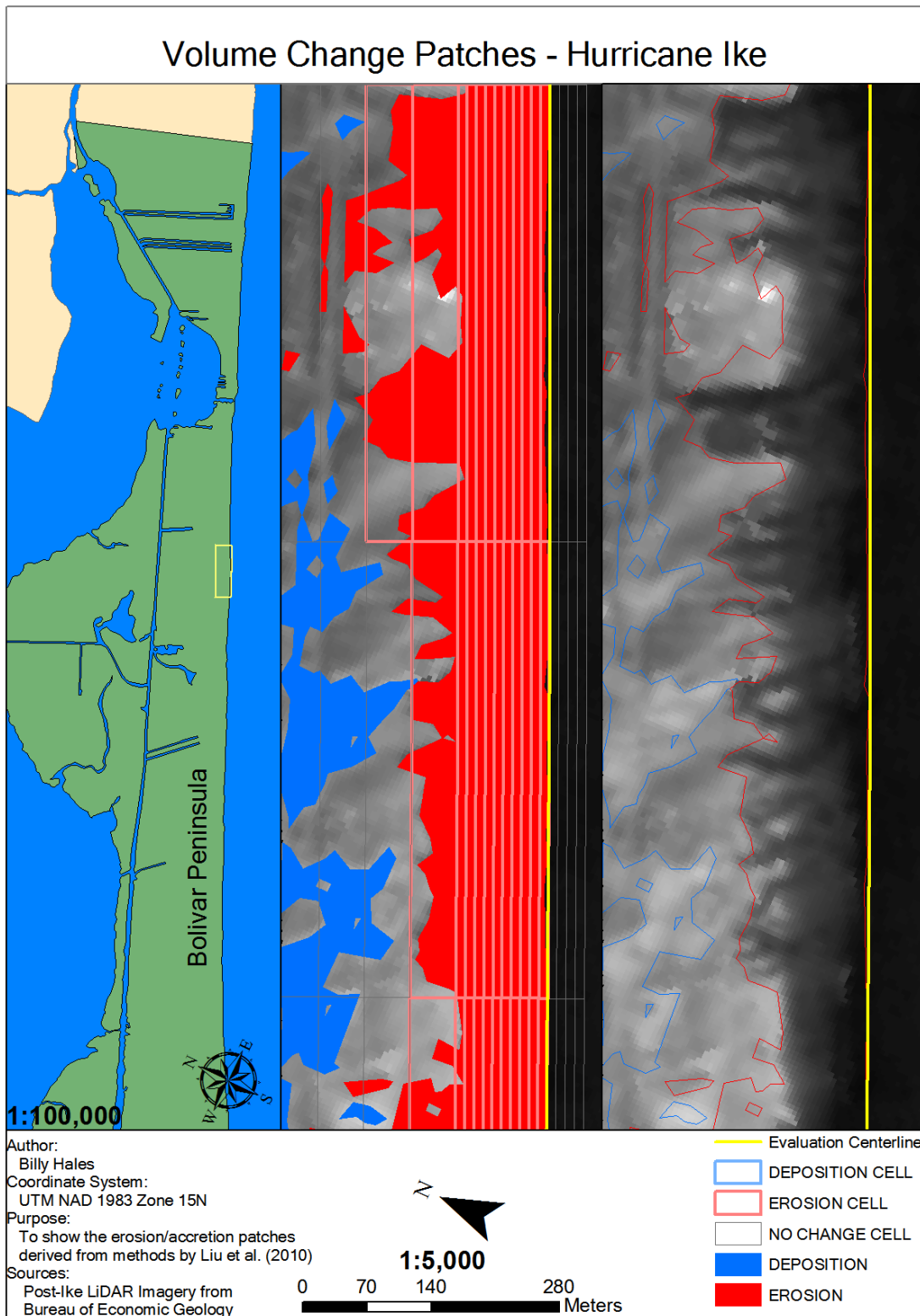


Figure D.77. Hurricane Ike section 21/28 of 1:5000 scale volumetric changes. Corresponds to M-N, N-O on Figure 4.35.

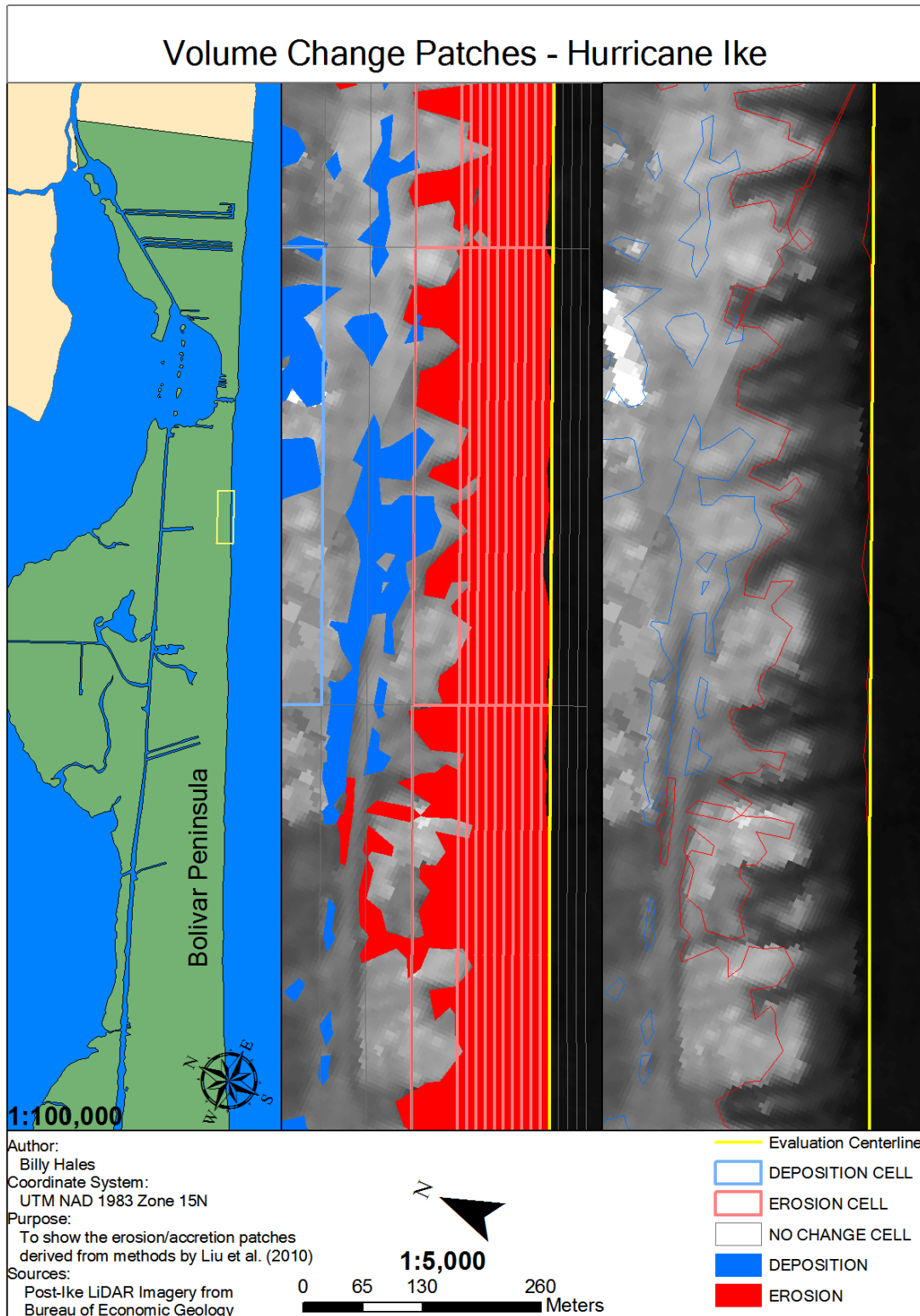


Figure D.78. Hurricane Ike section 22/28 of 1:5000 scale volumetric changes. Corresponds to N-O on Figure 4.35.

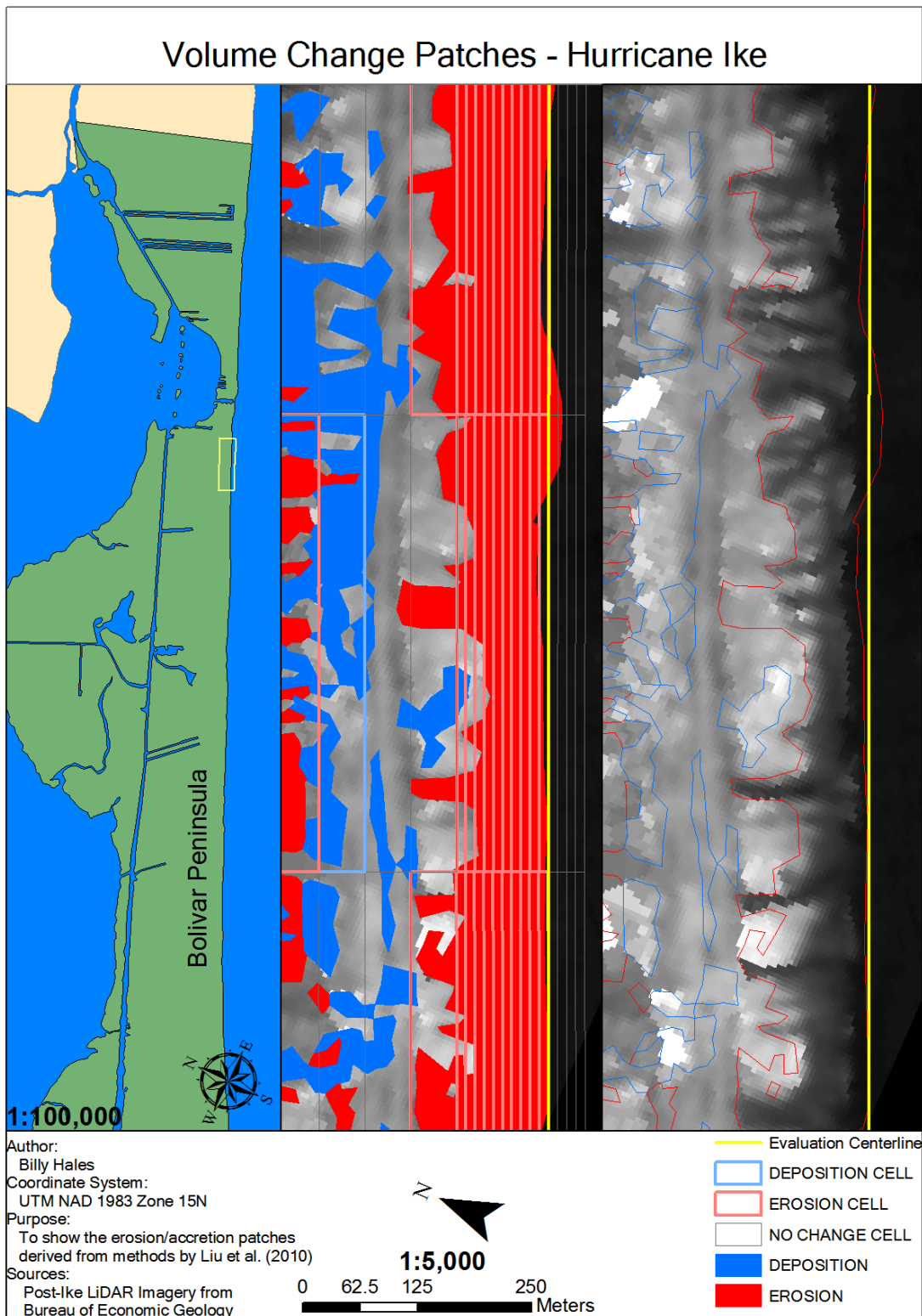


Figure D.79. Hurricane Ike section 23/28 of 1:5000 scale volumetric changes. Corresponds to O-P on Figure 4.35.

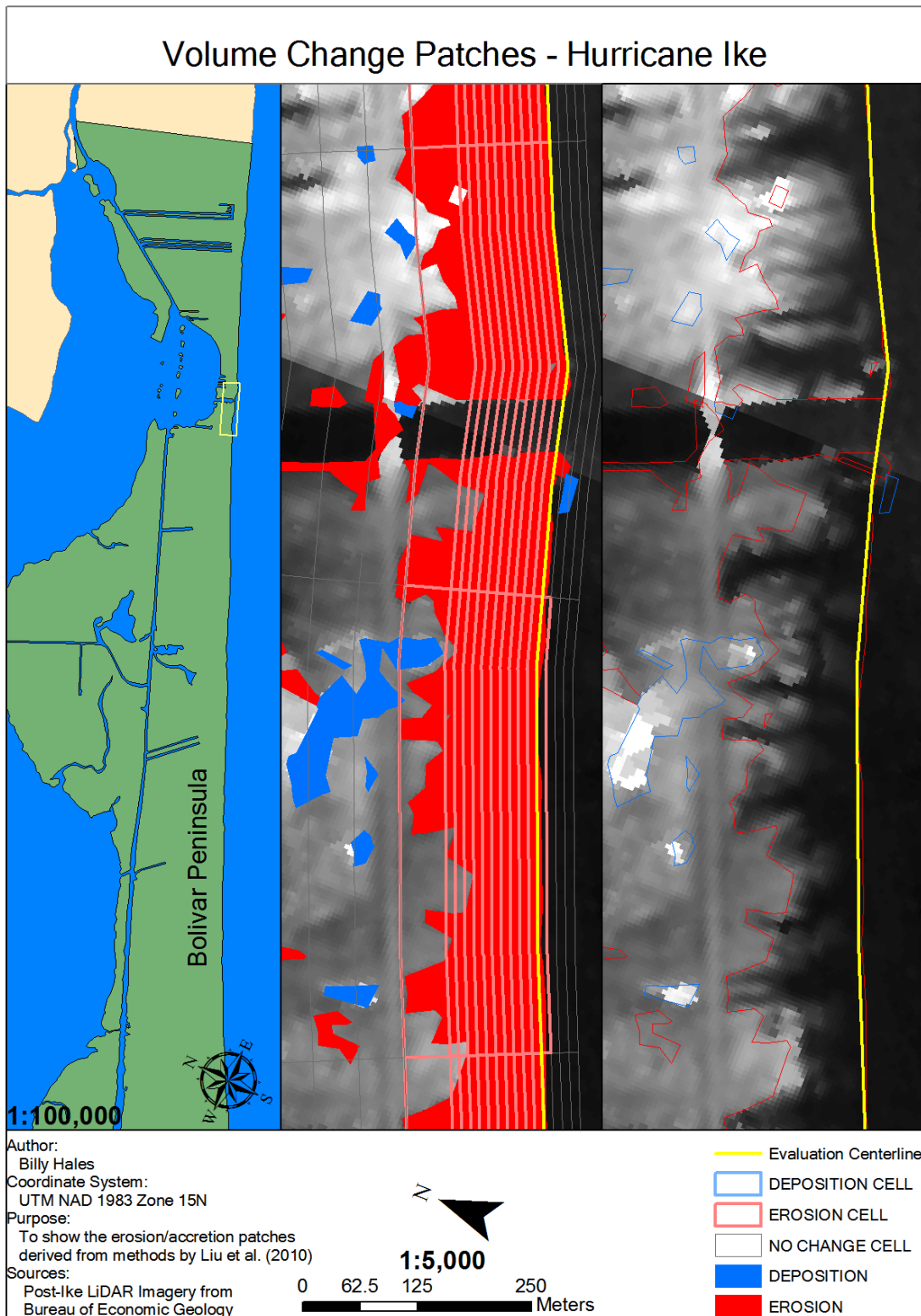


Figure D.80. Hurricane Ike section 24/28 of 1:5000 scale volumetric changes. Corresponds to O-P, P-Q on Figures 4.35 and 4.36.

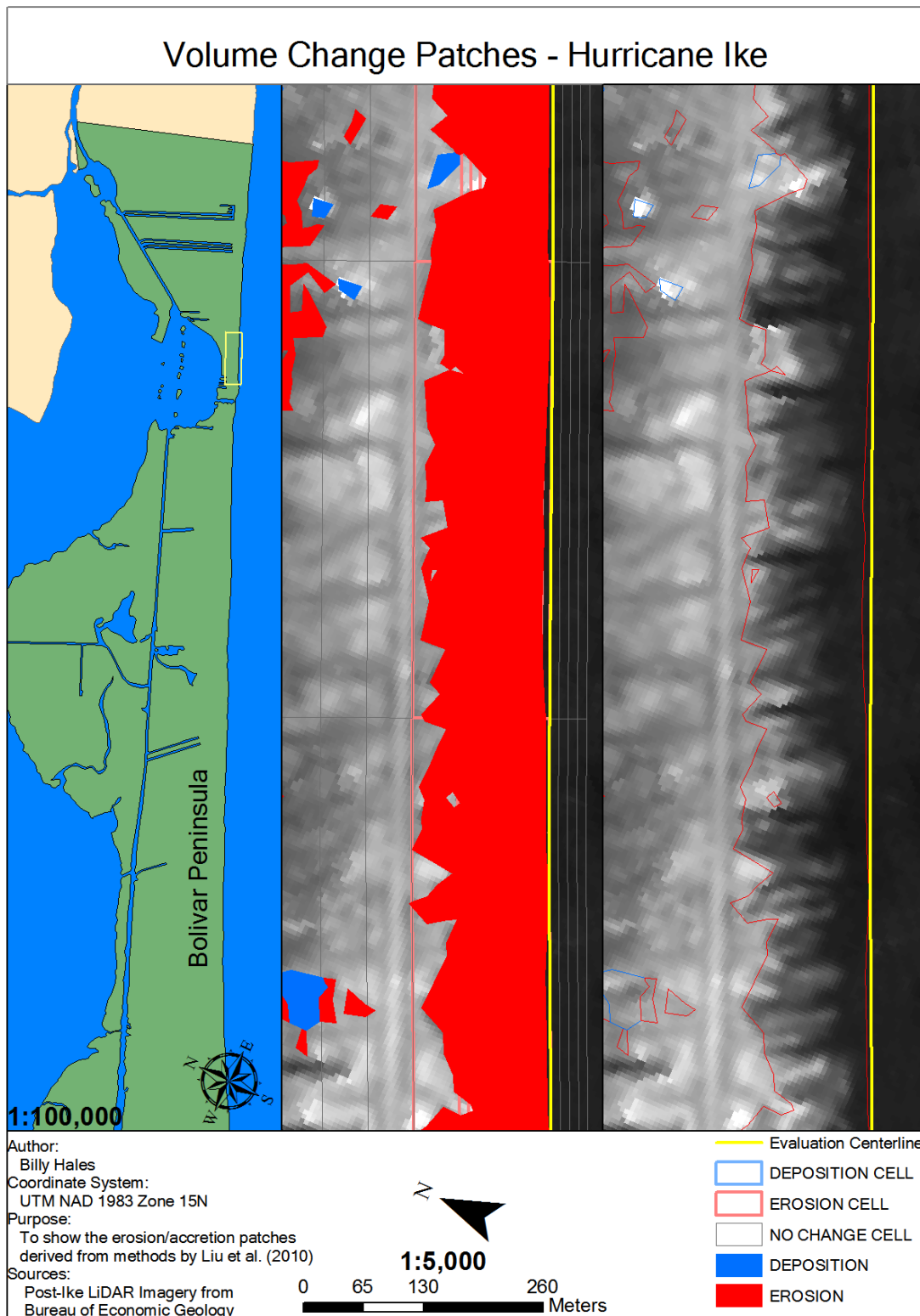


Figure D.81. Hurricane Ike section 25/28 of 1:5000 scale volumetric changes. Corresponds to P-O on Figure 4.36.

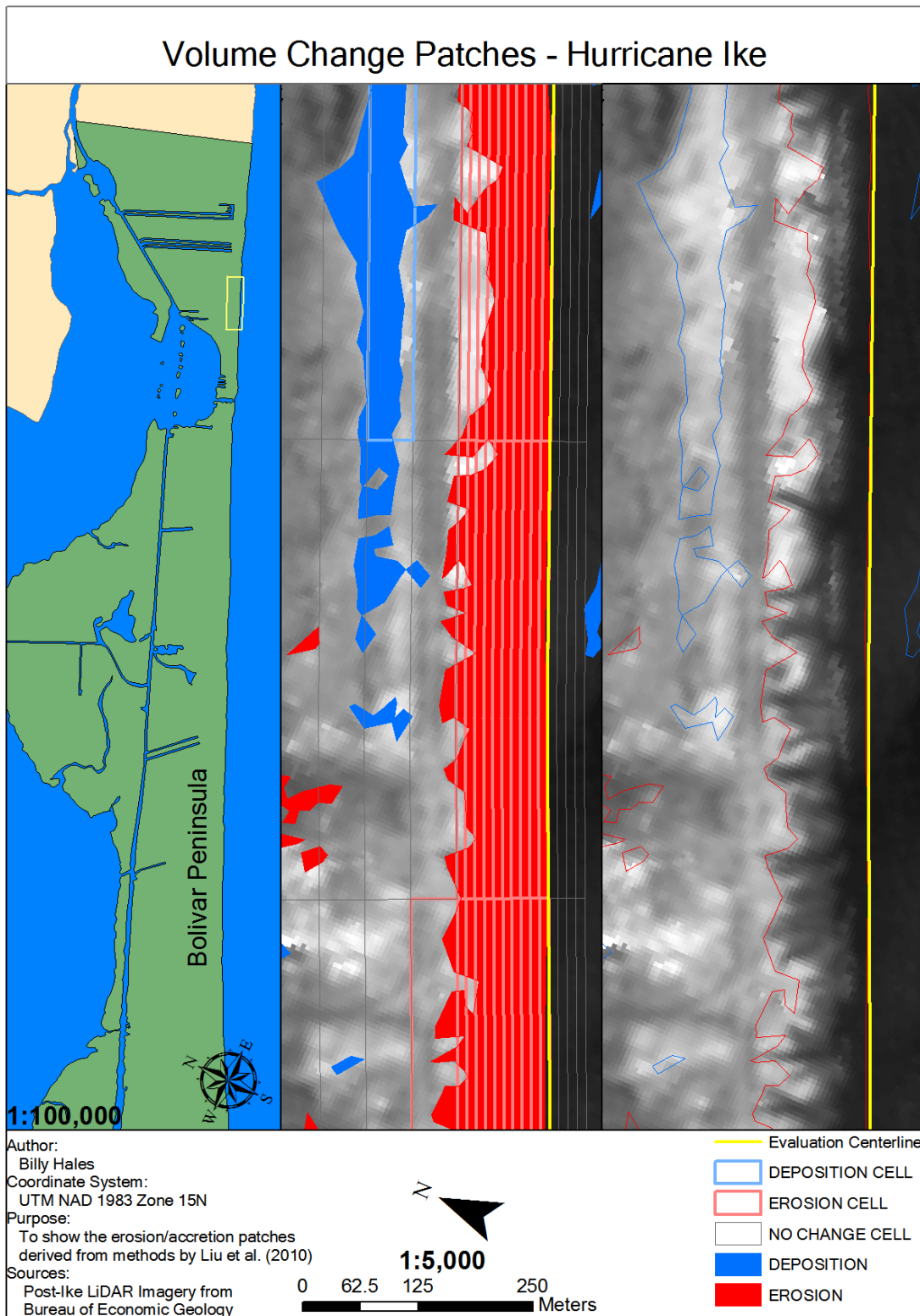


Figure D.82. Hurricane Ike section 26/28 of 1:5000 scale volumetric changes. Corresponds to P-Q, Q-R on Figure 4.36.

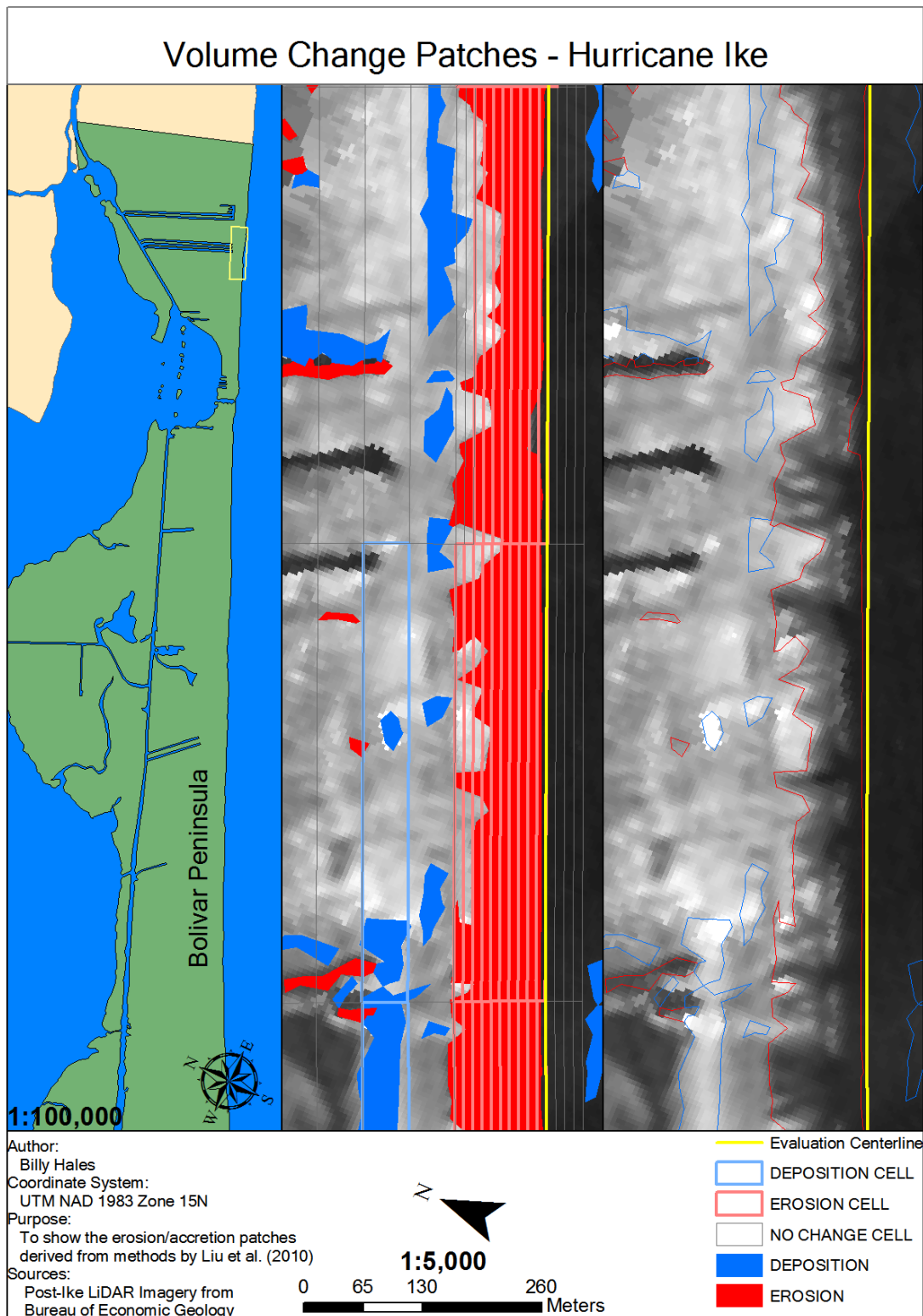


Figure D.83. Hurricane Ike section 27/28 of 1:5000 scale volumetric changes. Corresponds to Q-R on Figure 4.36.

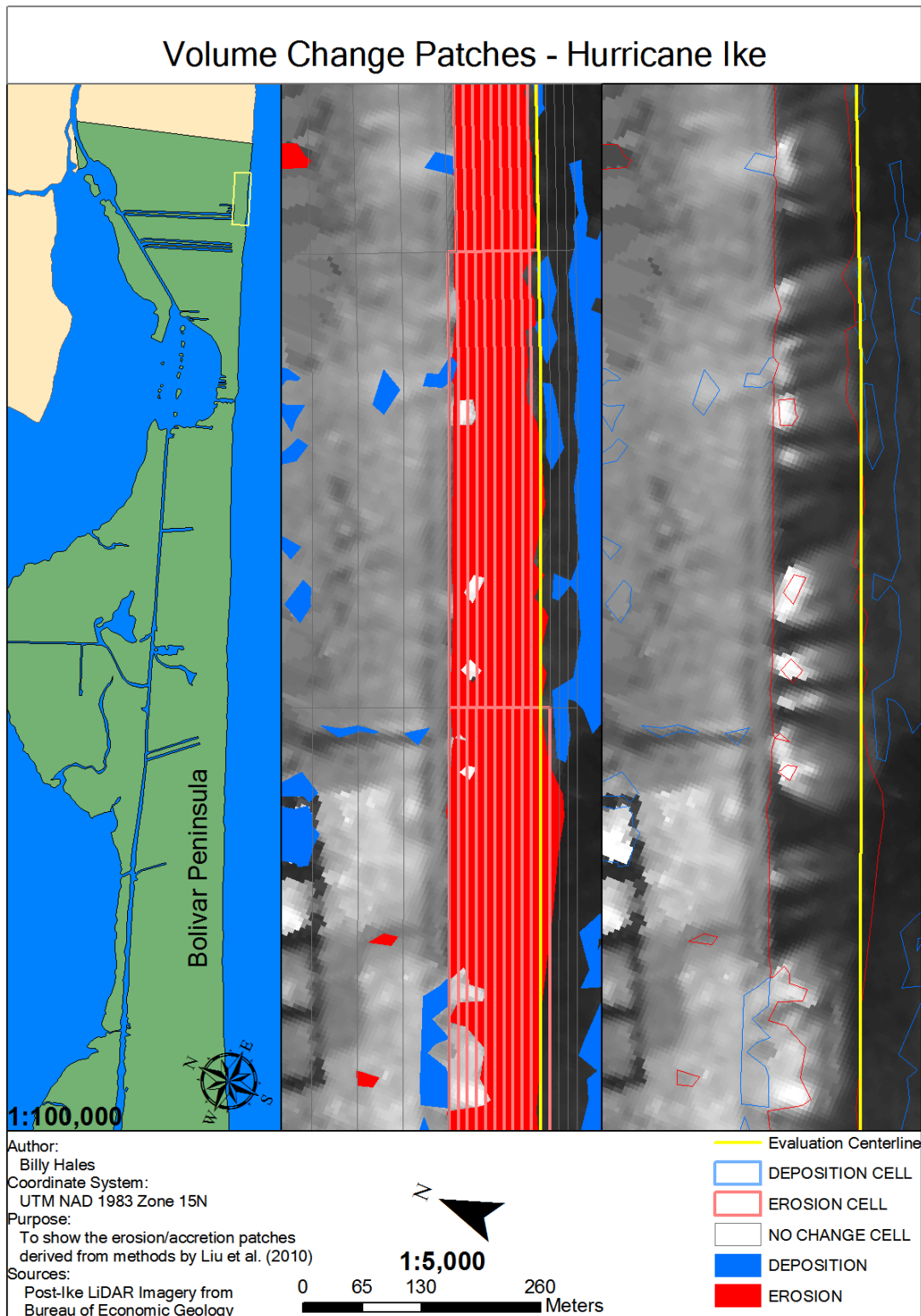


Figure D.84. Hurricane Ike section 28/28 of 1:5000 scale volumetric changes. Corresponds to Q-R, R-S on Figure 4.36.

APPENDIX E
SHORELINE CHANGE SPACING ANALYSIS

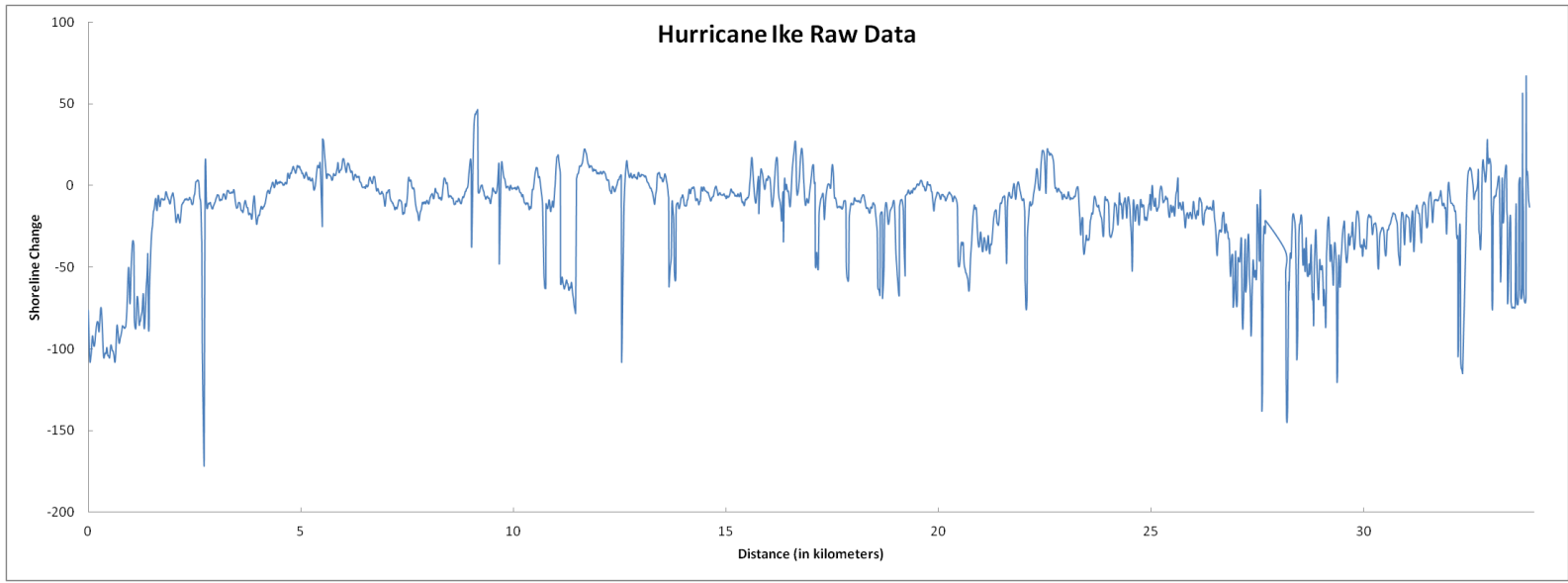


Figure E.1. Original Shoreline Change Data For Hurricane Ike

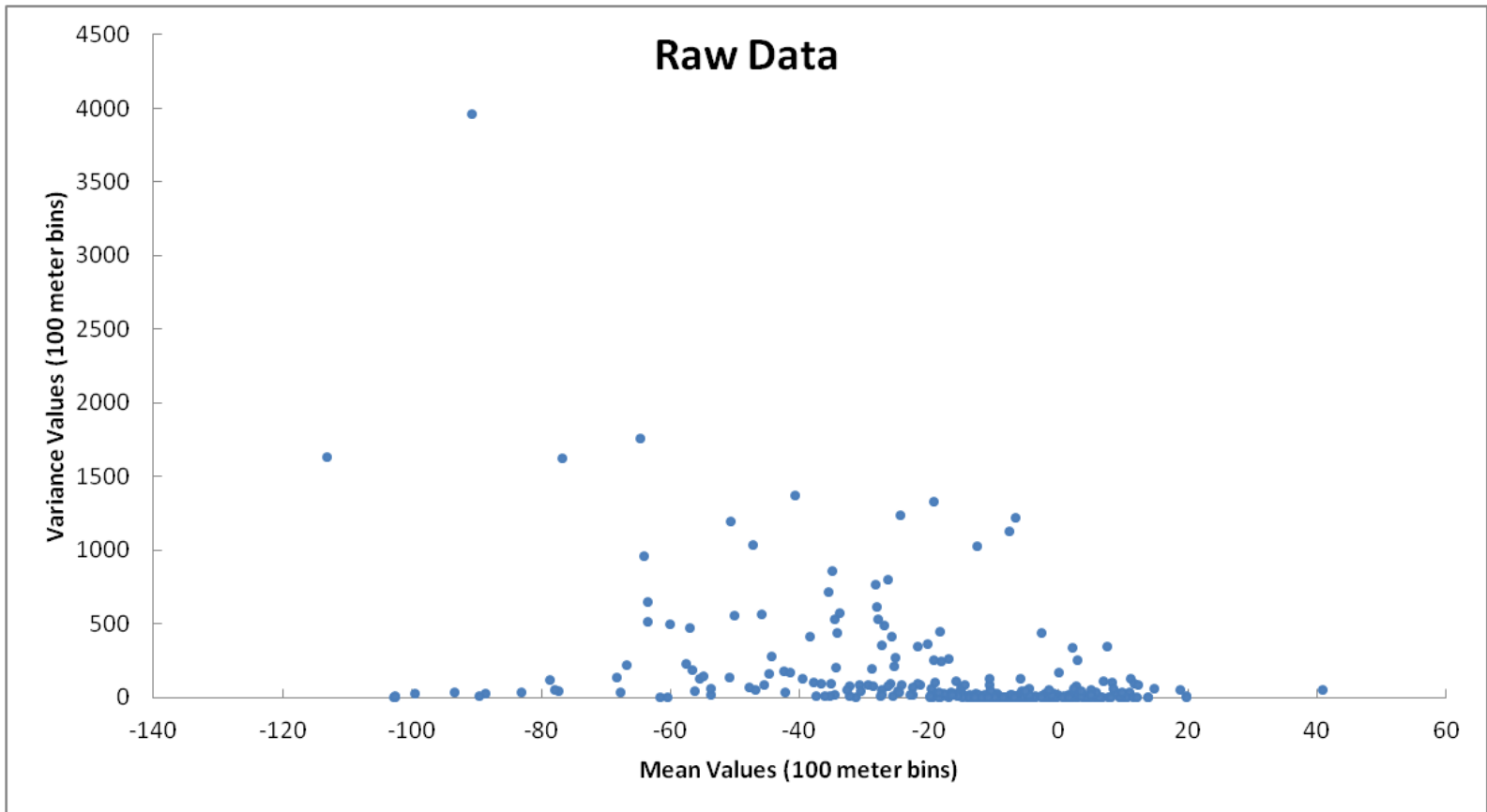


Figure E.2. Raw data for Hurricane Ike shoreline change to identify stationarity of the mean with respect to variance. Data suggest that there may be a relationship between the mean and variance.

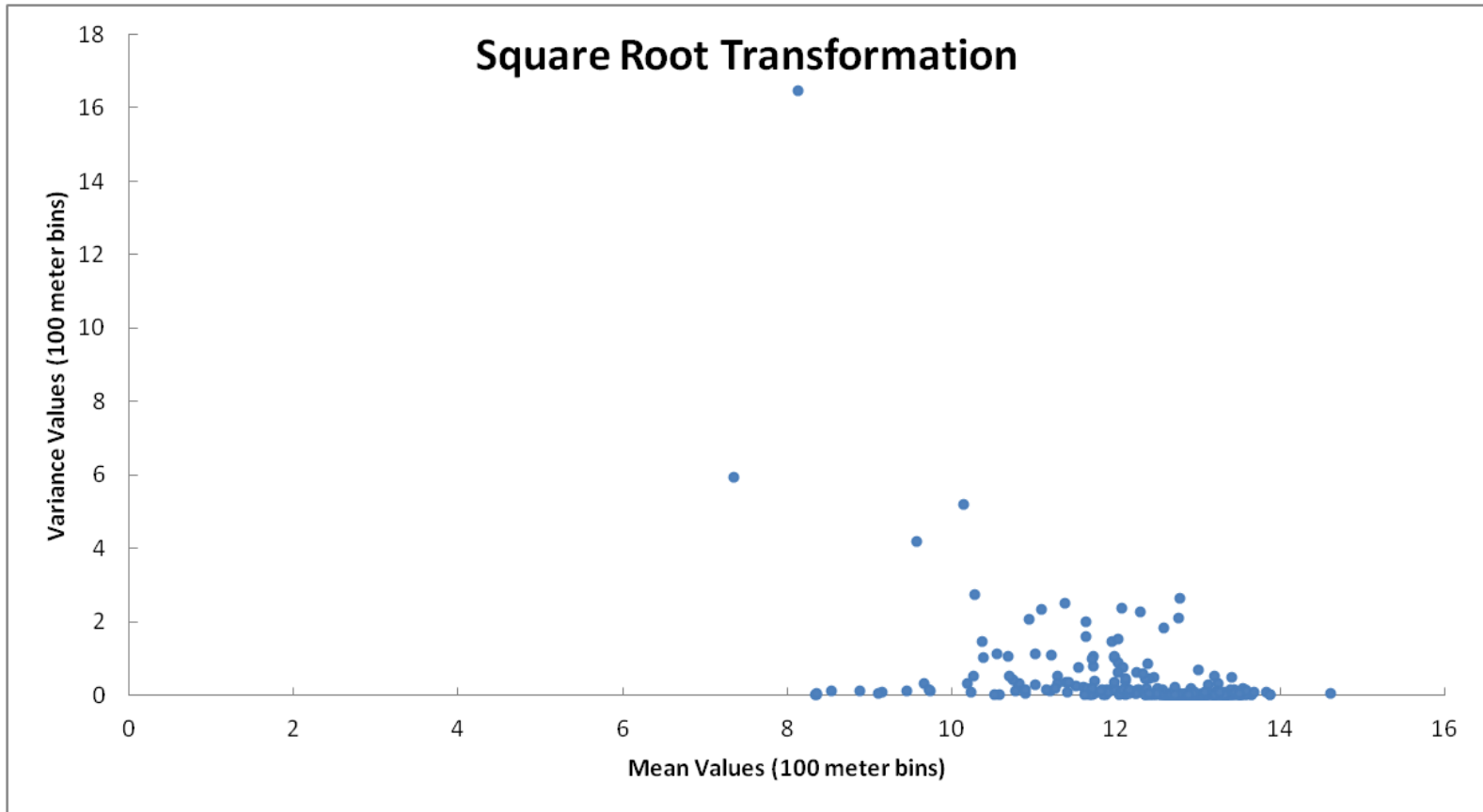


Figure E.3. Square root-transformed data for Hurricane Ike shoreline change to identify stationarity of the mean with respect to variance. Data suggest that there may be still be a relationship between the mean and variance, but data points suggesting this relationship appear to have decreased.

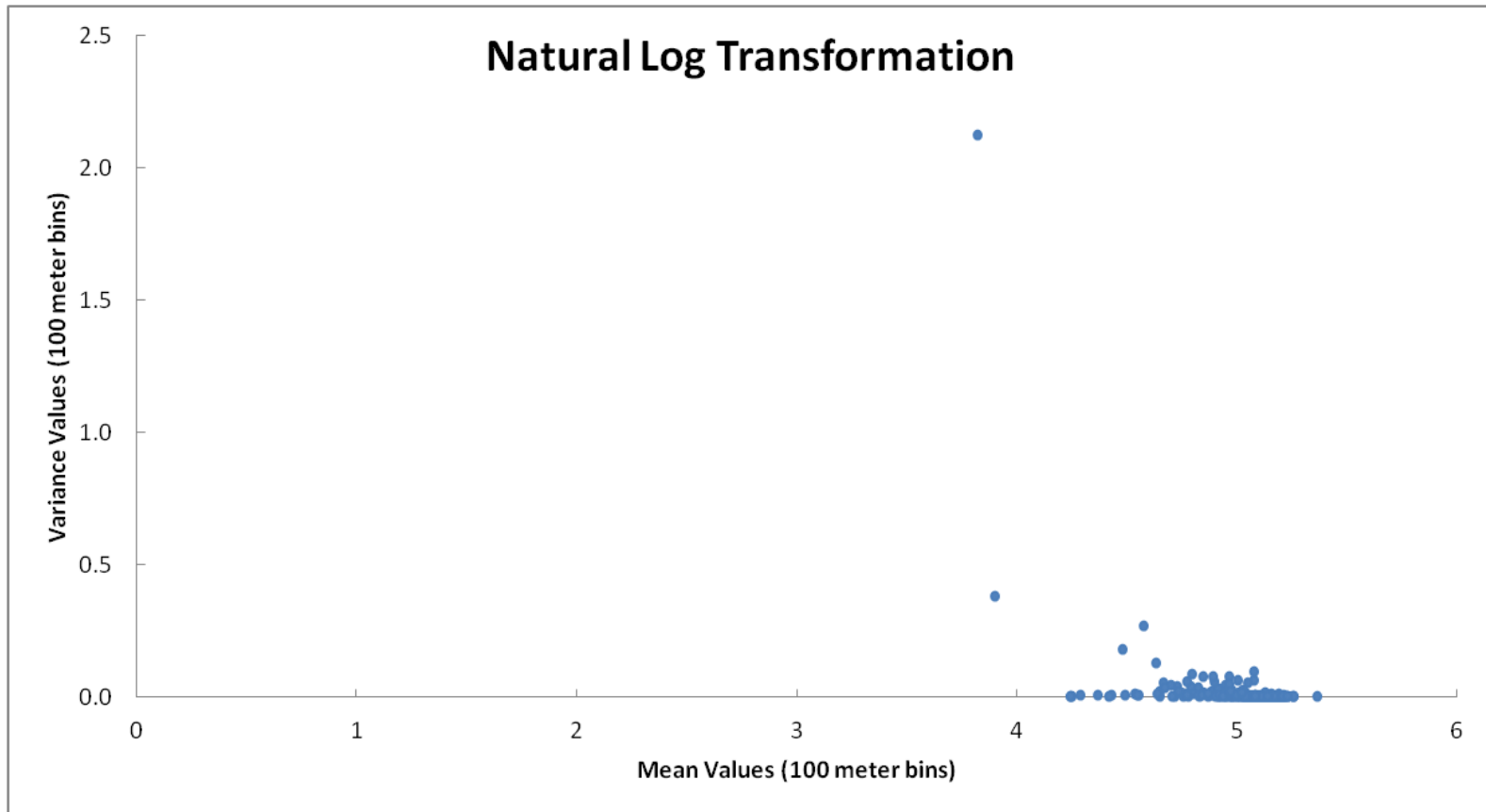


Figure E.4. Square root-transformed data for Hurricane Ike shoreline change to identify stationarity of the mean with respect to variance. Data suggest that there may be a relationship between the mean and variance, but only because of the trajectory of a few points.

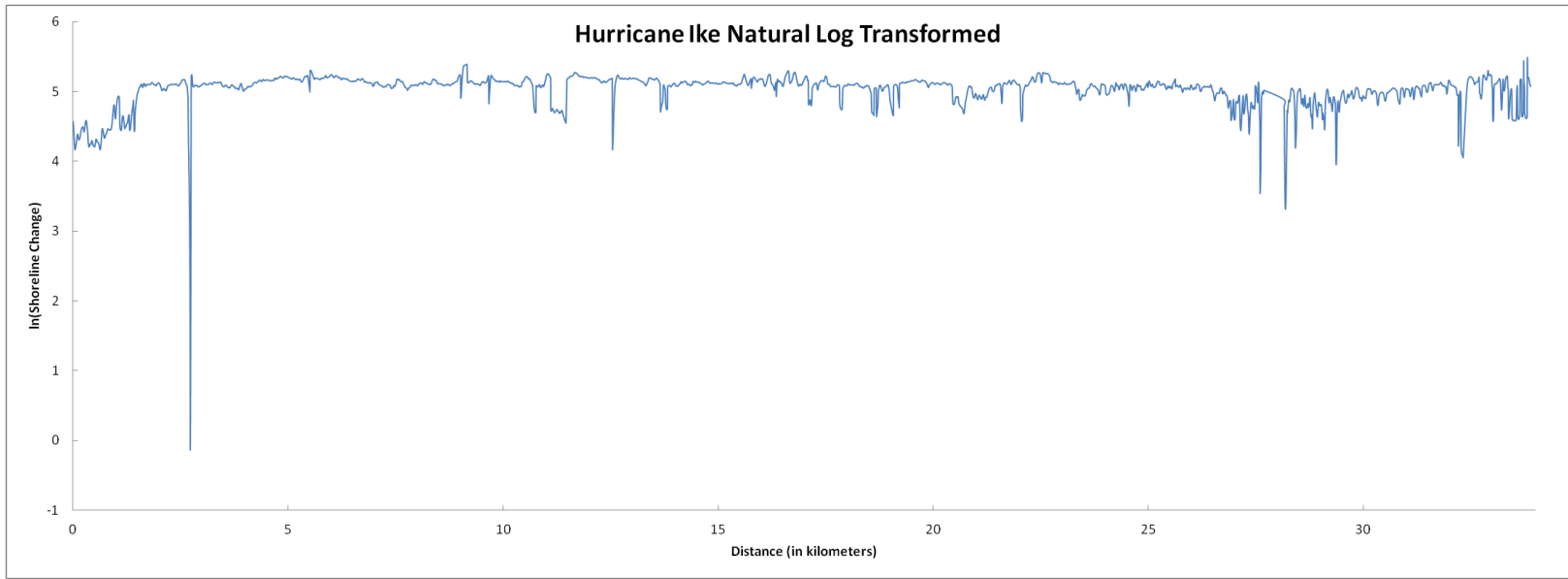


Figure E.5. Log-transformed Hurricane Ike shoreline changes. Variances have decreased, but a trend in the shoreline changes is still evident.

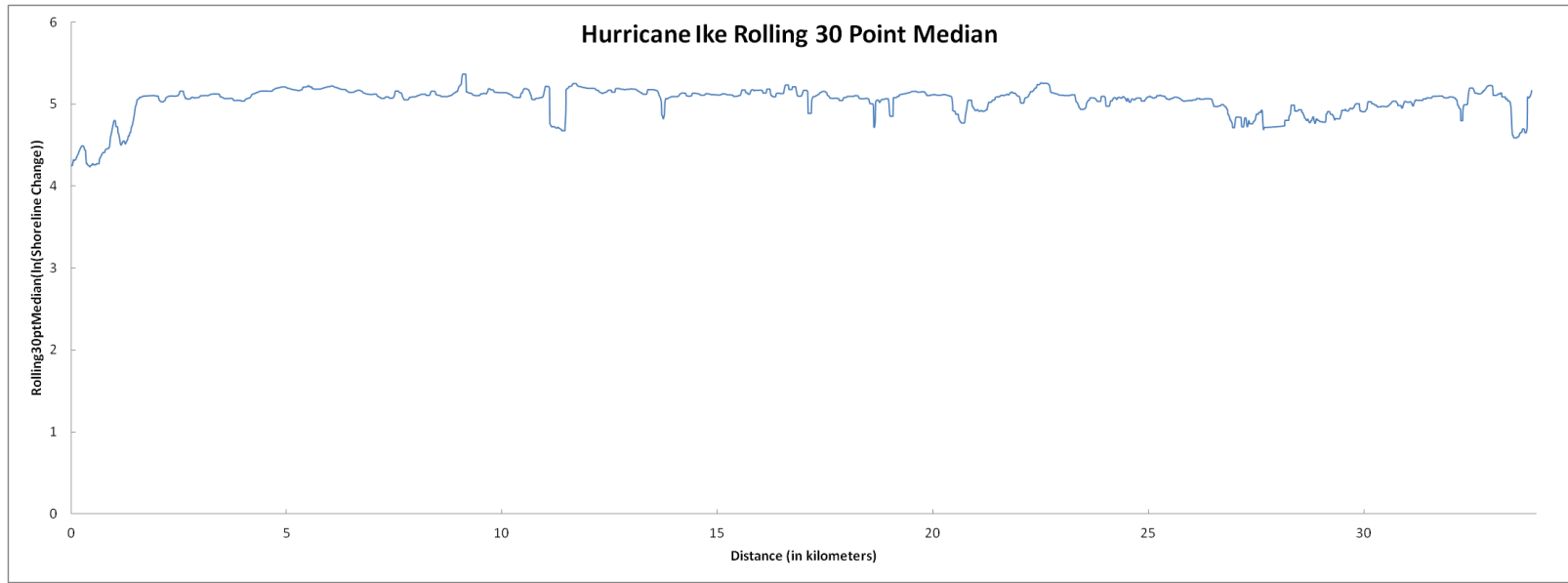


Figure. E.6. Thirty-point running median. This captures the larger-scale variability in the log-transformed Hurricane Ike shoreline change data.

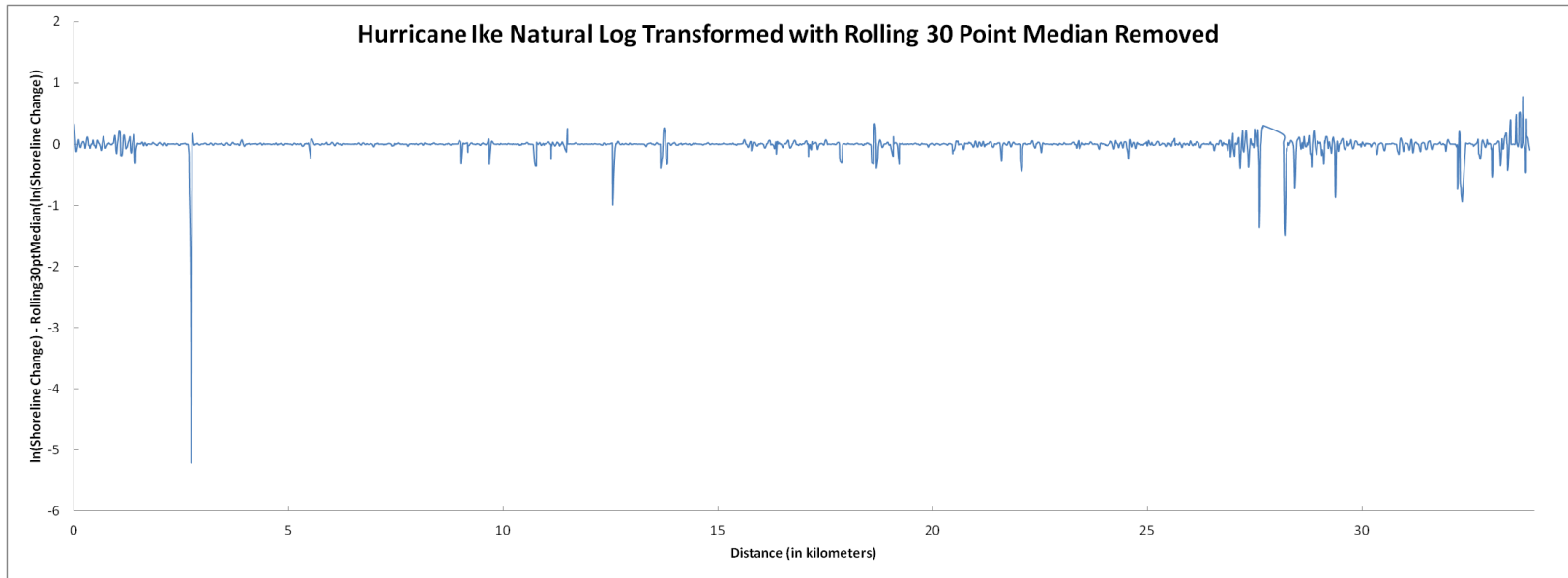


Figure E.7. Residuals of log-transformed as they are computed by subtracting median-smoothed data from log-transformed data. Notice the relative absence of a trend.

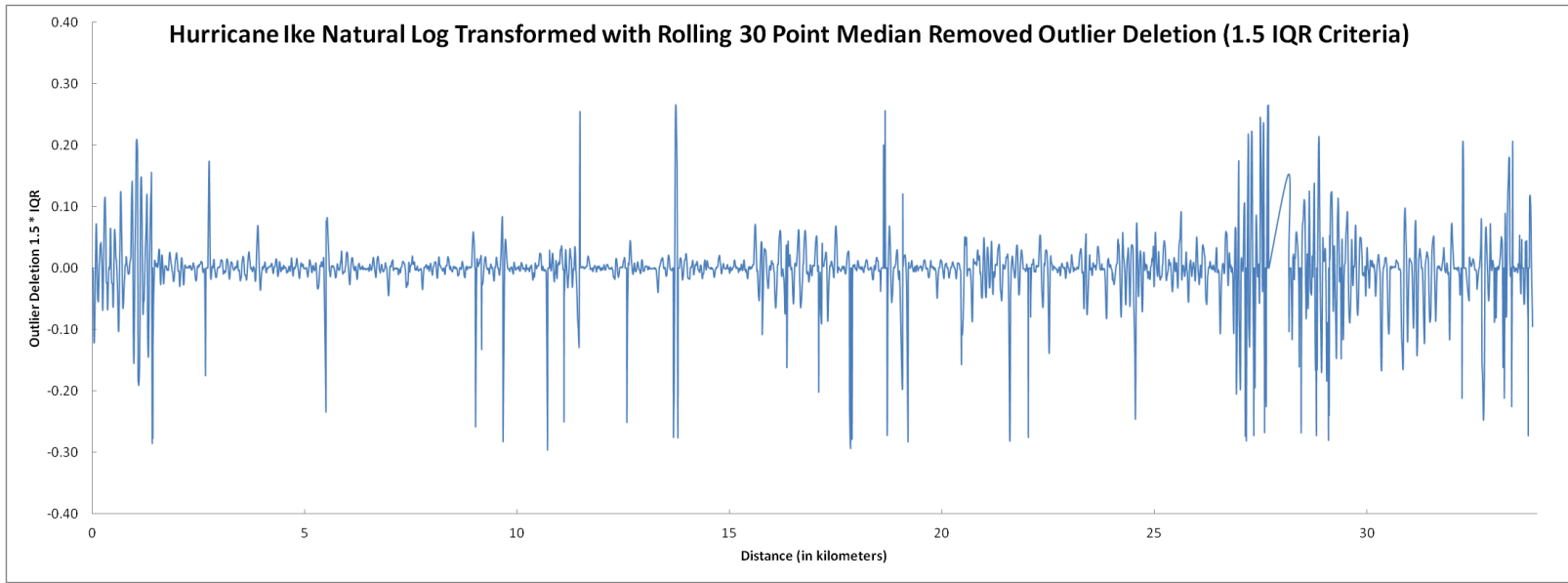


Figure E.8. Log-transformed shoreline change data with extreme value—above 1.5 multiplied by the interquartile range--removed.

VITA

Name: Billy Utah Hales, Jr.

Address: Department of Geography
College of Geosciences
Texas A&M University
810 Eller Oceanography and Meteorology Building
College Station, TX 77843-3147

Email Address: billy.hales@gmail.com

Education: A.A.S. Computer Information Technology, Coastal Bend College,
2002
B.S. Geology, Texas A&M University – Kingsville, 2009
M.S. Geography, Texas A&M University, 2012